UNIVERSITÉ DE STRASBOURG

ÉCOLE DOCTORALE ED269 : Mathématiques, Sciences de l'Informations et de l'Ingénieur

Laboratoire ICube, UMR7357, équipe Matériaux Multi-Échelles et Biomécanique

THÈSE présentée par :

Sumedha PREMI

soutenue le : **16 décembre 2019**

pour obtenir le grade de : **Docteur de l'université de Strasbourg**

Discipline / Spécialité : Mécanique / Biomécanique

Investigation of mechanical threshold to concussion

THÈSE dirigée par :

M. WILLINGER Rémy	Professeur, université de Strasbourg
Mme DECK Caroline	Chercheur, HDR CDI, université de Strasbourg

RAPPORTEURS :

M. ARNOUX Pierre Jean	Directeur de recherche, IFSTTAR / Aix-Marseille université
M. PELDSCHUS Steffen	Professeur, université de Ludwig-Maximilian, Munich

Table of Contents

Table of contents

Acknowledgement

I take this opportunity to express my heartfelt indebtedness to the people without whom I could not have completed this doctoral journey. I could progress in this delicate phase (apprentice researcher) of my life because of the generous support from several people.

At first, I would like to express my gratitude towards my thesis director, Professor Rémy Willinger, Co-Director of Multiscale Materials and Biomechanics (MMB) team at Department of Mechanics, ICube laboratory, University of Strasbourg, France, for welcoming me to his team and for continuously supporting and guiding me throughout the course of my research.

I would like to extend my gratitude towards my thesis co-director, Dr. Caroline Deck, Researcher at team MMB, Department of Mechanics, ICube laboratory, University of Strasbourg, France, for her valuable advices that helped me better understand things. Her incredible attention to detail drove me towards learning ways to better present my work. Her attention have been preponderant for the successful completion of this thesis.

I also extend my sincere thanks to Professor Brian D. Stemper, Medical College of Wisconsin, USA and his colleagues for providing the experimental data without which this study could not have been possible.

I am thankful to France Galop and The Grand Est regional council for funding my research.

In addition, I would like to acknowledge the contribution of my colleagues and friends, whose support made me complete this journey of three years pleasantly.

I am deeply thankful to Professor Anoop Chawla, Department of Mechanical Engineering, Indian Institute of Technology, Delhi, for his kind words of encouragement and his belief in me, which helped me during challenging times.

I express my profound gratitude to my parents, Deepti and Ajay, as well as to my siblings, Surbhi and Vibhor, for their continuous support, confidence and encouragement. In spite of being far away from home, their love never made me feel alone and a trip back home always reenergized me to work with greater enthusiasm and dedication. Thank you Mahi for bringing happiness into our lives.

Thank you Lalith for your support and affection, for proofreading my thesis and above all for the life that we share.

Thank you God.

General introduction

Concussion is a type of traumatic brain injury (TBI), which is also referred by many other names such as mild traumatic brain injury (mTBI), diffuse axonal injury (DAI), sports related concussion (SRC), traumatic axonal injury (TAI), inertial brain injury (IBI), diffuse brain injury (DBI) etc. Emerging scientific studies indicating long term psychiatric, cognitive and neurobehavioural impairments associated with concussion, have made it clear that concussion in sports is a serious health problem (Zhang et al., 2004; Murray et al., 2015). Theoretically, concussion can be defined as a disturbance in the functioning of brain, caused by a direct or indirect impulsive mechanical force transmitted to the head. Most common effects of concussion include impairment of neurological functions, such as consciousness, memory, thinking, movement, cognition, sensation and emotion. However, acute concussion may lead to a loss of consciousness or amnesia for an unspecified duration of time (CDC 2014; McCrory et al., 2017). Under normal circumstances, these disturbances are transient impairment of neurological functions, which resolve spontaneously. However, in certain circumstances, signs and symptoms of concussive impairments evolve over a period of time, from a few minutes to a couple of hours (McCrory et al., 2017).

Mostly, concussion signs and symptoms are not result of macroscopic structural injuries and hence, are not diagnosable by standard structural neuroimaging techniques (McCrory et al., 2017). Recovery after concussion may take a few hours, days, weeks, months or even longer. Recovery depends on various factors, such as concussion severity, age and health of the person at the time of concussion and care taken by the person after concussion (McCrory et al., 2017). It has been observed that repeated sub-concussive blows, in a short time, turn out to be more damaging than a single concussive blow (McCrory et al., 2004; Gysland et al., 2011). A person with a history of concussion is more vulnerable to concussive injuries in future, than those with no history. Also, there are chances that the slower recovery of neurological functions can be due to a previously encountered concussion (Guskiewicz et al., 2003). Inter injury interval plays an important role in identifying the duration and the extent of post injury cognitive deficits. It is also possible that the long term cognitive impairments occur even without any histological consequences, such as DAI (Tadepalli et al., 2019). Repetitive TBI can potentially lead to irreversible and progressive neurodegeneration, such as chronic traumatic encephalopathy (CTE) (Gysland et al., 2011; Briggs et al., 2016). Hence, in the context of social and economic consequences of concussion, it is essential to study brain injury mechanisms in order to minimize the rate of concussion by optimizing the design of safety measures, such as sports helmet. Let us now look at some statistics and epidemiology related to concussion.

TBI is the leading cause of disability and death in children as well as in young adults all over the world, causing nearly half of all the deaths due to trauma (WHO, 2006). Globally, TBI is one of the largest

contributors to disability and death amongst all trauma related injuries (Rubiano et al., 2015). By the year 2015, around 5.3 million people in USA and around 7.7 million people in Europe were living with a TBI related disability (Rubiano et al., 2015). Worldwide sixty-nine million people are estimated to suffer from a TBI each year (Dewan et al., 2018), among which 80-90% belong to mild injury category (WHO, 2006; Dewan et al., 2018). The frequency of occurrence of mild TBI is much greater (around ten times) than that of moderate or severe TBI (Dewan et al., 2018). Figure 1 shows the annual incidence of TBI (cases per 100,000 people) by World Health Organization (WHO) regions. The maximum number of overall incidents of TBI (per 100,000 people) was found in North America having an average count of 1299 cases, followed by Europe with an average count of 1012 cases and the least in Africa with an average count of 801 cases (Dewan et al., 2018).

Figure 1: Annual incidences of TBI (cases per 100,000 people) by WHO region (Dewan et al., 2018).

Based on clinical examination, approximately 90% of TBIs are identified as mild. Though mortality rate in case of mTBI is below 1%, the long term consequences are serious and adversely affect the lives of individuals, their family and the wider society (WHO, 2006). Between 2001 and 2012, approximately 90% of sports and recreation related TBIs in United States were treated and discharged from emergency departments, suggesting these injuries to be mild. However, previous researches indicate that 15% - 25% of people with mTBI may suffer long-term physical, cognitive and emotional consequences (Coronado et al., 2015). In 2013, approximately 2.8 million TBI related emergency department visits, hospitalizations and deaths (TBI-EDHDs) occurred in United States. Emergency department visits due to TBI in United States alone increased by more than 50% from 2007 to 2013. Though TBI related, hospitalizations and deaths increased by only approximately 8% and 2% respectively, it cannot be considered insignificant (Taylor et al., 2017).

The global influence of TBI, in terms of worldwide TBI burden, is illustrated in Figure 2. It is evident from the figure that South-East Asian region (SEAR) and Western Pacific region (WPR) have about

three times higher estimated TBI burdens than that of United States, Canada (AMR-US/Can), Latin America (AMR-L) and Eastern Mediterranean region (EMR). While estimated TBI burden of Africa (AFR) and Europe (EUR) lies somewhere in between (Dewan et al., 2018).

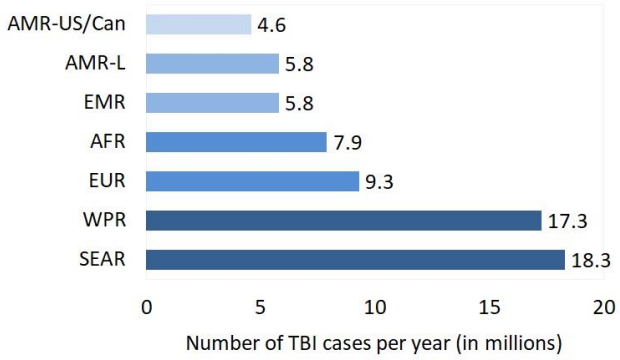

Figure 2: Diagram illustrating annual estimation of TBI volume across WHO regions (AMR-US/Can: America - United States and Canada; AMR-L: America - Latin America; EMR: Eastern Mediterranean Region; AFR: Africa; EUR: Europe; WPR: Western Pacific Region and SEAR: South-East Asian Region) (Dewan et al., 2018).

As per a review by Tagliaferri et al. (2006), a comparison of epidemiological parameters based on the TBI data from Europe, United States, Australia, Asia and India, for adults and from various years, is given in Table 1. Reported incident rate in Europe is much higher than that in United States and India. Here, it is important to consider that this data is based on hospitalizations; and variation in nationwide hospitalization policies and practices can impact this data to a great extent. Prevalence rate data is not available for Europe and Australia. Nonetheless, reported prevalence rate values vary drastically between United States, Asia and India. Mortality rate values are more or less in accordance. It can be observed from the reported severity percentage that mild TBIs take over moderate and severe TBIs.

Table 1: Epidemiological parameter values based on TBI data from Europe, United States, Australia, Asia and India (for adults and from various years) (Tagliaferri et al., 2006).

Europe	United States	Australia	Asia	India
Incidence rate (per 100,000 population, includes hospitalizations and deaths)				
235	103	226	344	160
Prevalence rate (per 100,000 population)				
NR	1893	NR	709	97
Mortality rate (per 100,000 population)				
15.4	18.1	NR	38	20
Severity percentage (mild – moderate – severe)				
79 – 12 – 9	80 – 10 – 10	76 – 12 – 11	76 – 12 – 11	71 – 15 – 13

NR: not reported

As shown in Figure 3, based on the data collected between 1988 – 2004 seasons by National Collegiate Athletic Association (NCAA) from 15 sports (more than a million exposures and total 182,000 injuries), analysis of injuries by body part showed that out of total head-neck injuries, about 44% accounted for concussion (Hootmann et al., 2007). Concussion caused by a single impact had been an area of interest for several decades. However, since last decade, a number of studies are focusing on repetitive concussion, also known as multiple concussion or repetitive mild traumatic brain injury (rmTBI). It has been hypothesized in literature that exposure to repetitive head impacts sustained by a sportsperson of a contact sport could be the reason behind concussion (Stemper et al., 2019). A study, based on 2015-2017 seasons, on 608 American football athletes from NCAA Division III, college and high school, at eight institutions, measured head impact accelerations to analyze concussion and repetitive head impact exposure (Stemper et al., 2018). It was found that on the date of concussion, 44% of concussed athletes experienced high risk head impacts, which directly correlates to concussion onset. For the remaining, 56% of concussed athletes, it was said that some other factors would have contributed to the concussion onset. Also, 33% of the concussed athletes had high repetitive head impact exposures during the season, which ultimately lead to concussion.

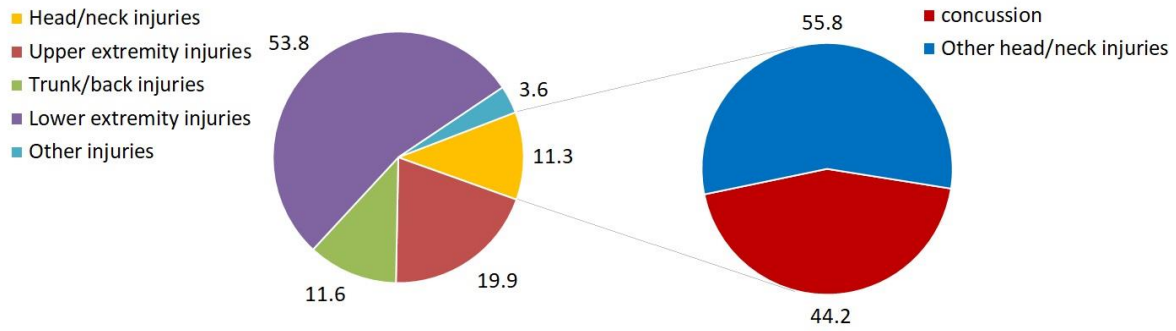

Figure 3: Diagram illustrating percentage distribution of injuries in sports by body parts (Hootman et al., 2007).

In spite of concussion being a mild injury, its long term outcomes affect a person's life adversely. The greatest challenge lies in the fact that the immediate consequences of concussion are usually only functional disturbances, which cannot be diagnosed by presently available standard structural neuroimaging techniques. It is well-known that concussion is caused by sudden movement of the head. Hence, it becomes essential to improve brain injury prediction tools and to optimize protection systems, such as sport helmets, in a manner that the severity and hence, the consequences of the concussion can at least be reduced, if not prevented completely. For this purpose, quantification of concussion in terms of a mechanical parameter will be of great assistance. Computational models have proved to be efficient in studying brain injuries. Hence, this study attempts to quantify concussion by means of a finite element rat brain model. This study is a first step towards better understanding of

the brain injury mechanism by getting insights into rat brain, in terms of axonal elongation, in case of concussion. This study as well opens the door to many more possibilities regarding concussion related investigations, such as repetitive concussion or rmTBI investigations. Let us look at the outline of this work in the following paragraphs.

The first chapter provides a review of literature regarding this study in order to better understand what has been done and why. The main objective of this study is to investigate mechanical threshold to concussion in terms of axonal stretch in case of concussion. This objective is achieved by developing an anisotropic finite element rat brain model and simulating concussion scenarios. As explained earlier, concussion is a kind of brain injury. Hence, to start with, the anatomy of head and brain, at macroscopic level and microscopic level, is presented. Knowledge of anatomy makes the comprehension of injury mechanisms easy. Main anatomical structures and their functions are described along with the similarities and differences of a human and a rat brain. A brief description about an advanced neuroimaging technique, commonly known as diffusion tensor imaging (DTI), is also provided. This neuroimaging technique makes use of diffusion of water molecules inside brain tissue and enables the identification of microscopic anatomy and properties of nerve fibers. As it is known that concussion is a mild kind of injury and results in functional disturbances, it is supposed that the structural injury happens at microstructural level. With this notion, potential injury mechanisms for concussion are presented next. Functional disturbances are result of interrupted neurotransmission caused by mechanical trauma. Axons are the main medium of neurotransmission and thus, potential injury mechanisms are thought to be impairments of axonal cytoskeleton elements due to sudden stretch. Therefore, this idea was conceived that estimation of axonal elongation can provide insights for concussion. In the next section, brain injury grading scales, criteria and tolerance limits, available in literature, are presented. An awareness about this not only broaden our horizon with respect to different possibilities of assessing concussion, but also make us realize how differently concussion has been defined in various studies. Towards the end, literature regarding finite element modelling of rat brain is presented. Finite element modelling is a systematic procedure comprising knowledge of material, development of meshed model, incorporation of material properties and model validation. Hence, the experimental studies available in literature for the determination of rat brain material properties are described briefly in the first part of this section. Next part sheds light on the existing finite element rat brain models and provides details about their meshing, material, validation and findings along with highlighting their limitations. Last part of this section talks briefly about the model validation methods available in literature. Validation of a computational model is an important and essential part of model development, because then only we can be sure of the

estimated results and put them in use. This chapter concludes by summarizing main aspects of reviewed literature and thus providing the motivation of this study.

Second chapter presents the development and validation of an anisotropic Finite Element Rat Brain Model (FERBM). The chapter starts with highlighting the advantages of computational models in studying injury biomechanics and the importance of validating a computational model before it can be put to use. The basis of the study i.e. Sprague Dawley rat is introduced next. This particular species of rat is chosen since the simulations of experimental concussion presented in the final chapter are based on similar kind of rats. A DTI atlas, available in literature, for the similar kind of rat is chosen next. This DTI atlas provides the geometry of the rat brain as well as the diffusion parameters. For the development of the model, at first the geometric boundaries are rendered from the DTI atlas. The details about geometric modelling and meshing of the rat brain is presented next. The rat brain is meshed as one single structure, as neither the segmented mesh of the rat brain was feasible, nor required. However, to identify regional and functional characteristics of the rat brain, the meshed model is categorized only for the analysis of simulation results. Hence, the details about this anatomical and functional categorization is presented next. The following section provides the methodology for the identification of the diffusion parameters. After meshing and knowing the diffusion parameters for every element of the meshed model, the next step is to decide upon the material model and the material properties. Hence, following section provides details about the chosen constitutive law and the material properties. Furthermore, incorporation of the material properties and the diffusion parameters in the FERBM is explained. Details about the material of cerebrospinal fluid and skull is also provided. Thus, the first half of this chapter detailed complete methodology of the development of an anisotropic finite element rat brain model. Second half of this chapter presents validation of developed anisotropic viscous hyperelastic FERBM. The developed model is validated against two experimentations available in literature. At first, validation against experimental dynamic cortical displacement on the application of vacuum pressure pulse is presented. Afterwards, validation against brain skull relative displacement on the application of rotational acceleration loading in the sagittal plane is presented. For both experimental specification are detailed first, followed by the simulation details and a comparison of results. A parametric study, presented at the end of the chapter, shows the importance of the choice of brain material law, compressibility of cerebrospinal fluid and the hourglass control on the brain response. The objective of this study is much more than just having a validated finite element rat brain model. This anisotropic model will provide detailed insights into the brain in terms of axonal elongation in case of concussion and open new doors to various concussion related investigations.

The final chapter provides simulations of experimental concussion. Data for twenty-six cases of experimental concussion was received from Medical College of Wisconsin (MCW), USA through a collaboration. At first, experimental approach is presented to detail the methodology used for inducing concussion in rats. This is followed by the experimental methodology used for the assessment of post-concussion behavioural responses. Acute injury severity was evaluated using the recovery time (unconscious time). Elevated plus maze (EPM) assessment was used to analyze the changes in behavioural aspects, activity and emotionality, following concussion. The Morris water maze (MWM) assessment was used to analyze the post traumatic anterograde amnesia and spatial learning after concussion. Details about simulation of these experimental cases in presented next. Simulation results are extracted for the brain in entirety as well as for anatomical and functional brain regions. For a better understanding of results, relation between simulation results and experimental results is established through different perspectives. Towards the end, statistical analysis of simulation results in terms of different statistical measures is provided. Statistical analysis is done to identify the best suitable predictor for concussion and to estimate the tolerance levels for concussion. Finally, this chapter concludes by highlighting the advantages of anisotropic finite element rat brain model.

In the end, general conclusion in the form of a synthesis of this research is exposed and the main results are reported. Further, prospects, as a number of steps needed in future for an advanced understanding of rmTBI is provided.

Chapter 1: Literature review

1 Anatomy of head and brain

1.1. Introduction

Knowledge of anatomy makes it easier to understand injury biomechanics more precisely. As the area of study here is brain, anatomy of brain, at macroscopic and microscopic level, is presented in this section. The basis of this study is the rat brain. However, for a better comprehension of the similarities and differences between the human and the rat brain, comparative anatomical details are provided. For both, humans and rats, brain is a part of central nervous system, enclosed in the head structure inside skull. Membranes, known as meninges, protect the brain and hold them in place inside the skull. Cerebrospinal fluid (CSF) filled in between the membrane layers, apart from acting as a cushion to protect the brain from mechanical shocks, serves many other neurological purposes. Anatomical details provided in the following paragraphs are not exhaustive, but sufficient for this study. For a detailed and precise description of brain anatomy, the standard anatomical atlases (e.g. human: Gray's anatomy 41st edition, 2015; rat: Rumple et al., 2013; Paxinos and Watson, 2013 and Papp et al., 2014) can be referred.

1.2. Macroscopic anatomy of head and brain

Broadly, the head is composed of skin, skull and brain. Skull provides a solid base to the head and protects the brain. Skull is made up of multiple bones and the bones housing the brain are known as frontal, parietal, occipital and temporal bones. Figure 1.1 portrays the skulls of a human and a rat, in different views at different scales.

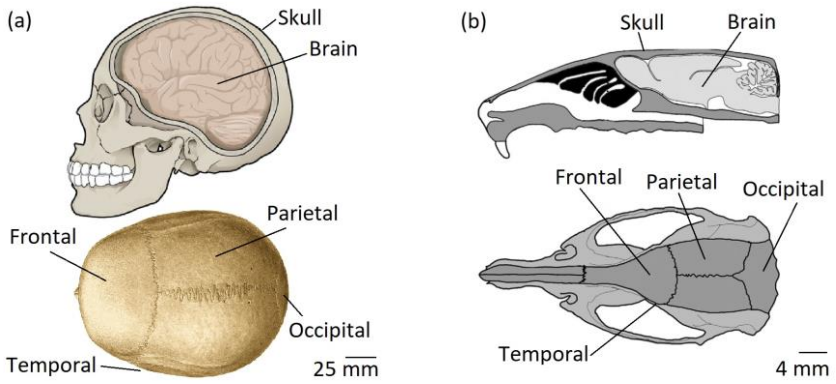

Figure 1.1: Diagram representing side view and top view of (a) a human skull and (b) a rat skull, along with illustrations of the placement of brain inside the skull. The length of a rat skull is around four to five times smaller, while the thickness is around ten times smaller than that of a human skull.

Length of a rat skull is around 4-5 times smaller than a human skull (Bollen and Bai, 2005; HEDDD, 2000). The thickness of an adult rat skull varies from 0.6 to 0.7 mm (Gefen et al., 2003; Mao et al.,

2011); whereas, that of an adult human varies from 5 to 8 mm (Li et al., 2007). As mentioned earlier, both, rat and human brain are held safe inside the skull by means of the membrane layers, known as meninges. Meninges is composed of dura mater, arachnoid mater and pia mater (Figure 1.2). CSF is found in the subarachnoid space between the arachnoid mater and the pia mater. The rat brain does not contain the layers falx cerebri, to distinguish left and right cerebellar hemispheres; and cerebellar tentorium, to distinguish between cerebellum and cerebrum, as in the human brain.

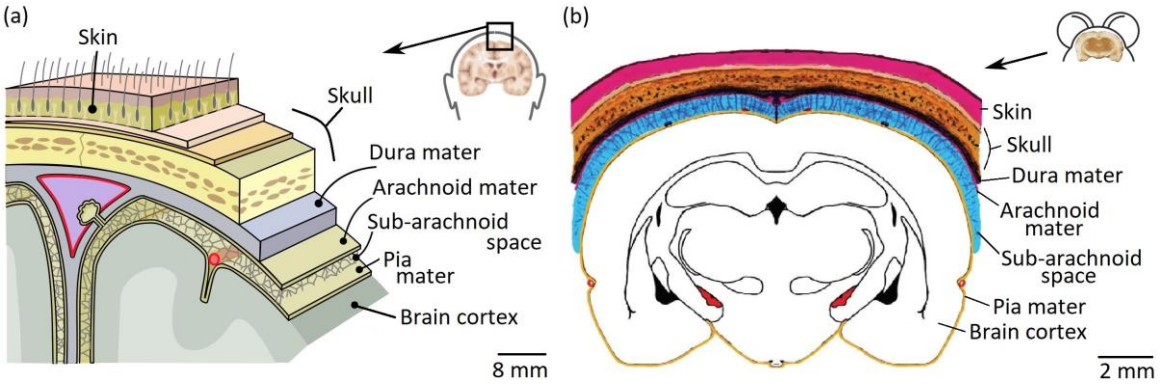

Figure 1.2: Diagram illustrating layers of (a) a human (based on NIH, SEER training module) and (b) a rat head (Nowak et al., 2011), which from outside to inside are skin or scalp, skull, meninges (dura mater, arachnoid mater, sub-arachnoid space and pia mater) and the brain cortex.

Normal intracranial pressure (ICP) in a supine adult human ranges from 7 mmHg to 15 mmHg (Steiner and Andrews, 2006); while, for a rat, normal ICP varies from 4 to 10 mmHg (Rooker et al., 2003; Uldall et al., 2014). The thickness of a rat meninges is at least three times smaller than that of a human. As reported by Nowak et al. (2011), in coronal plane at bregma = -3.6 mm or interaural = 5.4 mm, the thickness of rat brain dura mater, arachnoid mater, sub-arachnoid space and pia mater is around 300 µm, 75 µm, 750 µm and 25 µm respectively. The ventricular system in rodent and human is made up of four interconnected cavities (Figure 1.3), which are filled with cerebrospinal and interstitial fluid. The main constituents of ventricular system are lateral ventricles, third ventricle, fourth ventricle and the aqueduct (Snyder et al., 2018).

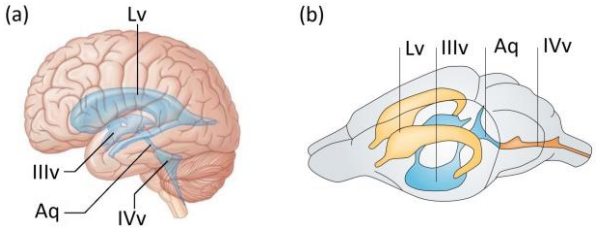

Figure 1.3: Diagram representing ventricular system in (a) human brain (Gray's anatomy 41st edition, 2015) and (b) rodent brain (Fliegauf et al., 2007) at different scales. Lv: lateral ventricle, IIIv: third ventricle, IVv: fourth ventricle and Aq: aqueduct.

Broadly, brain can be categorized into three major components - cerebrum, cerebellum and brainstem. Figure 1.4 represents the different views of human and rat brains, illustrating the major brain regions. Cerebrum is composed of left and right cerebral hemispheres and each hemisphere is composed of four lobes - frontal, parietal, occipital and temporal lobe, right beneath the corresponding skull bones. Further, every lobe can be subdivided into smaller regions, as every cortical layer technically have a unique name and function.

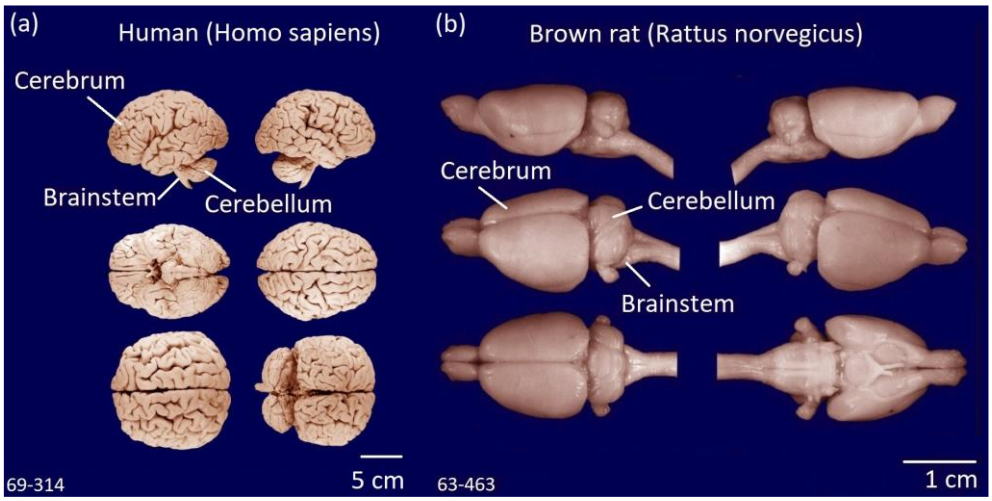

Figure 1.4: Diagram representing different views of (a) a human brain and (b) a rat brain, illustrating the main parts of the brain, i.e. cerebrum, cerebellum and brainstem (Univ. of Wisconsin-Madison Brain Collection).

Figure 1.5 gives an overview of approximate boundaries of main functional zones of a rodent brain and a human brain (Snyder et al., 2018). There exist more than hundred sub regions inside brain, which can be seen in any standard brain atlas and every region of the brain is usually associated with specific functions (Genon et al., 2018).

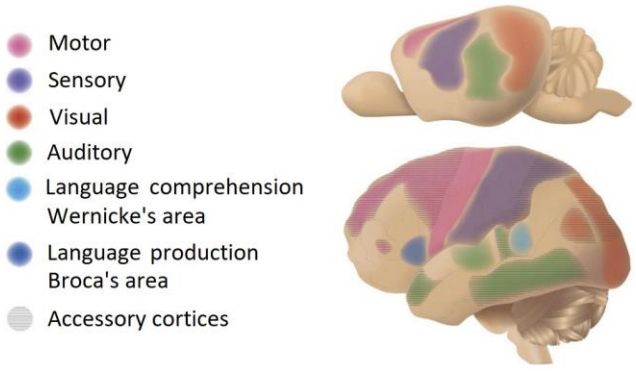

Figure 1.5: Diagram representing approximate boundaries of main functional zones of the brain; rodent (top), human (bottom) (Snyder et al., 2018).

Generally, left side of the brain is considered to be the scientific side, while the right one is considered artistic (Herrmann, 1991; Peschanel, 1996). Normally, the association of functions with different brain regions is supposed to be such as: frontal lobe with high level intellectual functions, and some memory and motor functions; parietal lobe with sensory and somatosensory functions; occipital lobe with visual functions; temporal lobe with memory related and auditory functions and cerebellum with motor functions (Snyder et al., 2018). Brainstem plays a role of conductive medium and controller. All information from cerebrum and cerebellum to body and from body to cerebrum and cerebellum transverse through brainstem. A specific sensory, cognitive or motor function is usually not performed by a single region alone, rather dynamic interplay and information exchange among different regions make all mental capabilities possible (Genon et al., 2018).

In human brain, the cerebral hemispheres consist of an external highly convoluted cortex, known as the cerebral cortex or the gray matter. The main constituents of brain gray matter are the neuron cell bodies. The grooves and folds of the cerebral cortex are known as sulci and gyri. Rat cerebrum is much simpler than the human cerebrum and does not have any grooves and folds. However, regions of rat cerebrum can also be divided into different lobes just like human brain. Underneath the gray matter lies an extensive mass of white matter (Figure 1.6).

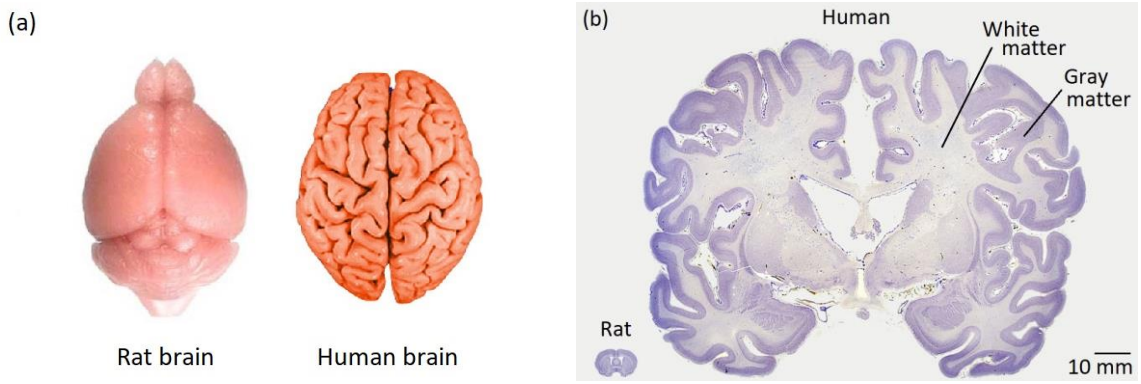

Figure 1.6: Diagram representing (a) the brain surface structure of a rat brain (left, scaled up) and a human brain (right, scaled down) illustrating the simplicity of rat brain over highly convoluted human brain; (b) gray matter and white matter representation of a rat brain (left) and a human brain (right) at a coronal section; the darker area outlining the brain slice is the gray matter and the remaining lighter area is the white matter (Univ. of Wisconsin-Madison Brain Collection).

The main constituent of the brain white matter is axons, explained in detail later. The two hemispheres are connected together by means of commissural fibers of corpus callosum. On the basis of the function and connection, the nerve fibers or the axons of the cerebral hemisphere are categorized into three types, which are association fibers, commissural fibers and the projection fibers.

Figure 1.7 represents a schematic diagram illustrating the nerve fibers in a human brain. The nerve fibers of a rat brain connects in a similar way.

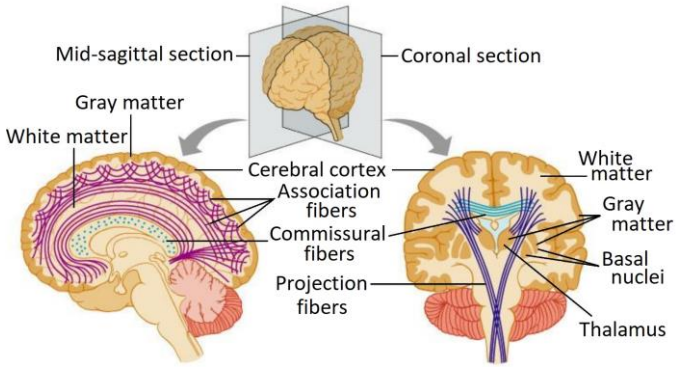

Figure 1.7: Diagram representing nerve fibers, i.e. association fibers, commissural fibers and projection fibers of a human brain in mid-sagittal section and coronal section along with the gray matter and white matter distinction (Heape, 2010).

Association fibers connects different cortical regions in the same hemisphere. Commissural fibers connects corresponding cortical regions in the two hemispheres. Projection fibers connects the cerebral cortex with the lower parts of the brain and the spinal cord. These nerve fibers group together to make fiber tracts or axon bundles and are responsible for brain anisotropy. Let us now look at the microscopic anatomy for a better understanding of the nerve fibers and neurotransmission.

1.3. Microscopic anatomy of brain

Brain is a part of central nervous system (CNS). It is the CNS that contains most of the neuronal cell bodies. These cell bodies are often grouped together in regions called nuclei or these may form more extensive layers of cells, frequently known as gray matter. Neurons and glial cells are the major constituent of CNS. Typically, there are billions of neurons in a human brain and millions in the rat brain. Approximately, sixteen-billion neurons are found in the cerebral cortex of a human brain (Azevedo et al., 2009) and thirty-million neurons in the cerebral cortex of a rat brain (Mortera and Herculano-Houzel, 2012). The main function of neurons is to transfer information by means of a nerve impulse, commonly known as action potential. Glial cells serve many different purposes and there are different kind of glial cells for different purposes. For instance, oligodendrocytes for myelination, astrocytes for guiding axons, synaptic support, managing blood-brain barrier and controlling blood flow, ependymal cells to enclose the cerebrospinal fluid filled ventricles and microglial cells for immune defense. In summary, glial cells surround the neurons to protect and keep them intact at their place while supplying nutrients and oxygen, insulating active neurons and destroying and removing the dead neurons (Jakel and Dimou, 2017). Schematic diagram of a neuron is shown in Figure 1.8.

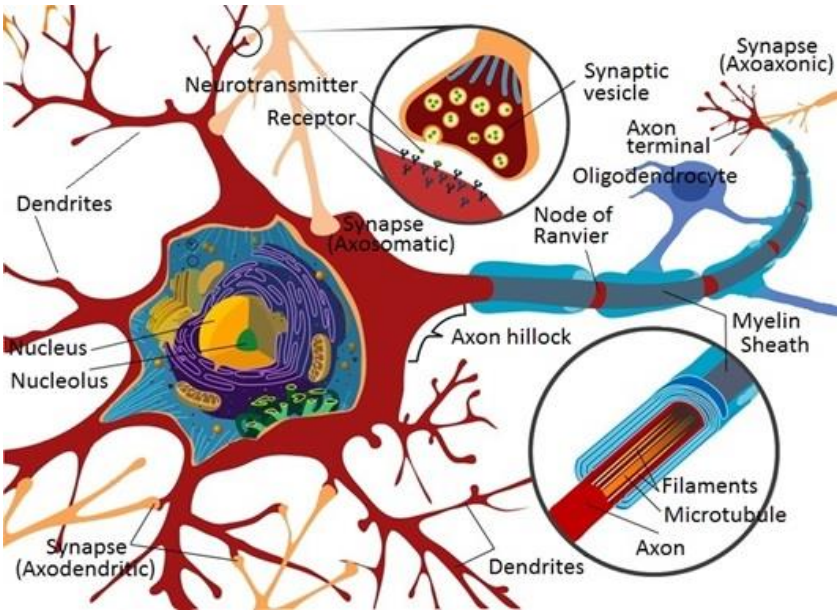

Figure 1.8: Schematic view of a neuron of the central nervous system with a myelinated axon.

There are three main parts of a neuron - cell body or soma, dendrites and axon. Soma is the compact central structure from which dendrites and axon extrude outwards. Centre of the soma is called nucleus. Typically, there can be multiple dendrites, but only a single axon coming out of a soma. Both dendrites and axon undergo branching; dendrites all along their length and axon towards the end terminal. But, the difference in branching between the two is that dendrites' branches get thinner while diverging; whereas axonal branches maintain their diameter intact, more or less. Dendrites can only be a few hundred micrometer long at maximum, while, axons can grow much longer. The region where an axon connects to the soma is referred as axon hillock. A contact between axon terminal and dendrite or soma or another axon is referred as synapse. Hence, there can be an axodendritic synapse, axosomatic synapse, axoaxonic synapse and dendrodendritic synapse. Typically, soma and dendrites of a neuron are used to receive synaptic signals from other neurons and axon is used to pass these signals to other neurons, in between soma may process this signal. The type, density, structure and function of cells varies from species to species, between genders as well as with age. Hence, the rodent brain differs from a human brain not only with its significantly lower number of neurons, but also by the size of cells, branching of dendrites, length of axons and transfer of nerve impulse (Bayer et al., 1993; Snyder et al., 2018; Azevedo et al., 2009). However, since the main anatomical structure and the functioning between a rodent and human brain are same, basic details are provided in this section.

Two types of axons, myelinated and unmyelinated, are found in CNS and the size of axons vary from neuron to neuron. In human CNS, an axon can have a minimum diameter of the order of 10^{-1} µm and maximum of the order of 10^{+1} µm (Perge et al., 2012); whereas, the maximum axonal diameter for a rat brain can be of the order of 1 µm (Pesaresi et al., 2015). Myelination is ensheathing or wrapping

of multiple layers of thin membrane like structures around the axon. As shown in Figure 1.9, myelination of axon is provided by oligodendrocytes. One axon is myelinated by various oligodendrocytes and one oligodendrocyte myelinates multiple axons at the same time. The gap between two myelinated spaces on an axon is called node of Ranvier.

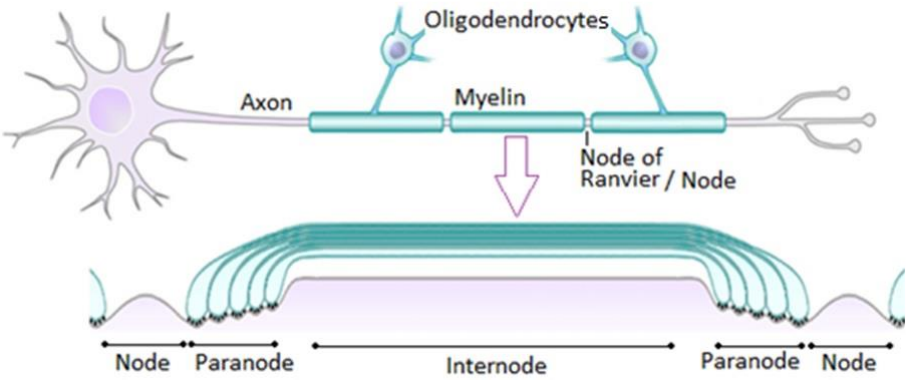

Figure 1.9: Diagram representing location of node, paranode and internode on a myelinated axon (Chang et al., 2016).

The main constituent of an axon is its cytoskeleton. It is composed of microtubules, neurofilaments or intermediate filaments and microfilaments or actin filaments. Axolemma, axoplasm, mitochondria, motor proteins and vesicles are other elements found inside an axon. Generally, a microtubule (Figure 1.10) is made up of 13 linear protofilaments of assembled α-tubulin and β-tubulin heterodimer subunits (Conde et al., 2009).

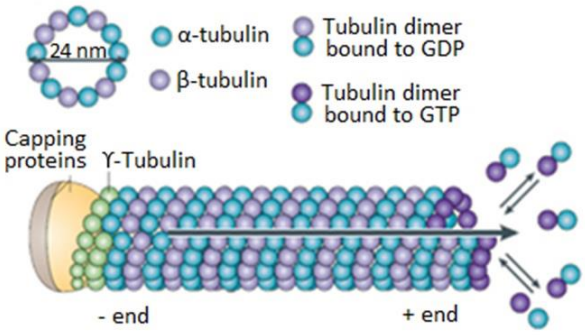

Figure 1.10: Structure of a microtubule (Conde et al., 2009).

Microtubule is a dynamic structure that keeps on growing on polymerization and continues to shrink on depolymerization. Typically, the diameter of microtubule is around 24 nm (human) and it looks like a hollow cylindrical tube (Conde et al., 2009). Various microtubules are kept organized together inside the axon by means of microtubule associated protein, commonly known as Tau.

Neurofilaments, also known as intermediate filaments, are made up of three subunits - neurofilament-light (NF-L), neurofilament-medium (NF-M) and neurofilament-heavy (NF-H) (Smith and Meaney,

2000). Structure of NF-L is straight like a rod, however NF-M and NF-H have side arms (Figure 1.11). Typically, the diameter of a neurofilament is around 10 nm (Yuan et al., 2012).

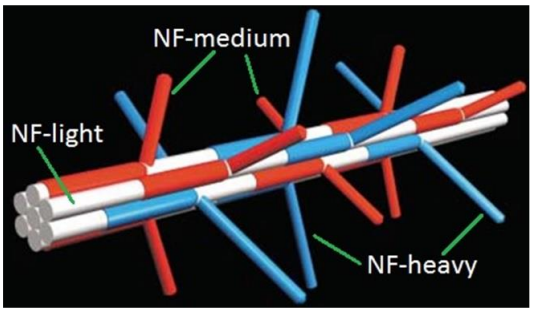

Figure 1.11: Structure of neurofilament (Smith and Meaney, 2000).

As shown in Figure 1.12, microfilaments or actin filaments are made up of two strands of polymers of globular actin protein. Microfilaments are dynamic structures of around 7 nm diameter (human), which keeps on polymerizing and depolymerizing (Flynn et al., 2013).

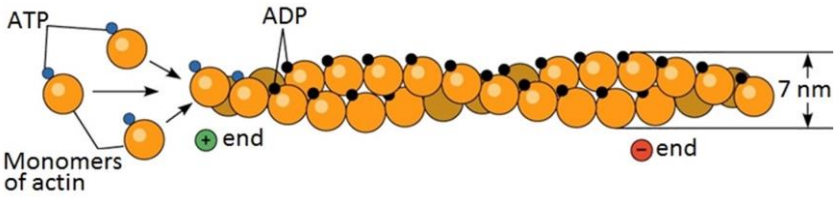

Figure 1.12: Structure of microfilament (Pearson Benjamin Cummings, 2006).

Main purpose of axonal cytoskeleton is to assist in axonal transport. This transportation can be categorized on the basis of speed such as slow transport (up to 8 mm per day) or fast transport (about 50-400 mm per day); or on the basis of direction such as anterograde transport, which is from cell body towards axon terminal or retrograde transport, which is from axon terminal towards cell body (Griffin et al., 1976; Maday et al., 2014). Kinesin is the motor protein that carries the material to be transported during the anterograde transport; and dynein does so during the retrograde transport. Next, let us get familiar with the basics of a medical imaging technique used to visualize the brain anatomy at microstructural level.

1.4. Visualizing microstructural brain anatomy

In the previous section, we saw that the axonal fibers, which are the main constituent of white matter, are responsible for neurotransmission. These axons make the brain an anisotropic structure, as they promote the flow along their length than in any other direction. Advanced medical imaging techniques have made it possible to look inside the brain to a great extent. Diffusion Tensor Imaging (DTI) or Diffusion-weighted magnetic resonance imaging (DW-MRI) is one such in-vivo and non-invasive

technique, which is basically an extension of commonly known Magnetic Resonance Imaging (MRI). There exist millions and billions neurons inside the brain and these neurons communicate with each other via axons and form the complex neural networks. Understanding of brain's structural connectivity is still a big challenge. However, DTI can measure the macroscopic organization of axons in the brain tissue (Mori and Zhang, 2006). In DTI, diffusion of water molecules is used to generate contrast in the medical images. For example, when a drop of water is dropped on a paper, sometimes it spreads in circular fashion and sometimes it is elongated in one direction. The circular dispersion or diffusion is known as isotropic diffusion, i.e. uniform dispersion along all the directions. However, the elongated dispersion is the result of the intrinsic paper structure. When high density of fibers are oriented in one particular direction than others, then such an elongated diffusion occurs and is known as anisotropic diffusion. This is exactly what happens inside the brain. Brain tissue, especially the white matter constituting the fiber bundles, is a highly anisotropic structure. Hence, water moves more easily along the axon bundles than orthogonally to these bundles making it possible to estimate axonal organization inside the brain through DTI. A brief description of the basics of DW-MRI is given in the following section for the understanding of diffusion technique.

As per Mori and Zhang (2006), MR contrast is generated based on the physical properties of water molecule. Proton density (PD), T_1 and T_2 relaxation times and the diffusion coefficient (D) are commonly used for this purpose. Water concentration is represented by the proton density. T_1 and T_2 are the signal decay (relaxation) times after excitation and depends upon surrounding conditions. The Brownian (thermal) motion of the water molecules is represented by the diffusion term, D. Equation 1.1 shows the contribution of these parameters to a MR signal (S) in a spin-echo image.

$$S = PD\left(1 - e^{-TR/T_1}\right) e^{-TE/T_2}\, e^{-bD} \qquad 1.1$$

Where, TR and TE are the repetition time i.e. the timing of excitation and the echo time i.e. the preparation period of the MR signal respectively (Figure 1.13) and b represents the diffusion weighting factor. MR scanner provides the magnitude of signal (S) from water and TR, TE and b are the controllable imaging parameters, which are used to modify the contribution of T_1, T_2 and D terms in the signal. By performing two MRI acquisitions for two different b values, we can determine the diffusion coefficient, D from Equation 1.1 as given in Equation 1.2.

$$D = \ln\left(\frac{S_2}{S_1}\right) / (b_1 - b_2) \qquad 1.2$$

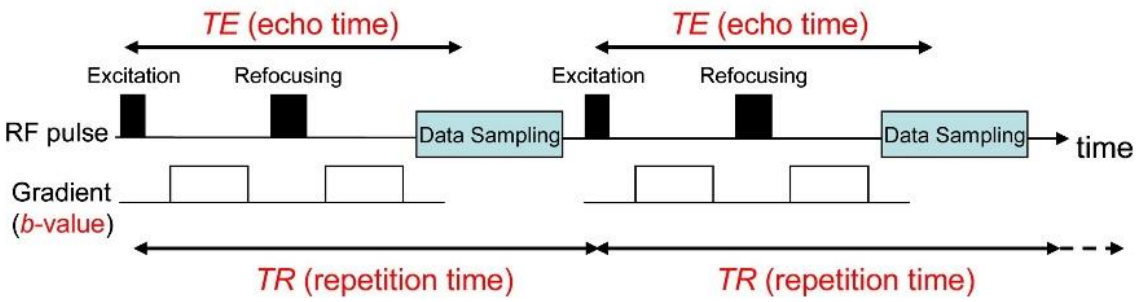

Figure 1.13: Diagram representing MRI pulse (spin-echo) sequence for the understanding of acquisition parameters (Mori and Zhang, 2006).

Usually, the first acquisition is done at a negligible b value ($b_1 \approx 0$) and the resultant image remains insensitive to the diffusion i.e. non-diffusion weighted image (signal intensity = S_1). In the second acquisition, a gradient is applied (high b_2 value) and a diffusion weighted image (S_2) is acquired. Because of the applied gradient, the signal intensity of the diffusion weighted image is lower due to the water movement. Hence, the diffusion coefficient can be obtained by solving Equation 1.2. Measurement of diffusion through MRI identifies the motion of water only along the axis of applied gradient. When the water molecule moves along the axon bundles, the principal fiber direction should be same as the measured orientation with the largest diffusion coefficient. If the X, Y and Z axes are assigned red, green and blue colors respectively, then the orientation of the largest diffusion coefficient can be used to develop a color coded orientation map indicating the principal fiber direction. However, it is not necessary that the fibers orient only along one of the three axes. Hence, to capture the exact fiber orientation, gradients need to be applied in thousands of direction, which is not feasible. To deal with this issue, a simplified concept of diffusion tensor was introduced by Basser et al. (1994). According to this concept, diffusion measurements along six directions are fitted to a three dimensional ellipsoid and then the properties of this ellipsoid can be defined by these six diffusion coefficients. These properties are the Eigen values (λ_1, λ_2 and λ_3) i.e. the longest, median and the shortest axes of the ellipsoid and the Eigen vectors (v_1, v_2 and v_3) i.e. the orientations of the longest, middle and the shortest axes of the ellipsoid. A 3 x 3 symmetric matrix containing these diffusion coefficients is known as diffusion tensor (Equation 1.3).

$$D = \begin{bmatrix} D_{xx} & D_{xy} & D_{xz} \\ D_{xy} & D_{yy} & D_{yz} \\ D_{xz} & D_{yz} & D_{zz} \end{bmatrix} \quad 1.3$$

Once, the diffusion tensor for every voxel of the image is known, diffusion parameters per voxel of the image can be calculated. Two of the most widely used diffusion parameters are fractional anisotropy (FA), which can be expressed as in Equation 1.4 and the principal fiber direction, which is the Eigen vector corresponding to the maximum Eigen value. However, since it is difficult to visualize the 3-

dimensional vectors per voxel, the principal fiber direction is converted to a color coded orientation map, where every color represents a direction. This makes it easier to understand the fiber orientation at a particular anatomical structure.

$$Fractional\ anisotropy, FA = \sqrt{\frac{3}{2}} \frac{\sqrt{(\lambda_1 - \tilde{\lambda})^2 + (\lambda_2 - \tilde{\lambda})^2 + (\lambda_3 - \tilde{\lambda})^2}}{\sqrt{\lambda_1{}^2 + \lambda_2{}^2 + \lambda_3{}^2}} \quad 1.4$$

Where, $\tilde{\lambda} = (\lambda_1 + \lambda_2 + \lambda_3)/3$ and $\lambda_1, \lambda_2, \lambda_3$ are the Eigen values.

Or an equivalent form can be expressed as in Equation 1.5.

$$Fractional\ anisotropy, FA = \sqrt{\frac{1}{2}} \frac{\sqrt{(\lambda_1 - \lambda_2)^2 + (\lambda_2 - \lambda_3)^2 + (\lambda_3 - \lambda_1)^2}}{\sqrt{\lambda_1{}^2 + \lambda_2{}^2 + \lambda_3{}^2}} \quad 1.5$$

Thus, the diffusion tensor imaging (DTI) helps in identifying the diffusion parameters per voxel of an anatomical medical image. Tractography is the three-dimensional visualization of nerve fiber tracts using the data collected through medical imaging (DW-MRI). Figure 1.14 shows an example of the white matter tractography for a human brain and a rat brain along axial plane, acquired through diffusion tensor imaging.

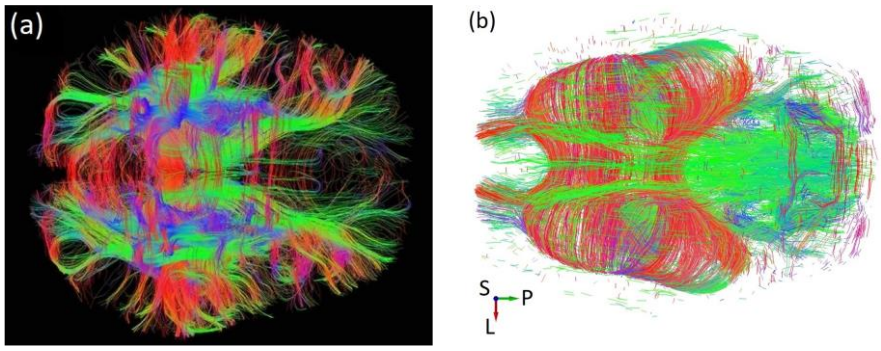

Figure 1.14: Image representing white matter tractography of (a) a human brain (Zeynep Saygin, mcgovern.mit.edu) and (b) a rat brain in axial plane, acquired through diffusion tensor imaging (L: left, P: posterior and S: superior).

1.5. Conclusion

The above section have presented a basic anatomy of the brain. Rat brain is very small in comparison to a human brain. An adult human brain weighs around 1400 g, whereas, the rat brain weighs only around 2 g. Although the basic anatomy of the rat brain and the human brain is similar, the rat brain is much simpler (structurally as well as functionally) than the human brain. We saw that at macroscopic level, the highly convolute cortex of human brain not only makes the physical structure

complicated, but also the reason behind high level functionalities of human brain. At microscopic level, the anatomy and the functioning of both the brains are same. Though, the size, types, density etc. of the neural constituents may vary, the variation is understandable because even for the same species, these variations occur with age and sex. Further, brain microstructures can be visualized with the help of advanced medical imaging techniques. Basics of one such imaging technique, known as diffusion weighted magnetic resonance imaging or diffusion tensor imaging, were described briefly. The data acquired through DTI of a brain makes it possible to identify the neural network in terms of fiber tracts as well as the diffusion parameters per voxel and hence, per brain region. This in turn can be useful in characterizing anisotropic mechanical behaviour of the brain. Following chapter sheds light on this aspect in an elaborative manner.

2 Potential injury mechanisms for concussion

2.1. Introduction

A very basic, yet sufficient information on brain anatomy was detailed in the previous section. This section gives a description of potential injury mechanisms associated with concussion. The knowledge of brain anatomy gained in the previous section will help in understanding the injury mechanisms more clearly. Concussion is a mild Traumatic Brain Injury (TBI). An important and one of the most common pathological features of TBI is axonal damage, also known as diffuse axonal injury (DAI) or traumatic axonal injury (TAI) (Smith and Meaney, 2000; Buki et al., 2006; Johnson et al., 2013; Ling et al., 2015). When a head is subjected to rapid acceleration and deceleration (translational or rotational), which is a very common phenomenon during sports, the brain tissue and all its constituents including neurons, glial cells and blood vessels, are stretched. This may lead to disruption in the normal functioning of the brain. Those axons, which span long distances from the cell bodies are especially vulnerable to stretching and the consequence could be DAI (Ling et al., 2015). TBI may result in a progressive, long term neurodegenerative process. This is evident through literary evidences highlighting axonal degeneration in human brain material, even years after the injury (Johnson et al., 2013). A developing brain is more susceptible to TBI than an adult brain, possibly due to factors, such as differences in the degree of myelination, volume ratio of brain to water, elastic properties and blood brain barrier integrity (Ling et al., 2015). Rapid tensile elongation or uniaxial stretch of axons is supposed to result in axonal cytoskeleton damage and in extreme cases, immediate disconnection, which is known as primary axotomy and is considered to be a comparatively rare event, except for severe brain injury (Smith and Meaney, 2000). On the other hand, in most cases, swelling, which follows cytoskeleton disruption can cause secondary axotomy (Smith and Meaney, 2000; Johnson et al., 2013). Primary axotomy is generally a result of dynamic injury, where application of force occurs in less than fifty milliseconds. Axons are thought to be viscoelastic in nature and it has been found that under quasi-static loading they can tolerate even 100% strains (Tang-Schomer et al., 2010). However, under dynamic loading conditions, where strain rates are greater than twenty-six per

second, they display undulations, indicating cytoskeleton damages (Ahmadzadeh et al., 2014). Hence, axonal injury depends on both the magnitude and the rate of strain during brain trauma (Smith and Meaney, 2000). It is supposed that in the end, the disconnected axons experience Wallerian degeneration (Johnson et al., 2013).

In spite of the transitory nature of clinical symptoms, functional neuroimaging, neurophysiological, electrophysiological, and neurochemical assessments show that the disturbance of concussion takes over a month to return to baseline and neuropathological assessment shows that concussion induced axonopathy possibly persist for years (Ling et al., 2015). The study also suggested that axonal injury related to acute TBI, breach of blood brain barrier, loss of microvascular integrity, resulting inflammatory cascade and astrocyte and microglia activation are probably the basis of TBI and Chronic Traumatic Encephalopathy (CTE) mechanisms. A review by Maxwell et al. (1997) provided the sequence of morphological responses shown by axons after exposure to mechanical loading or strain for a moderate to severe brain injury. The sequence is summarized as: first, a focal disruption of axolemma; second, mitochondrial swelling; third, the development of nodal blebs with or without focal decrease in the axonal diameter at internode; fourth, loss of axonal microtubules and disruption of the intra-axonal relationships of neurofilaments; fifth, involution of axolemma at intermodal region; sixth, formation of periaxonal spaces; seventh, occurrence of varicosities; eighth, development of myelin intrusions and finally, axonal disconnection, formation of axonal bulbs and degeneration. Although there is no consensus on potential injury mechanisms or on the sequence of their occurrence, yet on the basis of literature reviewed, potential injury (concussion) mechanisms at microscopic level are thought to be neuronal depolarization, myelin collapse, microtubule disruption, neurofilament compaction, microfilament disruption and mitochondria swelling. These mechanisms cause formation of axonal bulb and varicosities, which can be seen easily during histopathological examination (Johnson et al., 2013). Brief descriptions of these are given in the following sections.

2.2. Neuronal depolarization

The review by Giza and Hovda (2001) explains the neurometabolic cascade of concussion quite well. According to this review, post concussive impairments occur with minimal noticeable anatomic pathology and frequently resolve totally over time. It indicates that the impairments are due to temporary neuronal dysfunctions instead of cell death. Potential reasons behind neuronal dysfunction can be ionic shifts, impaired connectivity, altered metabolism or neurotransmission related changes. Hence, knowledge of underlying injury pathophysiology is essential to understand the phenomenon of concussion at microscopic level. It has been found that right after an injury to the brain, axonal stretching, disruption of neuronal membrane and opening of voltage dependent potassium channels occur, which lead to indiscriminant release of neurotransmitters and ionic fluxes. Subsequently,

binding of some of these transmitters with certain receptors causes neuronal depolarization with efflux of potassium and influx of calcium. Such ionic shifts lead to changes in acute and subacute physiology. In order to maintain the neuronal membrane potential, sodium-potassium pump works overtime triggering hypermetabolism, which further reduces the cerebral blood flow causing cellular energy crises. Persistent increment in calcium may impair mitochondrial metabolism, worsening the energy crises. Uncontrolled calcium accumulation can also disrupt the neurofilaments and microtubules, impairing the neural connectivity and may lead to cell death. Also, an abrupt increase in energy demand causes an increase in glycolysis, which in turn results in increased lactate production. Elevated levels of lactate leads to neuronal dysfunction by brining on acidosis, membrane damage, blood brain barrier permeability damage and cerebral edema. All this leads to post-concussive susceptibility, making the brain incapable of responding adequately to another injury and possibly leading to long lasting impairments.

2.3. Myelin collapse

Myelination of axon plays an important role. Myelination along with helping in rapid information transfer from one neuron to another, also provides a protective shield around axons. A mild traumatic brain injury may damage myelination, which consequently can either undergo recovery or lead to complete degeneration of an axon. Demyelination and excessive myelination, both are kind of myelin damages (Figure 1.15). It has been found that unmyelinated fibers are more susceptible to damage than myelinated fibers. Myelin damage can also cause myelin debris, which leads to the activation of microglia and further to chronic neuroinflammation. Myelin repair or remyelination is capable of not only recovering functionality, but also protecting denuded axons from progressive degeneration and disconnection (Mierzwa et al., 2015).

A study by Irvine and Blakemore (2008) also supports the fact that immediate remyelination of demyelinated axons protects the axons against demyelination associated axonal degeneration. In this study, the brains of experimental mice were exposed to X-irradiation (a process that inhibits remyelination) prior to cuprizone intoxication (a process that induces myelin damage by killing oligodendrocytes). Experimental results of another study by Staal and Vickers (2011) supports the fact that myelinated axon bundles are less vulnerable to stretch injury as compared to the non-myelinated ones. In this study, axon bundles of neuronal culture were exposed to stretch injury by the application of a 20 psi fluid pulse over a period of 13-20 ms to induce 3-6 % strain.

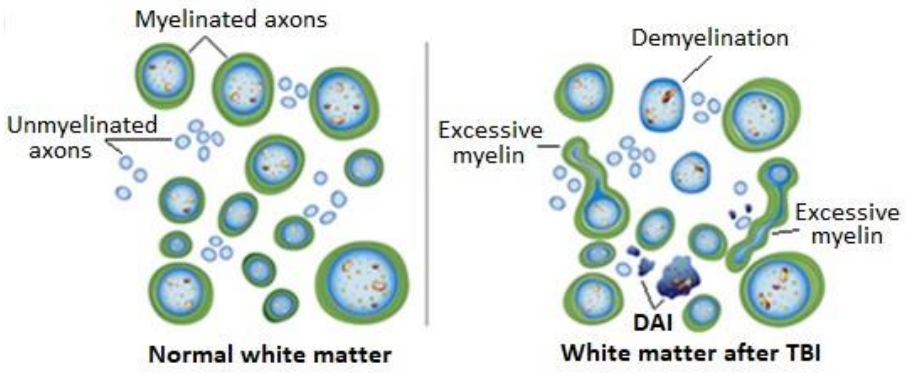

Figure 1.15: Cross sectional view of normal white matter (left) and white matter after TBI (right), illustrating normal myelinated and unmyelinated axons on the left hands side and same axons with multiple damages after TBI on the right hand side (axons are shown in blue and myelin in green) (Armstrong et al., 2016a).

Recent reviews by Armstrong et al. (2016a; 2016b) highlights the white matter pathology in terms of axon, myelin and oligodendrocyte damage and repair in quite elaborative manner. It is known that TAI/DAI is a major concern related to white matter injury resulting from TBI. Axonal projections that span long distances in white matter tracts get impaired during impact acceleration injuries to the head. The pattern of TAI is such that the injured axons remain distributed among intact axons within the white matter. TBI not only causes damage to axons, but to myelin as well. Development of axon and myelin pathology within white matter after a mTBI is shown in Figure 1.16. A three dimensional view of white matter illustrates myelinated and unmyelinated fibers along with oligodendrocyte and microglial cell. This figure displays the arrangement of fibers at different stages, i.e. from normal to mild then to moderate and then to severe damage, along with the enlarged sectional views of transportation through ultrastructural elements, such as microtubules and neurofilaments. Generally, axon and myelin pathology proceed sequentially. After an injury, the pathology starts from degeneration of unmyelinated fibers and progresses with damage of myelinated fibers at nodes of Ranvier. This initial phase of axon damage undergoes recovery and is reversible. Axons that do not recover and proceed towards degeneration cause swellings, atrophy of distal segments of axons and disruption of ensheathing myelin. Mitochondrial swelling, myelin collapse and cytoskeleton breakdown are the common features of axonal damage. Further, secondary processes can cause demyelination of intact axons, neuroinflammation and microglial activation, which may result in additional axonal degeneration that initiates at nodes of Ranvier. Proceeding axonal damage leads to irreversible degeneration and causes disconnected ends, commonly known as axon bulbs. Cytoskeleton debris and other transport materials, such as vesicles are found accumulated at the sites of swelling after a mTBI. Thus, demyelination can result in desynchronization of neural network. It further contributes to a variety of symptoms and specifically, diminished information processing speed. However, remyelination can restore the ability of denuded axons to get back the accurate

information processing speed. Thus, this might be a contributing factor in the high rate of symptom resolution in mTBI patients. However, extensive axonal degeneration in white matter may result in prolonged symptoms and vulnerability to chronic neurodegeneration.

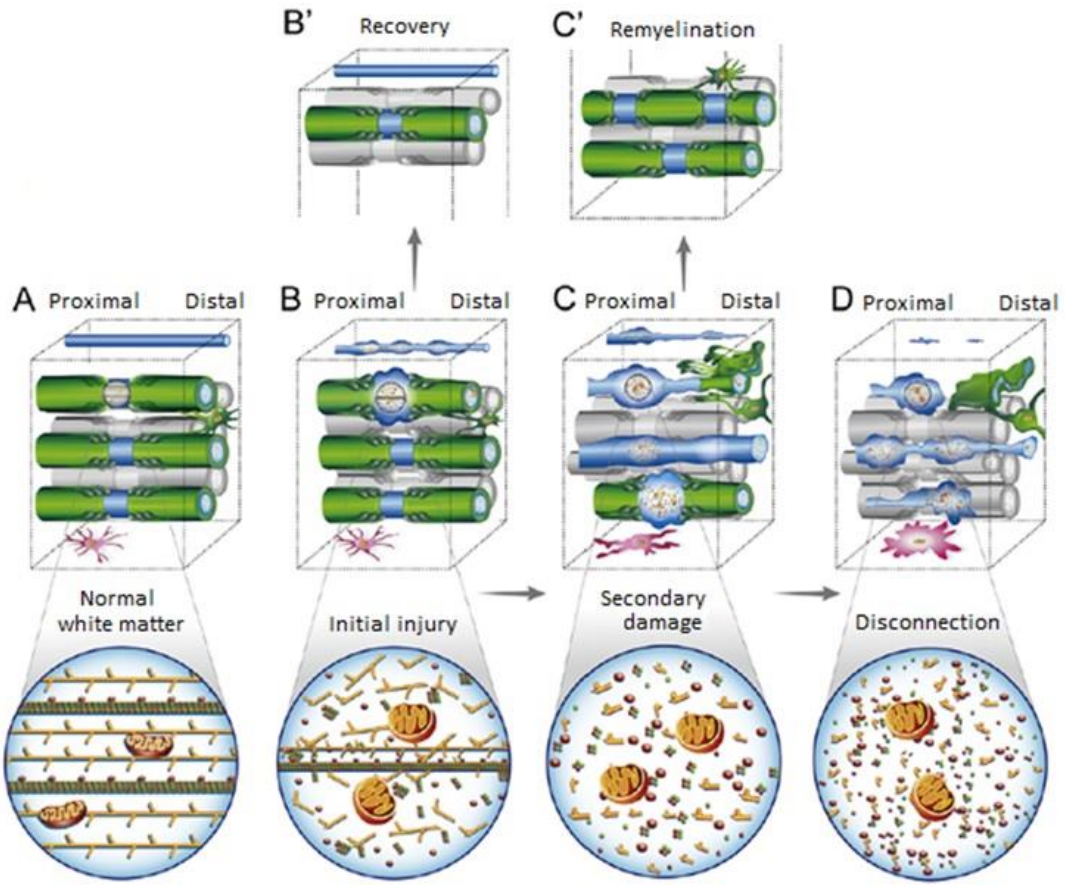

Figure 1.16: Progression of axon and myelin pathology in white matter after mild traumatic brain injury. White matter blocks show axon in blue, myelin around axons in green, oligodendrocyte as green cell and the microglial cell in pink. The enlargements show microtubules as brown and green structures carrying small brown elements i.e. vesicles, neurofilaments as yellow structures with side arms and mitochondria as red surface structures with yellow curved element inside. (Armstrong et al., 2016a).

2.4. Microtubule disruption

Microtubules are one of the most important components of axonal cytoskeleton, which assist in axonal transportation. It is believed that dynamic stretch causes axonal undulations and induces microtubule rupture at specific locations and eventually, microtubule depolymerization. Figure 1.17 shows the typical mechanism of microtubule rupture and varicosity formation after a TBI.

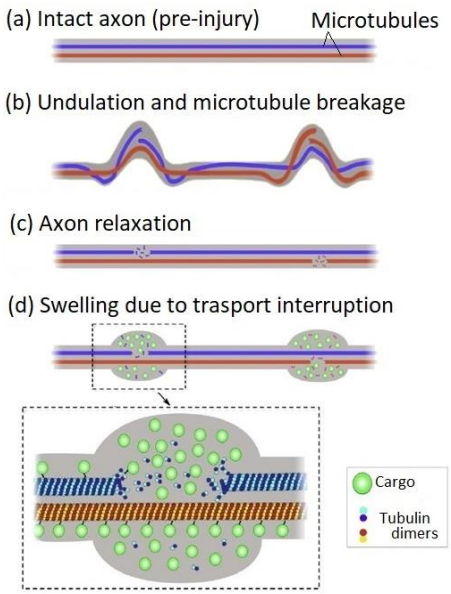

Figure 1.17: Varicosity formation mechanism after TBI; (a) intact axon, (b) disrupted axonal cytoskeleton, (c) axon relaxation and (d) varicosity formation (Tang-Schomer et al., 2012).

Axons return back to their straight position after stretch, but only after getting injured mechanically. Typically, this is evident from the subsequent focal swellings along the length of the axons within a few hours after trauma. These swellings are known as varicosities and are usually found to be filled with tubulin along with other transporting materials. Thus, loss of microtubule subsequently leads to transport interruption and ultimately to axon degeneration.

Tang-Schomer et al. (2010; 2012) performed in vitro experiments on micro-patterned neuronal cell cultures, placed on a silicon membrane, to induce dynamic tensile elongation exclusively to axon bundles. Mechanical strains of 30%, 50%, 70% and 75% were induced through controlled mechanical pressure loading of 1-30 ms duration and at a fixed strain rate of 44 per second. It is not yet clearly known that whether the damage to axon cytoskeleton after dynamic stretch is due to direct mechanical disruption or if it is a result of biochemical processes. Hence, in these studies, immediate and evolving effects of a dynamic stretch applied to axon bundles were examined. After an experimental injury, microtubule disruptions can be clearly seen through transmission electron micrograph (TEM) with or without immunohistochemistry (Figure 1.18). With regard to microtubules, the experimental results show that most of the time, the microtubules rupture at the peak points in undulations. Ruptured microtubules display frayed free ends just like depolymerizing ends of shortening microtubules. Some portions of microtubules can be found twisted. However, it was observed that not all the microtubules get ruptured at an undulating location.

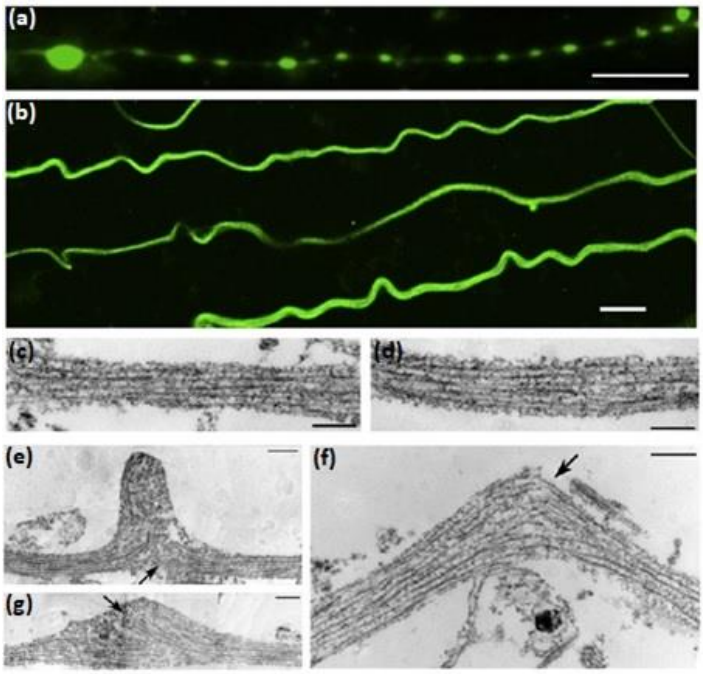

Figure 1.18: (a) Immunofluorescent image of an injured axon (3 h post dynamic stretch injury) displaying a series of swellings along the axonal length like beads on a string (scale bar: 10 µm); (b) Immunofluorescent image of injured axons (within 2 min post dynamic stretch injury) displaying multiple axons with undulations (scale bar 5 µm approximately), (c-d) Regions of uninjured axons with intact microtubules aligned parallelly and (e-g) TEM images (within 2 min post dynamic stretch injury) displaying injured axons with ruptured, unorganized, distored and twisted microtubules with discrete breaks (arrows) (scale bars: 500 nm) (Tang-Schomer et al., 2012).

Study by Tang-Schomer et al. (2012) suggested that although the transport within an axon may get blocked due to some broken microtubules, yet it can continue in the same region via other intact microtubules. Partial disruption of the transport at multiple places along the length of an injured axon could be the reason behind varicosities, a frequent feature of TBI. Broken microtubule at region of axonal undulation and highly dense accumulation of transport material in swollen areas are very common. Intrinsically, broken microtubules inhibit the relaxation of axons to their pre stretch length. However, depolymerization of broken microtubules may allow axons to relax back to their linear structure. Rupture or depolymerization of microtubules is not the only cause for microtubule disruption, it can also happen due to disarrangement of the microtubules. This disarrangement of the microtubules can be a result of defective Tau proteins, which otherwise is a microtubule stabilizer that keeps microtubules properly bound together. However, defective Tau protein is not an immediate consequence of TBI. Normally, it is evident only at a much later stage.

Another study by Ouyang et al. (2013) points out that microtubules are the main cytoskeleton component that contribute the most to the axonal stiffness. Microtubules also provide a supporting platform to other cytoskeleton components, such as neurofilaments and microfilaments. A

comparison of experimental results showed that the microtubule disrupted axons resulted in the lowest elastic modules.

2.5. Filament disruption

Microfilaments and neurofilaments are part of axonal cytoskeleton. It is believed that the spatial arrangement of the constituents of a cell is ensured by the wellbeing of cytoskeleton. Polymerization and depolymerization of an individual component can not only influence the network arrangement, but can also lead to alteration of mechanical properties of the cell. Experimental studies (Jafari et al., 1997, 1998; Ouyang et al., 2013; Fournier et al., 2014) have shown that after a stretch injury, filaments get disrupted. Some of the primary consequences of stretch injury are disarrangement of filaments, changes in the density of filaments at a particular location, loss of filaments and changes in the spacing between filaments etc., all of which could successively result in impaired neural behaviour.

2.6. Mitochondrial swelling

Mitochondria is an organelle containing enzymes responsible for producing energy. It has been found that axons after exposure to mechanical loading or strain caused by mTBI, at first experience focal perturbation of axolemma, followed by mitochondrial swelling (Maxwell et al., 1997). In other words, as explained earlier (Giza and Hovda, 2001), it has been found that right after an injury to the brain, axonal stretching, disruption of neuronal membrane and opening of voltage dependent potassium channels occur that lead to indiscriminant release of neurotransmitters and ionic fluxes. Subsequently, binding of some transmitters with certain receptors causes neuronal depolarization with efflux of potassium and influx of calcium. This excessive intracellular calcium can be sequestered in mitochondria and result in impaired oxidative metabolism, which ultimately results in mitochondrial swelling and energy crises. Alike filaments, not many studies are available specifically focusing on mitochondria behaviour after a mTBI.

2.7. Conclusion

To observe the post-injury response of axonal cytoskeleton elements, usually, stretch injuries are induced in axon bundles of cell cutlers by the application of controlled pressure loading. In spite of frequent studies, there is no universally accepted list of potential injury mechanisms for concussion or the exact sequence in which they occur. A review by Fehily and Fitzgerald (2017) can be referred to see the summary of outcomes and key findings of repetitive mTBI studies based on adult rodents. The complexity of brain, inability of current structural neuroimaging techniques in identifying ultrastructural details and complicated processes involving structural, biological, chemical and

electrical changes inside the brain makes the unavailability of global consensus in this regard understandable. After having understood potential injury mechanism for concussion, let us now look at various brain injury grading scales, criteria and tolerance limits available in literature.

3 Brain injury: grading scales, criteria and tolerance limits

3.1. Introduction

Injury, whether mild, moderate or severe, is a clear indicator of health deterioration. Injury grading scales help in identifying the severity of an injury based on the signs and symptoms expressed by the injured subject. On the other hand, injury criteria are the predictors based on some parameter values, which help in identifying the level of injury in a particular situation. Based on the predicted values through various studies, tolerance limits for different kind of injuries have been reported in literature. This section sheds light on the concussion grading scales, existing head/brain injury criteria and the tolerance limits available in literature.

3.2. Concussion grading scales

There are a number of concussion grading scales available in literature. However, many of those became obsolete with time. As reported by Cantu (2001), obsolete concussion scales based on the signs and symptoms shown by the injured person are:

- Nelson grading system for concussion, based on a five point scale, from disorientation to loss of consciousness, by Nelson et al. (1984)
- Ommaya grading system for concussion, based on a six point scale, from confusion to coma and death, by Ommaya (1985)
- Cantu grading system for concussion, based on a three point scale, from amnesia to loss of consciousness, by Cantu (1986)
- Jordan grading system for concussion, based on a four point scale, from confusion to loss of consciousness, by Jordan et al. (1989)
- Colorado Medical Society grading system for concussion, based on a three point scale, from confusion to loss of consciousness, in 1990
- Torg grading system for concussion, based on a six point scale, from confusion to death, by Torg (1991)

- Roberts grading system for concussion, based on a four point scale, from disorientation to loss of consciousness, by Roberts (1992)
- AAN practice parameter based grading system for concussion, based on a three point scale, from transient confusion to loss of consciousness, by Kelly et al. (1997).

A detailed description of grading for each of these is given in Annexure A. All these scales graded concussion on different levels. However, all of these were based on measurements of coma, loss of consciousness, amnesia and other symptoms such as disorientation, headache, dizziness and confusion etc. Duration was considered as important as the occurrence of any of these signs and symptoms. As mentioned earlier, these scales can measure the severity of concussion only after it has already occurred. These have nothing to do with the prevention of first occurrence of concussion, however, with the help of these grading, reoccurrence of concussion can be avoided by proper management.

Cantu grading system was modified in 2001 to include not only a checklist of 21 concussion signs and symptoms, but also the guidelines for return to play after concussion. At present, most widely used concussion grading scale is known as Sport Concussion Assessment Tool (SCAT), which is available for adults as well as for children. Its recent available versions are known as SCAT5 (Echemendia et al., 2017a, 2017b) for adults and child SCAT5 (Davis et al., 2017a, 2017b) for children. It was developed by concussion in sports group, to be used by medical professionals and is supported by International Ice Hockey Federation (IIHF), Fédération Internationale de Football Association (FIFA), Olympics, World Rugby and Fédération Équestre Internationale (FEI). It assesses the memory based on Maddocks questions (Table 1.1) (Maddocks et al., 1995). A higher correct response count on Maddock's questionnaire indicates better condition of the athlete.

Table 1.1: Maddock's questions for the memory assessment (Echemendia et al., 2017b).

Question No.	Question	Correct answer	Incorrect answer
1	What venue are we at today?	1 point	0 point
2	Which half is it now?	1 point	0 point
3	Who scored last in this match?	1 point	0 point
4	What team did you play last week/game?	1 point	0 point
5	Did your team win the last game?	1 point	0 point

The visual, verbal and motor responses are assessed based on Glasgow Coma Scale (GCS) (Table 1.2) (Teasdale and Jennett, 1974). For GCS also, better the response, higher the score and better the

condition of the athlete. Other assessments are made for concussion signs and symptoms, cognitive capabilities in terms of orientation and immediate memory, concentration, balance and delayed recall.

Table 1.2: Glasgow coma scale examination (Echemendia et al., 2017b).

Eye/visual response	**Points**
No eye opening	1
Eye opening in response to pain	2
Eye opening to speech	3
Eyes opening spontaneously	4
Verbal response	**Points**
No verbal response	1
Incomprehensible sounds	2
Inappropriate words	3
Confused	4
Oriented	5
Motor response	**Points**
No motor response	1
Extension to pain	2
Abnormal flexion to pain	3
Flexion/Withdrawal to pain 4 4	4
Localizes to pain	5
Obeys commands	6

The Abbreviated Injury Scale (AIS) is another injury grading scale that is not specifically for brain injury or concussion alone, but for injuries related to entire human body. This was developed in 1960's by a group of 75 specialists from around the world. It was introduced in 1971 and revised in 1976, 1980, 1985, 1990, 1998, 2005, 2008 and 2015. It is an anatomy based coding system, which does not assess the severity of injury, but the threat to life associated with an injury and it is the universally accepted standard for assessing the threat to life from an injury. It is a seven digit code, which describes the location of injury, the type of injury and the severity of injury all together. First digit specifies the body region, second digit specifies the type of anatomical structure, third and fourth digits specify the exact anatomical structure, fifth and sixth digits specify the level of injury and the seventh digit specifies the abbreviated injury score. This is the most widely used injury severity assessment score as it directly corresponds to the threat to life. As an example, for concussion with loss of consciousness, an abbreviated injury scale can be represented by ABCDEF.G = 161000.1, where A = 1, which indicates head; B = 6, which indicates loss of consciousness; CD = 10, which indicates concussion; EF = 00, which

indicates injury NFS (not further specified) and G = 1, which indicates minor injury. Table 1.3 provides the code for seventh digit of AIS code.

Table 1.3: Abbreviated injury score i.e. the seventh digit of AIS code.

Score value	Description of injury severity	Threat to life
1	Minor	0%
2	Moderate	1% to 2%
3	Serious	8% to 10%
4	Severe	5% to 50%
5	Critical	> 50%
6	Maximum	100 %

That is how injury grading scales help in identifying the occurrence and severity of concussion. This identification is based on the signs and symptoms expressed by the injured person and can only help in better managing the consequences of concussion, but cannot prevent it. Return to play policy is one such management, which, based on the response and condition of the athlete over a period of time, helps in deciding if the athlete can return to play or not and to what level of activity. The main limitation of these grading scales is that it is very subject specific. It is not always necessary that the injured person communicates the disease well, the person recording the details perceives it well and the medical report is absolutely accurate. Human error factor always plays some role. Having said that, it is but natural to think of some criteria or thresholds, which not only help in identifying the situation in which a concussion can occur, but also provide some guidelines, such as tolerance limits, so that every necessary measure can be taken to reduce the chances of injury. And that is why a better metric for the quantification of concussion is needed. Let us look at some existing head/brain injury criteria and tolerance limits.

3.3. Existing head/brain injury criteria and tolerance limits

Brain injury criteria, interchangeably referred to as head injury criteria, are nothing but ways of predicting the severity of an impact in terms of global mechanical parameters. Enormous studies have been done over the last six decades for the understanding of head injury biomechanics. The earliest records of research on head injury criteria date back to late 1950s and early 1960s. This is when the researchers started to quantify the injury in terms of mechanical correlation to be able to standardize the grading of injury severity. Initially, only the linear acceleration of head was chosen as the governing factor. However, importance of rotational head kinematic as well as combined linear and rotational head kinematics was understood and incorporated in the derivation of different injury criteria later.

In last few decades, the focus has shifted from global kinematic parameters and many model based injury criteria have come into picture. These criteria are based on tissue level injury parameters, such as stress, strain, strain rate, strain energy, pressure and force. In the following section, a brief description of these global kinematic parameter and tissue level injury parameter based head/brain injury criteria is given.

3.3.1. Global kinematic parameter based injury criteria

Global kinematic parameter based criteria are further subdivided into three categories. First, is based only on linear kinematic parameters; second, only on rotational kinematic parameters and third, on both linear and rotational kinematic parameters. Details of these criteria are given in the following subsections.

- **Linear kinematic parameter based criteria**

Studies by a team at Wayne State University, around 1960s, proved to be the basis for all future studies related to head injury criteria. In 1954, a research was funded in Wayne State University by Ford, to find out the human tolerance to head injuries, with the objective of improving motor vehicle safety. In 1960, study by Lissner and colleagues extended this research and the very first head injury tolerance curve came into picture (Rowson and Rowson, 2018). This tolerance curve was further extended by Gurdjian et al. (1966) and is now commonly known as Wayne State Tolerance Curve (WSTC). As shown in Figure 1.19, WSTC is an acceleration versus time curve, based on experiments.

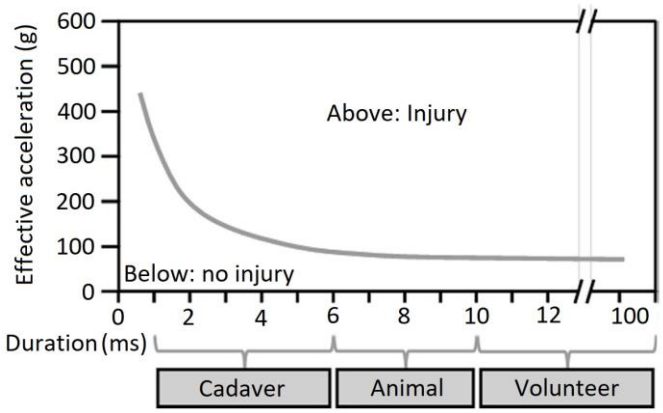

Figure 1.19: Diagram representing Wayne State Tolerance Curve (WSTC) indicating tolerance limit based on resultant linear acceleration magnitude and duration (Rowson and Rowson, 2018).

This tolerance curve indicated that high magnitude accelerations can be tolerated by a human head only if the duration is short enough and the magnitude of acceleration has to be really short in case the impact duration exceeds 10-15 milliseconds. After many revisions, the final WSTC was developed

by combining the results based on various pulse shapes, animals, cadavers, human volunteers, clinical research data and injury mechanisms (Fernandes and de Sousa, 2015). However, the study took into account only the resultant linear acceleration.

Another study by Gadd (1966) was based on the WSTC and proposed an impulse integration procedure for the estimation of the injury hazard. This study took into account the relative importance of intensity and the time of pulse. The severity index proposed by Gadd is commonly known as Gadd's Severity Index, GSI or SI and is expressed as in Equation 1.6.

$$G(SI) = \int_0^T a^{2.5}\, dt \qquad 1.6$$

Where, a is the magnitude of acceleration pulse in gravity unit g, T is the duration of acceleration pulse in seconds and t is the time in seconds. An index of 1000 was supposed to be the threshold for a serious internal injury in case of frontal impacts. Estimated tolerance levels for mTBI/Concussion in terms of Gadd's severity index are given below in Table 1.4 and in terms of peak linear accelerations in Table 1.5.

Table 1.4: Estimated tolerance levels for mTBI/Concussion in terms of GSI.

Tolerance	Description	Reference
5% probability: GSI = 23.5 50% probability: GSI = 291.2 95% probability: GSI = 558.9	24 cases of helmeted head impact from American football (9 concussed) replicated with Hybrid III ATDs	Newman et al., 2000a
GSI = 474	31 cases of helmeted head impact from NFL (25 concussed) replicated with Hybrid III ATDs	Pellman et al., 2003
GSI = 267	Based on data from 3312 impacts from 38 players from American collegiate football (1 concussion)	Duma et al., 2005

Table 1.5: Estimated tolerance levels for mTBI/concussion in terms of peak linear acceleration (Fernandes and de Sousa, 2015).

Tolerance	Description	Reference
5% probability: a = 392 m/s^2 (40 g) 50% probability: a = 762 m/s^2 (78 g) 95% probability: a = 1131 m/s^2 (115 g)	24 cases of helmeted head impact from American football (9 concussed) replicated with Hybrid III ATDs	Newman et al., 2000a
25% probability: a = 559 m/s^2 (57 g) 50% probability: a = 778 m/s^2 (79 g) 75% probability: a = 965 m/s^2 (98 g)	53 cases of helmeted head impact from American football (22 concussed) replicated with Hybrid III ATDs	King et al., 2003
a = 85 g (834 m/s^2) (duration: 10-30 ms)	24 cases of helmeted head impact from American football (9 concussed) replicated with Hybrid III ATDs	Zhang et al. 2004

Tolerance	Description	Reference
a = 81 g (795 m/s^2)	Based on data from 3312 head impacts from 38 players from American collegiate football (1 concussion)	Duma et al., 2005
a = 60.51 – 168.71 g (594 – 1655 m/s^2)	Based on data from 100,000 head impacts from 88 collegiate football players (13 concussions)	Guskiewicz et al., 2007
a = 96.1 g (943 m/s^2)	Based on data from 54,247 football related head impacts from 78 high school athletes (13 concussions)	Broglio et al., 2010
50% probability: a = 190 - 200 g (1864 - 1962 m/s^2)	Based on data from 62,974 sub-concussive and 32 concussive head impacts from collegiate and professional football linked to injury rates	Rowson and Duma, 2011
a = 73.6 ± 21 g (722 ± 20 m/s^2)	Based on data from 10 concussed athletes from high school and college football and college ice hockey	McAllister et al., 2012
50% probability: a = 65.1 g (639 m/s^2) 75% probability: a = 88.5 g (868 m/s^2)	Based on data from rigid body reconstructions of 27 concussion cases from Australian football and rugby league	McIntosh et al., 2014

a: Peak linear acceleration; ATD: anthropomorphic test dummy

In 1971, Versace criticized the severity index and proposed a correction, which proved to be the foundation of the head injury tolerance limit. This limit proposed by Versace (1971) was modified by National Highway Traffic Safety Administration (NHTSA) in 1999 and this modified version became the universally adopted criterion to access head injury severity. This criterion is known as Head Injury Criteria or HIC as expressed in Equation 1.7 and is frequently being used till date.

$$HIC = max\left[\frac{1}{t_2 - t_1}\int_{t_1}^{t_2} a(t)\,dt\right]^{2.5}(t_2 - t_1) \qquad 1.7$$

Where $a(t)$ is the magnitude of resultant linear acceleration in gravity unit (g) at time t and t_1 and t_2 are the times of beginning and end of the pulse in seconds. However, HIC only takes linear acceleration into consideration and has its own limitations. Hence, it cannot be very useful in every situation. HIC threshold values for mTBI/concussion are given in Table 1.6.

Table 1.6: Estimated tolerance levels for mTBI/concussion in terms of HIC (Fernandes and de Sousa, 2015).

Tolerance	Description	Reference
50% probability: HIC_{15} = 240 95% probability: HIC_{15} = 485	24 cases of helmeted head impact from American football (9 concussed) replicated with Hybrid III ATDs	Newman et al., 2000a

Tolerance	Description	Reference
25% probability: HIC_{15} = 136 50% probability: HIC_{15} = 235 75% probability: HIC_{15} = 333	53 cases of helmeted head impact from American football (22 concussed) replicated with Hybrid III ATDs and WSTC FEHM	King et al., 2003
HIC_{15} = 381	31 cases of helmeted head impact from NFL (25 concussed) replicated with Hybrid III ATDs	Pellman et al., 2003
HIC_{15} = 240	24 cases of helmeted head impact from American football (9 concussed) replicated with Hybrid III ATDs	Zhang et al. 2004
HIC_{15} = 200	Based on data from 3312 impacts from 38 players from American collegiate football (1 concussion)	Duma et al., 2005

- **Rotational kinematic parameter based injury criteria**

Takhounts et al. proposed a Brain Rotational Injury Criterion, commonly known as BrIC, which was first proposed in 2011, based on maximum angular velocity and acceleration as given in Equation 1.8 and then in 2013, which took into account the directional dependence of angular velocity as expressed in Equation 1.9.

$$BRIC = \frac{\omega_{max}}{\omega_{cr}} + \frac{\alpha_{max}}{\alpha_{cr}} \quad 1.8$$

Where, ω_{max}, ω_{cr} are the maximum and critical angular velocities and α_{max} and α_{cr} are maximum and critical angular accelerations respectively. ω_{cr} and α_{cr} for ATDs (anthropomorphic test dummy) were identified to range between 46.41 to 153.18 rad/s and 11,527.92 to 39,774.87 rad/s^2; and those for college football players were identified to be 42.05 rad/s and 363,268.91 rad/s^2 respectively. It was concluded that BRIC varies between 0.60 and 0.68 for Concussive (AIS 2+) injuries.

$$BrIC = \sqrt{\left(\frac{\omega_x}{\omega_{xC}}\right)^2 + \left(\frac{\omega_y}{\omega_{yC}}\right)^2 + \left(\frac{\omega_z}{\omega_{zC}}\right)^2} \quad 1.9$$

Where, ω_x, ω_y and ω_z are the maximum angular velocities along X, Y and Z axes respectively; ω_{xC}, ω_{yC} and ω_{zC} are the critical angular velocities along X, Y and Z axes respectively. These criteria were based on cumulative strain damage measures (CSDM) and maximum principal strain (MPS) to identify the probability of injury for a specific AIS level of injury severity. Critical maximum angular velocities, for ATDs and humans, in corresponding directions were identified to be 66.25 rad/s, 56.45 rad/s and 42.87 rad/s. Average critical value of BrIC for ATDs and humans was reported to be between 0.8 and

1.06. Brain injury risk curves for CSDM and MPS based BrIC for various AIS levels can be referred through Takhounts et al. (2013).

The most recent metric to predict brain strain response using kinematics of head is developed by Gabler et al. (2018). It is called universal brain injury criterion (UBrIC). This is based on the assumption that under rotational head motion, the maximum brain deformation can be considered analogous to the deformation from a second order system under excitation. As reported by Gabler and colleagues, this is applicable to wide range of kinematics encountered automotive and sport accidents. It is estimated as given in Equation 1.10.

$$UBrIC = \left\{\sum_i \left[\omega_i^* + (\alpha_i^* - \omega_i^*) e^{-\frac{\alpha_i^*}{\omega_i^*}}\right]^r\right\}^{\frac{1}{r}} \quad 1.10$$

Where, ω_i^* and α_i^* are the maximum magnitudes of head angular velocity and acceleration, corresponding to directions x, y and z (i = x, y, z), normalized by a corresponding critical value. This means $\omega_i^* = \omega_i / \omega_{icr}$ and $\alpha_i^* = \alpha_i / \alpha_{icr}$. The exponent r establishes the power to evaluate the magnitude. In this study, model performance was evaluated for two values of r, i.e. one and two. Total six parameters and corresponding six critical values were used to develop a complete 3D form of UBrIC. Using a database of 1595 head impacts (based on dummies, cadavers and volunteers), the critical angular velocities and angular accelerations in corresponding directions were found to be as given below in Table 1.7.

Table 1.7: Critical values for UBrIC metrics (Gabler et al., 2018).

Metrics	ω_{xcr} (rad/s)	α_{xcr} (krad/s^2)	ω_{ycr} (rad/s)	α_{ycr} (krad/s^2)	ω_{zcr} (rad/s)	α_{zcr} (krad/s^2)
UBrIC MPS	211	20.0	171	10.3	115	7.8
UBrIC CSDM	117	17.7	119	7.0	85.8	6.5

Table 1.8 provides the human brain tolerances to mTBI/concussion in terms of rotational acceleration and velocity as consolidated by Fernandes and de Sousa, 2015.

Table 1.8: Estimated tolerance levels for mTBI/concussion in terms of rotational acceleration and velocity (Fernandes and de Sousa, 2015).

Tolerance	Description	Reference
> 99% probability: α = 7500 rad/s^2 (duration: > 6.5 ms)	Based on experimental animal data scaling	Ommaya et al., 1967

Tolerance	Description	Reference
50% probability: α = 1800 rad/s^2 (duration: < 20 ms)	Based on experimental animal data scaling	Ommaya and Hirsch, 1971
α = 13600 – 16000 rad/s^2 ω = 25 – 48 rad/s	Based on data of 45 head blows from volunteer boxers (5 fights, 3 rounds each); exact injury type not specified	Pincemaille et al., 1989
5% probability: α = 3377 rad/s^2 50% probability: α = 6322 rad/s^2 95% probability: α = 9257 rad/s^2	24 cases of helmeted head impact from American football (9 concussed) replicated with Hybrid III ATDs	Newman et al., 2000a
α = 4500 - 18000 rad/s^2	Based on experimental animal data scaling	Ommaya et al., 2002
25% probability: α = 4384 rad/s^2 50% probability: α = 5757 rad/s^2 75% probability: α = 7130 rad/s^2	53 cases of helmeted head impact from American football (22 concussed) replicated with Hybrid III ATDs and WSTC FEHM	King et al., 2003
α = 6432 rad/s^2	31 cases of helmeted head impact from NFL (25 concussed) replicated with Hybrid III ATDs	Pellman et al., 2003
25% probability: α = 4600 rad/s^2 50% probability: α = 5900 rad/s^2 80% probability: α = 7900 rad/s^2 (duration: 10-30 ms)	24 cases of helmeted head impact from American football (9 concussed) replicated with Hybrid III ATDs	Zhang et al., 2004
α = 7912 rad/s^2	Based on data from 3312 impacts from 38 players from American collegiate football (1 concussion)	Duma et al., 2005
α = 6200 rad/s^2	Based on coronal plane angular acceleration loading experimentation on 26 rats, scaled to human equivalent from rat value of 368 krad/s^2	Fijalkowski et al., 2007a
α = 7600 rad/s^2 (duration: 15 ms) α = 7300 rad/s^2 (duration: 23 ms)	Based on coronal plane angular acceleration loading experimentation on 10 rats, scaled to human equivalent from rat value	Fijalkowski et al., 2007b
α = 5312 rad/s^2	Based on data from 100,000 head impacts from 88 collegiate football players (13 concussions)	Guskiewicz et al., 2007
α = 5582.3 rad/s^2	Based on data from 54,247 football related head impacts from 78 high school athletes (13 concussions)	Broglio et al., 2010
10% probability: α = 5260 rad/s^2 25% probability: α = 5821 rad/s^2 50% probability: α = 6383 rad/s^2 75% probability: α = 6945 rad/s^2 90% probability: α = 7483 rad/s^2	Based on data from 300,977 sub concussive and 57 concussive head impacts from 335 football players	Rowson et al., 2012
α = 5025 ± 1226 rad/s^2	Based on data from 10 concussed athletes from high school and college football and college ice hockey	McAllister et al., 2012

Tolerance	Description	Reference
50% probability: α = 1747 rad/s^2	40 head impact cases (27 concussions, 13 no injuries) from Australian football and Rugby replicated with KTH FEHM	Patton et al., 2013
50% probability: α = 1747 rad/s^2 75% probability: α = 2296 rad/s^2	Based on data from rigid body reconstructions of 27 concussion cases from Australian football and rugby league	McIntosh et al., 2014

α: rotational acceleration and ω: rotational velocity; NFL: National football league (American football)

- **Combined, linear and rotational parameters based injury criteria**

A brain injury criterion, known as GAMBIT (i.e. generalized acceleration model for brain injury threshold) was developed by Newman in 1986. GAMBIT took into account both, the linear and rotational accelerations as expressed in Equation 1.11.

$$G = \left[\left(\frac{a_{max}}{a_{cr}}\right)^2 + \left(\frac{\alpha_{max}}{\alpha_{cr}}\right)^2\right]^{\frac{1}{2}} \quad 1.11$$

Where, a_{max} is the maximum translational acceleration and α_{max} is the maximum rotational acceleration. a_{cr} and α_{cr} are the critical values of translational and rotational accelerations respectively. One of the suggested values is a_{cr} = 250 g and α_{cr} = 25000 rad/s^2. As per Newman et al., 2000a, for a 5% probability of mTBI, G > 0.22, for a 50% probability of mTBI, G > 0.39 and for a 95% probability of mTBI, G > 0.56. These values were based on the reconstruction of 24 cases of helmeted head impact from American football through Hybrid III ATD.

In the year 2000, Newman et al. proposed a new criterion for mTBI, known as HIP i.e. head impact power, based on the reconstruction of two American football players head collision via helmeted Hybrid III dummy heads. This power index (PI) takes into account head mass and the moment of inertia as well as both the linear and rotational accelerations as expressed through the generalized power index formula as in Equation 1.12.

$$PI = \left[C_1 a_x \int a_x dt + C_2 a_y \int a_y dt + C_3 a_z \int a_z dt\right] + \left[C_4 \alpha_x \int \alpha_x dt + C_5 \alpha_y \int \alpha_y dt + C_6 \alpha_z \int \alpha_z dt\right] \quad 1.12$$

Where a_x, a_y and a_z are the linear accelerations in m/s^2 and α_x, α_x and α_x are the rotational accelerations in rad/s^2 corresponding to x, y and z axes respectively and t is the duration of impact in seconds. When the coefficients C_i are set as C_1 = C_2 = C_3 = 4.5 kg i.e. the head mass; C_4 = 0.016 Nms^2, C_5 = 0.024 Nms^2 and C_6 = 0.022 Nms^2 i.e. the corresponding head moment of inertia; PI becomes HIP (Equation 1.13). Where the inertial reference frame is that of the head itself.

$$HIP = 4.5\left[a_x \int a_x dt + a_y \int a_y dt + a_z \int a_z dt\right] + \left[0.016\,\alpha_x \int \alpha_x dt + 0.024\,\alpha_y \int \alpha_y dt + 0.022\,\alpha_z \int \alpha_z dt\right] \quad 1.13$$

Where, a and α are corresponding linear and rotational accelerations in m/s^2 and rad/s^2 respectively. As per Newman et al., 2000b, for 5% probability of mTBI, HIP_{max} = 4.7 kW, for 50% probability of mTBI, HIP_{max} = 12.79 kW and for 95% probability of HIP_{max} = 20.88 kW. These values were based on the reconstruction of 24 cases of helmeted impact from American football through Hybrid III ATD.

Rowson and Duma (2013) developed a concussion injury risk function as a brain injury predictor by assessing the combined probability of concussion, utilizing linear and rotational accelerations of head. This was based on the data collected from 62,974 head impacts (37 concussions) from instrumented football players and adapted to take into account the underreporting of concussion. Figure 1.20 illustrates this brain injury risk function as given in Duma and Rowson (2014).

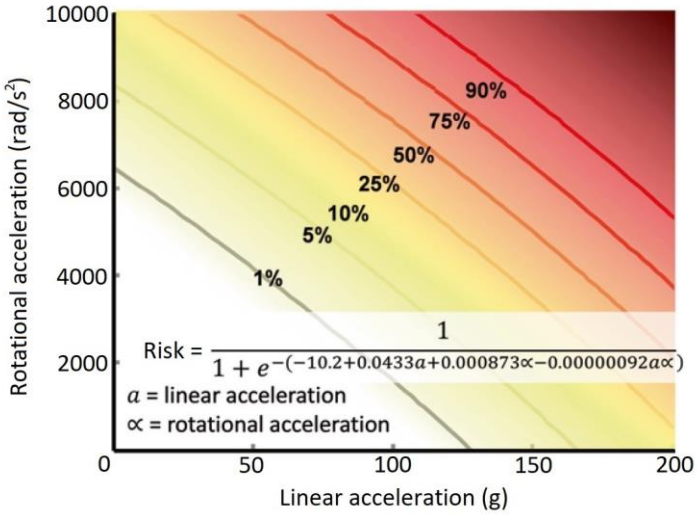

Figure 1.20: Concussion injury risk function highlighting combined probability of concussion contours based on the combination of linear and rotational accelerations (Duma and Rowson, 2014).

Recently, Antona-Makoshi et al. (2016) proposed a brain injury criterion for moderate and mild traumatic brain injuries and called it BITS i.e. Brain Injury Threshold Surface. This criterion took into account the translational and rotational kinematics as well as the time. A schematic diagram was provided to illustrate existing criteria and thresholds, all combined in one (Figure 1.21).

All these characteristics, as given in Figure 1.21, were captured into one simple generic surface equation as expressed in Equation 1.14.

$$\left(\frac{a}{C_1}\right)^2 + \left(\frac{\alpha}{C_2}\right)^2 - \left(\frac{C_3}{\Delta T}\right)^2 = 1 \quad 1.14$$

Where, a and α are the peak linear and rotational resultant accelerations of head respectively. ΔT is the duration of acceleration and C_1, C_2 and C_3 are the constant positive critical values having the same units as their corresponding variable. These critical values were chosen from their previous studies and ranged between 150-1300 g for C_1, 5500-55000 rad/s^2 for C_2 and 2-12 ms for C_3. 43 head impact experiments conducted on 15 monkeys were simulated.

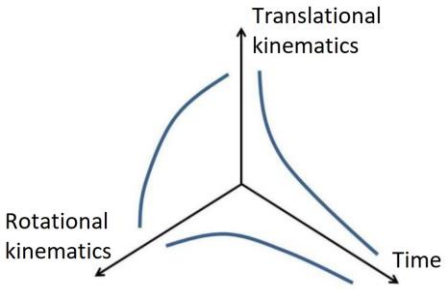

Figure 1.21: Combined translational and rotational head kinematics measures as well as time, all in one schematic diagram as given by Antona-Makoshi et al. (2016).

Based on simulation results, the accuracy of an injury was calculated by summing up the True Positives and True Negatives and dividing the sum by total number of observations as per the definition given below in Table 1.9.

Table 1.9: Definition to find out the accuracy of injury (Antona-Makoshi et al., 2016).

	Above surface	Below surface
Concussion	True Positive	False Negative
No concussion	False Positive	True Negative

This section provided an overview of kinematic parameter based head/brain injury criteria and estimated tolerance levels through various studies. It is evident that no single parameter can predict the biomechanics of injury with absolute accuracy. However, when multiple kinematic parameters, such as linear and rotational accelerations, along with time are taken into account together the predictions are close to reality. We can observe from the data given above that the reported values vary over a wide range. Some of the studies, in spite of being based on the same database, estimated different tolerance levels. There could be various reasons for this difference. At first, the very basic difference could be the assumed definition of concussion. We know that there does not exist a consensus for the definition of concussion. Hence, various researchers hypothesize different definitions for their studies. This variation in definition could definitely result in different estimated tolerance levels. Other reasons could be the differences in methodology, experimental protocol, chosen subject (i.e. human, cadaver, animal, dummy etc.) and method of analysis. These criteria could

not estimate the injury precisely and hence, a need for a better metric for the prediction of concussion arose. These factors lead to tissue level injury parameter based injury criteria. Finite element models have been very efficient in studying injury biomechanics. These models made it possible to derive tissue level injury parameter based injury criteria. Let us now have a look at these criteria.

3.3.2. Tissue level injury parameter based injury criteria

In the last few decades, computational models had been used to identify the injury tolerances in terms of mechanical parameters. These parameters can be extracted as a simulation outcome for any real world accidental or experimental scenario. Thus, the mechanical loading sustained by the brain tissue can be compared to the actual injuries reported medically. There are evidences in literature that the mechanical responses predicted by computational models more or less agree with the location and severity of the injuries described in the medical reports (Deck and Willinger, 2009). With regard to the cause of brain injury, it was hypothesized that the injury mechanism is governed by the brain response and not by the input acceleration (King et al., 2003). Hence, the mechanical response parameters of finite element head/brain model, specifically the strain rate should be investigated (King et al., 2003). Hence, this section details available tissue level injury parameter based injury criteria.

In 2003, Takhounts et al. (2003a) developed a software package, known as SIMon (Simulated Injury Monitor), to interpret the injury mechanism based on the dynamic data measured through experimentation on dummy and by implementing this measured data into the computational human model imbedded in SIMon. Three linear accelerations and three angular velocities of the head's center of gravity served as the input for the finite element human head model of SIMon (SIMon FEHM), in order to calculate the injury metrics. For diffuse axonal injury (DAI), a correlate, cumulative strain damage measure (CSDM) was calculated. The CSDM was based on the hypothesis that the DAI is linked to the cumulative volume of the brain tissue, which experiences tensile strains over a predefined critical level. From the animal data available in literature, it was found that when the 55% of the brain volume undergoes a strain of 15%, there is a 50% chance of concussion. On comparing this level of strain with what is observed in humans, the critical CSDM level was found to range between 40 to 70%. However, because of the lack of region specific experimental data, this version of CSDM assumed that every brain region contributes uniformly in the assessment of DAI and did not take into account the functional importance of different brain regions. Takhounts et al. (2008) investigated the traumatic brain injuries with a modified model and called it the next generation of SIMon FEHM. The brain of this modified model comprised of various parts. Based on 68 observations, two injury measures for DAI were provided. Probability of DAI can be calculated either based on CSDM or maximum principal strain. For a 50% probability of DAI, CSDM (0.25) was found to be 54% and the

MPS was found to be 0.87. CSDM (0.25) indicates the volume fraction of brain that experiences the maximum principal strain value of 25% or higher. It was concluded that CSDM (0.25) and MPS correlates well with the DAI (observed from animal tests available in literature). Based on impact simulations of 24 football players, it was found that biomechanical injury better correlates with the angular acceleration and angular velocity than with the linear acceleration. Also, the maximum principal stress did not correlate well with any of the kinematic measures. Hence, it was suggested that the angular injury criteria better predict TBI, than linear acceleration based injury criteria.

WSUHIM (Wayne State University Head Injury Model) is another finite element head model that had been used to predict injury tolerances (King et al., 2003). 22 concussion cases from NFL were reconstructed with WSUHIM, where average linear acceleration was 94 ± 27 g and average rotational acceleration was 6398 ± 1978 g. Another study on modified WSUBIM (Wayne State University Brain Injury Model) was done by Zhang et al., (2004). 24 cases of helmeted head impact from American football (9 concussed) were simulated. Peak resultant linear acceleration ranged from 61 – 144 g for injured cases with an average of 103 ± 30 g and from 32 – 102 g for non-injured cases with an average of 55 ± 21 g. Peak resultant rotational acceleration ranged from 4,168 – 12,832 rad/s^2 for injured cases with an average of 7354 ± 2897 rad/s^2 and from 2,087 ± 6265 rad/s^2 for non-injured cases with an average of 4,204 ± 1411 rad/s^2. Tolerance limits for mTBI, predicted by the studies based on WSUH/BIM are given in Table 1.10.

Table 1.10: Estimated tolerance levels for mTBI/Concussion in terms of tissue level injury parameter.

Injury predictor	Probability of mTBI			Description	Reference
	25%	50%	75-80%		
Strain x Strain rate (per second)	14	19	24	53 cases of helmeted head impact from American football (22 concussed) replicated with WSUHIM[#]	King et al., 2003
Strain rate (per second)	46	60	80		
Shear stress (kPa)	6.0	7.8	10.0	24 cases of helmeted head impact from American football (9 concussed) replicated with Hybrid III ATDs and with WSUBIM	Zhang et al., 2004
Strain	0.14	0.19	0.24		

[#] WSUH/BIM: Wayne State University Head/Brain Injury Model; ATD: anthropomorphic test dummy

Another study by Kleiven (2007) was based on the simulation of 58 NFL cases on finite element model of human head, commonly known as KTH FEHM, to compare the mTBI predictors. As the brain of KTH FEHM is made up of various parts, the partwise comparison (6 parts: brainstem, midbrain, corpus callosum, white matter, thalamus and gray matter; and for overall brain as well) was done for the mTBI predictors (8 predictors: maximum principal strain, strain rate, strain x strain rate, CSDM (0.1),

effective stress, strain energy density, maximum pressure and minimum pressure). As per the logistic regression plots of probability of concussion, based on the model response for every injury predictor after simulations of the NFL cases, it was found that for a 50% probability of concussion the regions of highest statistical significance were i) gray matter with a strain of 0.26, strain rate of 48.5 per second, strain x strain rate value equal to 10.1 per second, strain energy density of 2.1 kJ/m^3 and positive pressure equals to 65.8 kPa; ii) white matter with a CSDM (0.1) of 0.47 and negative pressure of 55.1 kPa and iii) corpus callosum with a strain of 0.21 and Von Mises stress of 8.4 kPa. However, it was concluded that the NFL database, though includes the head injury description, is not accurate enough to confidently determine the injury severity and location and hence, the need of medical imaging was highlighted. Another study, Patton et al. (2013) was also based on KTH FEHM. Finite element simulations were carried out to investigate deformation of brain tissue in case of sporting impacts to unprotected head. It was found that for a 50% chances of concussion, the mechanical thresholds of strain in thalamus, corpus callosum and white matter were 13%, 15% and 26% respectively. Study by Giordano and Kleiven (2014) was based on modified anisotropic KTH FEHM. Accident reconstruction based on the data from American National Football League (NFL: 58 accidents in total, 25 concussions and 33 with no injury), helped them conclude that maximum axonal strain best predict mTBI than any other traditional injury predictors. For corpus callosum and brainstem, a strain threshold of 7% and 15% were estimated for 50% probability of injury respectively. Latest study on the old version (not anisotropic) of KTH FEHM was based on the reconstruction of 40 unhelmeted head impacts (27 concussions and 13 no injury cases) from Australian football and Rugby leagues. For 50% chances of concussion, the estimated tolerance levels for thalamus were 2.24 kPa von Mises stress, 24 per second strain rate and 2.49 per second product of strain and strain rate. For corpus callosum, these values were 3.51 kPa, 25.1 per second and 2.76 per second respectively (Patton et al., 2015).

Dartmouth subject-specific finite element head model is another computational model that tried to correlate predicted high strain brain regions' association with diagnosed concussion. As reported in McAllister et al. (2012), with an automatic meshing technique, subject specific finite element head models could be generated with the help of subject specific MRI images. Head impacts sustained by 10 football and ice hockey players were recorded with the help of instrumented helmets. These head impacts were reconstructed to predict the regional strain responses and their association with diagnosed concussion. For these 10 concussed cases, the mean peak resultant linear acceleration was 73.6 ± 21.3 g and the mean peak resultant rotational acceleration was 5,025 ± 1,226 rad/s^2. Peak maximum principal strain of 28% and peak maximum principal strain rate of 54.3 was found in the corpus callosum i.e. the region of interest. The main motive was to associate these findings with the neuroimaging parameters.

Another computational model that helped in identifying brain injury tolerance level in terms of tissue level injury parameter is commonly known as SUFEHM i.e. Strasbourg University Finite Element Head Model. The initial version of the brain model was homogeneous. 109 head impact cases belonging to motorcycle accidents, American football player accidents, motorsport accidents, pedestrian accidents and experimental cases were reconstructed (Sahoo, 2013). The case was considered as a mild DAI case, when the coma duration was less than 24 hours. For a 50% risk of mild DAI, the tolerance level in terms of the best predictor i.e. von Mises stress was found to be 33 kPa. The most recent brain injury tolerance limit using latest version of SUFEHM, that is anisotropic and hence, heterogeneous, was identified by Sahoo et al. (2016). Existing SUFEHM was modified to incorporate the DTI information, which not only made the model anisotropic, but also made the calculation of axonal strains possible. A total of 109 TBI cases from real world accidents, involving American football players, motorsport, pedestrian and motorcycle accidents, were simulated to identify the brain injury tolerance in terms of axonal strain. Axonal strain was found to be the most suitable parameter for the prediction of DAI. Presence of loss of consciousness was considered as the basic characteristic of DAI. For a 50% risk of DAI, the proposed brain injury tolerance limit was 14.65% axonal strain.

This section described how computational models have been used as an efficient tool in identifying brain injury tolerance limits in terms of tissue level injury parameter. Although, injury biomechanics is very subject specific, yet standardized models can provide deep insights into brain. Table 1.11 below provides a synthesis of computational models used for identifying tissue level injury parameter based injury criteria and tolerance levels.

Table 1.11: Synthesis of computational models used for the identification of tissue level injury parameter based injury criteria and their latest estimated tolerance levels.

Model	Tolerance	Description	Reference
SIMon FEHM	50% probability of DAI: CSDM$^{\#}$ (0.25) = 54% MPS$^{\#}$ = 0.87	Based on 68 observations from animal experimental data, scaled and replicated with SIMon FEHM	Takhounts et al., 2008
WSUBIM	20% probability of mTBI: Shear stress = 6 kPa Strain = 0.14 50% probability of mTBI: Shear stress = 7.8 kPa Strain = 0.19 80% probability of mTBI: Shear stress = 10 kPa Strain = 0.24	Replication of 24 cases of helmeted head impact from American football (9 concussed)	Zhang et al., 2004

cont.

Model	Tolerance	Description	Reference
KTH FEHM (Homogeneous)	50% probability of concussion: Thalamus von Mises stress = 2.24 kPa Strain rate = 24 s^{-1} Strain x Strain rate = 2.49 s^{-1} Corpus callosum von Mises stress = 3.51 kPa Strain rate = 25.1 s^{-1} Strain x Strain rate = 2.76 s^{-1}	Replication of 40 cases of unhelmeted head impacts from Australian football and Rugby league (27 concussions)	Patton et al., 2015
KTH FEHM (Anisotropic)	50% probability of mTBI: Corpus callosum MAS# = 7% Brainstem MAS# = 15%	Replication of 58 cases of helmeted head impacts from NFL (25 concussions)	Giordano and Kleiven, 2014
DSS FEHM	Peak MPS# = 28% Peak maximum principal strain rate = 54.3 s^{-1}	Replication of 10 concussed cases from football and ice hockey players	McAllister et al., 2012
SUFEHM (Homogeneous)	50% probability of DAI: von Mises stress = 33kPa	Replication of 109 head impact cases belonging to motorcycle accidents, American football player accident, motorsport accidents, pedestrian accidents and experiments	Sahoo et al., 2013
SUFEHM (Anisotropic)	50% probability of DAI: MAS# = 14.65%	Replication of 109 TBI cases from real world accidents, involving American football players, motorsport, pedestrian and motorcycle accidents	Sahoo et al., 2016

#CSDM: cumulative strain damage measure, MPS: maximum principal strain, MAS: maximum axonal strain

3.4. Conclusion

A brief description of concussion grading scales and head/brain injury criteria was presented. On one hand, the concussion grading scales can only assess the severity of concussion after it has occurred. These can do nothing in preventing the first incident of concussion, but can help in managing the consequences and avoiding reoccurrences in future. On the other hand, injury criteria based on global mechanical parameters such as linear and rotational acceleration or rotational velocity has their own limitations. As some of these criteria take only linear acceleration into account, others only rotational acceleration; some do not take direction into account and others the duration. Hence, another category of injury criteria i.e. tissue level injury parameter based injury criteria has become popular in the last few decades. Assessing brain response in terms of mechanical parameters by simulating real world accidental or experimental scenarios and comparing these with the reported medical injuries

can help in identifying the tolerance limits undoubtedly. But, we can clearly see that there is a huge variation in the threshold values reported across studies for a specific type of injury. This variation is understandable because of two main reasons. First, finite element models used to identify these thresholds differ. Although, every study claims to have done the simulations on a validated model, yet a computational model, which has been validated against for instance intracranial pressure, will behave differently for say dynamic impacts. Also, the brain response is very subject specific. It differs from species to species, with age, with gender and with the loading conditions.

A recent study by Rowson et al. (2019) focused on the variations in concussion tolerances between individuals. A comparison was made between concussed football players and the physically matched control football players. It was found that concussed players not only experienced more head impacts, but also more high magnitude impacts and were exposed to higher risk. This clarifies the lack of understating about the connection between biomechanical input and the clinical outcome and hence, the variation in tolerances. Second and the most important reason behind variations is the definition of specific kind of injury e.g. mTBI or concussion with regard to the current study. Although, two studies report the tolerance limit for concussion in terms of same mechanical parameter, for example strain, yet the definition of concussion defined by these two studies may differ. In one study concussion could be defined based on the AIS value and in another based on the duration of coma or something else. Hence, the tolerance limits even in terms of same mechanical parameter and for same injury risk may differ from study to study.

King et al. (2003) reported some of the hypothesis, made in literature for the explanation of experimental results, on the mechanism of cerebral concussion. According to it, the cerebral concussion is caused by

- shear strains developed by rotation (Holbourn, 1943)
- relative displacement because of impact from different directions (Pudenz and Sheldon, 1946)
- relative displacement between brain and skull, which produces coup/countercoup cavitation (Gross, 1958)
- shear stress, distortion or mass movement in the brainstem because of pressure gradients of impact loading and high linear acceleration, whereas rotational acceleration, pressure and cavitation were said to be of negligible significance (Gurdjian et al., 1955, 1961, 1963; Hodgson et al., 1969)
- pressure waves (Goldsmith, 1972)

- disturbance of consciousness due to the disruptive effects of strain on brain function and structure in a centripetal sequence (Ommaya and Gennarelli, 1974)
- impact pulse comprising of frequencies close to modal frequencies of brain-skull complex, due to resonance (Willinger et al., 1995)

In one of the recent studies by Antona-Makoshi et al. (2016), concussion was supposed to have occurred after the experiment, when after the impact, the corneal reflex was lost for at least for 20 seconds or respiration was ceased for at least 20 seconds or two levels of blood pressure disturbances were present in the animals.

Actually, we can see a wide variety in the way concussion is defined in various studies. Other than the definition of concussion mechanism, even though the terms concussion, mTBI, mild DAI, mild neurological injury, diffuse brain injury etc. are used interchangeably, the injury definition taken into account for simulations differ. The definition of concussion used in earlier, around five decades back, studies were much more severe than what we use today (Rowson and Rowson, 2018). Some studies consider DAI as concussion, while some others classify even the DAI as mild, moderate and sever and concussion separately as mild, classical and severe (Gennarelli et al., 2003). The theoretical definition of concussion has got some consensus, but the pathological definition of concussion still involves huge ambiguity. Hence, the unavailability of any standardize definition for concussion is justified by the lack of consensus in this regard.

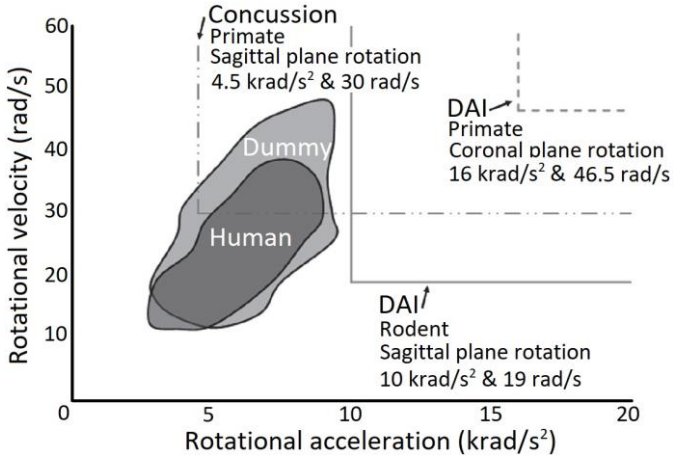

Figure 1.22: Diagram representing comparison of data from NFL reconstructions as dummy and instrumented football players as human with various brain injury thresholds scaled from animal models (Rowson and Rowson, 2018).

Brain tissue deformation for a given loading condition is modulated by brain mass/inertia. Hence, biomechanical scaling of mechanical parameters is possible (Holbourn, 1943; Ommaya et al., 1967; Gennarelli et al., 2003). This means that the tolerance limits can be scaled up to get the values for

primates from the animal data and vice versa. One such comparison, provided by Rowson and Rowson (2018) is given in Figure 1.22, which clearly illustrates that the primate concussion thresholds agree well with the human concussion data. However, scaled thresholds for DAI (severe injury) are greater than the concussion values. For rats, brain injury tolerance limit for concussion does not exist. However, many finite element rat brain models have been developed for different kinds of studies. In the following section, let us look briefly at these models and their findings, along with their model development strategies.

4 Finite element rat brain modelling

4.1. Introduction

Finite element modelling or computational modelling is a promising tool in the field of biomechanical studies. Finite element (FE) modelling not only allows the recreation of the complex anatomical structures in as much detail as required, but also makes it possible to implement diverse material properties. Experimentation on post-mortem human subjects (PMHS) could be thought of as an option. But, where the area of study is the brain, being in-vivo or in-vitro makes a lot of difference and thus the limitation of study on PMHS multiplies (Mao et al., 2006). FE modelling (FEM) of human brain has proven to be very efficient in studying injury biomechanics (Sahoo et al., 2014). FEM makes the understanding of the injury mechanism easier and the identification of injury locations possible by evaluating stress, strain and other such mechanical parameters at every desired location at each instance of time.

In-vivo animal models are widely used in the studies related to concussion. Low cost, small size and availability of extensive normative data of rodents have made them a preferred choice for various studies (Mao et al., 2006). In spite of the fundamental differences between human and rat brains (such as size, shape, organization, grey matter-white matter ratio, number of gyri and sulci etc.), at the tissue and cellular level, both the brains respond in a similar manner and the adult rat brain can be considered neurologically equivalent to the adult human brain (Shreiber et al., 1997; Gefen et al., 2003). Development of a finite element model is a systematic procedure. At first, the knowledge of material property is essential. Material properties can be identified either through experimentation or from the available literature based on the previously done experiments. Experimental characterization of brain material is necessary in order to replicate the actual brain by a finite element brain model. However, a finite element or computational model is considered efficient only when it is biofidelic, i.e. the end results are close to reality. Choice of appropriate material law plays an important role in achieving good biofidelity. In order to identify mechanical properties of the brain material,

different kind of experiments have been performed on a variety of subjects (humans as well as animals). In the following section, the experimental studies, conducted in the past, for the material characterization of rat brain are presented. Once the material properties are known, the geometric model can be built, meshed and then the material properties can be incorporated.

The succeeding section provides an overview of existing finite element rat brain models. A brief description of the material models used and the validation methods adopted is given along. A very important step before the developed model can be used for research is validation of the model. Once validated, the model can be used for a variety of systematic investigations. A FEM is validated by simulating the experimental scenarios computationally and then comparing the simulation results with the experimental results. Hence, finally, a description of experimental studies available in literature against which the finite element rat brain model can be validated is provided. Let us start with the experimentations conducted for the identification of material properties of a rat brain.

4.2. Experiments for the identification of rat brain material properties

Mechanical testing of rat brain has been done both, in-vivo and in-vitro and through different testing techniques, such as indentation testing, compression testing and magnetic resonance elastography. Although, the rat brain in itself is so small that performing experiments on it accurately is a difficult task, yet advanced technologies, such as atomic force microscopy (AFM), scanning force microscopy (SFM) and optical coherence tomography (OCT) etc., have made experimentations at microscopic level possible. Hence, although not exhaustive, material properties for overall rat brain as well as for different anatomical structures of the rat brain are available in literature.

Gefen et al. (2003) performed the very first experimentation to directly measure the mechanical properties of rat brain (Finan, 2019). Experimental protocol included controlled one mm indentation of the force probe into the rat brain. Preconditioned and non-preconditioned instantaneous and long-term shear modulus of brain tissue (in-situ and in-vitro) were calculated from the recorded force-displacement data. Basically, this study aimed at comparing age-dependent changes in material properties of the rat brain. Brain of immature rat was found to be significantly stiffer than the brain of an adult rat. Also, effective elastic modulus of braincase, estimated through reverse engineering finite element model approach, was found to be 6.3 MPa. Material properties for an adult rat, as reported in this study, are given in Table 1.12. Total eleven 13-days-old, ten 17-days-old, ten 43-days-old and eleven 90-days-old rats were tested. Statistically, mechanical characteristics of 43- and 90-days old rats were found to be similar.

Table 1.12: Material properties (mean value ± standard deviation) of an adult rat brain (Gefen et al., 2003).

	Non-preconditioned	Preconditioned
Instantaneous shear modulus, G_i (Pa)	1721 ± 680	1232 ± 343
Long-term shear modulus, G_∞ (Pa)	508 ± 252	398 ± 119

Vappou et al. (2008a, 2008b) used magnetic resonance elastography (MRE) to assess the mechanical properties of adult rat brain (Figure 1.23). MRE is a non-invasive method that makes use of propagating shear waves to find out the mechanical properties of soft tissue. In Vappou et al. (2008a), material properties were evaluated at three time points i.e. in-vivo, within thirty minutes post mortem (PM0.5h) and within 24 hours post mortem (PM24h), at a frequency of 180 Hz. Based on five experiments performed on a control rat, averaged values of storage and loss moduli were found to be 8450 ± 410 Pa and 7140 ± 610 Pa respectively.

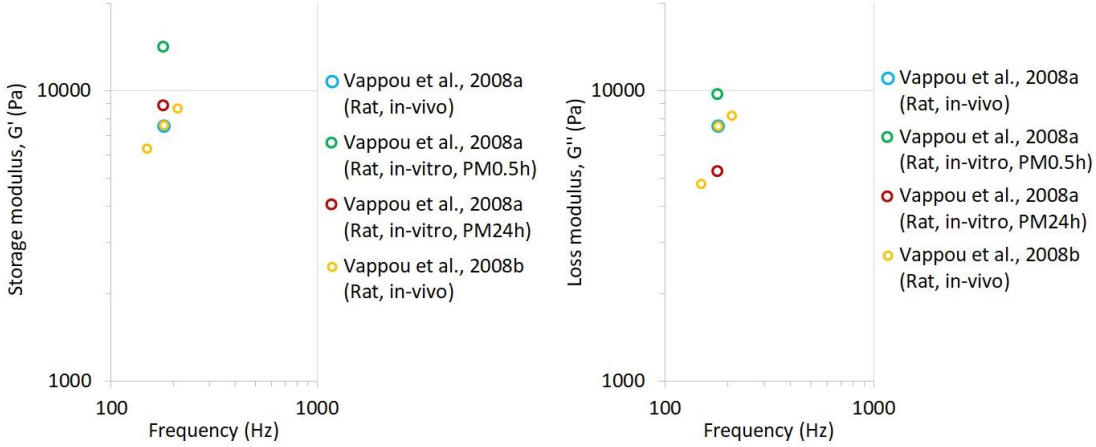

Figure 1.23: Storage modulus vs frequency (left) and loss modulus vs frequency (right) for in-vivo and in-vitro rat brain; measurements were taken at 180 Hz (Vappou et al., 2008a) and at 150 Hz, 180 Hz and 210 Hz (Vappou et al., 2008b).

It was observed that shear storage modulus increased significantly (approximately 100%) right after the death, however it came back near to in-vivo value around 24 hours post mortem. On the other hand, value of shear loss modulus right after death was closely similar to the in-vivo value; however 24 hours post mortem it reduced to about 50%. Vappou et al. (2008b) evaluated in-vivo rat brain (n = 7) material properties at three frequencies, i.e. 150 Hz, 180 Hz and 210 Hz. Storage moduli at these frequencies were found to be approximately 6325 Pa, 7595 Pa and 8660 Pa respectively. Loss moduli at these frequencies were found to be 4780 Pa, 7565 Pa and 8180 Pa respectively.

A comparison of rat brain storage and loss moduli with that of human brain at different frequencies is shown in Figure 1.24. Even though the rat brain moduli seems considerably higher than those of human, they are measured at higher frequency as well. A trend of increasing modulus value with an increase in frequency can be clearly seen from the diagram. Hence, it can be said that the storage and loss moduli of a rat and a human brain are more or less in accordance. In all the cases, we see that the value of loss modulus is usually lower than the corresponding storage modulus value.

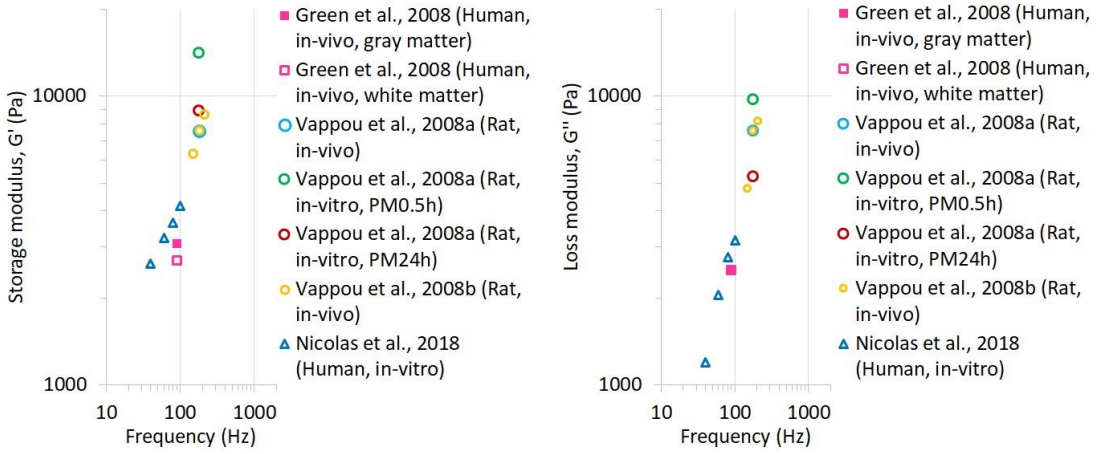

Figure 1.24: Storage modulus vs frequency (left) and loss modulus vs frequency (right) for in-vivo and in-vitro rat brain along with the human brain data; measurements were taken at 90 Hz (Green et al., 2008); at 180 Hz (Vappou et al., 2008a); at 150 Hz, 180 Hz and 210 Hz (Vappou et al., 2008b); at 40 Hz, 60 Hz, 80 Hz and 100 Hz (Nicolas et al., 2018).

Shafieian et al. (2009) performed indentation on brainstem samples of adult rats. Two regions of brainstem at corticospinal tract, which are ponto-medullary junction (PmJ) and pyramidal decussation (PDx) were selected for experimentation. In total, 8 injured and 11 uninjured animals were tested in this study. Instantaneous elastic force vs indentation depth and reduced relaxation function vs time data for non-preconditioned and preconditioned, uninjured and injured specimens were reported. Closed head injury model was used to induce DAI to compare the differences in brain material properties with and without injury. A significant reduction in the stiffness of injured tissue was observed. For different conditions, instantaneous elastic shear moduli were reported to range between 4 kPa to 9 kPa approximately.

Elkin et al. (2010) used atomic force microscopy (AFM) to measure region based mechanical properties of the cortical and the hippocampal sub regions of in-vitro adult rat brain. Experiments were performed on more than five rats and at each region, at least 16 force curves per region were deemed adequate for the analysis. AFM is a well suited technique to measure very local mechanical properties, as it indents the surface with very refined spatial resolution (Finan, 2019). 400 µm thick coronal slices were prepared for AFM. A 6 x 6 array with 6 µm spacing was examined within every distinct anatomical

region. It was found that apparent elastic modulus increases nonlinearly with indentation strain as well as with age. Later, displacement controlled (30% strain), stress relaxation, unconfined compression tests were performed to verify the material properties identified through AFM. 1 µm thick slices of cortex and hippocampus were prepared for unconfined compression tests. It was reported that the mean apparent elastic modulus as measured from AFM (at 30% indentation strain for each region and age) correlated well with the long-term elastic modulus measured from unconfined compression tests (at 30% strain). The average of all apparent elastic moduli for adult rat brain (at 30% strain, including all regions) was found to be approximately 1 kPa.

Christ et al. (2010) used scanning force microscopy (SFM) to find out the differences in the mechanical properties of white and gray matter of ex-vivo adult rat brain cerebellum. Four animals were used for the testing. Gray matter was found to be significantly stiffer than the white matter. The results were reported to be constant with a variation in indentation depth from 2 µm to 4 µm. As reported in Christ et al. (2010), exact median values of the effective elastic moduli (K) for gray and white matter at different indentation depths are given in Table 1.13.

Table 1.13: Medians of elastic moduli (K_g and K_w) of all four rats for indentation depths of 2-4 µm; n_g and n_w indicates number of measurements per animal per area (g: gray matter, w: white matter) (Christ et al., 2010).

	2 µm		3 µm		4 µm	
	K_g (Pa)	K_w (Pa)	K_g (Pa)	K_w (Pa)	K_g (Pa)	K_w (Pa)
Animal 1 (n_g = 61, n_w = 35)	496	334	486	380	508	384
Animal 2 (n_g = 36, n_w = 24)	438	315	409	341	387	347
Animal 3 (n_g = 109, n_w = 50)	397	215	397	263	384	266
Animal 4 (n_g = 39, n_w = 41)	546	152	524	190	502	207

Elkin et al. (2011) measured mechanical properties of various white and gray matter regions (alveus, brainstem, cerebellum gray, cerebellum white, corpus callosum, dentate gyrus, hippocampus CA1, hippocampus CA3, thalamus, inner cortex, middle cortex and outer cortex) in coronal slices of adult rat brain. One slice per region per animal was tested and slices were obtained from at least seven animals per region. Stress relaxation micro indentations (for 10% effective strain) were performed on 2 mm thick coronal slices. Shear moduli were reported at short (100 ms), intermediate (1 s) and long

(20 s) time points that ranged from about 1 kPa (short term moduli) to about 0.4 kPa (long term moduli). Both age and anatomical location were found to be significant factors influencing the time dependent shear modulus. Model fit parameters as well as shear modulus vs time curves for aforementioned anatomical regions were also reported. Figure 1.25 provides the reported shear modulus versus time curves for all the regions of adult rat brain measured through coronal slices.

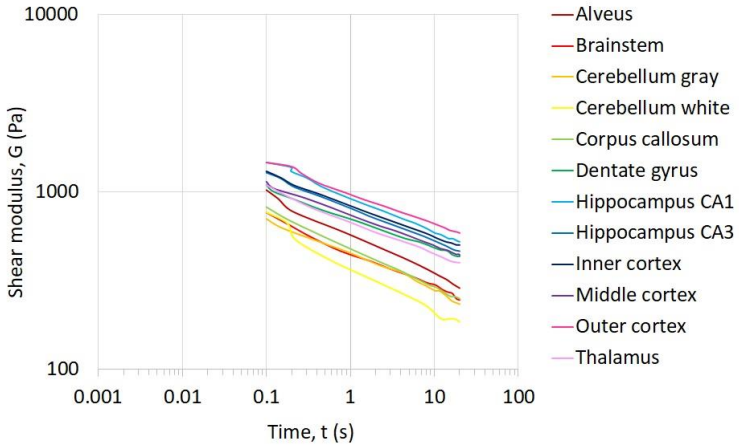

Figure 1.25: Shear modulus vs time curves of all twelve regions of adult rat brain measured in coronal plane (Elkin et al., 2011).

Finan et al. (2012a) performed micro indentation experiments on sagittal slices of adult rat brain to determine the viscoelastic properties of different anatomical regions (alveus, brainstem, cerebellum gray, cerebellum white, corpus callosum, dentate gyrus, hippocampus CA1, hippocampus CA3, thalamus, inner cortex, middle cortex and outer cortex). Figure 1.26 provides the reported shear modulus versus time curves for all the regions of adult rat brain measured through sagittal slices.

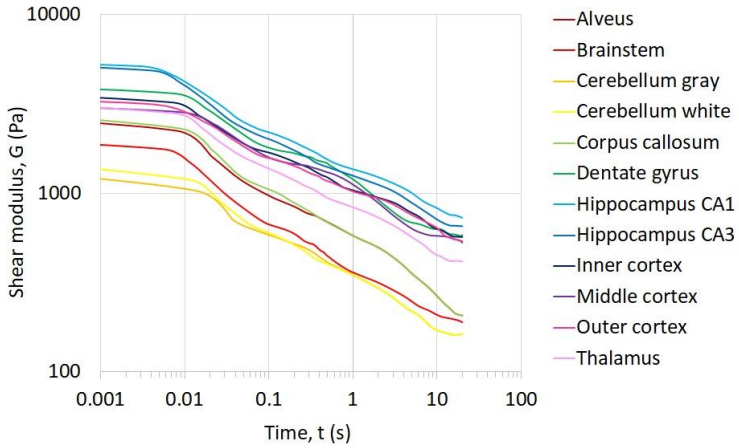

Figure 1.26: Shear modulus vs time curves of all twelve regions of adult rat brain measured in sagittal plane (Finan et al., 2012a).

Stress relaxation micro indentations (for 10% effective strain) were performed on 2 mm (1 mm in case of brainstem) thick sagittal slices. For all regions, number of animals used were more than or equal to six. Shear moduli were reported at three time points (10 ms, 50 ms and 20 s). Both age and anatomical location were found to be significant factors influencing time dependent shear modulus. Rat brain was found to be spatially heterogeneous in sagittal plane. Model fit parameters as well as shear modulus vs time curves for aforementioned anatomical regions were also reported.

In another study, Finan et al. (2012b) performed micro indentation experiments on horizontal slices of adult rat brain ($n \geq 5$) to determine the viscoelastic properties of different anatomical regions (alveus, brainstem, cerebellum gray, cerebellum white, corpus callosum, dentate gyrus, hippocampus CA1, hippocampus CA3, thalamus, inner cortex, middle cortex and outer cortex). Stress relaxation micro indentations (for 10% effective strain) were performed on 2 mm (1 mm in case of brainstem and cerebellum) thick sagittal slices. Shear moduli were reported at three time points (10 ms, 50 ms and 20 s). It was found that the brain properties in horizontal plane were dependent on age, time and region. Evidence of anisotropy was found in alveus and corpus callosum. Model fit parameters as well as shear modulus vs time curves for aforementioned anatomical regions were also reported. Figure 1.27 provides the reported shear modulus versus time curves for all the regions of adult rat brain measured through horizontal slices.

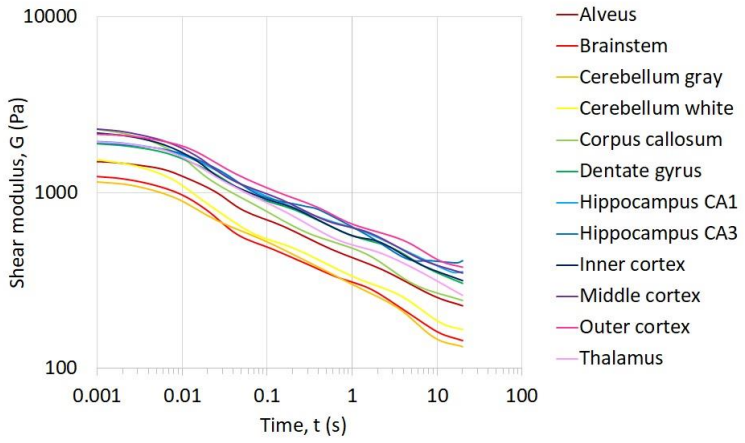

Figure 1.27: Shear modulus vs time curves of all twelve regions of adult rat brain measured in horizontal plane (Finan et al., 2012b).

Experimental study by Elkin et al. (2013) was actually a modification of Elkin et al. (2011), in order to assess the rat brain material properties more accurately. Mechanical properties of various white and gray matter regions (alveus, brainstem, cerebellum gray, cerebellum white, corpus callosum, dentate gyrus, hippocampus CA1, hippocampus CA3, thalamus, inner cortex, middle cortex and outer cortex) in coronal slices of adult rat brain were measured. At least 14 indentations were made per region and

not less than six adult rats were used per region. Stress relaxation micro indentations (for 10% effective strain) were performed on 2 mm thick coronal slices. Shear moduli were reported at three time points (10 ms, 50 ms and 20 s) and ranged from about 0.2 kPa to about 2.6 kPa based on age, region and time scale. Age, region and relaxation time were found to be significant factors affecting the stiffness. In general, regions were identified to be stiffer with age. Model fit parameters as well as shear modulus vs time curves for aforementioned anatomical regions were also reported. Figure 1.28 provides the reported shear modulus versus time curves for all the regions of adult rat brain measured through coronal slices.

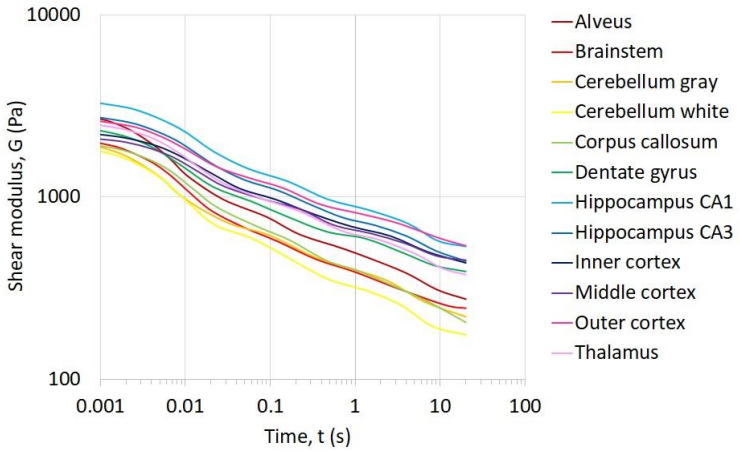

Figure 1.28: Shear modulus vs time curves of all twelve regions of adult rat brain measured in coronal plane (Elkin et al., 2013).

It can be observed from the diagrams that the properties for various rat brain regions identified through various studies not only follows the same pattern, but also lie within the same range. As per these studies (Elkin et al., 2011; Finan et al., 2012a, 2012b; Elkin et al., 2013) the instantaneous shear modulus for various brain regions varied from approximately 1.1 kPa to 3.3 kPa, except in one study up to 5.1 kPa; whereas the long term shear modulus ranged from 0.1 kPa to 0.7 kPa. Figure 1.29 illustrates the shear modulus versus time data obtained from these rat studies in comparison to the data obtained from studies based on human brain. The most recent study on human brain by Finan et al. (2017) more or less agrees with the rat brain data as well as the one by Takhounts et al. (2003b). However, the shear moduli values reported by Galford and McElhaney (1970) lies very high than all other values and on the contrary, those reported by Prange et al. (2000) lies at the bottom end. . It can be clearly observed from the figure that the value of shear modulus varies between wide ranges. Shear moduli for human brain as reported by Galford and McElhaney (1970) are the highest among all other reported values. Whereas, shear moduli reported by Prange et al. (2000) for human brain tissue (cortical gray matter) lie at the lowest. There could be various reasons for this variation in reported values, which are explained later. Nevertheless, we can see an overlap between rat brain

and human brain material properties and this supports the opinion that inter species brain at tissue or cellular level is the same (Shreiber et al., 1997; Gefen et al., 2003). However, consensus supporting this very fact is still unavailable.

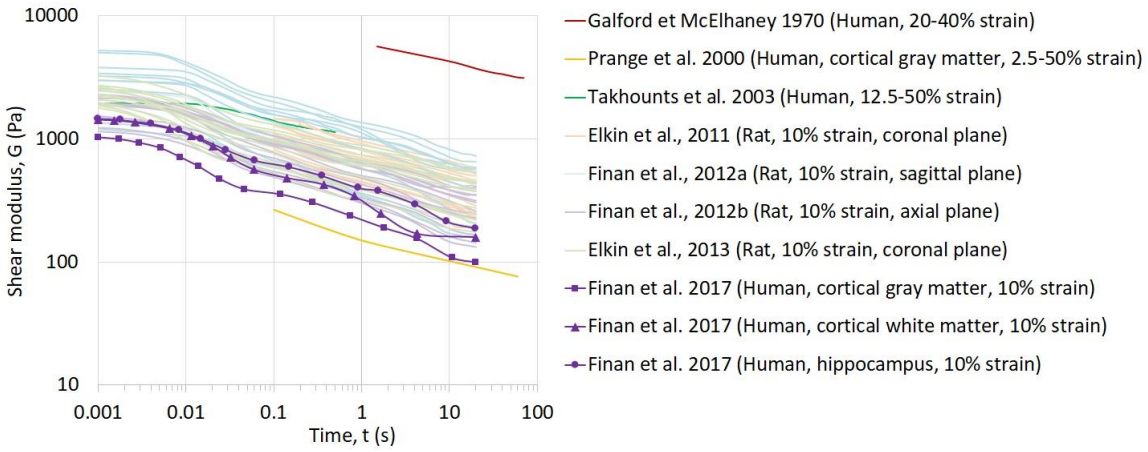

Figure 1.29: Diagram representing shear modulus vs time curves of adult rat brain (for various regions) in comparison to human brain data available in literature (Galford and McElhaney, 1970; Prange et al., 2000; Takhounts et al., 2003b; Elkin et al., 2011; Finan et al., 2012a; Finan et al., 2012b; Elkin et al., 2013; Finan et al., 2017).

Gabler et al. (2013) performed controlled indentation (0.6 mm) on 8 mm thick coronal slices of adult rat brain to assess the material properties at five specified regions. Hence, total eighty indentation tests were carried out on the tissue samples collected from sixteen animals. Brain tissue was found to be viscoelastic and spatially non-linear with region dependent mechanical properties. For all the five regions, instantaneous elastic response vs displacement data and reduced relaxation function vs time data was reported. Injured samples were found to have reduced stiffness than the uninjured samples.

Lee et al. (2014) measured the spatially heterogeneous viscoelastic properties of in-vitro rat brain (n = 3) tissue slices (six to seven slices per region) in coronal plane for different anatomical regions (cerebral cortex, caudate/putamen and hippocampus) through optical coherence tomography (OCT) indentation system. For every anatomical region, a non-linear decay with time was found in the shear modulus value. The range of instantaneous shear modulus to equilibrium shear modulus was found to be from 3.8 kPa to 0.54 kPa for cerebral cortex, from 1.4 kPa to 0.27 kPa for hippocampus and from 1 kPa to 0.17 kPa for caudate/putamen. In spite of the fact that all these regions are gray matter structures, their mechanical properties were found to be significantly different.

Moeendarbary et al. (2017) performed AFM on 2 mm thick coronal slices of adult rat brain (n = 2). Elastic modulus for uninjured cortical tissue ranged from 50 to 500 Pa with a median value of 285 Pa (1730 measurements). Raster indentation scanning was used to evaluate spatial heterogeneity of the

elastic properties of the brain tissue. It was found that the rectangular elasticity maps of brain tissue were heterogeneous. It was also observed that the brain mechanical properties were symmetrical with respect to the brain midline. Evidences of brain tissue getting softer after injury were reported as well.

As said earlier, these results are outcome of different kind of experimentations. Some from indentation tests, some from compression tests and others from magnetic resonance elastography. Not only the experimentation technique, but a number of other factors influence the differences in these results. One of the factors that causes differences in the values reported by various studies is age. There have been some studies assessing the influence of age on brain material properties, e.g. for rat brain (Gefen et al., 2003; Elkin et al., 2010; Finan et al., 2012a). Gefen et al. (2003) found that the immature rat brain was significantly stiffer than the matured rat brain. On the contrary, both Elkin et al. (2010) and Finan et al. (2012a) reported that the brain tissue gets stiffer with age. Specimens used for experimentation by different studies varies in age and hence, the results. It is now a well-known fact that brain material is anisotropic and heterogeneous structure. Other factors causing differences among results of various studies could be anisotropy and heterogeneity (Chatelin et al., 2010; Sahoo et al., 2014). Every region of brain has been found to have different material properties. Hence, sometimes the values reported, even for the same anatomical structure of brain, differs because of the difference in choice of location for the experimentation. Two samples from different regions of brainstem's corticospinal tract under same experimental protocol showed different mechanical properties (Shafieian et al., 2009). Another study by Elkin et al. (2010) showed a clear evidence of region and even sub-region dependent mechanical properties of a rat brain. Christ et al. (2010) reported the gray matter of cerebellum to be significantly stiffer than white matter of cerebellum (for the rat brain). Elkin et al. (2011) found out the regions of cerebellum and the white matter regions to be more compliant than regions of cortex, hippocampus and thalamus. Finan et al. (2012a) found enough evidences to state that brain becomes mechanically more heterogeneous as animal ages. Finan et al. (2012b) found out that the rat brain tissue is spatially heterogeneous and for an adult rat, tested forebrain regions were stiffer then tested hind brain regions and for young rats, cerebellum was softer than any other tested brain region. Gabler et al. (2013) did a study to find out region specific properties of an adult rat brain and their results confirmed heterogeneity. Elkin et al. (2013) reported hippocampal and cortical regions to be stiffer than the white matter and cerebellar regions of adult rat brain. Lee et al. (2014) performed some experiments to find out the mechanical properties of cerebral cortex, caudate/putamen and hippocampus. In spite of all these being gray matter regions, their mechanical properties were found to be significantly different. Moeendarbary et al. (2017) also found out the brain material to be heterogeneous and reported medial agranular

cortex region to be the softest among tested regions, with the lateral agranular cortex having medium stiffness and the anterior cingulate cortex nearer to brain mid-line to be the stiffest. Anisotropy could be one of the reasons that causes heterogeneity. Some other factors influencing the material properties of adult rat brain could be inter-species variation and variation in experimental parameters, such as temperature, preconditioning, protocol and postmortem time etc. Let us now look at existing finite element rat brain models and the material properties used by them.

4.3. Existing finite element rat brain models

Many two-dimensional (2D) (Gefen et al., 2003; Pena et al., 2005 and Fijalkowski et al., 2009) as well as three-dimensional (3D) (Shreiber et al., 1997; Levchakov et al., 2006; Mao et al., 2006; Baumgartner et al., 2009; Lamy et al., 2013; Ren et al., 2014, Antona-Makoshi et al., 2014, Antona-Makoshi et al., 2015, LaPlaca et al., 2019 and Unnikrishnan et al., 2019) FE rat brain models have been reported in the literature over the last two decades. These models, along with their characteristics and limitations, are explained briefly in the following paragraphs in chronological order.

Shreiber et al. (1997) developed a 3D model (Figure 1.30) of a rat brain as a single, homogeneous, isotropic structure with a non-linear, modified hyper-elastic material law and used 36,664 8-noded hexahedron elements. But, the brain was considered to be purely elastic in distension. The model geometry was created using a histological atlas of the rat brain. The model was developed to identify in-vivo thresholds of mechanical injury to blood brain barrier. This model was validated for peak displacements with regard to dynamic cortical deformation (DCD) experiments.

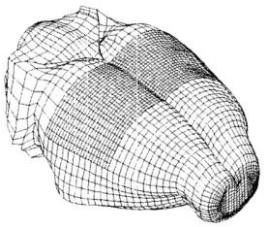

Figure 1.30: 3-dimensional finite element rat brain model developed by Shreiber et al. (1997).

Maximum principal strain was found to be the best predictor of blood brain barrier breakdown. The tolerance level for blood brain barrier breakdown in terms of peak principal logarithmic strain was found to be 18.8%. As the model was build homogeneous, there was no distinction of white and gray matter and no ventricular distinction as well. It was said that these assumptions could alter the identified threshold values to some extent. Also, the assumed boundary conditions were said to be influential in identifying the threshold values as the brain deformation on the application of pressure pulse would be affected. The choice of material constant was said to be one of the influential factors

too. However, it was said that the results would not change with these influences, but just the magnitude of threshold.

Gefen et al. (2003) developed three 2D brain slices or models for three different ages, which included braincase layer (Figure 1.31), representing half coronal plane cross-section of the brain. Quad elements were used for modelling and the model was assumed to be homogeneous, isotropic and incompressible. Initially, rat brain material properties were identified through experimentation, as described in the previous section and then, these properties were implemented in the FE model. Brain material properties clearly indicated the variation due to age difference. These FE models were used to predict the braincase material properties through simulations of indentation experiments.

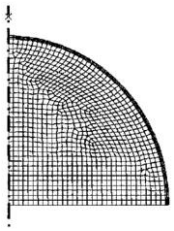

Figure 1.31: 2-dimensional finite element rat brain model developed by Gefen et al. (2003).

It was found that there was no significant age dependent variation in the effective elastic modulus of the braincase. In spite of the fact that the skulls of older rats were considerably thicker than that of the young ones. Hence, it was concluded that it is not the brain tissue that increases the structural rigidity of the braincase with age, but the increase in the skull thickness. Nothing with regard to model validation was reported in the study. It was a highly simplified model and hence, very limited information could be acquired through this model. Also, there was no certainty about biofidelity.

Another 2D rat brain model (Figure 1.32) developed by Pena et al. (2005) used triangular elements and considered the brain material to be linearly elastic. High resolution MRI data was used to build the geometry and to simulate different scenarios of closed cortical impact.

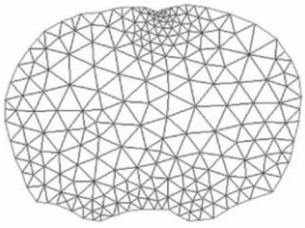

Figure 1.32: 2-dimensional finite element rat brain model developed by Pena et al. (2005).

The main purpose was to identify brain tissue biomechanics in terms of displacement, mean stress and shear stress with different tissue elasticity. This study demonstrated that regional tissue elasticity

has high influence on the transfer of forces, developed by initial tissue displacement, into the surrounding tissues. As per the observations, it was assumed that the linear relationship between the tissue intensity in the medical images and the elasticity of the brain provides more biofidelic results than the inverse linear relationship between them. Based on the results, it was also suggested that the finite element analysis is a suitable tool for biomechanical simulations. Nothing regarding the model validation was reported in the study. Again, high simplification of the model could be counted as one of its limitation as it could provide the brain response for only the region/brain-slice for which the model was built.

Another 3D rat brain model (Figure 1.33) developed by Levchakov et al. (2006) used 30,000 tetrahedron solid elements. The brain material was considered to be homogeneous, incompressible and viscoelastic with time dependent shear modulus taken from Gefen et al., 2003. The model was built to study the strain responses of neonatal and mature rat brains on the application of closed head impact. The model geometry was created using an anatomical digital database. Validation of this model was said to be found unfeasible, but the comparison of predictions made through closed head impact (indentation) simulations, against the findings of old histopathological studies, showed a good correspondence between them. This study basically compared neonatal rat brain response against adult rat brain response. It was concluded that as the neonatal rat brain demonstrated higher peak stresses and larger strain volumetric exposures in the study, the hypothesis that the infant brain are more susceptible to TBI because of stiffer tissue and smaller size of brain was supported. The major limitation of this model was the uncertainty of results as the model was not validated.

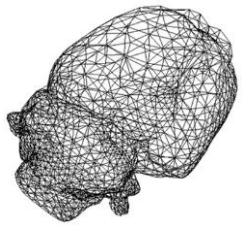

Figure 1.33: 3-dimensional finite element rat brain model developed by Levchakov et al. (2006).

Mao et al. (2006) developed a detailed FE model (Figure 1.34) consisting of 255,700 hexahedral and 250 pentahedral solid elements. The main objective of the study was to predict the intracranial response for different impact conditions. An isotropic and linear viscoelastic material was chosen. The shear modulus value for the gray matter region, as well as for brainstem and cerebellum, was taken from Gefen et al. (2003). Whereas for white matter regions, the shear modulus was assumed to be 70% of the gray matter region's value. The model was validated against DCD experimental data from Shreiber et al. (1997). The anatomical and geometrical details for the development of this 3D model

were taken from a rat brain atlas. Controlled cortical impact simulation results showed that the intracranial strains best correlate with the experimentally obtained injuries.

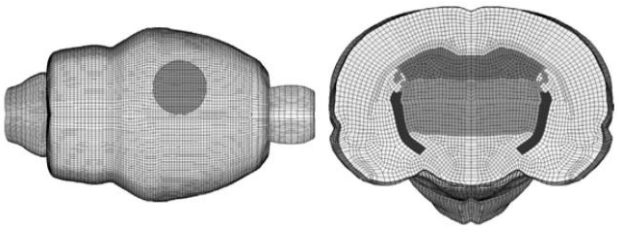

Figure 1.34: 3-dimensional finite element rat brain model developed by Mao et al. (2006).

Fijalkowski et al. (2009) developed a 2D rat brain model (Figure 1.35) to demonstrate region specific response in case of mild diffuse brain injuries. This model represented a mid-brain coronal section, whose anatomic and geometric details were imported digitally from an atlas. This head model contained 2,528 elements in total and the brain was assumed to be linear viscoelastic. The material properties were taken from literature. The model was validated against experiments of injurious and non-injurious angular acceleration loading, on rat, primate and human volunteers. A new concept of sustained maximum principal strain criterion (SMPS) was introduced. The region specific responses were compared with the histological data and then fractional areas were correlated with the time of unconsciousness to verify the compared results. It was found that for hippocampus and parietal cortex regions, 4-4 SMPS criterion best correlates with the histological results. A 4-4 SMPS criterion means, quantification of fractional tissue area exceeding 4% maximum principal strain for a time duration of 4 seconds. It was stated that linear viscoelastic brain material can be considered as one of the limitations of this model, since, if the tissue response is sensitive to strain, this material cannot take strain softening into account.

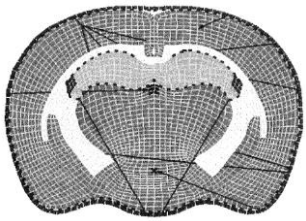

Figure 1.35: 2-dimensional finite element rat brain model developed by Fijalkowski et al. (2009).

Geometry of another 3D rat brain model developed by Baumgartner et al. (2009) was obtained through magnetic resonance imaging (MRI). The brain was modelled as a homogeneous, isotropic and viscoelastic material, containing 17,972 hexahedral elements and weighing 14.1 g. A complete validation of this 3D model was said to be found difficult due to the unavailability of experimental

data. This study was able to establish a correlation between the intracranial stresses and the observed injuries, as a result of sagittal plane rotational acceleration loading simulations.

The model developed by Lamy et al. (2013) was actually a refinement of the model developed by Baumgartner et al., 2009. Every hexahedral element of the old model was split into eight hexahedral elements and hence, the new model consisted of 143,776 hexahedral elements. The brain model was considered to be homogeneous and isotropic with an assumption of all gray matter. The model was validated against DCD experimental data from Shreiber et al. (1997). Two time-integrated metrics, strain-time and stress-time, proved to be better predictors of variation in injury severity associated with both, amplitude and duration of rotational acceleration (loading) as well as with experimentally observed recovery times.

Homogeneous model developed by Ren et al. (2014) was based on Baumgartner et al. (2009) and previously refined and validated in Lamy et al. (2013). However, the inhomogeneous model (Figure 1.36) developed in Ren et al. (2014) was validated against sagittal plane rotational impact experiments. As reported, the brain model consisted of 156,656 hexahedral elements. This model used inhomogeneous but isotropic and linear viscoelastic material properties. The material properties were taken from Finan et al. (2012a). The main objective of this study was to identify the effect of inhomogeneous material properties on brain response in case of trauma. It was found that on the application of rapid sagittal plane rotational acceleration on the rat head, the intracranial stress responses were more sensitive to inhomogeneity than intracranial strain responses. One of the limitations of this model was said to be the linear viscoelasticity of brain material. A nonlinear viscous hyperelastic material model is more biofidelic and better predicts the brain response. Another limitation was the abrupt boundaries of anatomical brain regions.

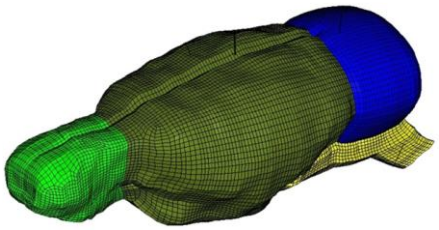

Figure 1.36: 3-dimensional finite element rat brain model developed by Ren et al. (2014).

The geometry of another 3D FE rat brain model (Figure 1.37) developed by Antona-Makoshi et al. (2014) was constructed combining information from the rat brain digital atlas, computed tomography (CT) scans and MRI. The brain was modeled as a heterogeneous, general viscoelastic material consisting of 79,469 hexahedral elements. This model was developed and validated hoping this could

be used to understand brain loading mechanism, to predict more accurate brain response and thus to develop brain injury threshold, for diffuse axonal injuries in future. Brain material properties were taken from Elkin et al. (2013). Initially, experiments of rotational acceleration loading in the sagittal plane were performed on rats to identify the brain-skull relative displacement at four depths. Later, averaged rotational acceleration pulse obtained through these experiments was employed to simulate this experimental scenario. Simulation results were compared with the experimental results in order to validate the model. This model was validated for local brain cortex kinematics through experimentation.

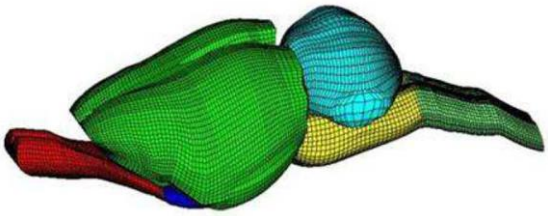

Figure 1.37: 3-dimensional finite element rat brain model developed by Antona-Makoshi et al. (2014).

Antona-Makoshi et al. (2015) modified this model a little bit in order to identify the aging effects on the prediction of brain injury in rotational head trauma. The space between brain and skull and the ventricular system of the modified model was filled with CSF. An increase in strain based thresholds was observed because of tissue stiffening from young adult to mature adult rats. Also, tissue softening and atrophy of old age brain demonstrated an increase in injury risk indicators (i.e. cumulative strain damage measure, CSDM; relative motion damage measure, RMDM and maximum principal strain, MPS).

A very recent high resolution 3D model (Figure 1.38) was developed by LaPlaca et al. (2019). The geometry of this rat head model was based on MicroCT images. Initially, the head model composed of 770,000 elements in total, of resolution 0.1 to 0.2 mm, out of which 220,000 elements belonged to brain. Later, to find out local mechanical response of specific brain regions, the brain model was refined to achieve a resolution of around 50 µm. Hence, the brain model consisted of more than 2,400,000 hexahedral elements. Heterogeneous, viscoelastic and nearly incompressible material properties were chosen for the brain. The rat brain model was validated against DCD experimental data from Shreiber et al. (1997). The model was developed to simulate closed cortical impacts and to correlate the results with acute membrane permeability following traumatic brain injury. It was concluded that experimentally induced TBI demonstrates mechanoporation and cell death, and this was found to correlate with the model output in term of maximum shear stress and maximum principal strain estimated through numerical simulations.

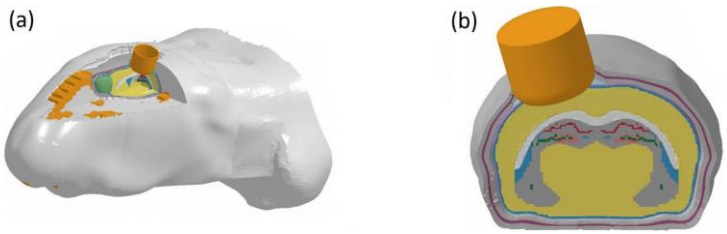

Figure 1.38: 3-dimensional high resolution finite element rat brain model developed by LaPlaca et al. (2019); (a) isometric view of sectioned model and (b) coronal sectional view demonstrating hippocampal sub regions, with impactor.

Another 3D rat brain model, published recently, was developed by Unnikrishnan et al. (2019). This model (Figure 1.39) was developed to study the effects of brain vasculature and material properties on blast wave exposure. This rat head model consisted of 250,935 quadratic tetrahedral elements having an average resolution of 0.7 mm. The vasculature was modeled as hollow pipes using linear triangular shell elements of average resolution of 0.07 mm and shell thickness of 0.1 mm. The cerebral vasculature was coupled with the rat brain model through rigid body transformation. The vascularized rat brain was modeled as incompressible hyperelastic material. The model was validated against experimental brain pressure data from blast scenarios. It was found that incorporation of vasculature and species specific brain material properties influence the strain predictions, but pressure predictions. One of the limitations of this model was said to be that the model was validated only against experimental pressure and not for experimental strain and hence, it is difficult to be sure of strain based results.

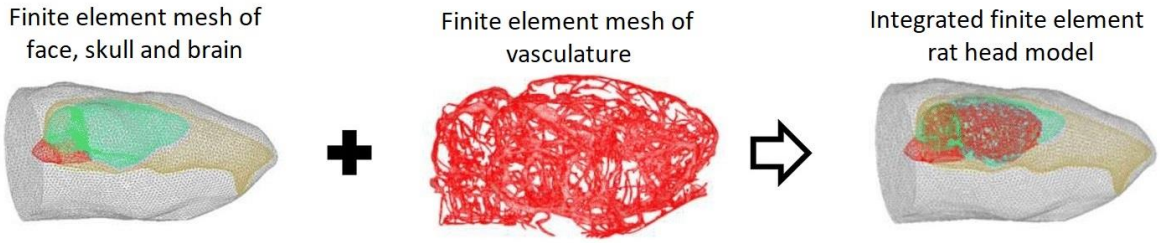

Figure 1.39: 3-dimensional finite element rat head model developed by Unnikrishnan et al. (2019).

A synthesis of the details of these models, in terms of a short description and validation, is provided in Table 1.14. Basically, with regard to concussion, there are two major limitations with existing finite element rat brain models. First, none of the available models took brain anisotropy into account. Anisotropy plays an important role in the brain kinematics, as it influences the regional material properties and hence, the brain response. Second, one of the reasons of not taking anisotropy into account, could be that mostly these models were used to simulate impact trauma cases related to severe injuries and not concussion. Apart from this, the material properties used by these models are either elastic or viscoelastic, except one which used hyperelastic material properties. Hence, to assess

the brain response in case of concussion, it is important to have a model that takes anisotropy into account and have a viscous hyperelastic material law to capture the overall behaviour of brain.

Table 1.14: Existing finite element rat brain models.

Model by	Description	Validation
Shreiber et al., 1997	• 3D model having 36,664 hexahedral solid elements • Homogeneous and isotropic structure with modified hyperelastic material properties	Validated against dynamic cortical displacement (DCD) measurements on application on vacuum pressure pulse
Gefen et al., 2003	• 2D model having quadrilateral elements • Homogeneous, isotropic and incompressible structure with linear viscoelastic material properties	Not validated
Pena et al., 2005	• 2D model having triangular elements • Homogeneous and isotropic structure with linear elastic material properties	Not validated
Levchakov et al., 2006	• 3D model having 30,000 tetrahedral solid elements • Homogeneous, isotropic and incompressible structure with viscoelastic material properties	Not validated
Mao et al., 2006	• 3D model having 255,700 hexahedral and 250 pentahedral solid elements • Heterogeneous and isotropic structure with linear viscoelastic material properties	Validated against DCD measurements on application on vacuum pressure pulse
Fijalkowski et al., 2009	• 2D model having 2,528 quadrilateral elements • Heterogeneous and isotropic structure with linear viscoelastic material properties	Validated against brain deformation on the application of rotational loading pulse
Baumgartner et al., 2009	• 3D model having 17,972 hexahedral solid elements • Homogeneous and isotropic structure with viscoelastic material properties	Not validated
Lamy et al., 2013	• 3D model having 143,776 hexahedral solid elements • Homogeneous and isotropic structure with viscoelastic material properties	Validated against DCD measurements on application on vacuum pressure pulse
Ren et al., 2014	• 3D model having 156,656 hexahedral solid elements • Heterogeneous and isotropic structure with linear viscoelastic material properties	Validated against brain-skull relative displacement (BSRD) measurements on the application of rotational loading pulse

Model by	Description	Validation
Antona-Makoshi et al., 2014	• 3D model having 79,469 hexahedral solid elements • Heterogeneous and isotropic structure with general viscoelastic material properties	Validated against BSRD measurements on the application of rotational loading pulse
Antona-Makoshi et al., 2015	• 3D model having 131,746 hexahedral and tetrahedral solid elements • Heterogeneous and isotropic structure with general viscoelastic material properties	Validated against BSRD measurements on the application of rotational loading pulse
LaPlaca et al., 2019	• 3D model having more than 2,400,000 hexahedral solid elements • Heterogeneous and isotropic structure with incompressible, viscoelastic material properties	Validated against DCD measurements on application on vacuum pressure pulse
Unnikrishnan et al., 2019	• 3D head model having 250,935 quadratic tetrahedral solid elements coupled with vasculature modeled with linear triangular shell elements • Heterogeneous and isotropic structure with hyperelastic material properties	Validated against brain pressure data on the application of blast overpressures

After looking at the details about existing finite element rat brain models available in literature, let us see what possibilities the literature holds for the validation of a computational model.

4.4. Model validation methods

Model validation is an important and essential step in developing a computational model. However, a model can be validated only when conclusive data is available based on extensive experimentation. When we look in the literature, there are two kinds of experiments that can be used for the validation of a finite element rat brain model. One is based on the measurement of dynamic cortical displacement (DCD) on the application of vacuum pressure pulse on the brain surface, after craniectomy. Another is measurement of brain deformation on the application of rotational acceleration loading, such as measurement of brain skull relative displacement (BSRD). These are the validations that has been used by many of existing finite element rat brain models as well. The experimental study by Shreiber et al. (1997) is used for DCD measurements and the experimental study by Antona-Makoshi et al. (2014) is used for BSRD measurements to validate a computational rat brain model. The details of these studies are given in the following chapter, where the development and validation of anisotropic finite element rat brain model is presented.

4.5. Conclusion

This section provided an overview of finite element rat brain modeling. The starting section presented available literature regarding the identification of rat brain material properties. This was followed by the description of existing finite element rat brain models along with the model validation methods available in literature. A computational model is considered efficient only when it is biofidelic. Good bio-fidelity of a model can be achieved by incorporating anatomical features in sufficient details, choosing appropriate material laws, selecting accurate injury measures and by extensively validating the model against well documented experimental data (Sahoo et al., 2014). In spite of the fact that the brain is a complicated heterogeneous anisotropic structure, none of the available finite element rat brain models (FERBM) took anisotropy into account, which indeed could provide more biofidelic results. Also, most of the existing rat brain models chose brain material to be elastic or general viscoelastic. However, it known that the nonlinear viscous hyperelastic material can replicate the actual brain response more accurately. Hence, an anisotropic viscous hyperelastic finite element rat brain model is the need of the hour to get additional insights into the rat brain in case of concussion.

5 Motivation of the study

Concussion in sports is a serious health problem and statistics provided in introductory section highlights the crucial requirement of preventive measures for concussion. Unfeasibility of experimentation on human brain restricts the in-depth investigation on concussion. However, small animals, such as rat, seem to be an interesting opportunity for such investigations. The observations that an adult rat brain can be considered neurologically equivalent to an adult human brain and at tissue level inter species brains respond similarly support the significance of the investigation through rat brain model. Further, a consolidation of brain material properties based on literature reviewed was furnished. Although, brain material properties for various species varies between wide ranges, yet they seemed to follow a similar pattern and this variation could be understood because of aforementioned reasons. A brief overview of brain anatomy, at macroscopic and microscopic level, was also provided to better understand the injury mechanisms. Although, no consensus on potential injury mechanisms of concussion or on their sequence of occurrence is available, yet it is supposed that it all happens at microstructural level and if managed properly, can heal over time. Unavailability of consensus is due to the fact that concussion results in neurological functional disturbances and usually no structural change can be seen through standard structural neuroimaging techniques. Diffuse axonal injury is one of the most common pathological features of acute concussion. A sudden loading on head causes rapid acceleration and deceleration of brain and subsequently results in axonal

stretch. This sudden stretch damages the axonal cytoskeleton, which is the main medium of neurotransmission and hence, disrupts the normal functioning of the brain. Hence, understanding the mechanical threshold of axonal stretch for concussion can help in improving the design of preventive measures, such as sports helmet. For this purpose, investigations through computational modelling seem a good option, since finite element models has proved to be an efficient tool for biomechanical studies. However, for a computational model, to accurately predict the brain response under loading, biofidelity is essential. This chapter shed light on the existing finite element rat brain models and the methods used for validation. It is observed that all of these models used isotropic material properties. Whereas, in spite of a few studies claiming brain material to be isotropic, it is a well-known fact that brain material is anisotropic.

There are two fundamental limitations with existing finite element rat brain models. First, these models use isotropic material properties, in spite of the fact that brain material is known to be anisotropic. Second, these models were built to study traumatic brain injuries (TBI) and not mild traumatic brain injury (mTBI) or concussion. Concussion is a very mild kind of injury and it is not possible to get any glimpse inside brain for concussion with the existing models without any further modification. Hence, an advanced anisotropic finite element rat brain model, which is more biofidelic and can capture the brain response in much detail, is very much needed. This model will not only help in identifying the mechanical threshold of axonal stretch to concussion, but can also prove to be a turning point for other concussion related investigations, specially investigations related to repetitive concussion, commonly known as rmTBI.

Chapter 2: Development and validation of an anisotropic finite element rat brain model

1 Introduction

Computational models, also known as finite element models have proved to be efficient tools in studying brain injuries. In comparison to experimentation, computational models are more accurate, economic and easier to use. Further, they do not involve any ethical concerns that are always present in case of experimentation on biological subjects. Previous chapter highlighted the need for an anisotropic finite element rat brain model (FERBM), for in depth investigation of concussion. This chapter presents the methodology for the development and validation of an anisotropic FERBM.

The first half of this chapter is about model development. This model was developed progressively in various stages, which are described in details in the following sections. As a first step, young adult Sprague Dawley rat, weighing approximately 290 g, was chosen as the basis for this study. After deciding upon the rat, an available DTI (diffusion tensor imaging) atlas, for the same kind of rat, was chosen to create the geometry of the rat brain. As a further step, the rat brain volume was meshed to create the geometric finite element model. Afterwards, the same DTI atlas, as mentioned earlier, was used to identify the diffusion parameters - fractional anisotropy (FA) and principal fiber direction (PFD), for every element of the FERBM. As a further step, a constitutive material law and the material properties for the FERBM, cerebrospinal fluid (CSF) and the skull were decided. Finally, the DTI implementation, to make the FERBM anisotropic, was completed by updating the brain material definition to incorporate the DTI information in terms of diffusion parameters.

The second half of this chapter is about model validation. Model validation is a very important step in biomechanical studies that employ computational modelling. It is the model validation that confirms that the results of the simulations conducted on this model have enough fidelity and are acceptable with respect to the real life responses. Thus, helping to achieve the objective of the investigation. For the validation of a computational model, experimental scenarios are recreated in terms of numerical simulations and the model response is compared with the experimental response. Simulation response of a biofidelic model is close to the experimental response. Hence, the model developed as a part of this study, i.e. FERBM, was validated with two kind of experiments available in literature. The first validation is against experimental dynamic cortical displacement on the application of a vacuum pressure pulse on the brain surface. The second validation is against experimental brain-skull relative displacement on the application of rotational acceleration loading in the sagittal plane. Both of these experiments were performed in-vivo. The details of these experiments are explained in the following sections. Ultimately, this anisotropic viscous hyperelastic FERBM provides insights into the rat brain, in case of concussion, in terms of axonal elongation, which is explained in the final chapter.

2 Geometric modeling and meshing of the rat brain

A three-dimensional anatomical atlas of the adult rat brain at postnatal day 72, developed by Rumple et al. (2013), was used for the geometrical construction of the rat brain model. A detailed description of the DTI atlas is provided later in the respective section. At first, the rat brain geometry was rendered from the DTI atlas in the form of STL representation. Then, HyperMesh software was used to generate the brain surface from the STL representation and to mesh the rat brain model (Figure 2.1).

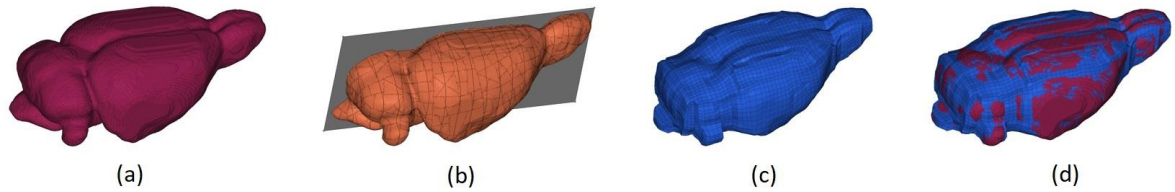

Figure 2.1: Geometric modeling and meshing process, (a) STL representation; (b) surfacing; (c) meshed model and (d) coincided STL representation and meshed model.

The meshing of the model was based on the hypothesis that the brain geometry is identical about mid-sagittal plane. Therefore, only the right half of the brain was meshed and replicated to the left, to generate the complete geometric meshed model of the rat brain. Figure 2.2 shows the dimensions of the meshed rat brain model. The final rat brain model weighed 1.94 g.

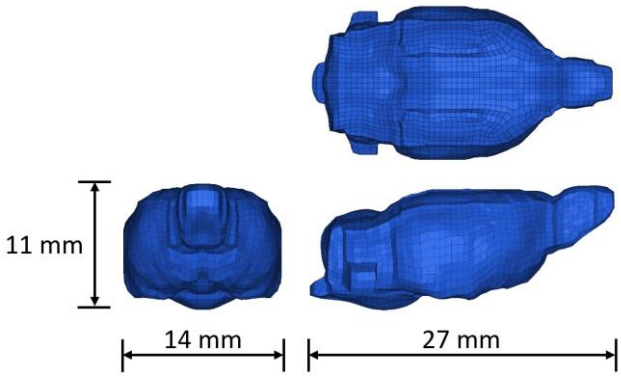

Figure 2.2: Diagram representing sagittal, axial and coronal views and the dimensions of the meshed rat brain.

This finite element rat brain model consists of 13,236 solid hexahedral elements. The element size varies from 0.4 mm to 0.8 mm, having an average value of around 0.5 mm. Meshing was done maintaining a good element quality. Thus, for all the brain elements, maximum warpage is less than 30 degrees, maximum aspect ratio is less than two, maximum skew is 45 degrees and the minimum Jacobian is equal to 0.5. The meshed rat brain is enwrapped within a layer of cerebrospinal fluid (CSF). The CSF was modelled as a layer of solid hexahedral elements, consisting 3,252 elements and having

an average thickness of 0.7 mm. The brain and the CSF model are enclosed inside the skull, which was modeled with 3,252 quadrilateral shell elements.

Earlier, it was thought that dividing the rat brain into main parts (as per the segmentation provided in the DTI atlas by Rumple et al., 2013) and meshing these parts separately, maintaining the continuity between the mesh of different parts would be a good idea. However, later it was found that neither it was feasible to develop such a mesh considering the restrictions in terms of element size and element quality, nor was it required for various reasons. Primarily, the rat brain being very simple in structure, unlike the human brain with multiple folds; and smaller in size, the parts can only be differentiated based on their functions, but not based on their geometrical structure. It is more like one single continuous structure, but with ventricular segregation. However, this ventricular segregation was supposed to be neglected because of the resolution restrictions. Furthermore, even if the brain would have been meshed with the partwise division, it would not have been possible to assign the partwise material properties to these regions at a later stage. There exist very limited experimental data in literature for the rat brain material properties, which was not enough for such a division of the brain. Hence, based on the hypothesis made, the model was meshed in the best possible way required for this study.

3 Categorization of the brain for the analysis of simulation results

Based on the segmentation provided in the DTI atlas by Rumple et al. (2013), the FERBM was categorized into twenty-four different regions for the analysis of simulation results. These regions are hippocampus, external capsule, caudate – putamen – globus pallidus as one, anterior commissure, substantia nigra, internal capsule, thalamus, cerebellum, superior colliculus, hypothalamus, inferior colliculus, central gray, neocortex, amygdala, olfactory bulb, brainstem, fimbria, fornix, ventral tegmental area (VTA), corpus callosum, genu, aqueduct, splenium and rest of brain as one. Later, this anatomical categorization provided further insights into simulation results on regional bases. Table 2.1 provides details about this anatomical categorization and Figure 2.3 displays the location of some of these parts in the rat brain as per the DTI atlas segmentation provided by Rumple et al. (2013).

Table 2.1: Details of anatomical categorization of rat brain regions.

#	Region description	Number of elements	% Brain volume
1	Hippocampus	614	4.6%
2	External capsule	1083	8.2%
3	Caudate – Putamen – Globus pallidus	572	4.3%
4	Anterior commissure	122	0.9%

#	Region description	Number of elements	% Brain volume
5	Substantia nigra	64	0.5%
6	Internal capsule	104	0.8%
7	Thalamus	434	3.3%
8	Cerebellum	2869	21.7%
9	Superior colliculus	92	0.7%
10	Hypothalamus	421	3.2%
11	Inferior colliculus	272	2.1%
12	Central gray	192	1.5%
13	Neocortex	3474	26.2%
14	Amygdala	124	0.9%
15	Olfactory bulb	676	5.1%
16	Brainstem	1459	11.0%
17	Fimbria	136	1.0%
18	Fornix	53	0.4%
19	Ventral tegmental area (VTA)	20	0.2%
20	Corpus callosum	118	0.9%
21	Genu	48	0.4%
22	Aqueduct	14	0.1%
23	Splenium	16	0.1%
24	Rest of the brain	259	2.0%

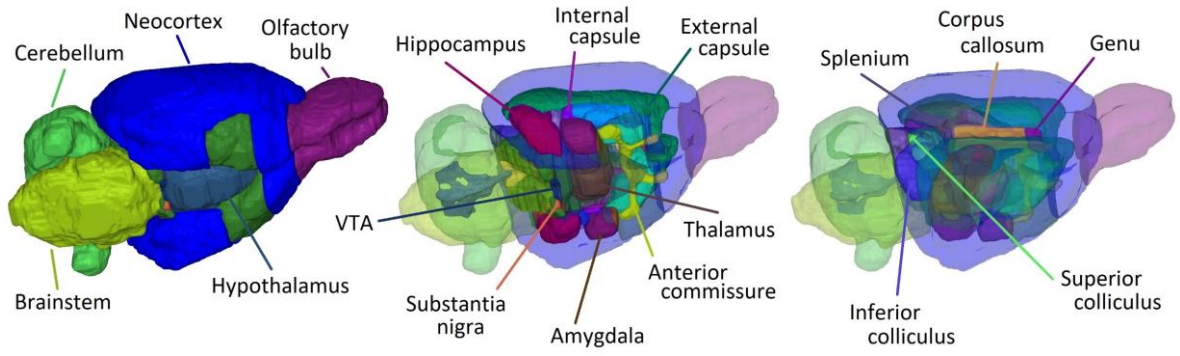

Figure 2.3: Diagram representing various parts of the rat brain as per brain segmentation provided by Rumple et al., 2013.

Another categorization of the brain was functional and was based on the behavioural aspects. The brain regions associated with four behavioural aspects - consciousness, activity, emotionality and cognition were identified. Due to the complexity of brain and the limited available-knowledge, it is not possible to clearly identify the brain regions associated with these behavioural aspects. However, it

was assumed that the consciousness is associated with thalamus, neocortex and brainstem; activity is associated with hippocampus, substantia nigra, cerebellum, central gray and neocortex; emotionality is associated with hippocampus, central gray, neocortex, amygdala, brainstem, fimbria and fornix; and cognition is associated with hippocampus, substantia nigra, cerebellum, neocortex, fimbria and fornix. Table 2.2 provides details about this functional categorization and Figure 2.4 displays the brain regions associated with these behavioural aspects. Later, based on this functional categorization, simulation results were analyzed for these functional regions or for different behavioural aspects.

Table 2.2: Details of functional categorization of rat brain regions.

#	Function / behavioural aspect	Region description	Number of elements
1	Consciousness	Thalamus, Neocortex and Brainstem	5367
2	Activity	Hippocampus, Substantia nigra, Cerebellum, Central gray and Neocortex	7213
3	Emotionality	Hippocampus, Central gray, Neocortex, Amygdala, Brainstem, Fimbria and Fornix	6052
4	Cognition capability	Hippocampus, Substantia nigra, Cerebellum, Neocortex, Fimbria and Fornix	7210

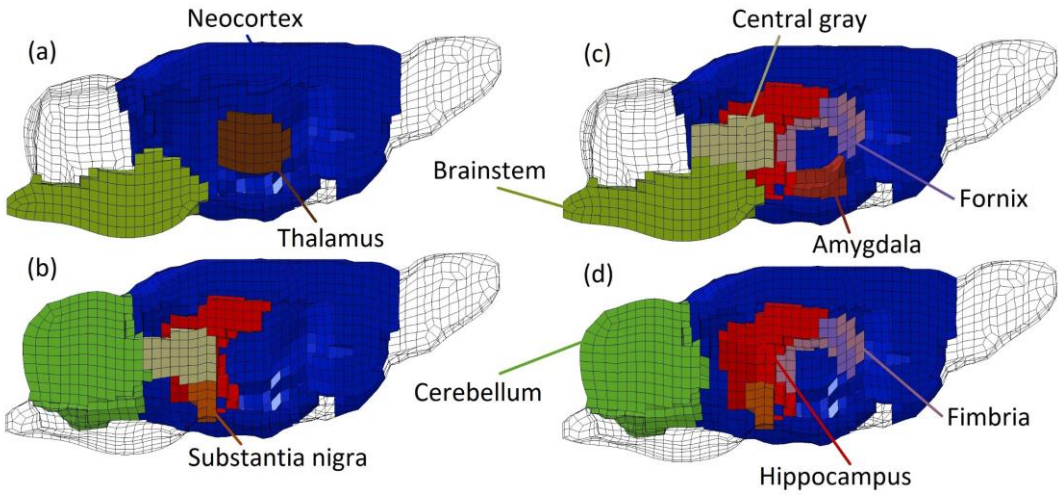

Figure 2.4: Diagram representing only the functional regions associated with different behavioural aspects: (a) consciousness, (b) activity, (c) emotionality and (d) cognition by means of a cut in mid-sagittal plane.

These anatomical and functional categorization of rat brain into various regions helped in correlating simulation results with experimental results on regional bases (presented in the final chapter).

4 Identification of diffusion parameters

4.1 Introduction

As mentioned earlier, a three-dimensional anatomical atlas of adult rat brain at postnatal day 72 developed by Rumple et al. (2013) was used for the identification of diffusion parameters of the rat brain. This atlas is based on the MRI acquisition of six female Sprague Dawley rats, weighing 289.3 ± 20.5 g. A 3-dimensional DTI RARE sequence with twin navigator echoes was used on Bruker horizontal 9.4 T scanner, with imaging parameters as TR = 700 ms, TE = 23.662 ms, RARE echo spacing = 11.9 ms and RARE factor = 3. The acquisition was made at a resolution of 0.16 x 0.125 x 0.16 mm^3 in twelve gradient directions with two base line images (b = 1600 s/mm^2). The total acquisition time was around 10 hours. The final isotropic resolution of the DTI atlas was 0.125 x 0.125 x 0.125 mm^3. Thus, this DTI atlas has a dimension of 192 x 256 x 103 voxels, with a voxel spacing of 0.125 x 0.125 x 0.125, origin at (0, 0, 0) and a L-P-S space orientation. This DTI atlas contains six volumes in total, each belonging to one of the six unique diffusion components of a typical diffusion tensor and thus, the diffusion data for every voxel of the rat brain.

Identification of diffusion parameters, fractional anisotropy and principal fiber direction, followed a systematic procedure, which is explained in detail in the following paragraphs. This methodology was adapted from Chatelin et al. (2011) and Sahoo et al. (2014). First, the diffusion parameters for every voxel of the brain were calculated mathematically from the diffusion data available for every voxel of the brain in the DTI atlas. As a second step, the developed FERBM was aligned with the DTI volume, so that both the volumes refer to the same location in space. Afterwards, since the voxel resolution is smaller than the model's element resolution, voxels falling inside every element of the FERBM were identified. Finally, as the diffusion parameters were already computed for every voxel, a weighted average, from the identified voxels per element was calculated to estimate the diffusion parameters per element. These estimated diffusion parameters were incorporated in the material definition per element, which will be explained later in this chapter. All this computation, alignment, identification, estimation and later incorporation was done through Python programming.

4.2 Computing fractional anisotropy and principal fiber direction per voxel

Fractional anisotropy (FA) and principal fiber direction (PFD) are two basic anisotropy parameters. FA is a quantitative and dimensionless (scalar) index to measure the fraction of the magnitude of diffusivity or in other words, to define how anisotropic the diffusion at a given location is. PFD is nothing but the orientation of the anisotropy vector at any location. FA value is evaluated from the

Eigen values (λ_1, λ_2, λ_3) of the diffusion tensor (D) as expressed in Equation 2.1 (Basser and Pierpaoli, 1996).

$$Fractional\ anisotropy, FA = \sqrt{\frac{3}{2}} \frac{\sqrt{(\lambda_1 - \tilde{\lambda})^2 + (\lambda_2 - \tilde{\lambda})^2 + (\lambda_3 - \tilde{\lambda})^2}}{\sqrt{\lambda_1{}^2 + \lambda_2{}^2 + \lambda_3{}^2}} \quad 2.1$$

Where, $\tilde{\lambda} = (\lambda_1 + \lambda_2 + \lambda_3) / 3$ and diffusion tensor, $D = \begin{bmatrix} D_{xx} & D_{xy} & D_{xz} \\ D_{xy} & D_{yy} & D_{yz} \\ D_{xz} & D_{yz} & D_{zz} \end{bmatrix}$

For an isotropic medium, FA value is equal to zero and for an anisotropic medium, which is cylindrically symmetric and where $\lambda_1 >> \lambda_2 = \lambda_3$, the FA value is equal to one. Hence, for a voxel, FA equals to zero indicates a perfect isotropy and FA equals to one indicates perfect anisotropy i.e. all axons are oriented along the anisotropy vector or in the principal fiber direction. Eigen vector associated with the maximum Eigen value of the diffusion tensor represents the principal fiber direction i.e. PFD. The DTI atlas contained the diffusion tensor data for every voxel of the brain. At first, Eigen values and Eigen vectors were calculated from this data and then the FA and PFD values per voxel were determined through python programming. Figure 2.5 displays the DTI maps of FA and PFD in the mid-sagittal plane of the rat brain obtained through the DTI atlas.

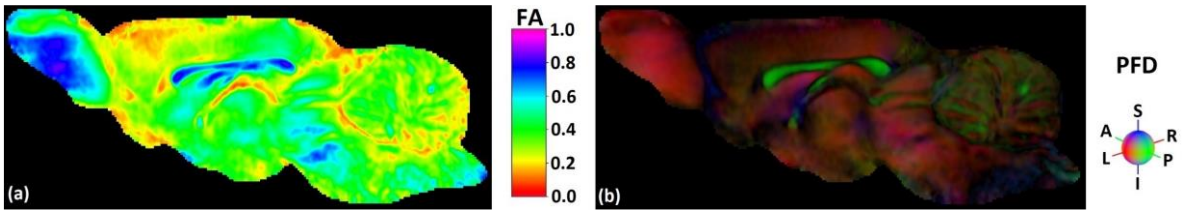

Figure 2.5: Diagram representing DTI data in terms of (a) fractional anisotropy (FA) map, and (b) principal fiber direction (PFD) map, in the mid-sagittal plane of the rat brain. FA=0 represents perfectly isotropic voxel, whereas FA=1 represents perfectly anisotropic voxel. For PFD, red represents right-left (R-L) direction, green represents anterior-posterior (A-P) direction and blue represents inferior-superior (I-S) direction.

4.3 Model alignment and identifying voxels per element

Before identifying voxels per element and estimating the diffusion parameters for FERBM, aligning FE model to the DTI volume is important. It is the alignment of the model that ensures both FE model and DTI volume are in the same coordinate frame and corresponds to the same location and orientation in space. The model alignment was performed in three main steps. First, seven landmarks (at center and on the outer brain surface at the right, left, anterior, posterior, inferior and the superior end) were identified on both DTI volume and FE model (Figure 2.6).

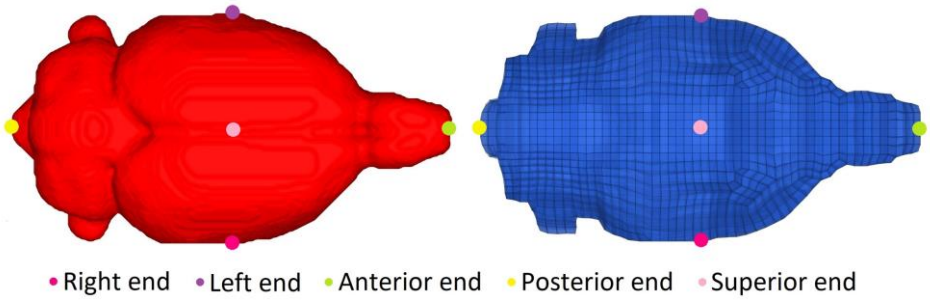

Figure 2.6: Diagram representing location of visible five landmarks on the DTI volume (on the left) and the FE model (on the right) for the alignment.

The landmarks on the FE model were taken as source landmarks and those on the DTI volume were taken as target landmarks. First, the transformation of FE model landmarks to DTI volume landmarks computed the best fit mapping in least square way and brought both the models close together. As a next step, iterative closest point (ICP) algorithm was used to optimize this alignment and a transformation matrix was identified to optimally align the FE model to the DTI volume. Finally, all the nodes of FERBM were transformed using this transformation matrix to optimally align the FERBM to the DTI volume. All the steps of model alignment were carried out through Python programming. Figure 2.7 depicts this model alignment briefly.

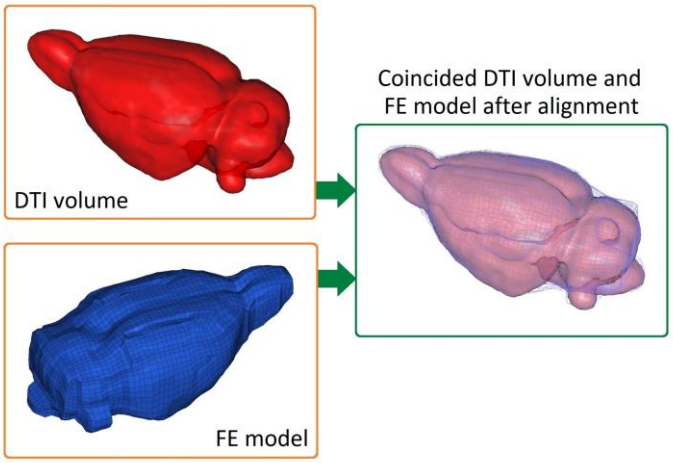

Figure 2.7: Diagram representing the DTI volume and the FE model before and after the alignment.

For the identification of voxels per element, a hexahedral voxel selection volume was built around the element such that the element falls completely inside this volume. For all the voxels inside this volume, it was checked if the voxel is within the element volume or on any of the element faces. All the voxels that either fell inside or on the boundary of the element were selected. Figure 2.8 illustrates an element, the voxel selection volume around the element and the selected voxels for the element.

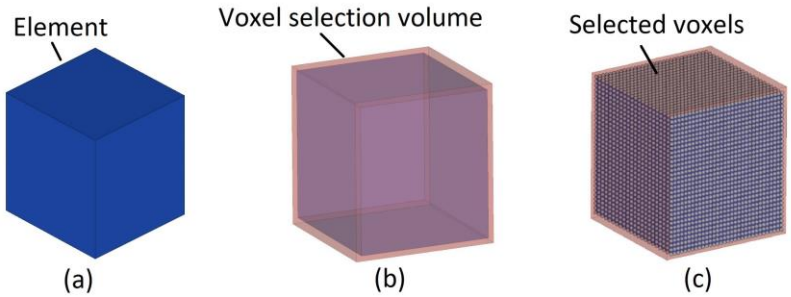

Figure 2.8: Diagram representing (a) an element, (b) voxel selection volume around the element and (c) selected voxels for the element.

Thus, voxels were selected for each of the 13,236 elements of the FERBM. This was also achieved through Python programming. Identification of voxels per element enabled the estimation of diffusion parameters per element, which is explained in the following section. Figure 2.9 depicts the number of voxels identified per element along with the minimum, maximum and the average number of voxels identified. The minimum, maximum and the average number of voxels identified for an element were 21, 177 and 68 respectively. Therefore, every element had good enough voxel count for the estimation of the diffusion parameters.

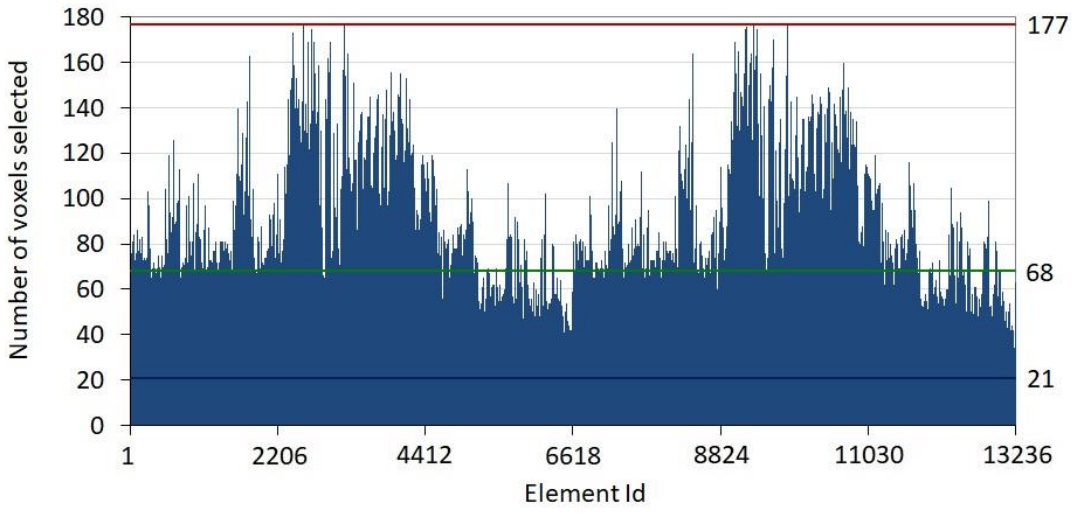

Figure 2.9: Diagram representing number of voxels selected per element, with the minimum selected equals to 21, maximum selected equals to 177 and an average selected equals to 68 ± 24.

4.4 Estimating fractional anisotropy and principal fiber direction per element

To estimate the diffusion parameters - fractional anisotropy (FA) and principal fiber direction (PFD) per element, a weighted average of FA and PFD values of all the voxels inside an element was calculated for every element of the FERBM. The average was weighted in such a way that the voxels near the center of the element had high influence than those at the element boundary. Hence, the

exponential weighting function was based on the distance of the voxel from the center of the element (D) and is given in Equation 2.2.

$$f(D_i) = e^{-D_i/L_e} \quad 2.2$$

Where, L_e is the half length of the maximum diagonal of the element and D_i is the distance of ith voxel from the element center. Figure 2.10 illustrates this weighting in a more comprehensible manner.

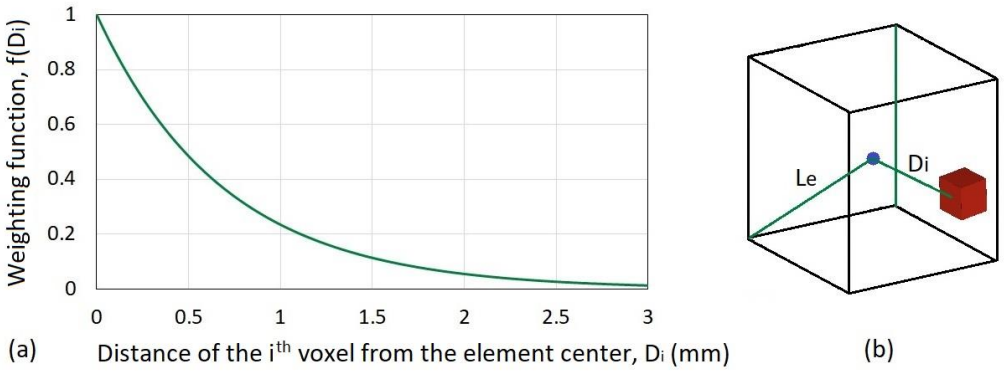

Figure 2.10: Diagram illustrating (a) the exponential weighting function based on the distance of the voxel from the element center and (b) a voxel (red) inside an element, the distance between the center of the element and the voxel (D_i) and the half length of the maximum diagonal of the element (L_e). Voxels near the center of the element have high influence than those at the element boundary (Sahoo et al., 2014).

Hence, the weighted diffusion parameters, FA and PFD per element were calculated based on the formulas given in Equation 2.3 and Equation 2.4.

$$FA_{element} = \frac{\sum_{i=1}^{n} FA_i \, e^{-\frac{D_i}{Le}}}{\sum_{i=1}^{n} e^{-\frac{D_i}{Le}}} \quad 2.3$$

$$\overrightarrow{PFD}_{element} = \frac{\sum_{i=1}^{n} \overrightarrow{PFD}_i \, e^{-\frac{D_i}{Le}}}{\sum_{i=1}^{n} e^{-\frac{D_i}{Le}}} \quad 2.4$$

Where, FA_i and $\overrightarrow{PFD}_i$ are the fractional anisotropy and principal fiber direction (anisotropy vector) for the ith voxel respectively and n is the total number of voxels selected inside an element.

Figure 2.11 depicts the estimated weighted averaged FA value for every element, along with the standard deviation and the overall averages. Actual minimum and maximum FA values were found to be zero and 0.9579 respectively. The weighted minimum and maximum FA values were found to be zero and 0.9595. Both the actual and the weighted FA values ranged similarly with an average of 0.31.

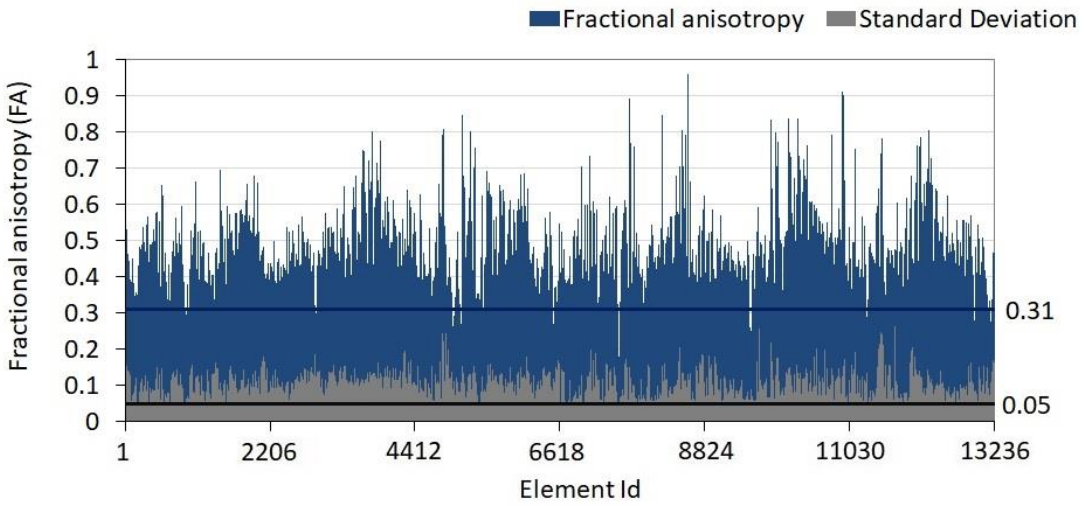

Figure 2.11: Diagram representing estimated weighted averaged FA value per element along with the standard deviation. Overall averaged FA equals to 0.31 and with a standard deviation of 0.05.

As mentioned earlier, brain regions having FA value equal to zero indicate perfectly isotropic regions and FA value approaching to one indicate highly anisotropic regions. In general, as gray matter is mostly composed of neuronal cell bodies, FA value in the gray matter regions is usually low. On the other hand, since the white matter is usually composed of axon bundles or fiber tracts, which are highly anisotropic, the FA value in white matter regions is mostly high.

Figure 2.12 represents a comparative illustration of the FA maps and the PFD maps, in the mid-sagittal plane of the rat brain, obtained through the DTI atlas and as estimated for the FERBM.

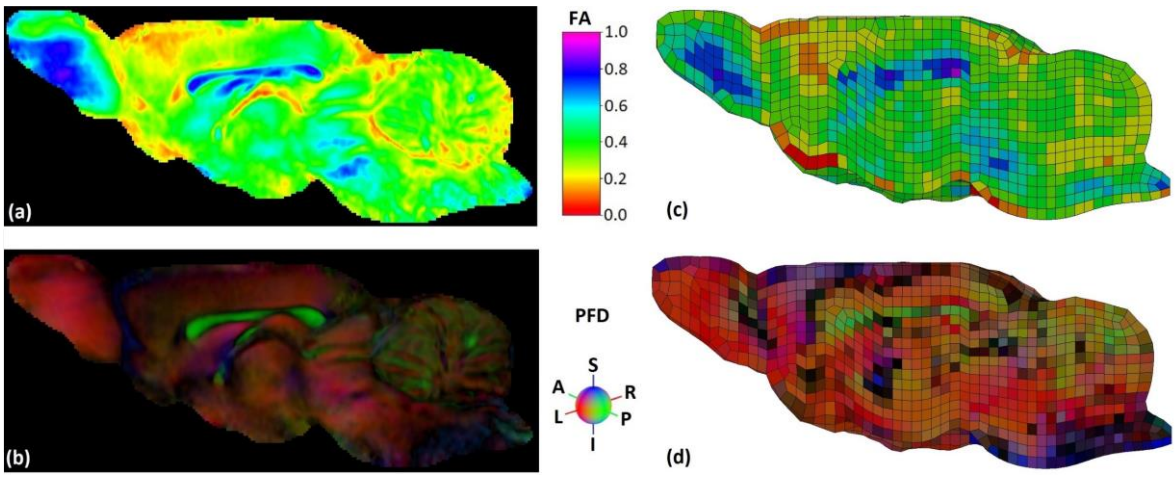

Figure 2.12: Diagram representing DTI data on the left and FERBM implementation on the right in terms of (a) and (c) fractional anisotropy (FA) map, and (b) and (d) principal fiber direction (PFD) map, in the mid-sagittal plane of the rat brain. FA=0 represents perfectly isotropic voxel/element, whereas FA=1 represents perfectly anisotropic voxel/element. For PFD, red represents right-left (R-L) direction, green represents anterior-posterior (A-P) direction and blue represents inferior-superior (I-S) direction.

It can be observed from the diagram that the diffusion parameters identified for the elements are in accordance with the actual imaging data. In Figure 2.12, FA and PFD maps of the imaging data are represented on the left and the FA and PFD maps of the FE model after the DTI implementation is displayed on the right. FA maps indicate the FA value of a voxel or of an element on a scale of zero to one. PFD maps are nothing but the directionally encoded colour maps, where every direction (i.e. the principal fiber direction in that voxel or the element) is indicated with a different colour, such that the red colour represents right-left (R-L) direction, the green colour represents anterior-posterior (A-P) direction and the blue colour represents inferior-superior (I-S) direction.

4.5 Conclusion

In this section methodology of identifying diffusion parameters for every element of the FERBM was explained. The identified diffusion parameters have demonstrated to be in accordance with the DTI imaging data.

5 Constitutive law and material properties

5.1 Introduction

After finding the diffusion parameters per element, the next step was to decide upon the constitutive law and the material properties for the developed FERBM. As described in the first chapter, after an extensive literature review, there is a huge variation in the understanding of the brain material. Based on a variety of experimentations conducted, brain material properties were found to differ when measured in-vitro or in-vivo; with location, with gray matter vs white matter, even within the subdivisions of brain regions; with age; with species; with experimental protocols etc. (Chatelin et al., 2010; Budday et al., 2019). However, when we look at microstructural level, it is the same soft tissue, where neuronal cell bodies and axons are spread in the glia. There also exist evidences in literature, which supports the fact that an adult rat brain can be considered neurologically equivalent to an adult human brain (Shreiber et al., 1997) and at tissue level the inter-species brain material responds similarly (Gefen et al., 2003). A comparison of material properties identified by different studies showed that the rat brain material properties follow the same pattern as that of other species and also lies within the same range. Hence, the constitutive law and the brain material properties, as identified by Chatelin et al. (2013) for adult human brain were adapted for the developed FERBM. These material properties were customized for rat by incorporating anisotropic diffusion properties of the rat brain through DTI implementation. A detailed description about this is provided in the following sections.

5.2 Brain material

Material model chosen for this study was developed by Chatelin et al. (2013) and is based on Weiss et al. (1996) and Puso and Weiss (1998). The chosen material model considered that the axonal fibers influence the mechanical behaviour of the brain tissue in a similar manner as the collagen fibers influence the ligaments. The complex brain tissue structure, where the neuron and the white matter tracts in the form of densely packed axons, remain spread within the neuroglia, was simplified as a fiber reinforced composite material. This simplification was based on the hypothesis that the axonal fibers are the main components, which influence the global anisotropic mechanical behaviour of the brain tissue and hence, the influence of surrounding neuroglia can be neglected. The brain tissue was supposed to consist of an isotropic matrix material with a fiber reinforcement in the principal fiber direction, a_0 as shown in Figure 2.13.

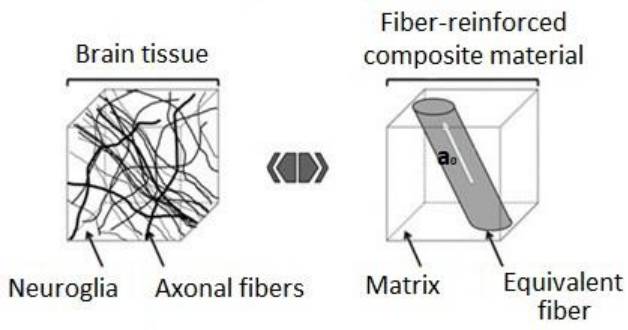

Figure 2.13: Diagram representing simplification of complex brain tissue structure as a fiber-reinforced composite material (Chatelin et al., 2013; Sahoo et al., 2014).

Strain energy of a fiber reinforced anisotropic hyperelastic material can be fully described by the five invariants of the right Cauchy-Green deformation 'C' as expressed in Equations 2.5 to 2.10 (Spencer, 1984).

$W = W(I_1, I_2, I_3, I_4, I_5)$, where 2.5

$$I_1 = tr(C) \quad 2.6$$

$$I_2 = \frac{1}{2}\,(tr(C)^2 - tr(C^2)) \quad 2.7$$

$$I_3 = det(C) = (J)^2 \quad 2.8$$

$$I_4 = a_0 \,.\, C \,.\, a_0 = \lambda^2 \quad 2.9$$

$$I_5 = a_0 . (C)^2 . a_0 \quad 2.10$$

Where, J is the Jacobian of deformation and equals to the determinant of the deformation gradient, a_0 is the unit vector in principal fiber direction and λ is the fiber stretch.

However, for the identification of the parametric coefficients of the brain tissue material from the experimental data of biaxial stretch, it was assumed that the strain energy can be described as a function of only first four invariants (Criscione et al., 2001). Hence, the strain energy function for the brain tissue material could be expressed as Equation 2.11.

$$W = W^d_{Matrix}(\tilde{I}_1, \tilde{I}_2) + W^d_{Fiber}(\tilde{I}_4) + W^v(\tilde{I}_3) \quad 2.11$$

Where, distortional strain energies of matrix and fiber are represented by W^d_{Matrix} and W^d_{Fiber} functions respectively. First and second distortional invariants of C can be expressed as in Equation 2.12 and Equation 2.13 and $\tilde{I}_4$ is the fourth distortional invariant of C.

$$\tilde{I}_1 = I_3^{-\frac{1}{3}} I_1 \quad 2.12$$

$$\tilde{I}_2 = I_3^{-\frac{2}{3}} I_2 \quad 2.13$$

Volumetric energy, $W^v(\tilde{I}_3)$, is represented in Equation 2.14.

$$W^v(\tilde{I}_3) = \frac{1}{2} K \ln(J)^2 \quad 2.14$$

Where K is the effective bulk modulus and hence, the volumetric energy depends upon the compressibility of the material. An assumption of perfect incompressibility makes the volumetric energy negligible.

Based on Franceschini et al. (2006), it was taken into consideration that the brain material exhibits non-linear mechanical behaviour and at large strains, the stiffness increases significantly. So, the brain tissue material was modeled as a non-linear solid with negligible volumetric incompressibility. Hence, Mooney-Rivlin material model, as given in Equation 2.15, was chosen for the matrix material of the brain tissue.

$$W^d_{Matrix}(\tilde{I}_1, \tilde{I}_2) = C_{10}(\tilde{I}_1 - 3) + C_{01}(\tilde{I}_2 - 3) \quad 2.15$$

Where, C_{10} and C_{01} are two model coefficients (Rivlin and Saunders 1951). It was assumed that the matrix strain energy is responsible for the brain tissue stiffening at large strains. The near

incompressibility was ensured by defining a very high value of bulk modulus K, at least three times larger than $(C_{10} + C_{01})/2$, which corresponds to initial isotropic shear modulus.

Based on experimental studies (Miller and Chinzei 2002), which demonstrated that the brain white matter exhibits different stiffness in tension and in compression, several assumptions were made for the fiber's strain energy model. First assumption was that the influence of fibers in compression can be considered negligible. Secondly, the influence of fibers in tension was assumed to increase the stiffness exponentially with the fiber stretch. Third assumption was that the deviatoric local fiber stretch, λ depends upon principal fiber direction, a_0 and can be expressed as given below in Equation 2.16.

$$\lambda = \sqrt{a_0 \,.\, C \,.\, a_0} = \sqrt{I_4} \qquad 2.16$$

Where, C is the deviatoric right Cauchy-Green deformation tensor.

Hence, the strain energy function for the fiber material of the brain tissue was adapted and is given by Equation 2.17 (Puso and Weiss, 1998).

$$\lambda \frac{\partial W^d_{Fibers}}{\partial \lambda}(\lambda) = \begin{cases} 0 & 0 \le \lambda < 1 \\ C_3\left(e^{FA*C_4(\lambda-1)} - 1\right) & \lambda \ge 1 \end{cases} \qquad 2.17$$

Where, C_3 and C_4 are the hyperelastic coefficients and depends upon mechanical properties and density of the axonal fibers. FA is the fractional anisotropy, which was included to weight the influence of fiber by anisotropic fraction. Consequently, axonal fibers have no mechanical influence on brain tissue either in compression or when the tension is perpendicular to the principal fiber direction.

Due to high strain rate sensitivity, viscosity plays an important role in the response of brain material to quasi-static loading as well as to impact loading (Prevost et al., 2011). As proposed by Fung et al. (1993), by considering the time dependent second Piola-Kirchhoff stress S(C, t), the viscoelastic behaviour can be described as given below in Equation 2.18.

$$S(C,t) = S^e(C) + S^v(C,t) \qquad 2.18$$

Where, $S^e(C)$ is the equilibrium stress and represents the long term elastic material behaviour.

Rate effects were taken into account by linear viscoelasticity, using a convolute integral representation as expressed in Equation 2.19.

$$S^v(C,t) = \int_0^t 2G(t-s)\,\frac{\partial W}{\partial C(s)}\,ds \qquad 2.19$$

Where, $G(t-s)$ is the reduced relaxation function, which can be expressed in terms of a n-order Prony series as shown in Equation 2.20.

$$G(t) = \sum_{i=1}^{n} S_i\, e^{-\frac{t}{T_i}} \qquad 2.20$$

Where, S_i is the shearing relaxation modulus and T_i is the characteristic relaxation time and these characterize the strain rate sensitivity of the model.

Parameters of this anisotropic viscous hyperelastic brain material model were identified based on various in-vivo and in-vitro studies available in literature (Chatelin et al., 2013). To identify the parameter values, the theoretical model was expressed in terms of stress-stretch for the uniaxial compression and tension, along the principal fiber direction (a_0). For this configuration, the hyperelastic first principal Cauchy stress, under the incompressibility assumption, is given by Equation 2.21.

$$\sigma^e(\lambda) = \lambda\,\frac{\partial W^d_{Matrix}}{\partial \lambda} + \lambda\,\frac{\partial W^d_{Fibers}}{\partial \lambda} - p \qquad 2.21$$

Where, λ is the stretch ratio and p is the hydrostatic pressure. In compression ($0 \le \lambda < 1$), when fibers have no influence, Equation 2.21 becomes Equation 2.22, as given below.

$$\sigma^e(\lambda) = 2\left(\lambda^2 - \frac{1}{\lambda}\right)\left(C_{10} + \frac{C_{01}}{\lambda}\right) \qquad 2.22$$

The Mooney-Rivlin hyperelastic coefficients (C_{10} and C_{01}) for the brain matrix were identified based on the data from in-vivo magnetic resonance elastography (MRE) experiments performed by Kruse et al. (2008) on healthy adult human subjects. The identified values were adapted to take into account the stiffening of brain tissue between 50% to 60% compression ($0.5 \le \lambda < 0.6$) at low as well as at high strain rates (Pervin et al., 2009 and Prevost et al., 2011). Under small stretch ($0 \le \lambda < 0.1$) the brain tissue behaviour was assumed to be linear (Nicolle et al., 2004). The parameter values were optimized using downhill simplex method. In tension ($\lambda \ge 1$), Equation 2.21 becomes Equation 2.23, where both, brain matrix and the fibers have a combined influence.

$$\sigma^e(\lambda) = 2\left(\lambda^2 - \frac{1}{\lambda}\right)\left(C_{10} + \frac{C_{01}}{\lambda}\right) + C_3\left(e^{FA*C_4\,(\lambda-1)} - 1\right) \qquad 2.23$$

Fractional anisotropy coefficient (FA) weights the projection of the principal stretch in the fiber direction. In case of pure isotropy, FA = 0 and hence, the fiber term becomes zero. Also, in case of

tension, orthogonal to principal fiber direction or compression, $\lambda = 1$ and hence, the fiber term becomes zero. The critical fiber stretch ratio was kept unusually high, so as to evaluate the material stresses under the influence of both, the matrix and the fiber. Identified Mooney-Rivlin hyperelastic coefficients enabled the interpolation of brain matrix behaviour in tension. For the identification of viscoelastic parameters, S_i and T_i, experimental relaxation data of dynamic mechanical analysis in shearing as reported by Shuck and Advani (1972) was utilized. The resulting relaxation modulus versus time curve was scaled to 13.6 kPa (Kruse et al., 2008), so that, the continuity between hyperelastic (non-linear) and viscoelastic (linear) models could be ensured. The brain fibers were modeled only as hyperelastic material because of the lack of experimental viscoelastic data on brain fibers.

This anisotropic viscous hyperelastic material model was validated against experimental data and was published in Chatelin et al. (2013). The same material model is incorporated in the developed FERBM along with some modifications required for the adaption to the rat brain. Figure 2.14 illustrates the stress stretch behaviour of this material model (Chatelin et al., 2013).

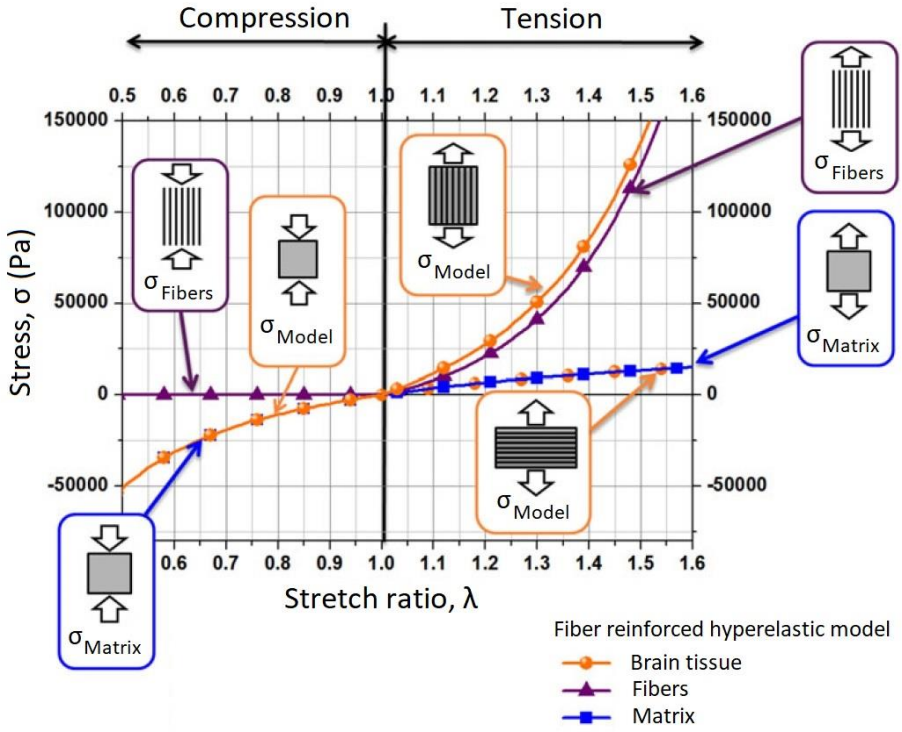

Figure 2.14: Diagram illustrating stress-stretch behaviour of fiber reinforced hyperelastic brain material model developed by Chatelin et al. (2013).

The parameters identified by Chatelin et al. (2013) were incorporated in *MAT_092 i.e. *MAT_SOFT_TISSUE_VISCO material model of LS-DYNA, along with the diffusion parameters, which were identified from the DTI atlas of Rumple et al. (2013). Table 2.3 reports these parameter's details, along with their equivalent LS-DYNA parameter. Diffusion parameter FA was incorporated along with

the hyperelastic coefficient C_4. Whereas, PFD, which is the anisotropy vector was incorporated by assigning its three components to LA_1, LA_2 and LA_3 parameters of the LS-DYNA material model (*MAT_SOFT_TISSUE_VISCO) respectively.

Table 2.3: Parametric details for the incorporation of anisotropic viscous hyperelastic material law in LS-DYNA's *MAT_092 i.e. *MAT_SOFT_TISSUE_VISCO material model.

LS-DYNA parameter	Model parameter	Unit	Description	Value
RO	ρ	Kg/m^3	Density	1040
C_1	C_{10}	kPa	Mooney-Rivlin hyperelastic coefficient for matrix	-1.034
C_2	C_{01}	kPa		7.809
C_3	C_3	kPa	Fiber reinforcement hyperelastic coefficient	13.646
C_4	C_4	-		4.64 x FA[#]
C_5	C_5	kPa	Hyperelastic coefficient	68.72
XK	K	MPa	Bulk modulus	1125
XLAM	λ	-	Critical fiber stretch ratio	11
AX, AY, AZ, BX, BY, BZ	-	-	To define local element axes	1, 0, 0, 1, 1, 0 (for AOPT = 2)
LA1, LA2, LA3	a_{0x}, a_{0y}, a_{0z}	-	Principal fiber direction vector (a_0) defined in local element frame	[#]
S1	S_i	kPa	Long-term shearing relaxation moduli	4.5
S2				9.11
T1	T_i	ms	Characteristic relaxation times	$1x10^{-6}$
T2				145

[#]DTI parameters, which were incorporated via python programming

Python programming was done to assign the material properties to every single element of the brain. Hence, all the 13,236 elements of the FERBM were assigned different material properties separately. All the elements have similar viscous hyperelastic material properties for the matrix material; but,

different fiber material properties in terms of fractional anisotropy (FA) and principal fiber direction (PFD) as determined from the DTI atlas.

5.3 Cerebrospinal fluid material

Cerebrospinal fluid (CSF) is found between the brain and the skull as a cushioning material to protect the brain from mechanical shocks and to serve various other neurological purposes. Many studies are found in literature, which characterizes the CSF material differently for use in biomechanical simulations. Some considered CSF as an elastic material, some others as viscoelastic material and others as elastic fluid. Most of the studies have provided arguments in support of their material characterization choices. However, the properties used highly depend upon the kind of loading and the boundary conditions. Jin et al. (2015) performed biomechanical simulations on the human head, with different material properties of CSF, to recreate some experimental cases. Upon comparison of the results, it was found that the CSF modeled as elastic fluid and with a very high bulk modulus replicated the results more closely than any other modelling ways. Hence, for the developed FERBM, the CSF material was assumed to be elastic fluid, having a density of 1000 kg/m^3 and a high bulk modulus of 6750 MPa. The LS-DYNA material model chosen for CSF is *MAT_001 i.e. *MAT_ELASTIC_FLUID.

5.4 Skull material

In this study, the skull was modeled as a rigid material, having a density of 1900 kg/m^3, Young's modulus of 10 GPa and Poisson's ratio of 0.22. LS-DYNA material model chosen for skull was *MAT_20 i.e. *MAT_RIGID. The skull was modelled as a rigid material, so that the loading on the brain can be applied in an appropriate manner by assigning proper boundary conditions on the skull.

5.5 Conclusion

This section provided details about material properties and how these have been incorporated in the anisotropic FERBM. Material model developed by Chatelin et al. (2013) had been utilized with human brain (in Strasbourg University Finite Element Head Model, SUFEHM) and has proved to be very useful. Hence, it was hypothesized that this material model, with the incorporation of rat brain diffusion properties, will be useful for the investigations on the rat brain as well. It is worth remembering here that this hypothesis is based on the literary evidences of tissue level similarities between rat and the human brains, which have been mentioned earlier as well. Hence, the developed FERBM consist of an anisotropic viscous hyperelastic material model.

6 Validation against experimental dynamic cortical displacement

6.1 Introduction

Shreiber et al. (1997) performed experiments on adult, male Sprague Dawley rats, weighing 350 to 400 g. Load application was in terms of a vacuum pressure pulse on the brain surface and the cortical displacement of the exposed cortex was measured through a laser displacement transducer. This experimental dynamic cortical displacement data was used to compare the response of the computational model for validation purpose. Following paragraph provides the experimental specifications, which were used for the reconstruction in terms of the numerical simulations.

6.2 Experimental specifications

To apply a vacuum pressure pulse on the rat brain surface, a 5 mm diameter craniectomy was performed over the parietal cortex on the left side of the brain. Dura was removed from this region, in order to avoid any mechanical resistance to the vacuum pressure pulse. The experiments were performed for three magnitudes of vacuum pressure pulse, which are 2 psi (13.8 kPa), 3 psi (20.7 kPa) and 4 psi (27.6 kPa) and for three different durations (25 ms, 50 ms and 100 ms). Thus, the experiments were performed on the rat brain for nine different loadings and a total of seven animals were tested for each loading condition. However, only six loading curves were available in literature, therefore, only six experimental loading conditions were simulated. Figure 2.15 displays these available experimental pressure vs time curves, which were also used for the model validation simulations.

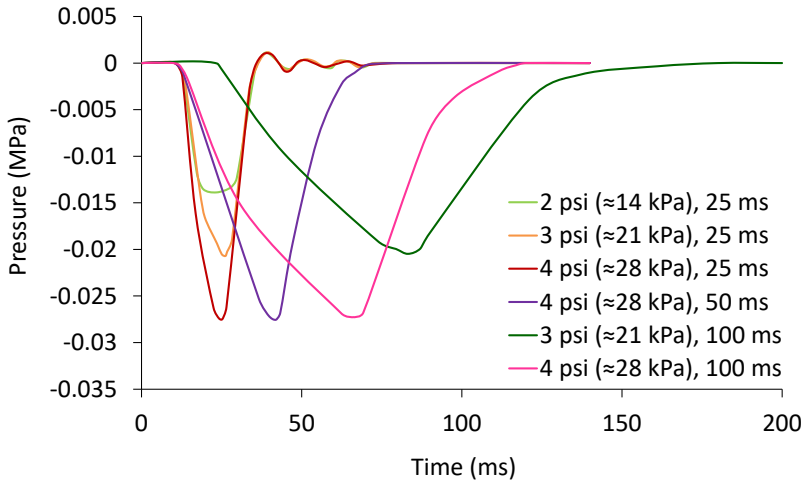

Figure 2.15: Diagram representing pressure versus time loading curves applied in dynamic cortical displacement experiments as well as validation simulations (Shreiber et al., 1997).

For every loading condition, mean peak cortical displacement was measured with the help of a laser displacement transducer. Experimental measurements of dynamic cortical displacement are given in Table 2.4.

Table 2.4: Experimental measurements of dynamic cortical displacement (DCD) (where number of animals per loading scenario, n = 7) (Shreiber et al., 1997).

Experimental DCD (mm)	2 psi, 25 ms	3 psi, 25 ms	4 psi, 25 ms	4 psi, 50 ms	3 psi, 100 ms	4 psi, 100 ms
Mean	1.0	1.1	1.2	1.5	1.3	1.7
Standard deviation	0.4	0.3	0.5	0.6	0.4	0.6

6.3 Numerical simulations

To reconstruct the dynamic cortical displacement experiments numerically, some modifications were made to the model. At first, to represent the craniectomy, skull shell elements and CSF solid elements, from over the left parietal cortex, were removed for an area of approximately 5 mm diameter. Secondly, a material erosion criterion was assigned to the elements of the CSF layer. This was done to reproduce the leakage of CSF from between the brain and the skull, as a result of craniectomy and dura removal. Based on the intracranial pressure (ICP) inside the rat head, which usually is equal to 4 mmHg - 10 mmHg (0.5 kPa – 1.3 kPa), the CSF elements were eroded, if the maximum pressure value was more than 1.1 kPa or the minimum pressure value was less than -1.1 kPa. In case of complete erosion of the CSF elements, a LS-DYNA contact, *CONTACT_AUTOMATIC_SURFACE_TO_SURFACE, was defined between the skull and the brain elements with a low coefficient of friction of 0.2. The skull was fixed in space and the loading was applied by means of a vacuum pressure pulse over the exposed brain elements (Figure 2.16).

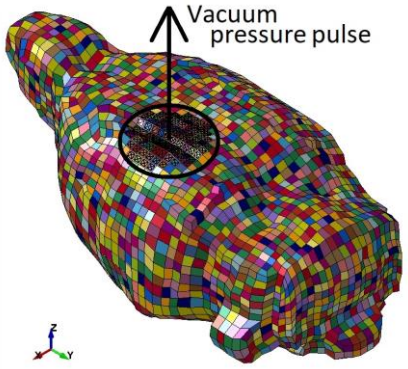

Figure 2.16: Diagram representing the model, highlighting the region where vacuum pressure pulse was applied.

A total of six simulations were conducted for the available pressure pulses as given in Figure 2.15. To measure the dynamic cortical displacement, maximum displacement of nodes at the center of craniectomy, in a region of one mm diameter, was measured and averaged to compare with the experimental results. One mm diameter was chosen according to the diameter of the displacement transducer's laser beam, which was used to measure the experimental DCD as given in Shreiber et al. (1997). Figure 2.17 displays the model before loading and after loading at the peak displacement position for 4 psi (≈28 kPa), 25 ms loading scenario.

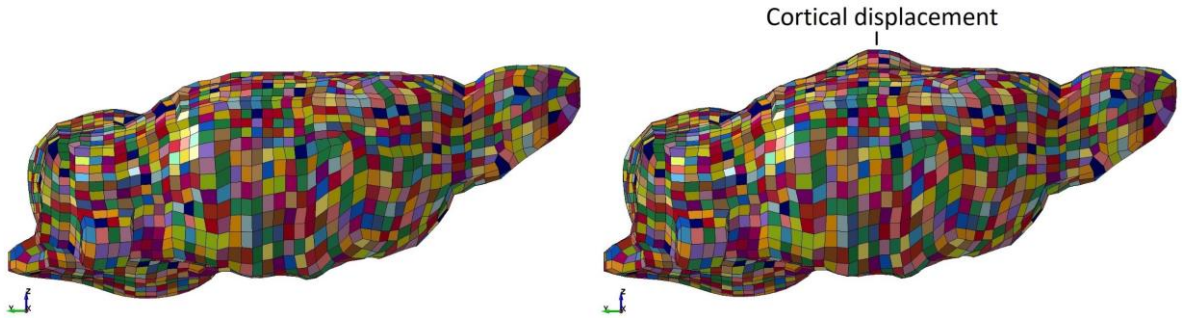

Figure 2.17: Diagram representing the model before loading (left) and after loading at the peak displacement position (right) for a 4 psi (≈28 kPa), 25 ms loading scenario.

Simulation results are given in Table 2.5 and a comparison of simulation results with the experimental results is provided in the following section.

Table 2.5: Simulation measurements of dynamic cortical displacement (DCD).

Simulation DCD (mm)	2 psi, 25 ms	3 psi, 25 ms	4 psi, 25 ms	4 psi, 50 ms	3 psi, 100 ms	4 psi, 100 ms
Mean	0.7	0.9	1.1	1.1	0.9	1.1
Standard deviation	0.01	0.02	0.04	0.04	0.03	0.04

All the simulations were performed on LS-DYNA platform and the average simulation time was around five hours.

6.4 Results of dynamic cortical displacement validation

For different loading scenarios, results of simulation and experimental dynamic cortical displacements are given in Figure 2.18. Experimental results are given as a mean peak cortical displacement value and the standard deviation, whereas simulation results are given as averaged maximum cortical displacement value.

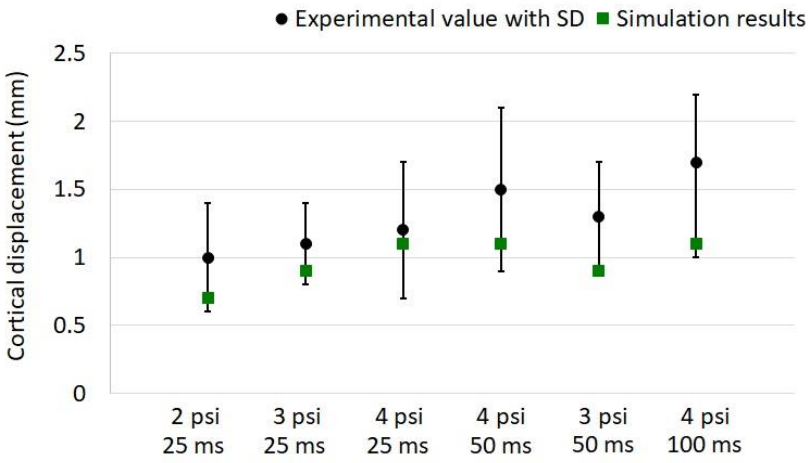

Figure 2.18: Diagram representing experimental and simulation dynamic cortical displacement measurements for different loading scenarios.

It is evident from the diagram that the simulation results are within the experimental range, almost for all the scenarios. Hence, we can conclude that the model was validated against experimental dynamic cortical displacement. If we observe closely, we can clearly see the influence of the magnitude of pressure pulse. As for similar duration of 25 ms, with an increase in the magnitude of pressure from 2 psi to 3 psi and to 4 psi the dynamic cortical displacement (DCD) increased from 0.7 mm to 0.9 mm and to 1.1 mm respectively. On the other hand, influence of the increase in the duration of pulse, which is clearly apparent from the experimental result was not seen in the simulation result. There could be multiple reasons for this difference in the results. One of the possible reasons could be material properties. The diffusion parameters of the material properties were identified through an in-vitro DTI atlas. However, in-vivo brain behaves differently than an in-vitro brain. Another reason could be the difference in the weight of the animal. All the required details (e.g. the DTI atlas and the experimental protocol) are not always available for the exact same subject. The DTI atlas was built from Sprague Dawley rats of around 290 g, whereas weight of the DCD experimental Sprague Dawley rats varied from 350 g to 400 g. A possibility that this might influence the brain response in some way or the other cannot be neglected. Other simulation parameters also influence the brain response, which are explained later in the parametric study section.

6.5 Conclusion

The validation of the developed anisotropic FERBM against experimental dynamic cortical displacement, on the application of vacuum pressure pulse was covered in this section. With different values of simulation parameters, it was possible to get even better simulation results, i.e. a response, which was more close to the experimental mean. However, for the model to pass the other validation (brain-skull relative displacement) as well, the one presented in Figure 2.18 was the best feasible

solution. Also, the main purpose of this study was not only the development of a validated model, but to go further and to be able to get additional insights into the rat brain in terms of axonal elongation in case of concussion. To the author's best knowledge, this is first of its kind study on the rat brain. Hence, the model was considered validated against experimental dynamic cortical displacement.

7 Validation against experimental brain-skull relative displacement

7.1 Introduction

Antona-Makoshi et al. (2014) performed experiments on three adult male Sprague Dawley rats, weighing around 500 g. Application of the load was in terms of rotational acceleration pulse in the sagittal plane to measure the displacement of the brain relative to the skull. This was done by inserting a needle in the brain, in such a manner that the needle was kept firmly fixed with the skull. Hence, the rotation of the head produced a scar on the brain due to the relative movement between the brain and the skull. This scar length was measured, at four depths from the brain surface, to identify the brain-skull relative displacement at four different depths. In order to validate the model, these experimental scar lengths at four depths were compared with the simulation results that were measured in terms of nodal displacements at those specific locations. Following paragraph provides the experimental specifications, which were used for the numerical simulations.

7.2 Experimental specifications

To apply a rotational acceleration loading on the rat head in sagittal plane, the rat was placed at a designated place on the base and the rat head was fitted to a rotating bar of the trauma producing equipment (Figure 2.19). To make this fit possible, at first a midline incision was made on the rat scalp and then the tissue was removed from above the frontal, parietal skull bone region. A metallic skull cap was then glued to the skull and was fastened with an attachment plate. This attachment plate made the fit between the rat head and the equipment possible.

The skull cap was designed in such a manner that a 0.6 mm diameter hole was drilled through the skull for the insertion of a 0.5 mm diameter needle. This needle was inserted until 3 mm depth inside the brain cortex at a location, 3.5 mm rear and 2.2 mm to the right of bregma and was firmly fixed with the skull. A short rearward rotation of the rat head in sagittal plane was induced through a rotational acceleration pulse, by hitting a striker on the targeted rubber block of the trauma producing equipment. This rearward rotation continues until the striker target comes in contact with the foam covered rigid cross beam as shown in Figure 2.19.

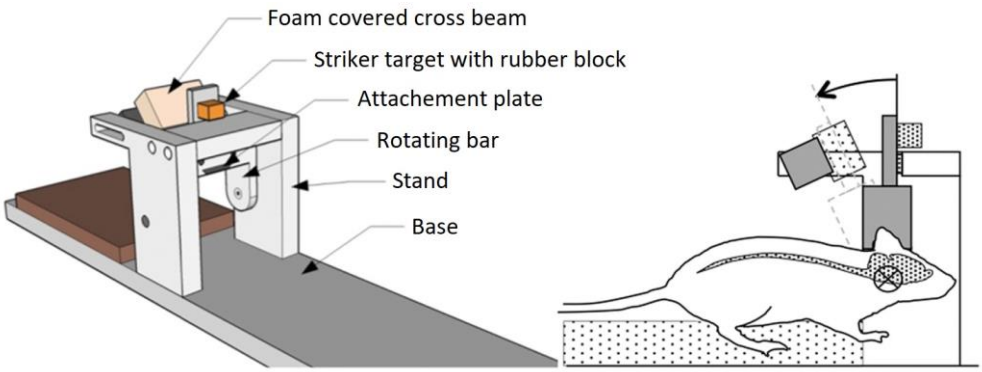

Figure 2.19: Diagram representing trauma producing equipment on the left and a schematic depiction of the side view of the rat head, fitted in the equipment (Davidsson and Risling, 2011).

The averaged experimental rotational acceleration versus time loading curve, which was also used to recreate the experiment through numerical simulation is furnished in Figure 2.20. Inserted needle caused a scar on the brain cortex because of the relative movement between brain and skull. Immediately after the trauma, the needle was removed and the brain was fixed. Afterwards, the brain was sliced, in a plane perpendicular to the inserted needle, at four depths from the brain surface, so as to measure the scar length at these four different depths, which are 0.5 mm, 1.0 mm, 1.5 mm and 2.0 mm. The measured scar length at these depths is the experimental brain-skull relative displacement data, against which the model was validated. Table 2.6 provides the experimental brain-skull relative displacement measurements as per Antona-Makoshi et al. (2014).

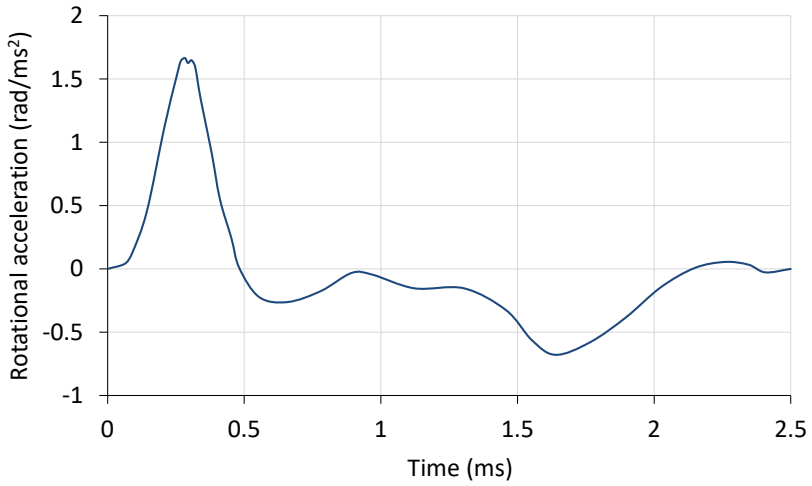

Figure 2.20: Diagram representing experimental averaged rotational acceleration versus time loading curve (Antona-Makoshi et al., 2014), also applied in the brain-skull relative displacement validation simulations.

Table 2.6: Experimental measurements of brain-skull relative displacement (BSRD).

Experimental BSRD (mm)	0.5 mm below surface	1.0 mm below surface	1.5 mm below surface	2.0 mm below surface
Rat 1	1.1	1.1	0.9	0.6
Rat 2	1.3	1.4	1.1	0.7
Rat 3	1.1	1.2	1.1	0.6
Average	1.2	1.2	1.0	0.6

7.3 Numerical simulations

As there was only one loading applied to the rat head, only one simulation was carried out to measure the brain-skull relative displacement. The load curve applied in terms of rotational acceleration versus time is given in Figure 2.20. The center of rotation was chosen in such a manner that the center of gravity of the brain was around 6.5 mm above the center of rotation (Davidsson and Risling, 2011). Figure 2.21 displays the model before and after the loading.

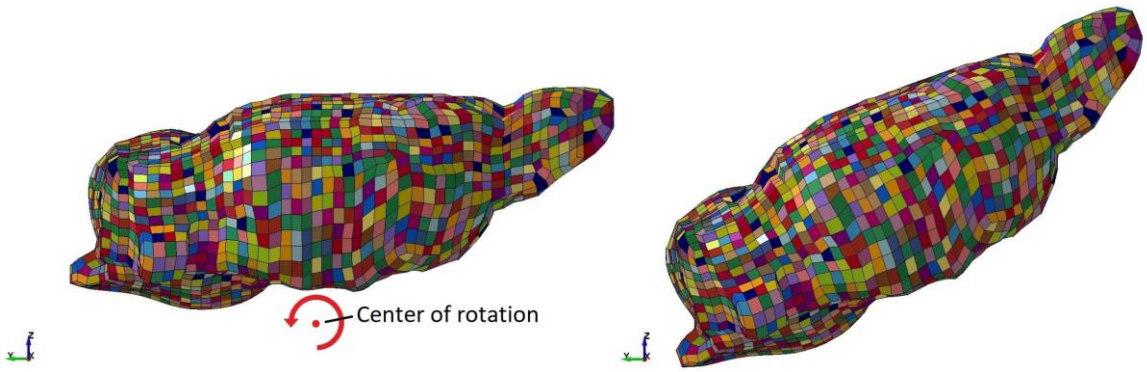

Figure 2.21: Diagram representing the model before (left) and after (right) the rotational acceleration loading in the sagittal plane.

Representative nodes chosen for the measurement of the brain-skull relative displacement at four different depths are illustrated in Figure 2.22. The top most node is on the skull, relative to which the movement of four nodes below were measured. The representative nodes were chosen at a location, 3.5 mm rear and 2.2 mm right to the bregma as per the needle location given in Antona-Makoshi et al. (2014).

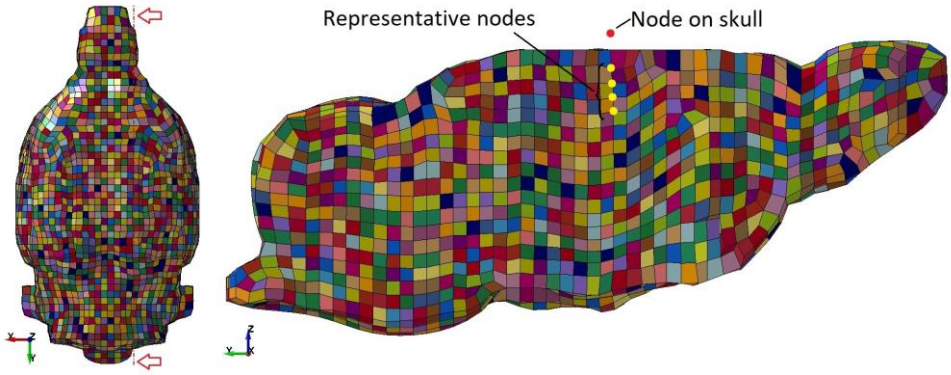

Figure 2.22: Diagram illustrating the representative nodes in yellow (right) through a sagittal plane cut (left) at 2.2 mm right to the bregma. Displacement of these nodes were measured relative to the node on the skull (red) to find out the brain-skull relative displacement at four depths below the brain surface.

The simulation was performed on LS-DYNA platform and the simulation time was around 20 minutes. The simulation was also checked for the stability and the maximum hourglass energy of the model was within 15% of the maximum internal energy. Simulation results of brain-skull relative displacement at four depths are given in Table 2.7.

Table 2.7: Simulation measurements of brain-skull relative displacement (BSRD).

Simulation BSRD (mm)	0.5 mm below surface	1.0 mm below surface	1.5 mm below surface	2.0 mm below surface
FERBM	1.1	1.1	1.1	1.2

7.4 Results of brain-skull relative displacement validation

On comparing the results of the simulation with that of the experiment (Figure 2.23), it is seen that there is a reasonable agreement between the two, at first three depths. This enables us to conclude that the model was validated against experimental brain-skull relative displacement. However, a significant difference is evident between the results at the fourth depth. There could be many possible reasons for this difference. As mentioned earlier, one of the possible reasons could be material properties. Another could be weight of the animal, which was quite significantly different in this case (290 g vs 500 g). The influence of a parametric variation is explained in the following section and can help us understand the brain response in a better way.

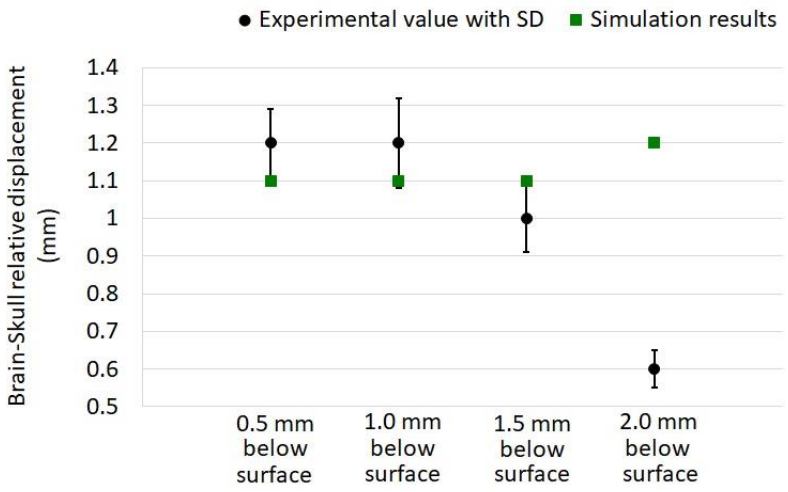

Figure 2.23: Diagram representing experimental and simulation brain-skull relative displacement measurements.

7.5 Conclusion

This section explained the validation of the developed anisotropic FERBM against brain skull relative displacement on the application of rotational acceleration loading in the sagittal plane. For first three depths, the simulation results are in good agreement with the experimental results. However, the difference in the BSRD measurement at the fourth depth is significant. Despite all other factors, we cannot neglect the fact that in the experimentation, there was a needle inserted in the brain, which would have influenced the response of the brain in some way or the other. However, in the simulations, that was not the case and it was supposed that the nodal behaviour of the selected nodes represents the actual behaviour as in the experiments. Hence, the model was considered validated against the experimental brain-skull relative displacement.

8 Parametric study

Parametric study plays an important role in adjudging the robustness of a developed finite element model. Varying the parameter value and checking the influence of this change on the brain response not only help in identifying critical parameters, but also in supporting the choice of parameter values. As a part of this study, at first, influence of the brain material variation was observed. Developed anisotropic finite element rat brain model (FERBM) uses an anisotropic viscous hyperelastic material law. For the parametric study, simulations performed for the dynamic cortical displacement (DCD) validation and for the brain-skull relative displacement (BSRD) validation were rerun with general viscoelastic material law of the rat brain. LS-DYNA material model *MAT_076 i.e. *MAT_GENERAL_VISCOELASTIC was used for this purpose. This variation was selected since many of the biomechanical studies on the rat brain have used this material for the brain tissue modeling. It

was found that DCD measurements increased significantly with the general viscoelastic material law of the brain tissue (Figure 2.24). For the loading of 2 psi - 25 ms, 3 psi - 25 ms, 4 psi - 25 ms, 4 psi - 50 ms, 3 psi - 100 ms and 4 psi - 100 ms the DCD measurements were found to increase by 21%, 22%, 18%, 18%, 22% and 27% respectively from the actual simulation values.

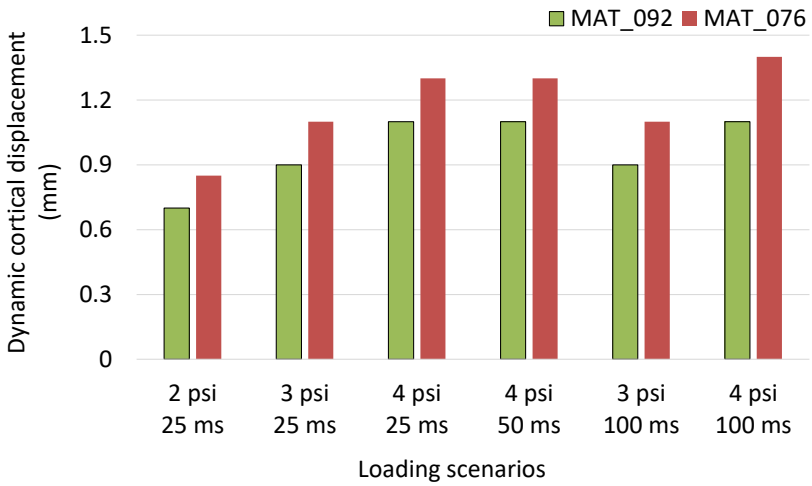

Figure 2.24: Diagram representing simulation dynamic cortical displacement measurements with MAT_092, i.e. anisotropic viscous hyperelastic brain material law and with MAT_076, i.e. general viscoelastic brain material law for different loading scenarios.

A similar trend was visible in the BSRD simulations as well. It was found that BSRD measurements as well increased significantly with the general viscoelastic material law of the brain tissue (Figure 2.25).

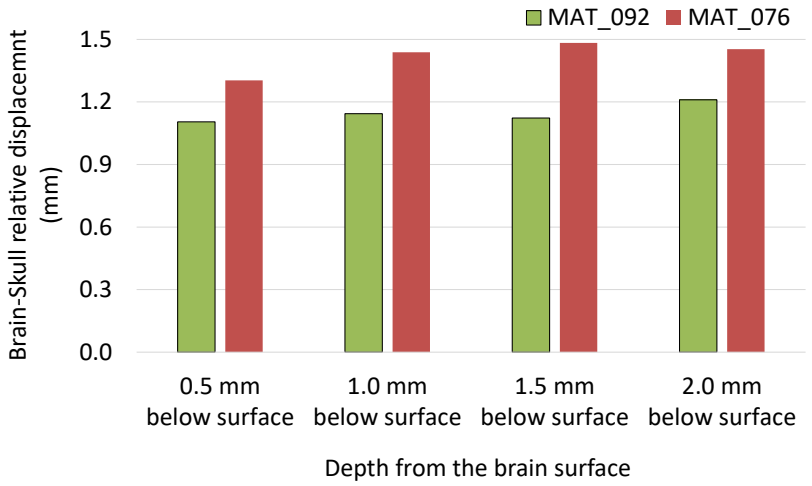

Figure 2.25: Diagram representing simulation brain-skull relative displacement measurements with MAT_092, i.e. anisotropic viscous hyperelastic brain material law and with MAT_076, i.e. general viscoelastic brain material law for different loading scenarios.

An increase of 18%, 22%, 34% and 24% was observed in the BSRD measurements at depths of 0.5 mm, 1.0 mm, 1.5 mm and 2.0 mm respectively. Thus, the influence of anisotropy and hyperelasticity is clearly evident from these results.

Another parametric variation was chosen in terms of just the anisotropy. The values of diffusion parameters, i.e. fractional anisotropy (FA) and the principal fiber direction (PFD), were made zero and the validation simulations were carried out again. This was done out of curiosity to see the influence of diffusion parameters on brain response. However, as both, the dynamic cortical displacement and the brain-skull relative displacement, are global measurements, there was no change in the brain response in case of the DCD measurements and negligible change in case of the BSRD measurements. Then, to check the influence of diffusion parameters locally, some random nodes were chosen in highly anisotropic regions as well as in highly isotropic regions and the displacement – time histories of these nodes were evaluated. As a result, it was observed that there exist a difference in the brain response, though very small, with and without the inclusion of diffusion parameters. However, due to the unavailability of any experimental data of this kind, this difference could not be assessed to be correct or incorrect.

Another parametric study was performed to observe the influence of cerebrospinal fluid's (CSF) bulk modulus (K) on the BSRD measurements. The CSF's bulk modulus value for the validated anisotropic FERBM is equal to 6570 MPa. For this parametric study, the brain response was identified at one-tenth, one-third, half, twice and ten times the actual bulk modulus value, which are 657 MPa, 2190 MPa, 3285 MPa, 13140 MPa and 65700 MPa respectively, while all other parameters were kept the same. The BSRD measurements of validated FERBM were taken as reference values and the deviation was measured in terms of percentage increase or decrease. It was found that with a decrease in the value of the bulk modulus, the brain-skull relative displacement measurement increases and vice versa. At first depth, i.e. 0.5 mm below the brain surface, there was a 100% increase in the value of BSRD measurement for the one-tenth value of actual K. However, a decrease in this increased value was observed, as the depth from the brain surface increased. The increase in BSRD measurement for this one-tenth K value at depths of 1.0 mm, 1.5 mm and 2.0 mm below the surface was found to be 82%, 64% and 25% respectively. Similar trend was visible at one-third K value as well. The increment in BSRD measurements, at depths of 0.5 mm, 1.0 mm, 1.5 mm and 2.0 mm below the surface, were 45%, 36%, 27% and 8%. At half the K value, there was an increment of 27% at first two depths, 18 % at third depth and no change at the fourth depth. On the other hand, at double the K value and at ten times K value, the BSRD measurements decreased and also, a further decrease in this decrement was observed by further going deep inside the brain. There was a decrease of 27%, 18%, 9% at first three depths, and no change at fourth depth at double the K value. These decrements were 45%, 27%, 18% and 8% at ten times the K value for four depths respectively. Figure 2.26 displays the actual BSRD measurements at four depths below brain surface for different bulk modulus (K) values.

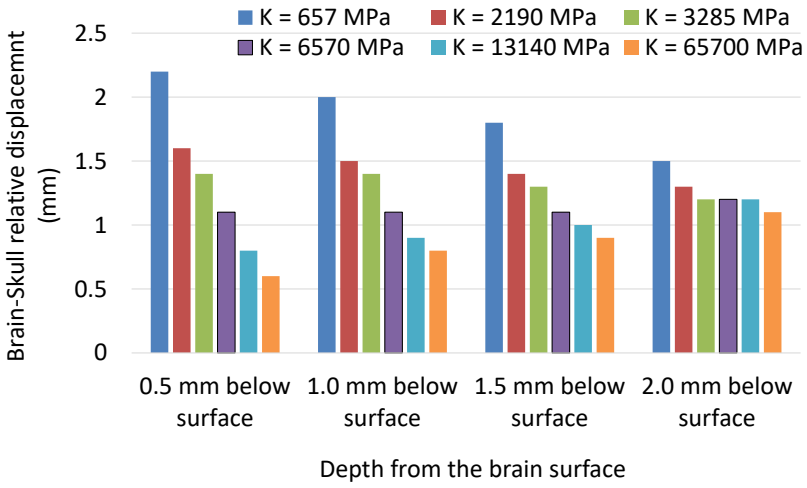

Figure 2.26: Diagram representing simulation brain-skull relative displacement measurements at four depths for different values of CSF's bulk modulus (K).

It was observed that the high value of CSF's bulk modulus restricts the movement of the brain inside the skull, whereas a smaller value of CSF's bulk modulus adds to the flexibility of the brain movement. This is understandable, since bulk modulus is nothing but the measure of compressibility of a substance. Both the brain and the CSF layer are closed inside the rigid skull. Hence, the overall flexibility of the brain movement was found to be highly influenced by the compressibility of CSF. However, this trend was highly prominent at initial depths than at the later ones.

The influence of CSF's bulk modulus on DCD measurements was found to be negligible, which is logical. As mentioned earlier, the CSF's bulk modulus value for the validated anisotropic FERBM is equal to 6570 MPa. For this parametric study, the brain response was observed for one of the loading scenarios, i.e. 4 psi (≈28 kPa) and 25 ms (the highest magnitude and the shortest duration scenario), at one-tenth, one-third, half, twice and ten times the actual bulk modulus value, which are 657 MPa, 2190 MPa, 3285 MPa, 13140 MPa and 65700 MPa respectively, while all other parameters were kept the same. The DCD measurements of validated FERBM were taken as reference values and the deviation was measured in terms of percentage increase or decrease. It was found that with a change in the value of the bulk modulus, the dynamic cortical displacement measurements does not change. Due to the craniectomy over left parietal cortex, on loading, CSF leakage occurs and hence, CSF's bulk modulus does not influence brain deformation.

Hourglass energy plays an important role in checking the accountability of any simulation. In LS-DYNA, one of the methods to control hourglass energy is to control the hourglass formulation. Hence, another parametric study was performed to see the influence of hourglass parameters on the BSRD measurements. Variation in two hourglass parameters, IHQ, i.e. hourglasses control type, and QH, i.e.

hourglass coefficient, were observed. Figure 2.27 displays the actual BSRD measurements at four depths below the brain surface for different hourglass coefficients.

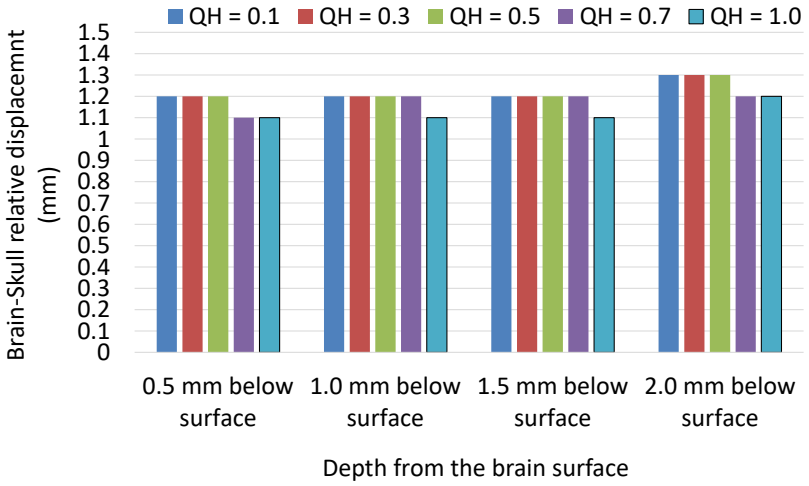

Figure 2.27: Diagram representing simulation brain-skull relative displacement measurements at four depths for different values of hourglass control parameter QH (hourglass coefficient).

The actual values of these control parameters in the validated FERBM are IHQ = 7 and QH = 1.0. Brain response was observed for IHQ values equal to 1, 2, 3 and 6 with a QH value of 1.0 and then for a QH value of 0.1, 0.3, 0.5 and 0.7 with an IHQ value of 7. As mentioned earlier QH is nothing but the hourglass coefficient. However, IHQ refers to different hourglass control types, as per LS_DYNA manual, IHQ = 1 belongs to standard viscous form, IHQ = 2 belongs to viscous form (Flanagan-Belytschko integration for solid element), IHQ = 3 belongs to viscous form (Flanagan-Belytschko with exact volume integration for solid element) and IHQ = 6 belongs to Belytschko-Bindeman assumed strain co-rotational stiffness form for 2D and 3D solid elements. It was seen that there was a small increase (within 10%) in the values of BSRD measurements as the QH reduced from 1.0 to 0.1 and the hourglass energy remained within 15% of the internal energy for all the cases.

For the IHQ variation, it was seen that for the first three IHQ values, i.e. 1, 2 and 3, not only the BSRD measurements decreased considerably (8% to 45%), but also the hourglass energy was much higher than the internal energy, to an extent that is not acceptable. This is understandable because hourglass control types (IHQ = 1, 2 and 3) are suitable only with a QH value less than 0.15. Hourglass energy came in control with the hourglass formulation of IHQ = 6, but the BSRD measurements were 10% to 20% higher. Influence of IHQ parameter on BSRD measurements at four depths are depicted in Figure 2.28.

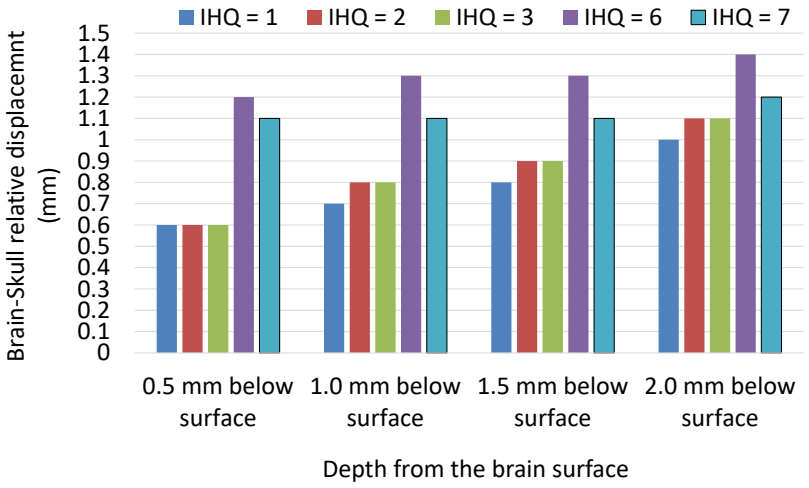

Figure 2.28: Diagram representing simulation brain-skull relative displacement measurements at four depths for different values of hourglass control parameter IHQ (hourglass control type).

With regard to DCD measurements for a 4 psi (≈28 kPa), 25 ms loading scenario, an increase was observed in the values of DCD measurements as the QH reduced from 1.0 to 0.1 and the hourglass energy remained within acceptable limits for all the cases. For a QH value equals to 0.7, there was a 4.5% increase in the DCD measurement and this increase further increased as the QH values reduced from 0.5 to 0.3 and to 0.1. The DCD measurements at these QH values were found to increase by 10%, 17.3% and 32.7% respectively. Figure 2.29 displays the actual DCD measurements for different hourglass coefficients for 4 psi (≈28 kPa), 25 ms loading scenario.

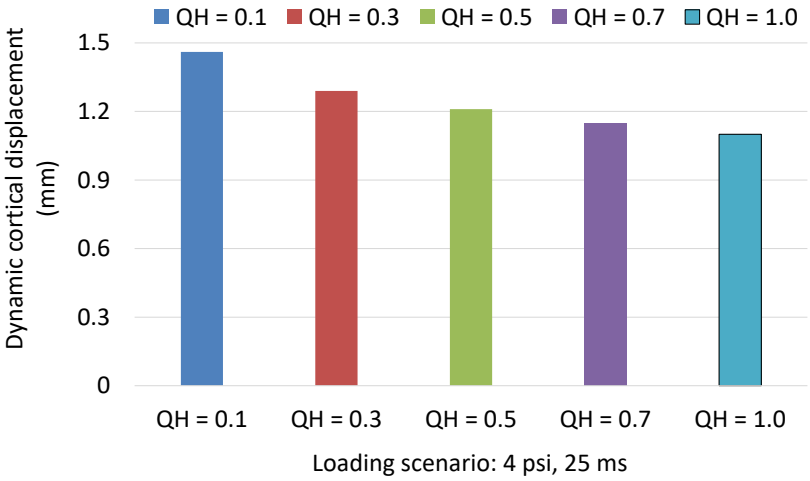

Figure 2.29: Diagram representing simulation dynamic cortical displacement measurements for different values of hourglass control parameter QH (hourglass coefficient) for 4 psi (≈28 kPa), 25 ms loading scenario.

With regard to DCD simulations, the parametric study for IHQ variation was not feasible. Since, the actual value of QH in the validated FERBM is equal to one and hourglass control types (IHQ = 1, 2 and 3) are suitable only with a QH value less than 0.15. On one hand, DCD simulations with a variation of

IHQ (1, 2 and 3) for a QH value equal to 0.1 showed no difference in the DCD measurements for 4 psi (≈28 kPa), 25 ms loading scenario. On the contrary, these values were 17.7% higher than the DCD measurement for IHQ = 7 and QH = 0.1 for 4 psi (≈28 kPa), 25 ms loading scenario. Also, the hourglass energy was much higher than the internal energy, to an extent that is not acceptable.

Thus, this parametric study revealed that the choice of brain material highly influence the brain response for a given loading condition. An isotropic general viscoelastic brain material law seemed to be more flexible than the anisotropic viscous hyperelastic brain material law. It was also observed that the compressibility of the cerebrospinal fluid influenced the brain response significantly. On the other hand, hourglass coefficient (QH) of the hourglass formulation, neither influences the hourglass energy considerably, nor the brain response; whereas for the hourglass control type (IHQ) of the hourglass formulation, a significant influence could be seen on both, the hourglass energy and the brain response.

9 Conclusion

This chapter presented the development of an anisotropic viscous hyperelastic finite element rat brain model (FERBM). To the author's knowledge, this is the first time that an anisotropic finite element model of a rat brain has been developed. As a starting point, a DTI atlas was chosen for the geometrical construction of the rat brain. Digitized brain surface was rendered from the DTI atlas as a STL representation and then surfacing and meshing of the enclosed brain volume was carried out on HyperMesh platform. The meshed brain model consists of 13,236 hexahedral solid elements. This meshed model was enclosed inside another layer of 3,252 hexahedral solid elements representing cerebrospinal fluid. Both of these were further enclosed inside a rigid skull, which was modeled by 3,252 quadrilateral shell elements. All the elements were meshed in a way that the continuities between the brain and the CSF elements and between the CSF and the skull elements were maintained.

In the second phase of the development, diffusion parameters for every element of the FERBM were estimated. The same DTI atlas, as mentioned earlier, was used to calculate the diffusion parameters per voxel. Once the voxels per element were identified, the diffusion parameters per element were estimated through a weighted average function, such that the voxels near the center of the element had higher weightage than those at the element boundary. Diffusion parameters estimated per element are fraction anisotropy (FA) and principal fiber direction (PFD). All of the above were done through Python programming.

The last phase of model development was to decide upon the constitutive law and the material properties. An anisotropic viscous hyperelastic material model developed by Chatelin et al. (2013) was chosen and adapted for the rat brain. Though this material model was developed for an adult human, based on the evidences available in literature, it was hypothesized that with the inclusion of rat brain's diffusion parameters, it could be used for the rat brain. At tissue level, it is the same neurons and axons spread inside glia. Hence, this material model was incorporated into FERBM through *MAT_SOFT_TISSUE_VISCO material model of LS-DYNA. The implementation of material properties and the diffusion parameters for every element of the FERBM was done through Python programming. Thus, the developed FERBM is an anisotropic viscous hyperelastic finite element rat brain model, where every element of the brain has a different material property.

The second half of this chapter presented the validation of a newly developed anisotropic finite element rat brain model. The model is validated against two kinds of experimentations available in literature. The first validation was against the dynamic cortical displacement measurements, as reported by Shreiber et al. (1997) and the second validation was against the brain-skull relative displacement measurements, as reported by Antona-Makoshi et al. (2014). This is the first time that a rat brain model has been validated for more than one experimentation available in literature. Though the model was validated, it cannot be concluded as an optimum validation. This is because of two reasons. First, the model was validated for two different experimental measurements simultaneously and hence, optimality was compromised. Second, the main objective of this study was to be able to get additional insights into the rat brain in terms of axonal elongation in case of concussion and not only the model validation. Nevertheless, the model can be considered validated reasonably. Parametric study showed the importance of brain material law, compressibility of cerebrospinal fluid and the hourglass control on the brain response. There always exists some uncertainties regarding the available experimental data. Regardless of all this, the overall behaviour of the developed anisotropic finite element rat brain model was validated. Now that we have a validated anisotropic FERBM, following and the final chapter provides simulations of experimental concussion, the results and the analysis.

The main motive behind developing an anisotropic FERBM was to be able to get insights into the rat brain in terms of axonal elongation in case of concussion. Once the diffusion parameters were incorporated in the rat brain and the principal fiber direction per element was known, the identification of axonal strain per element would become possible. Ultimately, after simulating a mild trauma, the elements of high axonal strain made it possible to identify the brain regions that are more

susceptible to injury. And finally, this helped in identifying the mechanical threshold to concussion in terms of axonal stretch.

Chapter 3: Simulations of experimental concussion

1 Introduction

As mentioned earlier, computational modelling has proved to be a promising tool in studying brain injury. A validated computational model comes to its best usage when real world or experimental scenarios are simulated, in order to investigate those biomechanical details, which cannot be recorded experimentally. With regard to an accidental scenario, the investigation of injury mechanism, analysis of causes and events, and conclusion in terms of injury tolerances can be best done through the scientific method of accident reconstruction, in the form of numerical simulation. Analysis of the results of numerical simulations enables the improvement of brain injury prediction tools and in turn optimization of protection systems. In the previous chapters, the need for an anisotropic finite element rat brain model (FERBM) was rationalized and the methodology of the development of one such model was explained, as well as the validation of this model was presented. This chapter presents the concussion related experiments chosen for the numerical simulations, along with the simulation results. Finally, statistical analysis of the simulation results was done to identify the head injury tolerance limit for concussion. Let us start by going through the experimental approach as given in the following section.

2 Experimental approach

A team at Medical College of Wisconsin (MCW), USA is doing concussion related experiments on rats since more than a decade. Experimental data of twenty-six such experiments was received through a collaboration with the MCW team. This data is a part of their published study, Stemper et al. (2016). In these experiments, mild traumatic brain injury or concussion was induced in the rat brain through rotational acceleration loading in the coronal plane as per MCW rotational injury model as shown in Figure 3.1.

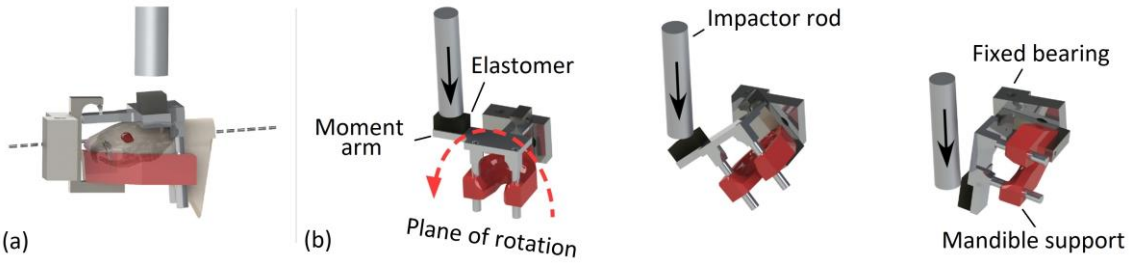

Figure 3.1: Diagram representing MCW rotational injury model, which was used to induce concussion in rats through rotational acceleration loading of the rat head in the coronal plane; (a) placement of the rat head in the device, (b) sequential helmet rotation (Stemper et al., 2016).

The rat head fitted securely in the helmet without any external fastener and the helmet was attached to the device with a pin joint, in such a way that allowed pure rotation of the rat head in the coronal plane about the cervical spine. It was reported that the use of this model resulted in zero mortality and no fracture or dislocation of the cervical spine (Stemper et al., 2016). Rotational acceleration loading on the rat head was materialized by impacting the laterally extended moment arm of the helmet by a pneumatically accelerated impactor. This controlled rotational acceleration vs time pulse resulted in rat head rotational acceleration, which was restricted to approximately 90˚ of rotation.

Experiments were performed on adult female Sprague Dawley rats, weighing 289 ± 22 g. Rats were anesthetized and placed in the helmet and then the helmet was attached to the test device. As soon as the anesthesia was removed, the impactor rod was launched to hit the moment arm so as to induce the rotational acceleration of the helmet. Immediately after the exposure to rotation, the rats were removed from the device and placed on a blanket to recover. Rats were returned to the cages after acquiring the righting reflex and were supervised continuously for the first thirty minutes and then periodically until six hours post exposure to the injury.

Acute injury severity was evaluated using the recovery time (unconscious time) i.e. the time between removal of anesthesia just before the exposer to the rotation and acquiring the righting reflex post injury. The elevated plus maze (EPM) assessment was used to analyze the changes in behavioural aspects, activity and emotionality, following concussion. Activity was monitored by observing the total distance travelled and the total number of arm changes in the EPM assessment. Whereas, emotionality was monitored by observing the total time spent in the open regions during the EPM assessment. Figure 3.2 depicts the kind of elevated plus maze used in the experiments for the behavioural assessment.

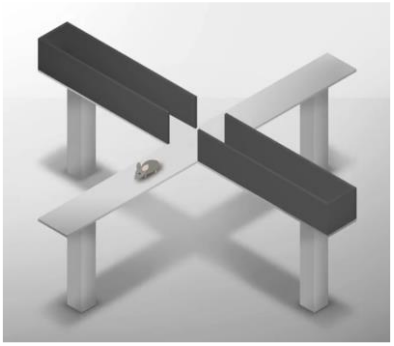

Figure 3.2: Diagram representing elevated plus maze (EPM) for the assessment of post-concussion activity and emotionality.

The Morris water maze (MWM) assessment was used to analyze the post traumatic anterograde amnesia and spatial learning after concussion. Changes in the cognitive capabilities after concussion

were monitored by observing the latency i.e. the time taken by rats to find the hidden platform during three different sessions (on three consecutive days after injury) of MWM assessment. Figure 3.3 illustrates the kind of Morris water maze used in the experiments for the behavioural assessment.

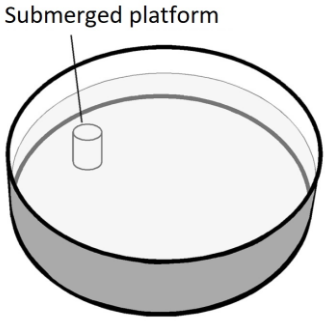

Figure 3.3: Diagram representing Morris water maze (MWM) for the assessment of post-concussion cognition capabilities.

The details of experimental inputs i.e. the peak magnitude and the positive duration of the applied rotational acceleration pulse for the twenty-six experimental cases are given in Table 3.1.

Table 3.1: Experimental inputs in terms of peak magnitude and duration of the applied rotational acceleration of the twenty-six experimental cases, as provided by MCW.

Animal ID	Peak rotational acceleration (rad/ms^2)	Duration (ms)	Animal ID	Peak rotational acceleration (rad/ms^2)	Duration (ms)
1RAT17	0.3903	3.2	**14RAT107**	0.3049	2.4
2RAT18	0.3932	2.9	**15RAT119**	0.3107	1.3
3RAT19	0.3903	3.7	**16RAT123**	0.1659	2.4
4RAT77	0.3457	1.4	**17RAT141**	0.1922	3.2
5RAT78	0.3700	1.6	**18RAT142**	0.2580	3.0
6RAT79	0.3061	3.4	**19RAT148**	0.2721	1.4
7RAT80	0.4596	1.5	**20RAT152**	0.3817	1.8
8RAT84	0.3923	1.5	**21RAT296**	0.2468	0.8
9RAT85	0.3640	1.7	**22RAT299**	0.2348	0.7
10RAT86	0.4629	1.3	**23RAT301**	0.2262	0.8
11RAT93	0.4146	1.5	**24RAT303**	0.2392	0.8
12RAT95	0.3836	1.6	**25RAT306**	0.1953	2.3
13RAT105	0.3953	1.5	**26RAT311**	0.2116	2.0

Based on the peak magnitude and the duration of the rotational acceleration, these twenty-six experimental cases could broadly be divided into four loading groups as in the publication, Stemper et al. (2016). These are low magnitude-short duration (M1D1) group, low magnitude-long duration (M1D2) group, high magnitude-short duration (M2D1) group and the high magnitude-long duration (M2D2) group. Table 3.2 consolidates the details of this categorization briefly. Eight rats fall in the M1D1 group, two in M1D2 group, twelve in M2D1 group and four in M2D2 group. The low magnitude, M1 was equal to 0.2242 ± 0.03 rad/ms^2 and the high magnitude, M2 was equal to 0.3791 ± 0.05 rad/ms^2. The short duration, D1 was equal to 1.5 ± 0.5 ms and the long duration was equal to 3.2 ± 0.3 ms.

Table 3.2: Details of categorization of twenty-six experimental cases into different loading groups based on the magnitude and duration of the applied rotational acceleration. Colour coding represents classification based on alike loading pulse.

	Short duration, D1 1.5 ± 0.5 ms	**Long duration, D2 3.2 ± 0.3 ms**
Low magnitude, M1 0.2242 ± 0.03 rad/ms^2	**n = 8 16RAT123, 19RAT148, 21RAT296, 22RAT299, 23RAT301, 24RAT303, 25RAT306, 26RAT311**	**n = 2 17RAT141, 18RAT142**
High magnitude (M2) 0.3791 ± 0.05 rad/ms^2	**n = 12 4RAT77, 5RAT78, 7RAT80, 8RAT84, 9RAT85, 10RAT86, 11RAT93, 12RAT95, 13RAT105, 14RAT107, 15RAT119, 20RAT152**	**n = 4 1RAT17, 2RAT18, 3RAT19, 6RAT79**

Acute post injury behavioural results of these twenty-six experimental cases provided by MCW and those of sham (control group without rotational injury) as given in Stemper et al. (2016) are provided below in Table 3.3.

Table 3.3: Acute post injury behavioural results of sham (as given in Stemper et al., 2016) and the twenty-six experimental cases as provided by MCW.

Animal ID	**Unconscious time (s)**	**EPM distance travelled (cm)**	**EPM arm changes (#)**	**EPM open duration (s)**	**MWM session I latency (s)**	**MWM session II latency (s)**	**MWM session III latency (s)**
Sham	178 ± 52 (n = 16)	724 ± 410 (n = 8)	15.6 ± 10.2 (n = 8)	42.2 ± 29.6 (n = 8)	48.8 ± 8.0 (n = 8)	17.8 ± 10.6 (n = 8)	21.2 ± 12.4 (n = 8)
1RAT17	256	1053	18	56.7	34.0	34.4	21.7

Animal ID	Unconscious time (s)	EPM distance travelled (cm)	EPM arm changes (#)	EPM open duration (s)	MWM session I latency (s)	MWM session II latency (s)	MWM session III latency (s)
2RAT18	134	1325	28	24.8	45.9	19.6	11.6
3RAT19	212	1067	26	86.7	60.0	33.7	10.4
4RAT77	99	1356	35	51.6	46.7	8.1	7.0
5RAT78	198	1293	24	30.8	45.4	2.9	6.9
6RAT79	298	2095	62	107.9	30.2	41.7	3.9
7RAT80	97	1604	42	73.0	38.8	25.2	15.7
8RAT84	179	1354	37	81.5	22.1	7.5	6.5
9RAT85	294	1092	22	31.6	32.3	8.7	7.8
10RAT86	394	572	19	36.2	43.6	19.1	47.4
11RAT93	318	715	20	49.2	32.2	19.8	8.8
12RAT95	180	1623	44	79.5	46.7	22.7	3.1
13RAT105	238	958	18	14.7	60.0	10.1	60.0
14RAT107	373	1429	36	49.1	49.7	5.0	5.9
15RAT119	264	1362	32	75.3	18.0	44.5	24.2
16RAT123	311	1235	29	33.3	26.7	22.9	33.5
17RAT141	190	1509	38	83.3	44.8	23.0	37.7
18RAT142	158	952	25	31.8	40.3	11.8	10.6
19RAT148	75	957	35	140.1	40.2	27.8	9.5
20RAT152	183	1778	44	109.4	25.6	30.7	23.0
21RAT296	165	1054	18	48.3	48.7	30.4	18.0
22RAT299	147	1169	25	82.0	27.0	15.2	17.1
23RAT301	135	1639	36	114.3	45.7	32.6	15.1
24RAT303	126	898	17	60.3	41.7	23.0	10.6
25RAT306	113	1869	39	144.6	26.3	10.1	18.2
26RAT311	144	932	21	55.2	15.0	15.2	23.9

A variation in the values of behavioural response measure of twenty-six experimental cases from that of sham is a clear indicator of change is behaviour post injury. Table 3.4 provides the association of experimental inputs (the peak magnitude and the duration of the applied rotational acceleration) with the experimental outputs (unconscious time, EPM distance travelled, EPM arm changes, EPM open duration and latency of MWM session I, II and III) to analyze the effect of applied loading pulse on behavioural response. As mentioned earlier, the experimental outputs associate with four behavioural aspects, such that unconsciousness time with consciousness; EPM distance travelled and EPM arm

changes with activity; EPM open duration with emotionality and MWM session latencies with the cognition capabilities. Even the load curves belonging to same loading group were not identical and hence, the groups were sub-divided. Group M1D1 had eight cases in total. Based on the nature of the loading pulse, the cases were further divided into two sub groups M1D1a and M1D1b, having four cases each. Loading curves in the sub-groups were more or less alike. Similarly, the groups M2D1a (7 cases), M2D1b (5 cases), M2D2a (3 cases) and M2D2b (1 case) were created. Colour coding provided in Table 3.2 represents these sub groups.

Table 3.4: Association between experimental inputs (the peak magnitude and duration of the applied rotational acceleration) and experimental outputs (unconscious time, EPM distance travelled, EPM arm changes, EPM open duration and latency in MWM session I, II and III) on the basis of loading groups.

Unconscious time

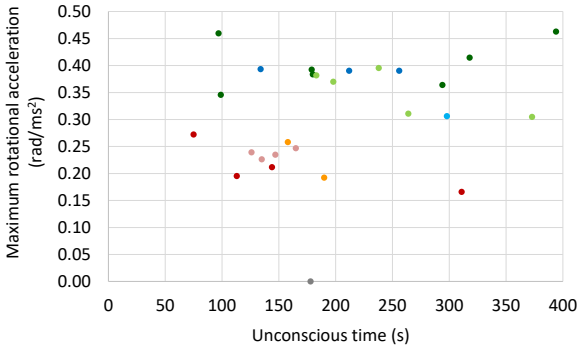

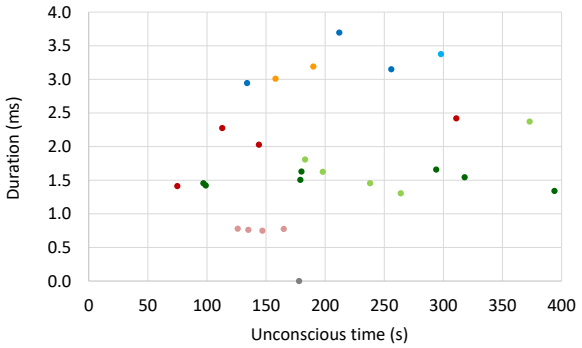

EPM distance travelled

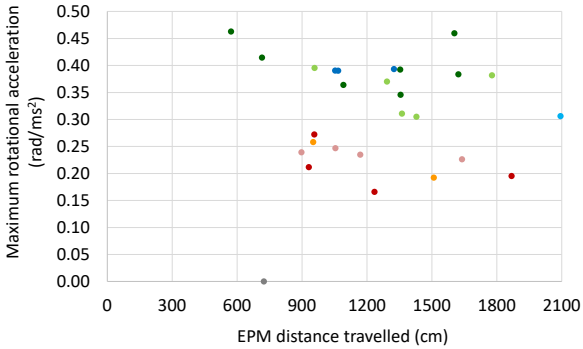

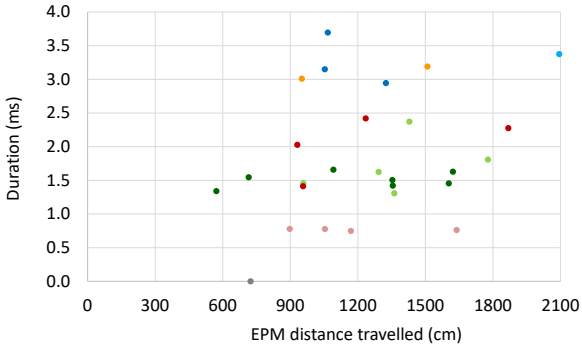

EPM arm changes

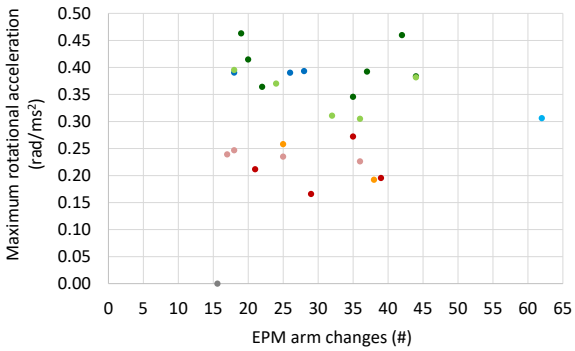

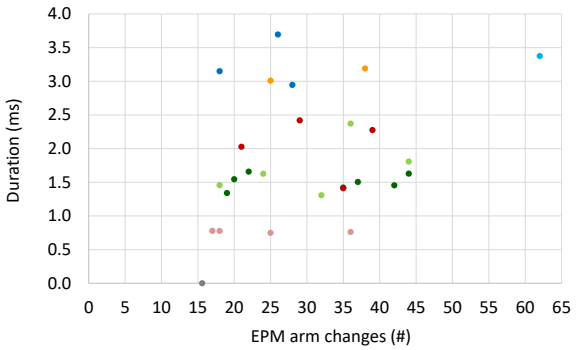

EPM open duration

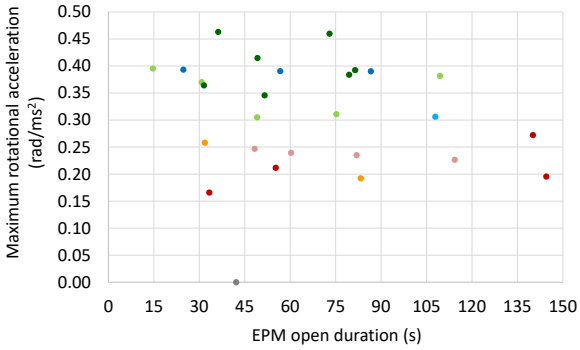

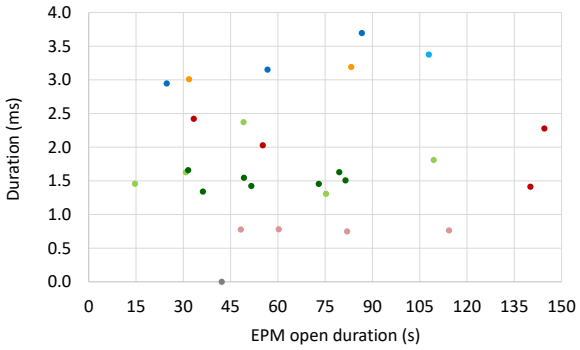

MCW Session I latency

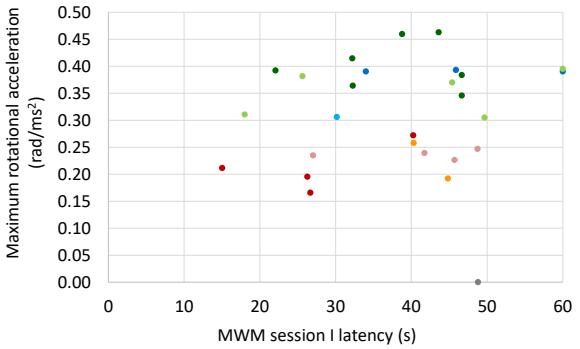

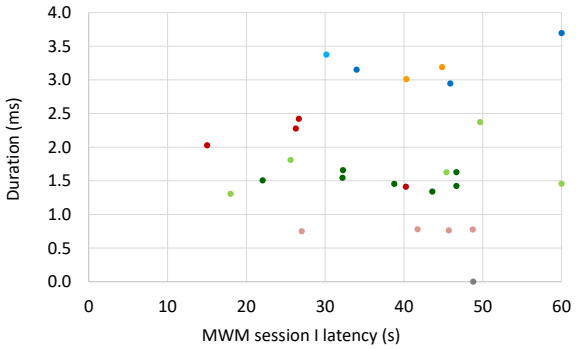

MCW Session II latency

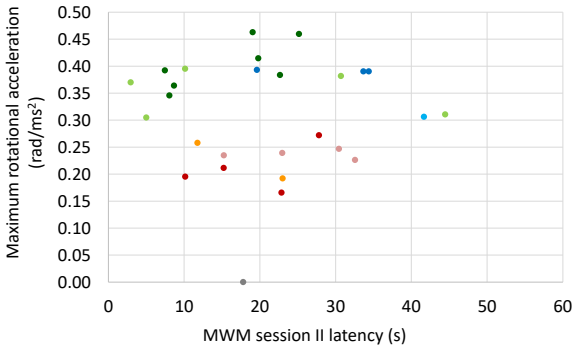

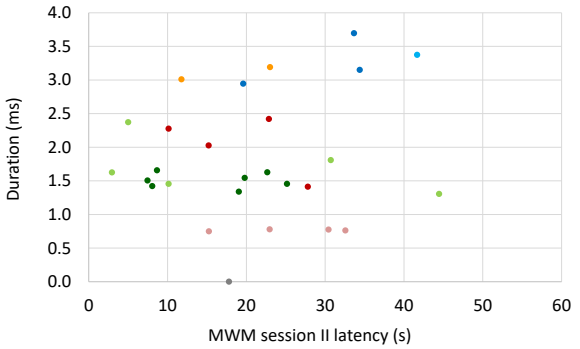

MCW Session III latency

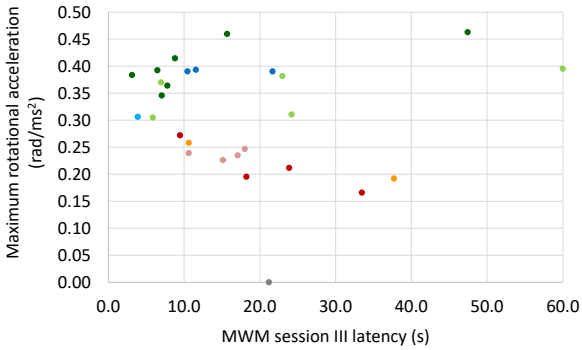

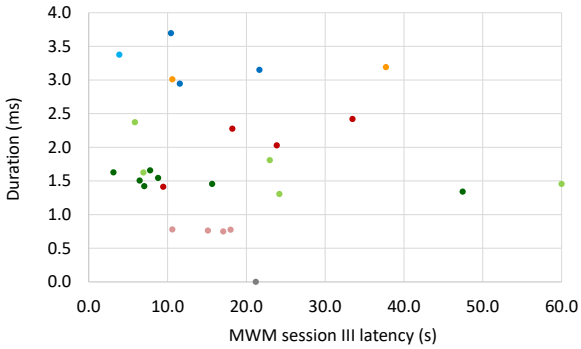

Sham[#] M1D1a M1D1b M1D2 M2D1a M2D1b M2D2a M2D2b

[#]Since, sham did not go through rotational loading, only their experimental response is marked.

It can be seen from the plots in Table 3.4 that even the cases of the same loading group have a wide variation in behavioural response. Hence, we do not see a direct correlation between the rotational acceleration characteristics and the experimental behavioural response measures. This means that it is difficult to explain behavioural changes based on maximum rotational acceleration and duration only. Experimental loading curves of twenty-six experimental cases depicting applied rotational acceleration pulses are provided in Annexure B for reference. Another way of looking at the relation between acceleration characteristics and behavioural responses is by categorizing the simulated cases in non-injured and injured groups. According to the behavioural response of sham, twenty-six cases can be categorized in two groups. Non-injured group, having behavioural response value less than that of sham and injured group, having behavioural response value greater than that of sham. Table 3.5 provides the association of experimental inputs (the peak magnitude and the duration of the applied rotational acceleration) with the experimental outputs (unconscious time, EPM distance travelled, EPM arm changes, EPM open duration and latency of MWM session I, II and III) to analyze the effect of applied loading pulse on behavioural response on the basis of non-injured and injured categories.

Table 3.5: Association between experimental inputs (the peak magnitude and duration of the applied rotational acceleration) and experimental outputs (unconscious time, EPM distance travelled, EPM arm changes, EPM open duration and latency in MWM session I, II and III) on the basis of non-injured and injured categories.

Unconscious time

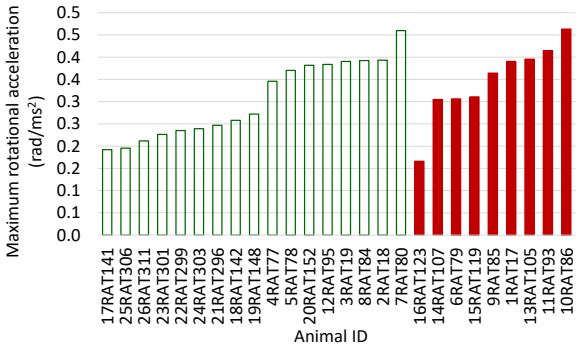

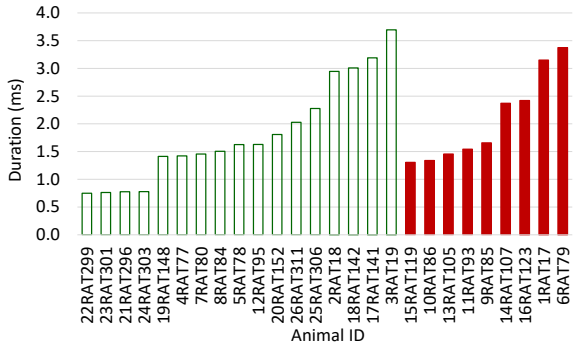

EPM distance travelled

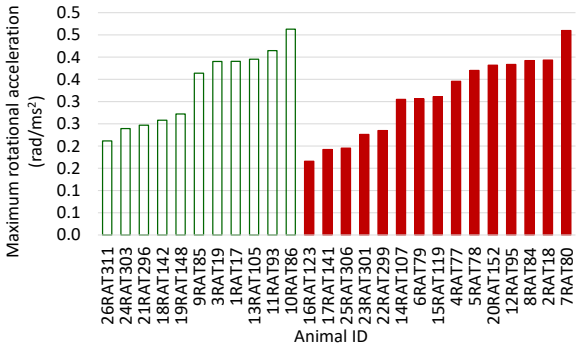

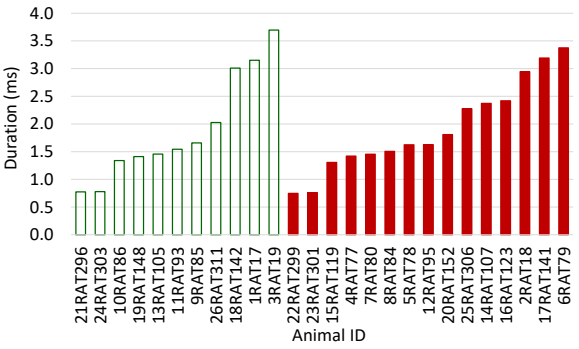

cont.

EPM arm changes

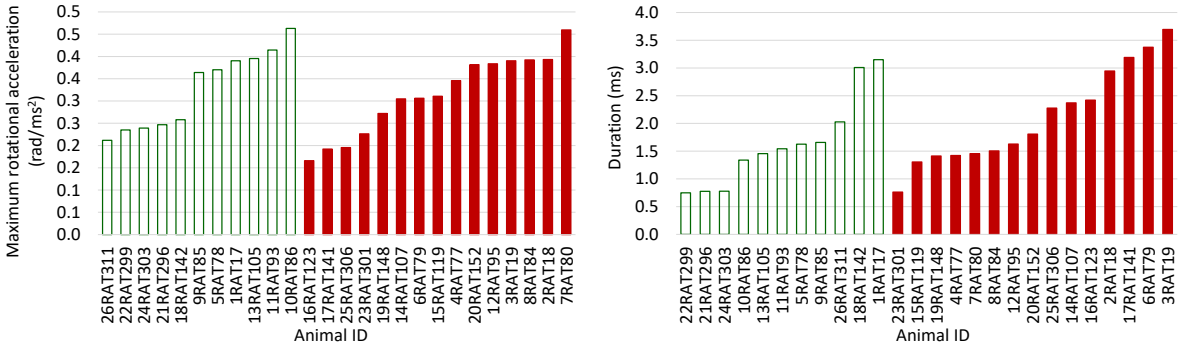

EPM open duration

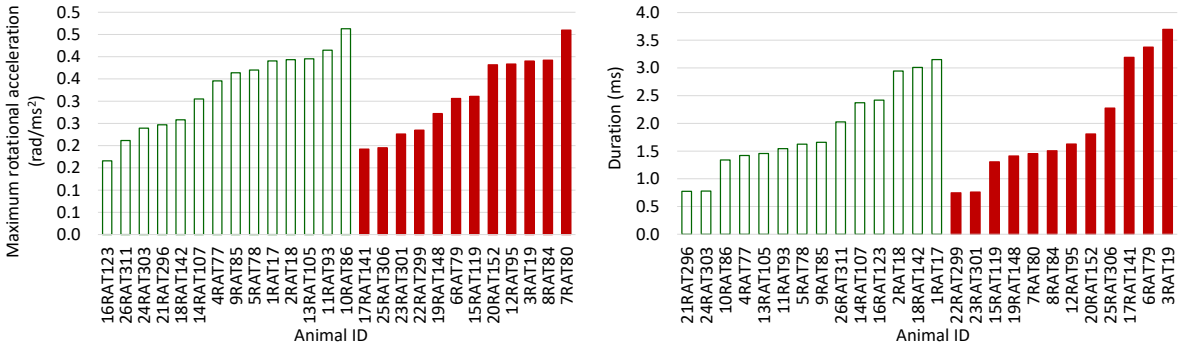

MCW Session I latency

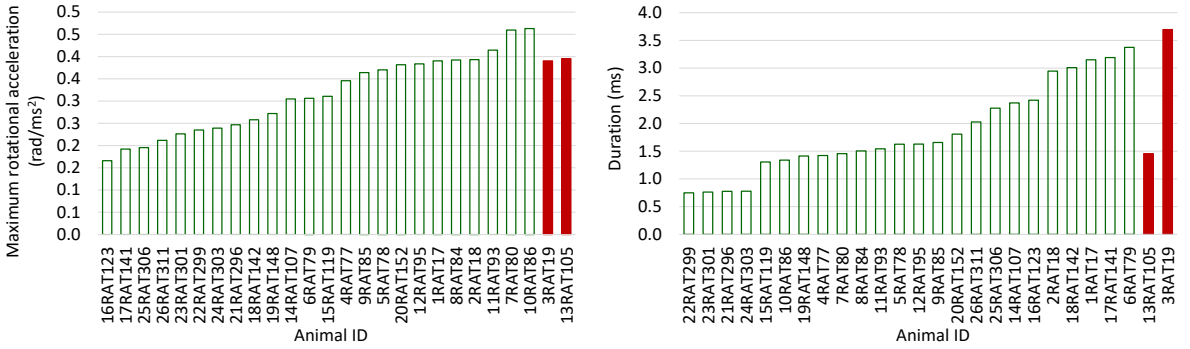

MCW Session II latency

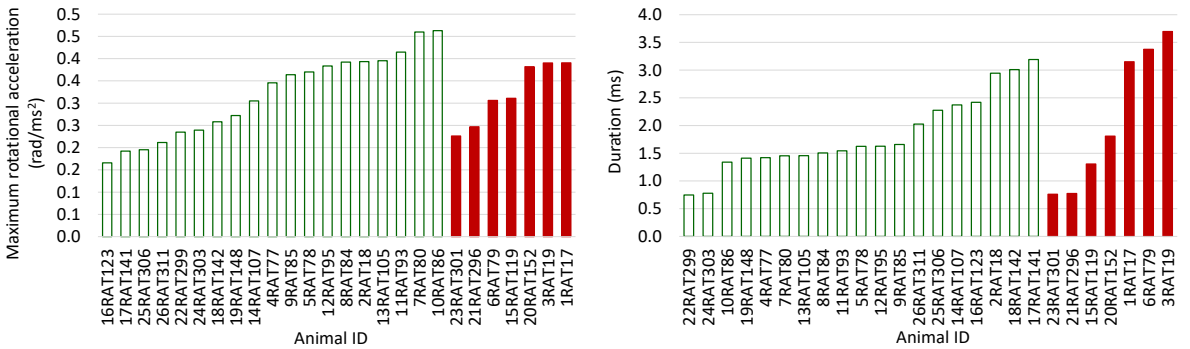

cont.

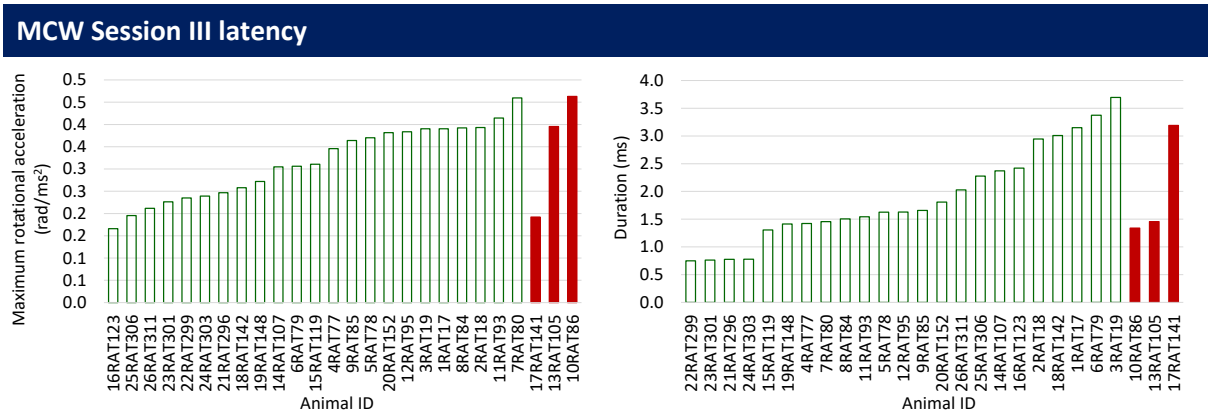

It can be seen from the plots in Table 3.5 that amplitudes of both non-injured and injured groups vary from low to high and there is no significance difference between the overall amplitudes of the two groups. Hence, we do not see a direct correlation between the rotational acceleration characteristics and the experimental behavioural response measures. This means that on the basis of non-injured and injured categorization also, it is difficult to explain behavioural changes based on maximum rotational acceleration and duration only.

3 Simulations of experimental cases

Aforementioned twenty-six experimental cases were simulated with the rat brain model developed in Chapter 2, based on the rotational acceleration pulses of rotational loading provided by MCW as given in Annexure B. Even the loading curves of the same loading group differ from each other. Hence, as mentioned before, for the better understanding of the simulation results, these groups were further sub divided in order to compare the behavioural response of rats based on the type of loading. As described in Chapter 2, the rat brain model was enclosed inside a rigid skull. To replicate the experiments, rotational acceleration pulse was applied to the skull about an axis in the lower half of the brain, which passes through the mid-sagittal plane, so as to have pure rotation of the rat brain in the coronal plane. The maximum rotation of the rat brain in all the twenty-six simulations remained within 90 degrees.

A nonlinear, dynamic, explicit finite element solver, LS-DYNA SMP version R10.1.0 (Livermore Software Technology Corporation (LSTC), CA) was used for the simulations. The simulation time varied between thirty minutes to three hours thirty minutes. Simulations were checked for the stability and the maximum hourglass energy of the model was within acceptable limits. Figure 3.4 displays the FERBM before and after one such simulation. As shown in the figure, right side view of the model before

simulation is shown on the left. After pure rotation in the coronal plane, the rotated view of the model is presented on the right.

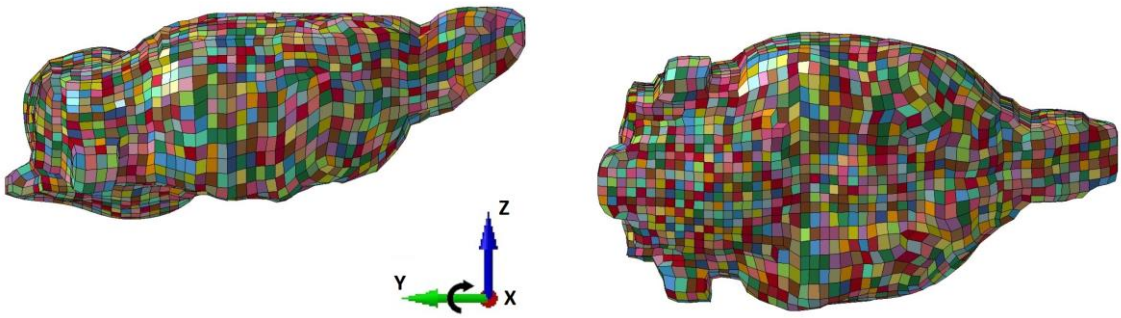

Figure 3.4: Diagram representing FERBM before and after the simulation based on MCW's concussion related experiment for one of the cases.

4 Simulation results

4.1 Introduction

After all twenty-six simulations were done, ten mechanical parameters were extracted, which are maximum von Mises stress and strain, maximum principal stress and strain, maximum shear stress and strain, minimum and maximum pressures, strain energy and the strain tensor, to calculate the axonal strain. Post processing of the simulation results was done on LS-PrePost software version 4.5 (LSTC). As the computational model is anisotropic, every element of the FERBM had a principal fiber direction (PFD) that is the orientation of the main axon bundle (explained in detail in Chapter 2). Hence, with the help of this orientation vector, axonal strain per element was calculated from the stain tensor data through python programming. This axonal strain data helped in estimating maximum axonal strain (MAS) for all the cases and also in identifying the brain regions experiencing high strains. All these mechanical parameters were calculated not only for the brain in entirety (Table 3.6), but also for each of the twenty-four anatomical brain regions as well as for the functional brain regions associated with consciousness, activity, emotionality and cognition capabilities (the categorization of brain regions for the analysis of simulation results is described in Chapter 2). These results can be looked upon in different manners. Following sections attempt to represent these simulation results with different perspectives.

Table 3.6: Simulation results of all twenty-six cases, in terms of ten mechanical parameters, for the entire brain.

Animal ID	Max. axonal strain	Max. strain energy (mJ)	Max. von Mises stress (kPa)	Max. von Mises strain	Max. shear stress (kPa)	Max. shear strain	Max. principal stress (kPa)	Max. principal strain	Min. pressure (kPa)	Max. pressure (kPa)
1RAT17	0.1169	6.6E-05	7.4	0.1431	4.2	0.1234	348.3	0.1402	-346.7	374.2
2RAT18	0.1102	6.1E-05	6.9	0.1358	4.0	0.1172	332.6	0.1324	-331.2	365.5
3RAT19	0.1020	5.3E-05	6.4	0.1269	3.7	0.1095	312.8	0.1230	-311.4	352.3
4RAT77	0.1088	5.7E-05	6.9	0.1341	3.9	0.1157	333.6	0.1308	-332.1	371.8
5RAT78	0.0846	3.7E-05	5.3	0.1084	3.0	0.0936	272.7	0.1040	-272.2	315.1
6RAT79	0.1080	5.7E-05	6.9	0.1344	3.9	0.1159	330.3	0.1310	-328.9	366.6
7RAT80	0.1232	6.9E-05	7.9	0.1502	4.5	0.1295	363.4	0.1483	-361.6	385.6
8RAT84	0.1187	6.7E-05	7.2	0.1422	4.1	0.1226	344.7	0.1395	-343.1	377.8
9RAT85	0.1144	6.2E-05	7.4	0.1421	4.2	0.1225	346.5	0.1394	-345.0	376.4
10RAT86	0.1195	6.9E-05	7.5	0.1461	4.3	0.1259	351.4	0.1434	-349.8	377.6
11RAT93	0.1239	7.1E-05	8.0	0.1510	4.5	0.1304	363.5	0.1504	-361.7	386.6
12RAT95	0.1197	6.7E-05	7.9	0.1493	4.5	0.1287	359.1	0.1483	-357.4	381.2
13RAT105	0.1286	7.9E-05	8.2	0.1576	4.7	0.1358	367.1	0.1558	-365.3	379.2
14RAT107	0.1225	7.3E-05	7.8	0.1522	4.4	0.1312	355.9	0.1499	-354.2	373.7
15RAT119	0.0934	4.3E-05	6.0	0.1177	3.4	0.1016	292.6	0.1137	-291.4	350.7
16RAT123	0.0731	2.8E-05	4.6	0.0951	2.6	0.0822	247.9	0.0911	-247.6	285.5
17RAT141	0.0767	3.1E-05	4.7	0.0984	2.7	0.0848	256.9	0.0946	-256.6	297.4
18RAT142	0.0789	3.2E-05	4.9	0.1001	2.8	0.0864	267.8	0.0961	-267.4	309.6
19RAT148	0.0869	3.8E-05	5.5	0.1100	3.1	0.0950	277.3	0.1057	-276.8	326.3
20RAT152	0.1462	9.7E-05	8.9	0.1745	5.1	0.1503	407.3	0.1743	-405.0	394.4
21RAT296	0.0569	1.4E-05	3.3	0.0734	1.9	0.0634	205.2	0.0688	-204.4	206.6
22RAT299	0.0577	1.4E-05	3.3	0.0746	1.9	0.0644	208.9	0.0700	-208.0	209.5
23RAT301	0.0560	1.3E-05	3.2	0.0722	1.8	0.0623	200.4	0.0675	-199.6	201.8
24RAT303	0.0571	1.4E-05	3.3	0.0737	1.9	0.0637	203.8	0.0690	-202.9	205.8
25RAT306	0.0725	2.8E-05	4.5	0.0934	2.6	0.0806	250.4	0.0897	-250.1	285.2
26RAT311	0.0708	2.8E-05	4.3	0.0921	2.5	0.0793	243.1	0.0885	-242.7	275.2

Broadly, case of animal id 20RAT152, which belongs to high magnitude short duration loading group went through most severe loading as the mechanical response of this case is the highest among all other cases. Although, for case ids 7RAT80 and 10RAT86, the magnitudes of applied rotational acceleration were higher and the durations were lower than case 20RAT152, yet the quality of

acceleration pulse of case 20RAT152 made the relative severity of this case understandable. Let us look at the simulation results for entire brain based on the loading group categorization in the following section.

4.2 For entire brain: based on loading group categorization

This section provides simulation results for entire brain. The results are furnished for maximum axonal strain and maximum von Mises stress (Table 3.7). Annexure C (Table C1 to Table C7) can be referred to see the results in terms of all ten mechanical parameters altogether in association with seven experimental behavioural response measures. These results are based on the loading groups, with regard to magnitude and duration of the experimental rotational acceleration.

Table 3.7: Simulation results for entire brain based on loading group categorization.

With respect to unconsciousness time

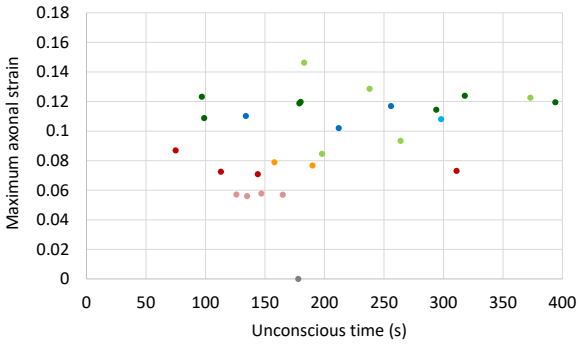

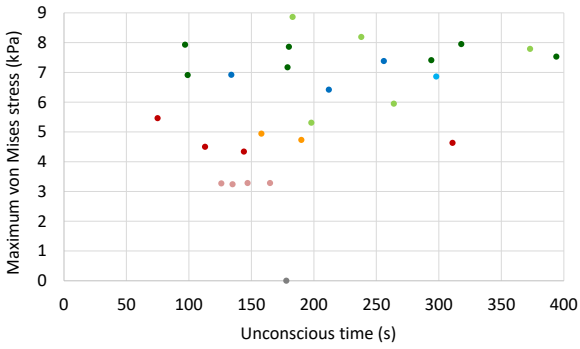

With respect to EPM distance travelled

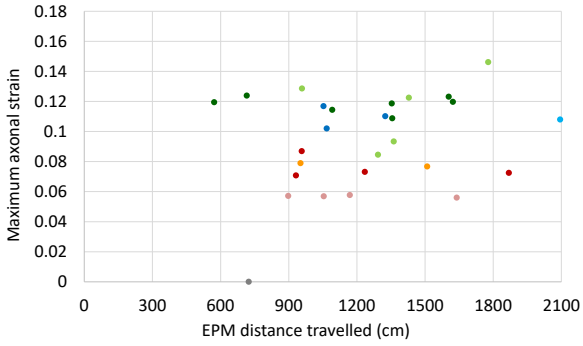

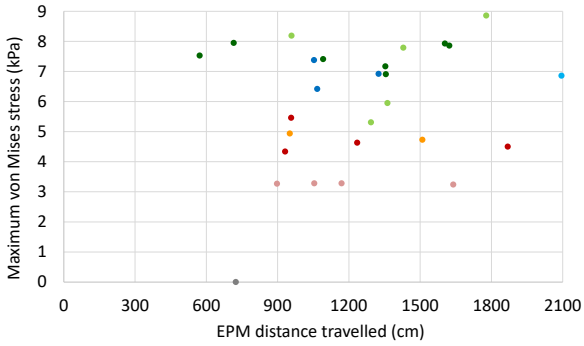

cont.

With respect to EPM arm changes

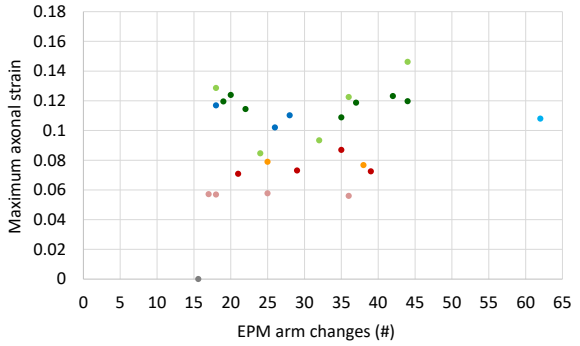

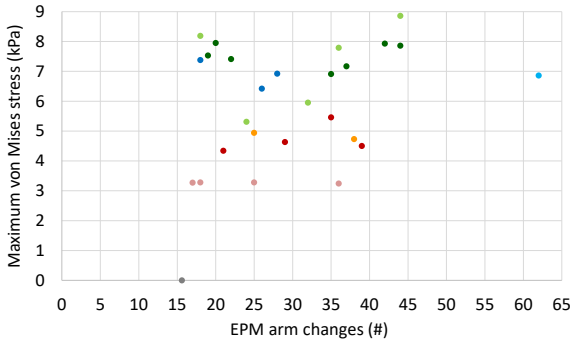

With respect to EPM open duration

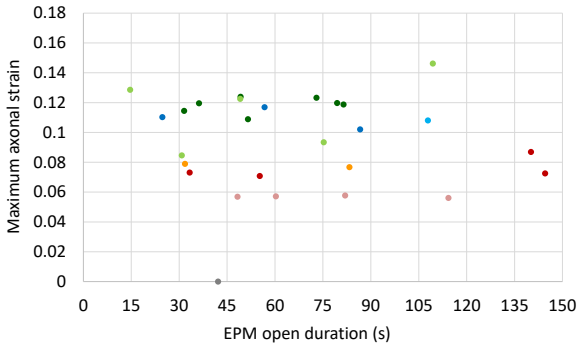

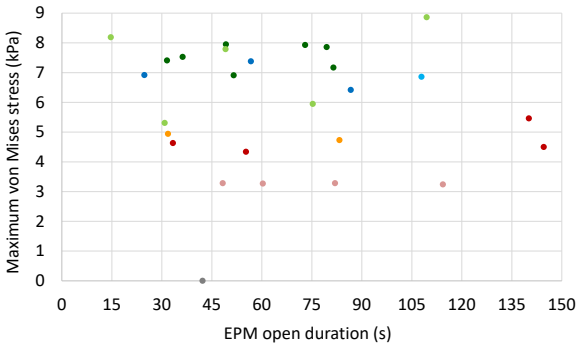

With respect to MWM session I latency

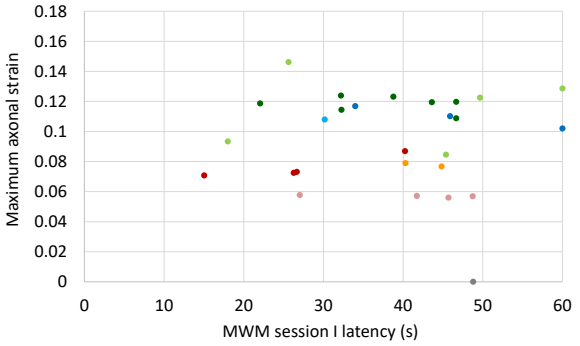

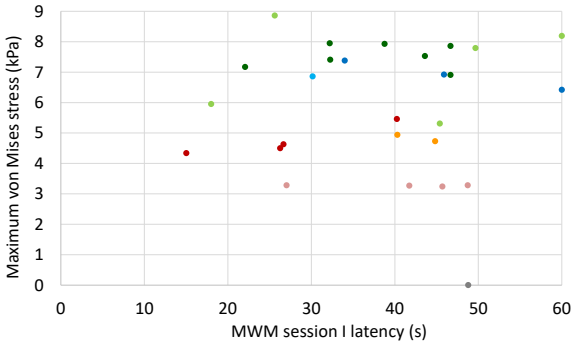

With respect to MWM session II latency

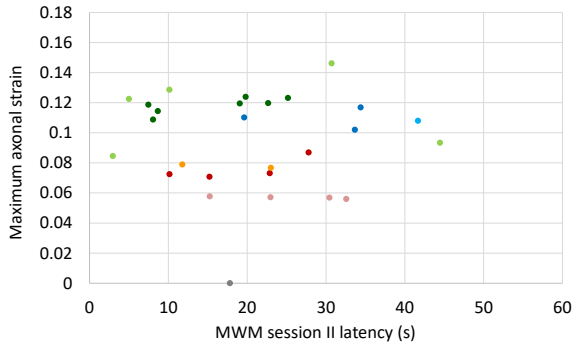

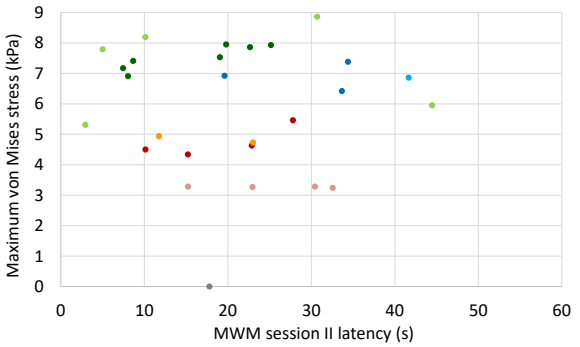

cont.

With respect to MWM session III latency

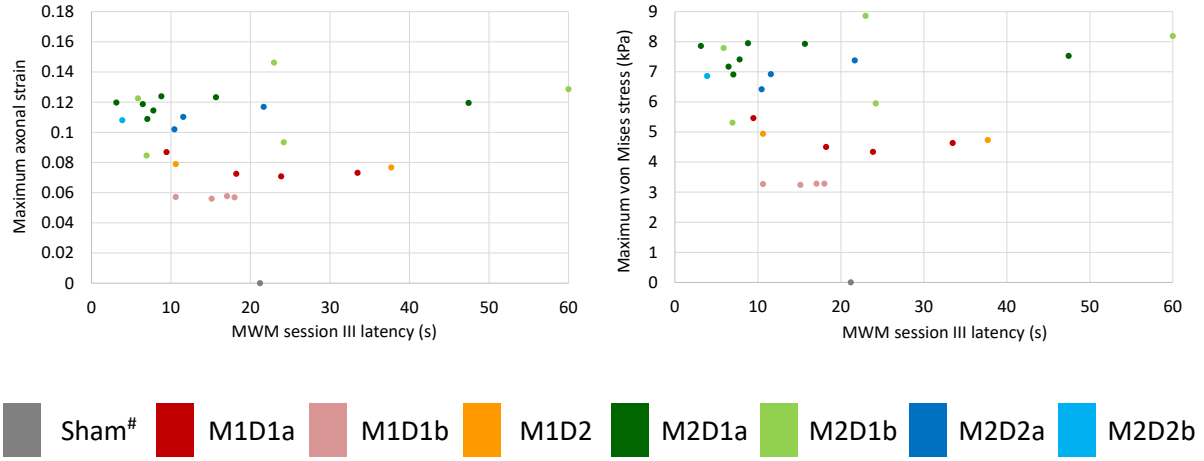

#Since, sham did not go through rotational loading, only their experimental response is marked.

There does not seem to be a direct correlation between the experimental behavioural response measures and the computed mechanical parameters, as the cases belonging to same loading group have a wide variation in the experimental behavioural response. Whereas, loading group wise mechanical outputs lie, more or less, within a reasonable narrow range. A deviation in response from that of the sham value clearly indicates post-injury changes in the mechanics of brain.

With regard to unconsciousness time, there are some cases, where the unconscious time of injured rats is less than that of sham. One of the possible reasons could be that for these cases, the rotational acceleration pulse acted as a stimulus in gaining consciousness early. Recovery of consciousness of an unconscious brain can be catalyzed by external stimuli in specific brain regions and the rotational loading might have triggered these stimulants.

With regard to EPM distance travelled, it is clearly evident that apart from a case or two, the distance travelled by the rats increased significantly after the application of rotational loading. This indicates a significant increase in activity post-injury.

With regard to EPM arm changes, it is clearly evident that the number of arm changes for all the cases increased considerably after the application of rotational acceleration. This indicates a significant increase in the activity post-injury.

With regard to EPM open duration, for some of the cases, the EPM open duration decreased. Whereas, for most of the cases an increase in the EPM open duration is clearly visible. This indicates that the rotational loading clearly influenced the emotionality of the rats.

With regard to MWM session I latency, for some of the cases, the MWM session I latency increased. Whereas, for most of the cases a decrease in the MWM session I latency is clearly visible. This indicates that the rotational acceleration loading influenced the cognition capability of the rats in such a manner that they were able to find out the hidden platform in lesser time. Most of the rats were able to find out the hidden platform within 30 to 50 seconds.

With regard to MWM session II latency, for some of the cases, the MWM session II latency decreased. Whereas, for most of the cases an increase in the MWM session II latency is clearly visible. However, most of the rats were able to find out the hidden platform within 10 to 30 seconds. This indicates that the session I enabled spatial learning and the cognition capability of most of the rats were improved such that they were able to find out the hidden platform in lesser time than session I. Significant improvement in cognition capability of sham is also clearly evident. However, for some of the injured rats the improvement was not so significant, which might be because of the influence of rotational acceleration loading.

With regard to MWM session III latency, for some of the cases, the MWM session III latency increased. Whereas, for most of the cases a decrease in the MWM session III latency is clearly visible. Most of the rats were able to find out the hidden platform within initial 20 seconds. This indicates that the session I and II enabled spatial learning and the cognition capability of most of the rats were improved such that they were able to find out the hidden platform in lesser time than session I or II. On the contrary, for sham, the latency of session III was slightly higher than the latency of session II. However, most of the injured rats showed significant improvement in the cognition capabilities. Those who could not, might have been influenced by the rotational acceleration loading adversely.

We observe that on the basis of loading group categorization, the simulation results, in term of maximum axonal strain and maximum von Mises stress, do not seem to have a direct correlation with the experimental behavioural response measures. This is consistent even with remaining eight mechanical parameters as well (Annexure C). However, it is important to consider that globally, for cases belonging to high magnitude short duration group, the mechanical response is the highest. This is followed by cases belonging to high magnitude long duration group and then by cases belonging to low magnitude long duration group. Mechanical response of the cases belonging to low magnitude short duration group lie at the lowest. Let us now look at these results from another perspective.

4.3 For entire brain: based on injured and non-injured group categorization

As mentioned earlier, for every behavioural aspect, the control or sham value was known from Stemper et al. (2016). Based on this sham value of experimental behavioural response measure, the twenty-six experimental cases were divided into two groups. Those, for which the experimental results were below the sham value, fall in the first group and were called non-injured cases and those for which the experimental results were above the sham value, fall in the second group and were called injured cases. Given below in Table 3.8 are the simulation results, in terms of two mechanical parameters (maximum axonal strain and maximum von Mises stress), of all twenty-six cases for every behavioural aspect i.e. consciousness, activity, emotionality and cognition capabilities. Annexure D can be referred to see the results in terms of all ten computed mechanical parameters altogether for seven experimental behavioural response measures. Blank green columns represent non-injured cases; whereas, solid red columns represents injured cases. Both are presented in an ascending order.

Table 3.8: Simulation results of all twenty-six experimental cases for two mechanical parameters, which are maximum axonal strain and maximum von Mises stress for the entire brain based on injured (solid red columns) and non-injured (blank green columns) categorization with regard to seven experimental behavioural response measures.

Injured and non-injured groups based on unconsciousness time

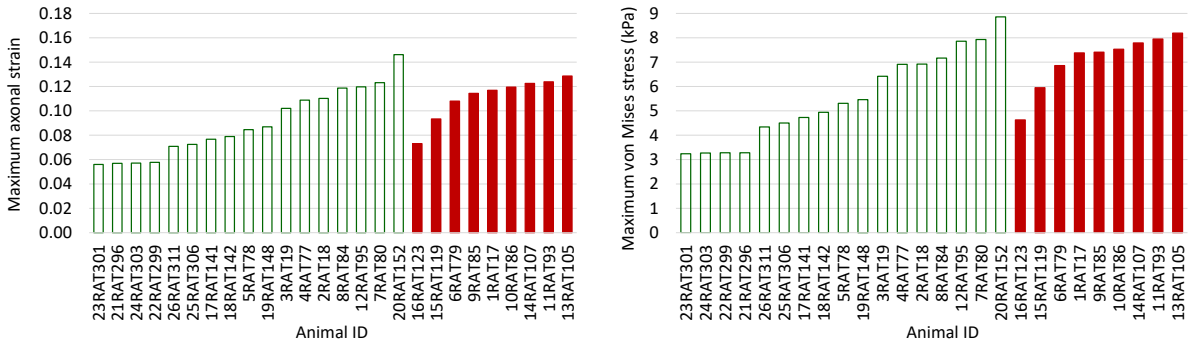

Injured and non-injured groups based on EPM distance travelled

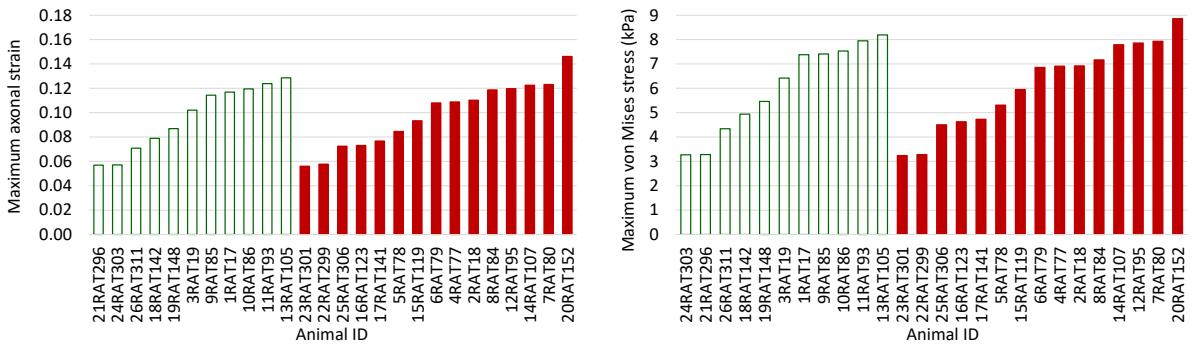

cont.

Injured and non-injured groups based on EMP arm changes

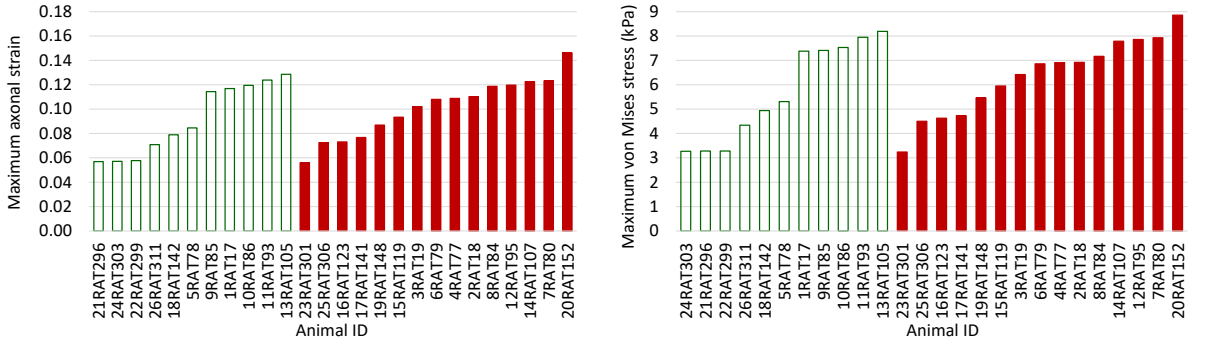

Injured and non-injured groups based on EPM open duration

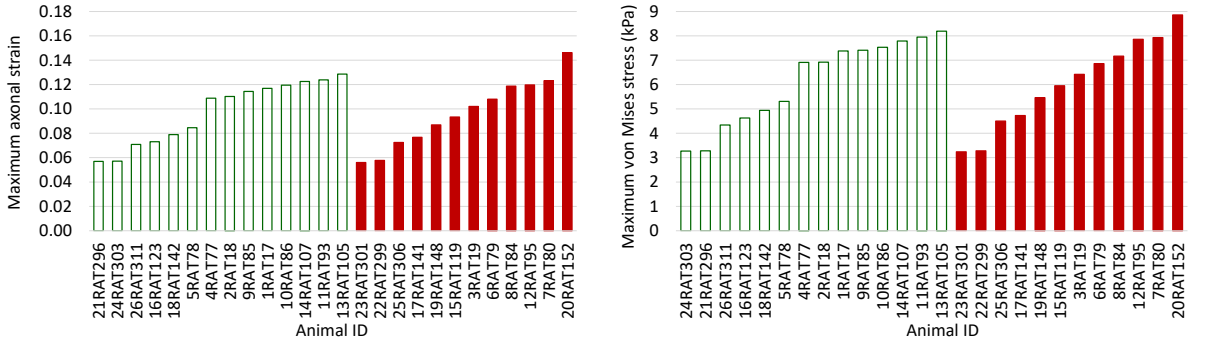

Injured and non-injured groups based on MWM session I latency

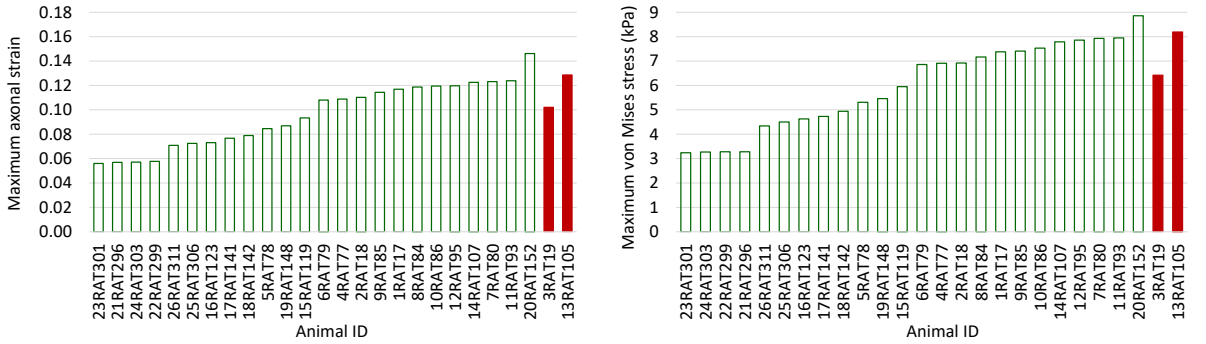

Injured and non-injured groups based on MWM session II latency

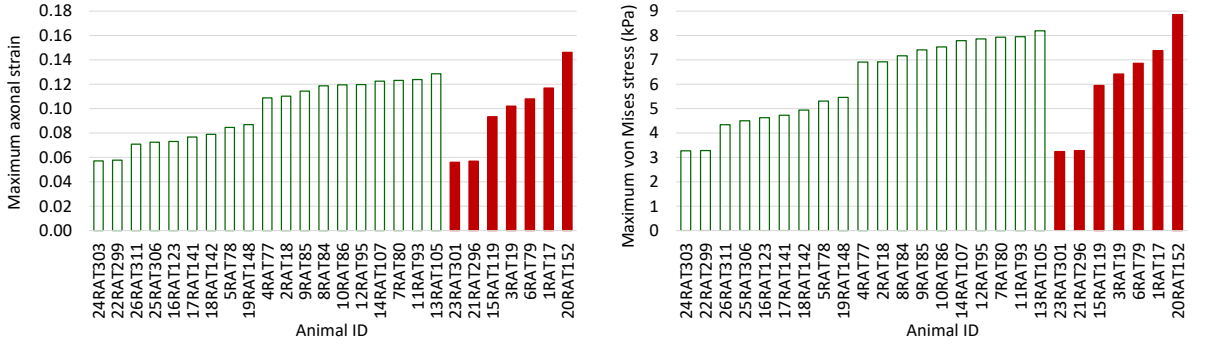

cont.

Injured and non-injured groups based on MWM session III latency

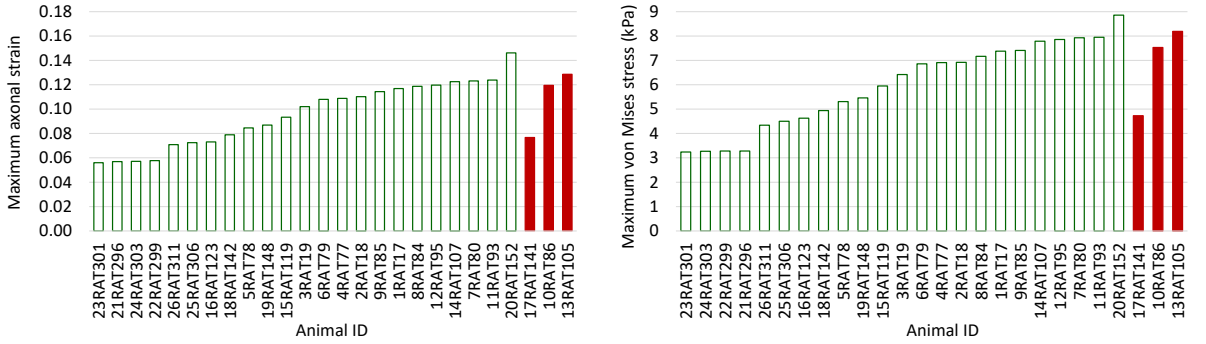

With regard to the consciousness measure i.e. unconsciousness time, we see that by taking the maximum unconsciousness time of the sham into consideration, nine out of twenty-six cases fall in the injured group and remaining seventeen in the non-injured group. This indicates that for only 35% of all the animals, which were exposed to rotational loading, the unconsciousness time increased post-injury. We also see that for one of the non-injured cases, i.e. animal id 20RAT152, the mechanical amplitude sustained is the highest, even higher than the injured group. For this animal, being in non-injured group does not actually mean that the rat was not injured. As told earlier, a mild loading can act as a stimulant in recovering consciousness early than causing any acute injury. This might be true for animal id 20RAT152 and for many others too. As can be seen from the plots, there is not much difference in the mechanical amplitude sustained by the injured group in comparison to that sustained by the non-injured group. Same was the case with all other selected mechanical parameters (Annexure D, Table D1). Thus, based on the unconsciousness time, we are not able to comment on the injury in terms of any chosen mechanical parameter.

With regard to the activity measures i.e. EPM distance travelled and EPM arm changes, we see that by taking either the maximum EPM distance travelled or the maximum number of EPM arm changes by the sham into consideration, fifteen out of twenty-six cases fall in the injured group and remaining eleven in the non-injured group. This indicates that for more than 50% animals, which were exposed to rotational loading, post-injury activity increased significantly. Also, both non-injured and injured groups sustained lowest to highest mechanical amplitudes and the range of mechanical amplitude sustained by both the groups is more or less the same. This was true even for all other selected mechanical parameters (Annexure D, Table D2 and Table D3). Thus, based on the EPM distance travelled and EPM arm changes, it is not possible to comment on the injury in terms of any chosen mechanical parameter. Nonetheless, we should keep in mind that an increase in activity as well as a decrease in activity, both are changes in behaviour. Although, here we are assuming the increased activity cases as the injured one, others had been concussed too.

With regard to the emotionality measure i.e. EPM open duration, we see that by taking the maximum EPM open duration of the sham into consideration, twelve out of twenty-six cases fall in the injured group and remaining fourteen in the non-injured group. This indicates that 46% animals, which were exposed to rotational loading, got significantly influenced emotionally post-injury. Also, both non-injured and injured groups sustained lowest to highest mechanical amplitudes and the range of mechanical amplitude sustained by both the groups is more or less the same. This was true even for all other selected mechanical parameters (Annexure D, Table D4). Thus, based on the EPM duration, it is not possible to comment on the injury in terms of any chosen mechanical parameter. Nonetheless, we should keep in mind that an increase in EPM open duration as well as a decrease in EPM open duration, both are changes in emotionality. Although, here we are assuming the increased EPM open duration cases as the injured one, others had been concussed too.

With regard to the cognition measures i.e. the latencies in MWM sessions, we see that by taking the maximum MWM session I latency of the sham into consideration, only two out of twenty-six cases fall in the injured group and remaining twenty-four in the non-injured group. This indicates that only 8% animals, which were exposed to rotational loading, got significantly influenced in such a manner that they took longer than sham in finding the hidden platform. As can be seen from the plots, the mechanical amplitude sustained by the injured group falls within the range of non-injured group. This was true even for all other selected mechanical parameters (Annexure D, Table D5). Thus, based on the MWM session I latency, it is not possible to comment on the injury in terms of any chosen mechanical parameter. Nonetheless, we should keep in mind that as the number of injured cases are too low, nothing conclusive could be stated anyways. As most of the cases were able to find the hidden platform with sham or before the sham could, that means the cognitive capabilities were altered positively by the rotational loading.

We see that by taking the maximum MWM session II latency of the sham into consideration, seven out of twenty-six cases fall in the injured group and remaining nineteen in the non-injured group. This indicates that only 27% animals, which were exposed to rotational loading, got significantly influenced in such a manner that they took longer than sham in finding the hidden platform. Also, both non-injured and injured groups sustained lowest to highest mechanical amplitudes and the range of mechanical amplitude sustained by both the groups is more or less the same. This was true even for all other selected mechanical parameters (Annexure D, Table D6). Thus, based on the MWM session II latency, it is not possible to comment on the injury in terms of any chosen mechanical parameter. Nonetheless, we should keep in mind that spatial learning in terms of improved cognitive capabilities

occurred for both injured and non-injured cases. As for all the animals, the time taken in finding the hidden platform was lesser than that of first session.

We see that by taking the maximum MWM session III latency of the sham into consideration, only three out of twenty-six cases fall in the injured group and remaining twenty-three in the non-injured group. This indicates that around 12% animals, which were exposed to rotational loading, got significantly influenced in such a manner that they took longer than sham in finding the hidden platform. As can be seen from the plots, the mechanical amplitude sustained by the injured group falls within the range of non-injured group. This was true even for all other selected mechanical parameters (Annexure D, Table D7). Thus, based on the MWM session III latency, it is difficult to comment on the injury in terms of any chosen mechanical parameter. Nonetheless, we should keep in mind that as the number of injured cases are too low, nothing conclusive could be stated anyways. As most of the cases were able to find the hidden platform with sham or before the sham could, that means the cognitive capabilities were altered positively by the rotational loading. We also see that spatial learning in terms of improved cognitive capabilities occurred for both injured and non-injured cases. As for most of the animals, the time taken in finding the hidden platform in third session was lesser than that of first or second session.

We see that on the basis of injured and non-injured categorization for the entire brain, the simulation results do not seem to have a direct correlation with the injury based on any of the experimental behavioural response measures. Not even for the axonal strain, which was clearly an evident predictor in the study by Sahoo (2013). From the results presented in Annexure D, similar conclusion can be drawn based on other eight computed parameters. Let us see if these results at the level of functional brain regions could provide some valuable insights.

4.4 For different functional brain regions

Let us now look at the simulation results for functional brain regions (detailed in Chapter 2, Table 2.2 and Figure 2.4) dedicated to specific behavioural aspect, i.e. consciousness, activity, emotionality and cognition. To recall, consciousness is associated with thalamus, neocortex and brainstem; activity is associated with hippocampus, substantia nigra, cerebellum, central gray and neocortex; emotionality is associated with hippocampus, central gray, neocortex, amygdala, brainstem, fimbria and fornix; and cognition is associated with hippocampus, substantia nigra, cerebellum, neocortex, fimbria and fornix. Instead of presenting the results for all ten mechanical parameters, results only in terms of axonal strain and von Mises stress are presented here. Annexure E can be referred to see the results in terms of all ten computed mechanical parameters altogether based on seven experimental behavioural

responses. The results are presented based on the categorization into injured and non-injured groups as per different experimental behavioural response measures. Blank green columns represent non-injured cases; whereas, solid red columns represents injured cases. Both are presented in an ascending order.

Table 3.9 represents the simulation results, in terms of maximum axonal strain and maximum von Mises stress, of all twenty-six cases for the brain regions associated with consciousness.

Table 3.9: Simulation results of all twenty-six experimental cases for two mechanical parameters, which are maximum axonal strain and maximum von Mises stress for the specific brain regions associated with consciousness; based on injured (solid red columns) and non-injured (blank green columns) categorization with regard to seven experimental behavioural responses.

Injured and non-injured groups based on unconsciousness time

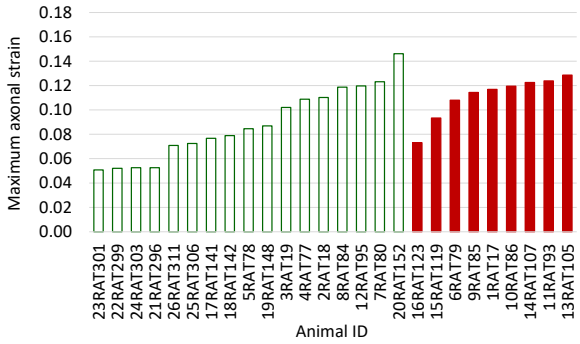

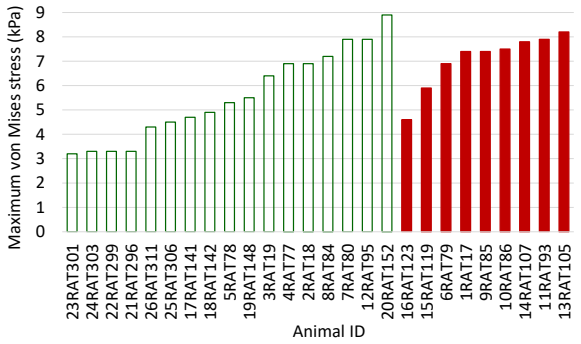

Injured and non-injured groups based on EPM distance travelled

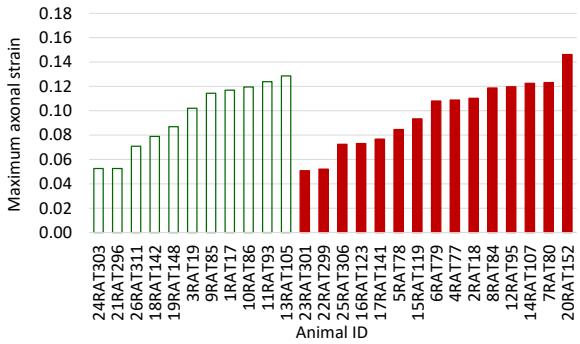

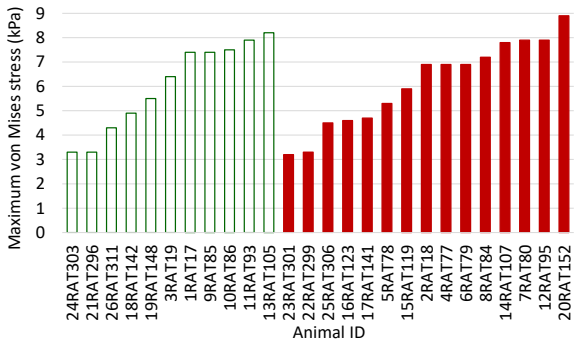

Injured and non-injured groups based on EPM arm changes

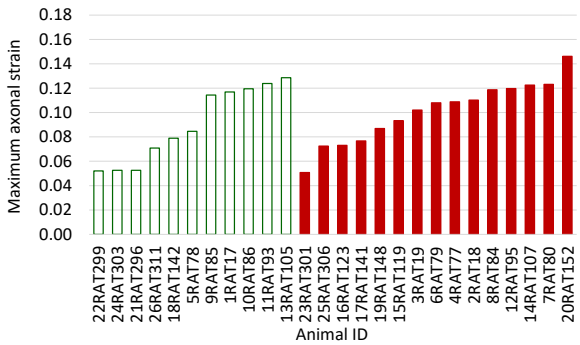

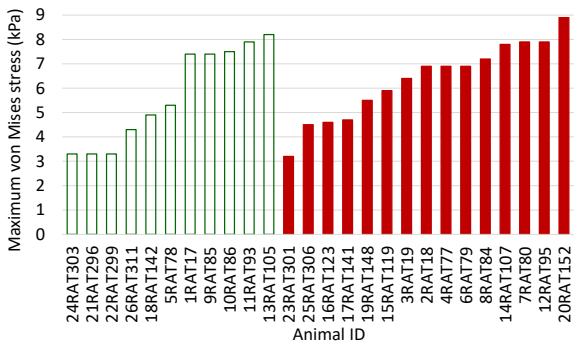

cont.

Injured and non-injured groups based on EPM open duration

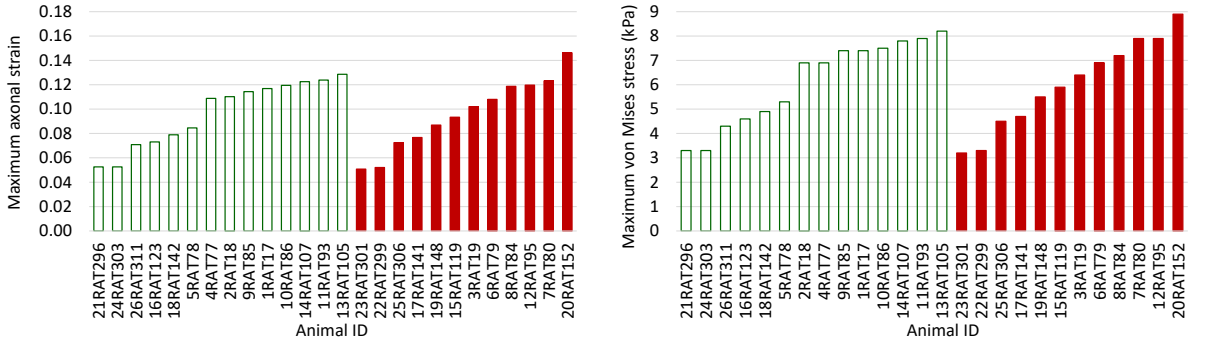

Injured and non-injured groups based on MWM session I latency

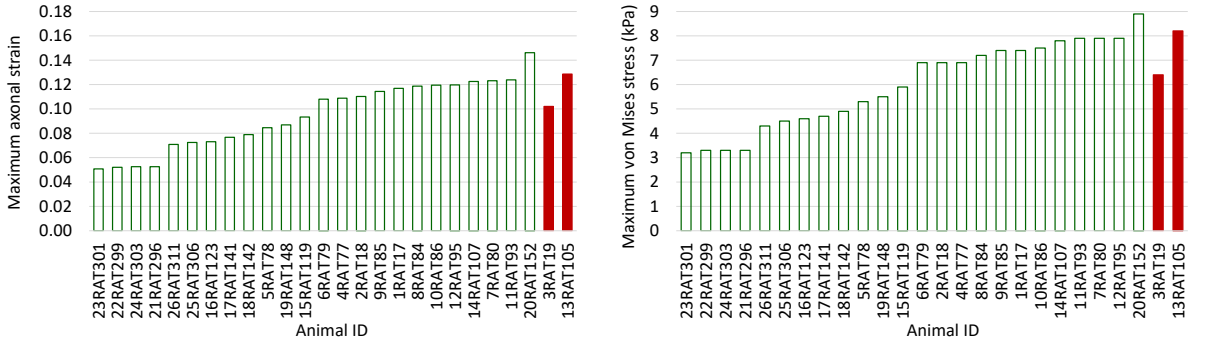

Injured and non-injured groups based on MWM session II latency

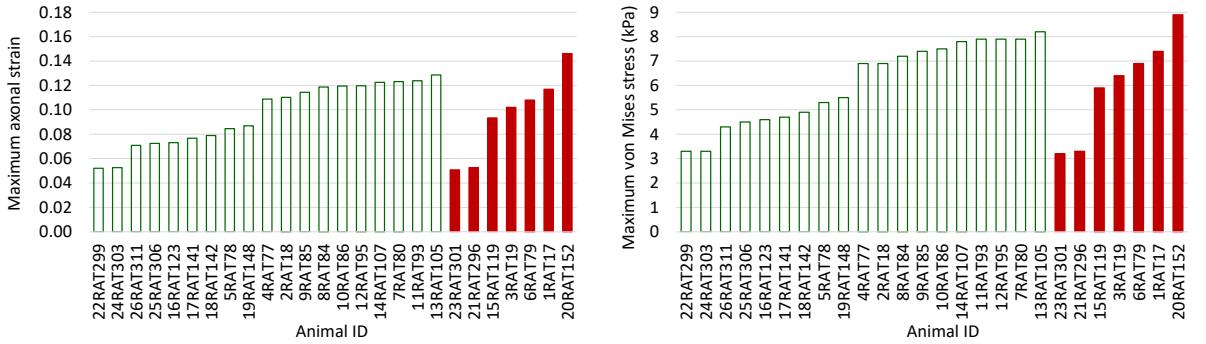

Injured and non-injured groups based on MWM session III latency

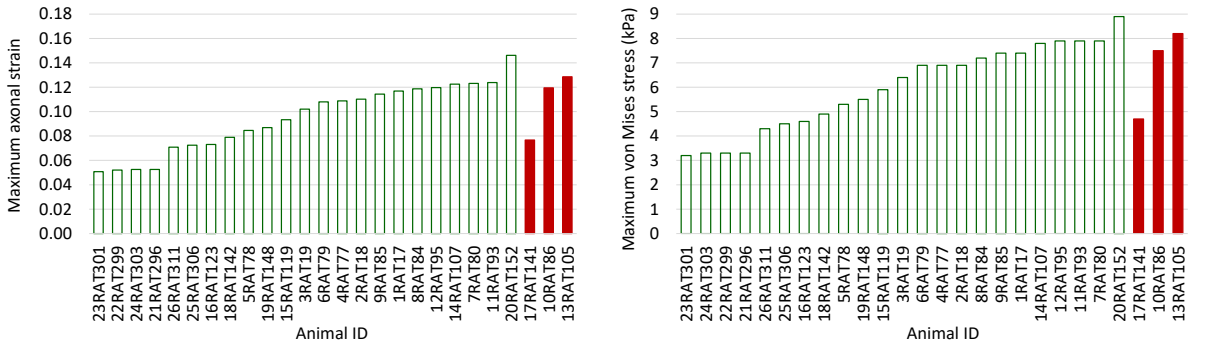

As can be seen from these plots, neither maximum axonal strain, nor maximum von Mises stress is able to predict the occurrence of concussion in association with any of the seven experimental

behavioural response measures for the brain regions associated with consciousness. It was true for other mechanical parameters as well (Annexure E, Table E1 to Table E7).

Table 3.10 represents the simulation results, in terms of maximum axonal strain and maximum von Mises stress, of all twenty-six cases for the brain regions associated with activity.

Table 3.10: Simulation results of all twenty-six experimental cases for two mechanical parameters, which are maximum axonal strain and maximum von Mises stress for the specific brain regions associated with activity; based on injured (solid red columns) and non-injured (blank green columns) categorization with regard to seven experimental behavioural responses.

Injured and non-injured groups based on unconsciousness time

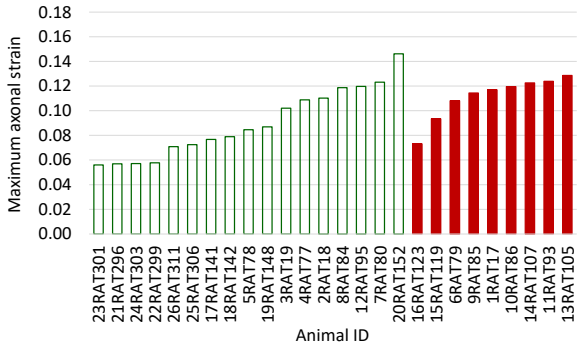

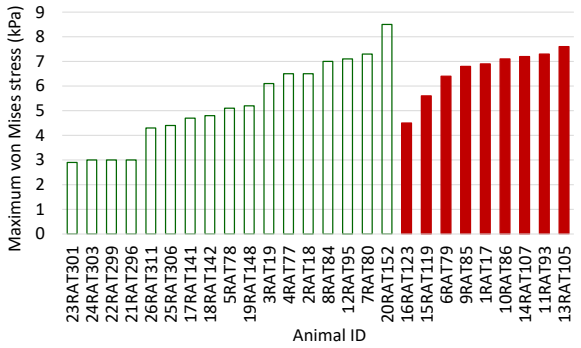

Injured and non-injured groups based on EPM distance travelled

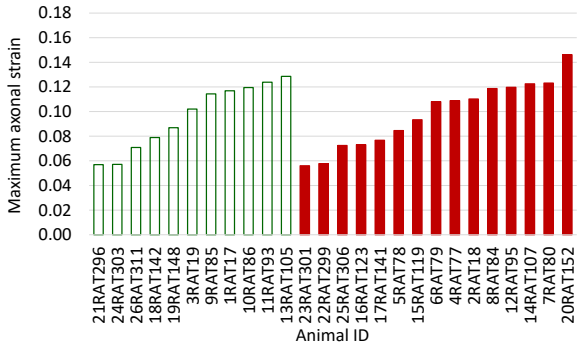

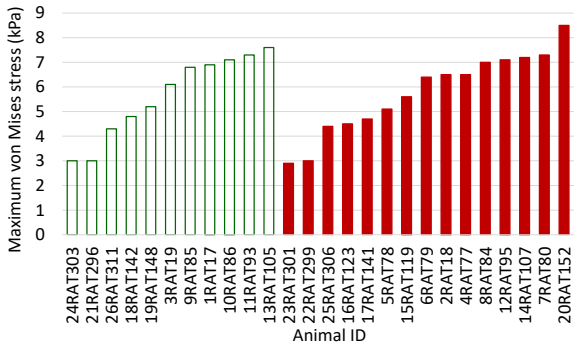

Injured and non-injured groups based on EPM arm changes

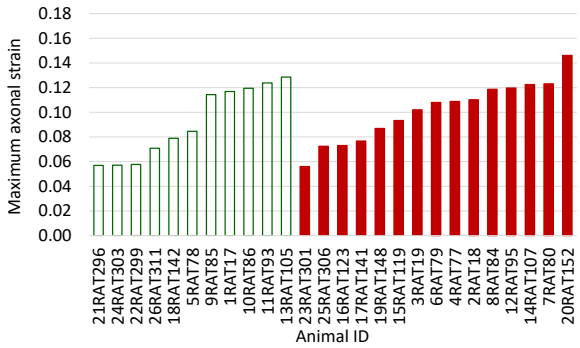

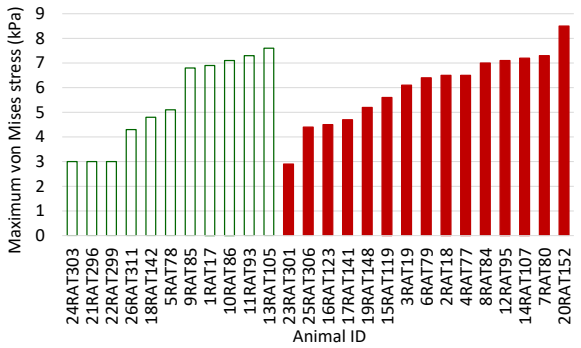

cont.

Injured and non-injured groups based on EPM open duration

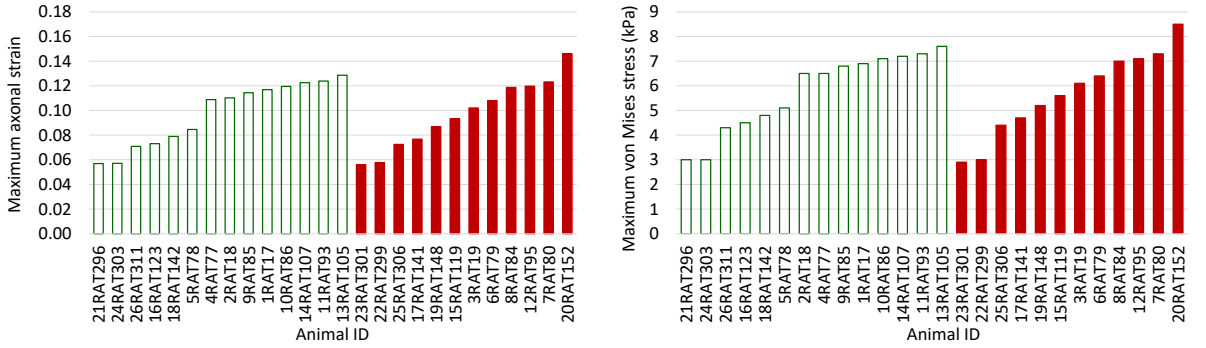

Injured and non-injured groups based on MWM session I latency

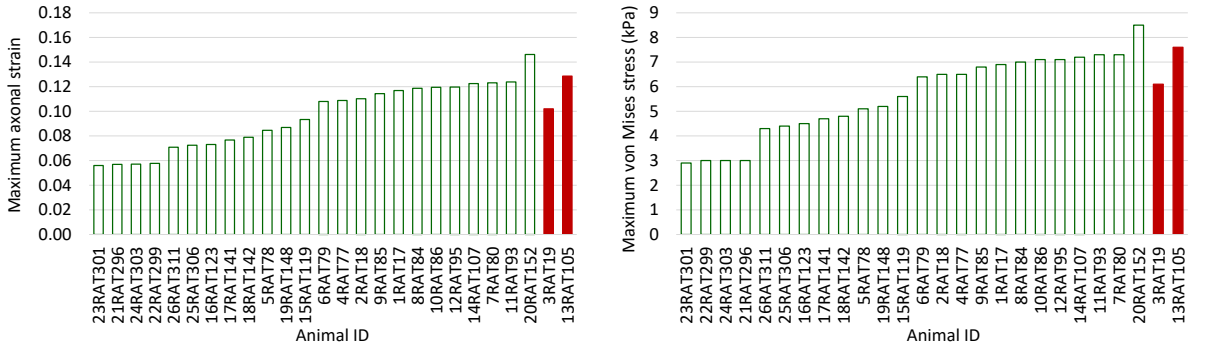

Injured and non-injured groups based on MWM session II latency

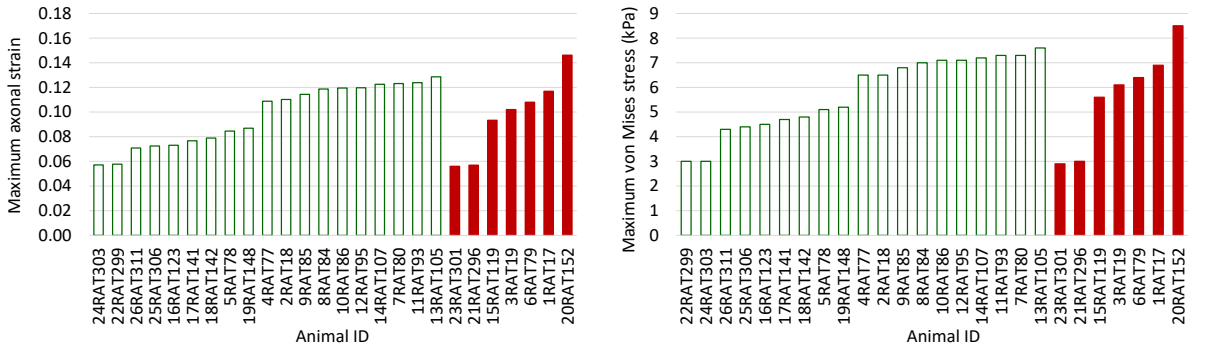

Injured and non-injured groups based on MWM session III latency

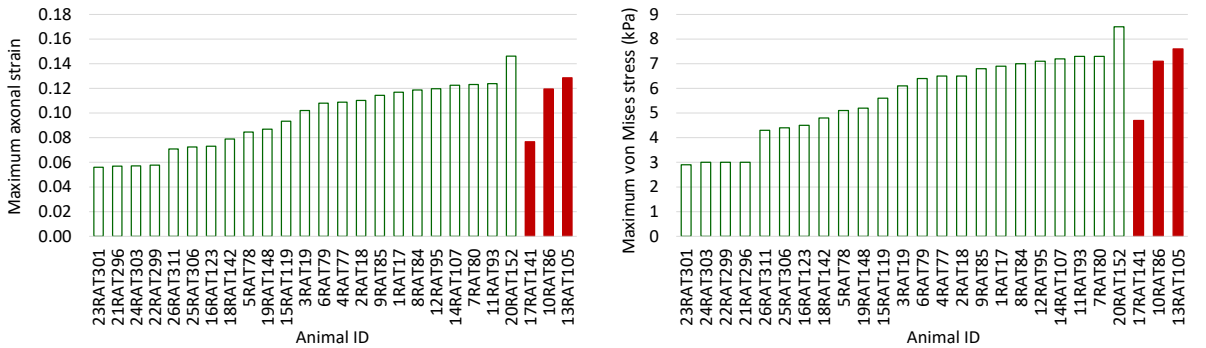

As can be seen from these plots, neither maximum axonal strain, nor maximum von Mises stress is able to predict the occurrence of concussion in association with any of the seven experimental

behavioural response measures for the brain regions associated with activity. It was true for other mechanical parameters as well (Annexure E, Table E8 to Table E14).

Table 3.11 represents the simulation results, in terms of maximum axonal strain and maximum von Mises stress, of all twenty-six cases for the brain regions associated with emotionality.

Table 3.11: Simulation results of all twenty-six experimental cases for two mechanical parameters, which are maximum axonal strain and maximum von Mises stress for the specific brain regions associated with emotionality; based on injured (solid red columns) and non-injured (blank green columns) categorization with regard to seven experimental behavioural responses.

Injured and non-injured groups based on unconsciousness time

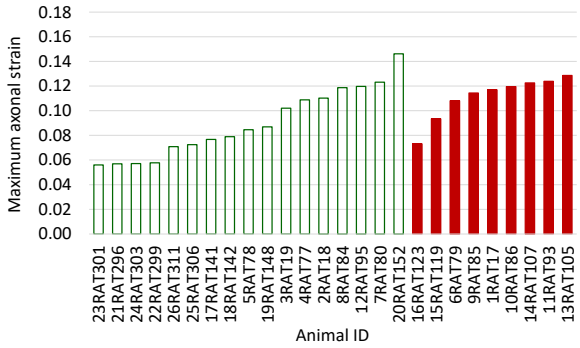

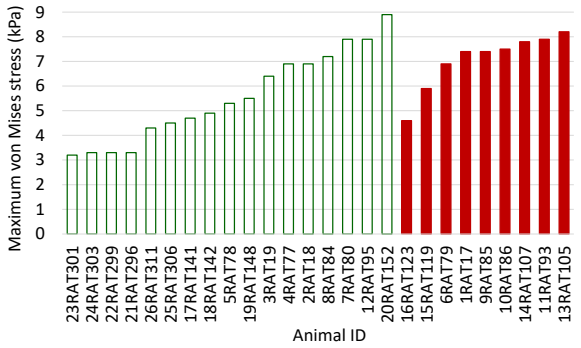

Injured and non-injured groups based on EPM distance travelled

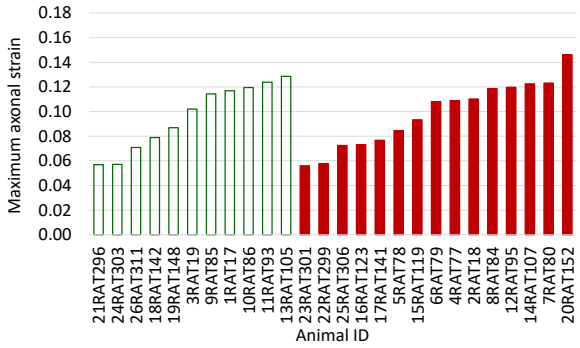

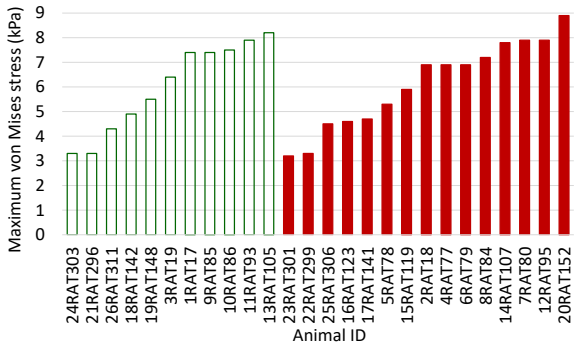

Injured and non-injured groups based on EPM arm changes

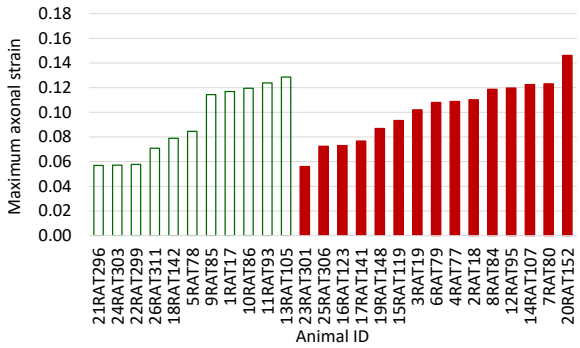

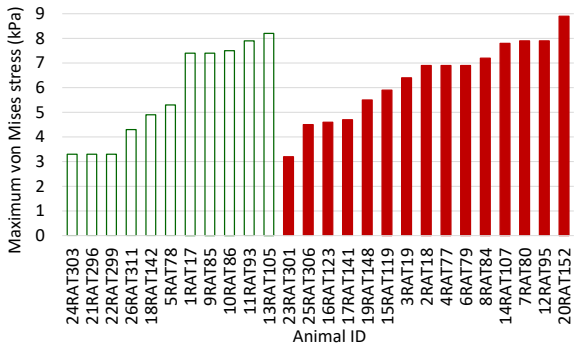

cont.

Injured and non-injured groups based on EPM open duration

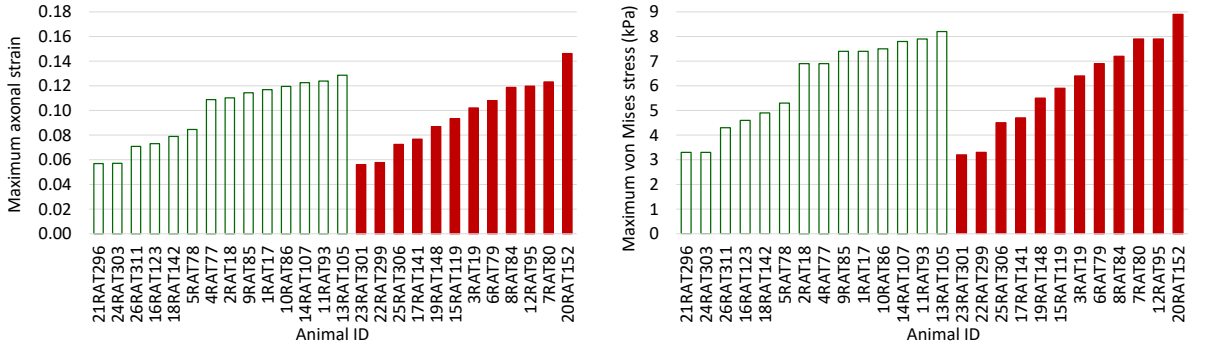

Injured and non-injured groups based on MWM session I latency

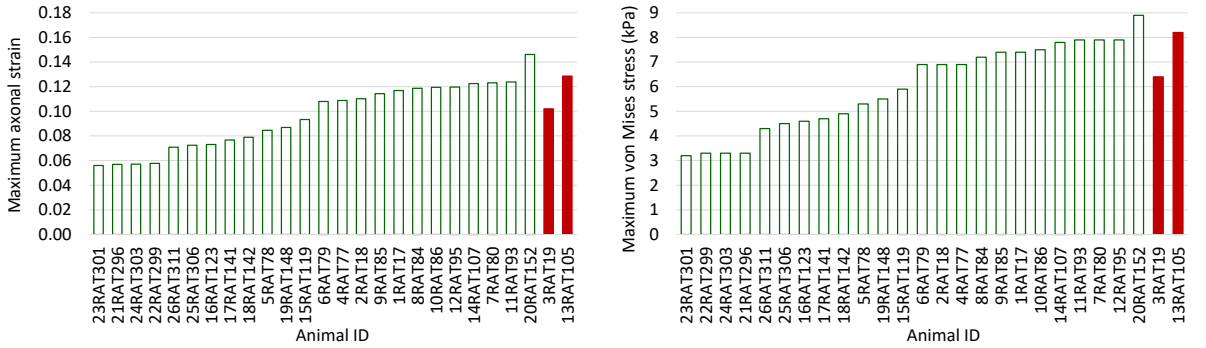

Injured and non-injured groups based on MWM session II latency

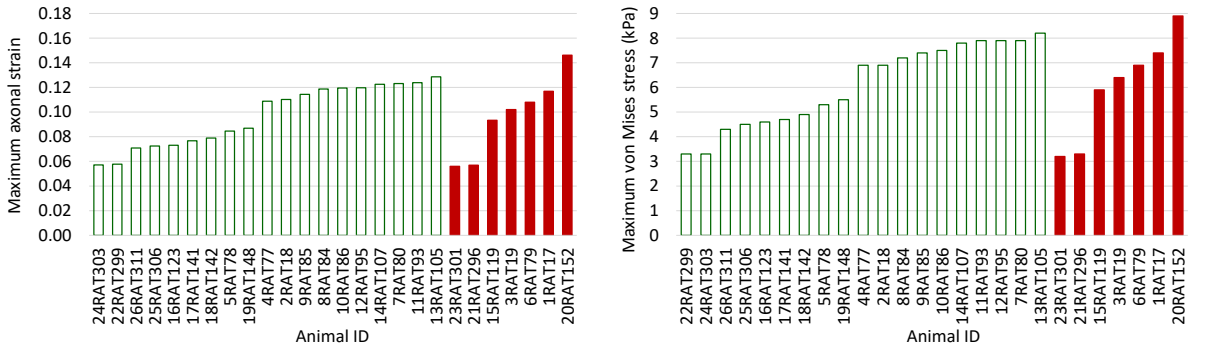

Injured and non-injured groups based on MWM session III latency

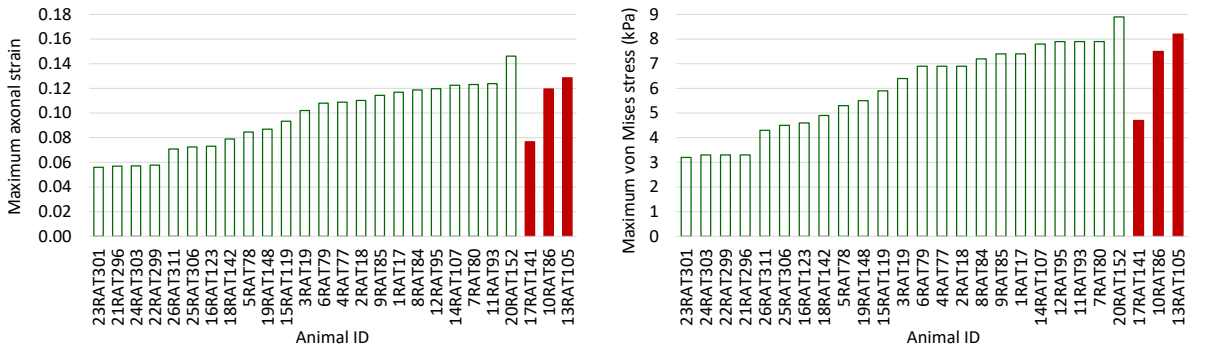

As can be seen from these plots, neither maximum axonal strain, nor maximum von Mises stress is able to predict the occurrence of concussion in association with any of the seven experimental

behavioural response measures for the brain regions associated with emotionality. It was true for other mechanical parameters as well (Annexure E, Table E15 to Table E21).

Table 3.12 represents the simulation results, in terms of maximum axonal strain and maximum von Mises stress, of all twenty-six cases for the brain regions associated with cognition.

Table 3.12: Simulation results of all twenty-six experimental cases for two mechanical parameters, which are maximum axonal strain and maximum von Mises stress for the specific brain regions associated with cognition; based on injured (solid red columns) and non-injured (blank green columns) categorization with regard to seven experimental behavioural responses.

Injured and non-injured groups based on unconsciousness time

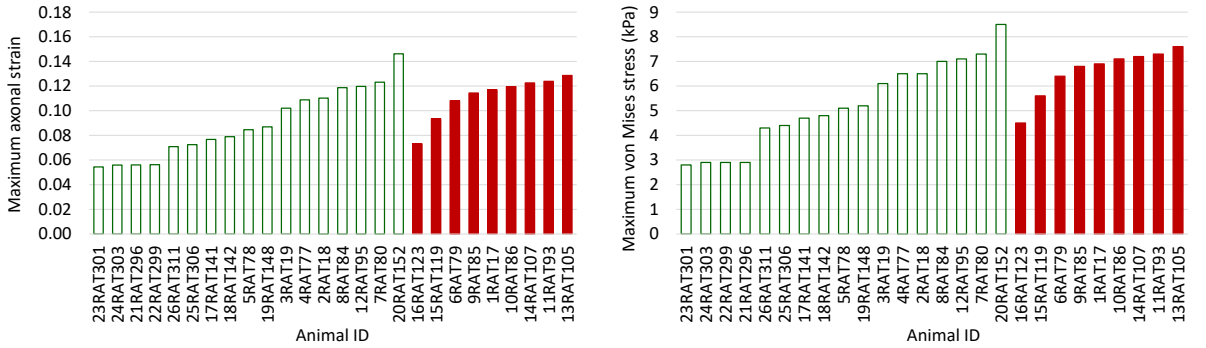

Injured and non-injured groups based on EPM distance travelled

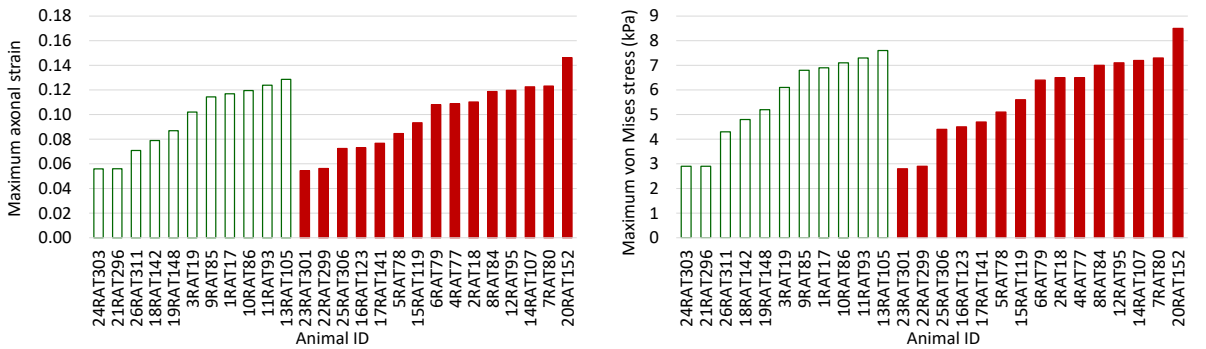

Injured and non-injured groups based on EPM arm changes

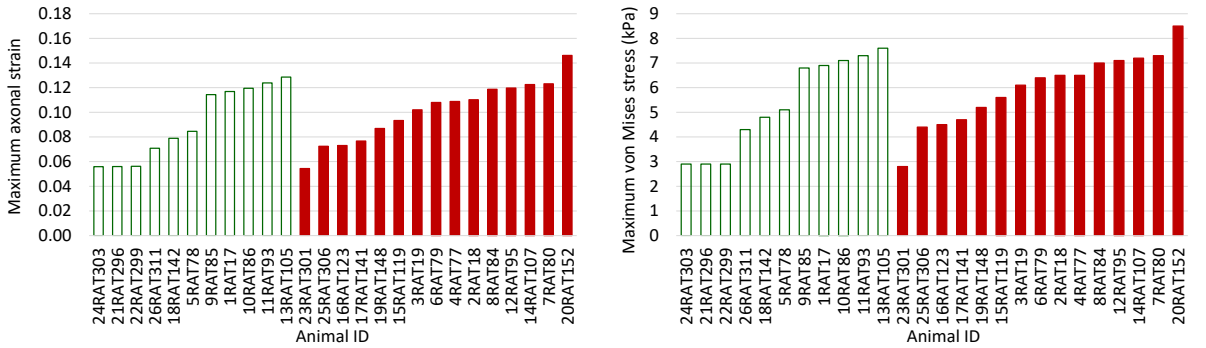

cont.

Injured and non-injured groups based on EPM open duration

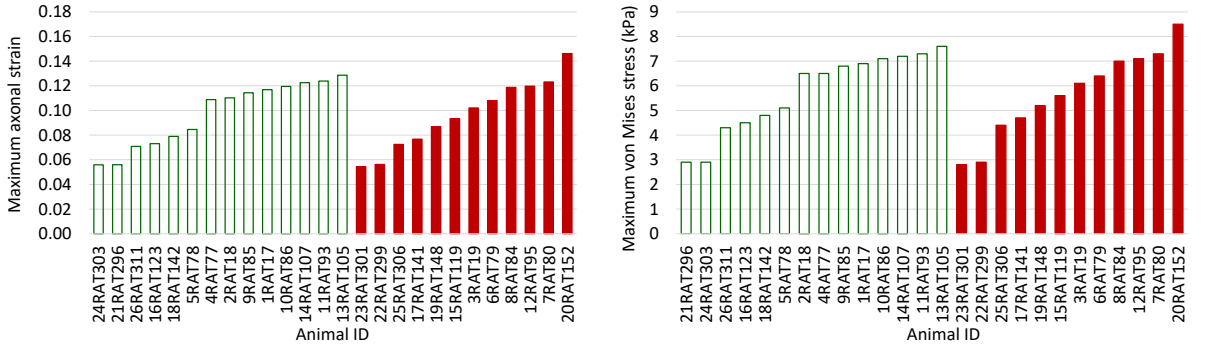

Injured and non-injured groups based on MWM session I latency

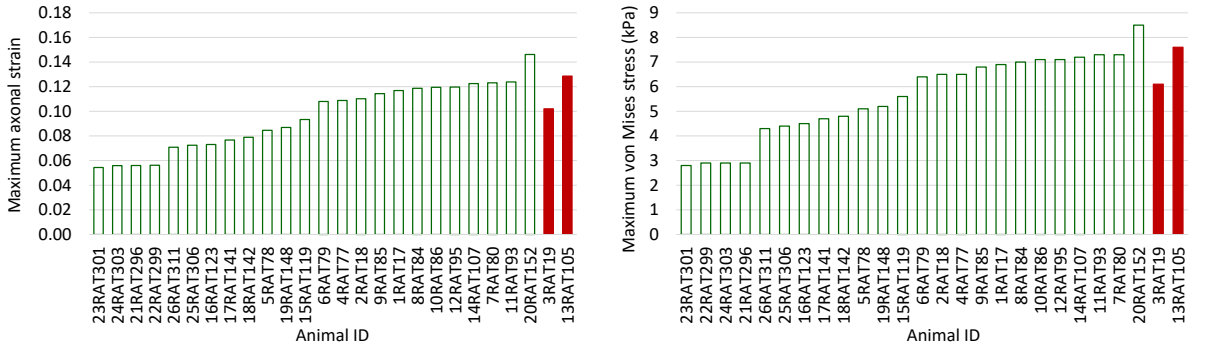

Injured and non-injured groups based on MWM session II latency

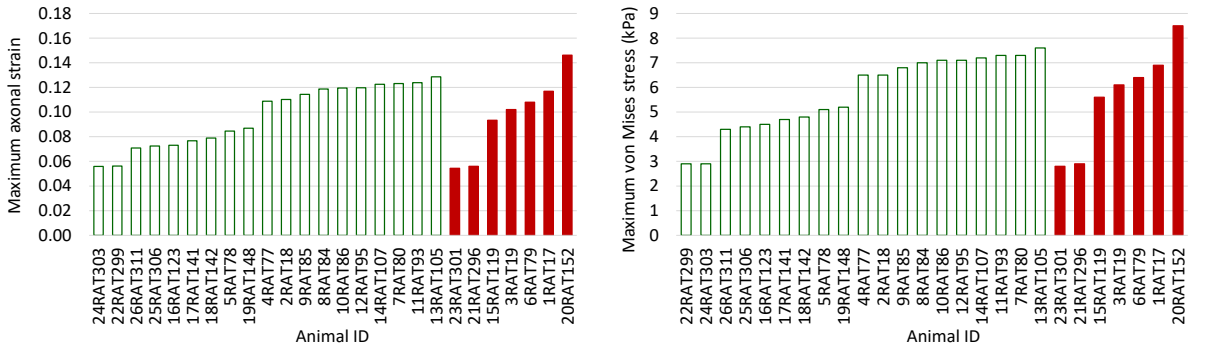

Injured and non-injured groups based on MWM session III latency

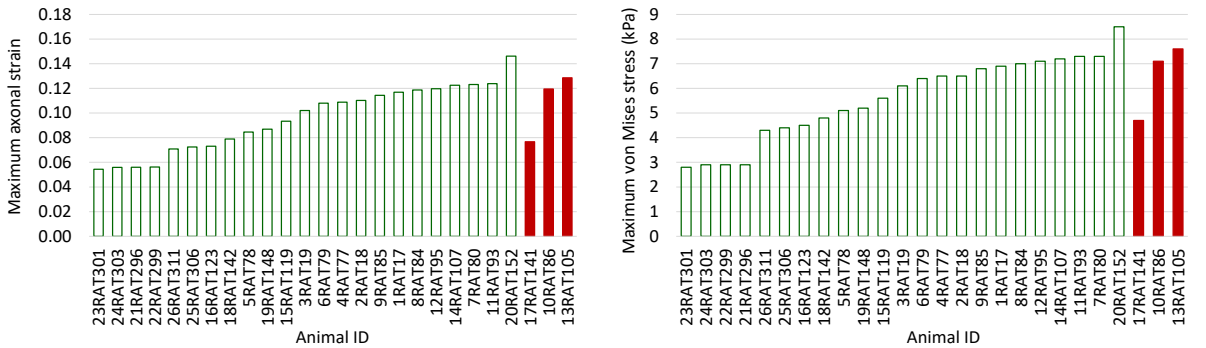

As can be seen from these plots, neither maximum axonal strain, nor maximum von Mises stress is able to predict the occurrence of concussion in association with any of the seven experimental

behavioural response measures for the brain regions associated with cognition. It was true for other mechanical parameters as well (Annexure E, Table E22 to Table E28).

We see that on the basis of injured and non-injured categorization for different functional brain regions, the simulation results do not seem to have a direct correlation with the injury based on the seven experimental behavioural response measures. However, it is important to notice that the relation with unconsciousness time seems better than any other computed mechanical parameter. Hence, let us now look at these results at individual brain regions with a different perspective.

4.5 For different anatomical brain regions

As mentioned in Chapter 2 (Figure 2.3), the anatomical categorization of brain divided the brain into twenty-four regions, recalled here for reference in Table 3.13. Simulation results for these anatomical brain regions are presented below. As seen earlier, the injured and non-injured categorization based on the seven experimental behavioural measures did not provide any valuable insights. Hence, instead of presenting the results based on injured and non-injured categorization, actual results, in term of maximum axonal strain, per brain region, per case is presented based on different loading groups.

Table 3.13: Anatomical categorization of rat brain into various regions.

#	Region description	#	Region description
1	Hippocampus	**13**	Neocortex
2	External capsule	**14**	Amygdala
3	Caudate – Putamen – Globus pallidus	**15**	Olfactory bulb
4	Anterior commissure	**16**	Brainstem
5	Substantia nigra	**17**	Fimbria
6	Internal capsule	**18**	Fornix
7	Thalamus	**19**	Ventral tegmental area (VTA)
8	Cerebellum	**20**	Corpus callosum
9	Superior colliculus	**21**	Genu
10	Hypothalamus	**22**	Aqueduct
11	Inferior colliculus	**23**	Splenium
12	Central gray	**24**	Rest of the brain

Figure 3.5 illustrates the maximum axonal strain values of all twenty-four brain regions for four cases belonging to M1D1a loading group. For this low magnitude short duration group, average maximum axonal strain was equal to 4.96%. As can be observed from the diagram, maximum axonal strain was

experienced by brain region number thirteen i.e. neocortex and the average MAS experienced by neocortex for M1D1a loading group was equal to 7.58% ± 0.6%.

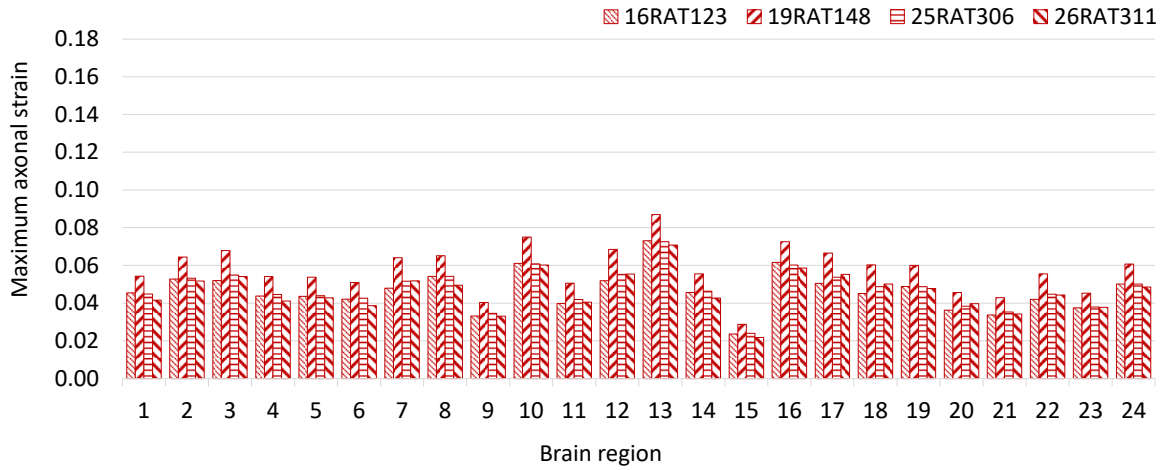

Figure 3.5: Diagram illustrating the maximum axonal strain values of all twenty-four brain regions for four cases belonging to M1D1a loading group.

Figure 3.6 illustrates the maximum axonal strain values of all twenty-four brain regions for four cases belonging to M1D1b loading group. For this low magnitude short duration group, average maximum axonal strain was equal to 4.04%. As can be observed from the diagram, maximum axonal strain was experienced by brain region number twelve i.e. central gray and seventeen i.e. fimbria. Average maximum axonal strain experienced by central gray for M1D1b loading group was equal to 5.69% ± 0.1% and that experienced by fimbria was 5.56% ± 0.1%.

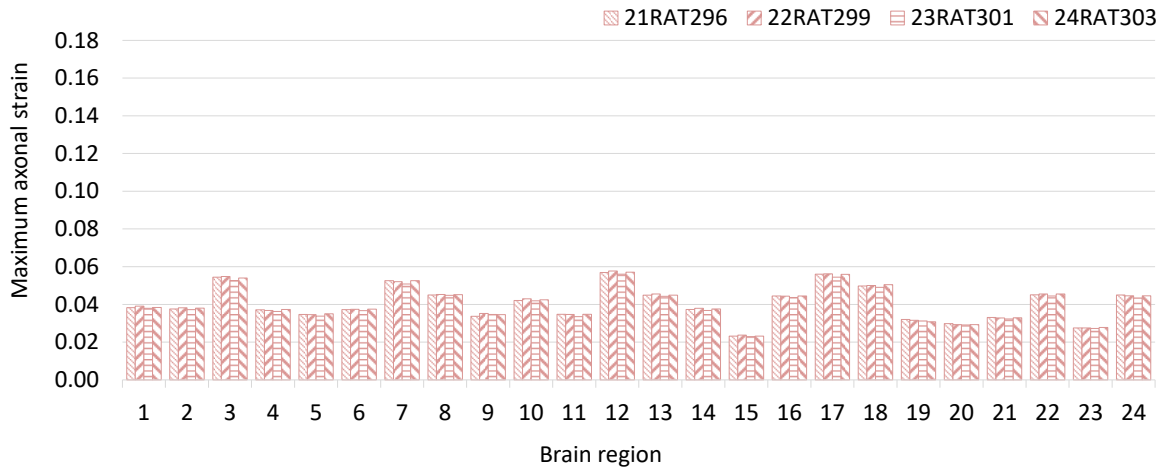

Figure 3.6: Diagram illustrating the maximum axonal strain values of all twenty-four brain regions for four cases belonging to M1D1b loading group.

Figure 3.7 illustrates the maximum axonal strain values of all twenty-four brain regions for two cases belonging to M1D2 loading group. For this low magnitude long duration group, average maximum axonal strain was equal to 5.2%. As can be observed from the diagram, maximum axonal strain was

experienced by brain region number thirteen i.e. neocortex. Average maximum axonal strain experienced by neocortex for M1D2 loading group was equal to 7.78% ± 0.1%.

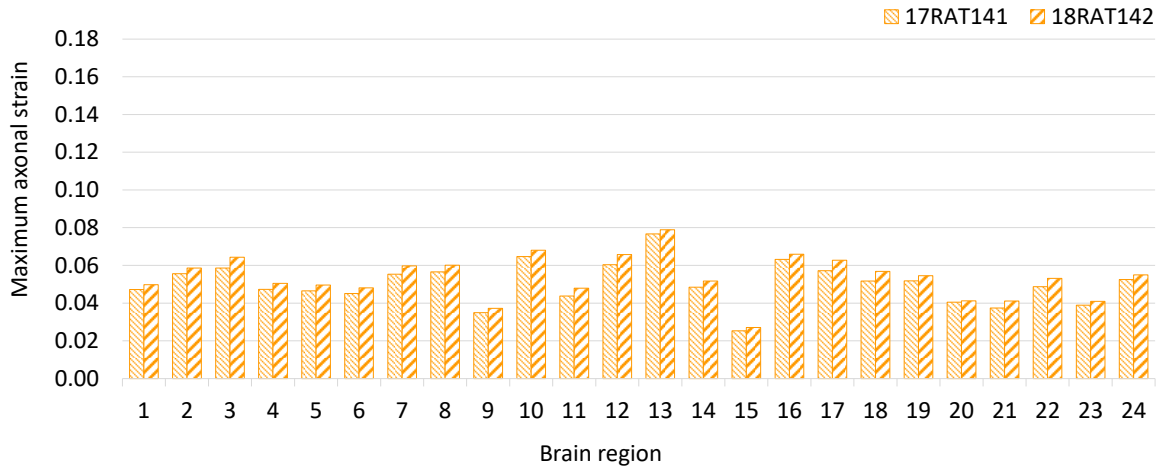

Figure 3.7: Diagram illustrating the maximum axonal strain values of all twenty-four brain regions for four cases belonging to M1D2 loading group.

Figure 3.8 illustrates the maximum axonal strain values of all twenty-four brain regions for seven cases belonging to M2D1a loading group. For this high magnitude short duration group, average maximum axonal strain was equal to 8.24%. As can be observed from the diagram, maximum axonal strain was experienced by brain region number thirteen i.e. neocortex. Average maximum axonal strain experienced by neocortex for this loading group was equal to 11.83% ± 0.5%.

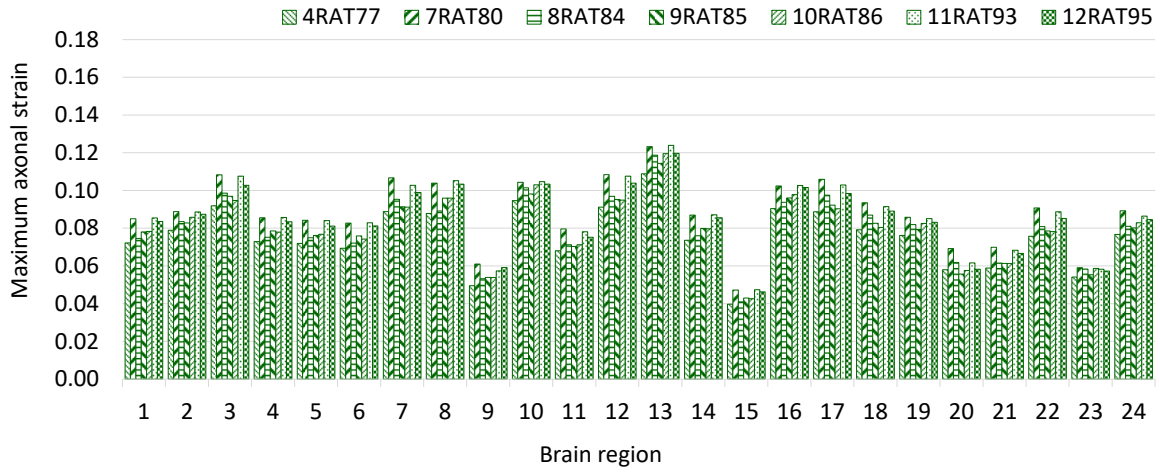

Figure 3.8: Diagram illustrating the maximum axonal strain values of all twenty-four brain regions for four cases belonging to M2D1a loading group.

Figure 3.9 illustrates the maximum axonal strain values of all twenty-four brain regions for five cases belonging to M2D1b loading group. For this high magnitude short duration group, average maximum axonal strain was equal to 7.45%. As can be observed from the diagram, maximum axonal strain was

experienced by brain region number thirteen i.e. neocortex. Average maximum axonal strain experienced by neocortex for this loading group was equal to 11.51% ± 2.3%.

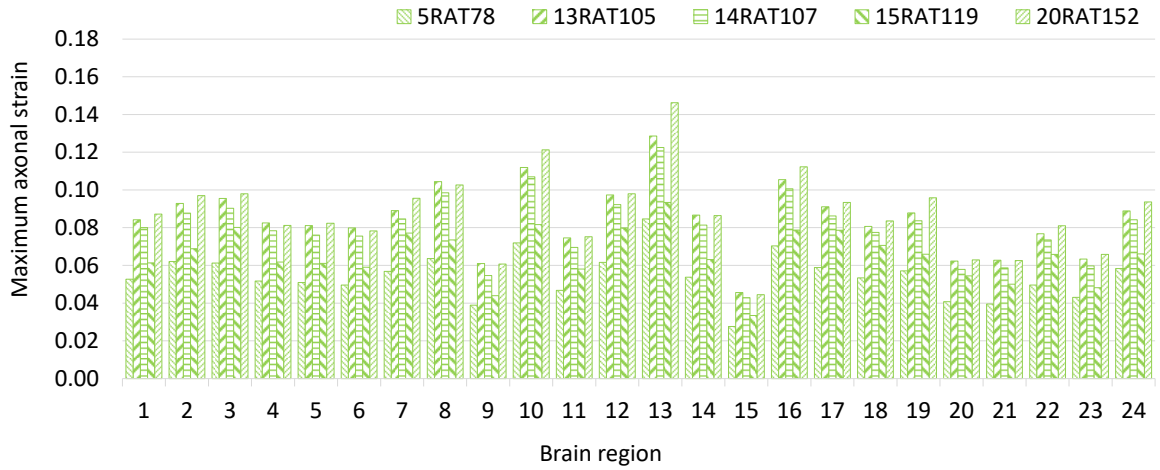

Figure 3.9: Diagram illustrating the maximum axonal strain values of all twenty-four brain regions for four cases belonging to M2D1b loading group.

Figure 3.10 illustrates the maximum axonal strain values of all twenty-four brain regions for four cases belonging to both groups of M2D2 loading group. For this high magnitude long duration group, average maximum axonal strain was equal to 7.31%. As can be observed from the diagram, maximum axonal strain was experienced by brain region number thirteen i.e. neocortex. Average maximum axonal strain experienced by neocortex for this loading group was equal to 10.93% ± 0.5%.

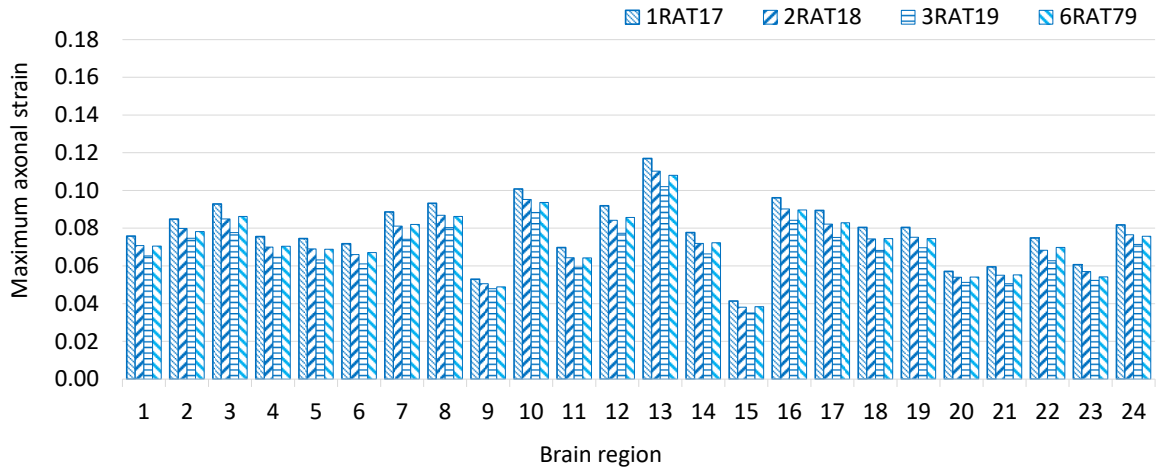

Figure 3.10: Diagram illustrating the maximum axonal strain values of all twenty-four brain regions for four cases belonging to M2D2 loading group.

Hence, we can see that the maximum axonal strain was experienced by cases belonging to high magnitude short duration loading group, which is in accordance with the literature. These results also helped in identifying brain regions, which experienced high strains and hence, were more vulnerable to injury. We can see from the diagrams that regions, which experienced high axonal strains were

neocortex (#13), hypothalamus (#10), brainstem (#16), central gray (#12), caudate-putamen-globus pallidus (#3), thalamus (#7), fimbria (#17) and cerebellum (#8). All these regions are known to influence the behavioural response (consciousness, activity, emotionality and cognition capabilities) in some way or the other.

4.6 Conclusion

In this section we saw the simulation results for the entire brain as well as for the functional and the anatomical brain regions with different perspectives. On one hand, it is disappointing that we could not see a direct relation between the simulation results, in terms of various mechanical parameters, and the injury, in terms of experimental behavioural response measures. Whereas, on the other hand, we could found out the axonal strains for each and every brain region and also could identify most vulnerable brain regions for concussion. This important finding could have been possible only because of the anisotropic finite element rat brain model.

Based on the simulation results of twenty-six experimental cases, there does not seem to be any direct relation between the acceleration characteristics and the experimental behavioural response measures. Cases having alike acceleration characteristics were found to have a wide variation in the values of experimental behavioural response measures. Also, both injured and non-injured cases ranged from low magnitudes, short durations to high magnitudes, long durations. Usually, acceleration characteristics in rotational acceleration loading, to induce injury, can correlate with the injury severity to some extent. However, that was not the case here. One of the possible reasons could be that the number of cases simulated were too low to be able to reveal any such relation.

Other mechanical parameters (maximum axonal strain, maximum strain energy, maximum von Mises stress and strain, maximum shear stress and strain, maximum principal stress and strain and minimum and maximum pressures) chosen for the analysis, does not show any direct relation with the injury, in terms of experimental behavioural response measures, either. Cases having alike acceleration characteristics were found to have a wide variation in the values of experimental behavioural response measures. Globally, it could be observed that for cases belonging to high magnitude short duration group, the mechanical response was the highest. This was followed by cases belonging to high magnitude long duration group and then by cases belonging to low magnitude long duration group. Mechanical response of the cases belonging to low magnitude short duration group laid at the lowest. Besides, the mechanical response of both, injured and non-injured cases ranged from low to high and also, though the overall amplitudes of these responses for injured cases were sometimes slightly higher than that of non-injured cases, the differences were not significant.

Cases were categorized into injured and non-injured groups based on the assumption that a behavioural response value that fall below the sham's response value can be considered non-injured and vice versa. This assumption may not be suitable for these experimental cases because concussion is a mild kind of traumatic brain injury. Impact of concussion is functional disturbances. Hence, a deviation in the response from sham's response indicates a change in behaviour. This change could be positive or negative. However, in both the situations, the change is because of the induced concussion. Hence, the cases, where the response fell below the sham's value is as well a change and might not have been considered not injured.

A part wise comparison of maximum axonal strain showed that the main regions experiencing the highest maximum axonal strains were neocortex, hypothalamus, brainstem, central gray, caudate-putamen-globus pallidus, fimbria, cerebellum and thalamus. All these regions are known to influence the behavioural response (consciousness, activity, emotionality and cognition capabilities) in some way or the other.

Based on low and high magnitudes (M1 and M2) and short and long durations (D1 and D2) of the rotational acceleration, a loading group wise comparison of maximum axonal strain showed that the brain regions experiencing the highest maximum axonal strain in all the four groups (M1D1, M1D2, M2D1 and M2D2) are more or less the same. However, the highest values of maximum axonal strain differ as expected. For example, for the low magnitude short duration group, the maximum axonal strain values were lower and lay around 7%, whereas that for high magnitude short duration group, the values were higher and lay around 11% and even 14.6% for one of the cases.

It would be interesting to get access to some more experimental cases, to be able to come to a point more clearly. However, to see the significance of these simulation results, let us proceed towards statistical analysis of the simulation data.

5 Statistical analysis

5.1 Introduction

With the objective of identifying best suitable parameter for the prediction of concussion, statistical analysis was done for different mechanical parameters computed numerically in association with different experimental behavioural response measures. Binary logistic regression method was utilized to statistically analyze the correlation between evaluated intracerebral parameters and the occurrence of concussion. The analysis was carried out using IBM SPSS Statics, Version 21 software package. As per Sahoo et al. (2016) based on the report by Hynd and colleagues (2004), binary logistic

regression was found to be the best statistical method over other measures of such assessment. Mechanical behaviour of the model, in terms of twelve mechanical parameters (two global and ten local), which are maximum rotational acceleration, duration of rotational acceleration, maximum axonal strain, maximum strain energy, maximum von Mises stress and strain, maximum shear stress and strain, maximum principal stress and strain and minimum and maximum pressures, was statistically analyzed based on seven experimental behavioural response measures, which are unconsciousness time, EPM distance travelled, EPM arm changes, EPM open duration and latencies of MWM session I, II and III to find out the best candidate parameters for predicting concussion. Binary logistic regression tries to fit a regression model between various possible brain injury (concussion) metrics. With this method, the probability of brain injury (concussion) is defined as given in Equation 3.1.

$$P(x) = 1/\left(1 + e^{-(b_0 + b_1 x)}\right) \quad 3.1$$

Where, b_0 and b_1 are two variables calculated by regression.

As described earlier, maximum value of experimental behavioural response measure of sham was used as the deciding factor to classify cases in non-injured and injured groups for the binarization. Nagelkerke R-squared values were calculated to identify the best injury predictor. The quality of logistic regression fit was tested through Hosmer-Lemeshow p-values. Additionally, receiver operating characteristic curve analysis was used to check the robustness of the estimated metric. Following sections provide a comparison of these injury predictors using three statistical methods, based on Nagelkerke R-squared value, Hosmer-Lemeshow p-value (HL p-value) and area under receiver operating characteristic curve (AUROC). Let us now look at the results of these statistical analyses.

5.2 Based on binary logistic regression for Nagelkerke R-squared value

Nagelkerke R-squared value was used to identify the significance of various injury predictors. The comparison of candidate parameters using Nagelkerke R-squared value helped in identifying which brain injury metric best correlate with the occurrence of concussion. Nagelkerke R-squared value ranges between zero and one, where zero represents a poor fit and one, a good fit. Table 3.14 provides the Nagelkerke R-squared values calculated for all twelve injury predictors based on seven experimental behavioural response measures for the entire brain.

Table 3.14: Nagelkerke R-squared values for the entire brain.

Injury predictor	Unconscious time	EPM distance travelled	EPM arm changes	EPM open duration	MWM session I latency	MWM session II latency	MWM session III latency
Max. rotational acceleration	0.071	0.019	0.006	0.009	0.163	0.000	0.034
Duration	0.025	0.000	0.096	0.001	0.112	0.033	0.002
Max. axonal strain	0.211	0.002	0.043	0.000	0.105	0.000	0.048
Max. strain energy	0.201	0.002	0.040	0.001	0.122	0.000	0.058
Max. von Mises stress	0.247	0.001	0.043	0.001	0.110	0.001	0.046
Max. von Mises strain	0.229	0.002	0.045	0.001	0.112	0.000	0.051
Max. shear stress	0.233	0.001	0.043	0.001	0.125	0.001	0.052
Max. shear strain	0.230	0.002	0.045	0.001	0.112	0.000	0.050
Max. principal stress	0.213	0.002	0.045	0.001	0.091	0.001	0.041
Max. principal strain	0.225	0.002	0.043	0.001	0.106	0.001	0.050
Min. pressure	0.214	0.002	0.045	0.001	0.090	0.001	0.042
Max. pressure	**0.261**	0.003	0.076	0.000	0.096	0.007	0.040

It can be observed that the Nagelkerke R-squared values for all the possible combinations are pretty low. Relatively, the best correlation of injury predictors is found with the unconsciousness time. The R-squared value of maximum pressure to predict concussion in 0.261 and is the highest. The second highest R-squared value is of von Mises stress and is equal to 0.247. The R-squared value of axonal strain is 0.211 only.

Based on this statistical analysis, injury risk curves for the entire brain to predict concussion with regard to the unconsciousness time are provided in Table 3.15.

Table 3.15: Injury risk curves for the entire brain to predict probability of concussion with regard to unconsciousness time in terms of different injury predictors (hollow green circles represent non-injured cases and solid red circles represent injured cases).

Maximum axonal strain (MAS)

For a 50% risk of concussion: MAS = 0.1182

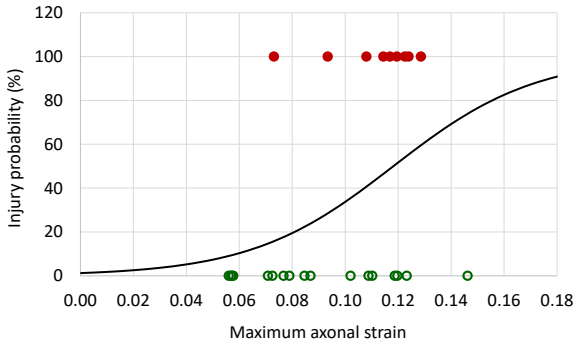

Maximum strain energy (MSE)

For a 50% risk of concussion: MSE = 6.77E-5 mJ

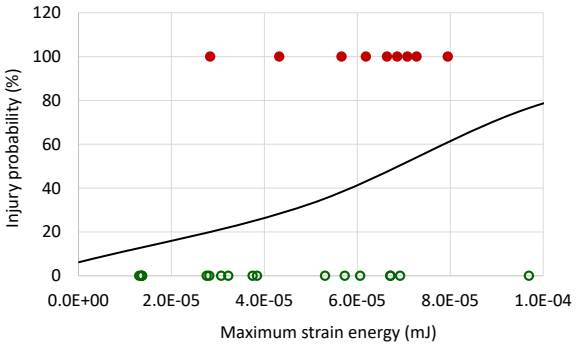

Maximum von Mises stress (MvMSs)

For a 50% risk of concussion: MvMSs = 7.4 kPa

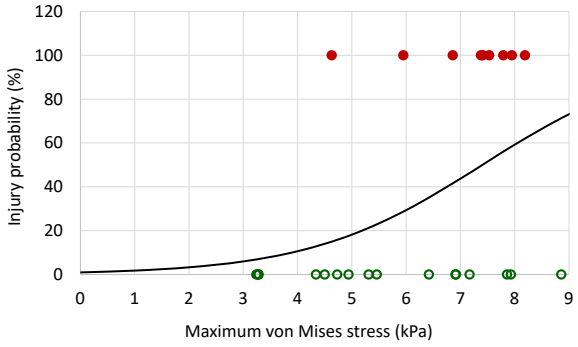

Maximum von Mises strain (MvMSn)

For a 50% risk of concussion: MvMSn = 0.1443

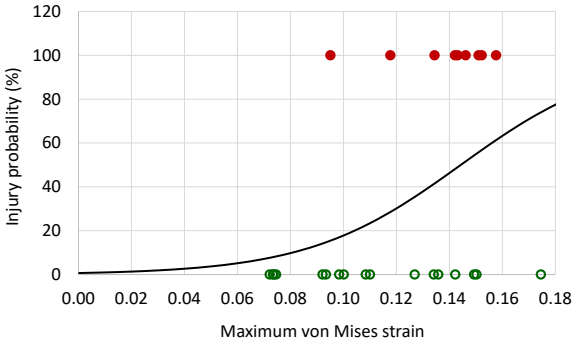

Maximum shear stress (MSSs)

For a 50% risk of concussion: MSSs = 4.2 kPa

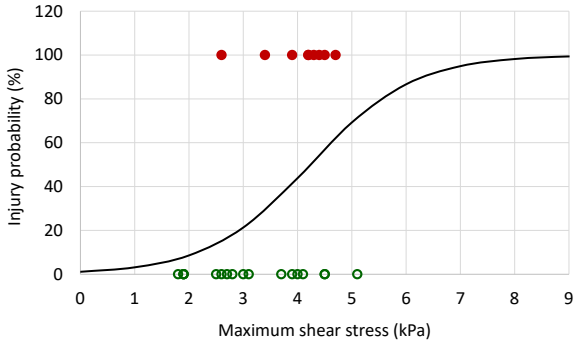

Maximum shear strain (MSSn)

For a 50% risk of concussion: MSSn = 0.1244

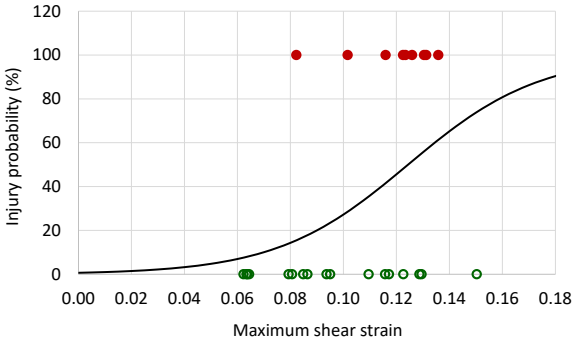

cont.

Maximum principal stress (MPSs)

For a 50% risk of concussion: MPSs = 349.6 kPa

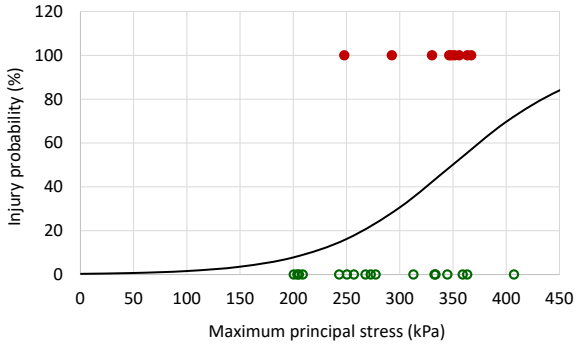

Maximum principal strain (MPSn)

For a 50% risk of concussion: MPSn = 0.1421

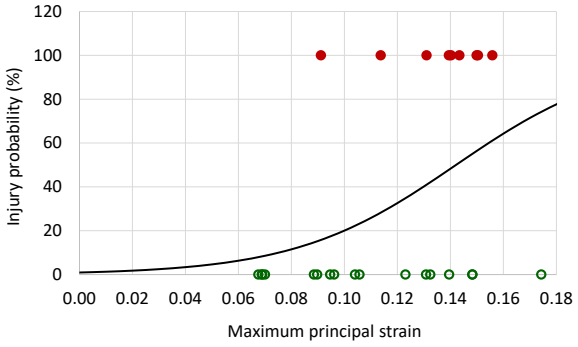

Minimum pressure (MinP)

For a 50% risk of concussion: MinP = -348 kPa

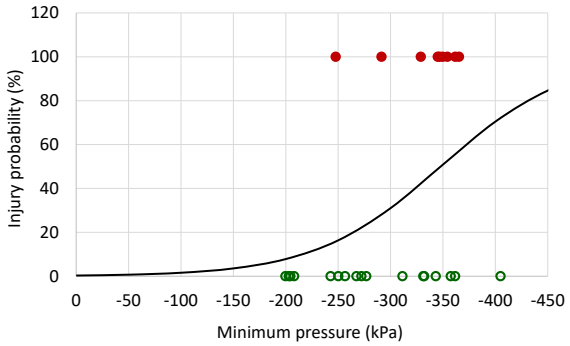

Maximum pressure (MaxP)

For a 50% risk of concussion: MaxP = 372.7 kPa

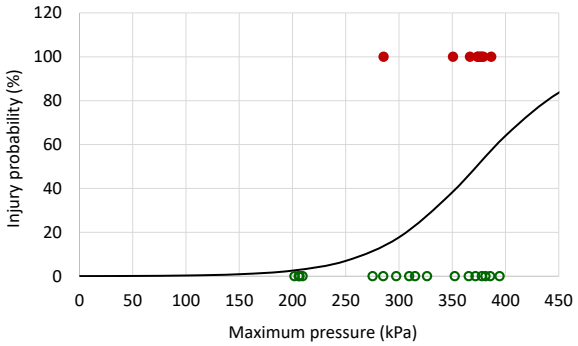

These injury risk curves indicate that based on unconscious time, for a 50% probability of concussion, the tolerance levels are 11.82% of axonal strain, 6.77E-5 mJ of strain energy, 7.4 kPa of von Mises stress, 14.43% of von Mises strain, 4.2 kPa of shear stress, 12.44% of shear strain, 349.6 kPa of principal stress, 14.21% of principal strain, -348 kPa of minimum pressure and 372.7 kPa of maximum pressure. Maximum axonal strain of 14.65% was identified by Sahoo et al. (2016) for a 50% risk of DAI in comparison to the value identified in this study, i.e. 11.82% of maximum axonal strain for a 50% risk of concussion with regard to unconsciousness time.

Table 3.16 provides the Nagelkerke R-squared values of ten injury predictors based on seven experimental behavioural response measures for the brain regions associated with consciousness.

Table 3.16: Nagelkerke R-squared values for the brain regions associated with consciousness.

Injury predictor	Unconscious time	EPM distance travelled	EPM arm changes	EPM open duration	MWM session I latency	MWM session II latency	MWM session III latency
Max. axonal strain	0.217	0.002	0.048	0.001	0.107	0.000	0.051

Injury predictor	Unconscious time	EPM distance travelled	EPM arm changes	EPM open duration	MWM session I latency	MWM session II latency	MWM session III latency
Max. strain energy	0.201	0.002	0.040	0.001	0.122	0.000	0.058
Max. von Mises stress	0.241	0.002	0.044	0.001	0.112	0.001	0.047
Max. von Mises strain	0.235	0.003	0.051	0.001	0.114	0.001	0.054
Max. shear stress	0.233	0.001	0.043	0.001	0.125	0.001	0.052
Max. shear strain	0.236	0.003	0.051	0.001	0.114	0.001	0.053
Max. principal stress	0.213	0.002	0.045	0.001	0.091	0.001	0.041
Max. principal strain	0.232	0.002	0.050	0.001	0.108	0.002	0.054
Min. pressure	0.214	0.002	0.045	0.001	0.090	0.001	0.042
Max. pressure	**0.261**	0.003	0.076	0.000	0.096	0.007	0.040

It can be observed that the Nagelkerke R-squared values for all the possible combinations are pretty low. Relatively, the best correlation is found with unconsciousness time. The R-squared value of maximum pressure to predict concussion in 0.261 and is the highest. The second highest R-squared value is of von Mises stress and is equal to 0.241. The R-squared value of axonal strain is 0.217 only. The injury risk curve (Table 3.20) for brain regions associated with consciousness indicates that based on unconscious time, for a 50% probability of concussion, the tolerance level is 11.80% of axonal strain.

Table 3.17 provides the Nagelkerke R-squared values of ten injury predictors based on seven experimental behavioural response measures for the brain regions associated with activity.

Table 3.17: Nagelkerke R-squared values for the brain regions associated with activity.

Injury predictor	Unconscious time	EPM distance travelled	EPM arm changes	EPM open duration	MWM session I latency	MWM session II latency	MWM session III latency
Max. axonal strain	0.211	0.002	0.043	0.000	0.105	0.000	0.048
Max. strain energy	0.201	0.002	0.040	0.001	0.122	0.000	0.058
Max. von Mises stress	0.226	0.002	0.052	0.001	0.114	0.002	0.059
Max. von Mises strain	0.225	0.002	0.043	0.001	0.106	0.000	0.049
Max. shear stress	0.233	0.003	0.055	0.000	0.105	0.001	0.049
Max. shear strain	0.226	0.002	0.043	0.001	0.106	0.000	0.048
Max. principal stress	0.213	0.002	0.045	0.001	0.091	0.001	0.041
Max. principal strain	0.215	0.002	0.045	0.000	0.107	0.000	0.050

Injury predictor	Unconscious time	EPM distance travelled	EPM arm changes	EPM open duration	MWM session I latency	MWM session II latency	MWM session III latency
Min. pressure	0.214	0.002	0.045	0.001	0.090	0.001	0.042
Max. pressure	**0.261**	0.003	0.076	0.000	0.096	0.007	0.040

It can be observed that the Nagelkerke R-squared values for all the possible combinations are pretty low. Relatively, the best correlation is found with unconsciousness time. The R-squared value of maximum pressure to predict concussion in 0.261 and is the highest. The second highest R-squared value is of shear stress and is equal to 0.233. The R-squared value of axonal strain and von Mises stress are only 0.211 and 0.225 respectively. The injury risk curve (Table 3.20) for brain regions associated with activity indicates that based on unconscious time, for a 50% probability of concussion, the tolerance level is 11.82% of axonal strain.

Table 3.18 provides the Nagelkerke R-squared values of ten injury predictors based on seven experimental behavioural response measures for the brain regions associated with emotionality.

Table 3.18: Nagelkerke R-squared values for the brain regions associated with emotionality.

Injury predictor	Unconscious time	EPM distance travelled	EPM arm changes	EPM open duration	MWM session I latency	MWM session II latency	MWM session III latency
Max. axonal strain	0.211	0.002	0.043	0.000	0.105	0.000	0.048
Max. strain energy	0.201	0.002	0.040	0.001	0.122	0.000	0.058
Max. von Mises stress	0.241	0.002	0.044	0.001	0.112	0.001	0.047
Max. von Mises strain	0.229	0.002	0.045	0.001	0.112	0.000	0.051
Max. shear stress	0.233	0.001	0.043	0.001	0.125	0.001	0.052
Max. shear strain	0.230	0.002	0.045	0.001	0.112	0.000	0.050
Max. principal stress	0.213	0.002	0.045	0.001	0.091	0.001	0.041
Max. principal strain	0.225	0.002	0.044	0.001	0.106	0.001	0.050
Min. pressure	0.214	0.002	0.045	0.001	0.090	0.001	0.042
Max. pressure	**0.261**	0.003	0.076	0.000	0.096	0.007	0.040

It can be observed that the Nagelkerke R-squared values for all the possible combinations are pretty low. Relatively, the best correlation is found with unconsciousness time. The R-squared value of maximum pressure to predict concussion in 0.261 and is the highest. The second highest R-squared value is of von Mises stress and is equal to 0.241. The R-squared value of axonal strain is 0.211 only.

The injury risk curve (Table 3.20) for brain regions associated with emotionality indicates that based on unconscious time, for a 50% probability of concussion, the tolerance level is 11.82% of axonal strain.

Table 3.19 provides the Nagelkerke R-squared values of ten injury predictors based on seven experimental behavioural response measures for the brain regions associated with cognition.

Table 3.19: Nagelkerke R-squared values for the brain regions associated with cognition.

Injury predictor	Unconscious time	EPM distance travelled	EPM arm changes	EPM open duration	MWM session I latency	MWM session II latency	MWM session III latency
Max. axonal strain	0.213	0.002	0.044	0.000	0.106	0.000	0.049
Max. strain energy	0.201	0.002	0.040	0.001	0.122	0.000	0.058
Max. von Mises stress	0.227	0.002	0.053	0.001	0.115	0.002	0.060
Max. von Mises strain	0.233	0.002	0.046	0.001	0.109	0.001	0.052
Max. shear stress	0.235	0.002	0.055	0.001	0.105	0.001	0.050
Max. shear strain	0.234	0.002	0.045	0.001	0.109	0.001	0.052
Max. principal stress	0.213	0.002	0.045	0.001	0.091	0.001	0.041
Max. principal strain	0.224	0.002	0.048	0.001	0.110	0.001	0.053
Min. pressure	0.214	0.002	0.045	0.001	0.090	0.001	0.042
Max. pressure	**0.261**	0.003	0.076	0.000	0.096	0.007	0.040

It can be observed that the Nagelkerke R-squared values for all the possible combinations are pretty low. Relatively, the best correlation is found with unconsciousness time. The R-squared value of maximum pressure to predict concussion in 0.261 and is the highest. The second highest R-squared value is of shear stress and is equal to 0.235. The R-squared value of axonal strain and von Mises stress are only 0.213 and 0.233 respectively. The injury risk curve (Table 3.20) for brain regions associated with cognition indicates that based on unconscious time, for a 50% probability of concussion, the tolerance level is 11.82% of axonal strain.

The Nagelkerke R-squared values for functional brain regions are in the same range as that for the entire brain, which are very low and hence, not significant. Thus, the injury risk curves for functional brain regions for all ten computed mechanical parameter are not provided. However, injury risk curves for the functional brain regions to predict concussion in terms of maximum axonal strain with regard to the unconsciousness time are given below in Table 3.20.

Table 3.20: Injury risk curves for functional brain regions to predict probability of concussion with regard to unconsciousness time in terms of maximum axonal strain (MAS) (hollow green circles represent non-injured cases and solid red circles represent injured cases).

For regions associated with consciousness

For a 50% risk of concussion: MAS = 0.1180

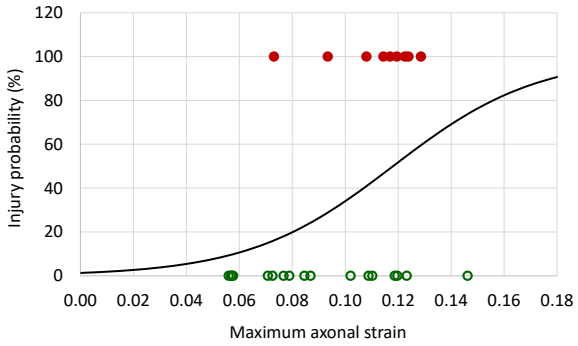

For regions associated with activity

For a 50% risk of concussion: MAS = 0.1182

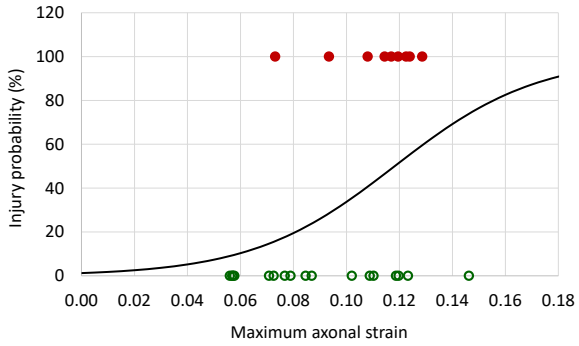

For regions associated with emotionality

For a 50% risk of concussion: MAS = 0.1182

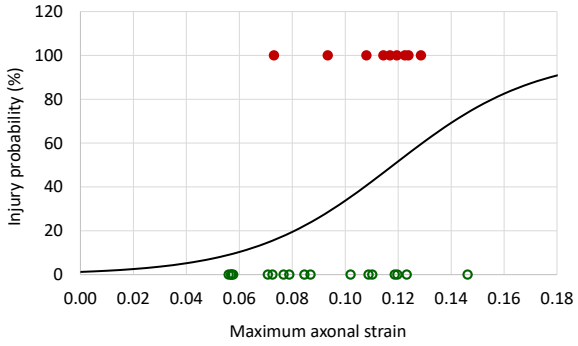

For regions associated with cognition

For a 50% risk of concussion: MAS = 0.1182

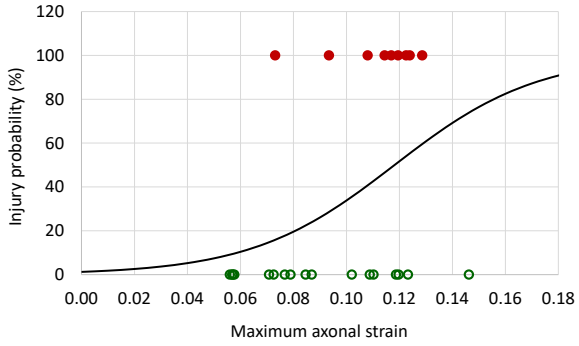

5.3 Based on binary logistic regression for Hosmer-Lemeshow p-value

The Hosmer-Lemeshow test was conducted and the p-values were identified to see the goodness of fit of the logistic regression. This test checks if the observed event rates in the sub-groups of model population correspond to the expected event rates. This test specifically identifies sub-groups as deciles of fitted risk values. Probability values or p-values are calculated based on chi-square distribution, in order to test the fit of logistic model (Hosmer and Lemeshow, 1980). A p-value in the range 0.7 to 0.8 indicates acceptable discrimination, in the range 0.8 to 0.9 indicates excellent discrimination and greater than 0.9 indicates outstanding discrimination. Table 3.21 provides the HL p-values of all twelve injury predictors based on seven experimental behavioural response measures for the entire brain.

Table 3.21: HL p-values for the entire brain.

Injury predictor	Unconscious time	EPM distance travelled	EPM arm changes	EPM open duration	MWM session I latency	MWM session II latency	MWM session III latency
Max. rotational acceleration	0.318	0.488	0.218	0.936	0.800	0.586	0.314
Duration	0.257	0.679	0.250	0.406	0.254	0.099	0.485
Max. axonal strain	0.906	0.956	0.736	0.345	0.619	0.008	0.432
Max. strain energy	0.893	0.955	0.725	0.348	0.629	0.192	0.440
Max. von Mises stress	0.869	0.513	0.200	0.304	0.348	0.338	0.536
Max. von Mises strain	0.939	0.954	0.719	0.926	0.621	0.092	0.429
Max. shear stress	0.649	0.760	0.407	0.247	0.357	0.296	0.338
Max. shear strain	0.939	0.954	0.720	0.925	0.621	0.092	0.429
Max. principal stress	0.532	0.955	0.728	0.347	0.609	0.065	0.442
Max. principal strain	0.927	0.964	0.695	0.925	0.651	0.093	0.547
Min. pressure	0.532	0.955	0.729	0.347	0.608	0.065	0.443
Max. pressure	0.941	0.960	0.774	0.632	0.705	0.469	0.543

It can be observed that the HL p-values in association with unconsciousness time, EPM distance travelled and EPM open duration show good discrimination. Table 3.22 provides the HL p-values of ten injury predictors based on seven experimental behavioural response measures for the brain regions associated with consciousness.

Table 3.22: HL p-values for the brain regions associated with consciousness.

Injury predictor	Unconscious time	EPM distance travelled	EPM arm changes	EPM open duration	MWM session I latency	MWM session II latency	MWM session III latency
Max. axonal strain	0.839	0.650	0.291	0.085	0.405	0.065	0.515
Max. strain energy	0.893	0.955	0.725	0.348	0.629	0.192	0.440
Max. von Mises stress	0.647	0.759	0.404	0.248	0.360	0.297	0.340
Max. von Mises strain	0.946	0.949	0.725	0.925	0.624	0.097	0.436
Max. shear stress	0.649	0.760	0.407	0.247	0.357	0.296	0.338
Max. shear strain	0.946	0.949	0.726	0.925	0.624	0.097	0.436
Max. principal stress	0.532	0.955	0.728	0.347	0.609	0.065	0.442
Max. principal strain	0.802	0.650	0.297	0.412	0.400	0.482	0.524
Min. pressure	0.532	0.955	0.729	0.347	0.608	0.065	0.443

Injury predictor	Unconscious time	EPM distance travelled	EPM arm changes	EPM open duration	MWM session I latency	MWM session II latency	MWM session III latency
Max. pressure	0.941	0.960	0.774	0.632	0.705	0.469	0.543

It can be observed that the HL p-values in association with unconsciousness time, EPM distance travelled and EPM open duration show good discrimination for brain regions associated with consciousness. Table 3.23 provides the HL p-values of ten injury predictors based on seven experimental behavioural response measures for the brain regions associated with activity.

Table 3.23: HL p-values for the brain regions associated with activity.

Injury predictor	Unconscious time	EPM distance travelled	EPM arm changes	EPM open duration	MWM session I latency	MWM session II latency	MWM session III latency
Max. axonal strain	0.906	0.956	0.736	0.345	0.619	0.008	0.432
Max. strain energy	0.893	0.955	0.725	0.348	0.629	0.192	0.440
Max. von Mises stress	0.848	0.650	0.298	0.608	0.398	0.348	0.516
Max. von Mises strain	0.942	0.955	0.721	0.346	0.613	0.008	0.434
Max. shear stress	0.814	0.703	0.355	0.248	0.663	0.385	0.396
Max. shear strain	0.943	0.955	0.722	0.346	0.611	0.008	0.434
Max. principal stress	0.532	0.955	0.728	0.347	0.609	0.065	0.442
Max. principal strain	0.940	0.954	0.718	0.345	0.616	0.008	0.438
Min. pressure	0.532	0.955	0.729	0.347	0.608	0.065	0.443
Max. pressure	0.941	0.960	0.774	0.632	0.705	0.469	0.543

It can be observed that the HL p-values in association with unconsciousness time and EPM distance travelled show good discrimination for brain regions associated with consciousness. Table 3.24 provides the HL p-values of ten injury predictors based on seven experimental behavioural response measures for the brain regions associated with emotionality.

Table 3.24: HL p-values for the brain regions associated with emotionality.

Injury predictor	Unconscious time	EPM distance travelled	EPM arm changes	EPM open duration	MWM session I latency	MWM session II latency	MWM session III latency
Max. axonal strain	0.906	0.956	0.736	0.345	0.619	0.008	0.432
Max. strain energy	0.893	0.955	0.725	0.348	0.629	0.192	0.440

Injury predictor	Unconscious time	EPM distance travelled	EPM arm changes	EPM open duration	MWM session I latency	MWM session II latency	MWM session III latency
Max. von Mises stress	0.647	0.759	0.404	0.248	0.360	0.297	0.340
Max. von Mises strain	0.939	0.954	0.719	0.926	0.621	0.092	0.429
Max. shear stress	0.649	0.760	0.407	0.247	0.357	0.296	0.338
Max. shear strain	0.939	0.954	0.720	0.925	0.621	0.092	0.429
Max. principal stress	0.532	0.955	0.728	0.347	0.609	0.065	0.442
Max. principal strain	0.927	0.964	0.695	0.925	0.651	0.093	0.546
Min. pressure	0.532	0.955	0.729	0.347	0.608	0.065	0.443
Max. pressure	0.941	0.960	0.774	0.632	0.705	0.469	0.543

It can be observed that the HL p-values in association with unconsciousness time, EPM distance travelled and EPM open duration show good discrimination for brain regions associated with emotionality. Table 3.25 provides the HL p-values of ten injury predictors based on seven experimental behavioural response measures for the brain regions associated with cognition.

Table 3.25: HL p-values for the brain regions associated with cognition.

Injury predictor	Unconscious time	EPM distance travelled	EPM arm changes	EPM open duration	MWM session I latency	MWM session II latency	MWM session III latency
Max. axonal strain	0.908	0.956	0.738	0.345	0.620	0.065	0.433
Max. strain energy	0.893	0.955	0.725	0.348	0.629	0.192	0.440
Max. von Mises stress	0.851	0.650	0.300	0.608	0.400	0.350	0.518
Max. von Mises strain	0.945	0.950	0.726	0.346	0.620	0.065	0.440
Max. shear stress	0.792	0.474	0.196	0.248	0.299	0.387	0.425
Max. shear strain	0.945	0.951	0.726	0.346	0.618	0.065	0.440
Max. principal stress	0.532	0.955	0.728	0.347	0.609	0.065	0.442
Max. principal strain	0.809	0.650	0.294	0.345	0.406	0.065	0.520
Min. pressure	0.532	0.955	0.729	0.347	0.608	0.065	0.443
Max. pressure	0.941	0.960	0.774	0.632	0.705	0.469	0.543

It can be observed that the HL p-values in association with unconsciousness time and EPM distance travelled show good discrimination for brain regions associated with cognition.

In comparison to Nagelkerke's R squared value assessment, it can be observed that in addition to unconsciousness time, EPM distance travelled seems to be a significant measure as well. For a very few computed mechanical parameters, EPM open duration also demonstrates significant discrimination. Let us look at AUROC statistics in the following section.

5.4 Based on receiver operating characteristic curves

Receiver operating characteristic (ROC) curves were plotted for different candidate parameters in association with experimental behavioural response measures in order to predict the occurrence of concussion. The diagnostic capability of a binary classifier (in this study, injured as 1 and non-injured as 0) with the variation in its threshold value is illustrated by the ROC curve. A ROC curve is created by plotting the sensitivity i.e. true positive rate against 1 – specificity i.e. false positive rate in order to predict a dichotomous outcome. Another measure to test performance is area under ROC curve (AUROC). When, sensitivity is equal to one and specificity is equal to zero, the AUROC value is 1 and the test is 100% accurate. Whereas, a test, which is not able to discriminate between normal and abnormal, results in a diagonal line from (0, 0) to (1, 1) and for this AUROC is equal to 0.5. Hence, the metric corresponding to AUROC equals to one is supposed to be the best suitable predictor for concussion. Table 3.26 provides the AUROC values of different injury predictors based on seven experimental behavioural response measures for the entire brain.

Table 3.26: AUROC values for the entire brain.

Injury predictor	Unconscious time	EPM distance travelled	EPM arm changes	EPM open duration	MWM session I latency	MWM session II latency	MWM session III latency
Max. rotational acceleration	0.650	0.400	0.445	0.438	0.823	0.496	0.652
Duration	0.588	0.521	0.636	0.476	0.688	0.541	0.493
Max. axonal strain	0.745	0.509	0.570	0.476	0.729	0.436	0.681
Max. strain energy	0.758	0.509	0.570	0.464	0.729	0.444	0.696
Max. von Mises stress	0.758	0.491	0.558	0.470	0.729	0.455	0.681
Max. von Mises strain	0.765	0.509	0.570	0.470	0.729	0.451	0.681
Max. shear stress	0.745	0.497	0.564	0.476	0.729	0.451	0.681
Max. shear strain	0.765	0.509	0.570	0.470	0.729	0.451	0.681
Max. principal stress	0.745	0.497	0.558	0.476	0.729	0.451	0.681
Max. principal strain	0.765	0.503	0.564	0.470	0.729	0.451	0.681
Min. pressure	0.255	0.503	0.442	0.524	0.271	0.549	0.319
Max. pressure	0.719	0.509	0.570	0.512	0.667	0.451	0.638

It can be observed that for the entire brain, AUROC is significant only in association with unconsciousness time and MWM session I latency. Based on this statistical analysis, ROC curves to predict concussion with regard to the unconsciousness time are given below in Table 3.27.

Table 3.27: ROC curves for the entire brain to predict probability of concussion with regard to unconsciousness time in terms of different injury predictors.

Maximum axonal strain

AUROC = 0.745

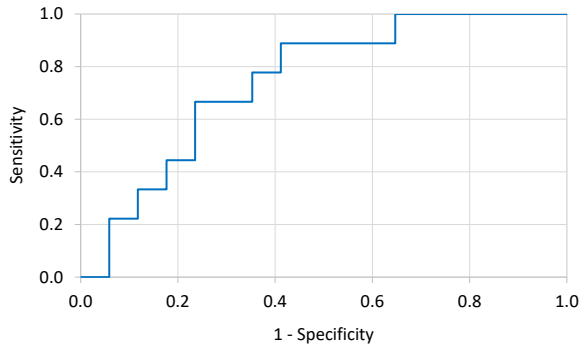

Maximum strain energy

AURCO = 0.758

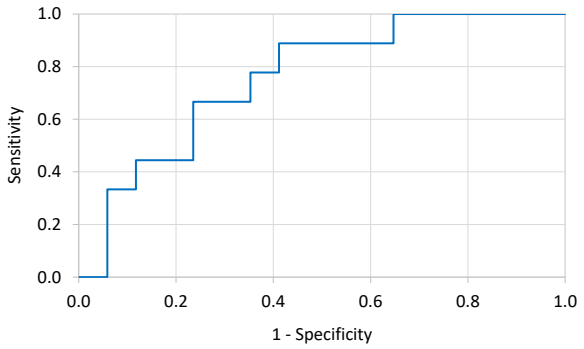

Maximum von Mises stress

AUROC = 0.758

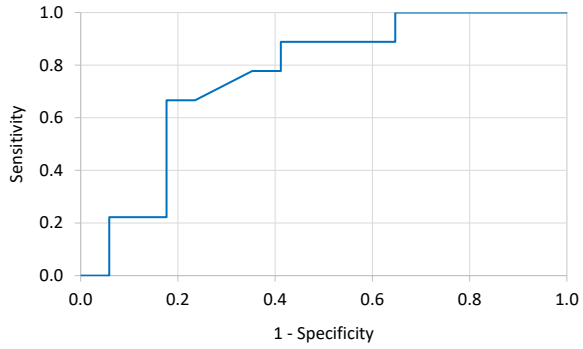

Maximum von Mises strain

AUROC = 0.765

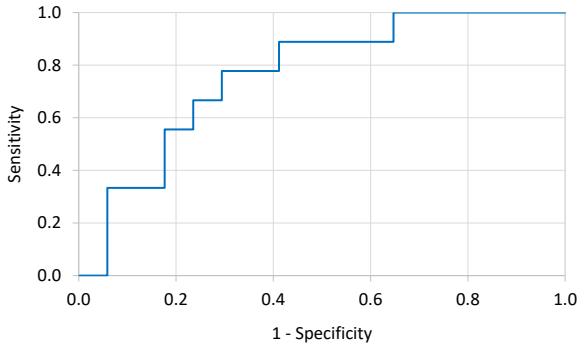

Maximum shear stress

AUROC = 0.745

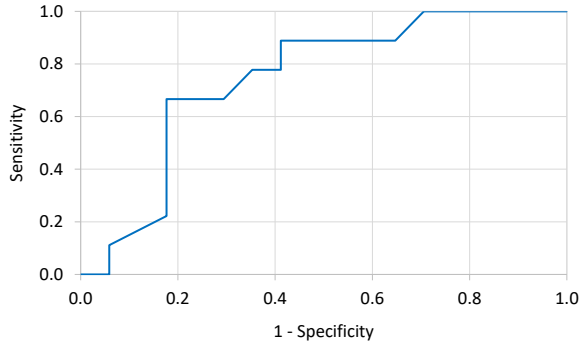

Maximum shear strain

AUROC = 0.765

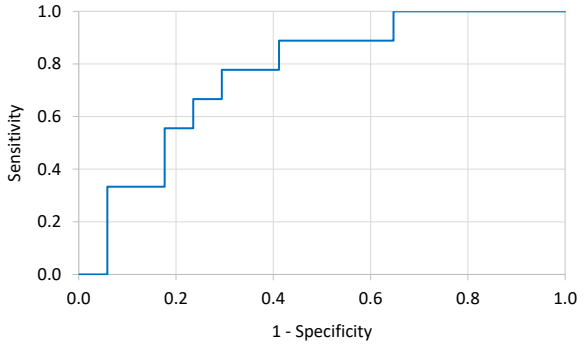

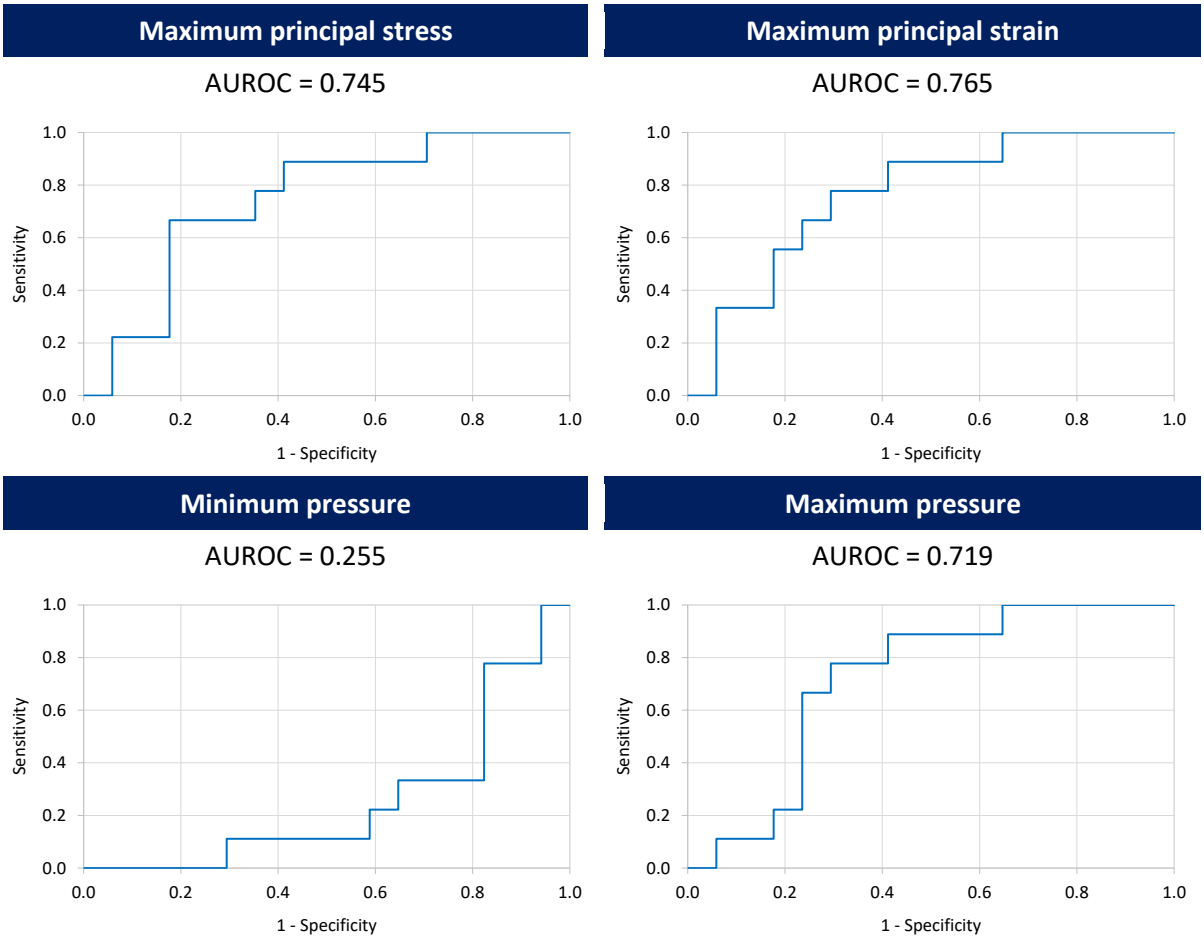

These ROC curves indicate that based on unconscious time, the AUROC values are 0.745 for axonal strain, 0.758 for strain energy, 0.758 for von Mises stress, 0.765 for von Mises strain, 0.745 for shear stress, 0.765 for shear strain, 0.745 for principal stress, 0.765 for principal strain, 0.255 for minimum pressure and 0.719 for maximum pressure. Table 3.28 provides the AUROC values of ten injury predictors based on seven experimental behavioural response measures for the brain regions associated with consciousness.

Table 3.28: AUROC values for the brain regions associated with consciousness.

Injury predictor	Unconscious time	EPM distance travelled	EPM arm changes	EPM open duration	MWM session I latency	MWM session II latency	MWM session III latency
Max. axonal strain	0.745	0.497	0.570	0.464	0.729	0.447	0.681
Max. strain energy	0.758	0.509	0.570	0.464	0.729	0.444	0.696
Max. von Mises stress	0.752	0.497	0.564	0.476	0.729	0.455	0.681
Max. von Mises strain	0.765	0.503	0.570	0.464	0.729	0.451	0.681
Max. shear stress	0.745	0.497	0.564	0.476	0.729	0.451	0.681
Max. shear strain	0.765	0.503	0.570	0.464	0.729	0.451	0.681

Injury predictor	Unconscious time	EPM distance travelled	EPM arm changes	EPM open duration	MWM session I latency	MWM session II latency	MWM session III latency
Max. principal stress	0.745	0.497	0.558	0.476	0.729	0.451	0.681
Max. principal strain	0.765	0.491	0.564	0.458	0.729	0.462	0.681
Min. pressure	0.255	0.503	0.442	0.524	0.271	0.549	0.319
Max. pressure	0.719	0.509	0.570	0.512	0.667	0.451	0.638

It can be observed that for the brain regions associated with consciousness, AUROC is significant only in association with unconsciousness time and MWM session I latency. Table 3.29 provides the AUROC values of ten injury predictors based on seven experimental behavioural response measures for the brain regions associated with activity.

Table 3.29: AUROC values for the brain regions associated with activity.

Injury predictor	Unconscious time	EPM distance travelled	EPM arm changes	EPM open duration	MWM session I latency	MWM session II latency	MWM session III latency
Max. axonal strain	0.745	0.509	0.570	0.476	0.729	0.436	0.681
Max. strain energy	0.758	0.509	0.570	0.464	0.729	0.444	0.696
Max. von Mises stress	0.745	0.503	0.570	0.470	0.729	0.444	0.688
Max. von Mises strain	0.752	0.503	0.564	0.470	0.729	0.444	0.681
Max. shear stress	0.758	0.518	0.579	0.482	0.729	0.459	0.674
Max. shear strain	0.752	0.503	0.564	0.470	0.729	0.444	0.681
Max. principal stress	0.745	0.497	0.558	0.476	0.729	0.451	0.681
Max. principal strain	0.752	0.503	0.564	0.470	0.729	0.444	0.681
Min. pressure	0.255	0.503	0.442	0.524	0.271	0.549	0.319
Max. pressure	0.719	0.509	0.570	0.512	0.667	0.451	0.638

It can be observed that for the brain regions associated with activity, AUROC is significant only in association with unconsciousness time and MWM session I latency. Table 3.30 provides the AUROC values of ten injury predictors based on seven experimental behavioural response measures for the brain regions associated with emotionality.

Table 3.30: AUROC values for the brain regions associated with emotionality.

Injury predictor	Unconscious time	EPM distance travelled	EPM arm changes	EPM open duration	MWM session I latency	MWM session II latency	MWM session III latency
Max. axonal strain	0.745	0.509	0.570	0.476	0.729	0.436	0.681
Max. strain energy	0.758	0.509	0.570	0.464	0.729	0.444	0.696
Max. von Mises stress	0.752	0.497	0.564	0.476	0.729	0.455	0.681
Max. von Mises strain	0.765	0.509	0.570	0.470	0.729	0.451	0.681
Max. shear stress	0.745	0.497	0.564	0.476	0.729	0.451	0.681
Max. shear strain	0.765	0.509	0.570	0.470	0.729	0.451	0.681
Max. principal stress	0.745	0.497	0.558	0.476	0.729	0.451	0.681
Max. principal strain	0.765	0.503	0.564	0.470	0.729	0.451	0.681
Min. pressure	0.255	0.503	0.442	0.524	0.271	0.549	0.319
Max. pressure	0.719	0.509	0.570	0.512	0.667	0.451	0.638

It can be observed that for the brain regions associated with emotionality, AUROC is significant only in association with unconsciousness time and MWM session I latency. Table 3.31 provides the AUROC values of ten injury predictors based on seven experimental behavioural response measures for the brain regions associated with cognition.

Table 3.31: AUROC values for the brain regions associated with cognition.

Injury predictor	Unconscious time	EPM distance travelled	EPM arm changes	EPM open duration	MWM session I latency	MWM session II latency	MWM session III latency
Max. axonal strain	0.745	0.509	0.570	0.476	0.729	0.444	0.681
Max. strain energy	0.758	0.509	0.570	0.464	0.729	0.444	0.696
Max. von Mises stress	0.745	0.503	0.570	0.470	0.729	0.444	0.688
Max. von Mises strain	0.758	0.497	0.564	0.458	0.729	0.459	0.681
Max. shear stress	0.758	0.506	0.573	0.470	0.729	0.459	0.674
Max. shear strain	0.758	0.497	0.564	0.458	0.729	0.459	0.681
Max. principal stress	0.745	0.497	0.558	0.476	0.729	0.451	0.681
Max. principal strain	0.758	0.500	0.564	0.461	0.729	0.455	0.681
Min. pressure	0.255	0.503	0.442	0.524	0.271	0.549	0.319
Max. pressure	0.719	0.509	0.570	0.512	0.667	0.451	0.638

It can be observed that for the brain regions associated with cognition, AUROC is significant only in association with unconsciousness time and MWM session I latency.

In comparison to Nagelkerke's R squared value assessment, it can be observed that in addition to unconsciousness time, MWM session I latency seems to be a significant measure as well.

5.5 Conclusion

This section presented the statistical analysis of simulation results based on experimental behavioural response measures in order to identify the best suitable parameter to predict concussion. Table 3.32 provides a synthesis of this analysis for the entire brain in association with one of the experimental behavioural response measure i.e. unconsciousness time.

Table 3.32: Comparison of results of logistic regression for different mechanical parameters calculated from twenty-six rotational loading simulations to predict concussion (for entire brain and based on unconsciousness time).

Injury predictor	Estimated tolerance level for 50% risk of concussion	Nagelkerke R-squared value	HL p-value	AUROC
Max. axonal strain	0.1182	0.211	0.906	0.745
Max. strain energy	6.77E-5 mJ	0.201	0.893	0.758
Max. von Mises stress	7.4 kPa	0.247	0.869	0.758
Max. von Mises strain	0.1443	0.229	0.939	0.765
Max. shear stress	4.2 kPa	0.233	0.649	0.745
Max. shear strain	0.1244	0.230	0.939	0.765
Max. principal stress	349.6 kPa	0.213	0.532	0.745
Max. principal strain	0.1421	0.225	0.927	0.765
Min. pressure	-348 kPa	0.214	0.532	0.255
Max. pressure	372.7 kPa	0.261	0.941	0.719

Sahoo et al. (2016) also derived brain injury tolerance limits based on the computation of axonal strain. However, their study was based on human brain and SUFEHM (Strasbourg University Finite Element Head Model) was utilized to reconstruct 109 TBI (traumatic brain injury) cases for this purpose. From the results of their statistical analysis, it was absolutely clear that axonal strain is the best injury predictor for DAI (diffuse axonal injury) among various selected parameters. The present study does not see such a clear distinction in the results. Out of seven experimental behavioural response

measures only unconsciousness time seems to be significant relatively. However, the Nagelkerke R-squared values for unconsciousness time also are pretty low in general. Although, HL p-value and AUROC do provide additional insight, yet, none of the injury predictor can be said to correlate well certainly. This might be because the number of cases simulated were very low and were not identical. As stated earlier, these cases can be divided into four major loading groups and based on the magnitude and duration of applied rotational acceleration, the severity of injury would have been different for each case, which further reduces the number of cases evaluated per loading group. Another important factor is the choice of binary classifier. We divided the cases into injured and non-injured groups based on the sham value of experimental behavioural response measure. As per this hypothesis, case with a response value lower than that of sham was considered as non-injured and vice versa. Nevertheless, this classification may not be appropriate for concussion. Concussion is a mild kind of traumatic brain injury and results in functional disturbances. An increase in the response value in comparison to sham is a change in behaviour post-injury, so is the decrease in the response value. Hence, another binary classifier may be required to suitably differentiate between the injured and non-injured groups to be able to identify the best injury predictor for concussion with certainty.

6 Benefit of an anisotropic finite element rat brain model

Anisotropic finite element rat brain model developed in this study prevails among other existing models. It was with this model that we were able to identify axonal strains per brain region. Table 3.33 provides the details about maximum axonal strain (MAS) experienced by every brain region among all twenty-six cases as well as the average MAS along with the standard deviation. Among all the cases and all the brain regions maximum axonal strain of 14.62% experienced by neocortex was the highest. Average MAS experienced by neocortex was 9.54% ± 2.89%.

Table 3.33: Details about regional maximum axonal strain among all twenty-six cases.

#	Brain region	Maximum axonal strain	Average maximum axonal strain
1	Hippocampus	0.0872	0.0631 ± 0.0173
2	External capsule	0.0970	0.0696 ± 0.0188
3	Caudate - Putamen - Globus pallidus	0.1083	0.0783 ± 0.0195
4	Anterior commissure	0.0857	0.0625 ± 0.0174
5	Substantia nigra	0.0842	0.0613 ± 0.0174
6	Internal capsule	0.0829	0.0601 ± 0.0165
7	Thalamus	0.1067	0.0747 ± 0.0191
8	Cerebellum	0.1052	0.0765 ± 0.0219

#	Brain region	Maximum axonal strain	Average maximum axonal strain
9	Superior colliculus	0.0610	0.0461 ± 0.0100
10	Hypothalamus	0.1213	0.0823 ± 0.0238
11	Inferior colliculus	0.0796	0.0576 ± 0.0155
12	Central gray	0.1084	0.0789 ± 0.0188
13	Neocortex	**0.1462**	0.0954 ± 0.0289
14	Amygdala	0.0871	0.0642 ± 0.0180
15	Olfactory bulb	0.0474	0.0345 ± 0.0091
16	Brainstem	0.1123	0.0797 ± 0.0214
17	Fimbria	0.1059	0.0762 ± 0.0178
18	Fornix	0.0935	0.0684 ± 0.0157
19	Ventral tegmental area (VTA)	0.0958	0.0654 ± 0.0197
20	Corpus callosum	0.0692	0.0491 ± 0.0120
21	Genu	0.0699	0.0499 ± 0.0129
22	Aqueduct	0.0907	0.0642 ± 0.0160
23	Splenium	0.0658	0.0482 ± 0.0120
24	Rest of the brain	0.0936	0.0681 ± 0.0166

As can be observed from Table 3.33, brain regions, which experienced high axonal strain are neocortex, hypothalamus, brainstem, central gray, caudate-putamen-globus pallidus, fimbria, cerebellum and thalamus. Figure 3.11 illustrates the cumulative top hundred elements of twenty-six cases that experienced highest maximum axonal strain (232 elements in total).

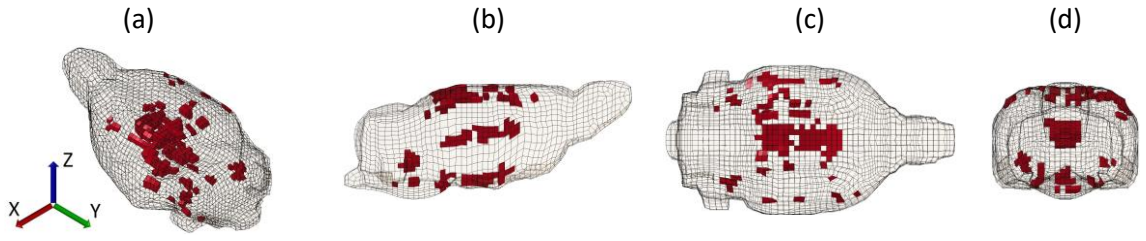

Figure 3.11: Diagram illustrating cumulative top hundred elements of twenty-six cases that experienced the highest maximum axonal strain; (a) isometric view, (b) sagittal view, (c) axial view and (d) coronal view of the rat brain.

Location of the highest strain elements is within the brain regions, which some way or the other influence the behavioural response and this in turn in accordance with the experimental results, as changes in behavioural response were evident in the experimental results. Knowledge of axonal strain

and the regions experiencing high axonal strain can help is concussion related investigations as diffuse axonal injury is one of the most prominent characteristic of traumatic brain injury. Nonetheless, extensive real world accidental data or experimental data is required to be able to come to any definite conclusions.

7 Conclusion

This chapter presented simulations of concussion related experiments. Total twenty-six experimental cases were simulated with the developed anisotropic viscous hyperelastic finite element rat brain model. In the beginning of the chapter, details about the experimental approach and the experimental results were given. As a part of the experimentation, rotational acceleration loading of the rat head was supposed to induce concussion. Post injury behavioural response of animals was measured through seven parameters, which are unconsciousness time, EPM distance travelled, EPM arm changes, EPM open duration (through elevated plus maze assessment) and latency in MWM session I, II and III (through Morris water maze assessment). A comparison of rotational loading acceleration characteristics with these seven experimental behavioural response measures did not bring out any relation among them. Afterwards, information related to simulations was provided, which was followed by the simulation results. With regard to simulation results, total ten mechanical parameters were extracted, which are maximum axonal strain, maximum strain energy, maximum von Mises stress and strain, maximum shear stress and strain, maximum principal stress and strain and minimum and maximum pressures. Simulation results were assessed for entire brain as well as for functional and anatomical brain regions. Basic assessment of results was based on two assumptions. First assumption was that the twenty-six cases can be divided into four loading groups (and further seven subgroups) based on the characteristics of the applied rotational acceleration. Second assumption was based on sham's experimental behavioural response. Twenty-six cases were divided into injured and non-injured groups based on the experimental results of sham animal. It was hoped that this categorization would help in better identify brain tolerance limits. However, analysis of results based on these two assumptions was not very fruitful. As none of the mechanical parameters was found to be in strong link with any of the experimental behavioural response measure. Hence, in the end, statistical analysis was carried out to see the significance of these simulation results in association with the experimental results and to find out the most suitable mechanical parameter to predict concussion. Binary logistic regression was employed to analyze the data in terms of Nagelkerke R-squared statistics, Hosmer-Lemeshow p-value statistics and receiver operating characteristic curve statistics. It was found that the overall Nagelkerke R-squared values were very low. Relatively, the only experimental behavioural response measure that could correlate with the simulation data was

unconsciousness time with a MAS value of 11.8% for a 50% risk of concussion. Overall, no candidate parameter was able to predict concussion expeditiously. Based on studies available in literature, at least axonal strain should have been evident to predict concussion. But, that was not strongly demonstrated in this study. One of the possibility is that the number of cases simulated were too low to be able to reveal anything in this regard. Secondly, a parameter other than selected ten parameters may be a suitable candidate to predict concussion.

Although the results of statistical analysis did not show any interesting correlation, yet the importance of anisotropic viscous hyperelastic finite element rat brain model prevails. It was with this model that we were able to identify the most vulnerable brain regions and their tolerance levels for concussion.

General conclusion and prospects

Concussion, in spite of being a *mild* traumatic brain injury, involves serious long term consequences and can adversely affect the life of an individual, their family and the society. Concussion is a neurological disturbance caused by a direct or indirect impulsive mechanical force to the head. These neurological disturbances result in functional impairments of the brain. As diffuse axonal injury (DAI) is found to be one of the most frequent pathological features of traumatic brain injury, knowledge of mechanical threshold to concussion in terms of axonal elongation can help in developing better brain injury prediction tools and in optimizing head protection systems. Computational models have proved to be efficient means for such studies. In comparison to experimentation, computational models are more accurate, economic and easier to use. Further, they do not involve any ethical concerns that are always present in case of experimentation on biological subjects. Still, experimental data is essential for the validation of a computational model. Unfeasibility of experimentation on human brain restricts the detailed investigation on concussion. However, small animals, such as rat, seemed to be an interesting opportunity for such investigations. The literary observations that an adult rat brain can be considered neurologically equivalent to an adult human brain and that at tissue level inter species brains respond similarly further support the significance of investigations through rat brain model. Hence, as a part of this doctoral thesis work, an anisotropic viscous hyperelastic finite element rat brain model was developed, validated and utilized for the investigation of mechanical threshold to concussion. This doctoral work contributes to the research on the development of better brain injury prediction tools and the optimization of head protection systems.

This study began with an extensive literature review about the anatomy of brain, potential injury mechanisms for concussion, brain injury - grading scales, criteria and tolerance levels, and the finite element rat brain modelling. A summary of this literature review is given below.

- Anatomy of brain, presented at macroscopic and microscopic level, clarified the similarities and differences between a human and a rat brain and got us familiarized with the inside of the brain.
- Potential concussion mechanisms highlighted the importance of axonal elongation quantification, since, the impairment of axonal cytoskeleton elements seemed to be the primary reason for the onset of concussion.
- An awareness about brain injury - grading scales, criteria and tolerance levels not only broadened our horizon with respect to different possibilities of assessing concussion, but also made us realize how differently concussion had been defined in various studies. Furthermore, we came to know that for the rat brain, tolerance limits for concussion, in terms of mechanical parameters, does not exist.

- The experimental data available in literature regarding rat brain material properties is very limited. Nevertheless, the rat brain material properties seemed to be in accordance with that of the human brain.
- Existing finite element rat brain models are isotropic and were developed to analyze moderate and severe traumatic brain injuries. They cannot be used for concussion related investigations without further modifications.
- Experimental data on brain deformation from Shreiber et al. (1997) and Antona-Makoshi et al. (2014) can be used for the validation of a finite element rat brain model.

Therefore, the restriction on in-depth investigations of the human brain and the incapability of existing finite element rat brain models in investigating concussion, made us realize the need for an anisotropic finite element rat brain model for the investigation of mechanical threshold to concussion in terms of axonal elongation.

For this purpose, an anisotropic viscous hyperelastic finite element rat brain model (FERBM) was developed. Summary of the model development methodology is given below.

- Adult Sprague Dawley rat, weighing approximately 290 g, was chosen as the basis for this study.
- A three-dimensional DTI (diffusion tensor imaging) atlas of the adult Sprague Dawley rat (weighing approximately 290 g) brain at postnatal day 72, developed by Rumple et al. (2013), was used to identify the geometry and the diffusion parameters of the rat brain.
- Based on the rat brain geometry rendered from the DTI atlas, the model was meshed using HyperMesh software. Meshed FERBM consisted of 13,236 solid hexahedral elements, with an average element size of 0.5 mm. The brain model was enwrapped within a layer of cerebrospinal fluid (CSF), modelled with 3,252 solid hexahedral elements, having an average thickness of 0.7 mm. The brain and the CSF model were further enclosed inside the skull, modeled with 3,252 quadrilateral shell elements.
- Two diffusion parameters – fractional anisotropy (FA) and principal fiber direction (PFD) were identified from the DTI atlas. Anisotropy of developed FERBM was achieved by implementing this DTI information into the model.
- The DTI atlas had the diffusion data stored for every voxel (the cubical subdivision (size: 0.125 mm) of the rat brain volume). Thus initially, FA and PFD values for every voxel of the rat brain were computed from the data stored in the DTI atlas.

- The FERBM was aligned with the DTI volume, so that both corresponds to the same location and orientation in space. Voxels falling inside every element of FERBM were identified next. Average number of voxels inside an element were equal to 68 ± 24.
- FA and PFD values for every element of the FERBM were estimated next. It was done by taking weighted average of FA and PFD values of all the voxels inside an element. The exponential weighting function was chosen in such a manner that the voxels near the center of the element had high influence than those at the element boundary. The FA value ranged from zero to 0.96 with a weighted average FA value equals to 0.31 ± 0.12.
- The entire process, i.e. computation of diffusion parameters for every voxel, alignment of FE model and DTI volume, identification of voxels per element and estimation of diffusion parameters per element was achieved through coding in a high-level programming language - Python. A comparison of identified diffusion parameters with that of the DTI atlas demonstrated a good agreement.
- A validated anisotropic viscous hyperelastic constitutive law for brain material developed by Chatelin et al. (2013) was found suitable for this study. This law hypothesized that the brain tissue consists of an isotropic matrix material with an anisotropic fiber reinforcement in the principal fiber direction. Furthermore, it was assumed that fibers have no influence in compression and in situation, where tension is applied orthogonally to the principal fiber direction. The matrix material took into account both the hyperelasticity and the viscosity. However, the fiber material was modelled only as hyperelastic due to the lack of experimental viscoelastic data on brain fibers.
- Brain material properties were incorporated into developed FERBM by means of *MAT_092 i.e. *MAT_SOFT_TISSUE_VISCO material model of LS-DYNA. This model included both viscous hyperelastic brain material properties and anisotropic diffusion parameters of the rat brain. Based on the literary evidences, it was hypothesized that at tissue level, the adult rat brain and the adult human brain are neurologically equivalent. Thus, the brain material properties used by Chatelin et al. (2013) for the adult human were adapted for the rat brain by including rat brain diffusion parameters.
- Since the anisotropic material property for every element of the FERBM differs, the incorporation of material properties into FERBM, along with the diffusion parameters, was achieved through coding in a high-level programming language - Python.

- CSF was modeled with *MAT_001 i.e. *MAT_ELASTIC_FLUID material model of LS-DYNA and the skull with *MAT_20 i.e. *MAT_RIGID. The skull was modelled as rigid to apply the loading on the brain in an appropriate manner, by assigning proper boundary conditions on the skull.
- Developed anisotropic viscous hyperelastic FERBM was validated against two experimentations available in literature. First validation was against experimental dynamic cortical displacement on the application of vacuum pressure pulse as per Shreiber et al. (1997). A total of six simulations were performed for different combinations of pressure magnitudes and pulse durations. Second validation was against experimental brain-skull relative displacement (BSRD) on the application of rotational acceleration loading in the sagittal plane as per Antona-Makoshi et al. (2014). One simulation was performed for the available rotational acceleration pulse.
- A parametric study revealed that the choice of brain material highly influences the brain response for a given loading condition. An isotropic general viscoelastic brain material law seemed to be more flexible than the anisotropic viscous hyperelastic brain material law. Also, the compressibility of the cerebrospinal fluid was found to influence the brain response significantly. Furthermore, the hourglass control type (IHQ) demonstrated a significant influence on both, the hourglass energy and the brain response; but not the hourglass coefficient (QH).

Thus, a validated anisotropic viscous hyperelastic finite element rat brain model was developed for the investigation of mechanical threshold to concussion.

Simulations of experimental concussion were performed to get insight into the rat brain. Summary of experiments chosen for simulations and the details of simulations, their results and the statistical analysis is given below.

- Data of twenty-six cases of experimental concussion was received from Medical College of Wisconsin (MCW), USA through collaboration. This data was a part of their published study - Stemper et al. (2016).
- The subject of experiments were adult Sprague Dawley rats (weighing approximately 290 g) and concussion was induced through rotational acceleration loading of the rat head in the coronal plane. For the twenty-six experimental cases, the average magnitude of peak rotational acceleration was 319.5 ± 85.5 krad/s^2 and the average duration was 1.9 ± 0.8 ms.
- Experimental acute injury severity was assessed through unconsciousness time. Elevated plus maze (EPM) assessment was used to analyze post-concussion changes in activity and emotionality. Morris water maze (MWM) assessment was used to analyze post-concussion changes in cognition capabilities. A total of seven experimental behavioural response measures were used to analyze

the post-concussion responses. These were unconsciousness time, EPM distance travelled, EPM arm changes, EPM open duration and the latencies in MWM session I, II and III.

- As experimental output, values of these seven experimental behavioural response measures were available for all twenty-six cases. Corresponding values for sham (control subject that did not go through rotational loading) were taken from Stemper et al. (2016).
- For the analysis of post-concussion response, based on the peak magnitude and the duration of the rotational acceleration, these twenty-six experimental cases were divided into four loading groups as in the publication, Stemper et al. (2016). These were low magnitude-short duration (M1D1) group, low magnitude-long duration (M1D2) group, high magnitude-short duration (M2D1) group and the high magnitude-long duration (M2D2) group. Average low magnitude M1 was equal to 224.2 ± 31.2 krad/s^2 and average high magnitude M2 was equal to 379.1 ± 45.2 krad/s^2. Average short duration D1 was equal to 1.5 ± 0.5 ms and average long duration D2 was equal to 3.2 ± 0.3 ms.
- Furthermore, for the analysis of post-concussion response with another perspective, based on the response value of sham, these twenty-six experimental cases were divided into two groups. Those, for which the experimental results were below the sham value, fall in the first group and were called non-injured cases and those for which the experimental results were above the sham value, fall in the second group and were called injured cases.
- Association of the acceleration characteristics with the experimental behavioural response measures was analyzed. No relation was found between the acceleration characteristics and the experimental behavioural response measures. Based on loading group wise association, cases having similar acceleration characteristics were found to have a wide variation in the values of experimental behavioural response measures. This variation was observed even with cases having dissimilar acceleration characteristics. This means, experimental outcome of low magnitude or short duration cases ranged from low to high and so did the experimental outcome of high magnitude or long duration cases. Moreover, based on the other classification, both injured and non-injured cases ranged from low magnitudes, short durations to high magnitudes, long durations with no significant difference between the overall amplitudes.
- A total of twenty-six simulations were performed corresponding to twenty-six experimental cases. Simulation results or the mechanical responses were extracted in terms of ten mechanical parameters. These parameters were maximum von Mises stress and strain, maximum principal stress and strain, maximum shear stress and strain, minimum and maximum pressures, strain energy and the strain tensor, to calculate the axonal strain.

- Based on the principal fiber direction (PFD) per element estimated earlier, axonal strain for every element of FERBM was calculated through Python programming. Hence, the maximum axonal strain (MAS) value was identified for every element of the FERBM.
- Globally, it was observed that for the cases belonging to high magnitude short duration group (M2D1), the amplitude of mechanical responses were the highest. This was followed by the cases belonging to high magnitude long duration group (M2D2) and then by the cases belonging to low magnitude long duration group (M1D2). The amplitude of mechanical responses of the cases belonging to low magnitude short duration group (M1D1) were the lowest.
- Computed mechanical parameters (maximum axonal strain, maximum strain energy, maximum von Mises stress and strain, maximum shear stress and strain, maximum principal stress and strain and minimum and maximum pressures) did not show any direct relation with the injury, in terms of experimental behavioural response measures. Cases having similar acceleration characteristics were found to have a wide variation in the values of experimental behavioural response measures. Besides, the mechanical response of both, injured and non-injured cases ranged from low to high and though the overall amplitudes of these responses for injured cases were sometimes slightly higher than that of non-injured cases, the differences were not significant. With regard to unconsciousness time, the average maximum axonal strain for non-injured group was 8.98% ± 2.69%. Whereas, the average maximum axonal strain for injured group was 11.11% ± 1.66%.
- A loading group wise comparison of maximum axonal strain showed that the brain regions experiencing the highest maximum axonal strain in all four loading groups (M1D1, M1D2, M2D1 and M2D2) are more or less the same. However, the highest values of maximum axonal strain differ, which is logical. For example, for the low magnitude short duration group, the maximum axonal strain values were around 7% only, whereas that for high magnitude short duration group were around 11% and even 14.6% for one of the cases.
- For further analyzing the simulation results on regional basis, FERBM was subdivided into anatomical and functional regions. Anatomical categorization divided the brain into twenty-four regions - hippocampus, external capsule, caudate – putamen – globus pallidus as one, anterior commissure, substantia nigra, internal capsule, thalamus, cerebellum, superior colliculus, hypothalamus, inferior colliculus, central gray, neocortex, amygdala, olfactory bulb, brainstem, fimbria, fornix, ventral tegmental area (VTA), corpus callosum, genu, aqueduct, splenium and rest of brain as one. Functional categorization was based on four behavioural aspects – consciousness, activity, emotionality and cognition. It was assumed that the consciousness is associated with thalamus, neocortex and brainstem; activity is associated with hippocampus, substantia nigra,

cerebellum, central gray and neocortex; emotionality is associated with hippocampus, central gray, neocortex, amygdala, brainstem, fimbria and fornix; and cognition is associated with hippocampus, substantia nigra, cerebellum, neocortex, fimbria and fornix. However, computed mechanical parameters demonstrated a similar trend for anatomical and functional brain regions as with the entire brain.

- An anatomical region wise comparison of maximum axonal strain showed that the main regions experiencing the highest maximum axonal strains were neocortex (MAS = 14.62%, average: 9.54% ± 2.89%), hypothalamus (MAS = 12.13%, average: 8.23% ± 2.38%), brainstem (MAS = 11.23%, average: 7.97% ± 2.14%), central gray (MAS = 10.84%, average: 7.89% ± 1.88%), caudate-putamen-globus pallidus (MAS = 10.83%, average: 7.83% ± 1.95%), thalamus (MAS = 10.67%, average: 7.47% ± 1.91%), fimbria (MAS = 10.59%, average: 7.62% ± 1.78%) and cerebellum (MAS = 10.52%, average: 7.65% ± 2.19%). All these regions are known to influence the behavioural response (consciousness, activity, emotionality and cognition capabilities) in some way or the other.
- Statistical analysis of simulation results was carried out by means of binary logistic regression, in terms of Nagelkerke R-squared statistics, Hosmer-Lemeshow (HL) p-value statistics and area under receiver operating characteristics (AUROC) statistics.
- None of the chosen mechanical parameter showed a strong correlation with experimental behavioural response measures. This might be because the number of cases simulated are quite low, since the experimental data was available only for twenty-six cases. Relatively, unconsciousness time fairly correlated with the mechanical responses.
- Based on unconsciousness time, for a 50% risk of concussion, the estimated tolerance level was found to be 11.82% of maximum axonal strain, with a Nagelkerke R-squared value of 0.211, HL p-value of 0.906 and AUROC equals to 0.745.
- Sahoo et al. (2016) reconstructed 109 TBI (traumatic brain injury) cases using SUFEHM (Strasbourg University Finite Element Head Model) to identify the brain injury tolerance limit in terms of axonal strain. For a 50% risk of DAI, the estimated tolerance level was found to be 14.65% of maximum axonal strain. Tolerance level for concussion identified in current study is in good proximity with the tolerance level for DAI identified by Sahoo et al. (2016).

This is the first time that an anisotropic finite element rat brain model is developed. It is because of this model that we could get insights into the rat brain in terms of axonal elongation, which was not possible with any of the existing finite element rat brain models. Identification of maximum axonal strains made it possible to identify those brain regions which were more vulnerable to concussion. Experimental results clearly indicated post-concussion changes in behavioural responses and the

simulation results seemed to be in link, since the brain regions identified to be vulnerable to concussion are known to influence the behaviour in some way or the other. Nevertheless, it would be interesting to get access to more experimental data, in order to clearly see a strong correlation and identify the best injury predictor and the tolerance level. Hence, this study is a first step towards concussion related investigations through finite element rat brain modelling.

An anisotropic viscous hyperelastic finite element rat brain model was developed, validated and utilized in order to get insights into the rat brain in case of concussion. Investigation of mechanical threshold to concussion demonstrated that for a 50% risk of concussion, the estimated tolerance level of maximum axonal strain is 11.82%. This result is in good proximity with the tolerance level estimated by Sahoo et al. (2016) with the human brain, which is 14.65% of axonal strain for a 50% risk of DAI. This study opens the door to many more possibilities regarding concussion related investigations.

In future, when the experimental rat brain material properties for individual anatomical brain regions will become available, it would be interesting to know how incorporation of this kind of heterogeneity influences the tolerance levels. In this case, even the mesh of the model can be refined to have distinct smooth boundaries between various anatomical regions, which will make model even more realistic.

Experimental results, available for the current study, were only behavioural responses. Accessibility to post-concussion histological data or medical imaging data will enable us to get better insights into the rat brain and will help in predicting concussion more accurately. In addition, more number of experimental cases will make it possible to carry out statistical analysis in a more robust manner and further, to identify best injury predictor and the tolerance level for concussion more efficiently.

Another interesting possibility is to investigate repetitive mild traumatic brain injuries (rmTBI) or multiple concussion. Recently, many studies have started focusing on rmTBI, since it is supposed that multiple concussion could be the primary reason behind long term consequences of concussion. In this regard, an anisotropic finite element rat brain model can be insightful for such studies.

References

Ahmadzadeh, H., Smith, D. H. and Shenoy, V. B. Viscoelasticity of Tau proteins leads to strain rate-dependent breaking of microtubules during axonal stretch injury: predictions from a mathematical model. Biophysical Journal, 2014, 106(4):1123-1133.

Antona-Makoshi, J., Davidsson, J., Ejima, S. and Ono, K. Development of a comprehensive injury criterion for moderate and mild traumatic brain injuries. International Journal of Automotive Engineering, 2016, 7(1):69-75.

Antona-Makoshi, J., Davidsson, J., Risling, M., Ejima, S. and Ono, K. Validation of local brain kinematics of a novel rat brain finite element model under rotational acceleration. International Journal of Automotive Engineering, 2014, 5(1):31-37.

Antona-Makoshi, J., Eliasson, E., Davidsson, J., Ejima, S. and Ono, K. Effect of ageing on brain injury prediction in rotational head trauma – a parameter study with a rat finite element model. Traffic Injury Prevention, 2015, 16:sup1, S91-S99.

Armstrong, R. C., Mierzwa, A. J., Marion, C. M. and Sullivan, G. M. White matter involvement after TBI: clues to axon and myelin repair capacity, Experimental Neurology, 2016a, 275(3):328-333.

Armstrong, R. C., Mierzwa, A. J., Sullivan, G. M. and Sanchez, M. A. Myelin and oligodendrocyte lineage cells in white matter pathology and plasticity after traumatic brain injury. Neuropharmacology, 2016b, 110(B):654-659.

Azevedo, F. A. C., Carvalho, L. R. B., Grinberg, L. T., Farfel, J. M., Ferretti, R. E. L., Leite, R. E. P., Filho, W. J., Lent, R. and Herculano-Houzel, S. Equal numbers of neuronal and nonneuronal cells make the human brain an isometrically scaled-up primate brain. The Journal of Comparative Neurology, 2009, 513(5):532-541.

Basser, P. J. and Pierpaoli, C. Microstructural and physiological features of tissues elucidated by quantitative-diffusion-tensor MRI. Journal of Magnetic Resonance, Series B, 1996, 111(3):209-219.

Basser, P. J., Mattiello, J. and LeBihan, D. MR diffusion tensor spectroscopy and imaging. Biophysical Journal, 1994, 66(1):259-267.

Baumgartner, D., Lamy, M., Willinger, R., Choquet, P., Goetz, C., Constantinesco, A. and Davidsson, J. Finite element analysis of traumatic brain injuries mechanisms in the rat. Proceedings of IRCOBI Conference, 2009, York, United Kingdom, 97-108.

Bayer, S. A., Altman, J., Russo, R. J. and Zhang, X. Timetables of Neurogenesis in the human brain based on experimentally determined patterns in the rat. NeuroToxicology, 1993, 14(1):83-144.

Bollen, A. and Bai, X. Effects of long-term calcium intake on body weight, body fat and bone in growing rats. Osteoporosis International, 2005, 16(12):1864-1870.

Briggs, D. I., Angoa-Perez, M. and Kuhn, D. M. Prolonged repetitive head trauma induces a singular chronic traumatic encephalopathy-like pathology in white matter despite transient behavioural abnormalities. The American Journal of Pathology, 2016, 186(11):2869-2886.

Broglio, S. P., Schnebel, B., Sosnoff, J. J., Shin, S., Feng, X., He, X. and Zimmerman, J. The biomechanical properties of concussions in high school football. Medicine and Science in Sports and Exercise, 2010, 42(11):2064-2071.

Budday, S., Ovaert, T. C., Holzapfel, G. A., Steinmann, P. and Kuhl, E. Fifty shades of brain: a review on the mechanical testing and modelling of brain tissue. Archives of Computational Methods in Engineering, 2019, https://doi.org/10.1007/s11831-019-09352-w.

Buki, A. and Povlishock, J. T. All roads lead to disconnection? – Traumatic axonal injury revisited. Acta Neurochirurgica, 2006, 148(2):181-194.

Cantu, R. C. Guidelines for return to contact sports after a cerebral concussion. The Physicians and Sportsmedicine, 1986, 14(10):75-83.

Cantu, R. C. Posttraumatic retrograde and anterograde amnesia: pathophysiology and implications in grading and safe return to play. Journal of Athletic Training, 2001, 36(3):244-248.

CDC, Centers for Disease Control and Prevention, Report to Congress on traumatic brain injury in the United States: epidemiology and rehabilitation. National Center for Injury Prevention and Control; Division of Unintentional Injury Prevention, 2014, Atlanta, GA.

Chang, K., Redmond, S. A and Chan, J. R. Remodeling myelination: implications for mechanisms of neural plasticity. Nature Neuroscience, 2016, 19(2):190-197.

Chatelin, S., Constantinesco, A. and Willinger, R. Fifty years of brain tissue mechanical testing: from in vitro to in vivo investigations. Biorheology, 2010, 47(5-6):255-276.

Chatelin, S., Deck, C. and Willinger, R. An anisotropic viscous hyperelastic constitutive law for brain material finite-element modeling. Journal of Biorheology, 2013, 27(1-2):26-37.

Chatelin, S., Deck, C., Renard, F., Kremer, S., Heinrich, C., Armspach, J. and Willinger, R. Computation of axonal elongation in head trauma finite element simulation. Journal of the Mechanical Behavior of Biomedical Materials, 2011, 4(8):1905-1919.

Christ, A. F., Franze, K., Gautier, H., Moshayedi, P., Fawcett, J., Franklin, R. J. M., Karadottir, R. T. and Guck, J. Mechanical difference between white and gray matter in the rat cerebellum measured by scanning force microscopy. Journal of Biomechanics, 2010, 43(15):2986-2992.

Colorado medical society - guidelines for the management of concussion in sports. Report of the Sports Medicine Committee, Denver, CO, 1990.

Conde C. and Caceres, A. Microtubule assembly, organization and dynamics in axons and dendrites. Nature review, Neuroscience, 2009, 10:319-332.

Coronado, V. G., Haileyesus, T., Cheng, T. A., Bell, J. M., Haarbauer-Krupa, J., Lionbarger, M. R., Flores-Harrera, J., McGuire, L. C. and Gilchrist, J. Trends in sports- and recreation- related traumatic brain injuries treated in US emergency departments: the national electronic injury surveillance system-all injury program (NEISS-AIP) 2001-2012. Journal of head trauma rehabilitation, 2015, 30(3):185-197.

Criscione, J. C., Douglas, A. S. and Hunter, W. C. Physically based strain invariant set for materials exhibiting transversely isotropic behavior. Journal of Mechanics and Physics of Solids, 2001, 49(4):871-897.

Davidsson, J. and Risling, M. A new model to produce sagittal plane rotational induced diffuse axonal injuries. Frontiers in Neurology, 2011, 2(41):58-68.

Davis, G. A., Purcell, L., Schneider, K. J., Yeates, K. O., Gioia, G. A., Anderson, V., Ellenbogen, R. G., Echemendia, R. J., Makdissi, M., Sills, A., Iverson, G. L., Dvorak, J., McCrory, P., Meeuwisse, W., Patricios, J, Giza, C. C. and Kutcher, J. S. The child sport concussion assessment tool 5th edition (Child SCAT5): background and rationale. British Journal of Sports Medicine, 2017a, 51(11):859-861.

Davis, G. A., Purcell, L., Schneider, K. J., Yeates, K. O., Gioia, G. A., Anderson, V., Ellenbogen, R. G., Echemendia, R. J., Makdissi, M., Sills, A., Iverson, G. L., Dvorak, J., McCrory, P., Meeuwisse, W., Patricios, J, Giza, C. C. and Kutcher, J. S. The child sport concussion assessment tool 5th edition (Child SCAT5): background and rationale. British Journal of Sports Medicine, 2017b, 51(11):862-869.

Deck, C. and Willinger, R. Head injury prediction tool for protective systems optimisation. Proceedings of 7th European LS-DYNA Conference, 2009.

Dewan, M. C., Rattani, A., Gupta, S., Baticulon, R. E., Hung, Y., Punchak, M., Agrawal, A., Adeleye, A. O., Shrime, M. G., Rubiano, A. M., Rosenfeld, J. V., and Park, K. B. Estimating the global incidence of traumatic brain injury. Journal of Neurosurgery, 2018, 130(4):1080-1097.

Duma, S. M. and Rowson, S. Chapter 7 – The biomechanics of concussion: 60 years of experimental research. In: Slobounov S., Sebastianelli W. (eds) Concussions in Athletics. Springer, New York, NY, 2014, 115-137.

Duma, S. M., Manoogian, S. J., Bussone, W. R., Brolinson, P. G., Goforth, M. W., Donnenwerth, J. J., Greenwald, R. L., Chu, J. J. and Crisco, J. J. Analysis of real-time head accelerations in collegiate football players. Clinical Journal of Sport Medicine, 2005, 15(1):3-8.

Echemendia, R. J., Meeuwisse, W., McCrory, P., Davis, G. A., Putukian, M., Leddy, J., Makdissi, M., Sullivan, S. J., Broglio, S. P., Raftery, M., Schneider, K., Kissick, J., McCrea, M., Dvorak, J., Sills, A. K., Aubry, M., Engebretsen, L., Lossemore, M., Fuller, G., Kutcher, J., Ellenbogen, R., Guskiewicz, K., Patricios, J and Herring, S. The sport concussion assessment tool 5th edition (SCAT5): background and rationale. British Journal of Sports Medicine, 2017a, 51(11):848-850.

Echemendia, R. J., Meeuwisse, W., McCrory, P., Davis, G. A., Putukian, M., Leddy, J., Makdissi, M., Sullivan, S. J., Broglio, S. P., Raftery, M., Schneider, K., Kissick, J., McCrea, M., Dvorak, J., Sills, A. K., Aubry, M., Engebretsen, L., Lossemore, M., Fuller, G., Kutcher, J., Ellenbogen, R., Guskiewicz, K., Patricios, J and Herring, S. The sport concussion assessment tool 5th edition (SCAT5). British Journal of Sports Medicine, 2017b, 51(11):851-858.

Elkin, B. S. and Morrison, B. Viscoelastic properties of the P17 and adult rat brain from indentation in the coronal plane. ASME, Journal of Biomechanical Engineering, 2013, 135(11):114507.

Elkin, B. S., Ilankovan, A. and Morrison III, B. Age-dependent regional mechanical properties of the rat hippocampus and cortex. ASME, Journal of Biomechanical Engineering, 2010, 132(1):011010.

Elkin, B. S., Ilankovan, A. I. and Morrison III, B. A detailed viscoelastic characterization of the P17 and adult rat brain. Journal of Neurotrauma, 2011, 28(11):2235-2244.

Fehily, B. and Fitzgerald, M. Repeated mild traumatic brain injury: potential mechanisms of damage. Cell Transplantation, 2017, 26(7):1131-1155.

Fernandes, F. A. O. and de Sousa, R. J. A. Head injury predictors in sports trauma – a state-of-the-art review. Journal of Engineering in Medicine, 2015, 229(8):592-608.

Fijalkowski, R. J., Stemper, B. D., Pintar, F. A., Yoganandan, N., Crowe, M. J. and Gennarelli, T. A. New rat model for diffuse brain injury using coronal plane angular acceleration. Journal of Neurotrauma, 2007a, 24(8):1387-1398.

Fijalkowski, R. J., Stemper, B. D., Pintar, F. A., Yoganandan and Gennarelli, T. A. Influence of angular acceleration duration on functional outcomes following mild diffuse brain injury. Proceedings of IRCOBI Conference, Maastricht, The Netherlands, 2007b, 161-171.

Fijalkowski, R. J., Yoganandan, N., Zhang, J. and Pintar, F. A. A finite element model of region-specific response for mild diffuse brain injury. Stapp Car Crash Journal, 2009, 53:193-213.

Finan, J. D. Biomechanical simulation of traumatic brain injury in the rat. Clinical Biomechanics, 2019, 64:114-121.

Finan, J. D., Elkin, B. S., Pearson, E. M., Kalbian, I. L. and Morrison III, B. Viscoelastic properties of the rat brain in the sagittal plane: effects of anatomical structure and age. Annals of Biomedical Engineering, 2012a, 40(1):70-78.

Finan, J. D., Pearson, E. M. and Morrison III, B. Viscoelastic properties of the rat brain in the horizontal plane. Proceedings of IRCOBI Conference, Dublin, Ireland, 2012b, 474-485.

Finan, J. D., Sundaresh, S. N., Elkin, B. S., McKhann II, G. M. and Morrison III, B. Regional mechanical properties of human brain tissue for computational models of traumatic brain injury. Acta Biomaterialia, 2017, 55:333-339.

Fliegauf, M. Benzing, T and Omran, H. When cilia go bad: cilia defects and ciliopathies. Nature Reviews Molecular Cell Biology, 2007, 8:880-893.

Flynn, K. C., Stiess, M. and Bradke, F. Chapter 2 - Role of the cytoskeleton and membrane trafficking in axon-dendrite morphogenesis. Cellular Migration and Formation of Neuronal Connections: Comprehensive Developmental Neuroscience, 2013, 2:19-50.

Fournier, A. J., Rajbhandari, L., Shrestha, S. and Venkatesan, A. In vitro and in situ visualization of cytoskeletal deformation under load: traumatic axonal injury, The FASEB Journal, 2014, 28(12):5277-5287.

Franceschini, G., Bigoni, D., Regitnig, P. and Holzapfel, G. A. Brain tissue deforms similarly to filled elastomers and follows consolidation theory. Journal of Mechanics and Physics of Solids, 2006, 54(12):2592-2620.

Fung, Y. C. Biomechanics: mechanical properties of living tissues. Second edition, Springer-Verlag New York, 1993.

Gabler, L. F., Crandall, J. R. and Panzer, M. B. Development of a metric for predicting brain strain responses using head kinematics. Annals of Biomedical Engineering, 2018, 46(7):972-985.

Gabler, L. F., Stone, J. R., Mourad, P. D., Crandall, J. R. and Salzar, R. S. Region specific viscoelastic properties of the adult rat brain under indentation following traumatic brain injury. Proceedings of IRCOBI Conference, Gothenburg, Sweden, 2013, 470-482.

Gadd, C. W. Use of a weighted-impulse criterion for estimating injury hazard. Proceedings of 10th Stapp Car Crash Conference, SAE Technical Paper 660793, 1966, 164-174.

Galford, J. E. and McElhaney, J. H. A viscoelastic study of scalp, brain and dura. Journal of Biomechanics, 1970, 3(2):211-221.

Gefen, A., Gefen, N., Zhu, Q., Raghupathi, R. and Margulies, S. S. Age-dependent changes in material properties of the brain and braincase of the rat. Journal of Neurotrauma, 2003, 20(11):1163-1177.

Gennarelli, T. A., Pintar, F. A. and Yoganandan, N. Biomechanical tolerances for diffuse brain injury and a hypothesis for genotypic variability in response to trauma. 47th Annual Proceedings, Association for the Advancement of Automotive Medicine, 2003, 47:624-628.

Genon, S., Reid, A., Langner, R., Amunts, K. and Eickhoff, S. B. How to characterize the function of a brain region. Trends in Cognitive Sciences, 2018, 22(4):350-364.

Giordano, C. and Kleiven, S. Evaluation of axonal strain as a predictor for mild traumatic brain injuries using finite element modeling. Stapp Car Crash Journal, 2014, 58:1-33.

Giza, C. C. and Hovda, D. A. The neurometabolic cascade of concussion. Journal of Athletic Training, 2001, 36(3):228-235.

Goldsmith, W. Biomechanics of head injury. In: Fung, Y. C., Perrone N. and Anliker, M. (eds) Biomechanics. Its foundation and objectives. Prentice-Hall, Englewood Cliffs, NJ, 1972, 585–634.

Gray's anatomy 41st edition, 2015.

Green, M. A., Bilston, L. E. and Sinkus, R. In vivo brain viscoelastic properties measured by magnetic resonance elastography. NMR in Biomedicine, 2008, 21(7):755-764.

Griffin, J. W., Price, D. L., Drachman, D. B. and Engel, W. K. Axonal transport to and from the motor nerve ending. Annals New York Academy of Sciences, 1976, 274(1):31-45.

Gross, A. G. Impact thresholds of brain concussion. The Journal of Aviation Medicine, 1958, 29(10):725-732.

Gurdjian, E. S., Webster, J. E. and Lissner, H. R. Observations on the mechanism of brain concussion, contusion and laceration. Surgery, Gynecology and Obstetrics, 1955, 101(6):680-690.

Gurdjian, E. S., Lissner, H. R. and Evans, F. G. Intracranial pressure and acceleration accompanying head impacts in human cadavers. Surgery, Gynecology, and Obstetrics, 1961, 113:185-190.

Gurdjian, E. S., Lissner H. R. and Patrick, L. M. Concussion-mechanism and pathology. 7th Stapp Car Crash Conference, 1963, 470-482.

Gurdjian, E. S., Roberts, V. L. and Thomas, L. M. Tolerance curves of acceleration and intracranial pressure and protective index in experimental head injury. The Journal of Trauma, 1966, 6(5):600-604.

Guskiewicz, K. M., McCrea, M., Marshall, S. W., Cantu, R. C., Randolph, C., Barr, W., Onate, J. A. and Kelly, J. P. Cumulative effects associated with recurrent concussion in collegiate football players: the NCCA concussion study. The Journal of the American Medical Association, 2003, 290(19):2549-2555.

Guskiewicz, K. M., Mihalik, J. P., Shankar, V., Marshall, S. W., Crowell, D. H., Oliaro, S. M., Ciocca, M. F. and Hooker, D. N. Measurement of head impacts in collegiate football players: relationship between head impact biomechanics and acute clinical outcome after concussion. Neurosurgery, 2007, 61(6):1244-1253.

Gysland, S. M., Mihalik, J. P., Register-Mihalik, J. K., Trulock, S. C., Shields, E. W. and Guskiewicz, K. M. The relationship between subconcussive impacts and concussion history on clinical measures of neurological function in collegiate football players. Annals of Biomedical Engineering, 2011, 40(1):14-22.

Heape, A., Cells of the nervous system, Neurobiology, 2010.

HEDDD - Human engineering design data digest, Department of defense human factors engineering technical advisory group, USA, 2000.

Herrmann, N. The creative brain. The Journal of Creative Behavior, 1991, 25(4):275-295.

Hodgson, V. R., Thomas, L. M., Gurdjian, E. S., Fernando, O. U., Greenberg, S. W. and Chason, J. L. Advances in understanding of experimental concussion mechanisms. Proceedings of 13th Stapp Car Crash Conference, SAE Technical Paper 690796, 1969, 18-37.

Holbourn, A. H. S. Mechanics of head injuries. The Lancet, 1943, 438-441.

Hootman, J. M., Dick, R. and Agel, J. Epidemiology of collegiate Injuries for 15 Sports: summary and recommendations for Injury prevention initiatives. Journal of athletic training, 2007, 42(2):311-319.

Hosmer, D. W. and Lemeshow, S. Goodnss of fit tests for the multiple logistic regression model. Communications in Statistics – Theory and Methods, 1980, 9(10):1043-1069.

Irvine, K. A. and Blakemore, W. F. Remyelination protects axons from demyelination-associated axon degeneration. Brain, 2008, 131(6):1464-1477.

Jafari, S. S., Maxwell, W. L., Neilson, M. and Graham, D. I. Axonal cytoskeletal changes after non-disruptive axonal injury, Journal of Neurocytology, 1997, 26(4):207-221.

Jafari, S. S., Nielson, M., Graham, D. I. and Maxwell, W. L. Axonal cytoskeleton changes after nondisruptive axonal injury. II. Intermediate sized axons, Journal of Neurotrauma, 1998, 15(11):955-966.

Jakel, S. and Dimou, L. Glial cells and their function in the adult brain: a journey through the history of their ablation. Frontiers in Neurology, 2017, 11(24):1-17.

Jin, J., Zhang, J., Song, X., Hu, H., Sun, X. and Gao, Z. Effect of cerebrospinal fluid modeled with different material properties on a human finite element head model. Journal of Mechanics in Medicine and Biology, 2015, 15(1):1550027(1-19).

Johnson, V. E., Stewart, W. and Smith, D. H. Axonal pathology in traumatic brain injury. Experimental Neurology, 2013, 246:35-43.

Jordan, B. D., Tsairis, P., Warren, R. F. (eds) Head injury in sports, Sports Neurology, Aspen Publications, 1989, 227.

Kelly, J. P. and Rosenberg, J. H. Diagnosis and management if concussion in sports. Neurology, 1997, 48(3):575-580.

King, A. I., Yang, K. H., Zhang, L., Hardy, W. and Viano, D. C. Is head injury caused by linear or angular acceleration? Proceedings of IRCOBI Conference, Lisbon, Portugal, 2003, 1-12.

Kleiven, S. Predictors for traumatic brain injuries evaluated through accident reconstructions. Stapp Car Crash Journal, 2007, 51:81-114.

Kruse, S. A., Rose, G. H., Glaser, K. J., Manduca, A., Felmlee, J. P., Jack Jr., C. R. and Ehman, R. L. Magnetic resonance elastography of the brain. NeuroImage, 2008, 39(1):231-237.

Lamy, M., Baumgartner, D., Yoganandan, N, Stemper, B. D. and Willinger, R. Experimentally validated three-dimensional finite element model of the rat for mild traumatic brain injury. Medical & Biological Engineering & Computing, 2013, 51(3):353-365.

LaPlaca, M. C., Lessing, M. C., Prado, G. R., Zhou, R., Tate, C. C., Geddes-Klein, D., Meaney, D. F. and Zhang, L. Mechanoporation is a potential indicator of tissue strain and subsequent degeneration following experimental traumatic brain injury. Clinical Biomechanics, 2019, 64:2-13.

Lee, S. J., King, M. A., Sun, J., Xie, H. K., Subhash, G. and Sarntinoranont, M. Measurement of viscoelastic properties in multiple anatomical regions of acute rat brain tissue slices. Journal of the Mechanical Behavior of Biomedical Materials, 2014, 29:213-224.

Levchakov, A., Linder-Ganz, E., Raghupathi, R., Margulies, S. S. and Gefen, A. Computational studies of strain exposures in neonate and mature rat brains during closed head impact. Journal of Neurotrauma, 2006, 23(10):1570-1580.

Li, H., Raun, J., Xie, Z., Wang, H. and Liu, W. Investigation of the critical geometric characteristics of living human skulls utilizing medical image analysis techniques. International Journal of Vehicle Safety, 2007, 2(4):345-367.

Ling, H., Hardy, J. and Zetterberg, H. Neurological consequences of traumatic brain injuries in sports. Molecular and Cellular Neuroscience, 2015, 66(B):114-122.

Lissner, H. R., Lebow, M. and Evans, F. G. Experimental studies on the relation between acceleration and intracranial pressure changes in man. Surgery, Gynecology and Obstetrics, 1960, 111:329–338.

Maday, S., Twelvetrees, A. E., Moughamian, A. J. and Holzbaur, E. L. F. Axonal transport: cargo-specific mechanisms of motility and regulation. Neuron, 2014, 84(2):292-309.

Maddocks, D. L., Dicker, G. D. and Saling, M. M. The assessment of orientation following concussion in athletes. Clinical Journal of Sport Medicine, 1995, 5(1):32-35.

Mao, H., Zhang, L., Yang, K. H. and King, A. I. Application of a finite element model of the brain to study traumatic brain injury mechanisms in rat. Stapp Car Crash Journal, 2006, 50:583-600.

Mao, H., Wagner, C., Guan, F., Yeni, Y. N. and Yang, K. H. Material properties of adult rat skull. Journal of Mechanics in Medicine and Biology, 2011, 11(5):1199-1212.

Maxwell, W. L., Povlishock, J. T. and Graham, D. L. A mechanistic analysis of nondisruptive axonal injury: a review. Journal of Neurotrauma, 1997, 14(7):419-440.

McAllister, T. W., Ford, J. C., Ji, S., Beckwith, J. G., Flashman, L. A., Paulsen, K. and Greenwald, R. M. Maximum principal strain and strain rate associated with concussion diagnosis correlates with changes in corpus callosum white matter indices. Annals of Biomedical Engineering, 2012, 40(1):127-140.

McCrory, P., Matser, E., Cantu, R. and Ferrigno, M. Sports neurology. The LANCET Neurology, 2004, 3(7):435-440.

McCrory, P., Meeuwisse, W., Dvorak, J., Aubry, M., Bailes, J., Broglio, S., Cantu, R. C., Cassidy, D., Echemendia, R. J., Castellani, R. J., Davis, G. A., Ellenbogen, R., Emery, C., Engebresten, L., Feddermann-Demont, N., Giza, C. C., Guskiewicz, K. M., Herring, S., Iversonm G. L., Johnston, K. M., Kissick, J., Kutcher, J., Leddy, J., J., Maddocks, D., Makdissi, M., Manley, G. T., McCrea, M., Meehan, W. P., Nagahiro, S., Patricios, J., Putukian, M., Schneider, K. J., Sills, A., Tator, C. H., Turner, M. and Vos, P. E. Consensus statement on concussion in sport-the 5th international conference on concussion in sport held in Berlin, October 2016. British Journal of Sports Medicine, 2017, 51(11):838-847.

McIntosh, A. S., Patton, D. A., Frechede, B., Pierre, P., Ferry, E. and Barthels, T. The biomechanics of concussion in unhelmeted football players in Australia: a case-control study. BMJ Open, 2014, 4(5): e005078.

Mierzwa, A. J., Marion, C. M., Sullivan, G. M., McDaniel, D. P. and Armstrong, R. C. Components of myelin damage and repair in the progression of white matter pathology after mild traumatic brain injury. Journal of Neuropathology and Experimental Neurology, 2015, 74(3):218-232.

Miller, K. and Chinzei, K. Mechanical properties of brain tissue in tension. Journal of Biomechanics, 2002, 35(4):483-490.

Moeendarbary, E., Weber, I. P., Sheridan, G. K., Koser, D. E., Soleman, S., Haenzi, B., Bradbury, E. J., Fawcette, J. and Franze, K. The soft mechanical signature of glial scars in the central nervous system. Nature communications, 2017, 8:14787.

Mori, S. and Zhang, J. Principals of diffusion tensor imaging and its applications to basic neuroscience research. Neuron, 2006, 51(5):527-539.

Mortera, P. and Herculano-Houzel, S. Age-related neuronal loss in the rat brain starts at the end of adolescence. Frontiers in Neuroanatomy, 2012, 6(45):1-9.

Murray, I. R., Murray, A. D. and Robson, J. Sports concussion: time for a culture change. Clinical Journal of Sports Medicine, 2015, 25(2):75-77.

Nelson, W. E., Jane, J. A. and Gieck, J. H. Minor head injury in sports: a new system of classification and management. The Physicians and Sportsmedicine, 1984, 12(3):103-107.

Newman, J. A. A generalized acceleration model for brain injury threshold (GAMBIT). Proceedings of IRCOBI Conference, Zurich, Switzerland, 1986, 121-131.

Newman, J., Barr, C., Beusenberg, M., Fournier, E., Shewchenko, N., Welbourne, E. and Withnall, C. A new biomechanical assessment of mild traumatic brain injury Part II – results and conclusions. Proceedings of IRCOBI Conference, Montpellier, France, 2000a, 223-233.

Newman, J. A., Shewchenko, N and Welbouren, E. A proposed new biomechanical head injury assessment function – the maximum power index. Proceedings of 44th Stapp Car Crash Conference, SAE Technical Paper 2000-01-SC16, 2000b, 362-394.

NHTSA (National Highway Traffic Safety Administration), Development of improved injury criteria for the assessment of advanced automotive restraint systems – II. 1999.

Nicolas, E., Calle, S., Nicolle, S., Mitton, D. and Remenieras, J. Biomechanical characterization of ex vivo human brain using ultrasound shear wave spectroscopy. Ultrasonics, 2018, 84:119-125.

Nicolle, S., Lounis, M. and Willinger, R. Shear properties of brain tissue over a frequency range relevant for automotive impact simulations: new experimental results. Stapp Car Crash Journal, 2004, 48():239-258.

Nowak, K., Mix, E., Gimsa, J., Strauss, U., Sriperumbudur, K. K., Benecke, R. and Gimsa, U. Optimizing a rodent model of Parkinson's disease for exploring the effects and mechanisms of deep brain stimulations. Parkinson's disease, 2011, 414682:1-19.

Ommaya, A. K., Yarnell, P., Horsch, A. E. and Harris, E. H. Scaling of experimental data on cerebral concussion in sub-human primates to concussion threshold for man. Proceedings of 11th Stapp Car Crash Conference, SAE Technical Paper 670906, 1967, 73-80.

Ommaya, A. K. and Hirsch, A. E. Tolerances for cerebral concussion from head impact and whiplash in primates. Journal of Biomechanics, 1971, 4(1):13-21.

Ommaya, A. K. and Gennarelli, T. A. Cerebral concussion and traumatic unconsciousness: correlation of experimental and clinical observations on blunt head injuries. Brain, 1974, 97(1):633-654.

Ommaya, A. K. Biomechanics of head injury: experimental aspects. In: Nahum AM, Melvin JW (eds) The Biomechanics of Trauma. Appleton-Century-Crofts, Norwalk, Connecticut, 1985, 245–269.

Ommaya, A. K., Goldsmith, W. and Thibault, L. Biomechanics and neuropathology of adult and paediatric head injury. British Journal of Neurosurgery, 2002, 16(3):220-242.

Ouyang, H., Nauman, E. and Shi, R. Contribution of cytoskeletal elements to the axonal mechanical properties, Journal of Biological Engineering, 2013, 7(21):1-8.

Papp, E. A., Leergaard, T. B., Calabrese, E., Johnson, G. A. and Bjaalie, J. G. Waxholm space atlas of the Sprague Dawley rat brain. NeuroImage, 2014, 97:374-386.

Patton, D. A., McIntosh, A. S. and Kleiven, S. The biomechanical determinants of concussion: finite element simulations to investigate brain tissue deformations during sporting impacts to the unprotected head. Journal of Applied Biomechanics, 2013, 29(6):721-730.

Patton, D. A., McIntosh, A. S. and Kleiven, S. The biomechanical determinants of concussion: finite element simulations to investigate tissue-level predictors of injury during sporting impacts to the unprotected head. Journal of Applied Biomechanics, 2015, 31(4):264-268.

Paxinos, G. and Watson, C. The rat brain in stereotaxic coordinates 7th edition, 2013.

Pellman, E. J., Viano, D. C., Tucker, A. M., Casson, I. R. and Waeckerle, J. F. Concussion in professional football: reconstruction of game impacts and injuries. Neurosurgery, 2003, 53(4):799-814.

Pena, A., Pickard, J. D., Stiller, D., Harris, N. G. and Schuhmann, M. U. Brain tissue biomechanics in cortical contusion injury: a finite element analysis. Acta Neurochirurgica Supplementum, 2005, 95:333-336.

Perge, J. A., Niven, J. E., Mugnaini, E., Balasubramanian, V. and Sterling, P. Why do axons differ in caliber? The Journal of Neuroscience, 2012, 32(2):626-638.

Pervin, F. and Chen, W. W. Dynamic mechanical response of bovine gray matter and white matter brain tissues under compression. Journal of Biomechanics, 2009, 42(6):731-735.

Pesaresi, M., Soon-Shiong, R., French, L., Kaplan, D. R., Miller, F. D. and Paus, T. Axon diameter and axonal transport: in vivo and in vitro effects of androgens. Neuroimage, 2015, 115:191-201.

Peschanel, F. D. The creative mind, the creative brain. Kyoto Conference on Japanese Studies 1994 II, 1996, .non01-02:50-58.

Pincemaille, Y., Trosseille, X., Tarriere, C., Breton, F. and Renault, B. Some new data related to human tolerance obtained from volunteer boxers. Proceedings of 33rd Stapp Car Crash Conference, SAE Technical Paper 892435, 1989, 177-190.

Prange, M. T., Meaney, D. F. and Margulies, S. S. Defining brain mechanical properties: effects of region, direction, and species. Stapp Car Crash Journal, 2000, 44:205-214.

Prevost, T. P., Balakrishnan, A., Suresh, S. and Socrate, S. Biomechanics of brain tissue. Acta Biomaterialia, 2011, 7(1):83-95.

Pudenz, R. H. and Shelden, C. H. The Lucite calvarium - a method for direct observation of the brain - cranial trauma and brain movement. Journal of Neurosurgery, 1946, 3(6):487-505.

Puso, M. A. and Weiss, J. A. Finite element implementation of anisotropic quasi-linear viscoelasticity using a discrete spectrum approximation. Journal of Biomechanical Engineering, 1998, 120(1):62-70.

Ren, L., Baumgartner, D., Davidsson, J., Yang, J. and Willinger, R. Effect of the inhomogeneous brain material characteristic on dynamic responses of head under trauma. Proceedings of IRCOBI Conference, 2014, Berlin, Germany, 93-105.

Rivlin, R. S. and Saunders, D. W. Large elastic deformations of isotropic materials VII. Experiments on the deformation of rubber. Philosophical Transactions of the Royal Society of London, Series B, Mathematical and Physical Sciences, 1951, 243(865):251-288.

Roberts, W. O. and Johnson, R. Who plays? Who sits? The Physician and Sportsmedicine, 1992, 20(6):66-72.

Rooker, S., Jorens, P. G., Reempts, J. V., Borgers, M. and Verlooy, J. Continuous measurement of intracranial pressure in awake rats after experimental closed head injury. Journal of Neuroscience methods, 2003, 131(1-2):75-81.

Rowson, S. and Duma, S. M. Development of the STAR evaluation system for football helmets: integrating player head impact exposure and risk of concussion. Annals of Biomedical Engineering, 2011, 39(8):2130-2140.

Rowson, S., Duma, S. M., Beckwith, J. G., Chu, J. J., Greenwald, R. M., Crisco, J. J., Brolinson, P. G., Duhaime, A., McAllister, T. W. and Maerlender, A. C. Rotational head kinematics in football impacts: an injury risk function for concussion. Annals of Biomedical Engineering, 2012, 40(1):1-13.

Rowson, S. and Duma, S. M. Brain injury prediction: assessing the combined probability of concussion using linear and rotational head acceleration. Annals of Biomedical Engineering, 2013, 41(5):873-882.

Rowson, S. and Rowson, B. Chapter 4 – Biomechanics of Head Trauma, Chronic Traumatic Encephalopathy, 2018, 51-62.

Rowson, S., Campolettano, E. T., Duma, S. M., Stemper, B. D., Shah, A., Harezlak, J., Riggen, L., Mihalik, J. P., Guskiewicz, K. M., Giza, C., Brooks, A., Cameron, K., McAllister, T., Broglio, S. P. and McCrea, M. Accounting for variance in concussion tolerance between individuals: comparing head accelerations between concussed and physically matched control subjects. Annals of Biomedical Engineering, 2019, 1-9.

Rubiano, A. M., Carney, N., Chesnut, R. and Puyana, J. C. Global neurotrauma research challenges and opportunities. Nature, 2015, 527(7578):S193-S197.

Rumple, A., McMurray, M., Johns, J., Lauder, J., Makam, P., Radcliffe, M. and Oguz, I. 3-Dimensional diffusion tensor imaging (DTI) atlas of the rat brain, PLOS ONE, 2013, 8(7):e67334.

Sahoo, D. Brain injury criteria based on computation of axonal elongation. PhD Thesis, University of Strasbourg, France, 2013.

Sahoo, D., Deck, C. and Willinger, R. Development and validation of an advanced anisotropic visco-hyperelastic human brain FE model. Journal of the Mechanical Behavior of Biomedical Materials, 2014, 33:24-42.

Sahoo, D., Deck, C. and Willinger, R. Brain injury tolerance limit based on computation of axonal strain. Accident Analysis and Prevention, 2016, 92:53-70.

Shafieian, M., Darvish, K. K. and Stone, J. R. Changes to the viscoelastic properties of brain tissue after traumatic axonal injury. Journal of Biomechanics, 2009, 42(13):2136-2142.

Shreiber, D. I., Bain, A. C. and Meaney, D. F. In vivo thresholds for mechanical injury to the blood-brain barrier. Proceedings of 41st Stapp Car Crash Conference, SAE Technical Paper 973335, 1997.

Shuck, L. Z. and Advani, S. H. Rheological response of human brain tissue in shear. ASME, Journal of Basic Engineering, 1972, 94(4):905-911.

Smith, D. H. and Meaney, D. F. Axonal damage in traumatic brain injury. The Neuroscientist, 2000, 6(6):483-495.

Snyder, J. M., Hagan, C. E., Bolon, B. and Keene, C. D. Chapter 20 - Nervous system. Comparative Anatomy and Histology (Second edition), Academic press, 2018, 403-444.

Spencer, A. J. M. Continuum theory of the mechanics of fibre-reinforced composites. Springer-Verlag New York, 1984.

Staal, J. A. and Vickers, J. C. Selective vulnerability of non-myelinated axons to stretch injury in an in vitro co-culture system. Journal of Neurotrauma, 2011, 28(5):841-847.

Steiner, L. A. and Andrews, P. J. D. Monitoring the injured brain: ICP and CBF. British Journal of Anaesthesia, 2006, 97(1):26-38.

Stemper, B. D., Shah, A. S., Chiariello, R., Olsen, C. M., Budde, M. D., Glavaski-Joksimovic, A., McCrea, M., Kurpad, S. N. and Pintar, F. A. Prediction of post-concussive behavioral changes in a rodent model based on head rotational acceleration characteristics. Annals of Biomedical Engineering, 2016, 44(11):3252-3265.

Stemper, B. D., Shah, A. S., Wild, A., Humm, J. R., Pintar, F. A., Broglio, S. P., McAllister, T. W. and McCrea, M. Role of repetitive head impact exposure in the onset of concussion: evidence of a possible second mechanism of concussion for contact sports. Proceedings of IRCOBI Conference, Athens, Greece, 2018, 334-335.

Stemper, B. D., Shah, A., Harezlak, J., Rowson, S., Duma, S. M., Mihalik, J. P., Riggen, L. D., Brooks, A., Cameron, K. L., Giza, C. C., Houston, M. N., Jackson, J., Posner, M. A., McGinty, G., DiFiori, J., Broglio, S. P., McAllister, T. W., McCrea, M. and the CARE Consortium Investigators. Repetitive head impact exposure in college football following an NCAA rule change to eliminate two-a-day preseason practices: a study from the NCAA-D0D CARE Consortium. Annals of Biomedical Engineering, 2019, 1-13.

Tadepalli, S. A., Bali, Z. K., Bruszt, N., Nagy, L. V., Amrein, K., Fazekas, B., Buki, A, Czeiter, E. and Hernadi, I. Long-term cognitive impairment without diffuse axonal injury following repetitive mild traumatic brain injury in rats. bioRxiv preprint, 2019.

Tagliaferri, F., Compagnone, C., Korsic, M., Servadei, F. and Kraus, J. A systematic review of brain injury epidemiology in Europe. Acta Neurochirurgica, 2006, 148:255-268.

Takhounts, E. G., Eppinger, R. H., Campbell, J. Q., Tannous, R. E., Power, E. D. and Shook, L. S. On the development of the SIMon finite element head model. Stapp Car Crash Journal, 2003a, 47:107-133.

Takhounts, E. G., Crandall, J. R. and Darvish, K. On the importance of nonlinearity of brain tissue under large deformations. Stapp Car Crash Journal, 2003b, 47:79-92.

Takhounts, E. G., Ridella, S. A., Hasija, V., Tannous, R. E., Campbell, J. Q., Malone, D., Danelson, K., Stitzel, J., Rowson, S. and Duma, S. M. Investigation of traumatic brain injuries using the next generation of simulated injury monitor (SIMon) finite element head model. Stapp Car Crash Journal, 2008, 52:1-31.

Takhounts, E. G., Hasija, V., Ridella, S. A., Rowson, S. and Duma, S. M. Kinematic rotational brain injury criterion (BRIC). International Technical Conference on the Enhanced Safety of Vehicles, Washington DC, 2011, 11-0263.

Takhounts, E. G., Craig, M. J., Moorhouse, K. and McFadden, J. Development of brain injury criteria (BrIC). Stapp Car Crash Journal, 2013, 57:243-266.

Tang-Schomer, M. D., Patel, A. R., Baas, P. W. and Smith, D. H. Mechanical breaking of microtubules in axons during dynamic stretch injury underlies delayed elasticity, microtubule disassembly, and axon degeneration, The FASEB Journal, 2010, 14(5):1401-1410.

Tang-Schomer, M. D., Johnson, V. E., Baas, P. W., Stewart, W. and Smith, D. H. Partial interruption of axonal transport due to microtubule breakage accounts for the formation of periodic varicosities after traumatic axonal injury, Experimental Neurology, 2012, 233(1):364-372.

Taylor, C. A., Bell, J. M., Breiding, M. J. and Xu L. Traumatic Brain Injury–Related Emergency Department Visits, Hospitalizations, and Deaths — United States, 2007 and 2013. Centers for disease control and prevention (CDC), Morbidity and mortality weekly report (MMWR), Surveillance summaries, 2017, 66(9):1-16.

Teasdale, G. and Jennett, B. Assessment of coma and impaired consciousness: a practical scale. The Lancet, 1974, 304(7872):81-84.

Torg, J. S. Athletic Injuries to the Head, Neck and Face. St Louis, MO: Mosby-Year Book; 1991:226.

Uldall, M., Juhler, M., Skjolding, A. D., Kruuse, C., Jansen-Olesen, I. and Jensen, R. A novel method for long-term monitoring of intracranial pressure in rats. Journal of Neuroscience Methods, 2014, 227:1-9.

Unnikrishnan, G., Mao, H., Sundaramurthy, A., Bell, E. D., Yeoh, S., Monson, K. and Reifman, J. A 3-D rat brain model for blast-wave exposure: effects of brain vasculature and material properties. Annals of Biomedical Engineering, 2019, 47(9):2033-2044.

Vappou, J., Breton, E., Choquet, P., Willinger, R. and Constantinesco, A. Assessment of in vivo and post-mortem mechanical behavior of brain tissue using magnetic resonance elastography. Journal of Biomechanics, 2008a, 41(14):2954-2959.

Vappou, J., Breton, E., Choquet, P., Constantinesco, A. and Willinger, R. Brain viscoelasticity measured by magnetic resonance elastography. Proceedings of IRCOBI Conference, Bern, Switzerland, 2008b, 441-444.

Versace, J. A review of the severity index. Proceedings of 15th Stapp Car Crash Conference, SAE Technical Paper 710881, 1971, 771-796.

Weiss, J. A., Maker, B. N. and Govindjee, S. Finite element implementation of incompressible, transversely isotropic hyperelasticity. Computer methods in applied mechanics and engineering, 1996, 135(1-2):107-128.

WHO, World Health Organization, Neurological disorders: public health challenges, 2006.

Willinger, R., Taleb, L. and Kopp, C. Modal and temporal analysis of head mathematical models. Journal of Neurotrauma, 1995, 12(4):743-754.

Yuan, A., Rao, M. V., Veeranna and Nixon, R. A. Neurofilaments at a glance. Journal of Cell Science, 2012, 125(14):3257-3263.

Zhang, L., Yang, K. H. and King, A. I. A proposed injury threshold for mild traumatic brain injury. Journal of Biomechanical Engineering, 2004, 126(2):226-236.

Annexures

Annexure A: Obsolete concussion grading scales

As reported by Cantu, 2001, concussion grading scales, which are obsolete now, are given hereunder in chronological order.

Nelson Grading System (1984)	
Grade 0	Head struck or moved rapidly; not stunned or dazed initially; subsequently complains of headache and difficulty in concentrating
Grade 1	Stunned or dazed initially; no loss of consciousness or amnesia; sensorium clears in less than 1 minute
Grade 2	Headache; cloudy sensorium longer than 1 minute in duration, no loss of consciousness; may have tinnitus or amnesia; may be irritable, hyper excitable, confused or dizzy
Grade 3	Loss of consciousness less than 1 minute in duration; no coma (arousable with noxious stimuli); demonstrates grade 2 symptoms during recovery
Grade 4	Loss of consciousness for more than 1 min; no coma; demonstrates grade 2 symptoms during recovery

Ommaya Grading System (1985)	
Grade 1	Confusion without amnesia (stunned)
Grade 2	Amnesia without coma
Grade 3	Coma lasting less than 6 hours (includes classic cerebral concussion, minor and moderate head injuries)
Grade 4	Coma lasting 6 to 24 hours (severe head injuries)
Grade 5	Coma lasting more than 24 hours (severe head injuries)
Grade 6	Coma, death within 24 hours (fatal head injuries)

Cantu Grading System (1986)	
Grade 1	No loss of consciousness; posttraumatic amnesia less than 30 minutes
Grade 2	Loss of consciousness less than 5 minutes in duration or posttraumatic amnesia lasting longer than 30 minutes but less than 24 hours in duration
Grade 3	Loss of consciousness for more than 5 minutes or posttraumatic amnesia for more than 24 hours

cont.

Jordan Grading System (1989)	
Grade 1	Confusion without amnesia; no loss of consciousness
Grade 2	Confusion with amnesia lasting less than 24 hours; no loss of consciousness
Grade 3	Loss of consciousness with an altered level of consciousness not exceeding 2 to 3 minutes; posttraumatic amnesia lasting more than 24 hours
Grade 4	Loss of consciousness with an altered level of consciousness exceeding 2 to 3 minutes

Colorado Medical Society Grading System (1989)	
Grade 1	Confusion without amnesia; no loss of consciousness
Grade 2	Confusion with amnesia; no loss of consciousness
Grade 3	Loss of consciousness

Torg Grading System (1991)	
Grade 1	Bell rung; short-term confusion; unsteady gait; dazed appearance; no amnesia
Grade 2	Posttraumatic amnesia only; vertigo; no loss of consciousness
Grade 3	Posttraumatic retrograde amnesia; vertigo; no loss of consciousness
Grade 4	Immediate transient loss of consciousness
Grade 5	Paralytic coma; cardiorespiratory arrest
Grade 6	Death

Roberts Grading System (1992)	
Bell ringer	No loss of consciousness; no posttraumatic amnesia; symptoms less than 10 minutes
Grade 1	No loss of consciousness; posttraumatic amnesia less than 30 minutes; symptoms greater than 10 minutes
Grade 2	Loss of consciousness less than 5 minutes; posttraumatic amnesia greater than 30 minutes
Grade 3	Loss of consciousness greater than 5 minutes; posttraumatic amnesia greater than 24 hours

AAN Practice Parameter Grading System (1997)	
Grade 1	Transient confusion; no loss of consciousness; concussion symptoms or mental status abnormalities on examination resolve in less than 15 minutes
Grade 2	Transient confusion; no loss of consciousness; concussion symptoms or mental status abnormalities on examination last more than 15 minutes
Grade 3	Any loss of consciousness, either brief (seconds) or prolonged (minutes)

Annexure B: Experimental rotational acceleration loading curves

As provided by Medical College of Wisconsin, USA, the loading curves of twenty-six experimental cases depicting applied rotational acceleration pulse are given hereunder.

1RAT17

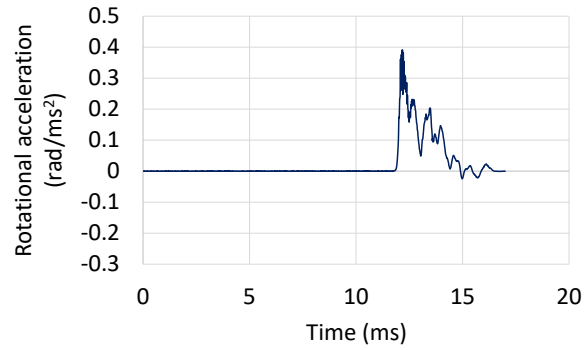

2RAT18

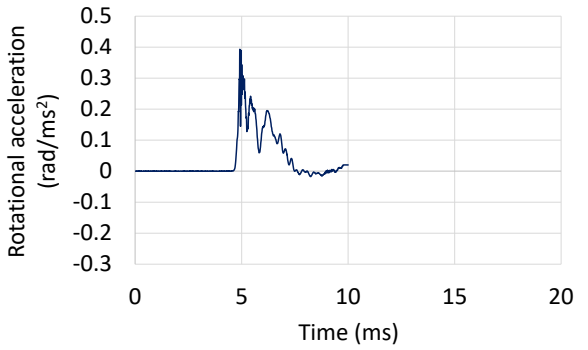

3RAT19

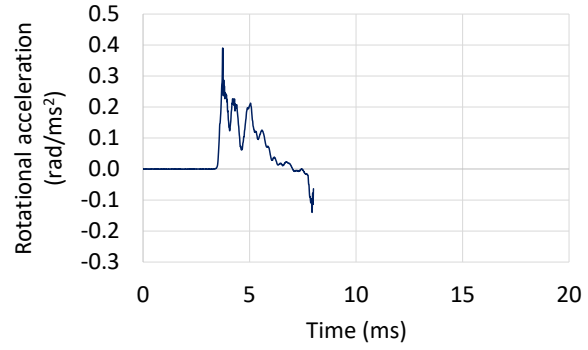

4RAT77

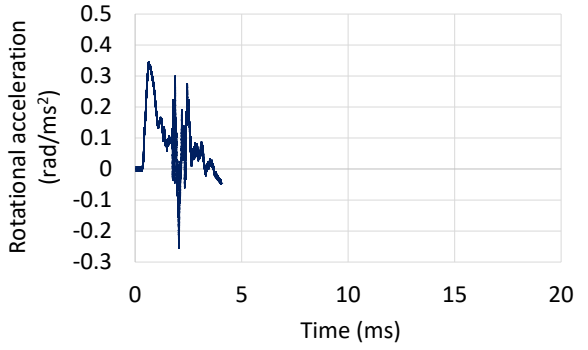

5RAT78

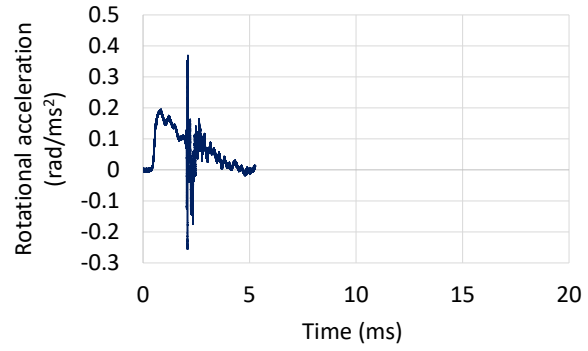

6RAT79

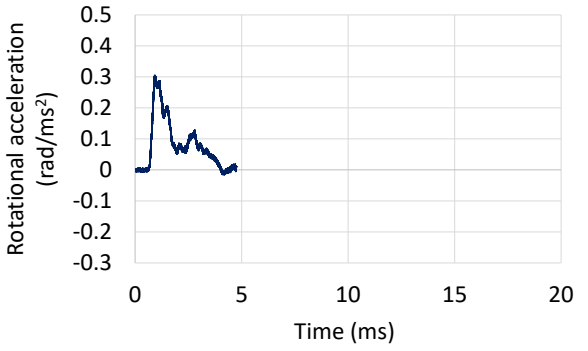

7RAT80

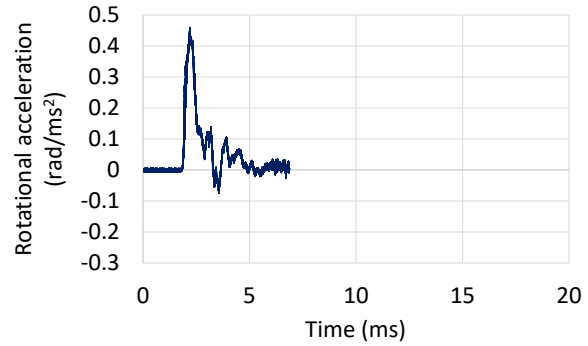

8RAT84

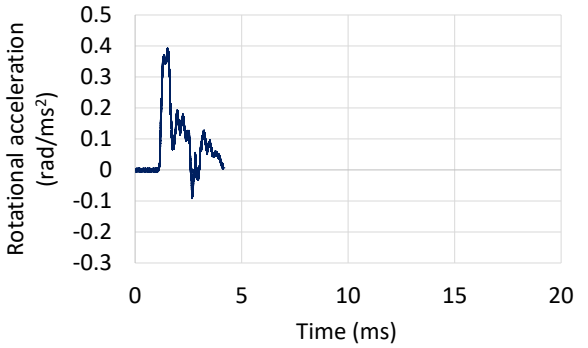

9RAT85

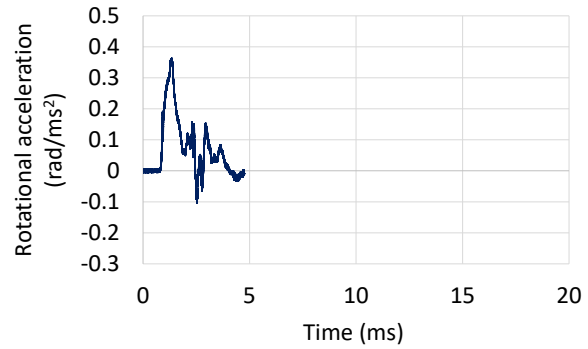

10RAT86

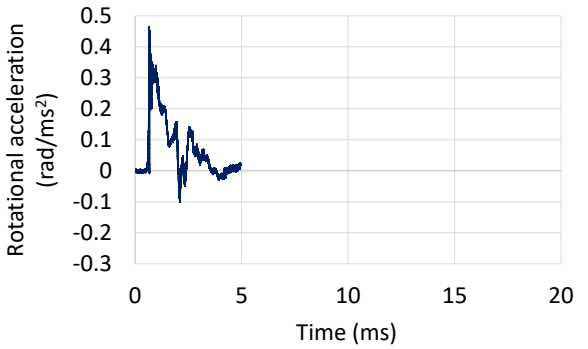

11RAT93

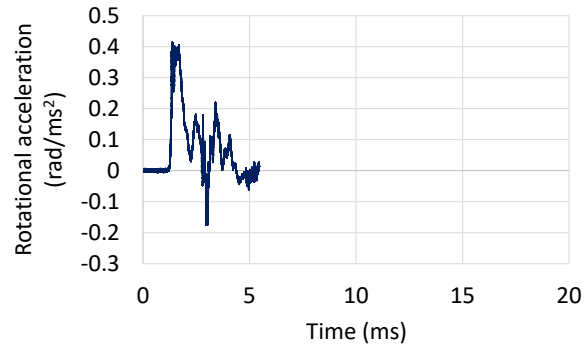

12RAT95

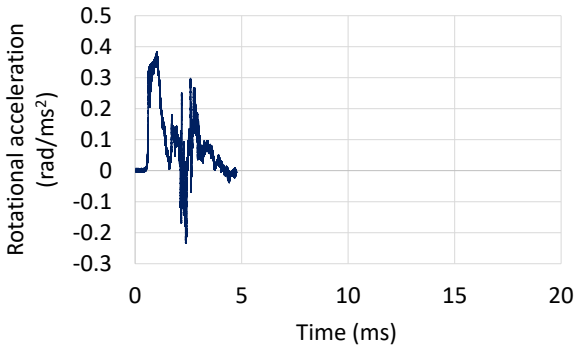

13RAT105

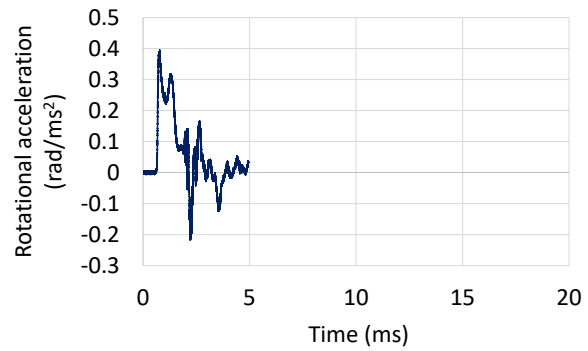

14RAT107

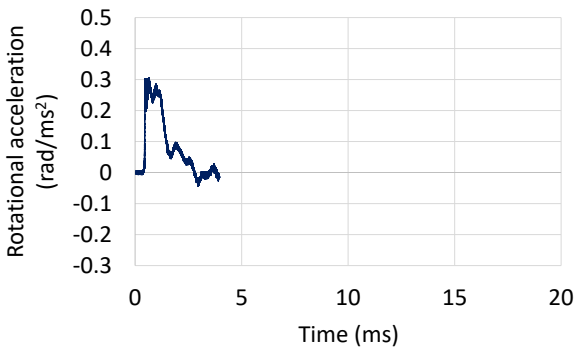

15RAT119

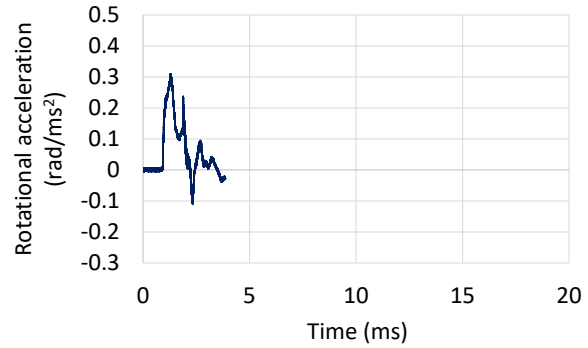

16RAT123

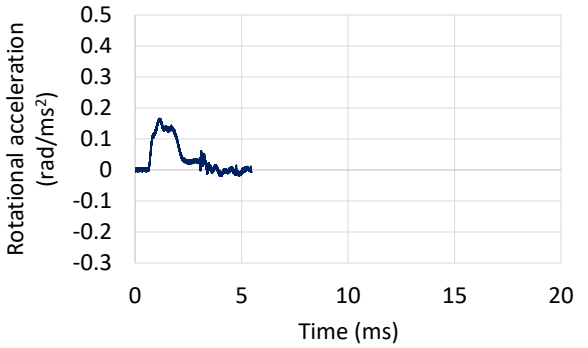

17RAT141

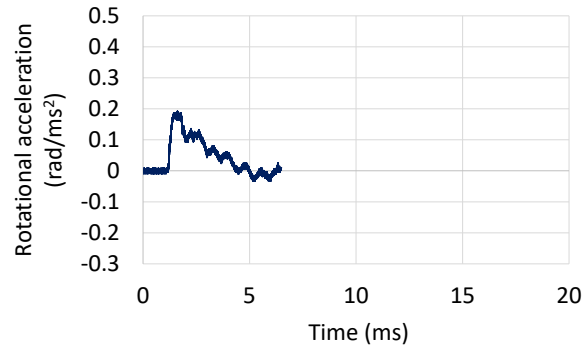

18RAT142

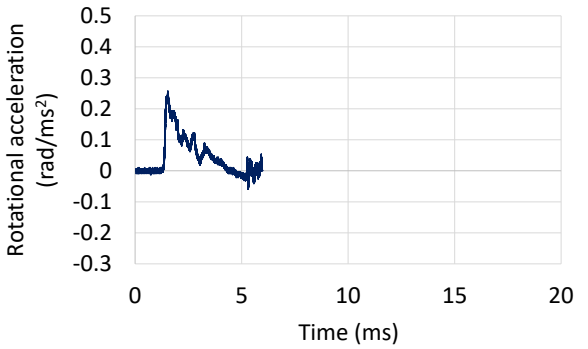

19RAT148

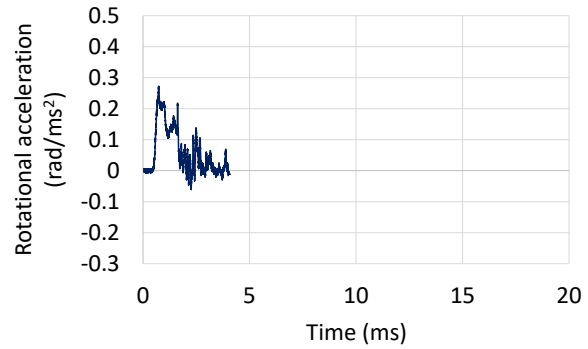

20RAT152

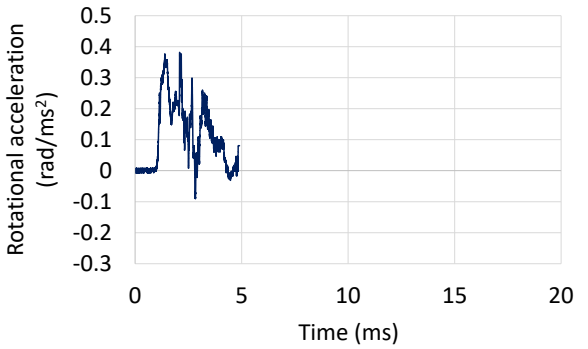

21RAT296

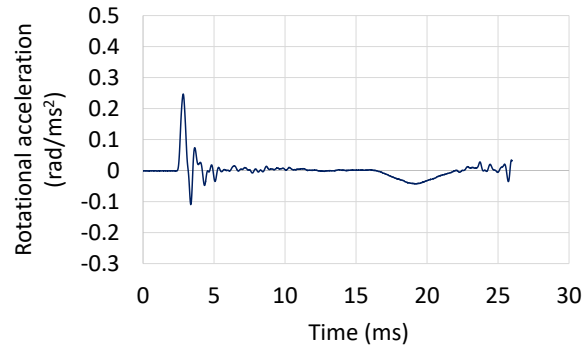

22RAT299

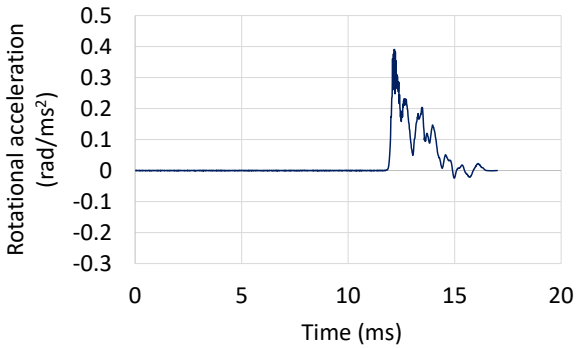

23RAT301

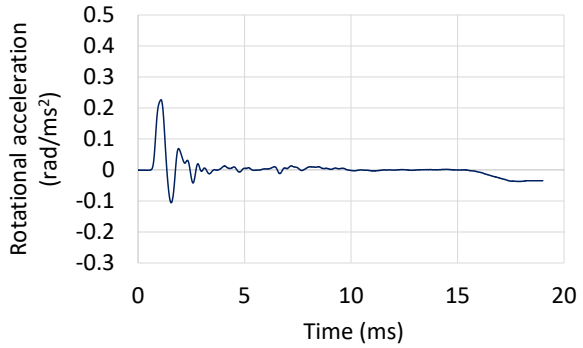

24RAT303

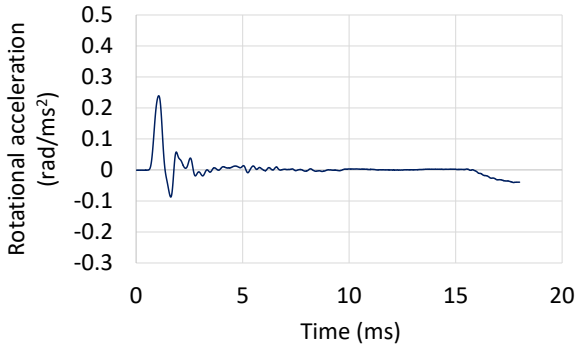

25RAT306

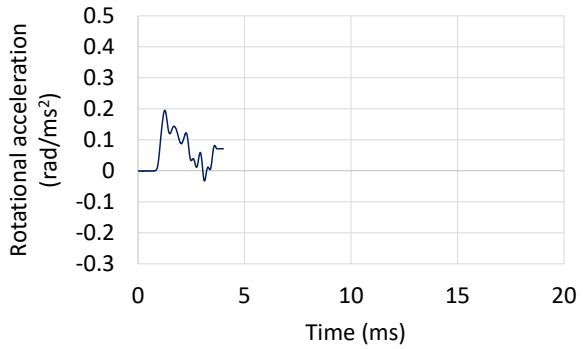

26RAT311

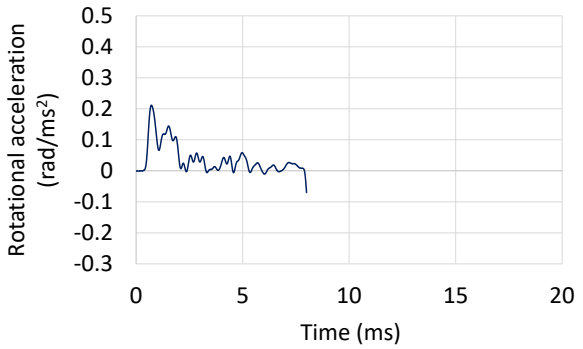

Annexure C: Simulation results for entire brain based on loading groups

Simulation results of all twenty-six experimental cases for all ten mechanical parameters, which are maximum axonal strain, maximum strain energy, maximum von Mises stress and strain, maximum shear stress and strain, maximum principal stress and strain and minimum and maximum pressures for the entire brain based on loading group categorization are presented here in Table C1 to Table C7.

Table C1: Simulation results for entire brain with respect to unconsciousness time based on loading group categorization.

Maximum axonal strain

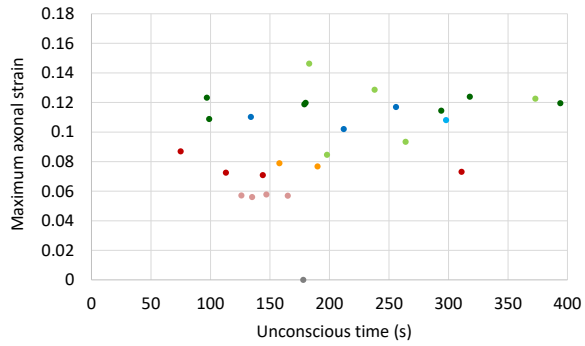

Maximum strain energy

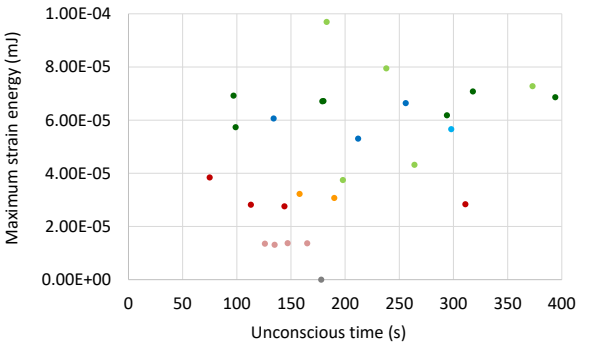

Maximum von Mises stress

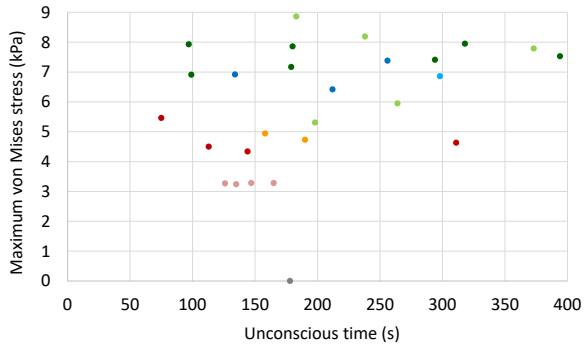

Maximum von Mises strain

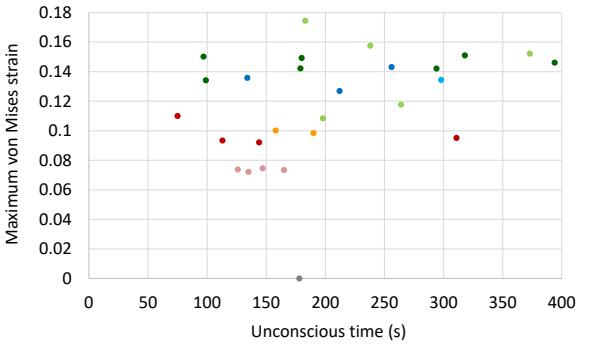

Maximum shear stress

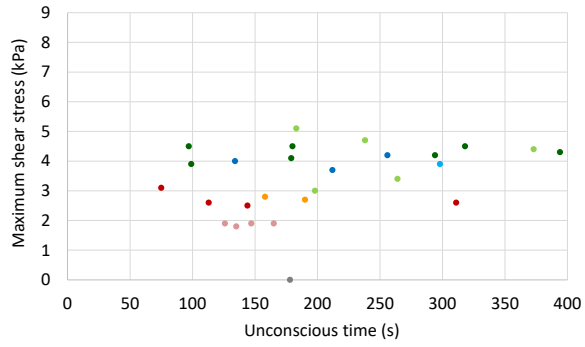

Maximum shear strain

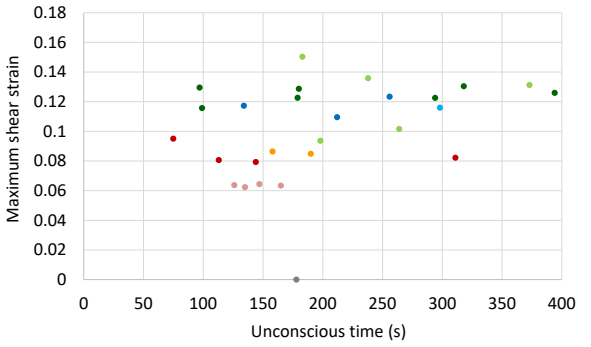

cont.

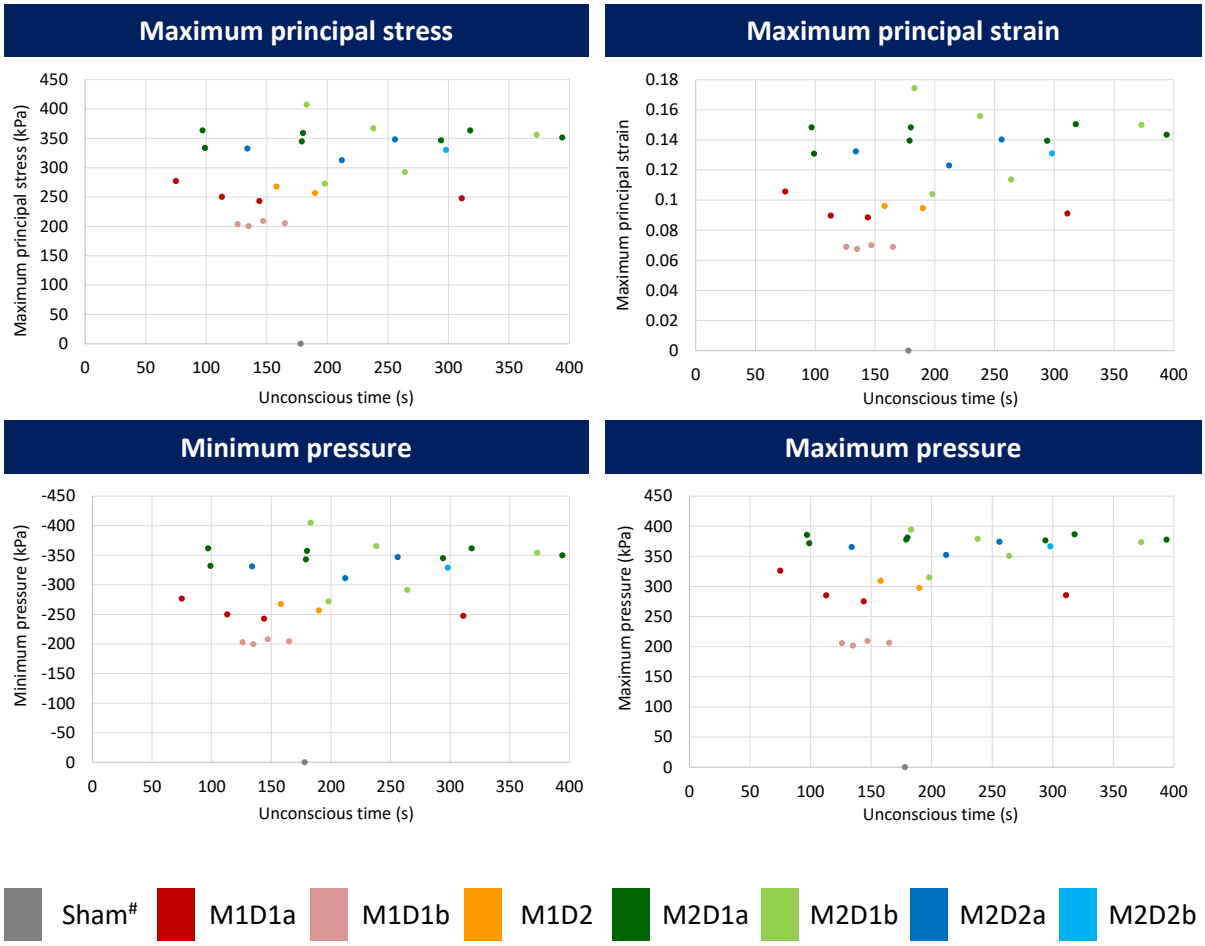

#Since, sham did not go through rotational loading, only their experimental response is marked.

Table C2: Simulation results for entire brain with respect to EPM distance travelled based on loading group categorization.

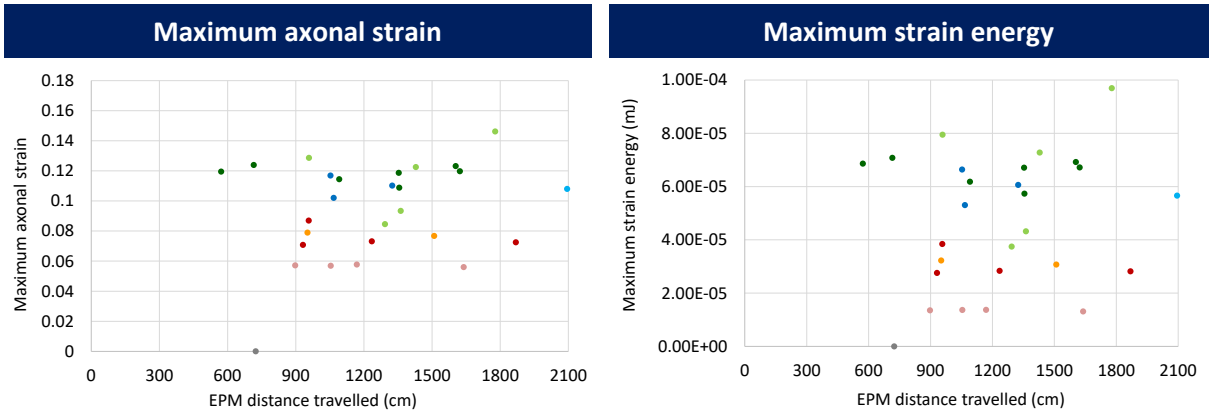

cont.

Maximum von Mises stress

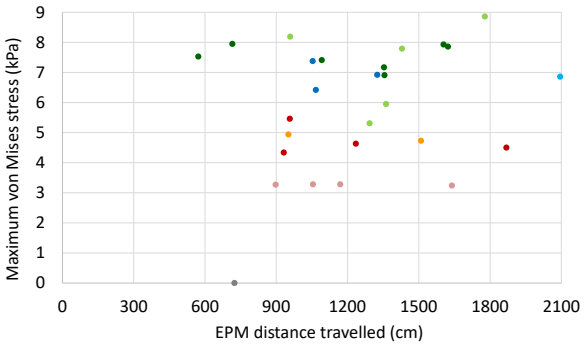

Maximum von Mises strain

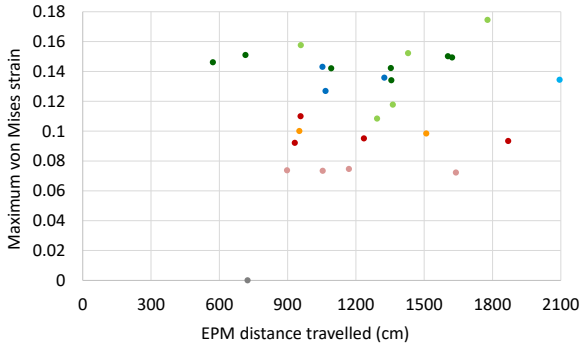

Maximum shear stress

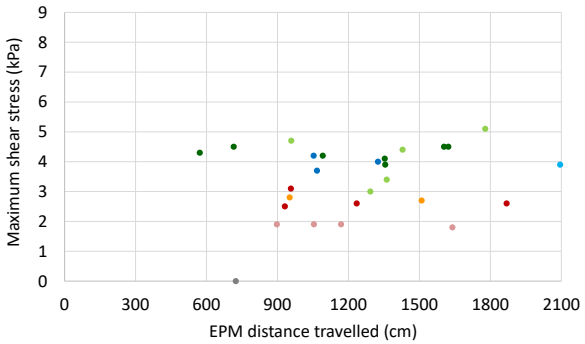

Maximum shear strain

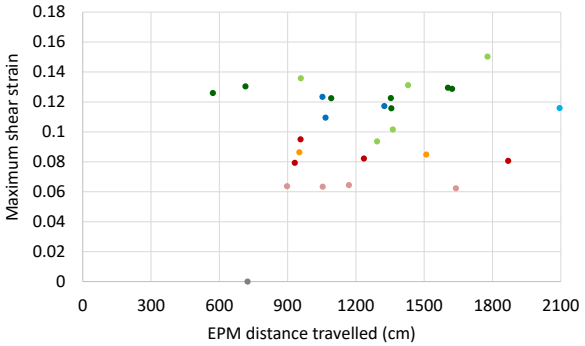

Maximum principal stress

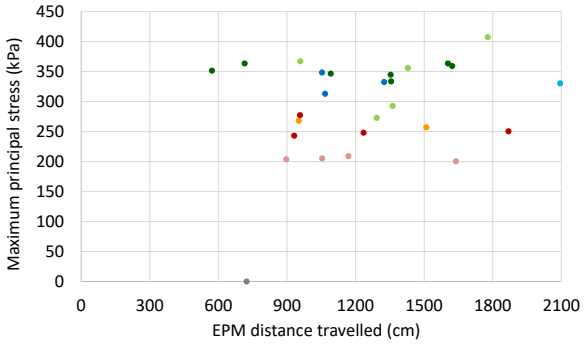

Maximum principal strain

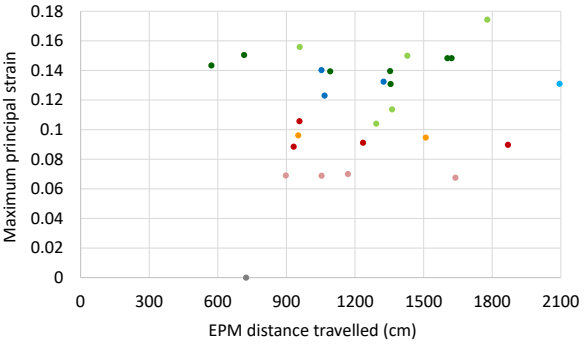

Minimum pressure

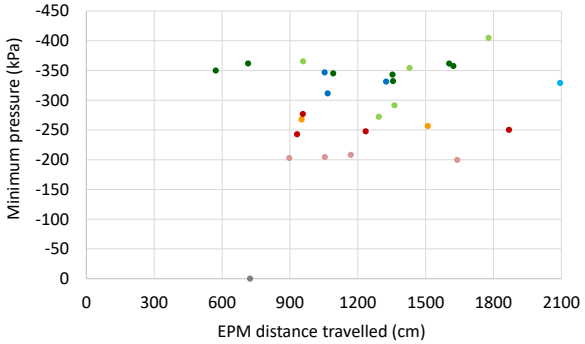

Maximum pressure

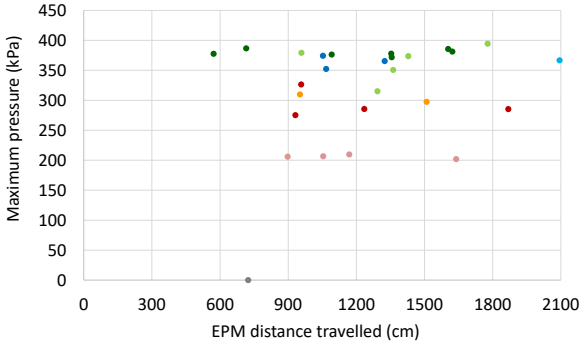

Sham[#] M1D1a M1D1b M1D2 M2D1a M2D1b M2D2a M2D2b

[#]Since, sham did not go through rotational loading, only their experimental response is marked.

Table C3: Simulation results for entire brain with respect to EPM arm changes based on loading group categorization.

Maximum axonal strain

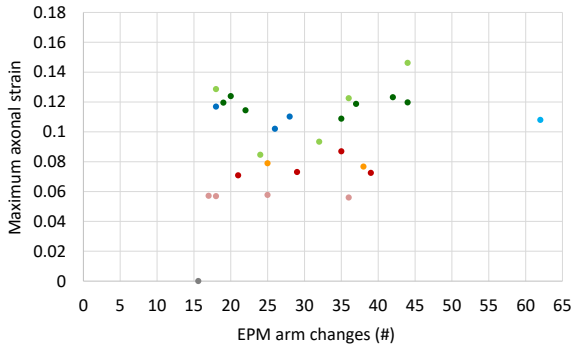

Maximum strain energy

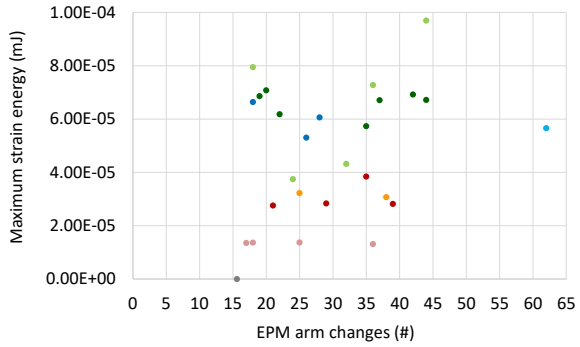

Maximum von Mises stress

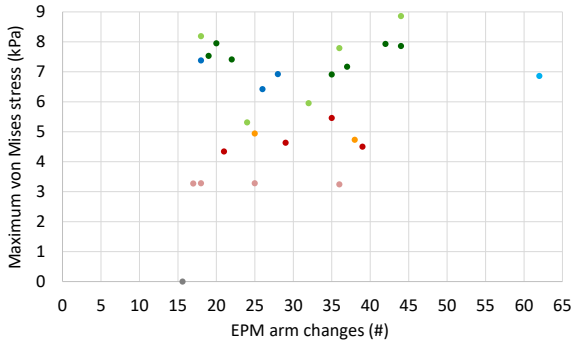

Maximum von Mises strain

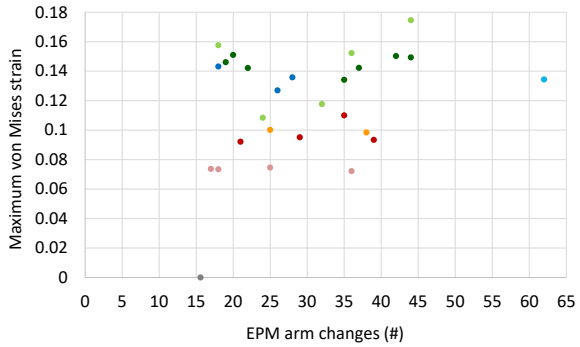

Maximum shear stress

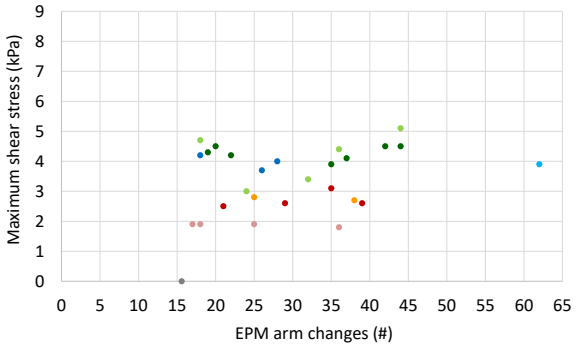

Maximum shear strain

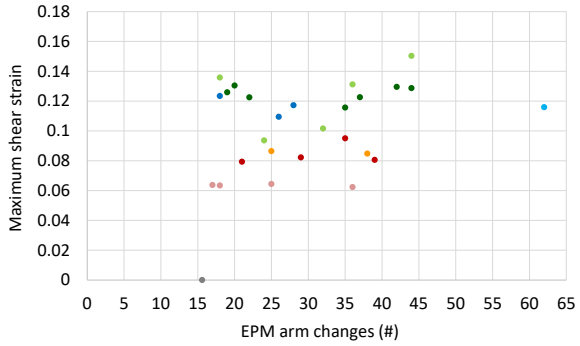

Maximum principal stress

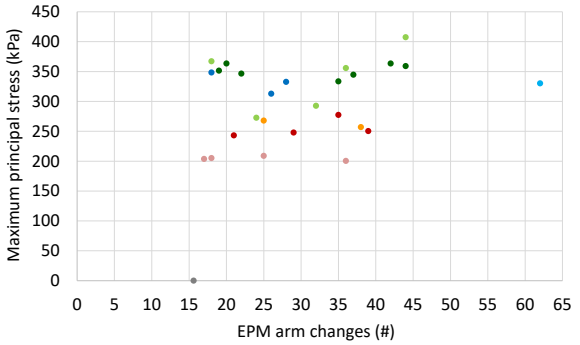

Maximum principal strain

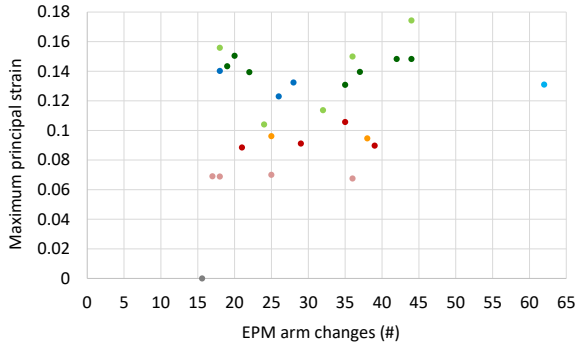

cont.

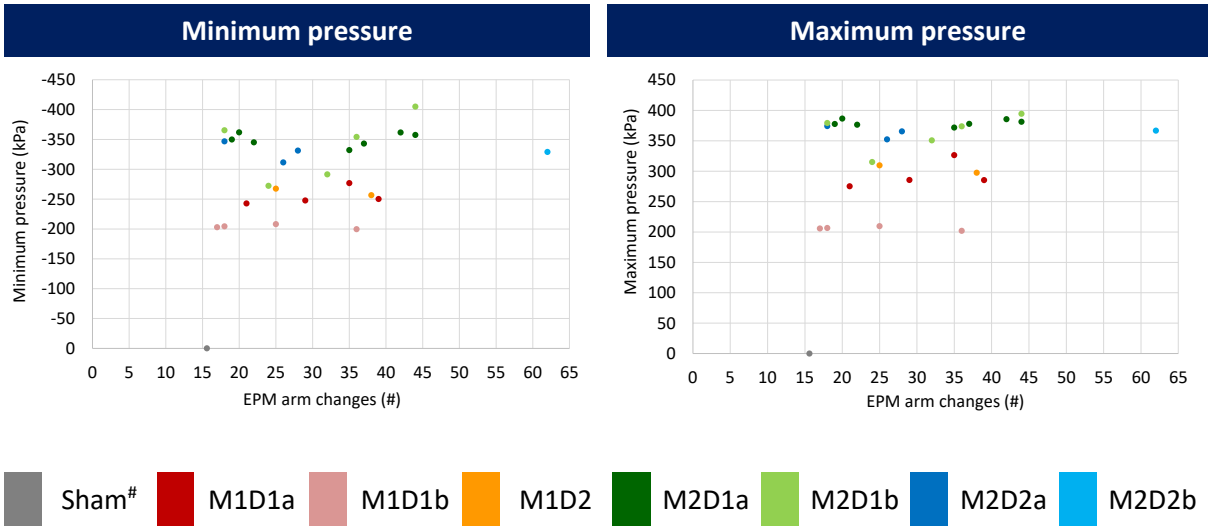

#Since, sham did not go through rotational loading, only their experimental response is marked.

Table C4: Simulation results for entire brain with respect to EPM open duration based on loading group categorization

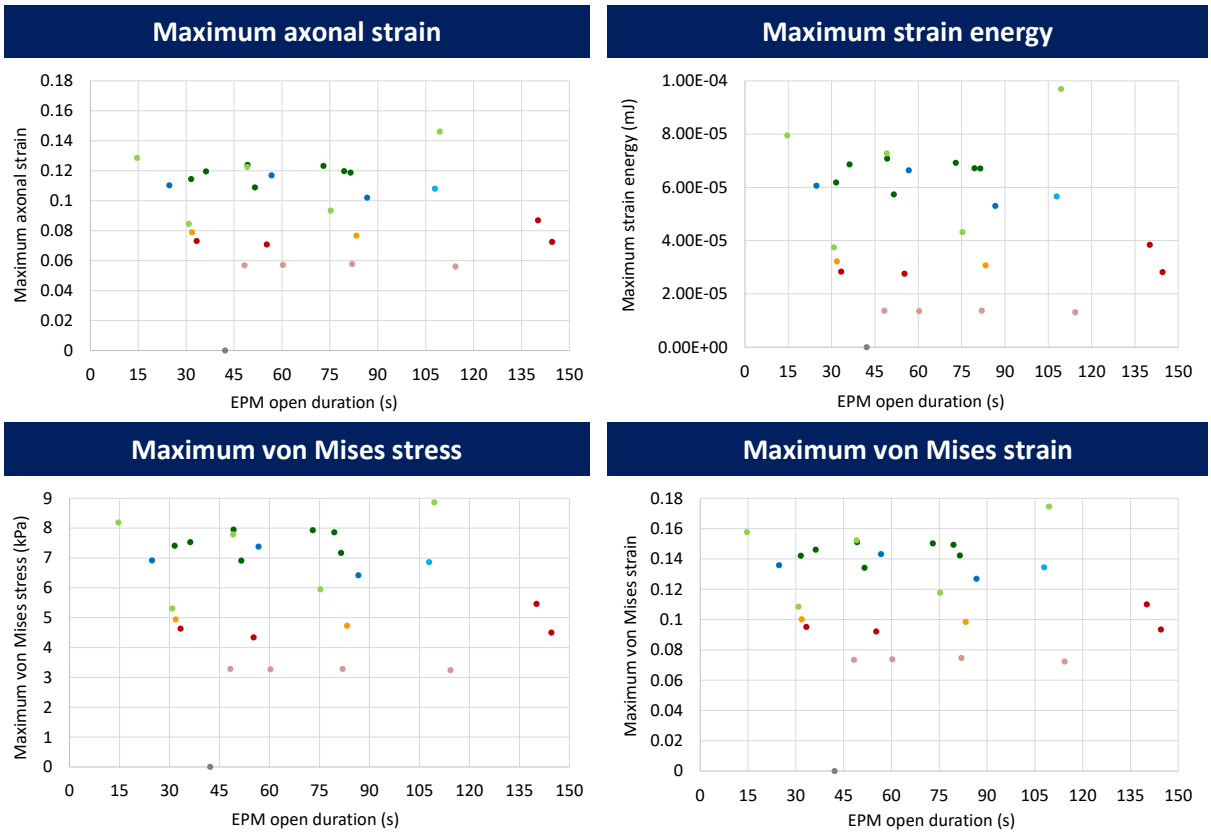

cont.

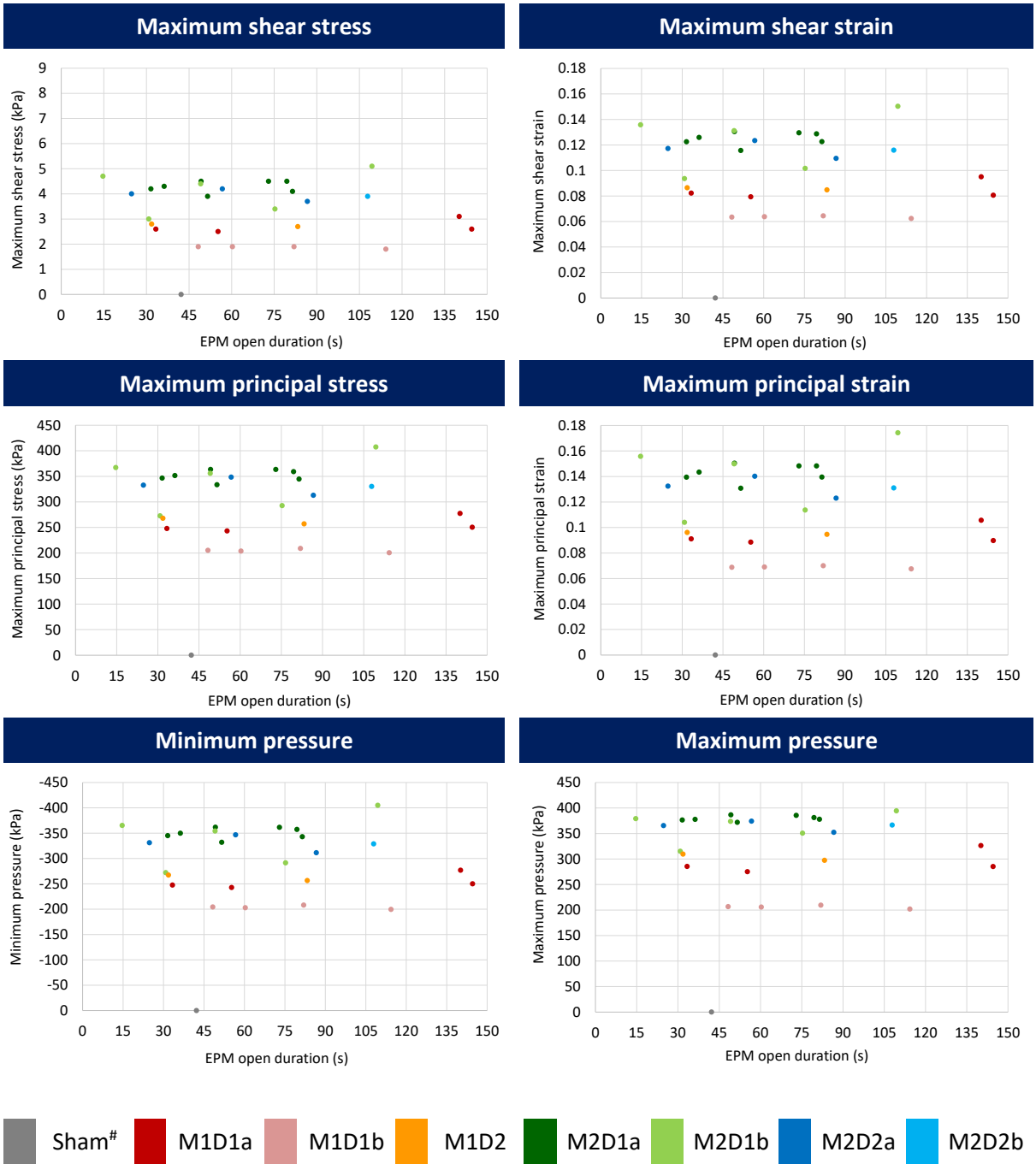

#Since, sham did not go through rotational loading, only their experimental response is marked.

Table C5: Simulation results for entire brain with respect to MWM session I latency based on loading group categorization

Maximum axonal strain

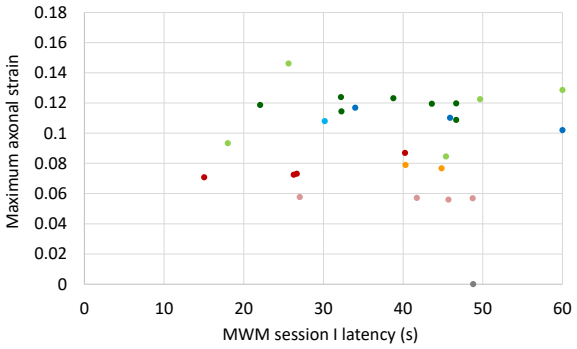

Maximum strain energy

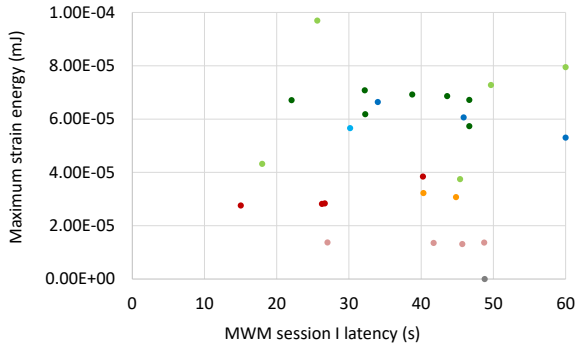

Maximum von Mises stress

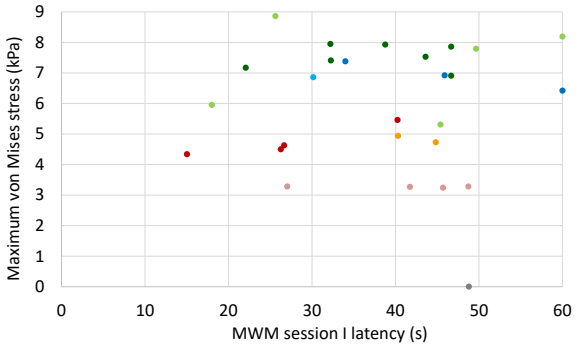

Maximum von Mises strain

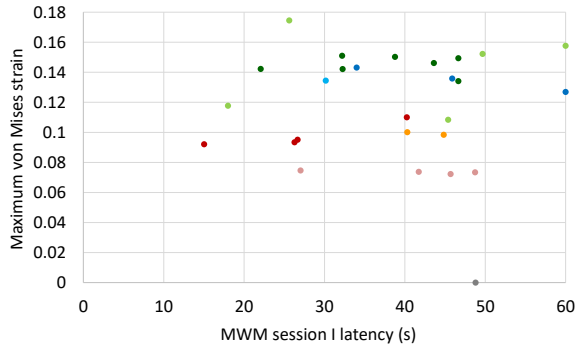

Maximum shear stress

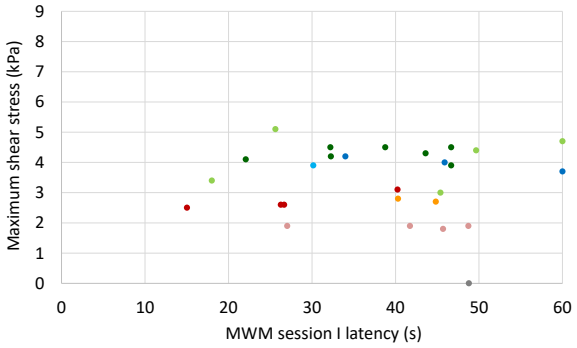

Maximum shear strain

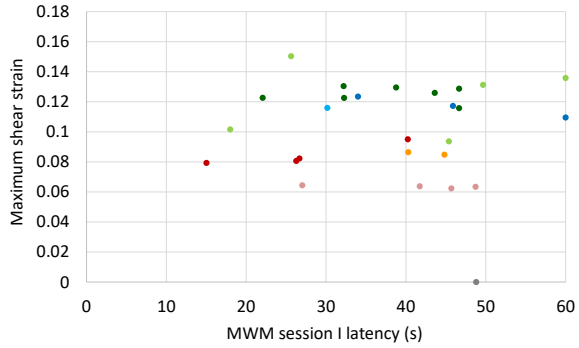

Maximum principal stress

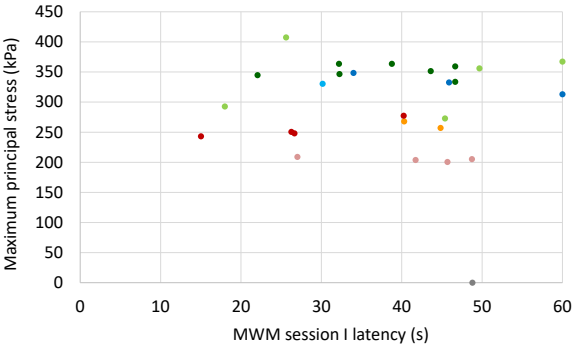

Maximum principal strain

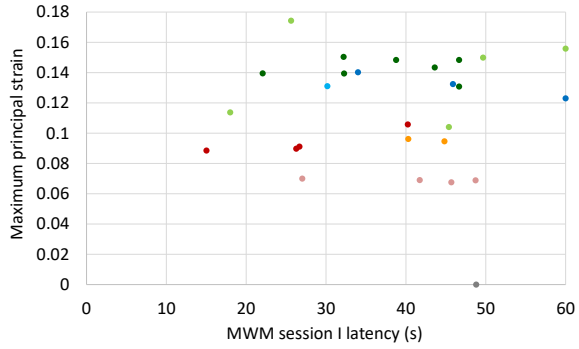

cont.

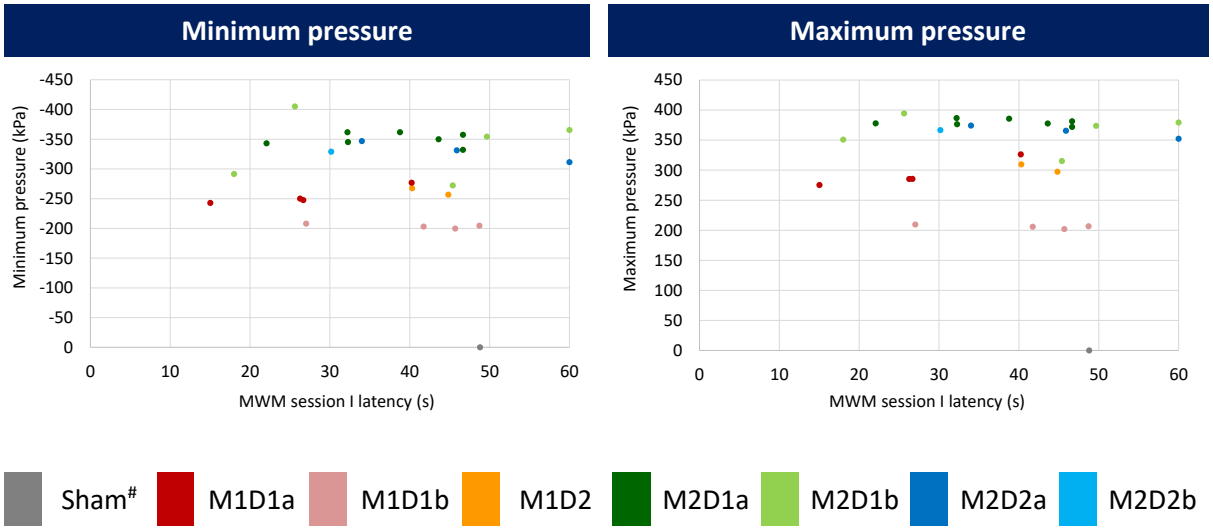

#Since, sham did not go through rotational loading, only their experimental response is marked.

Table C6: Simulation results for entire brain with respect to MWM session II latency based on loading group categorization

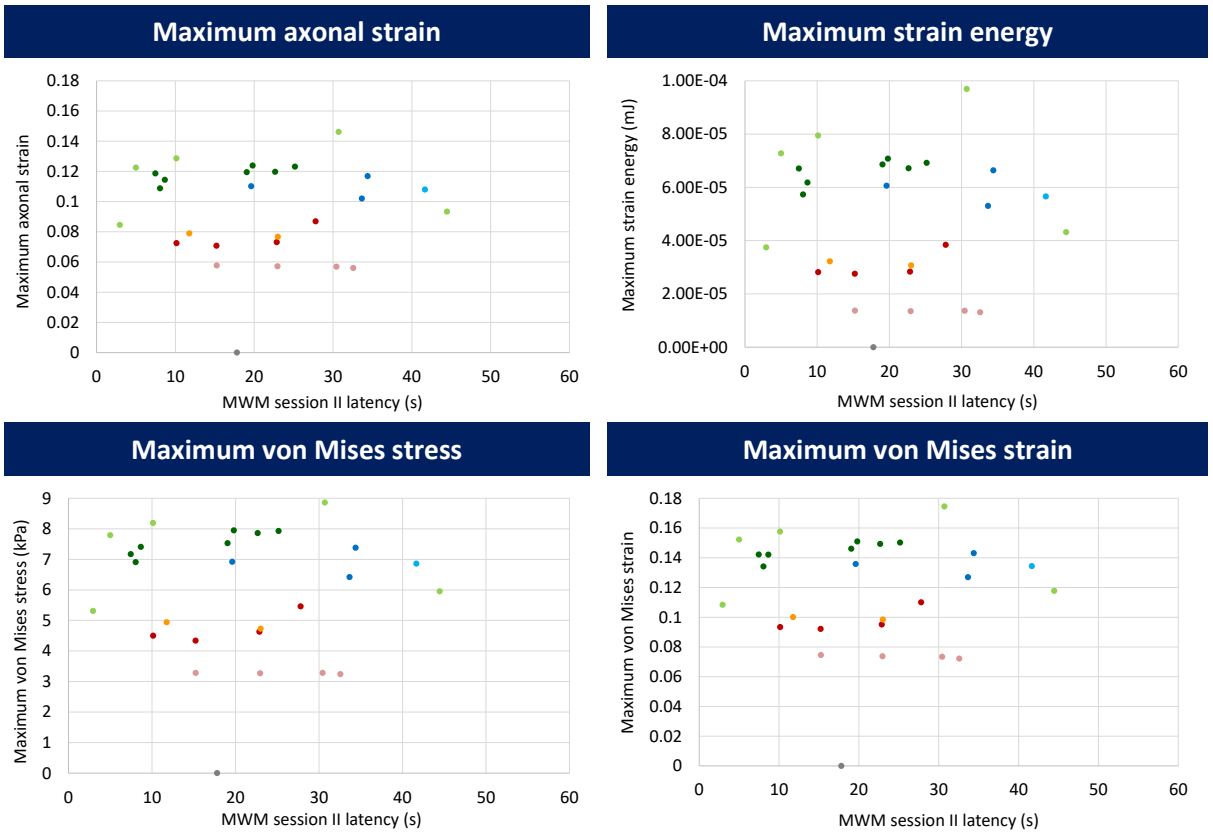

cont.

Maximum shear stress

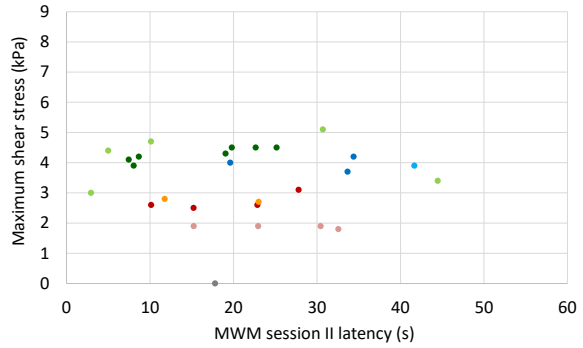

Maximum shear strain

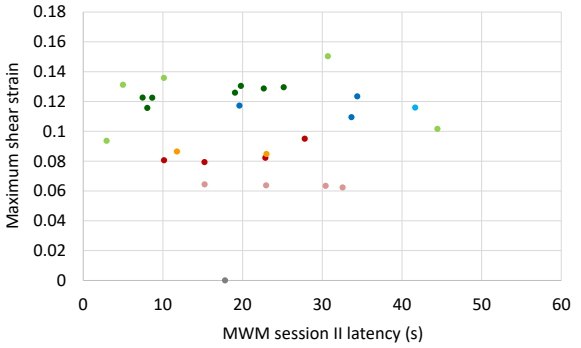

Maximum principal stress

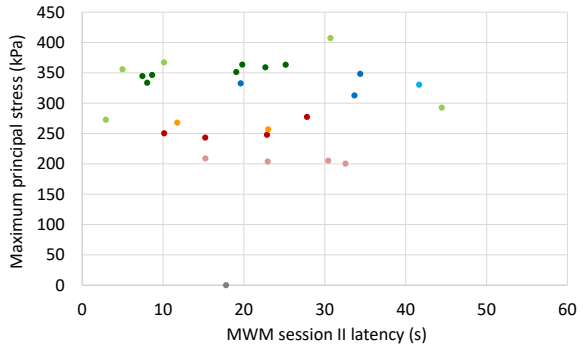

Maximum principal strain

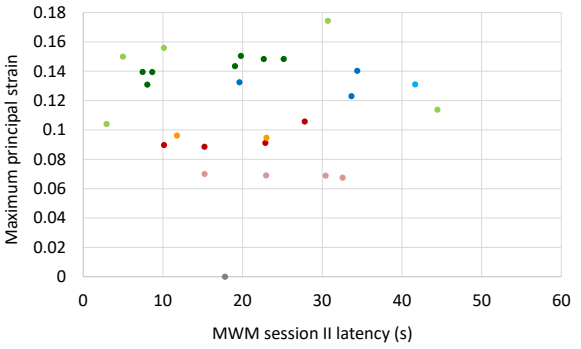

Minimum pressure

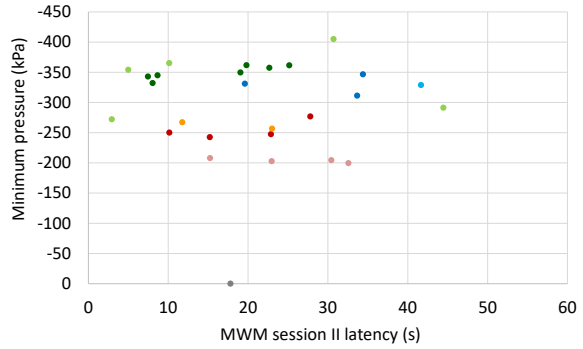

Maximum pressure

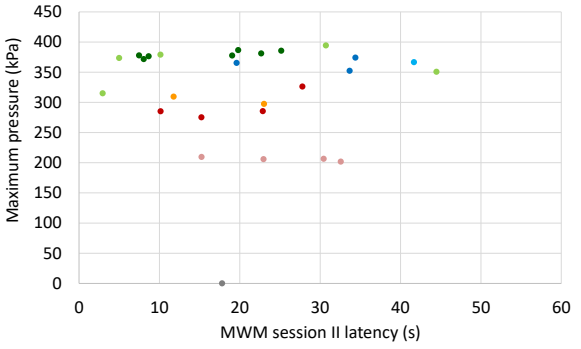

Sham[#] M1D1a M1D1b M1D2 M2D1a M2D1b M2D2a M2D2b

[#]Since, sham did not go through rotational loading, only their experimental response is marked.

Table C7: Simulation results for entire brain with respect to MWM session III latency based on loading group categorization

Maximum axonal strain

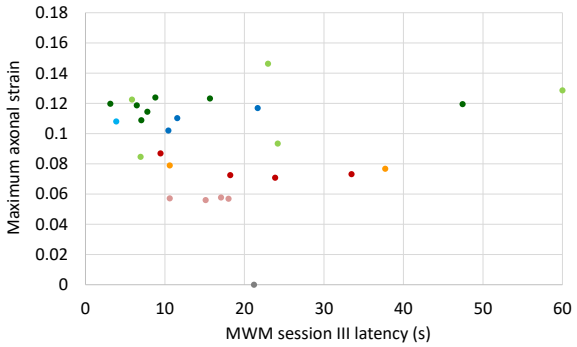

Maximum strain energy

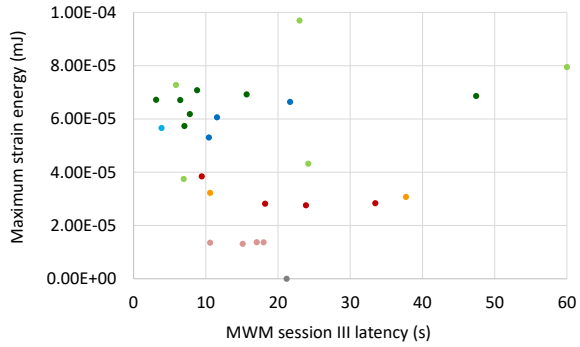

Maximum von Mises stress

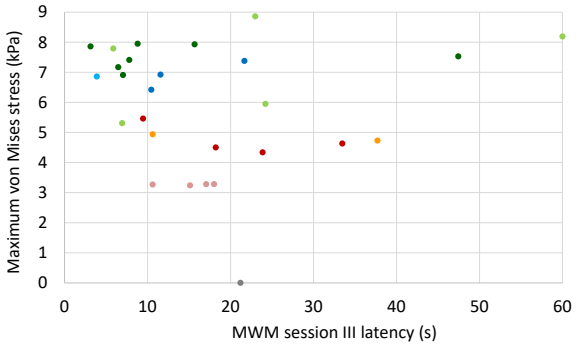

Maximum von Mises strain

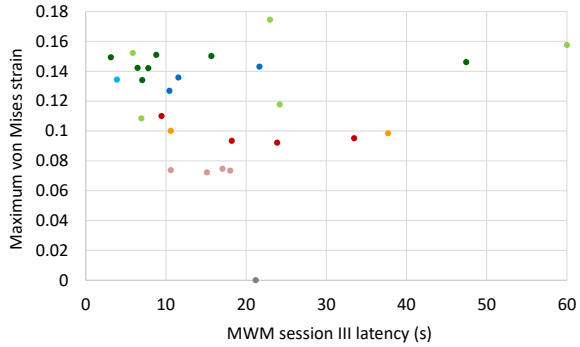

Maximum shear stress

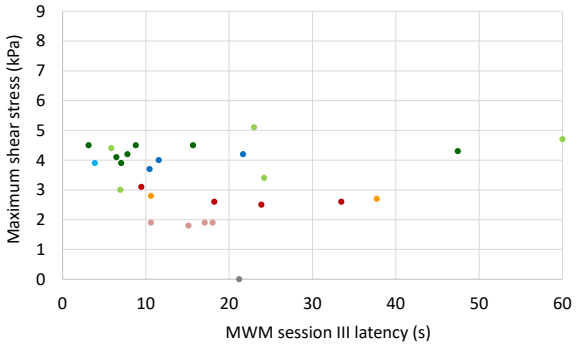

Maximum shear strain

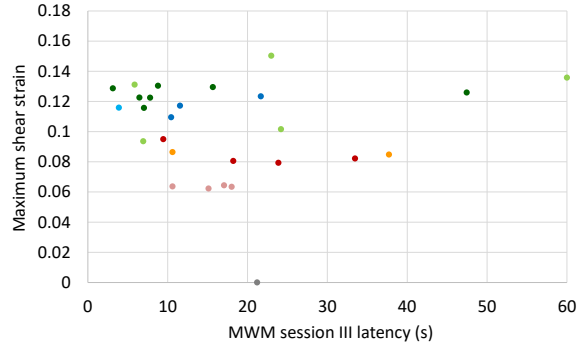

Maximum principal stress

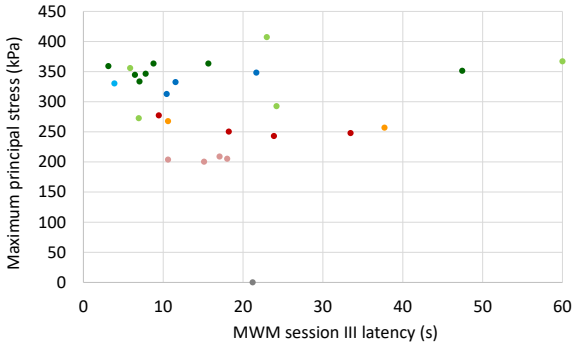

Maximum principal strain

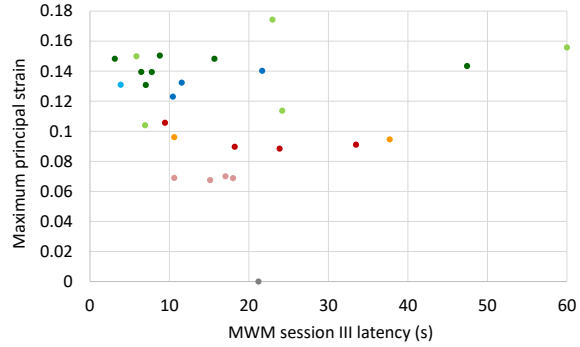

cont.

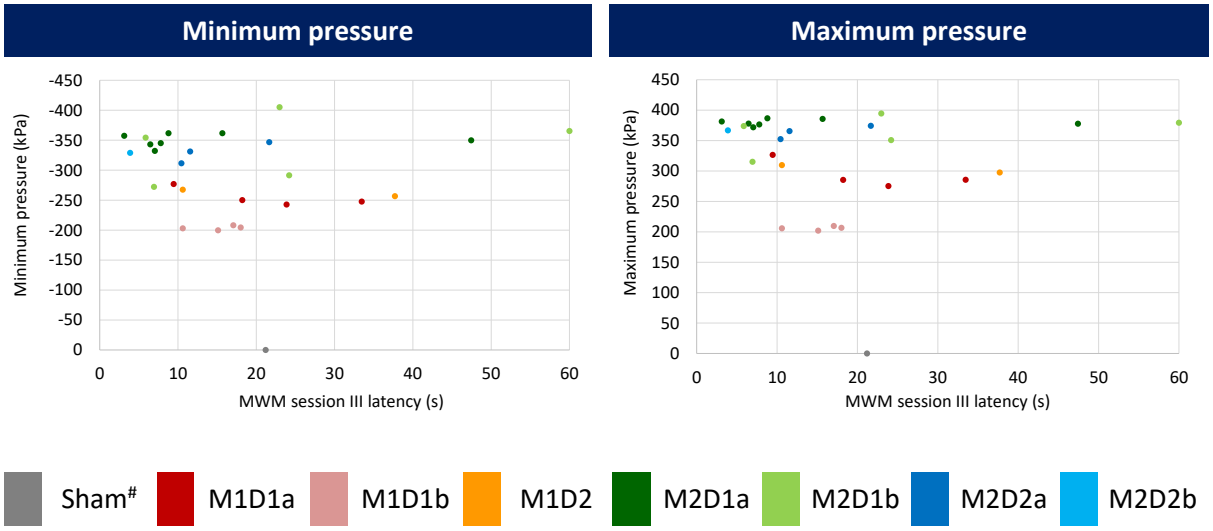

#Since, sham did not go through rotational loading, only their experimental response is marked.

Annexure D: Simulation results for entire brain based on injured and non-injured groups

Simulation results of all twenty-six experimental cases for all ten mechanical parameters, which are maximum axonal strain, maximum strain energy, maximum von Mises stress and strain, maximum shear stress and strain, maximum principal stress and strain and minimum and maximum pressures for the entire brain associated with consciousness, activity, emotionality and cognition are given below in Table D1 to Table D7. Results are categorized based on seven experimental behavioural responses in injured (solid red columns) and non-injured (blank green columns) groups.

Table D1: Simulation results for the entire brain. Case categorization into non-injured and injured groups is based on unconsciousness time.

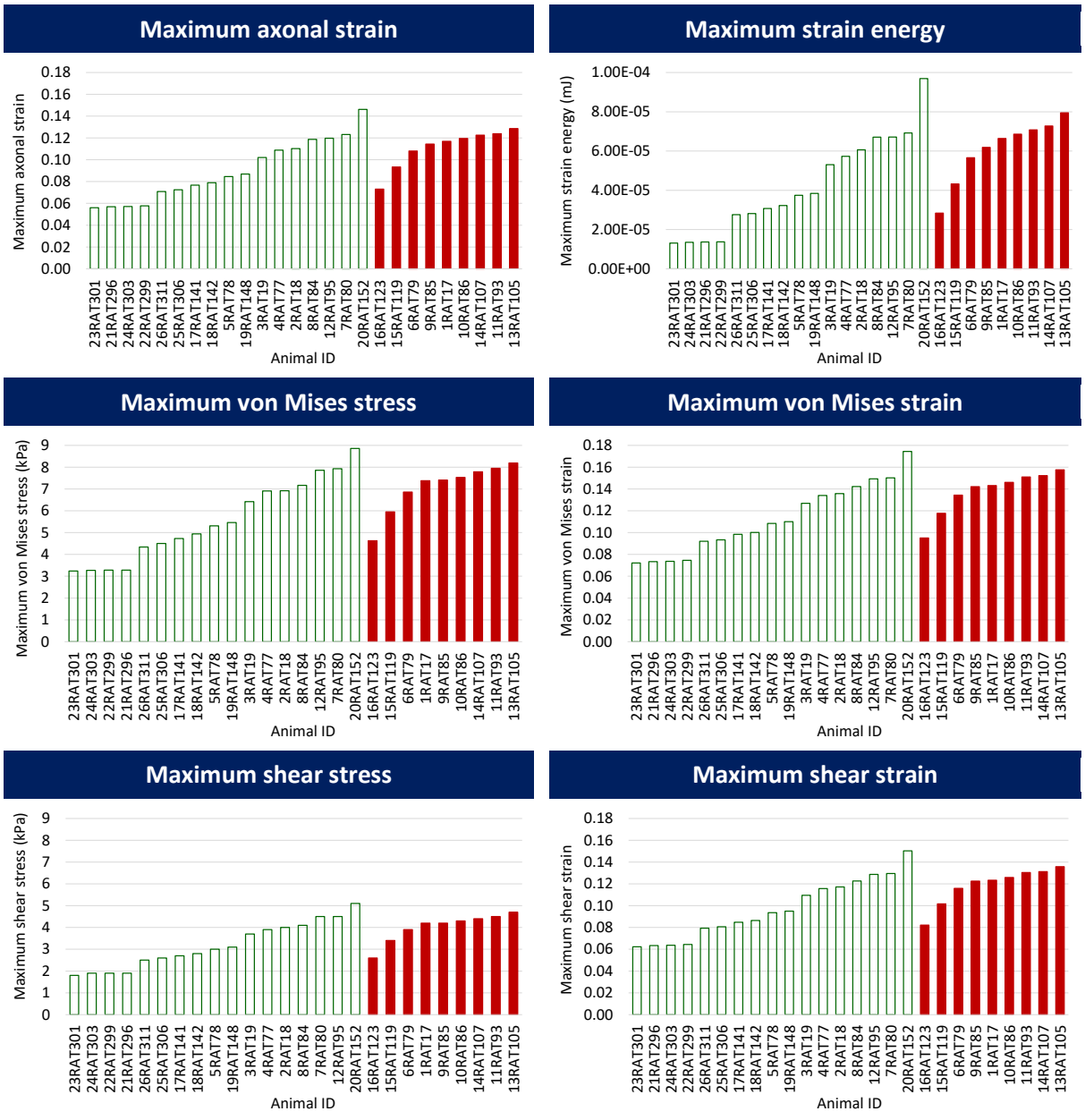

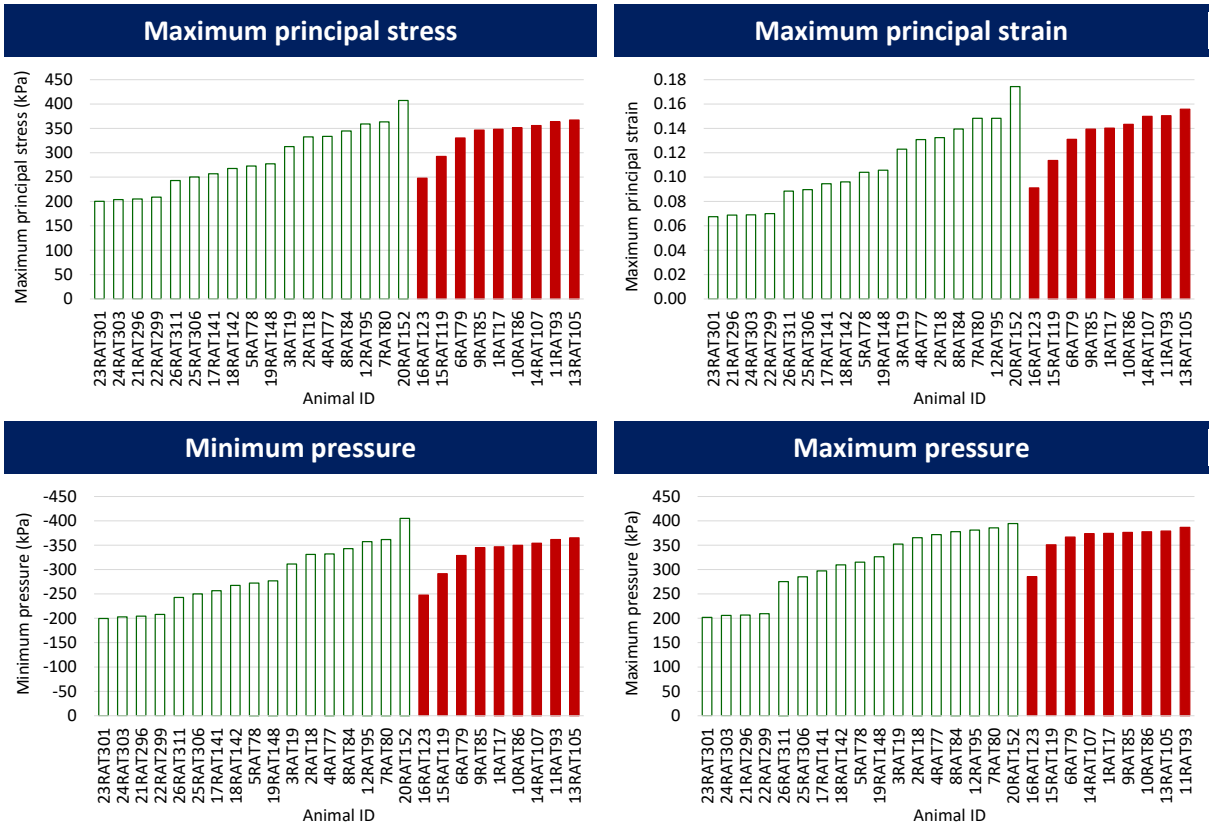

Table D2: Simulation results for the entire brain. Case categorization into non-injured and injured groups is based on EPM distance travelled.

cont.

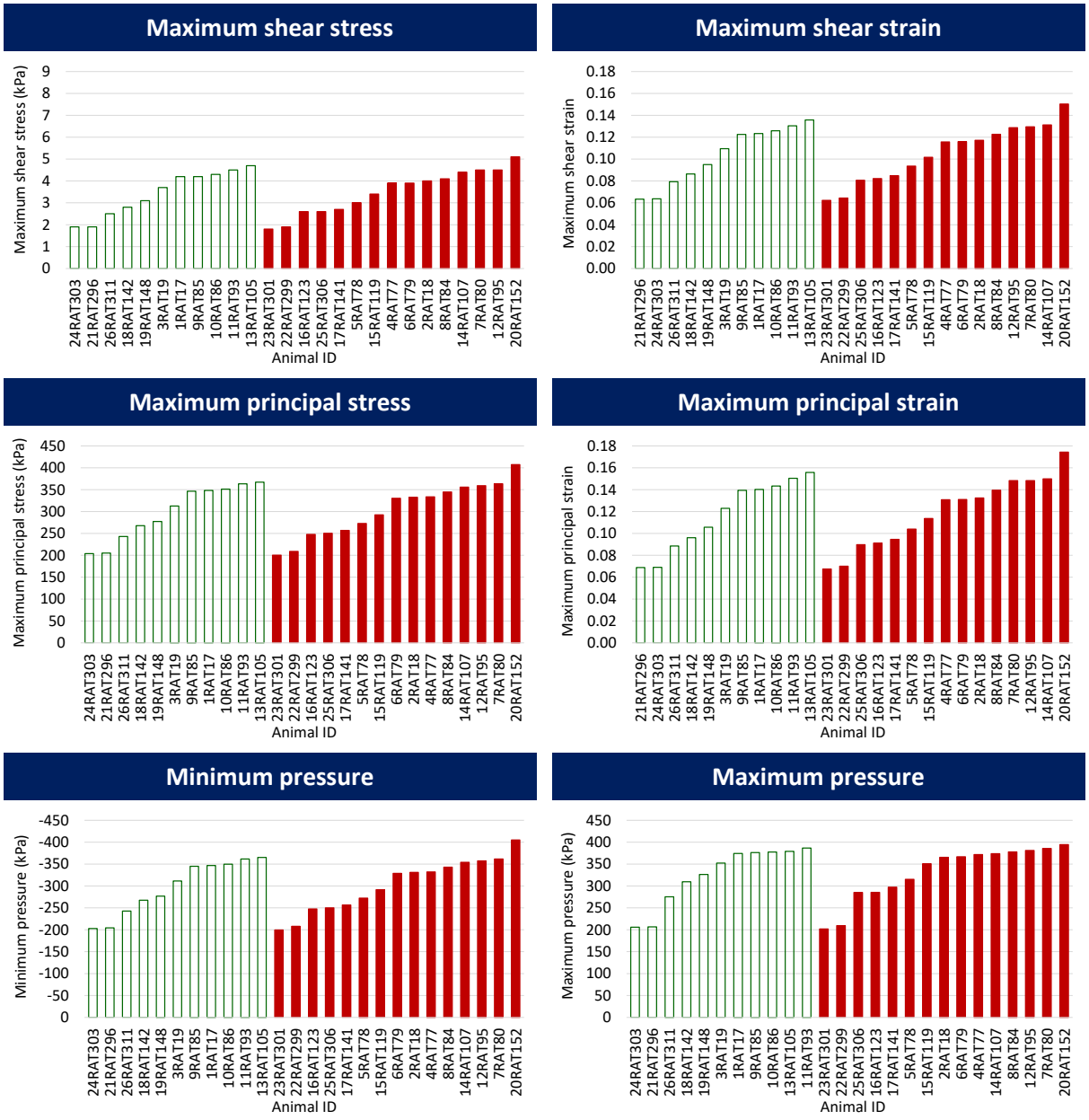

Table D3: Simulation results for the entire brain. Case categorization into non-injured and injured groups is based on EPM arm changes.

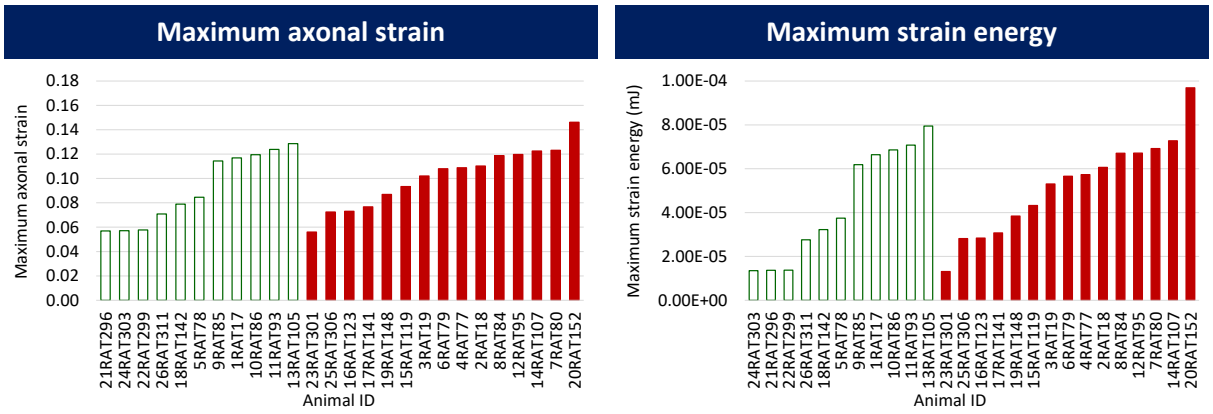

cont.

Maximum von Mises stress

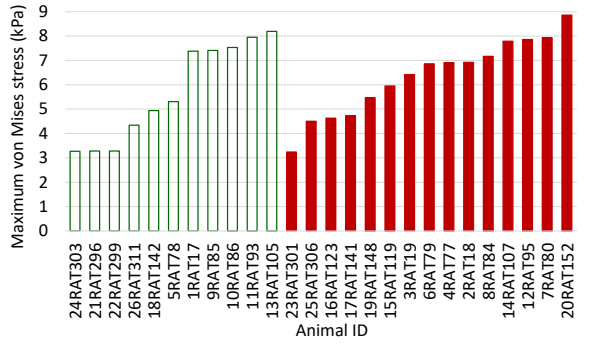

Maximum von Mises strain

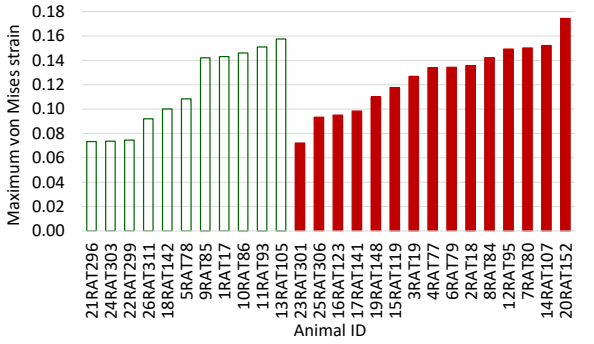

Maximum shear stress

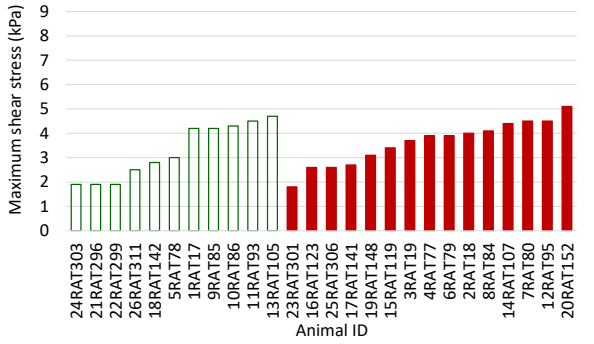

Maximum shear strain

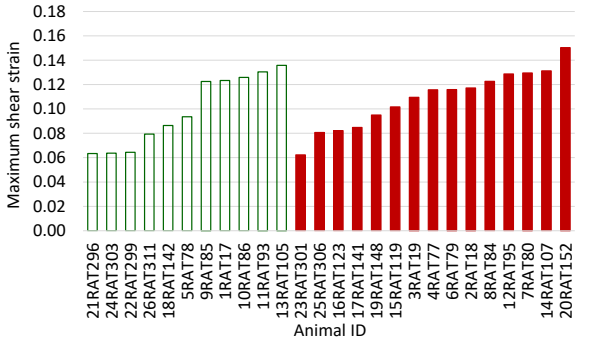

Maximum principal stress

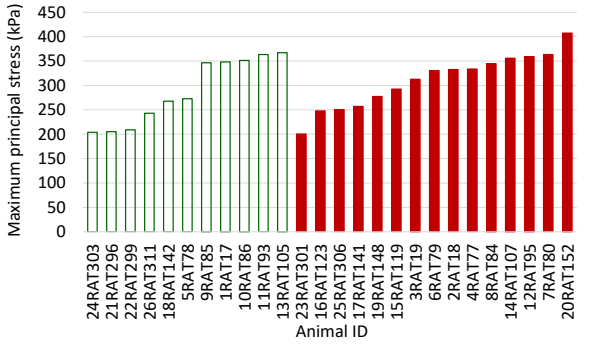

Maximum principal strain

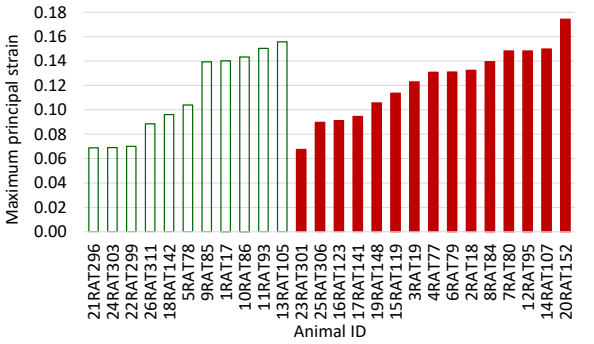

Minimum pressure

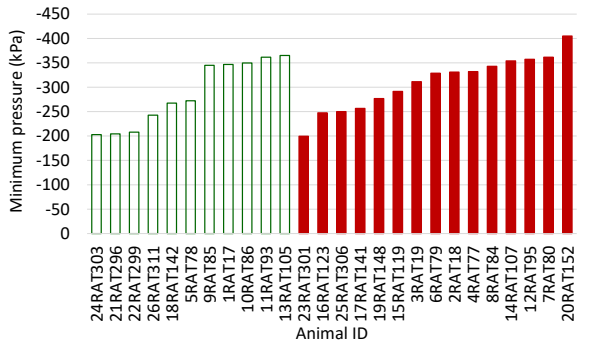

Maximum pressure

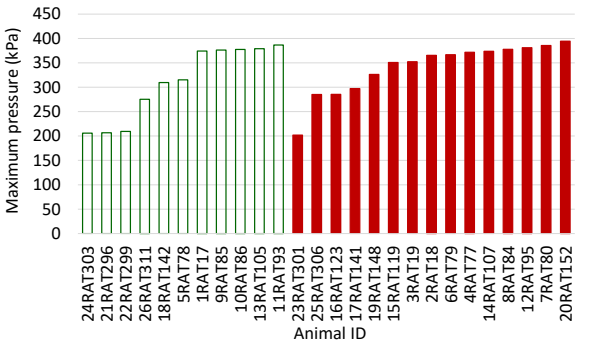

Table D4: Simulation results for the entire brain. Case categorization into non-injured and injured groups is based on EPM open duration.

Maximum axonal strain

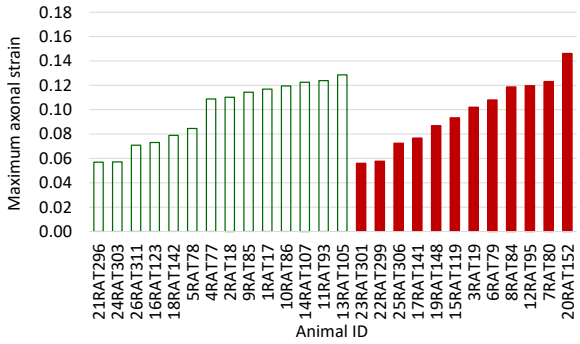

Maximum strain energy

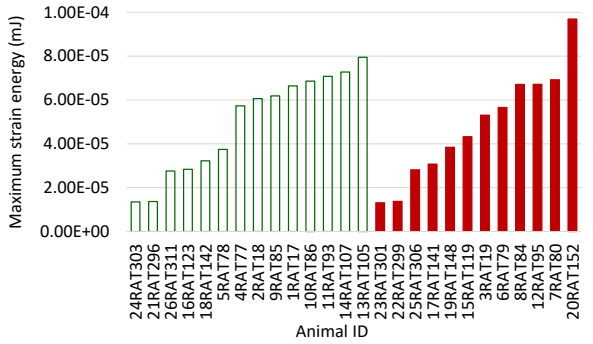

Maximum von Mises stress

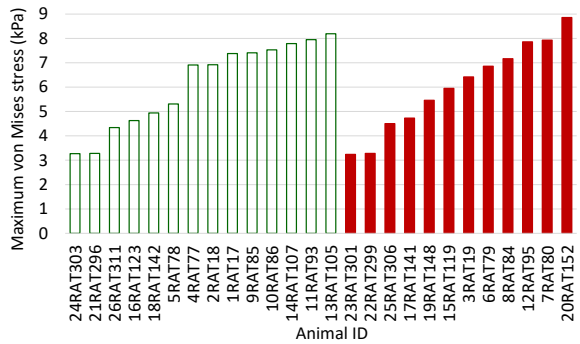

Maximum von Mises strain

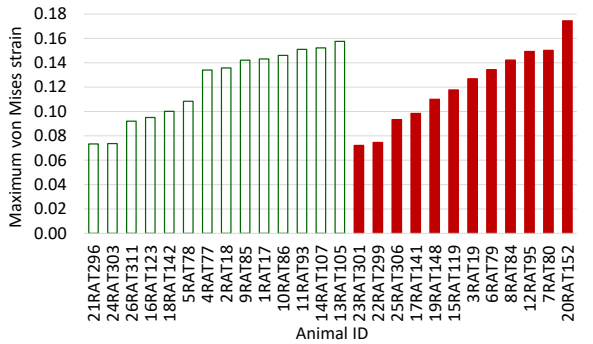

Maximum shear stress

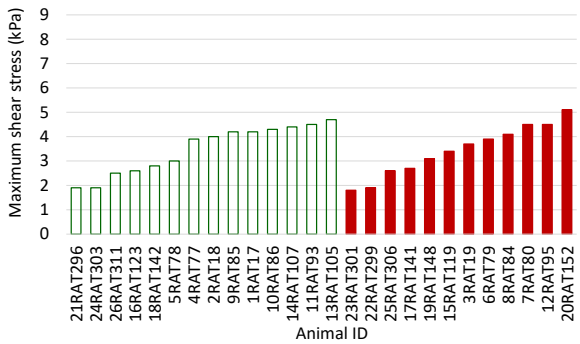

Maximum shear strain

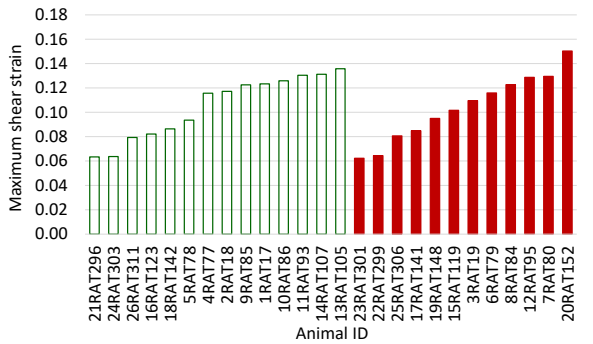

Maximum principal stress

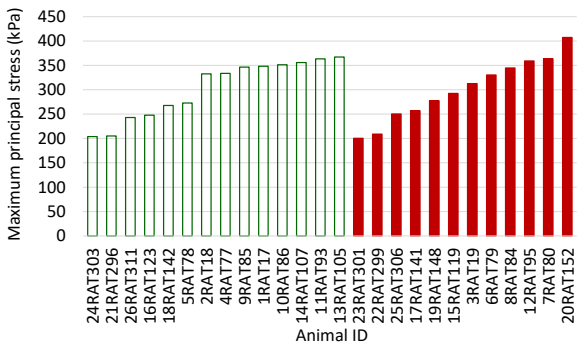

Maximum principal strain

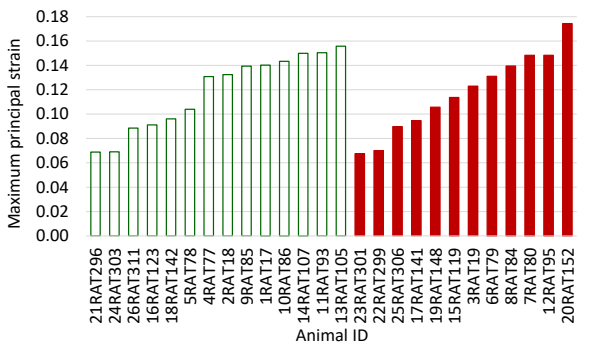

cont.

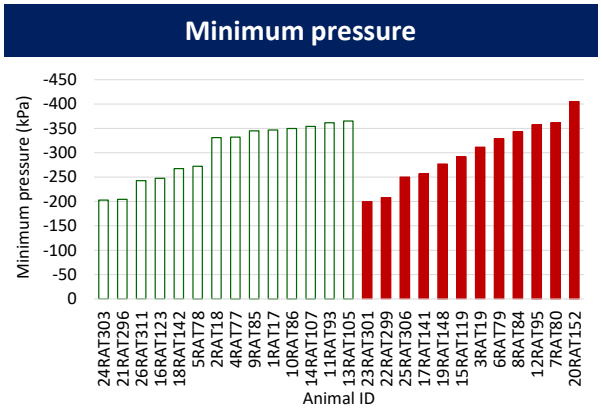

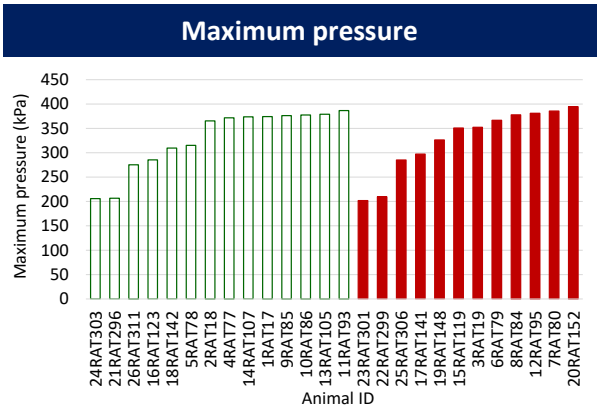

Table D5: Simulation results for the entire brain. Case categorization into non-injured and injured groups is based on MWM session I latency.

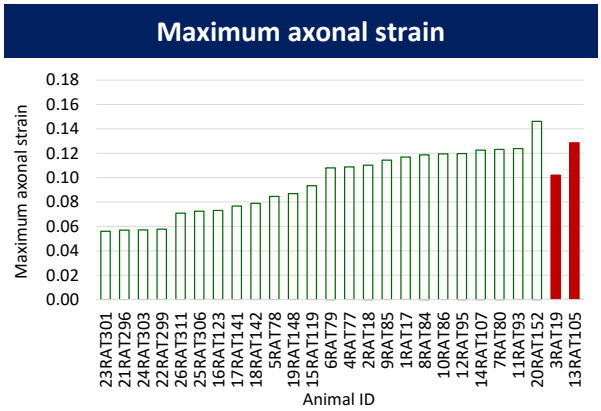

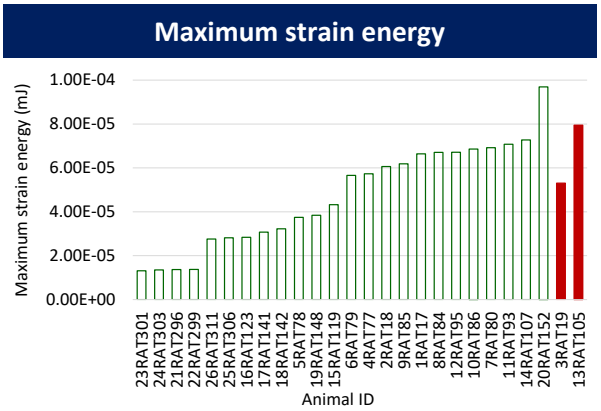

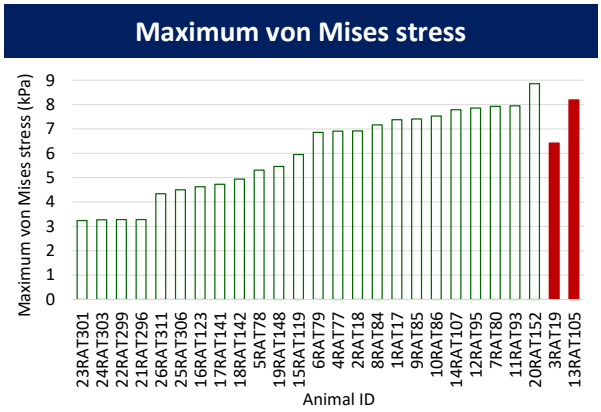

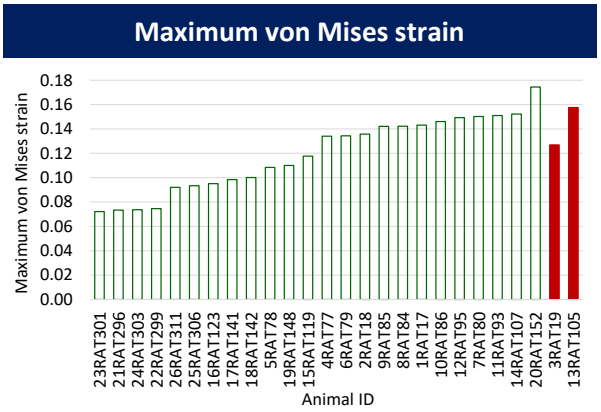

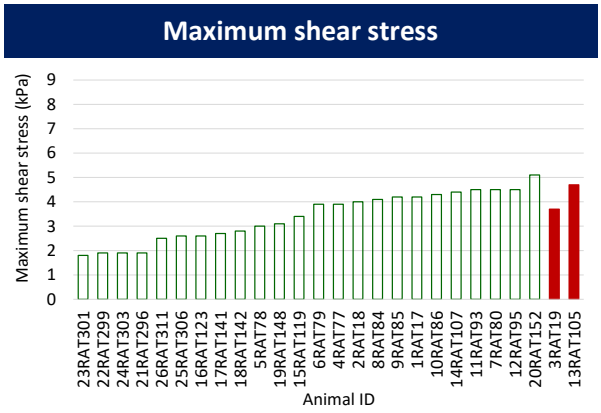

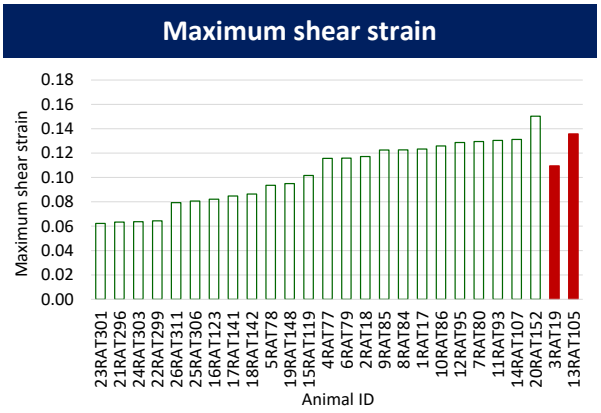

cont.

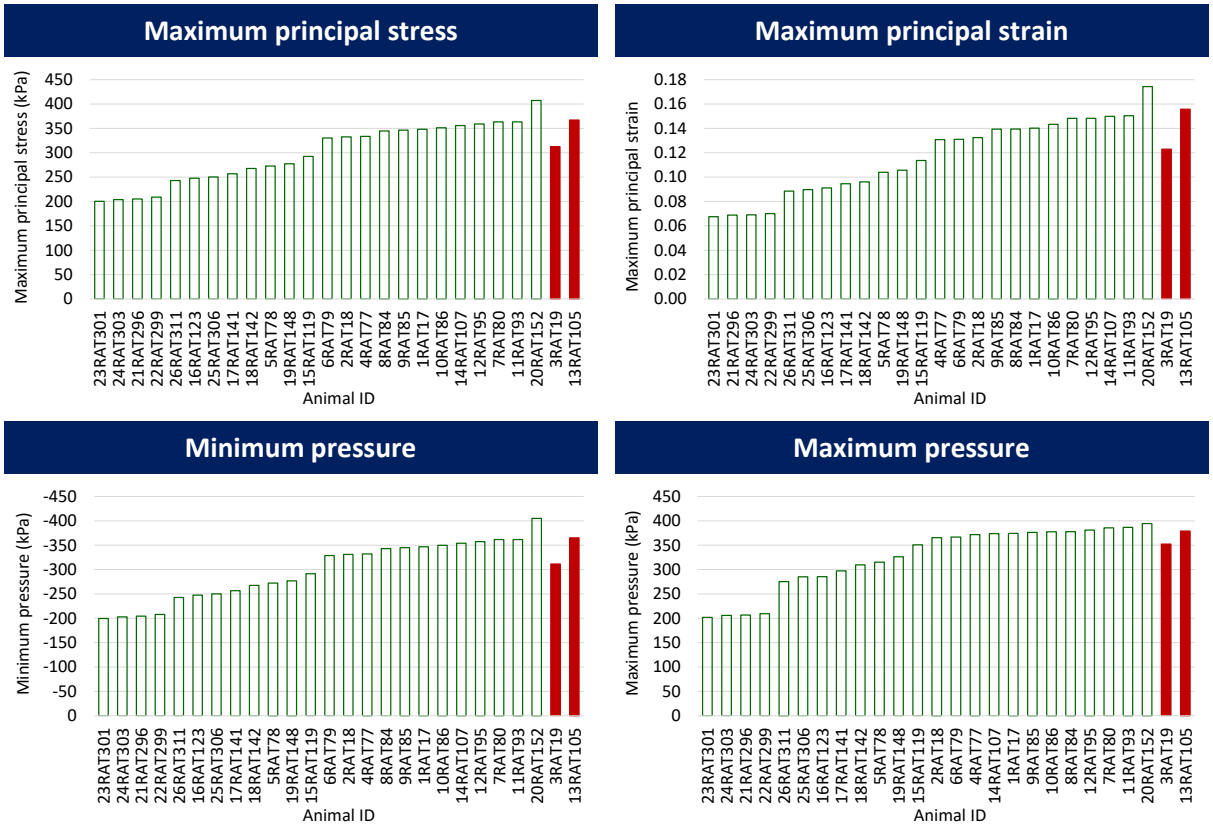

Table D6: Simulation results for the entire brain. Case categorization into non-injured and injured groups is based on MWM session II latency.

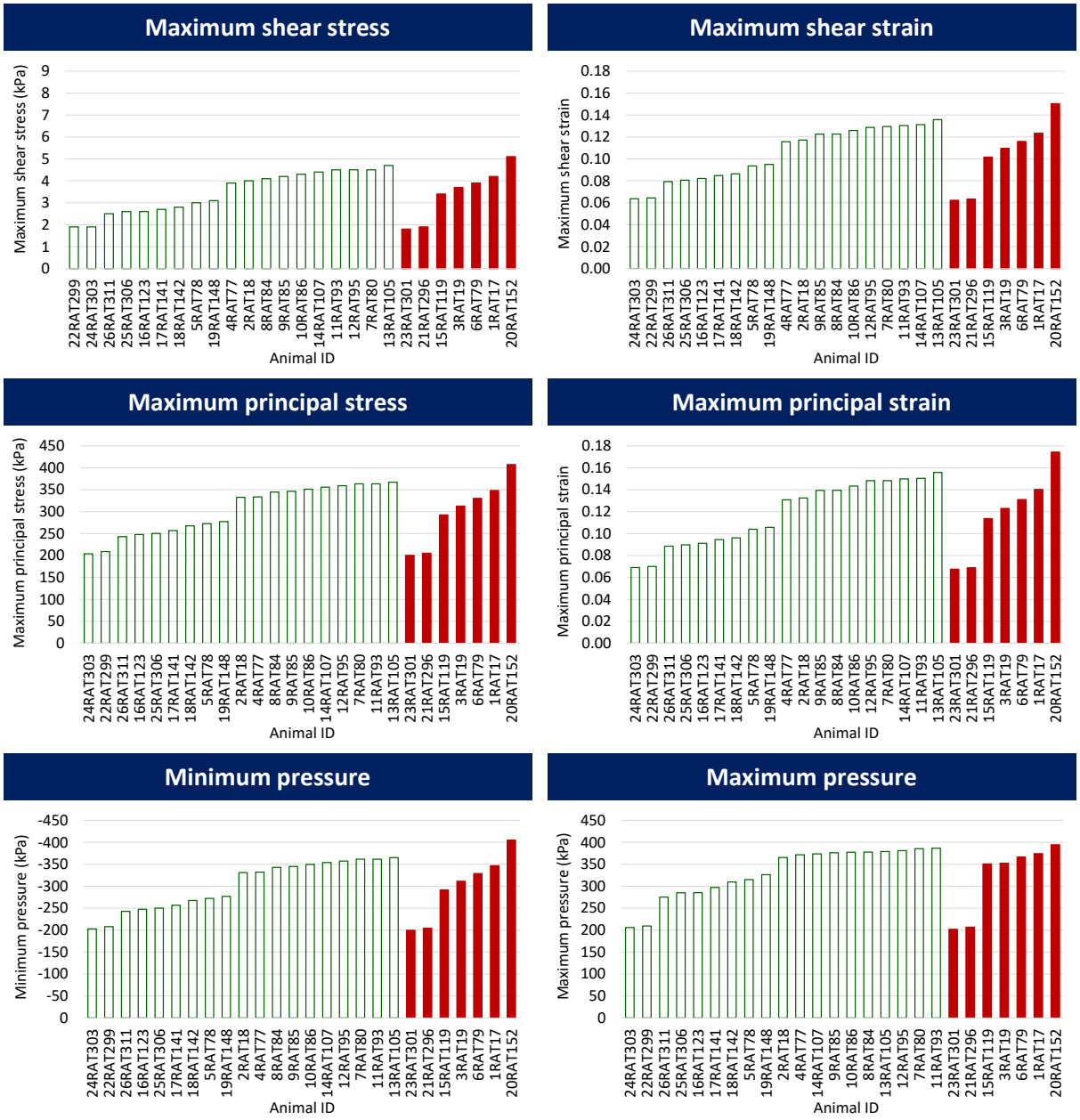

Table D7: Simulation results for the entire brain. Case categorization into non-injured and injured groups is based on MWM session III latency.

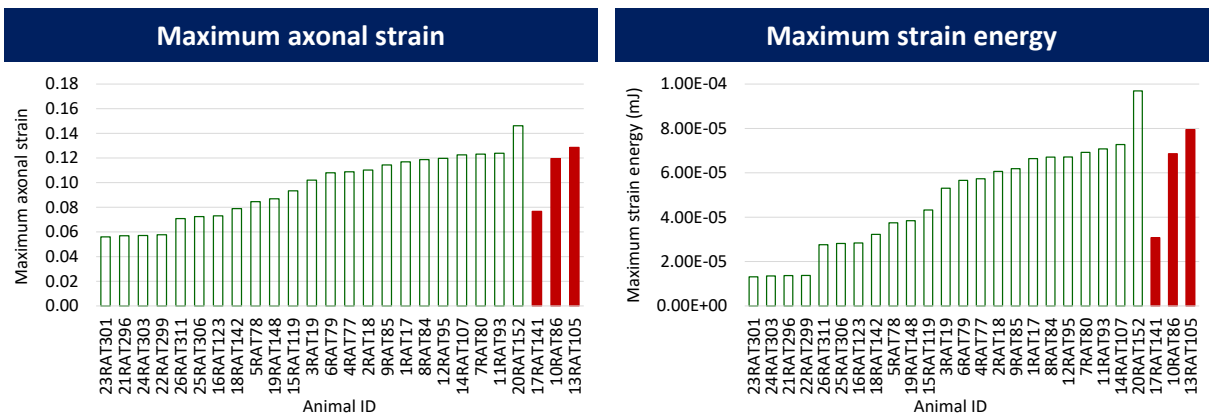

Maximum von Mises stress

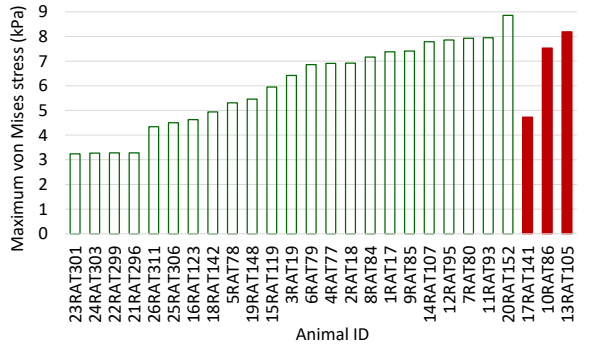

Maximum von Mises strain

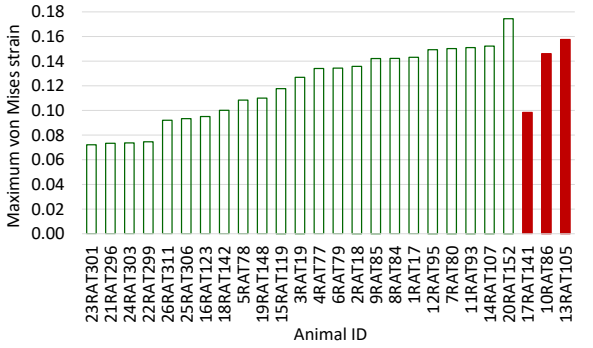

Maximum shear stress

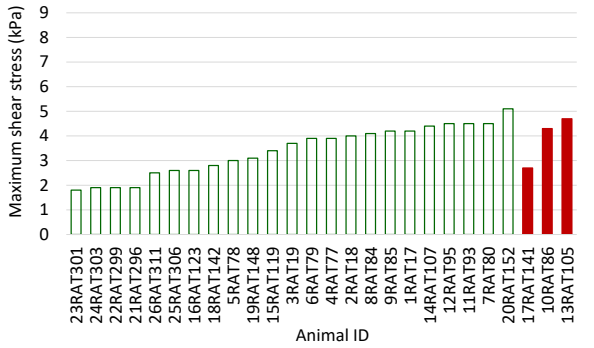

Maximum shear strain

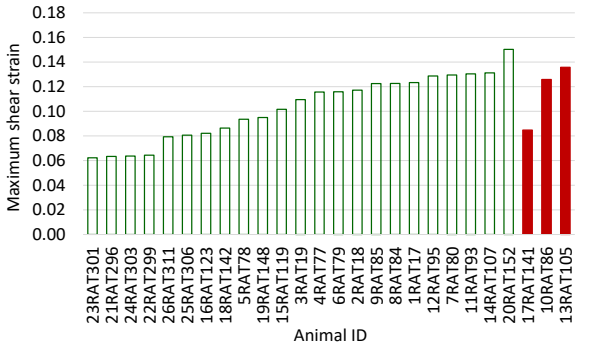

Maximum principal stress

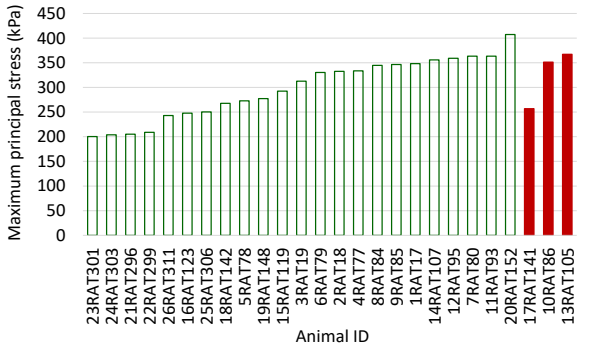

Maximum principal strain

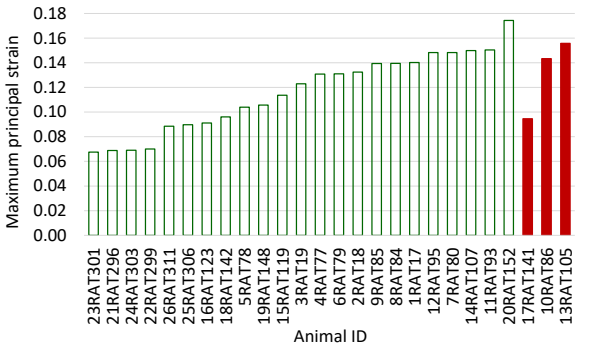

Minimum pressure

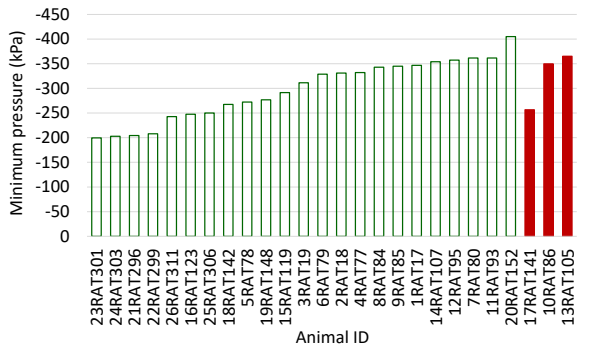

Maximum pressure

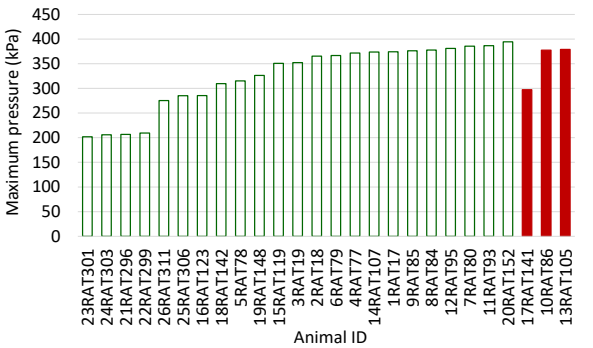

Annexure E: Simulation results for functional brain regions

Simulation results of all twenty-six experimental cases for all ten mechanical parameters, which are maximum axonal strain, maximum strain energy, maximum von Mises stress and strain, maximum shear stress and strain, maximum principal stress and strain and minimum and maximum pressures for the specific brain regions associated with consciousness are given below in Table E1 to Table E7. Results are categorized based on seven experimental behavioural responses in injured (solid red columns) and non-injured (blank green columns) groups.

Table E1: Simulation results for brain regions associated with consciousness. Case categorization into non-injured and injured groups is based on unconsciousness time.

Maximum axonal strain

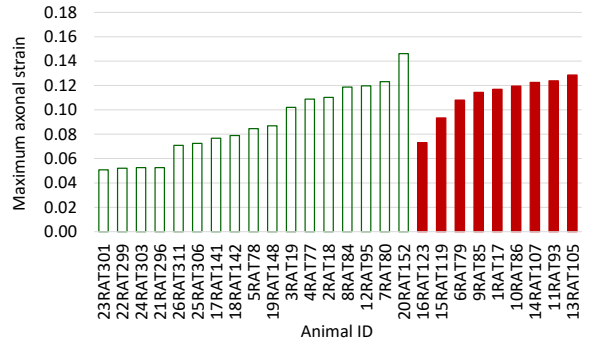

Maximum strain energy

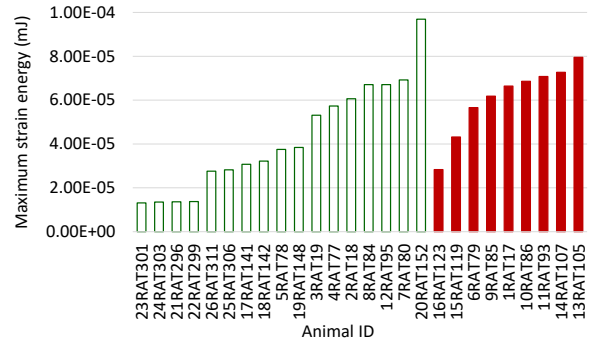

Maximum von Mises stress

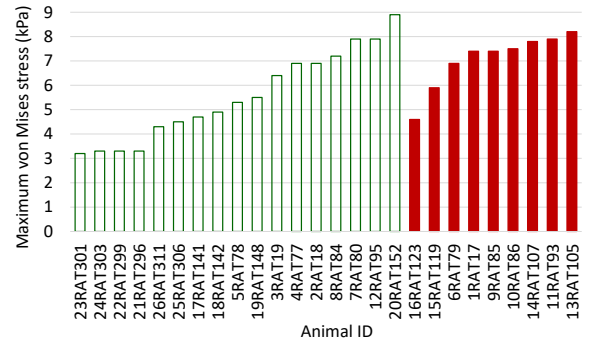

Maximum von Mises strain

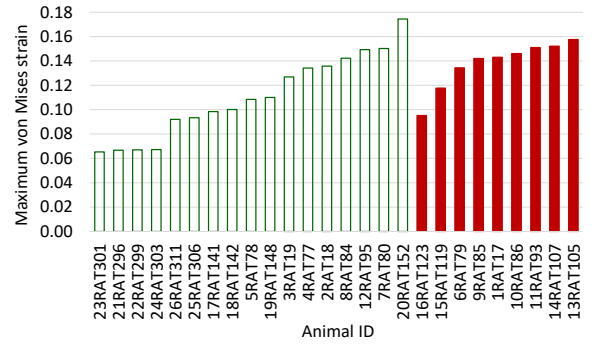

Maximum shear stress

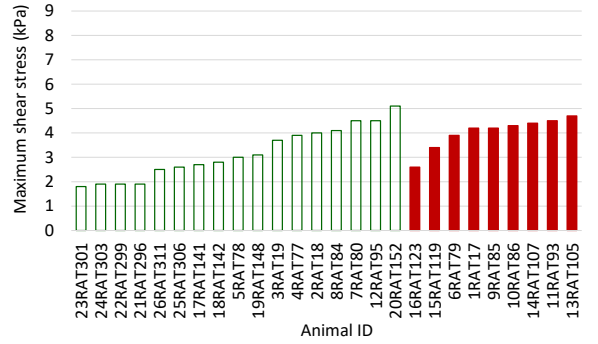

Maximum shear strain

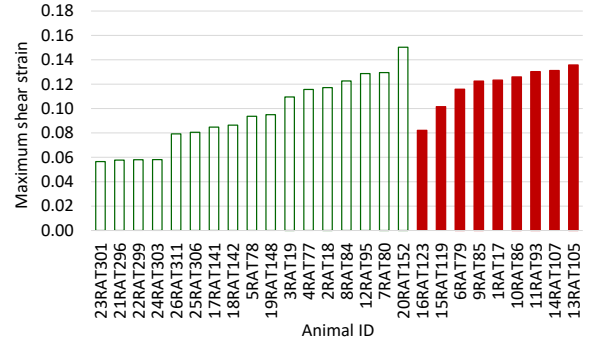

cont.

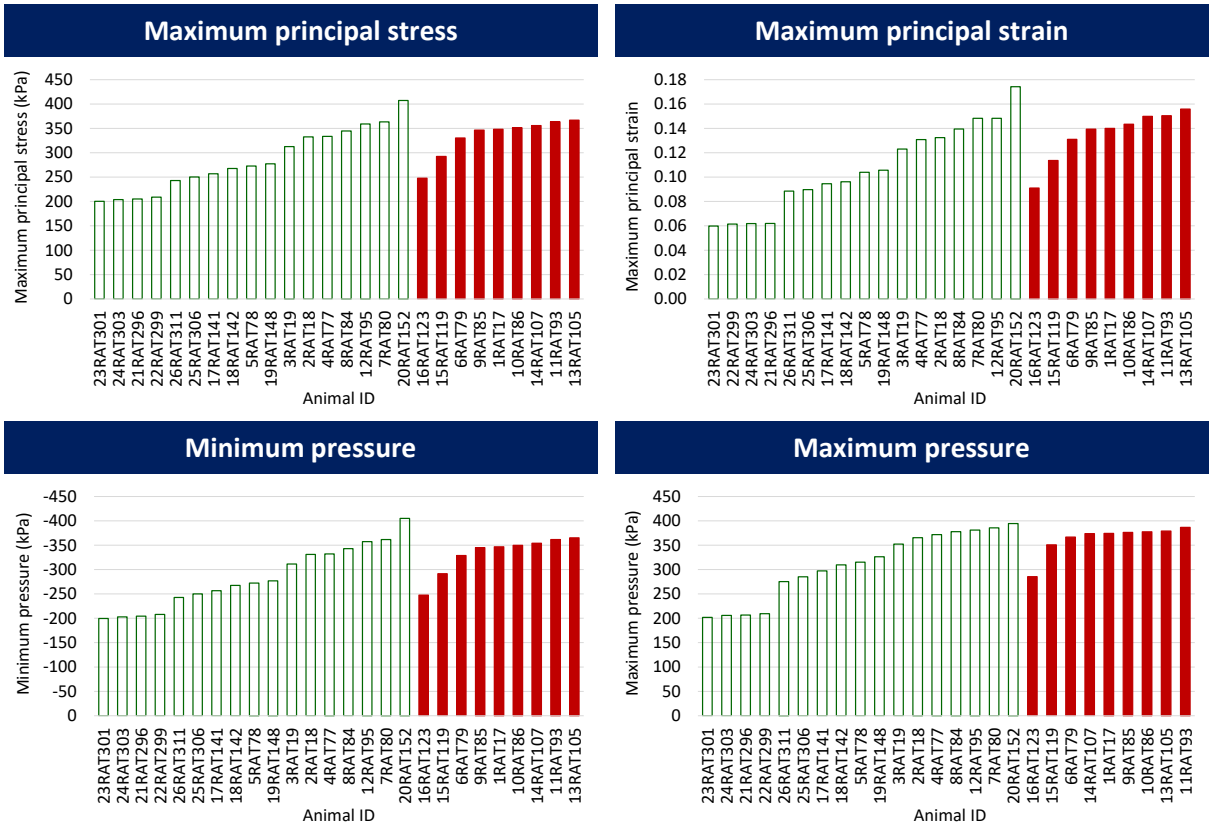

Table E2: Simulation results for brain regions associated with consciousness. Case categorization into non-injured and injured groups is based on EPM distance travelled.

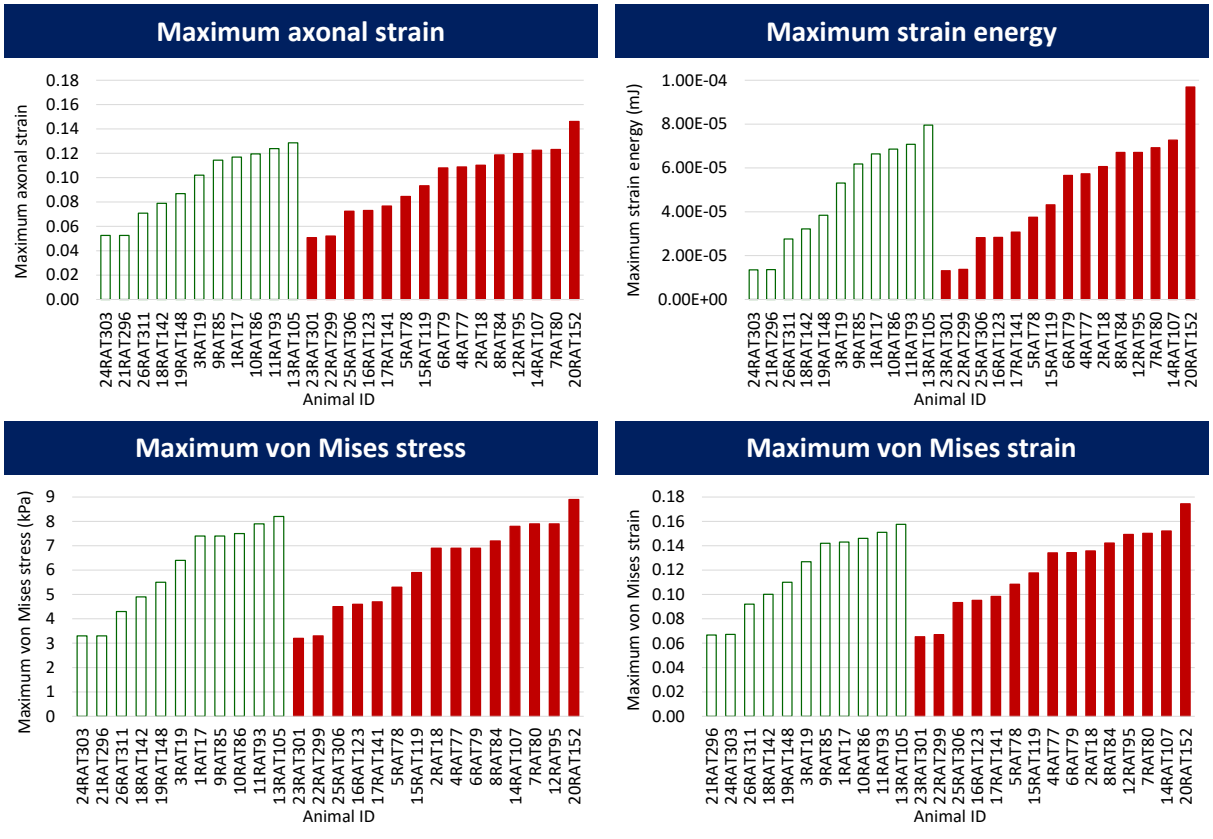

cont.

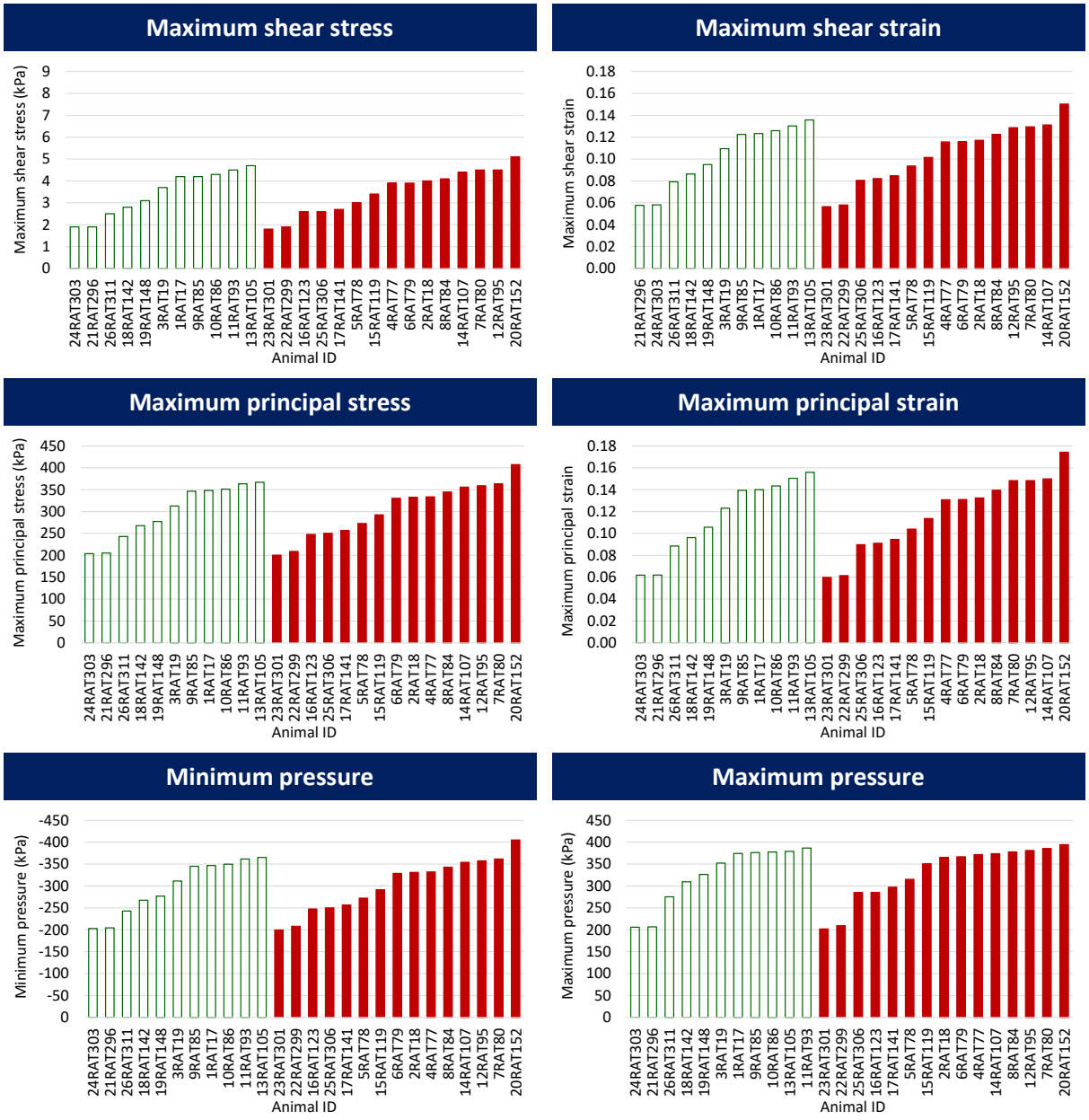

Table E3: Simulation results for brain regions associated with consciousness. Case categorization into non-injured and injured groups is based on EPM arm changes.

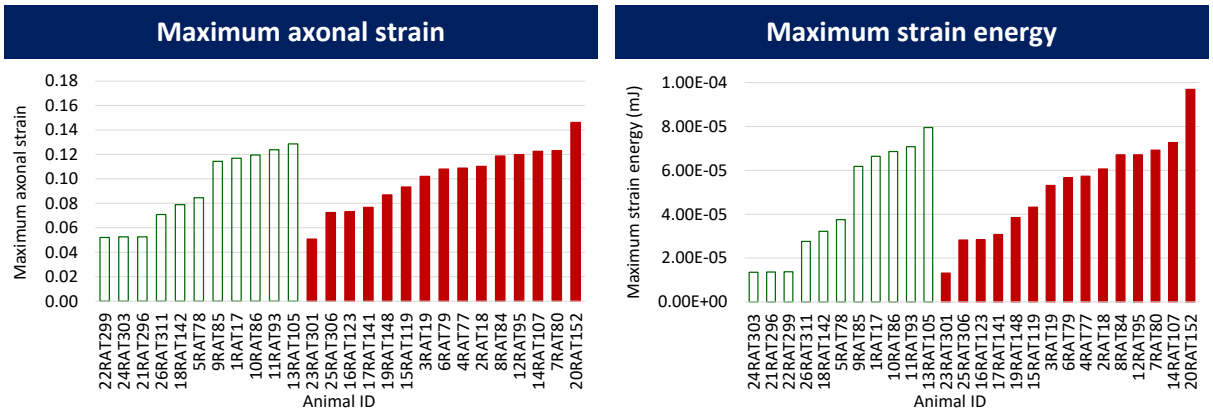

cont.

Maximum von Mises stress

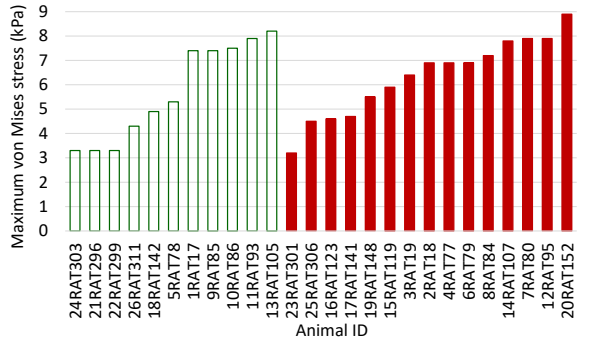

Maximum von Mises strain

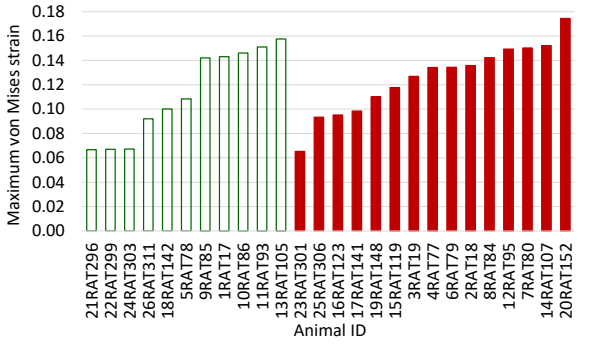

Maximum shear stress

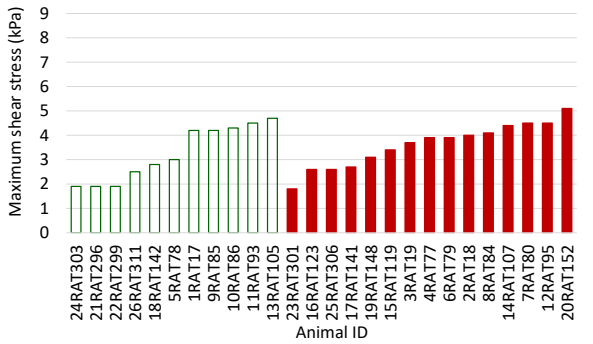

Maximum shear strain

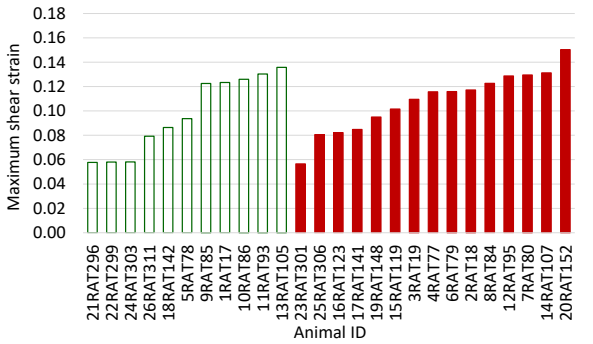

Maximum principal stress

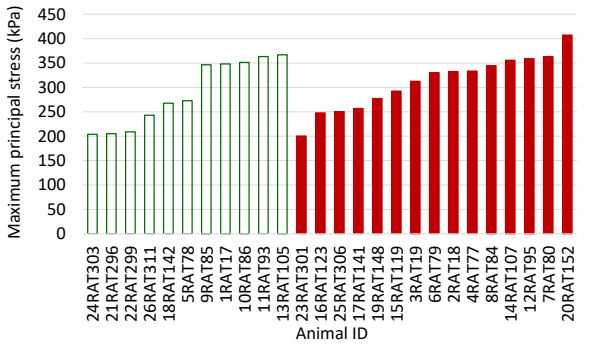

Maximum principal strain

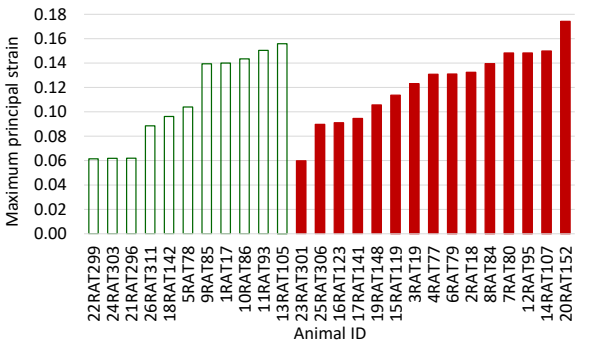

Minimum pressure

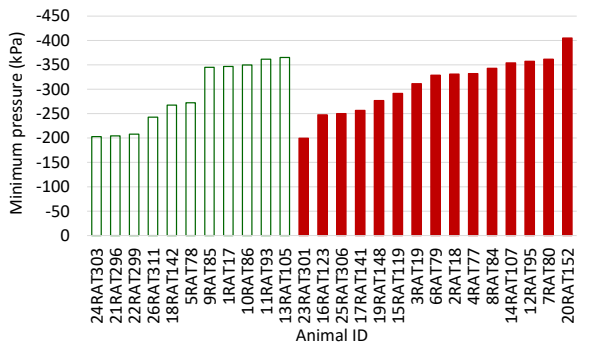

Maximum pressure

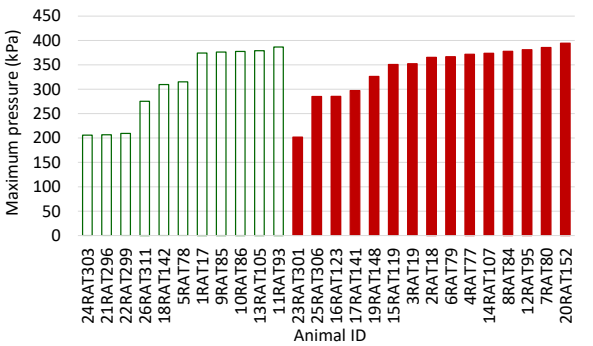

Table E4: Simulation results for brain regions associated with consciousness. Case categorization into non-injured and injured groups is based on EPM open duration.

Maximum axonal strain

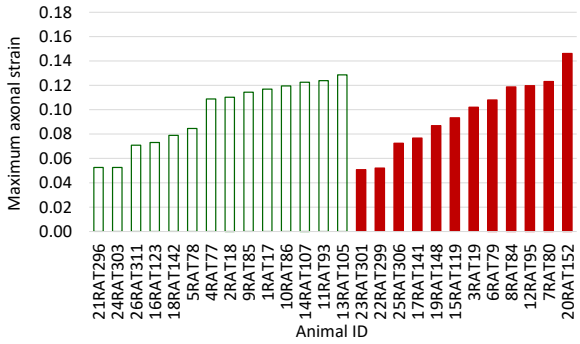

Maximum strain energy

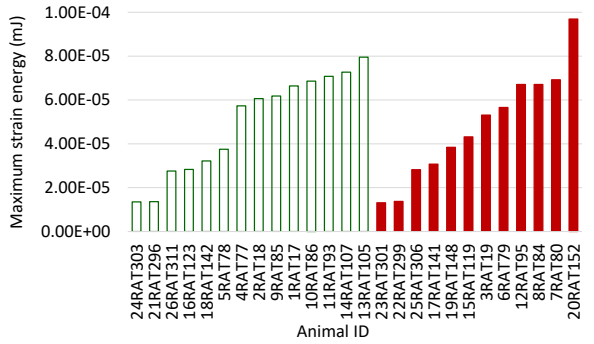

Maximum von Mises stress

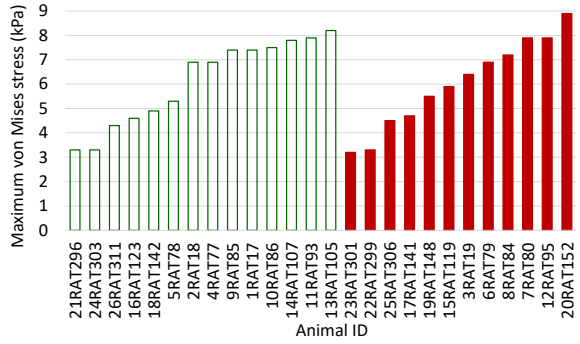

Maximum von Mises strain

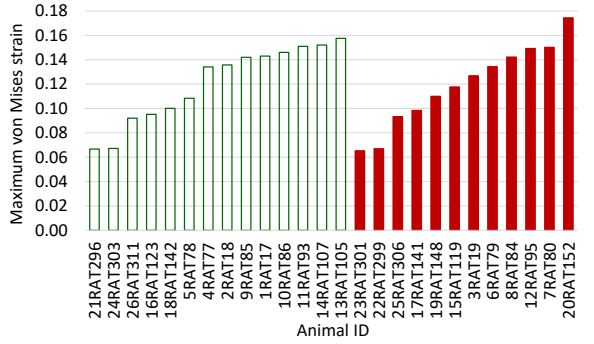

Maximum shear stress

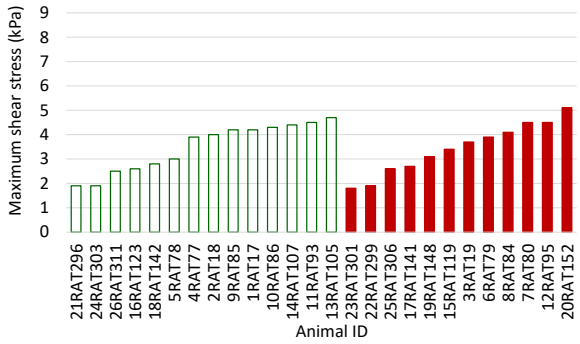

Maximum shear strain

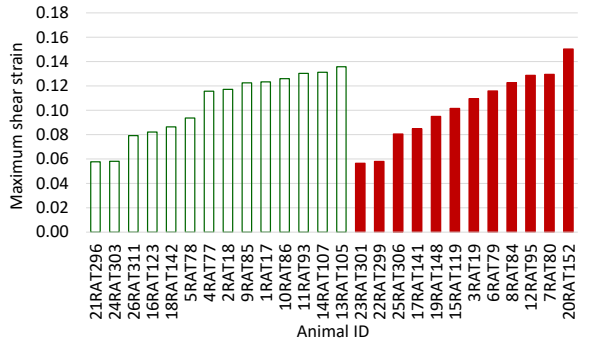

Maximum principal stress

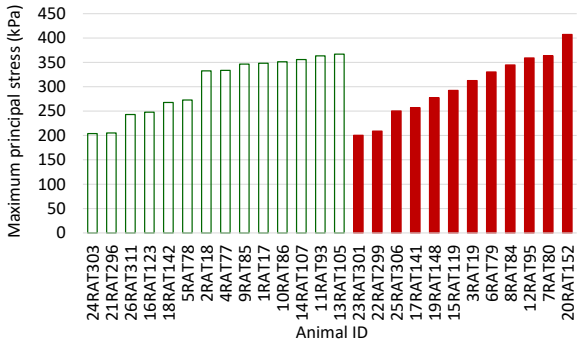

Maximum principal strain

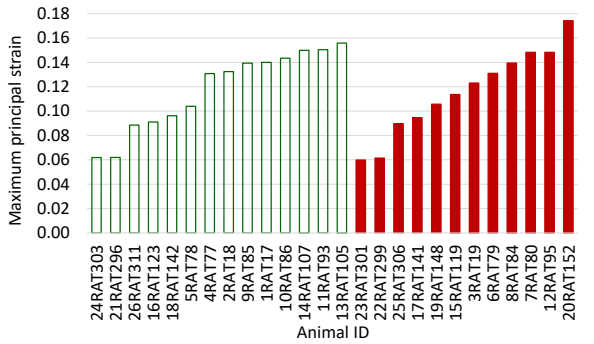

cont.

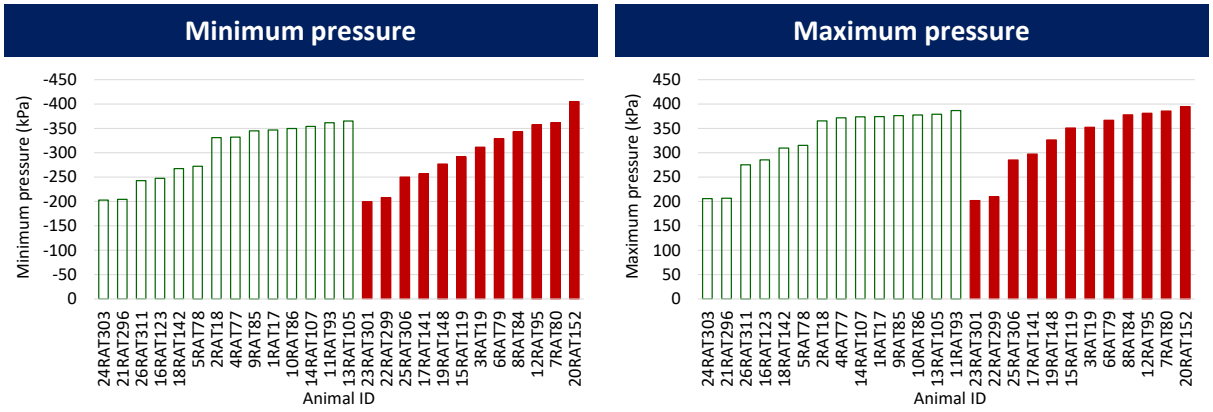

Table E5: Simulation results for brain regions associated with consciousness. Case categorization into non-injured and injured groups is based on MCW session I latency.

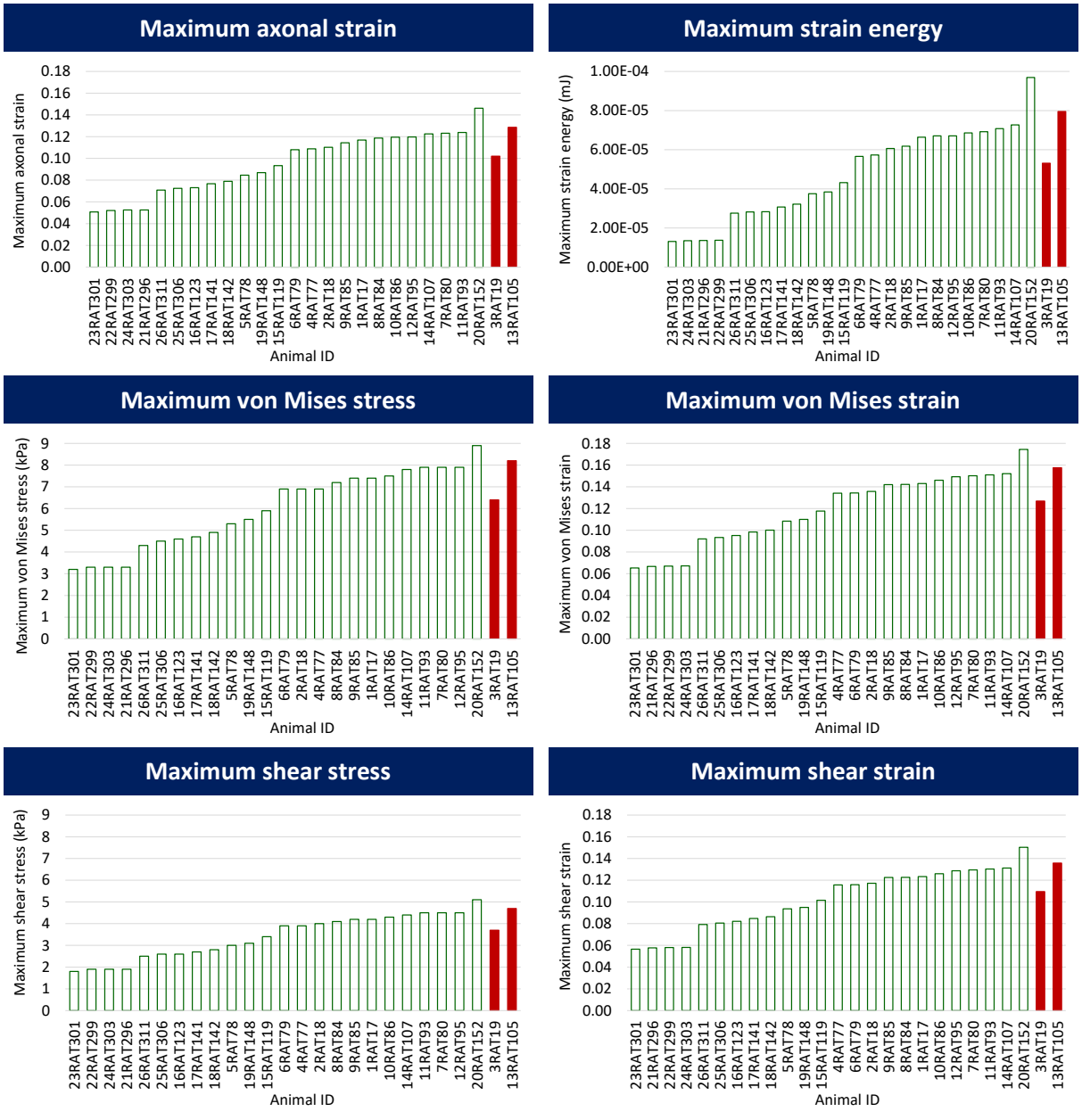

cont.

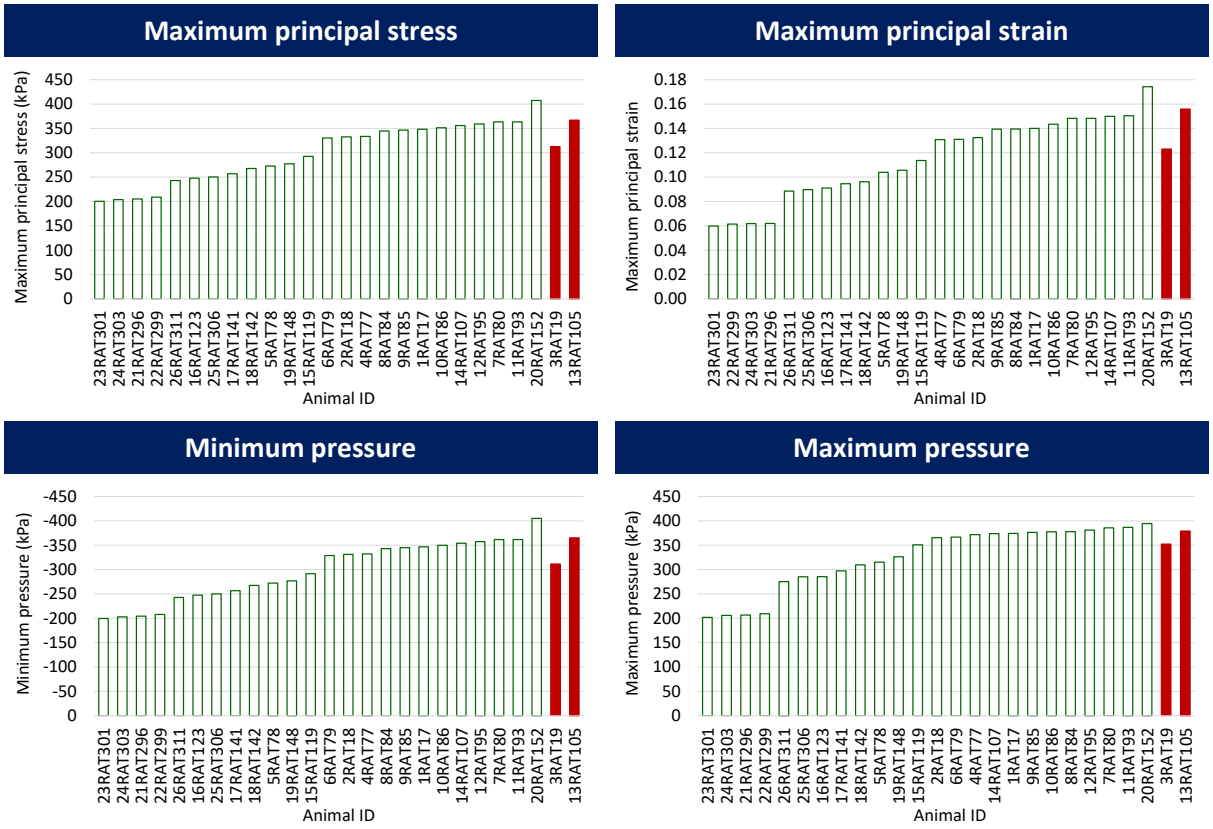

Table E6: Simulation results for brain regions associated with consciousness. Case categorization into non-injured and injured groups is based on MCW session II latency.

cont.

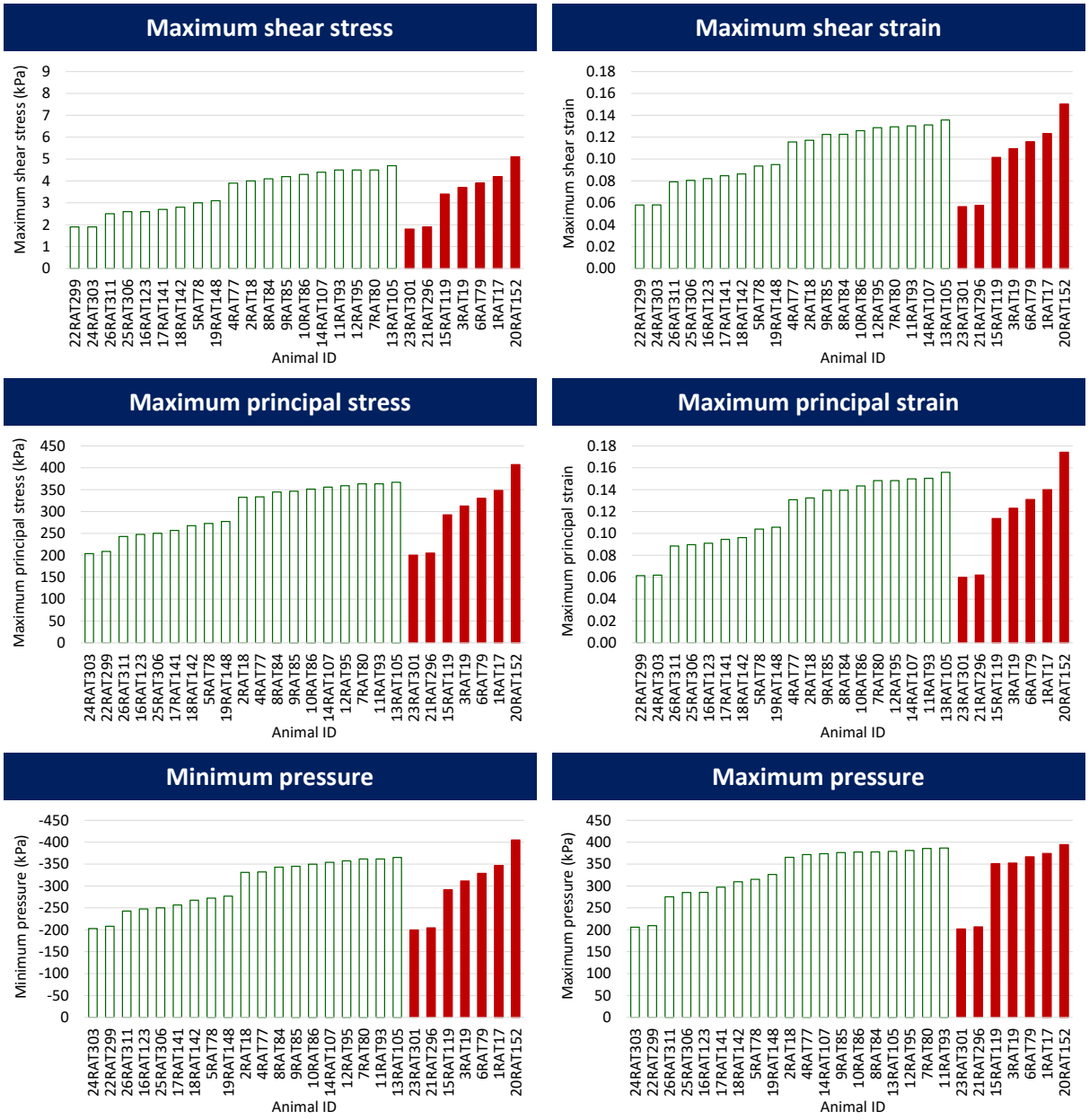

Table E7: Simulation results for brain regions associated with consciousness. Case categorization into non-injured and injured groups is based on MCW session III latency.

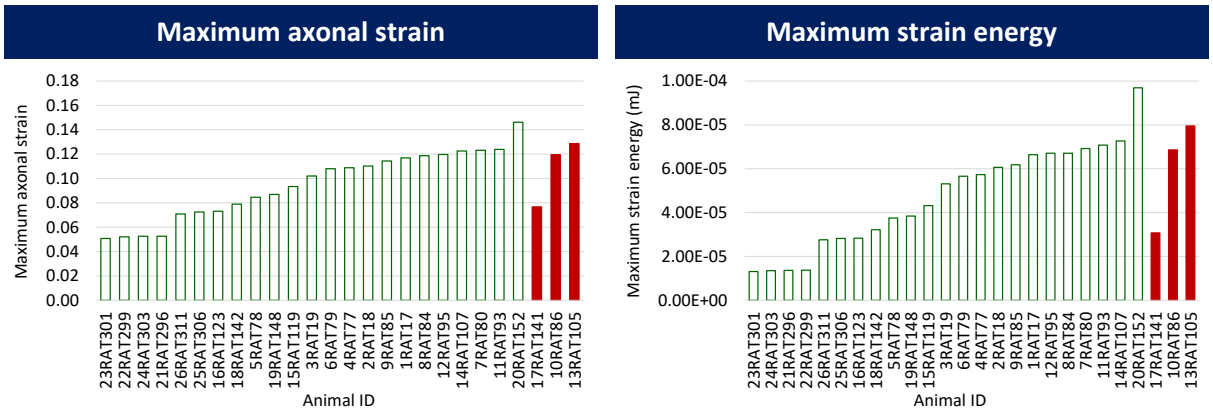

cont.

Maximum von Mises stress

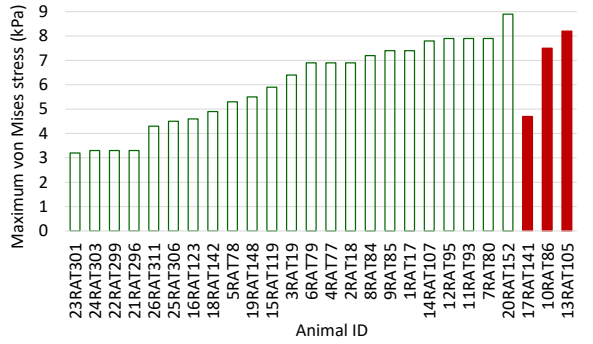

Maximum von Mises strain

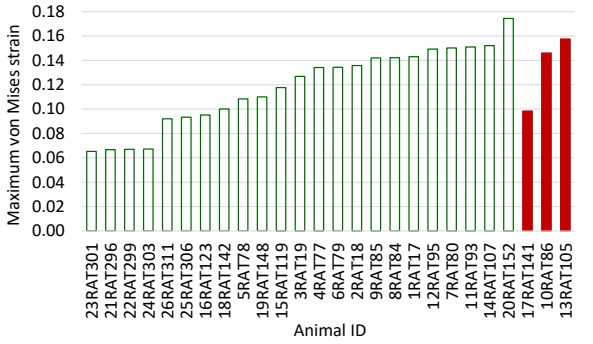

Maximum shear stress

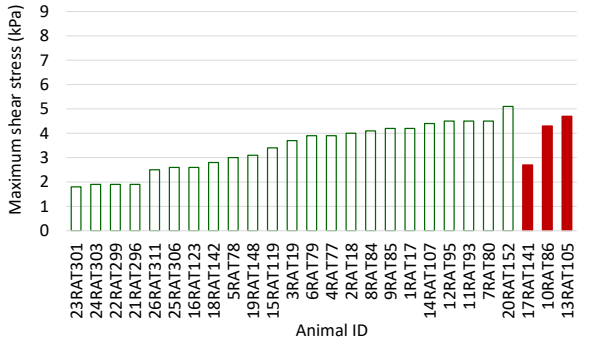

Maximum shear strain

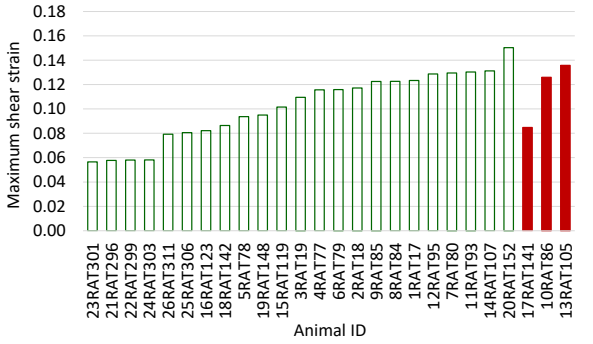

Maximum principal stress

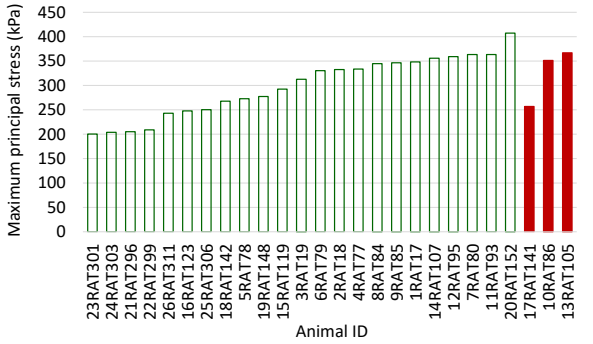

Maximum principal strain

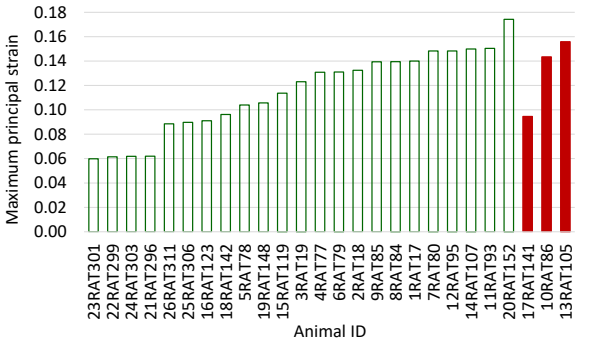

Minimum pressure

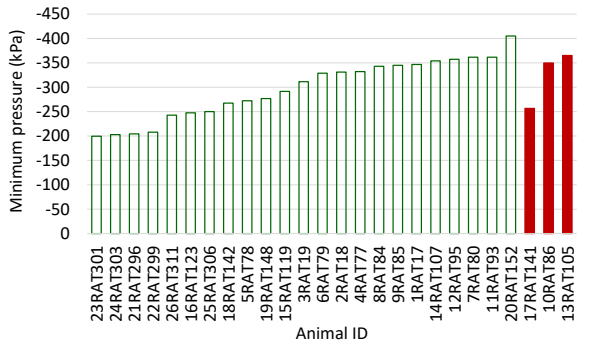

Maximum pressure

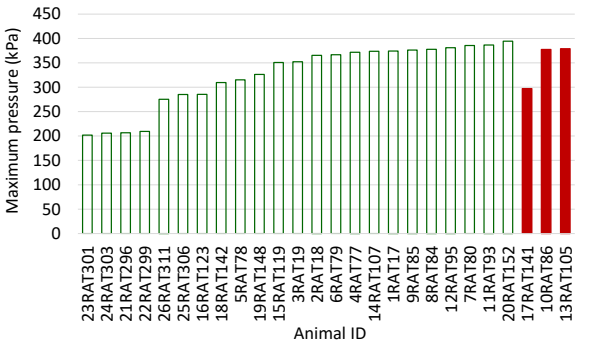

Simulation results of all twenty-six experimental cases for all ten mechanical parameters, which are maximum axonal strain, maximum strain energy, maximum von Mises stress and strain, maximum shear stress and strain, maximum principal stress and strain and minimum and maximum pressures for the specific brain regions associated with activity are given below in Table E8 to Table E14. Results are categorized based on seven experimental behavioural responses in injured (solid red columns) and non-injured (blank green columns) groups.

Table E8: Simulation results for brain regions associated with activity. Case categorization into non-injured and injured groups is based on unconsciousness time.

Maximum axonal strain

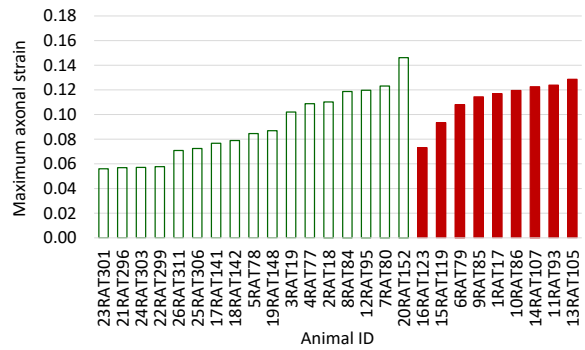

Maximum strain energy

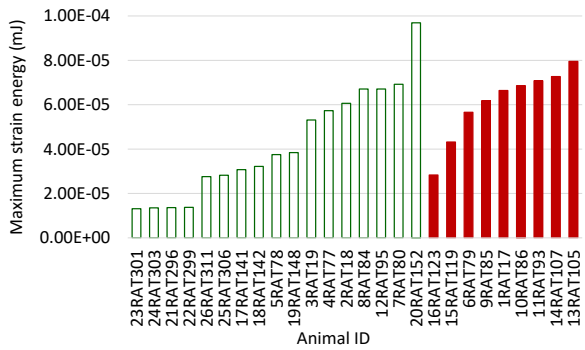

Maximum von Mises stress

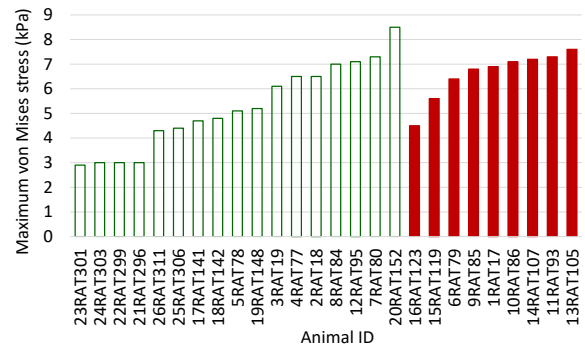

Maximum von Mises strain

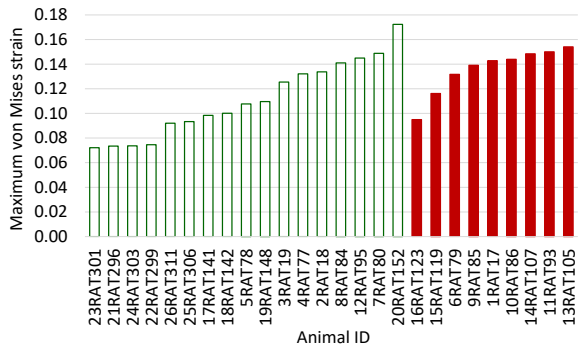

Maximum shear stress

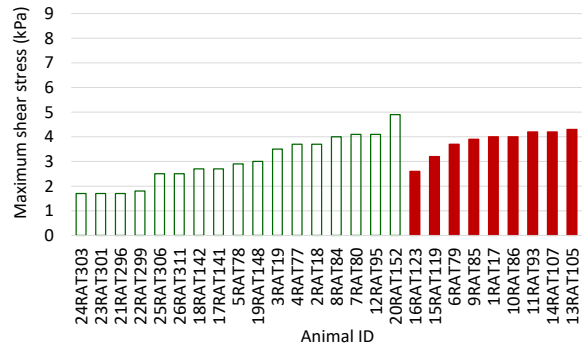

Maximum shear strain

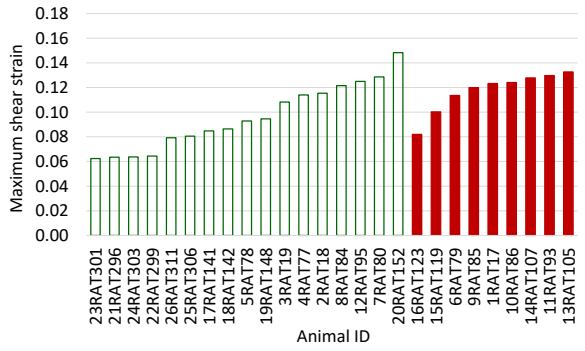

cont.

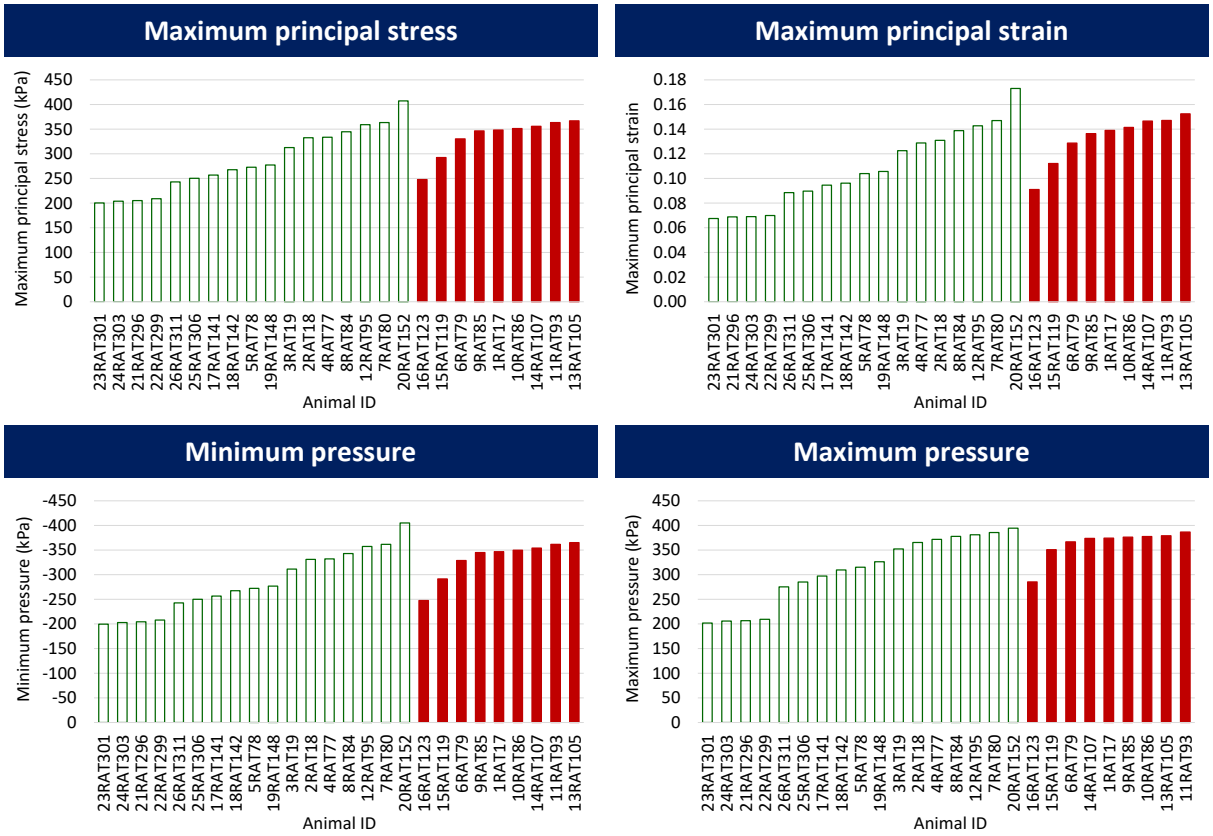

Table E9: Simulation results for brain regions associated with activity. Case categorization into non-injured and injured groups is based on EPM distance travelled.

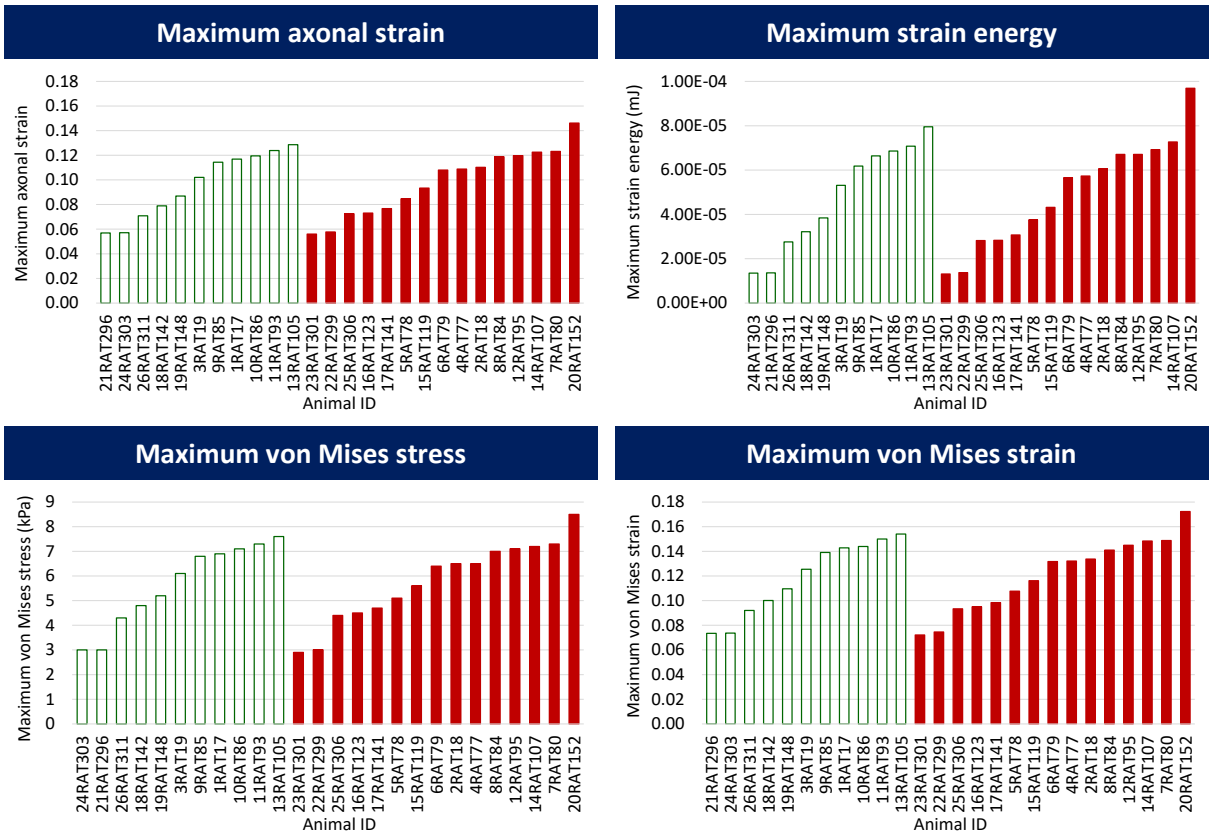

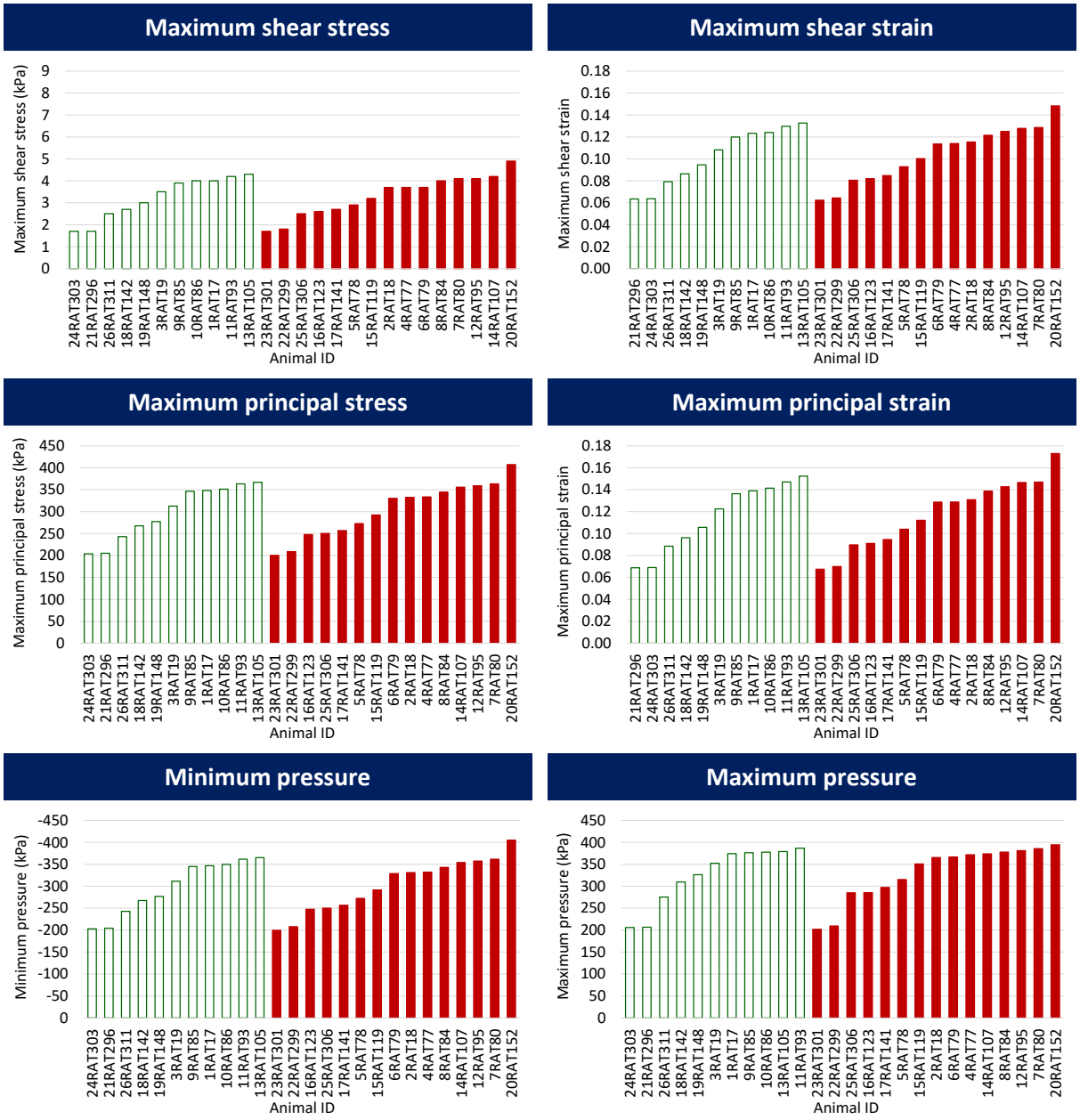

Table E10: Simulation results for brain regions associated with activity. Case categorization into non-injured and injured groups is based on EPM arm changes.

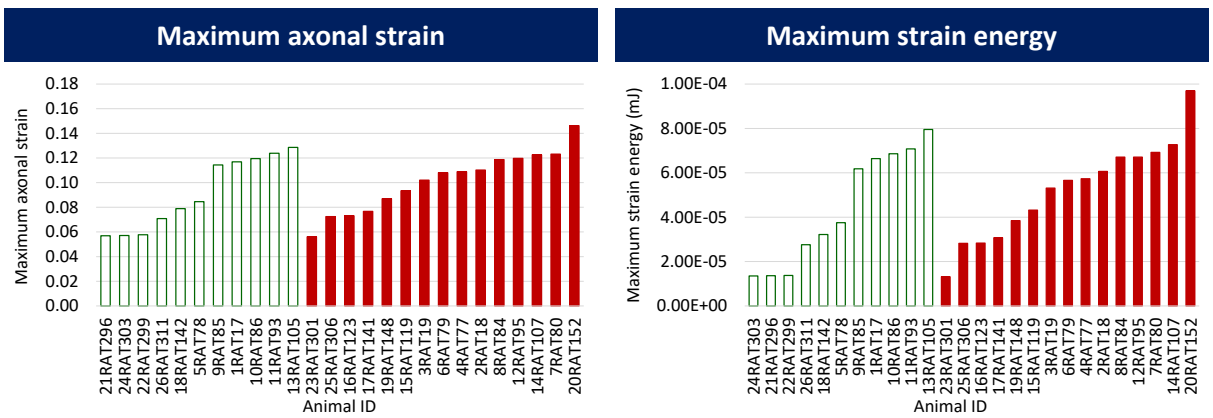

Maximum von Mises stress

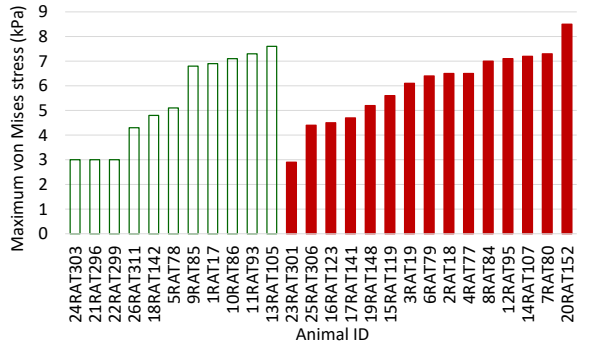

Maximum von Mises strain

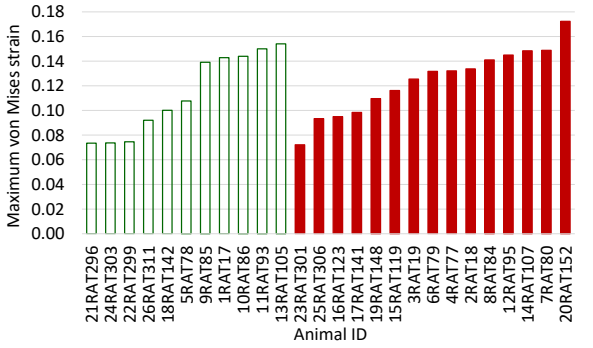

Maximum shear stress

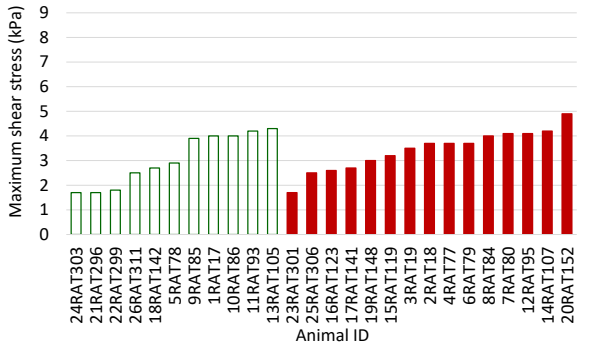

Maximum shear strain

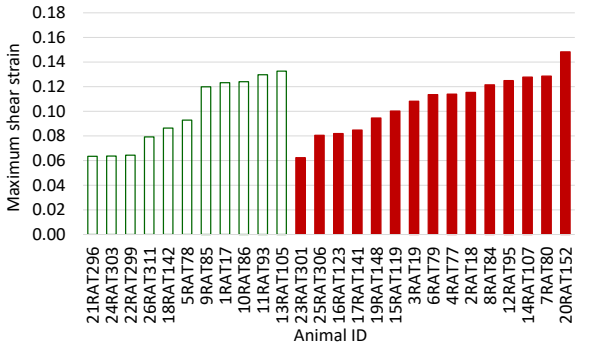

Maximum principal stress

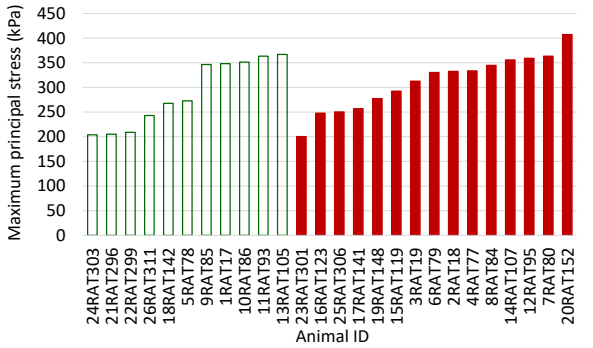

Maximum principal strain

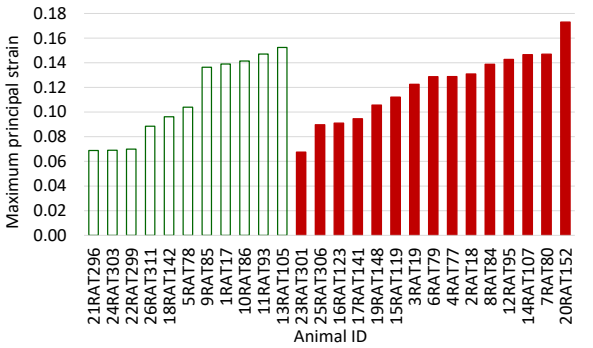

Minimum pressure

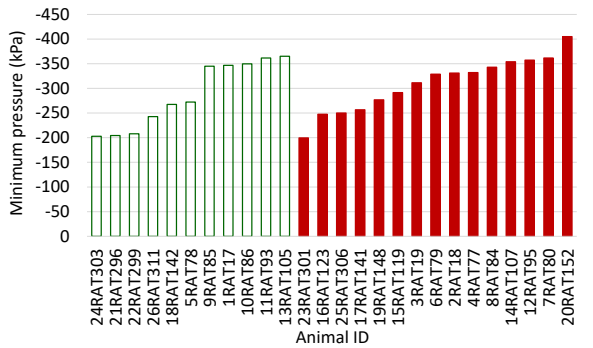

Maximum pressure

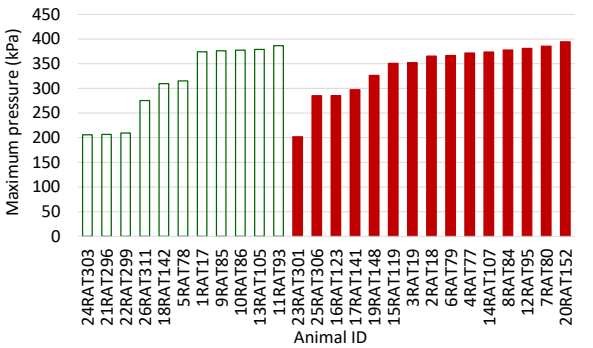

Table E11: Simulation results for brain regions associated with activity. Case categorization into non-injured and injured groups is based on EPM open duration.

Maximum axonal strain

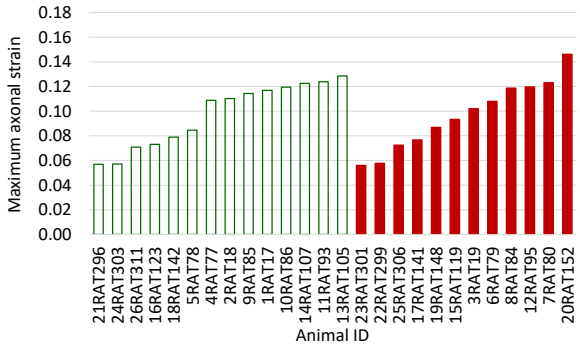

Maximum strain energy

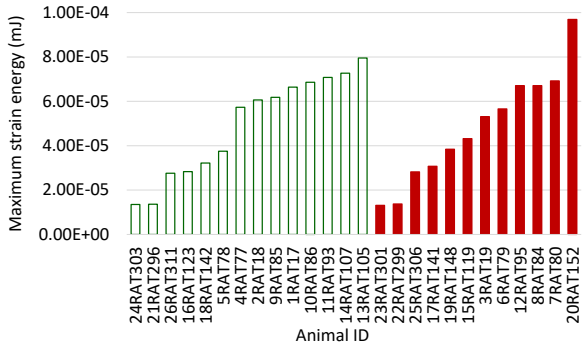

Maximum von Mises stress

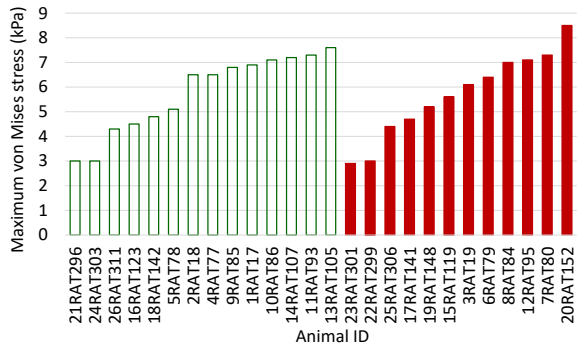

Maximum von Mises strain

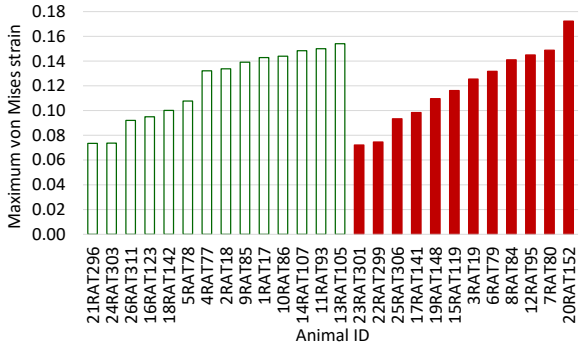

Maximum shear stress

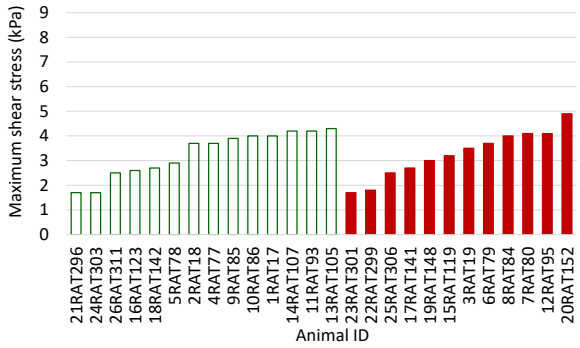

Maximum shear strain

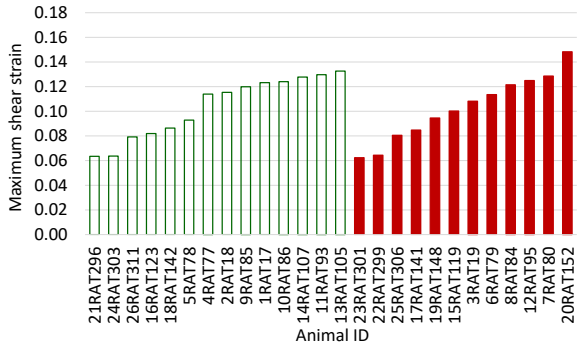

Maximum principal stress

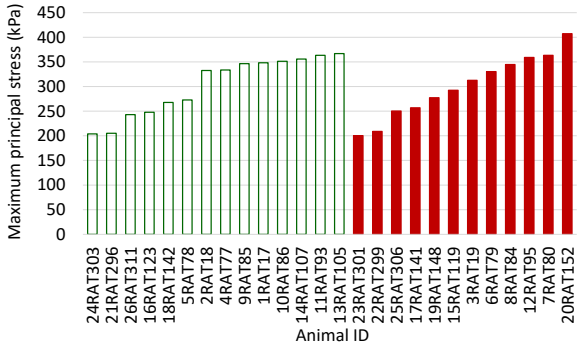

Maximum principal strain

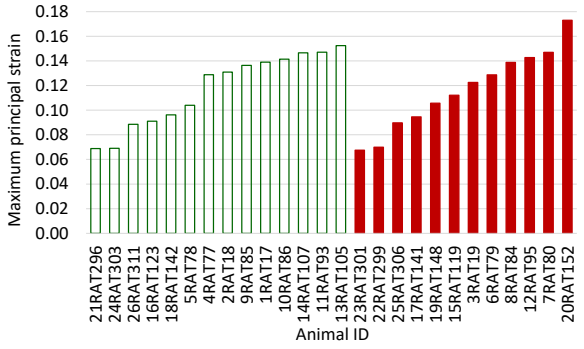

cont.

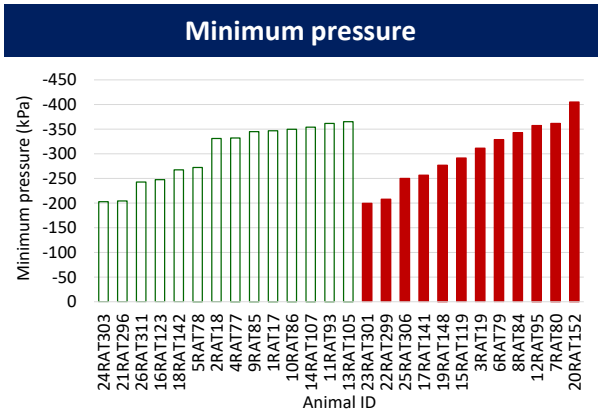

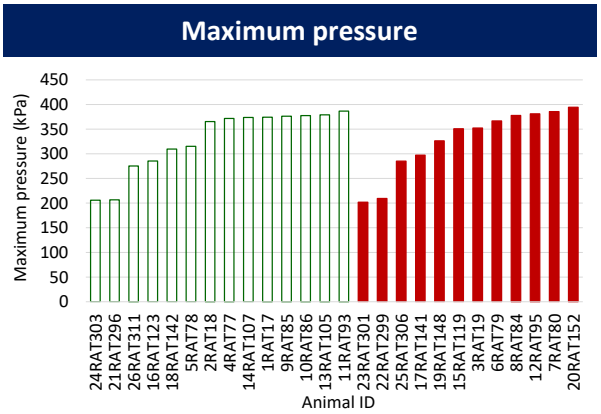

Table E12: Simulation results for brain regions associated with activity. Case categorization into non-injured and injured groups is based on MCW session I latency.

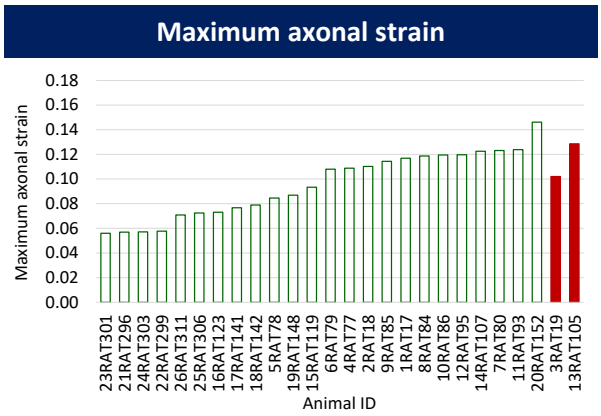

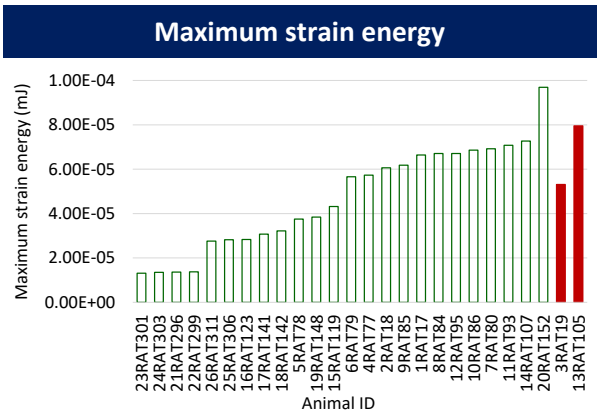

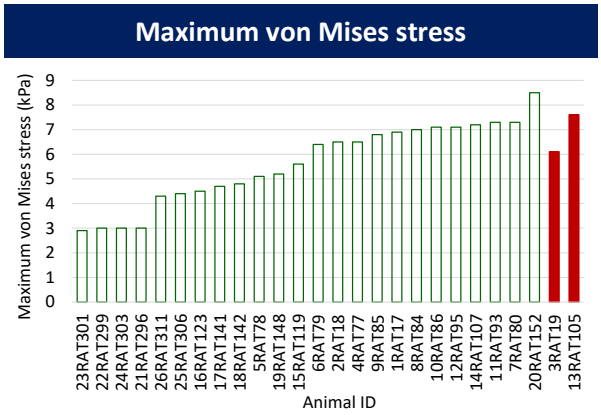

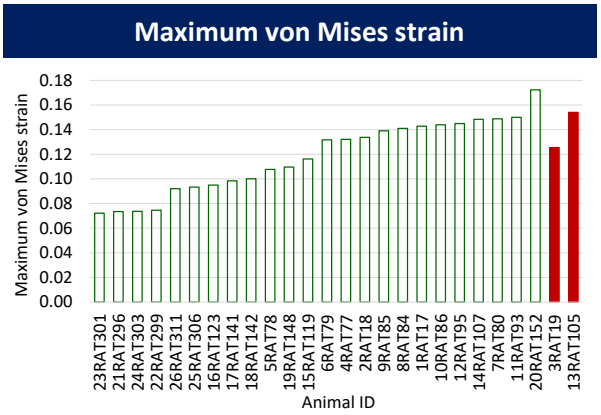

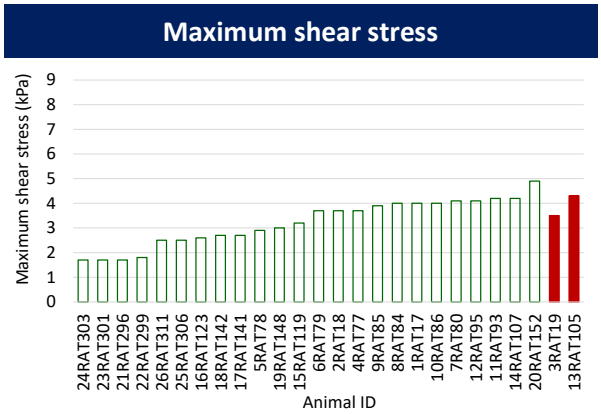

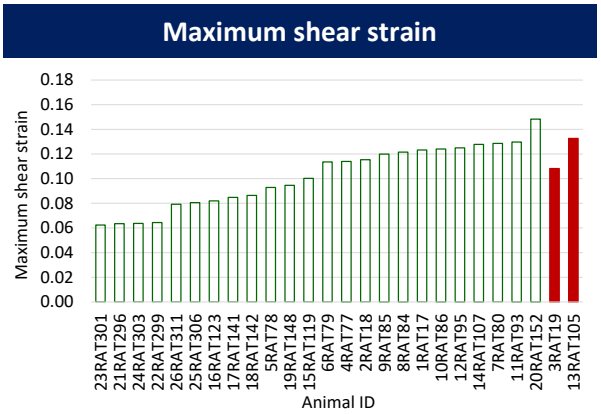

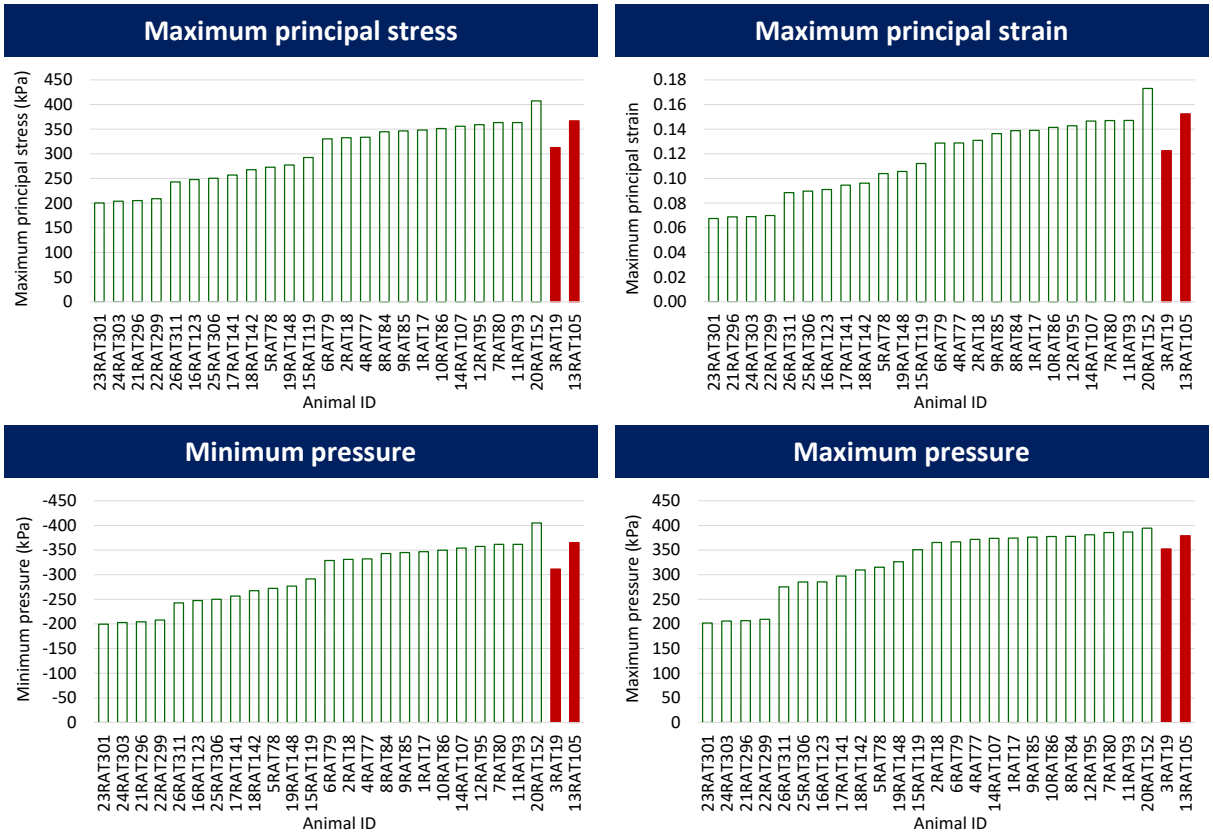

Table E13: Simulation results for brain regions associated with activity. Case categorization into non-injured and injured groups is based on MCW session II latency.

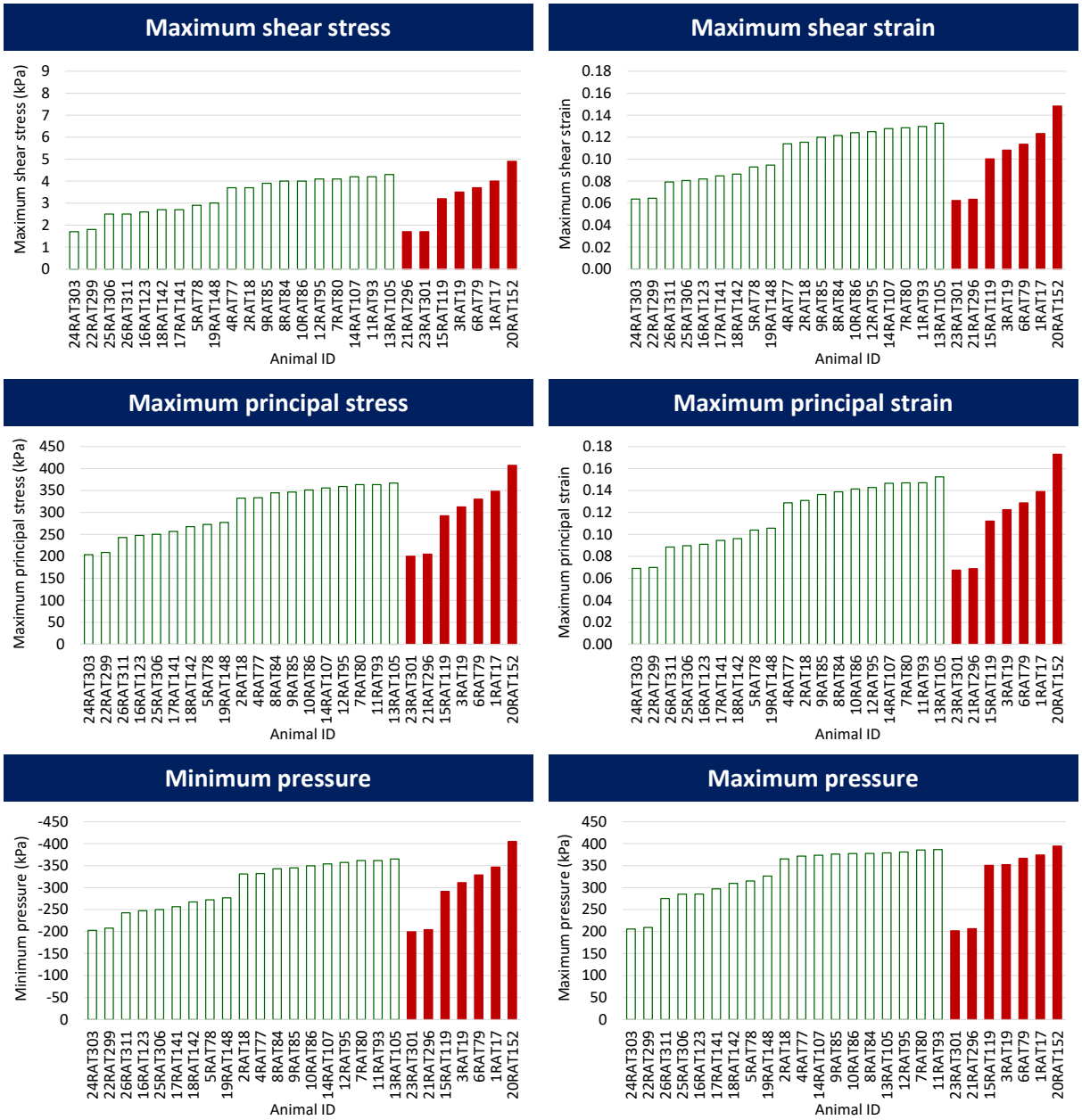

Table E14: Simulation results for brain regions associated with activity. Case categorization into non-injured and injured groups is based on MCW session III latency.

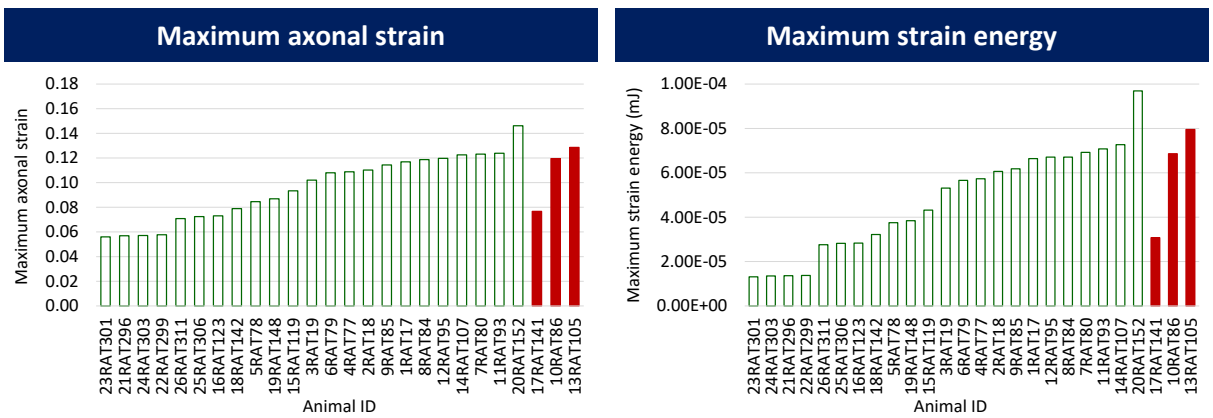

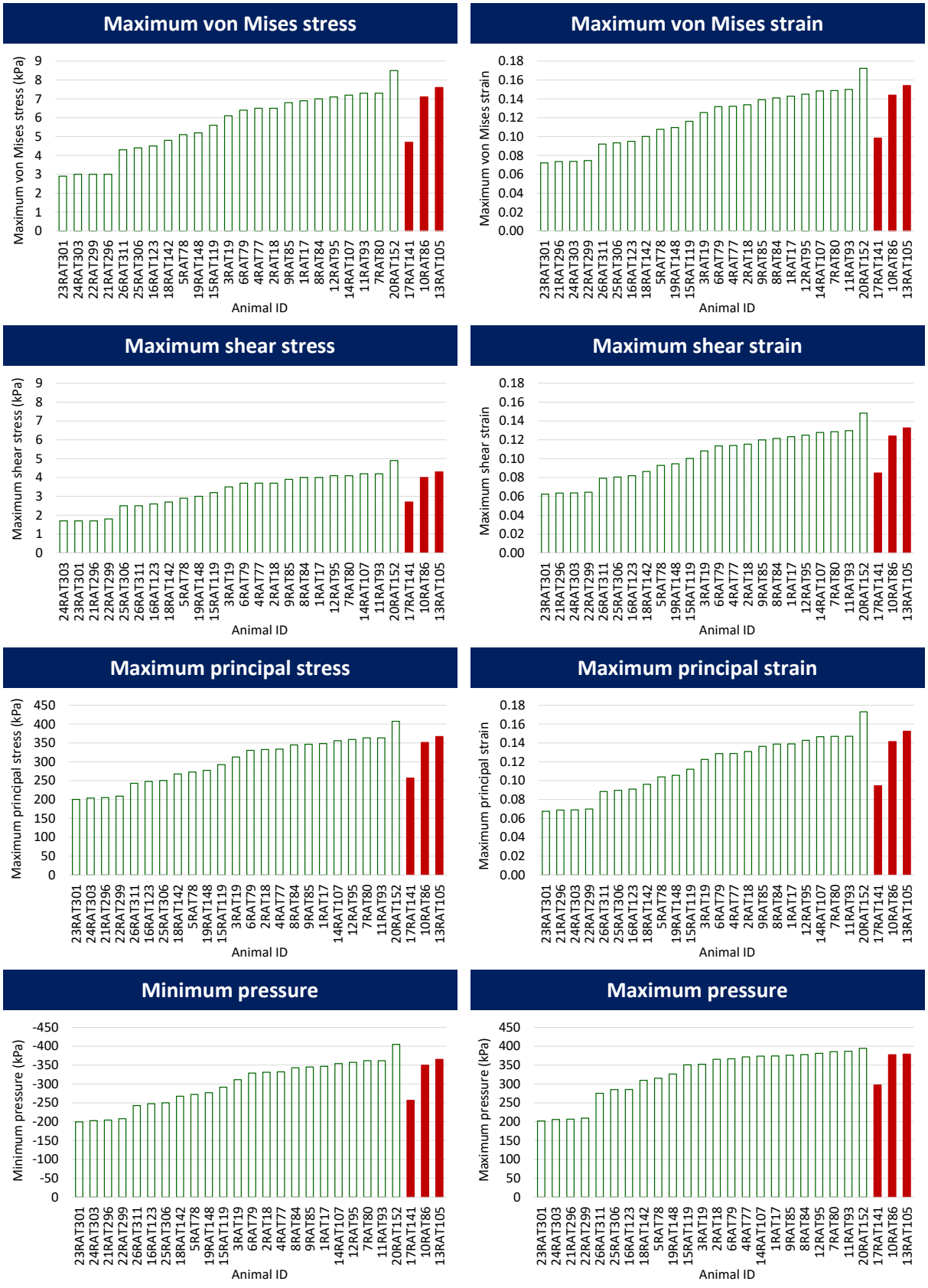

Simulation results of all twenty-six experimental cases for all ten mechanical parameters, which are maximum axonal strain, maximum strain energy, maximum von Mises stress and strain, maximum

shear stress and strain, maximum principal stress and strain and minimum and maximum pressures for the specific brain regions associated with emotionality are given below in Table E15 to Table E21. Results are categorized based on seven experimental behavioural responses in injured (solid red columns) and non-injured (blank green columns) groups.

Table E15: Simulation results for brain regions associated with emotionality. Case categorization into non-injured and injured groups is based on unconsciousness time.

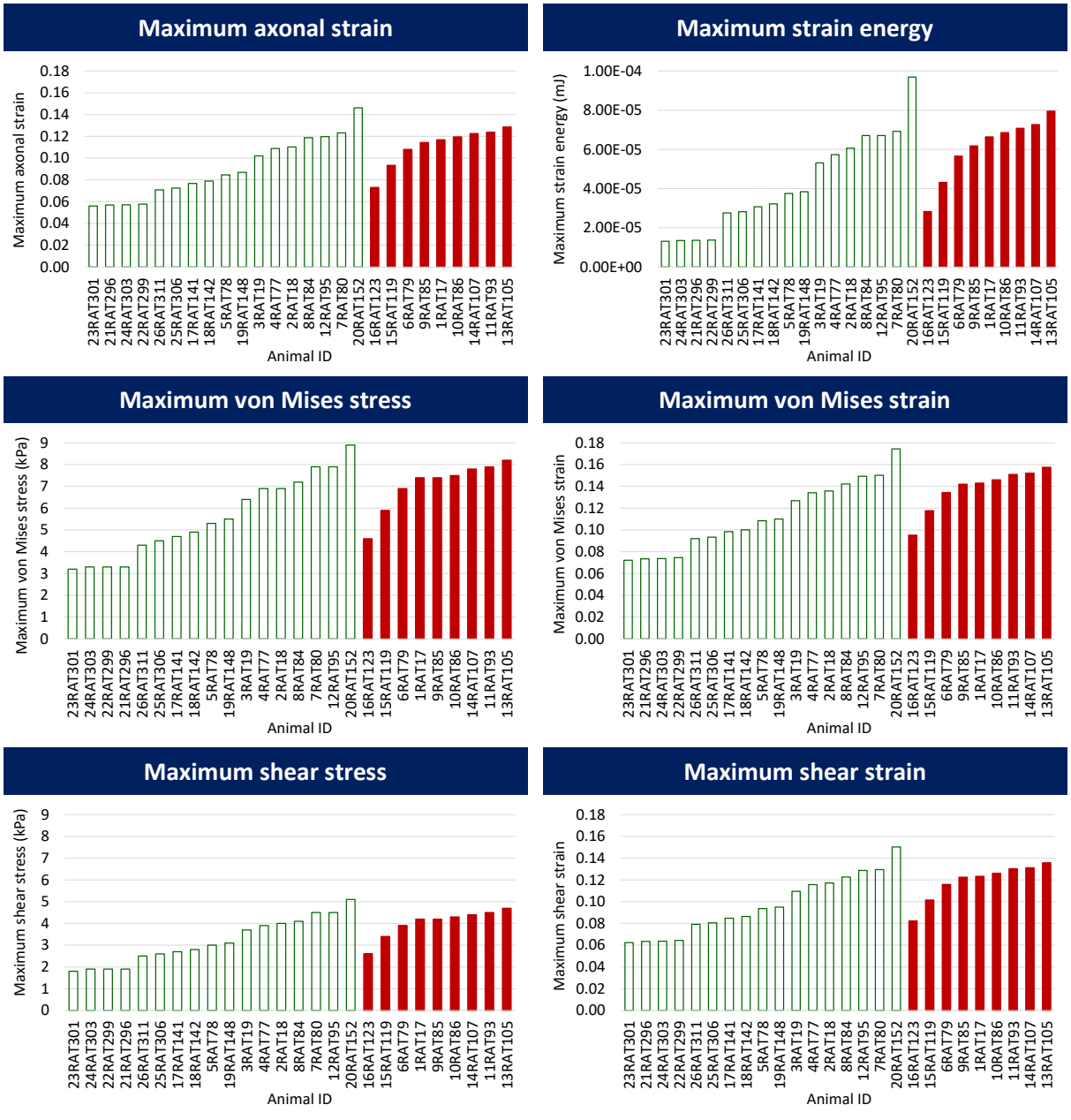

cont.

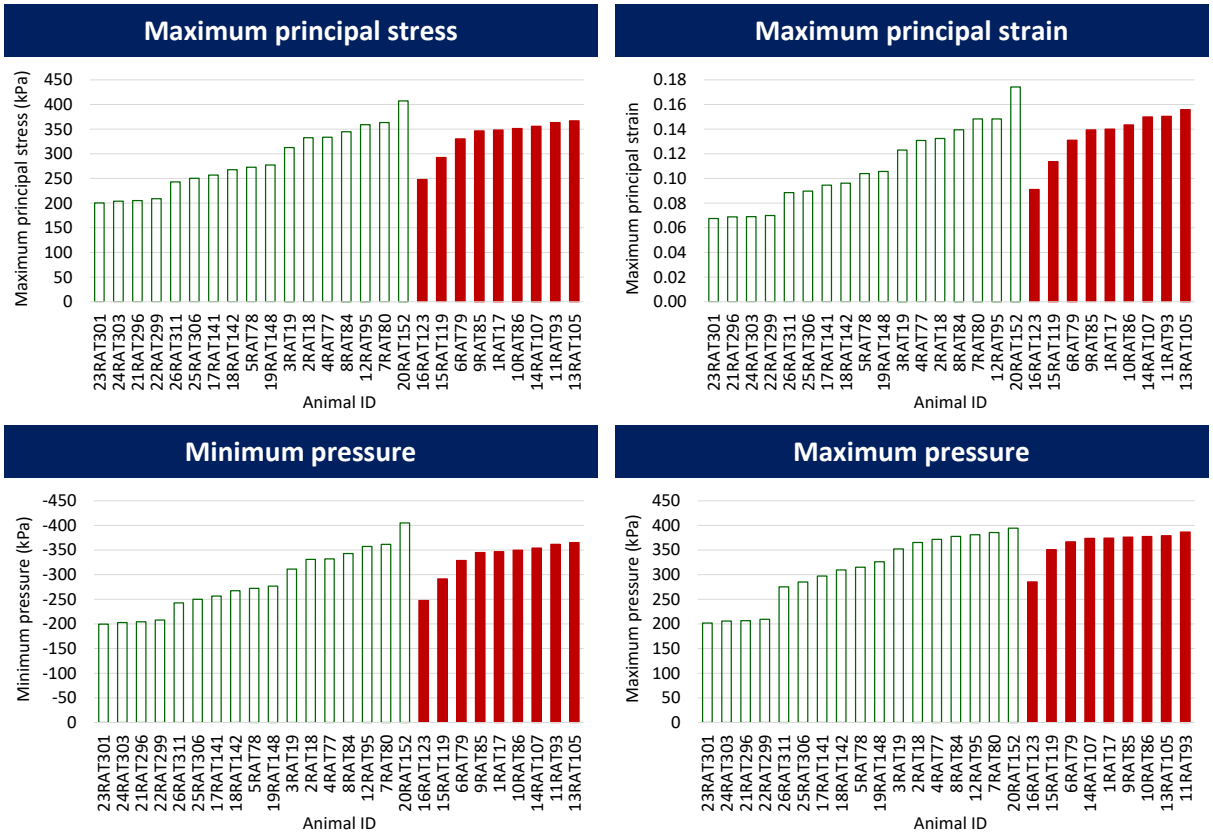

Table E16: Simulation results for brain regions associated with emotionality. Case categorization into non-injured and injured groups is based on EPM distance travelled.

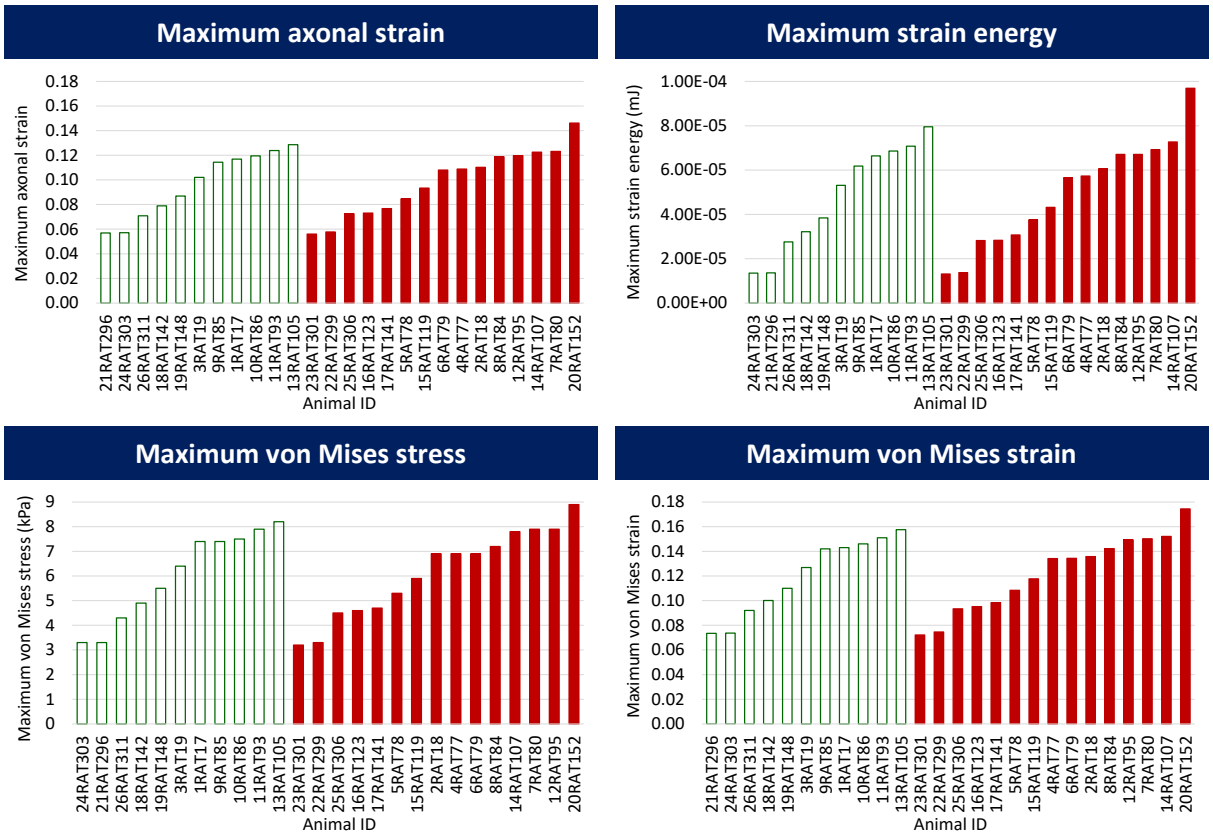

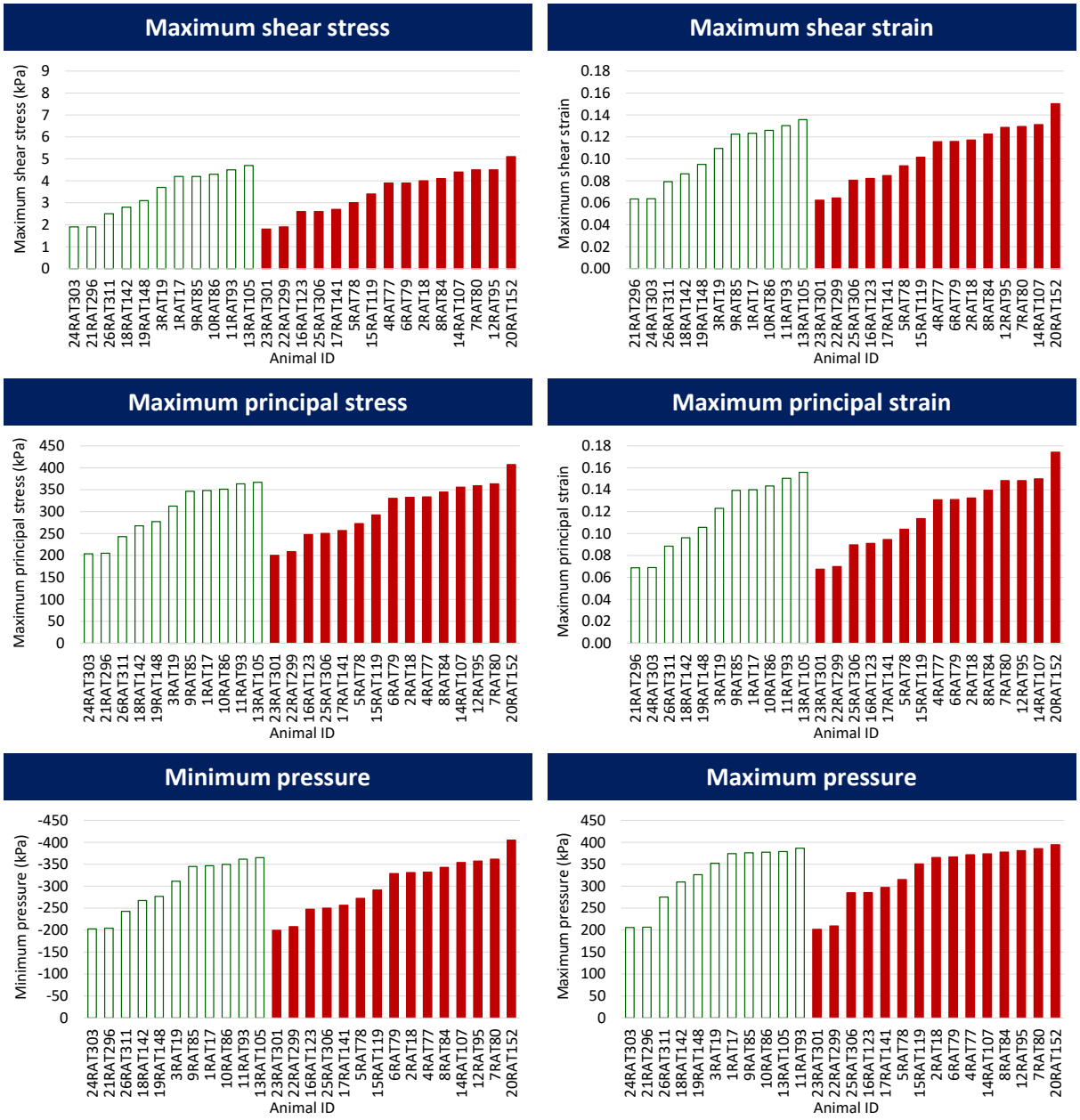

Table E17: Simulation results for brain regions associated with emotionality. Case categorization into non-injured and injured groups is based on EPM arm changes.

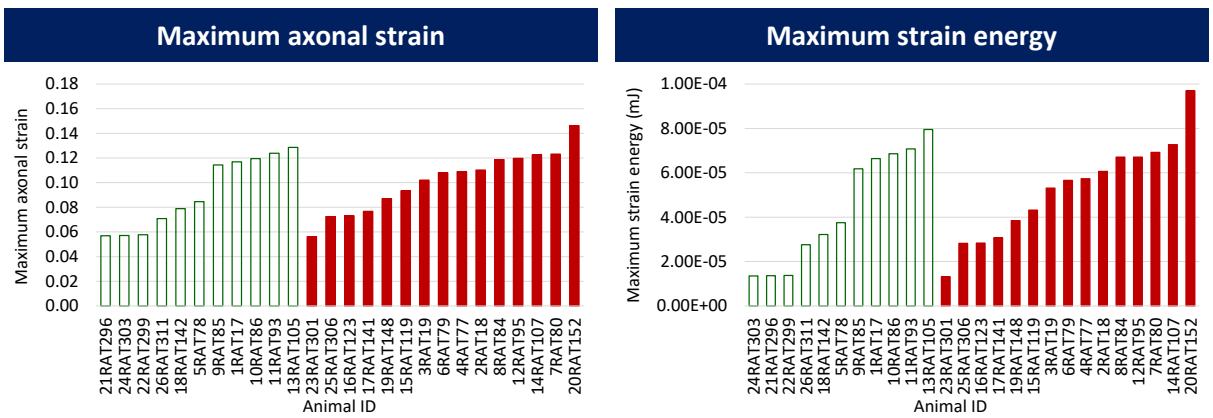

Maximum von Mises stress

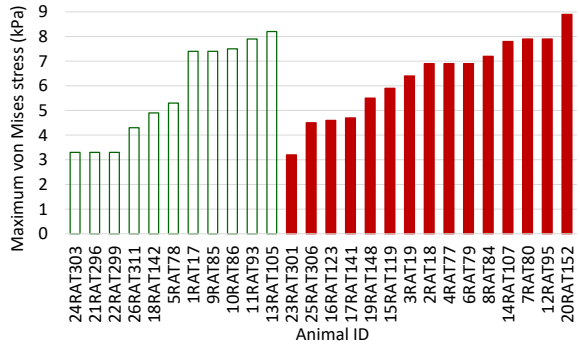

Maximum von Mises strain

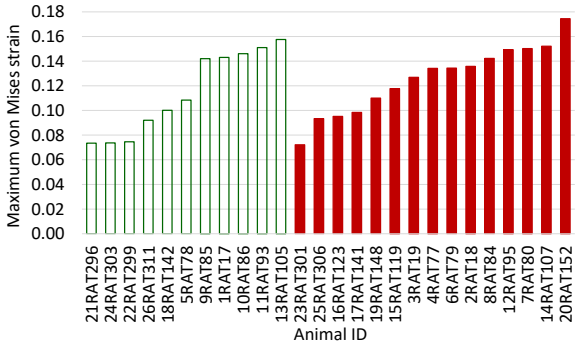

Maximum shear stress

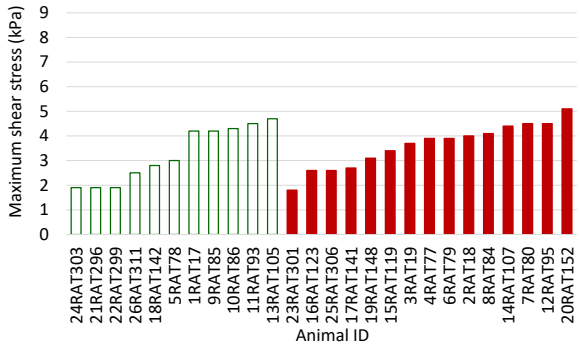

Maximum shear strain

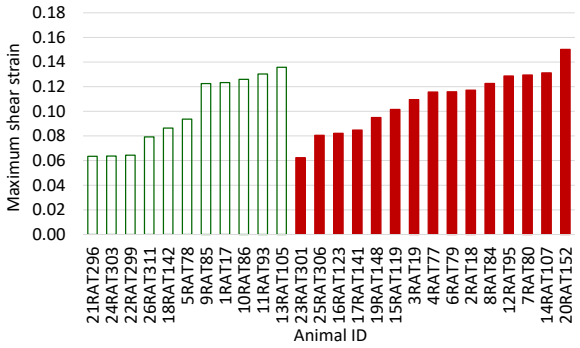

Maximum principal stress

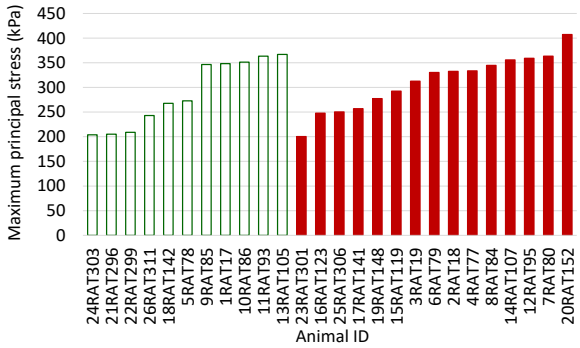

Maximum principal strain

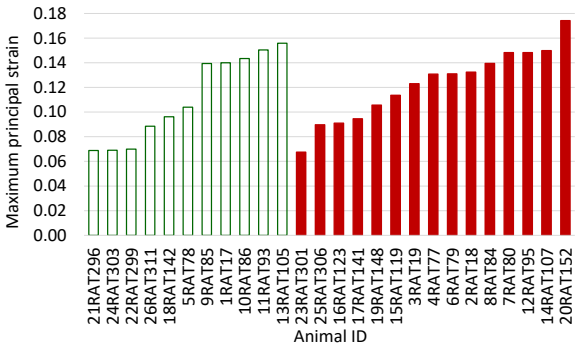

Minimum pressure

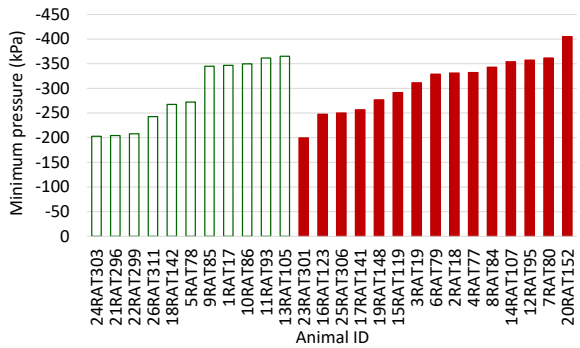

Maximum pressure

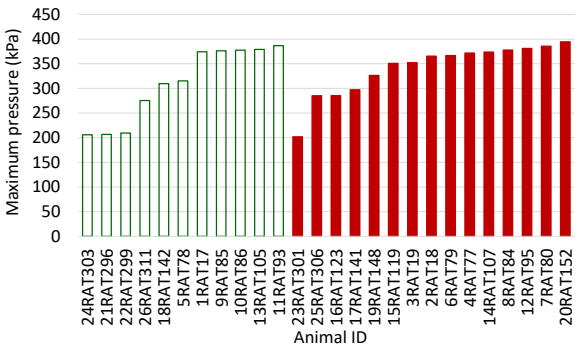

Table E18: Simulation results for brain regions associated with emotionality. Case categorization into non-injured and injured groups is based on EPM open duration.

Maximum axonal strain

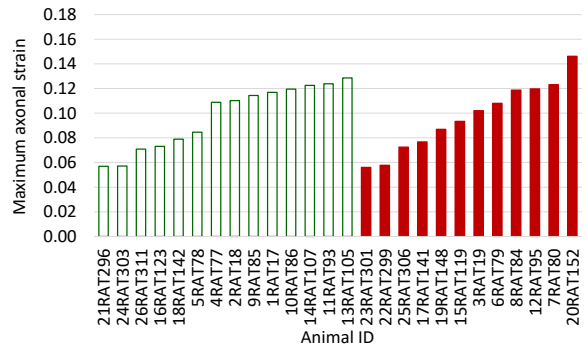

Maximum strain energy

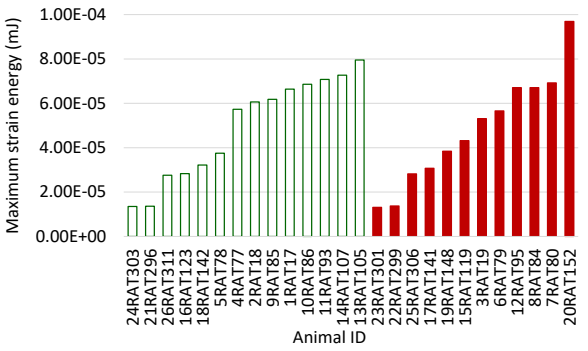

Maximum von Mises stress

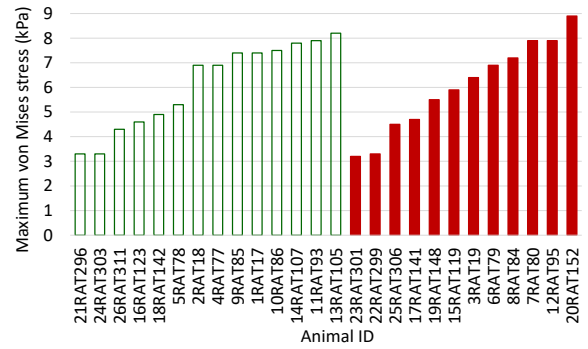

Maximum von Mises strain

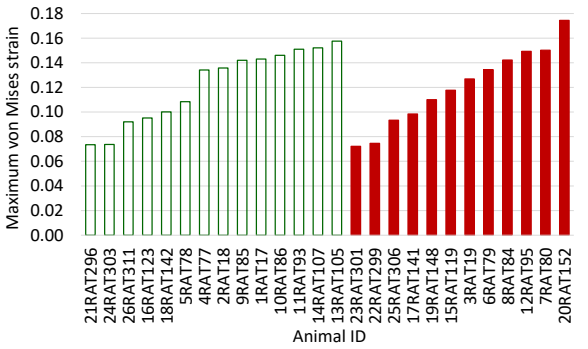

Maximum shear stress

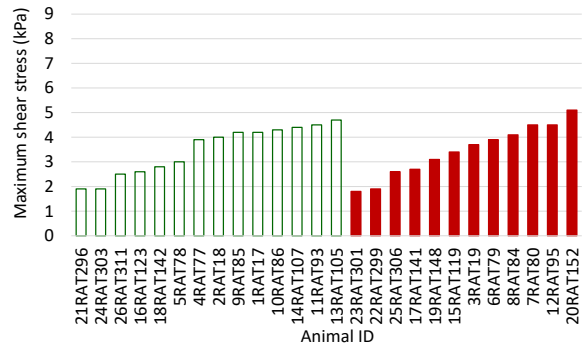

Maximum shear strain

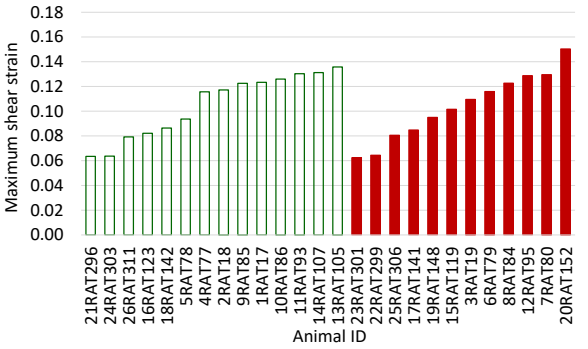

Maximum principal stress

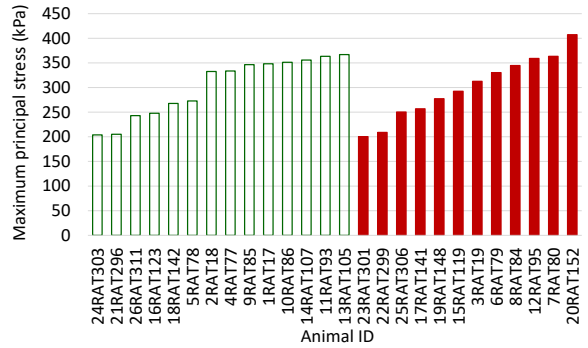

Maximum principal strain

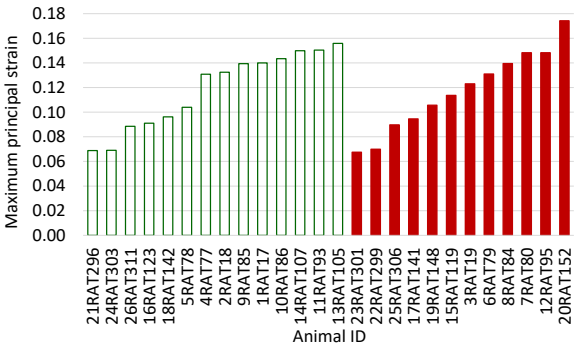

cont.

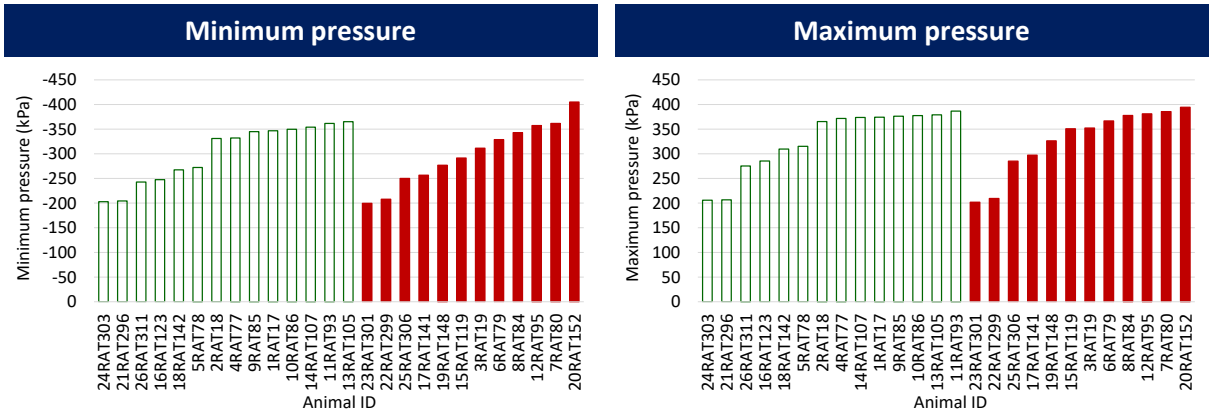

Table E19: Simulation results for brain regions associated with emotionality. Case categorization into non-injured and injured groups is based on MCW session I latency.

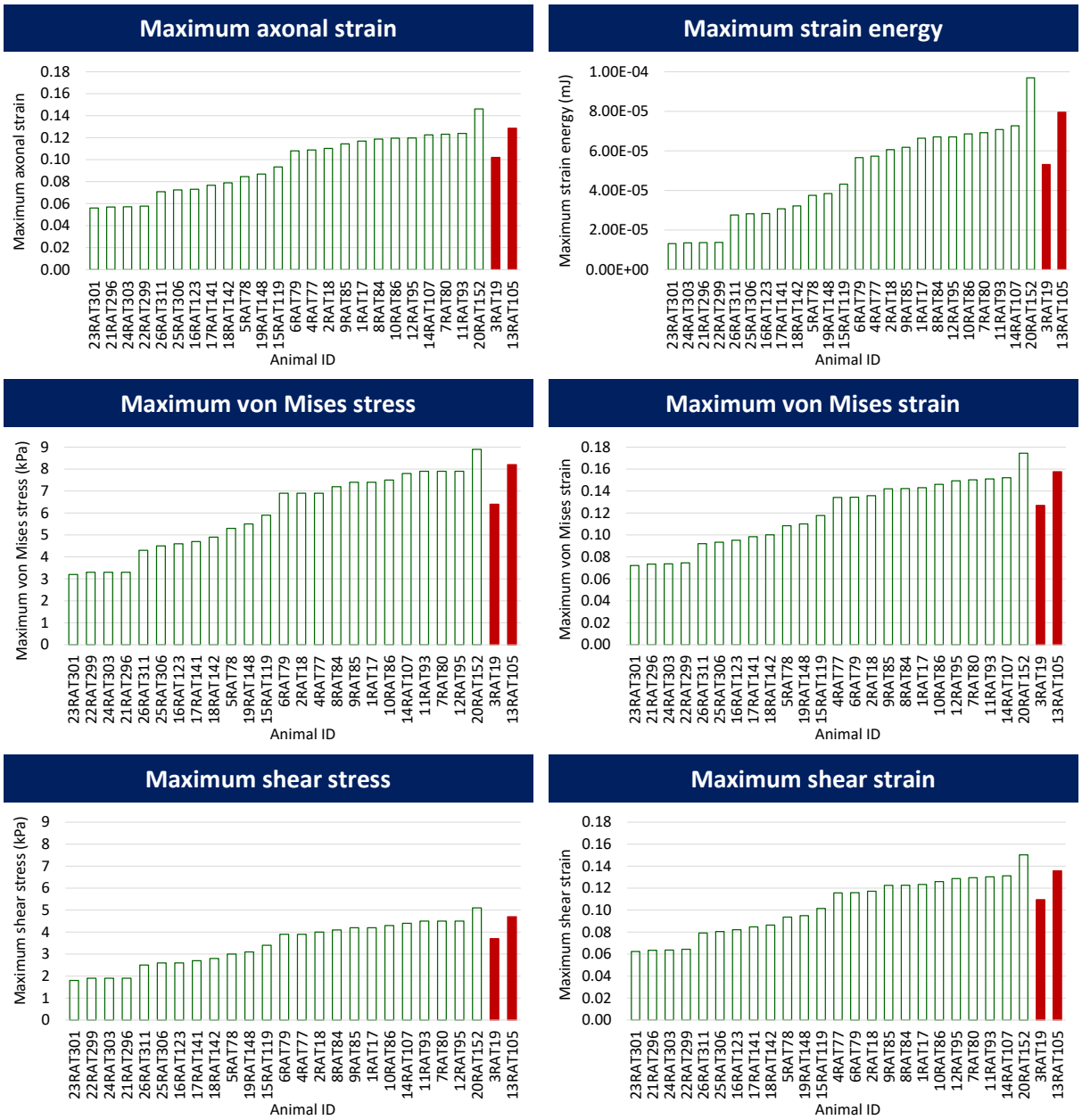

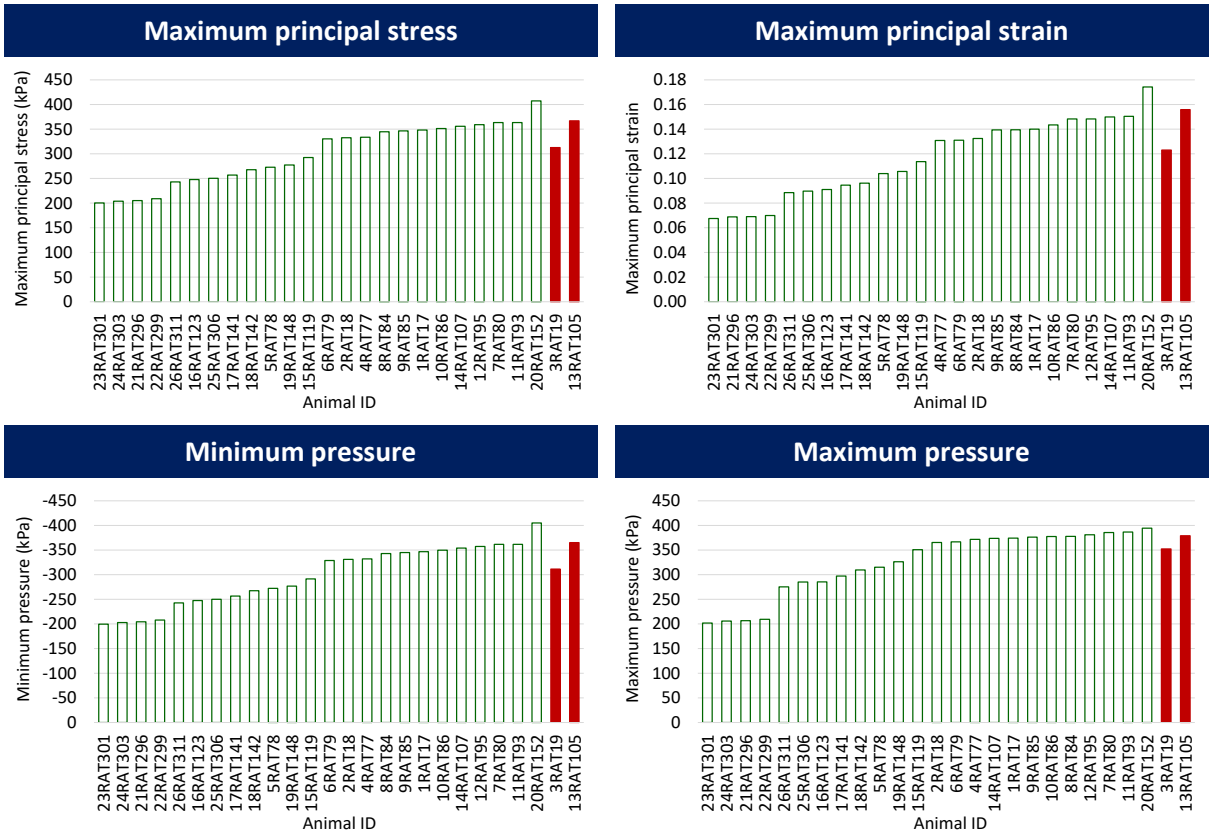

Table E20: Simulation results for brain regions associated with emotionality. Case categorization into non-injured and injured groups is based on MCW session II latency.

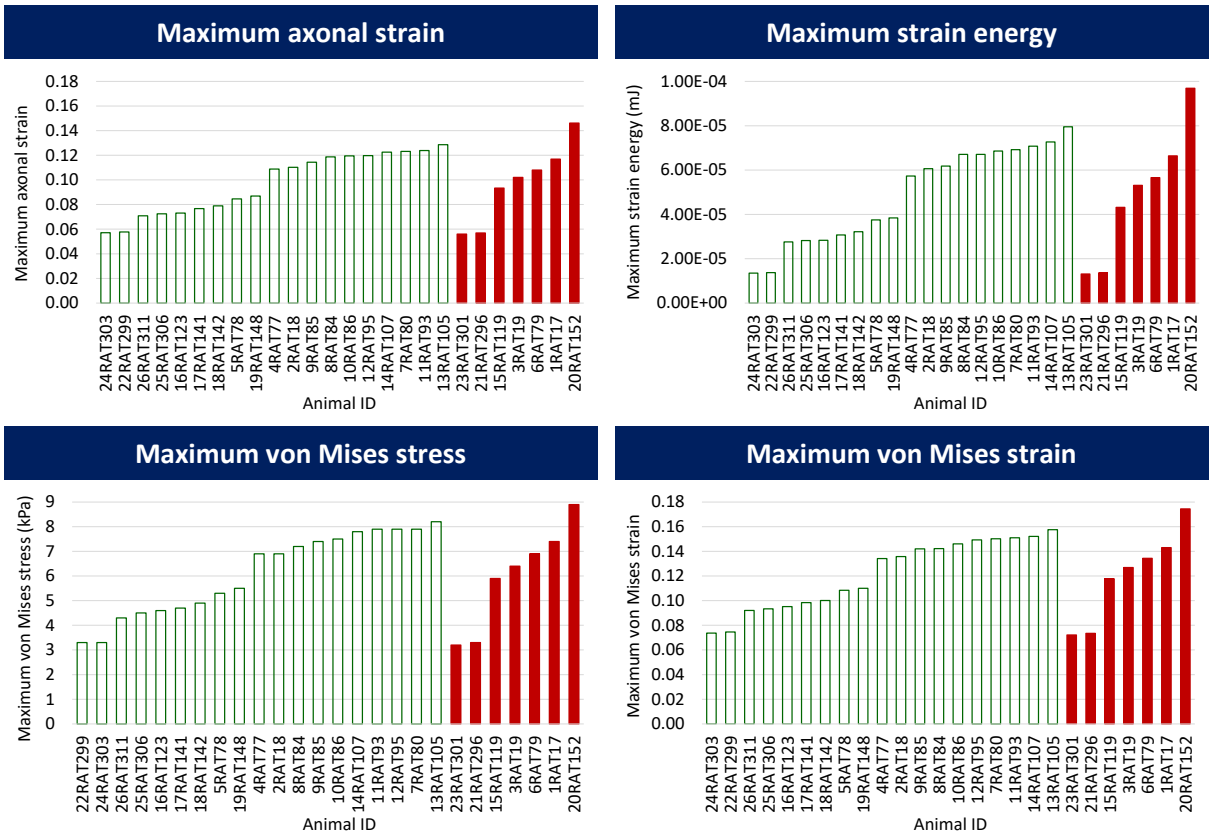

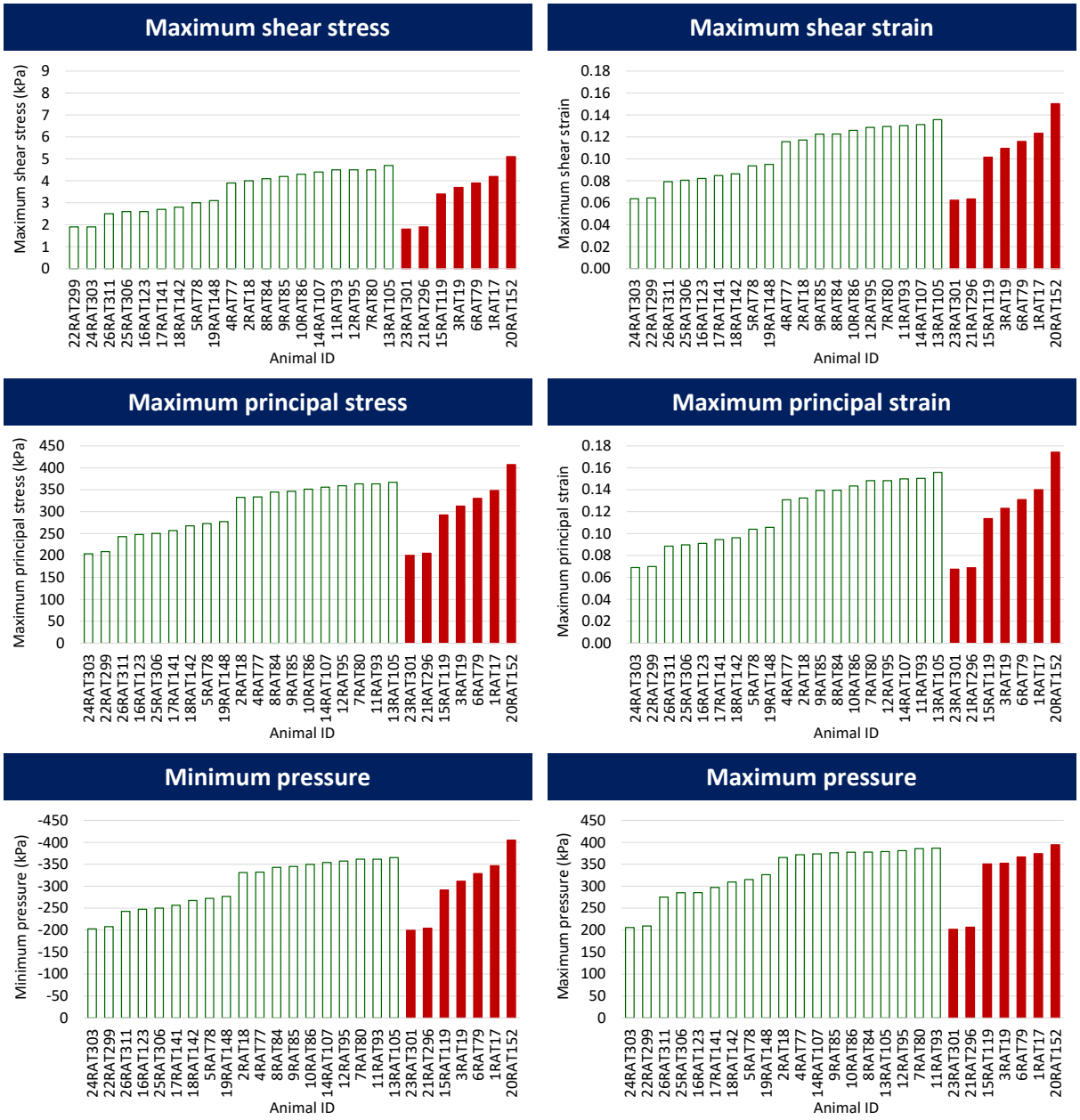

Table E21: Simulation results for brain regions associated with emotionality. Case categorization into non-injured and injured groups is based on MCW session III latency.

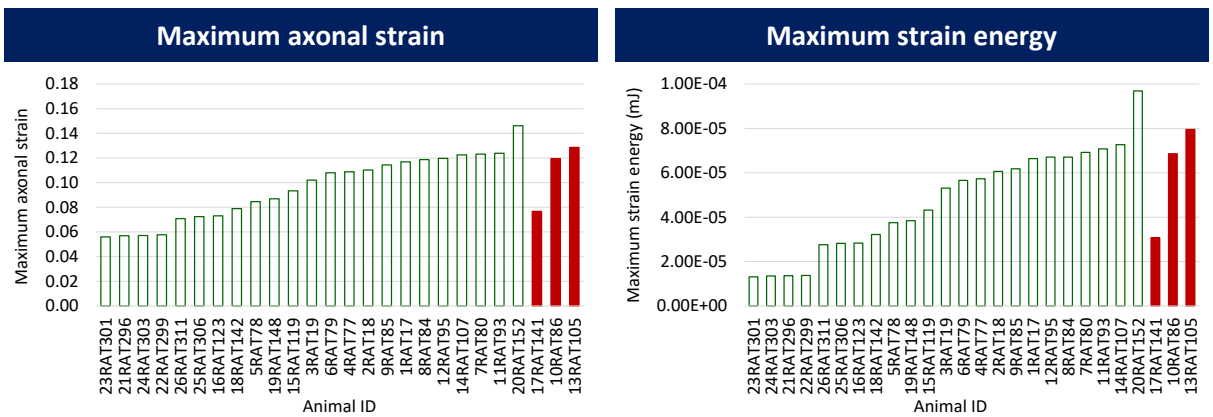

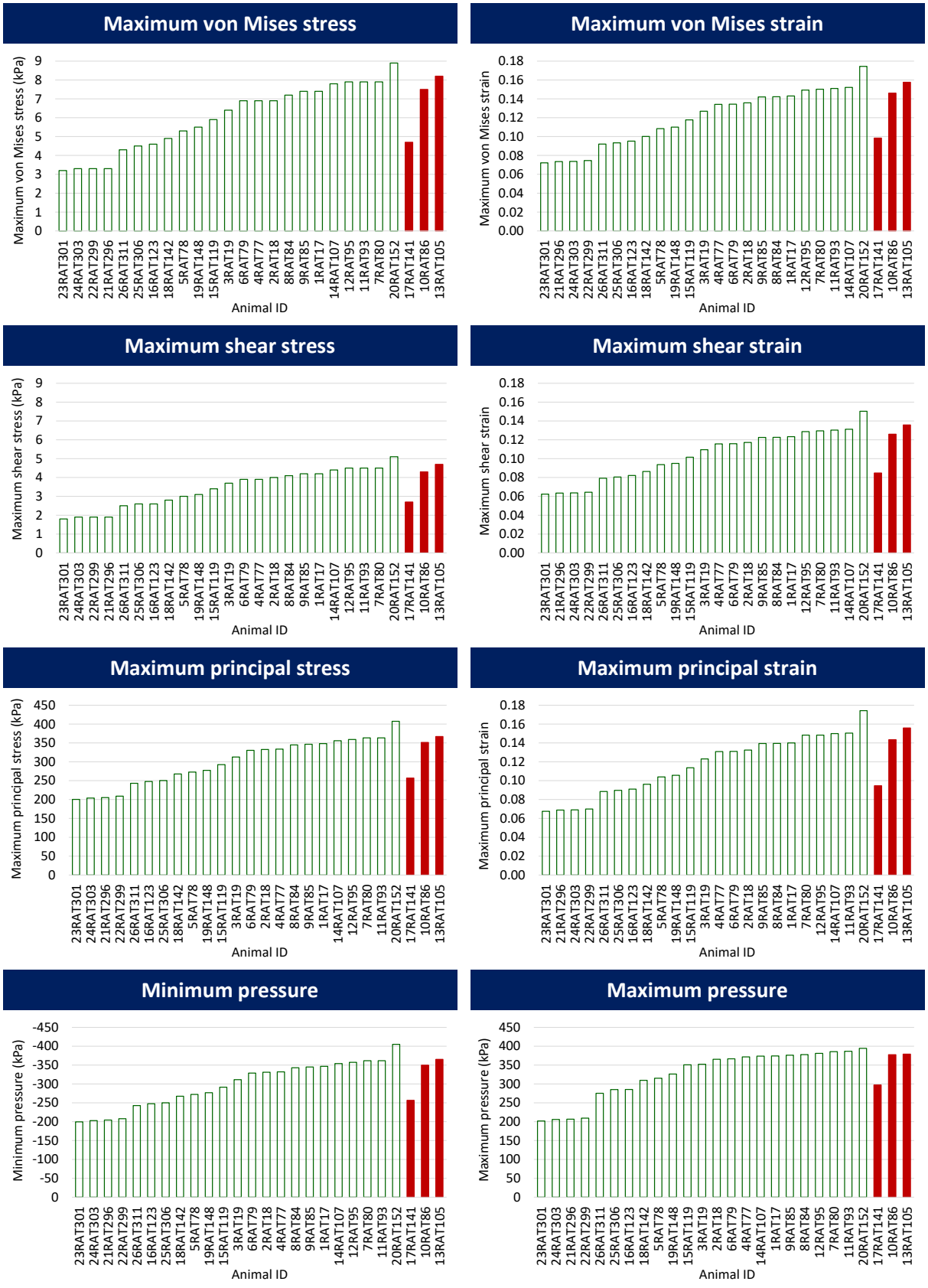

Simulation results of all twenty-six experimental cases for all ten mechanical parameters, which are maximum axonal strain, maximum strain energy, maximum von Mises stress and strain, maximum

shear stress and strain, maximum principal stress and strain and minimum and maximum pressures for the specific brain regions associated with cognition are given below in Table E22 to Table E28. Results are categorized based on seven experimental behavioural responses in injured (solid red columns) and non-injured (blank green columns) groups.

Table E22: Simulation results for brain regions associated with cognition. Case categorization into non-injured and injured groups is based on unconsciousness time.

Maximum axonal strain

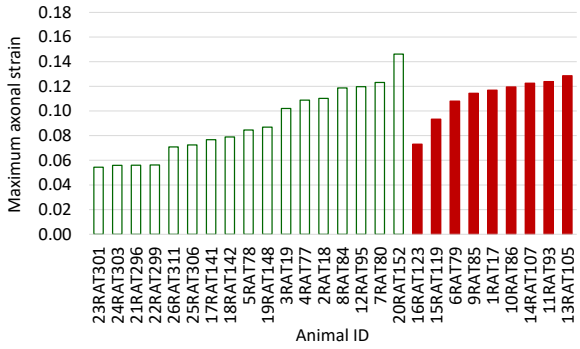

Maximum strain energy

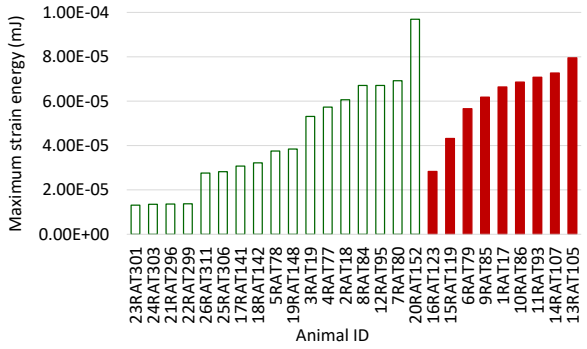

Maximum von Mises stress

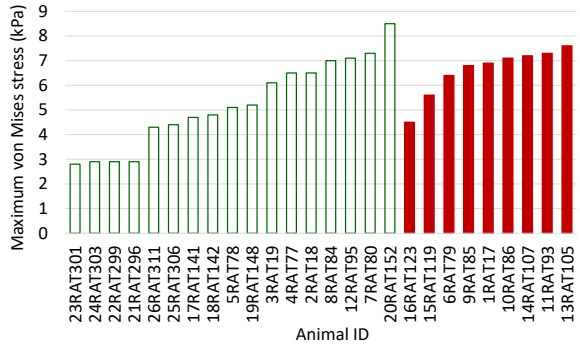

Maximum von Mises strain

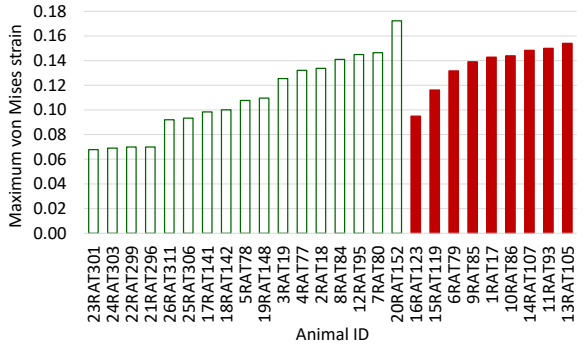

Maximum shear stress

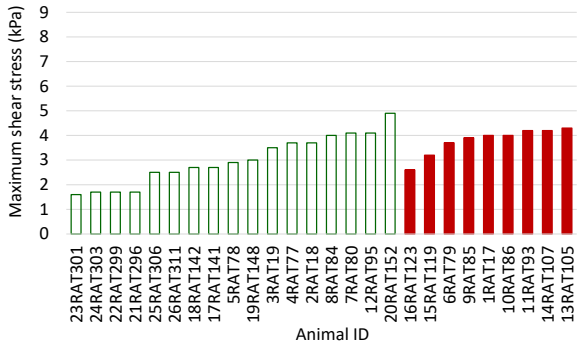

Maximum shear strain

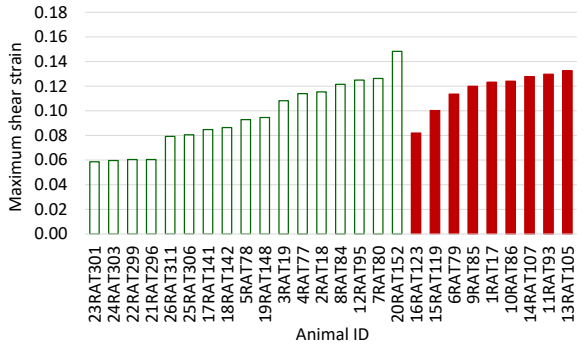

cont.

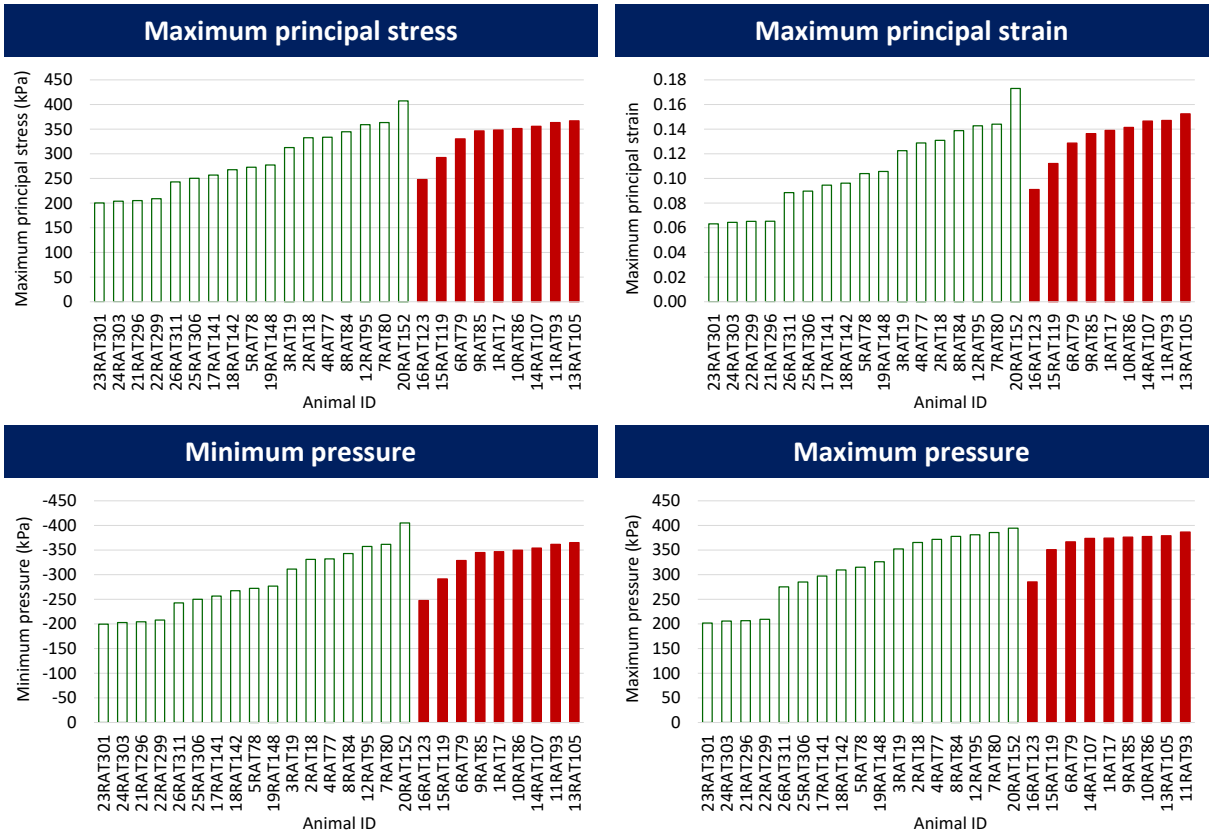

Table E23: Simulation results for brain regions associated with cognition. Case categorization into non-injured and injured groups is based on EPM distance travelled.

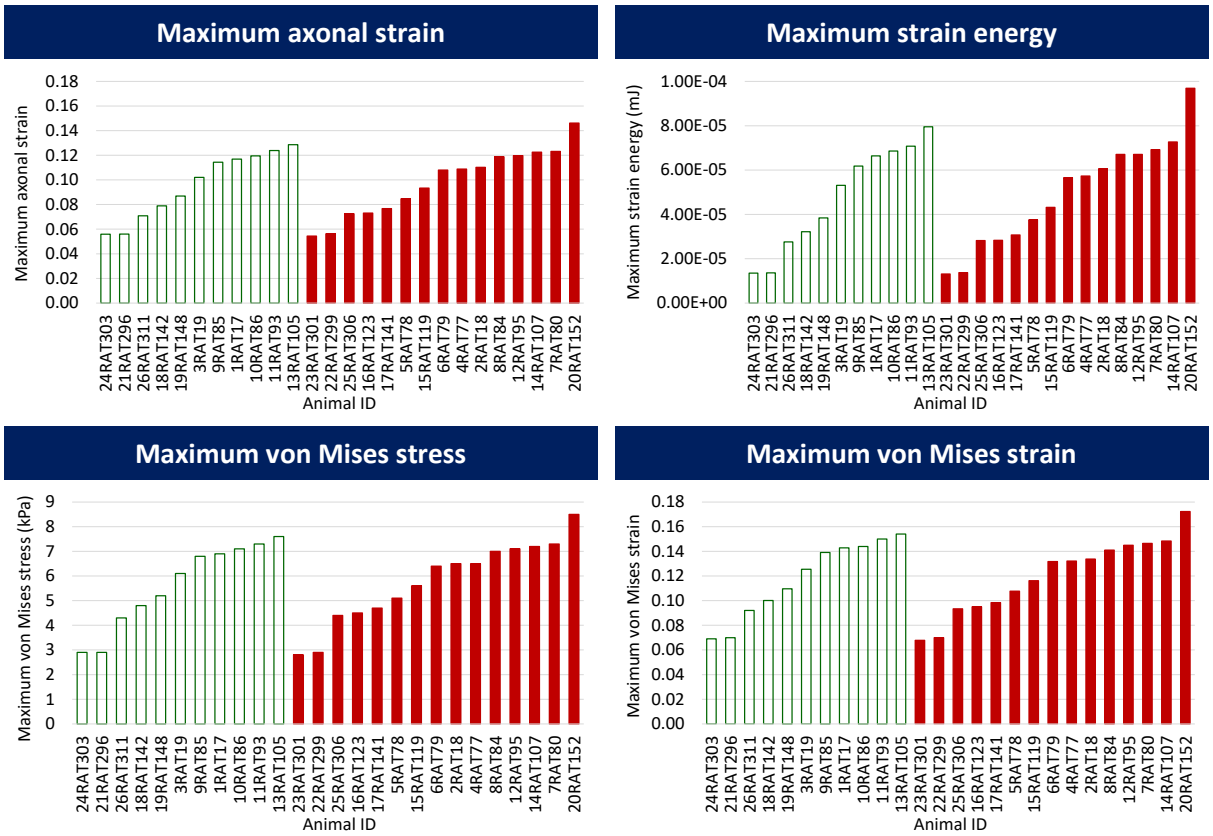

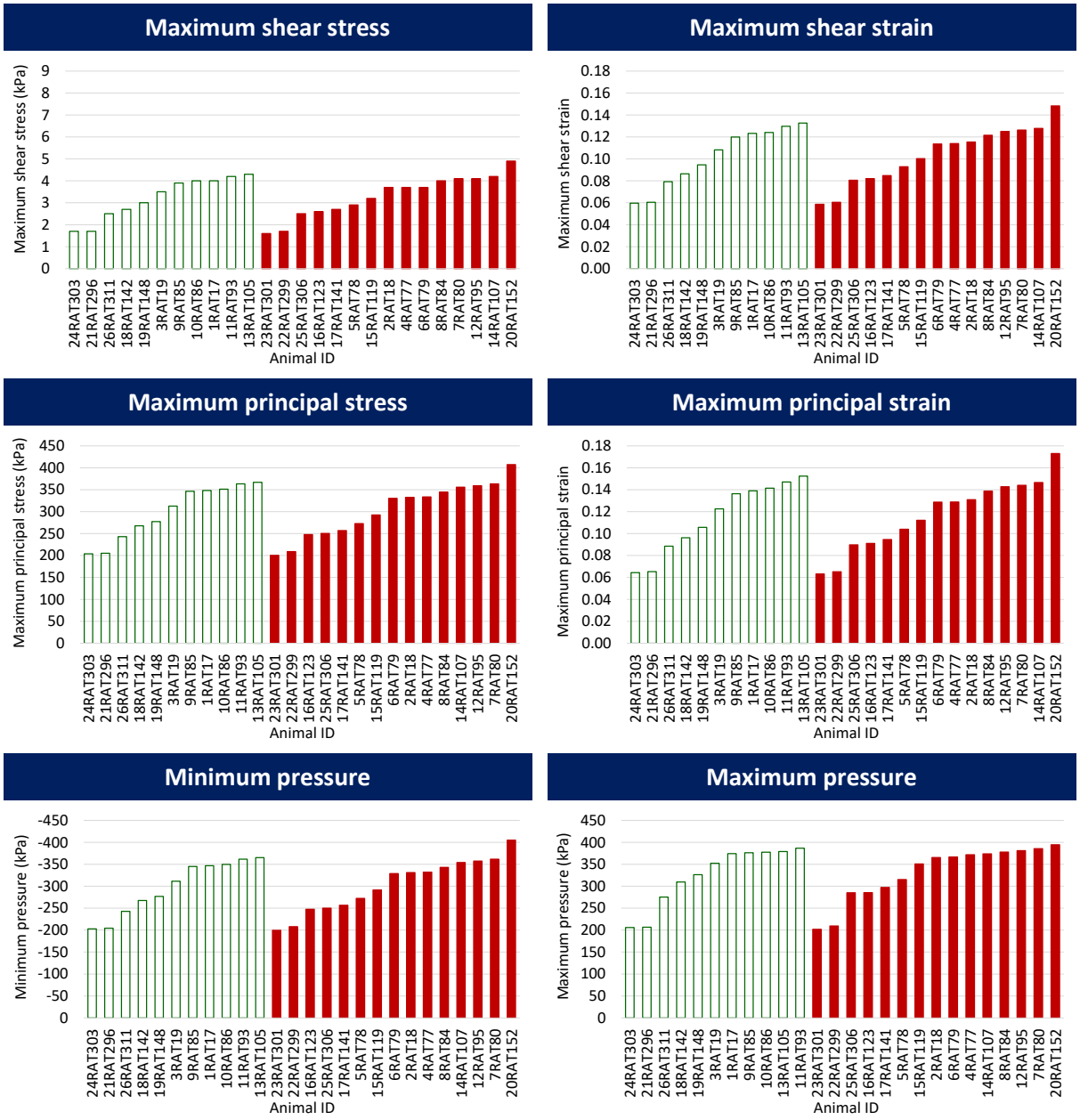

Table E24: Simulation results for brain regions associated with cognition. Case categorization into non-injured and injured groups is based on EPM arm changes.

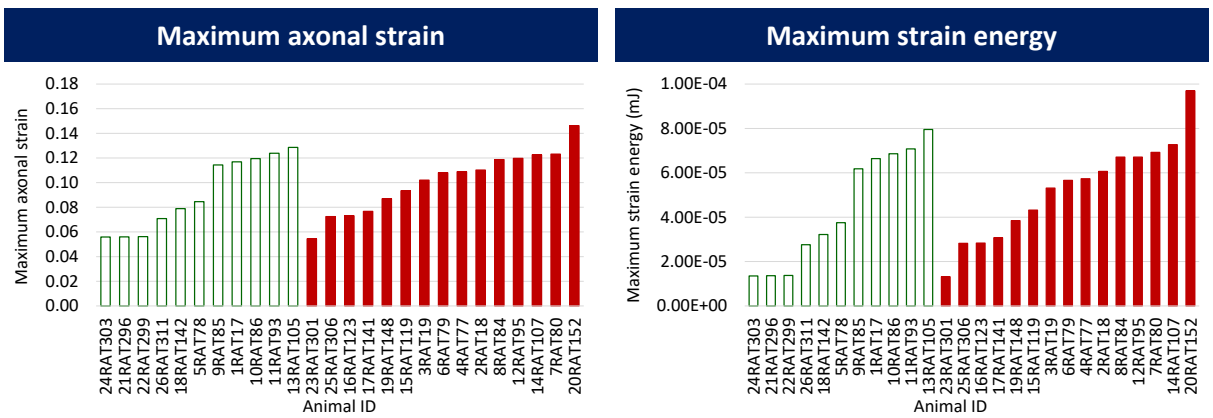

Maximum von Mises stress

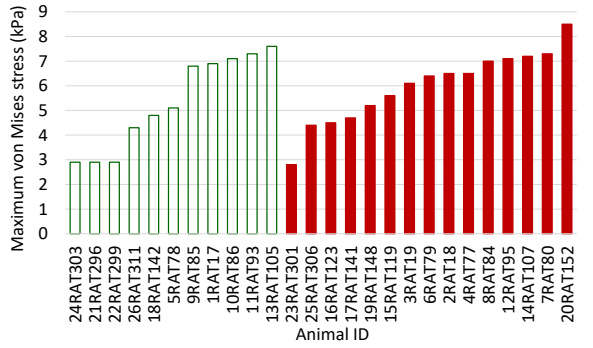

Maximum von Mises strain

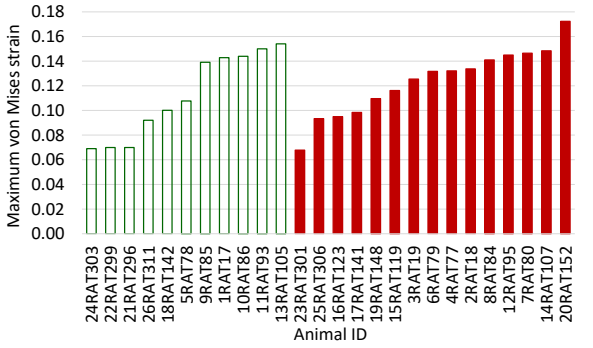

Maximum shear stress

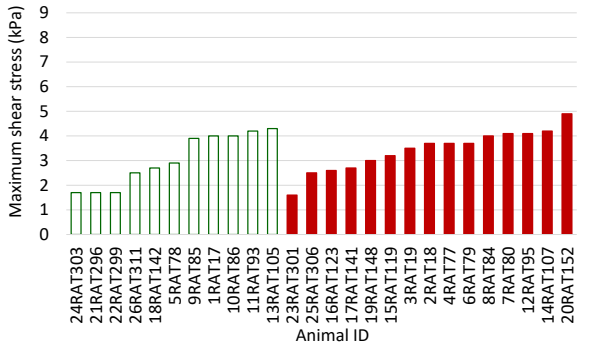

Maximum shear strain

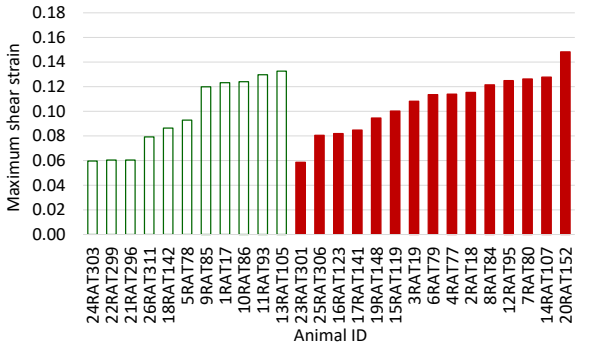

Maximum principal stress

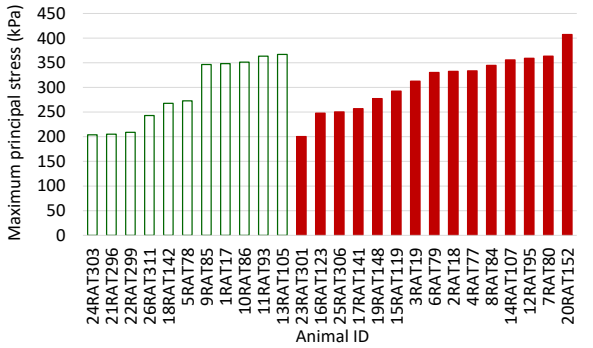

Maximum principal strain

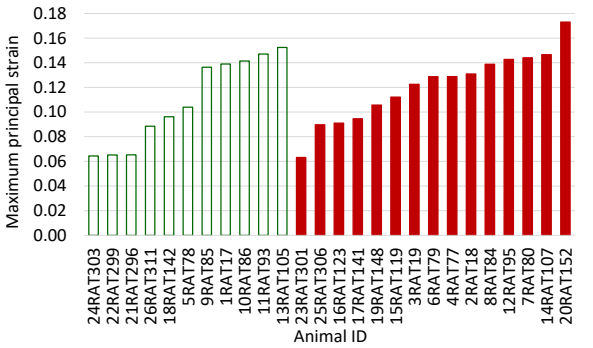

Minimum pressure

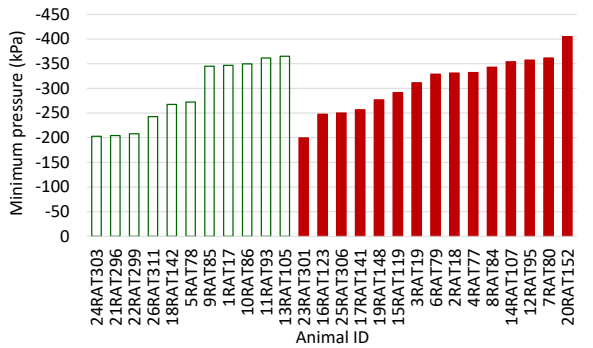

Maximum pressure

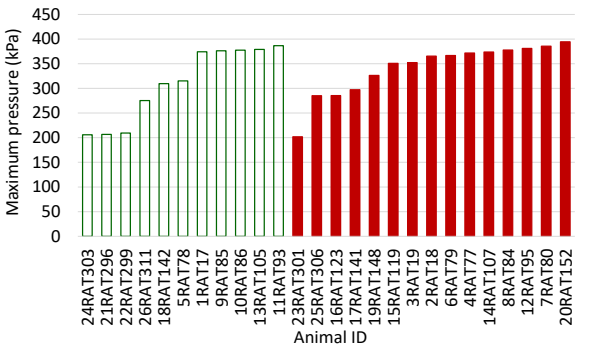

Table E25: Simulation results for brain regions associated with cognition. Case categorization into non-injured and injured groups is based on EPM open duration.

Maximum axonal strain

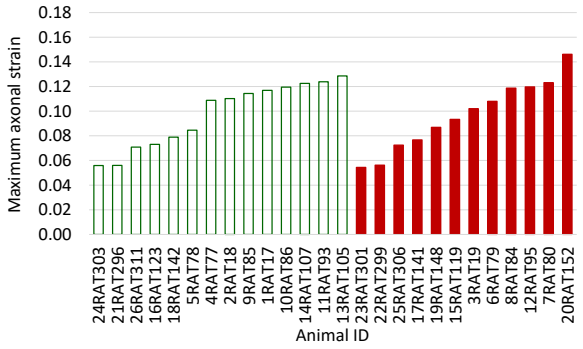

Maximum strain energy

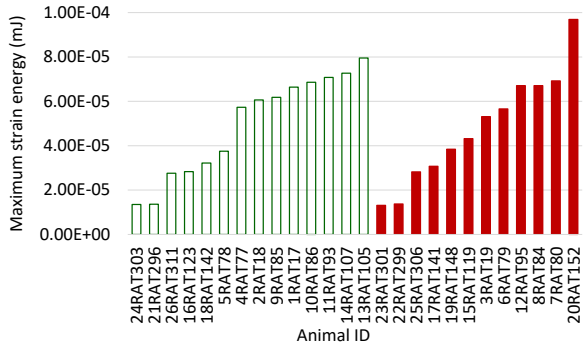

Maximum von Mises stress

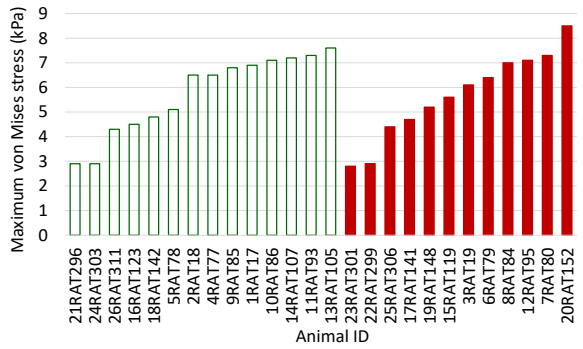

Maximum von Mises strain

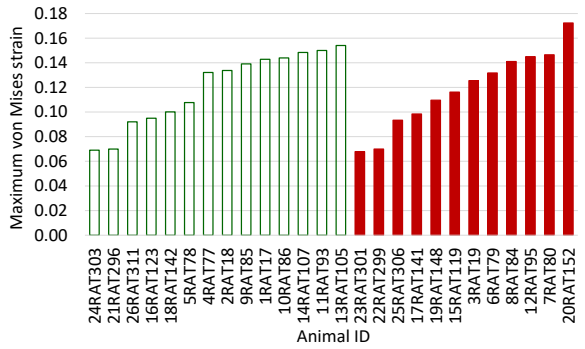

Maximum shear stress

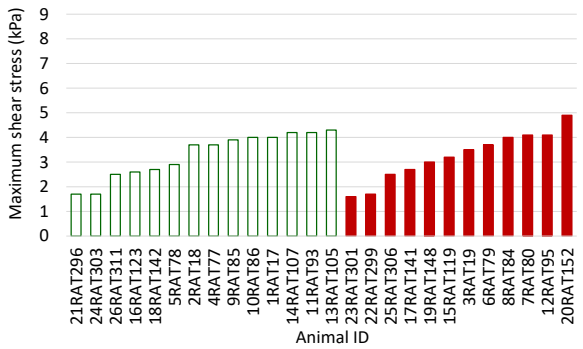

Maximum shear strain

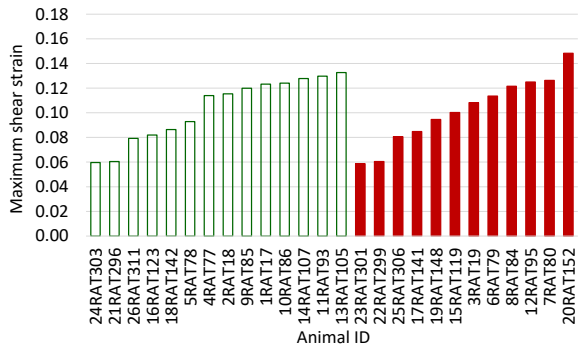

Maximum principal stress

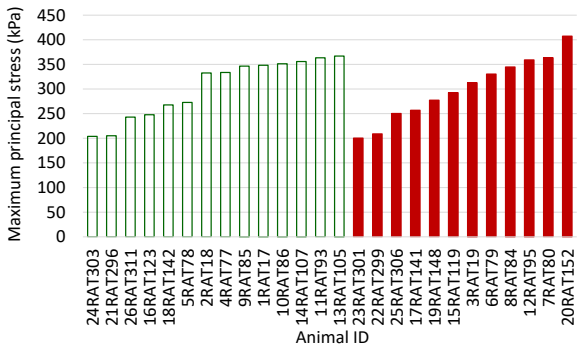

Maximum principal strain

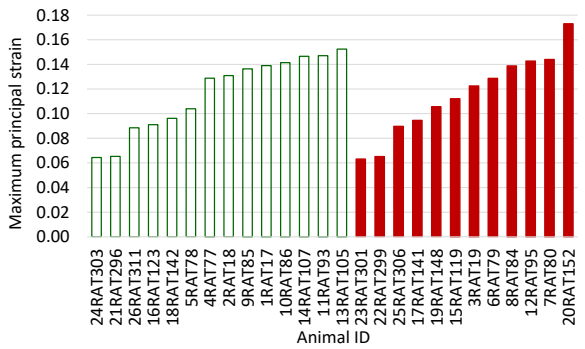

cont.

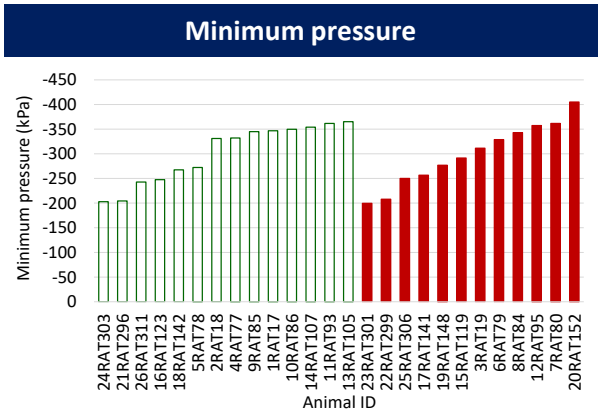

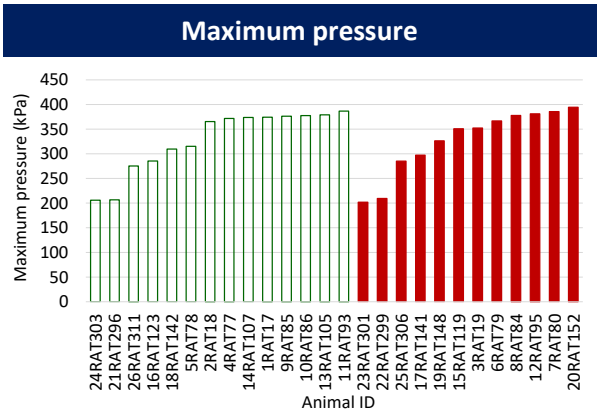

Table E26: Simulation results for brain regions associated with cognition. Case categorization into non-injured and injured groups is based on MCW session I latency.

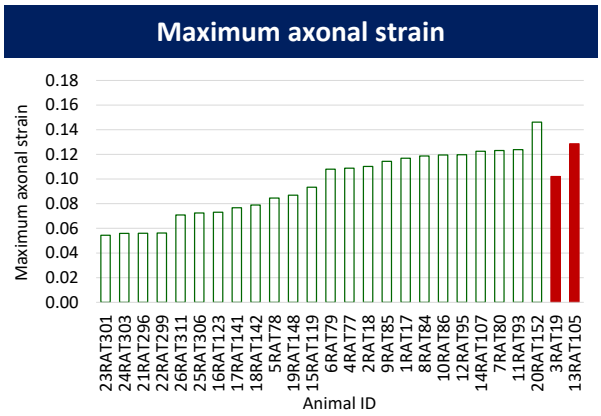

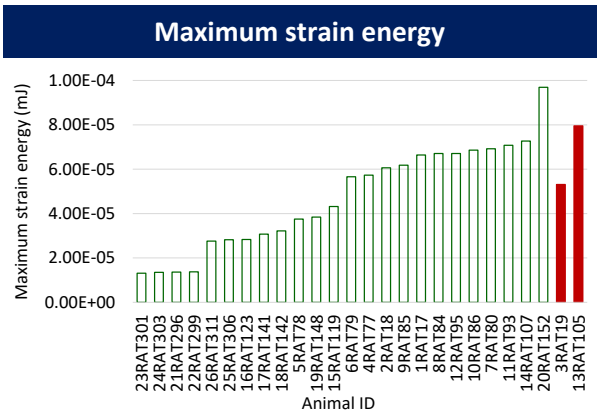

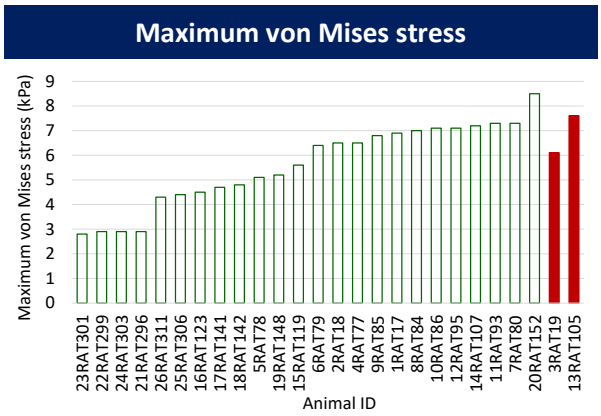

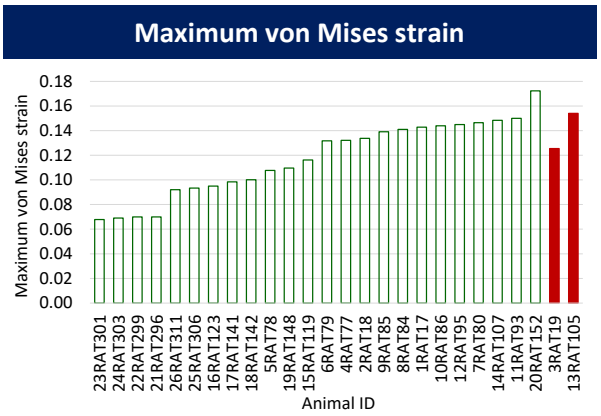

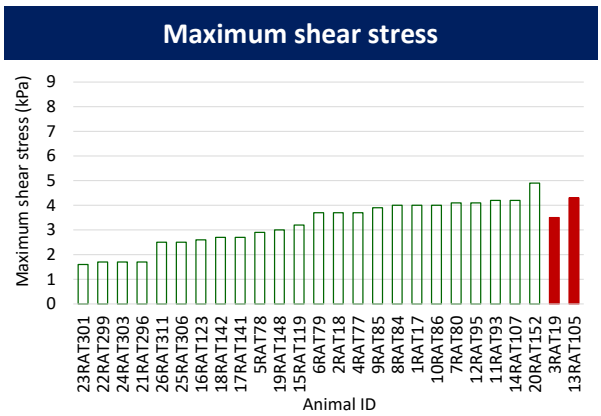

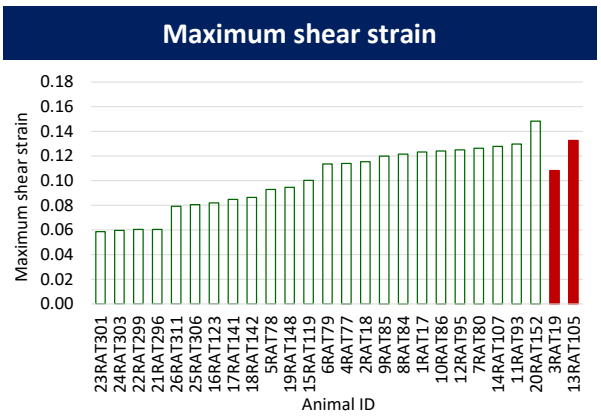

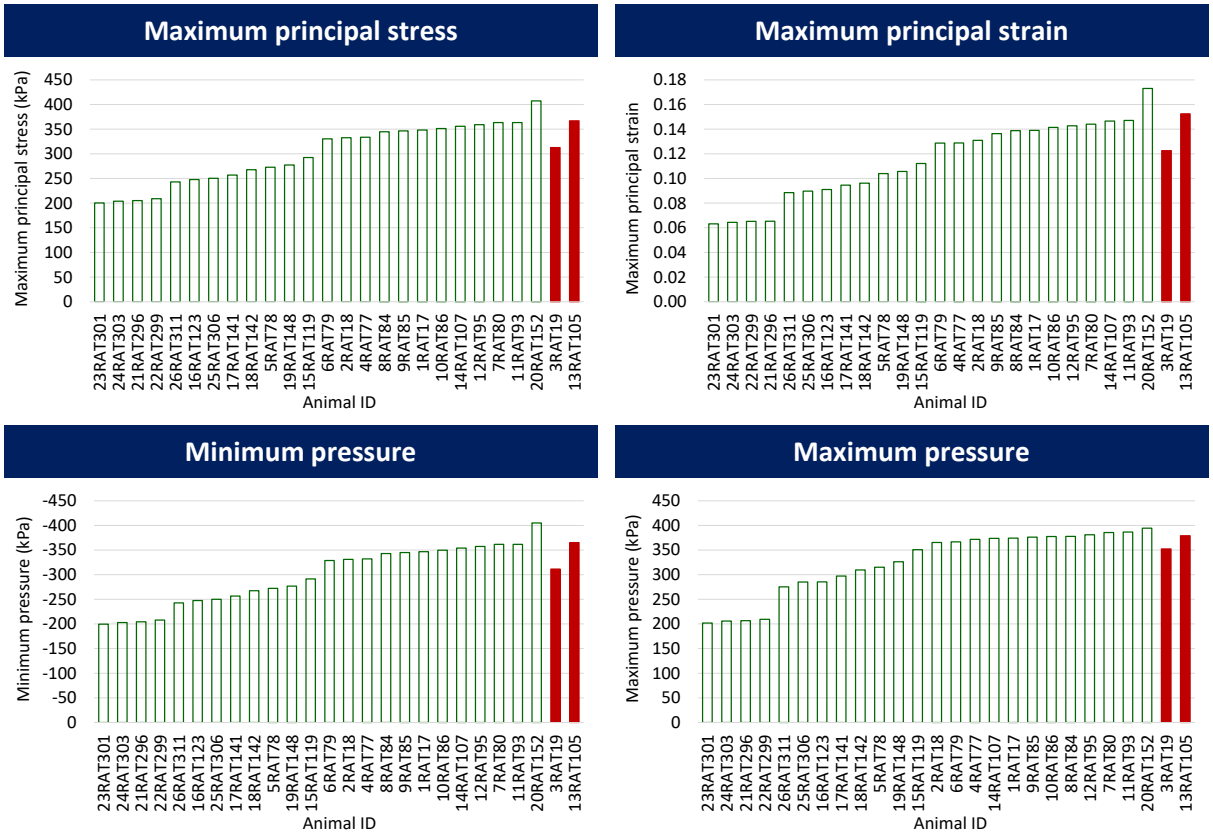

Table E27: Simulation results for brain regions associated with cognition. Case categorization into non-injured and injured groups is based on MCW session II latency.

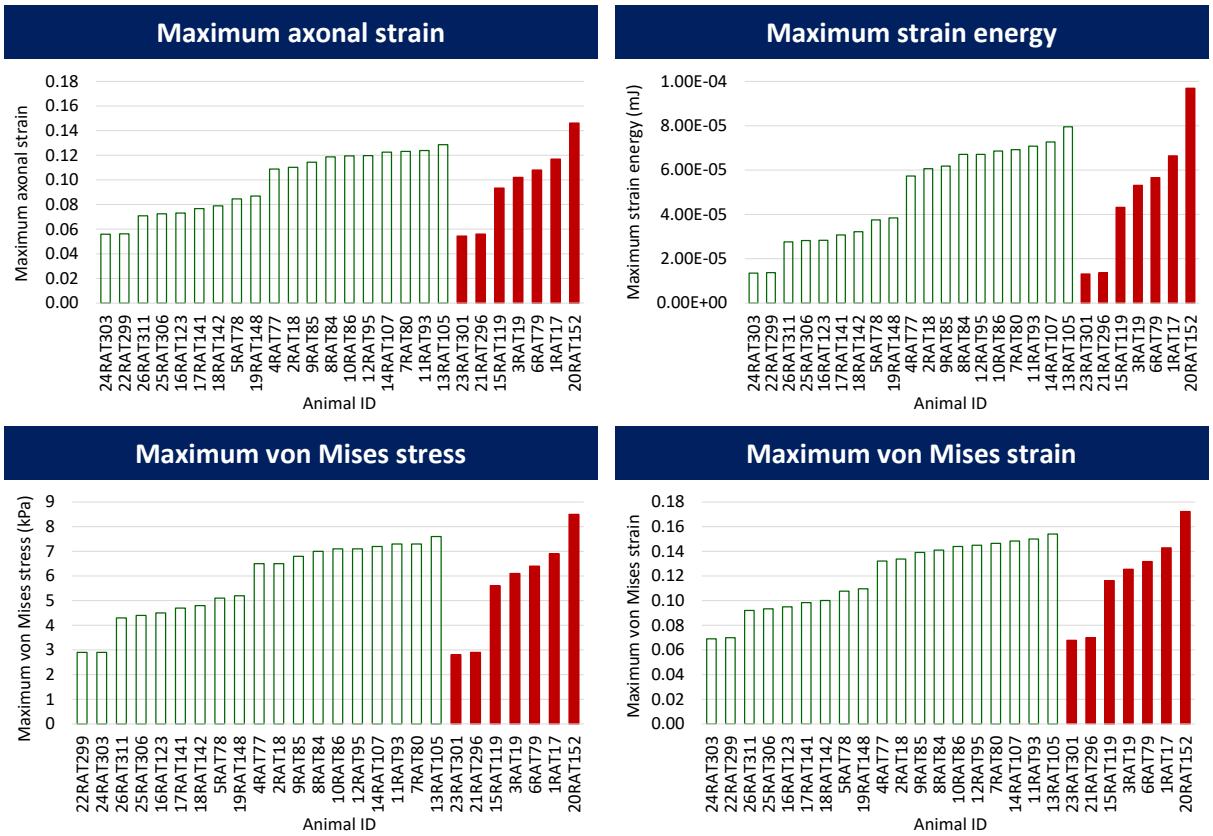

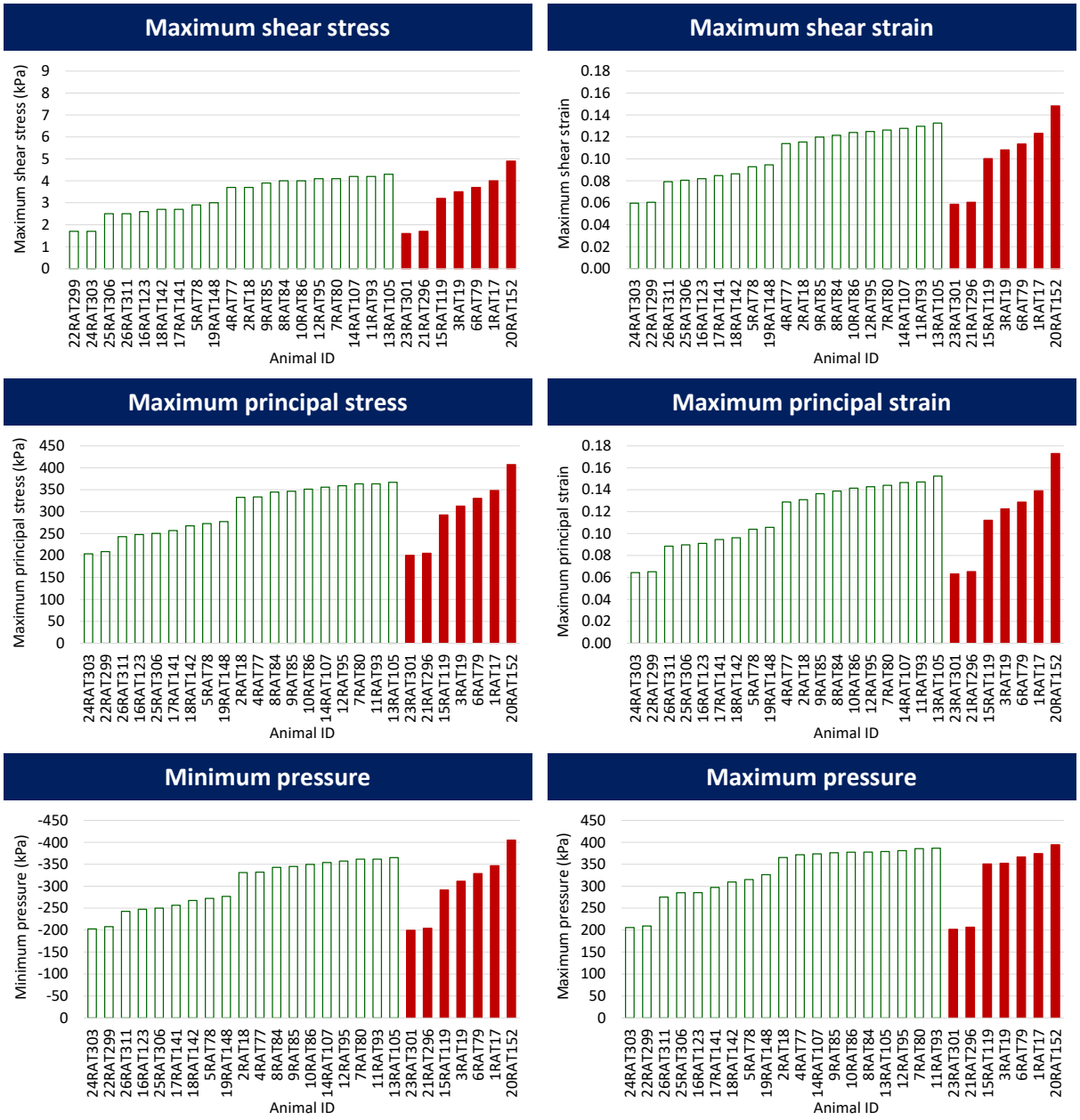

Table E28: Simulation results for brain regions associated with cognition. Case categorization into non-injured and injured groups is based on MCW session III latency.

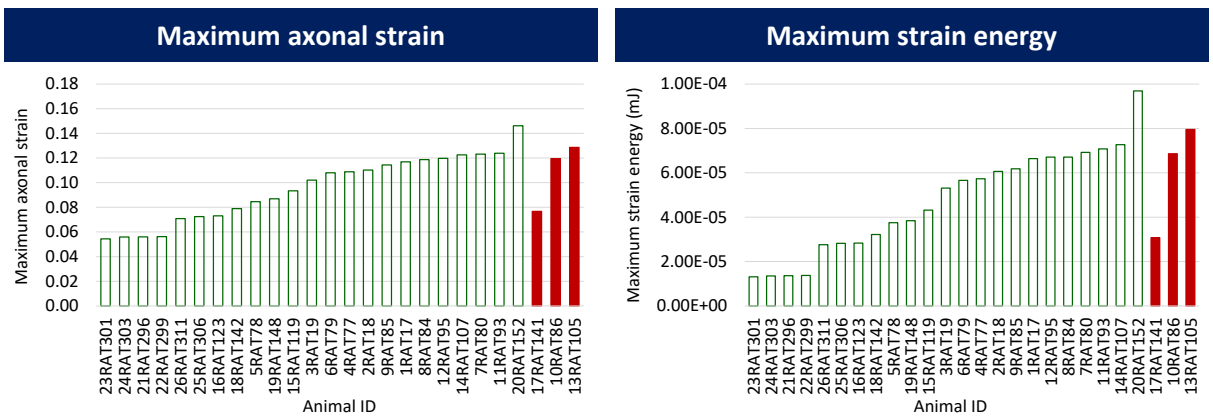

Maximum von Mises stress

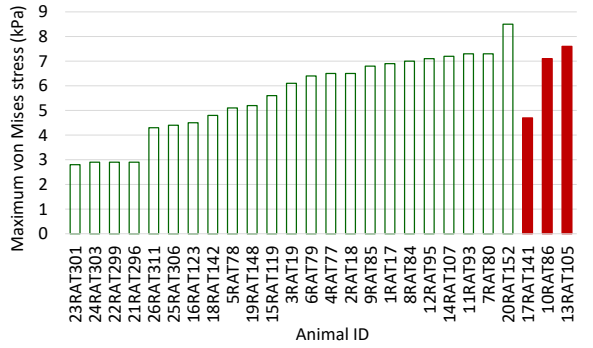

Maximum von Mises strain

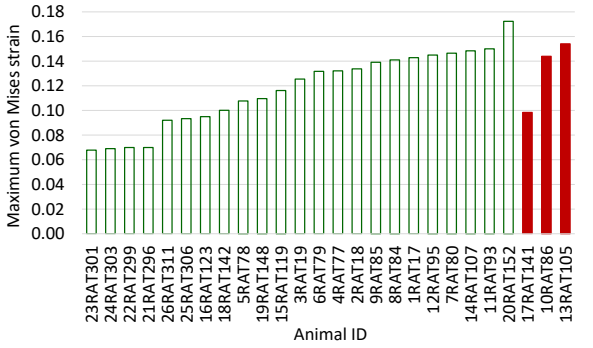

Maximum shear stress

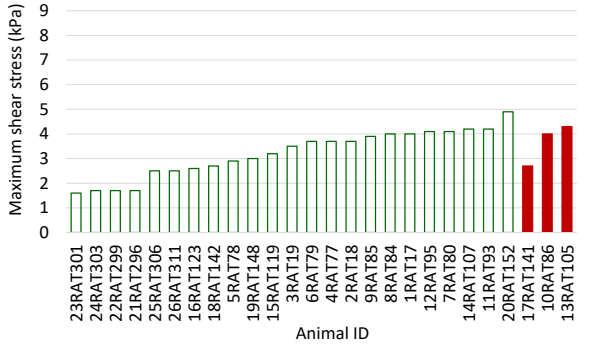

Maximum shear strain

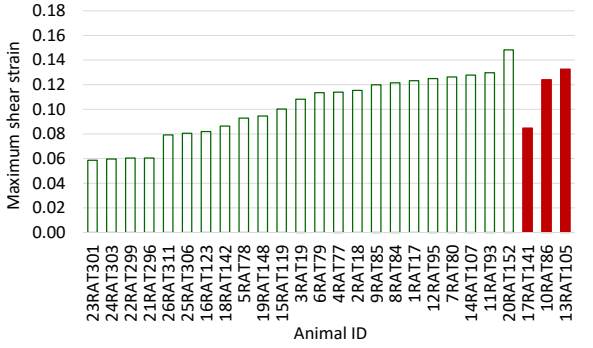

Maximum principal stress

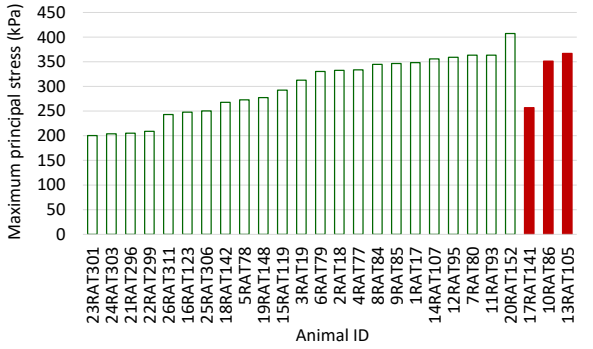

Maximum principal strain

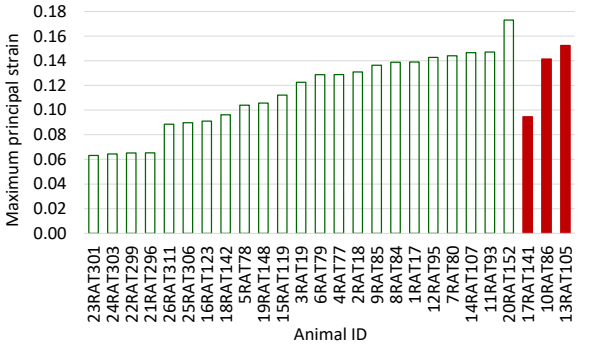

Minimum pressure

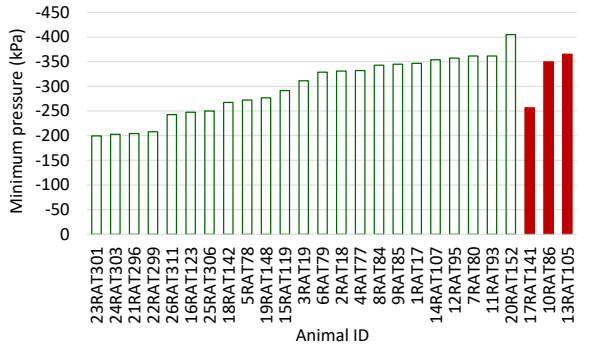

Maximum pressure

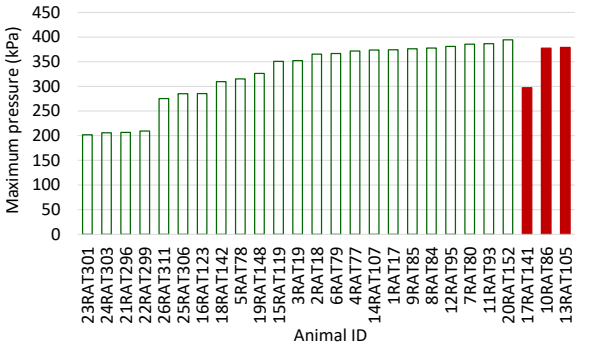

Sumedha PREMI

Limites de tolérance à la commotion cérébrale

Résumé

Bien qu'il s'agisse d'un traumatisme crânien léger, la commotion cérébrale entraîne de graves conséquences à long terme et peut nuire à la vie d'une personne, à sa famille et à la société. La commotion cérébrale est une perturbation neurologique causée par une impulsion mécanique directe ou indirecte à la tête. Ces troubles neurologiques entraînent des dysfonctionnements du cerveau. Comme les lésions axonales diffuses (DAI) sont l'une des caractéristiques pathologiques les plus fréquentes des lésions cérébrales traumatiques, la connaissance du seuil mécanique de la commotion cérébrale en termes d'allongement axonal peut aider à développer de meilleurs outils de prédiction des lésions cérébrales et à optimiser les systèmes de protection des têtes. Les modèles numériques se sont avérés être des moyens efficaces pour de telles études. Comparés à l'expérimentation, les modèles numériques sont plus précis, plus économiques et plus faciles à utiliser. De plus, ils n'impliquent pas de préoccupations éthiques qui sont toujours présentes en cas d'expérimentation sur des sujets biologiques. Néanmoins, les données expérimentales sont essentielles à la validation d'un modèle informatique. L'impossibilité d'expérimenter sur le cerveau humain restreint l'étude détaillée sur les commotions cérébrales. Cependant, les petits animaux, comme le rat, semblent être un substitut intéressante pour de telles recherches. La littérature confirme qu'un cerveau de rat adulte peut être considéré comme neurologiquement équivalent à un cerveau humain adulte et que, au niveau tissulaire, les cerveaux interespèces réagissent de la même façon, ce qui a conduit à de nombreuses recherches effectuées au moyen du modèle du cerveau du rat. Ainsi, dans le cadre de cette thèse de doctorat, un modèle cérébral anisotrope visqueux hyperélastique à éléments finis du rat a été développé, validé vis à vis d'expériences rapportées dans la littérature puis utilisé pour l'étude du seuil mécanique à la commotion en termes d'allongement axonal basé sur les simulations de traumatismes crâniens expérimentaux. Ce travail de doctorat contribue à la recherche sur le développement d'outils de prédiction des lésions cérébrales et à l'optimisation des systèmes de protection de la tête.

Mots clés: commotion cérébrale, modélisation du cerveau, élongation axonales

Sumedha PREMI

Investigation of mechanical threshold to concussion

Abstract

Concussion, in spite of being a mild traumatic brain injury, involves serious long term consequences and can adversely affect the life of an individual, their family and the society. Concussion is a neurological disturbance caused by a direct or indirect impulsive mechanical loading of the head. These neurological disturbances result in functional impairments of the brain. As diffuse axonal injury (DAI) is found to be one of the most frequent pathological features of traumatic brain injury, knowledge of mechanical threshold to concussion in terms of axonal elongation can help in developing better brain injury prediction tools and in optimizing head protection systems. Computational models have proved to be efficient means for such studies. In comparison to experimentation, computational models are more accurate, economic and easier to use. Further, they do not involve any ethical concerns that are always present in case of experimentation on biological subjects. Still, experimental data is essential for the validation of a computational model. Unfeasibility of experimentation on human brain restricts the detailed investigation on concussion. However, small animals, such as rat, seem to be an interesting opportunity for such investigations. The literary observations that an adult rat brain can be considered neurologically equivalent to an adult human brain and that at tissue level inter species brains respond similarly further support the significance of investigations through rat brain model. Hence, as a part of this doctoral thesis work, an anisotropic viscous hyperelastic finite element rat brain model is developed, validated and utilized for the investigation of mechanical threshold to concussion in terms of axonal elongation. This doctoral work contributes to the research on the development of better brain injury prediction tools and the optimization of head protection systems.

Keywords: concussion, mild traumatic brain injury, brain modelling, axonal strain, brain anisotropy

UNIVERSITÉ DE STRASBOURG

ÉCOLE DOCTORALE ED269 : Mathématiques, Sciences de l'Informations et de l'Ingénieur

Laboratoire ICube, UMR7357, équipe Matériaux Multi-Échelles et Biomécanique

THÈSE présentée par :

Sumedha PREMI

soutenue le : **16 décembre 2019**

pour obtenir le grade de : **Docteur de l'université de Strasbourg**

Discipline / Spécialité : Mécanique / Biomécanique

Limites de tolérance à la commotion cérébrale

THÈSE dirigée par :

M. WILLINGER Rémy	Professeur, université de Strasbourg
Mme DECK Caroline	Chercheur, HDR CDI, université de Strasbourg

RAPPORTEURS :

M. ARNOUX Pierre Jean	Directeur de recherche, IFSTTAR / Aix-Marseille université
M. PELDSCHUS Steffen	Professeur, université de Ludwig-Maximilian, Munich

Table des matières

Introduction générale

La commotion cérébrale est un type de traumatisme crânien (TBI), qui est également désigné par de nombreux autres noms tels que traumatisme crânien léger (mTBI), lésion axonale diffuse (DAI), commotion cérébrale liée au sport (SRC), lésion axonale traumatique (TAI), lésion cérébrale inertielle (IBI), lésion cérébrale diffuse (DBI). De récent études scientifiques indiquant des déficiences psychiatriques, cognitives et neurocomportementales à long terme associées aux commotions cérébrales ont clairement montrés que les commotions cérébrales dans le sport constituent un grave problème de santé publique (Zhang et al., 2004; Murray et al., 2015). Théoriquement, la commotion cérébrale peut être définie comme une perturbation du fonctionnement du cerveau, causée par une force mécanique impulsive directe ou indirecte transmise à la tête. Les effets les plus courants de la commotion cérébrale comprennent l'altération des fonctions neurologiques, comme la conscience, la mémoire, la pensée, le mouvement, la cognition, les sensations et les émotions. Cependant, une commotion cérébrale aiguë peut entraîner une perte de conscience ou une amnésie pendant une durée indéterminée (CDC 2014; McCrory et al., 2017). Dans des circonstances normales, ces troubles sont des altérations transitoires des fonctions neurologiques, qui se résolvent spontanément. Cependant, dans certaines circonstances, les signes et les symptômes des troubles commotionnels évoluent sur une période de temps, allant de quelques minutes à quelques heures (McCrory et al., 2017).

La plupart du temps, les signes et les symptômes de commotion cérébrale ne résultent pas de lésions structurelles macroscopiques et ne peuvent donc pas être diagnostiqués par les techniques standard de neuroimagerie structurelle (McCrory et al., 2017). Le rétablissement après une commotion cérébrale peut prendre quelques heures, jours, semaines, mois ou même plus longtemps. Le rétablissement dépend de divers facteurs, comme la gravité de la commotion, l'âge et l'état de santé de la personne au moment de la commotion et les soins qu'elle a reçus après la commotion (McCrory et al., 2017). Il a été observé que des coups sub-commotionnels répétés, en peu de temps, s'avèrent plus dommageables qu'un seul coup de commotion (McCrory et al., 2004; Gysland et al., 2011). Une personne ayant des antécédents de commotion cérébrale est plus vulnérable aux blessures par commotion cérébrale à l'avenir que celle qui n'en a pas. De plus, il y a des chances que le rétablissement plus lent des fonctions neurologiques soit dû à une commotion cérébrale déjà survenue (Guskiewicz et al., 2003). L'intervalle entre les blessures joue un rôle important dans l'identification de la durée et de l'étendue des déficits cognitifs post-traumatiques. Il est également possible que les déficiences cognitives à long terme se produisent même sans conséquences histologiques, telles que l'IAD (Tadepalli et al., 2019). Les lésions traumatiques répétitives peuvent potentiellement conduire à une neurodégénérescence irréversible et progressive, comme l'encéphalopathie traumatique chronique (ETC) (Gysland et al., 2011; Briggs et al., 2016). Par

conséquent, dans le contexte des conséquences sociales et économiques des commotions cérébrales, il est essentiel d'étudier les mécanismes des lésions cérébrales afin de minimiser le taux de commotion en optimisant la conception des mesures de sécurité, comme le port d'un casque de sport. Examinons maintenant quelques statistiques et l'épidémiologie liées aux commotions cérébrales.

La TBI est la principale cause d'invalidité et de décès chez les enfants ainsi que chez les jeunes adultes dans le monde entier, causant près de la moitié des décès dus aux traumatismes (WHO, 2006). À l'échelle mondiale, la TBI est l'un des facteurs qui contribuent le plus à l'invalidité et au décès parmi toutes les blessures liées à un traumatisme (Rubiano et al., 2015). En 2015, environ 5,3 millions de personnes aux Etats-Unis et environ 7,7 millions de personnes en Europe vivaient avec un handicap lié au TBI (Rubiano et al., 2015). On estime que 69 millions de personnes dans le monde souffrent d'un TBI chaque année (Dewan et al., 2018), dont 80-90 % appartiennent à la catégorie des blessures légères (WHO, 2006; Dewan et al., 2018). La fréquence d'apparition des commotions légère est beaucoup plus élevée (environ dix fois) que celle de la commotion modérée ou grave (Dewan et al., 2018). Figure 1 montre l'incidence annuelle de la commotion (cas pour 100 000 personnes) par région de l'Organisation mondiale de la santé (OMS). Le nombre maximum d'incidents globaux de TB (pour 100 000 personnes) a été constaté en Amérique du Nord avec un compte moyen de 1 299 cas, suivi par l'Europe avec un compte moyen de 1 012 cas et le moins en Afrique avec un compte moyen de 801 cas (Dewan et al., 2018).

Figure 1: Incidence annuelle de la commotion (cas pour 100 000 personnes) par région de l'OMS (Dewan et al., 2018).

D'après l'examen clinique, environ 90 % des ICT sont identifiés comme étant légers. Bien que le taux de mortalité en cas de mTBI soit inférieur à 1 %, les conséquences à long terme sont graves et affectent négativement la vie des individus, de leur famille et de la société en général (WHO, 2006). Entre 2001 et 2012, environ 90 % des traumatismes liés aux sports et aux loisirs aux États-Unis ont été traités et

renvoyés des services d'urgence, ce qui laisse supposer que ces blessures sont bénignes. Cependant, des recherches antérieures indiquent que 15 à 25 % des personnes atteintes de TBIm peuvent souffrir de conséquences physiques, cognitives et émotionnelles à long terme (Coronado et al., 2015). En 2013, environ 2,8 millions de visites aux urgences, d'hospitalisations et de décès liés à des TBI (TBI-EDHD) sont survenus aux États-Unis. Les visites aux urgences dues à la TBI aux États-Unis seulement ont augmenté de plus de 50 % de 2007 à 2013. Bien que les hospitalisations et les décès liés à la tuberculose n'aient augmenté que d'environ 8 % et 2 % respectivement, ils ne peuvent pas être considérés comme négligeables (Taylor et al., 2017).

L'influence mondiale des TBI, en termes de charge mondiale de la TBI, est illustrée dans la Figure 2. Il ressort clairement de la figure que la région de l'Asie du Sud-Est (SEAR) et la région du Pacifique occidental (WPR) ont des charges estimées de TBI environ trois fois plus élevées que celles des États-Unis, du Canada (AMR-US/Can), de l'Amérique latine (AMR-L) et de la région de la Méditerranée orientale (EMR). Alors que le fardeau estimé de la TBI de l'Afrique (AFR) et de l'Europe (EUR) se situe quelque part entre (Dewan et al., 2018).

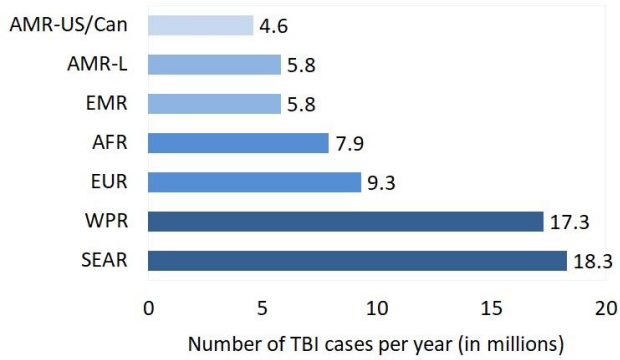

Figure 2: Diagramme illustrant l'estimation annuelle du volume des TBI dans les régions de l'OMS (AMR-US/Can : Amérique - États-Unis et Canada ; AMR-L : Amérique - Amérique latine ; EMR : Région de la Méditerranée orientale ; AFR : Afrique ; EUR : Europe ; WPR : Région du Pacifique occidental et SEAR : Région de l'Asie du Sud-Est) (Dewan et al., 2018).

Selon un examen effectué par le Tagliaferri et al. (2006), une comparaison des paramètres épidémiologiques fondée sur les données relatives à l'ITS en Europe, aux États-Unis, en Australie, en Asie et en Inde, pour les adultes et pour diverses années, est présentée dans le Table 1. Le taux d'incidents signalés en Europe est beaucoup plus élevé qu'aux États-Unis et en Inde. Ici, il est important de considérer que ces données sont basées sur les hospitalisations ; et les variations dans les politiques et pratiques d'hospitalisation à l'échelle nationale peuvent avoir un impact important sur ces données. Les données sur les taux de prévalence ne sont pas disponibles pour l'Europe et l'Australie. Néanmoins, les valeurs des taux de prévalence signalés varient considérablement entre les

États-Unis, l'Asie et l'Inde. Les valeurs des taux de mortalité sont plus ou moins conformes. On peut observer, à partir du pourcentage de gravité déclaré, que les TBL légères prennent le pas sur les TBL modérées et graves.

Table 1: Valeurs des paramètres épidémiologiques basées sur les données de l'IBT en Europe, aux États-Unis, en Australie, en Asie et en Inde (pour les adultes et pour diverses années) (Tagliaferri et al., 2006).

Europe	United States	Australia	Asia	India
Incidence rate (per 100,000 population, includes hospitalizations and deaths)				
235	103	226	344	160
Prevalence rate (per 100,000 population)				
NR	1893	NR	709	97
Mortality rate (per 100,000 population)				
15.4	18.1	NR	38	20
Severity percentage (mild – moderate – severe)				
79 – 12 – 9	80 – 10 – 10	76 – 12 – 11	76 – 12 – 11	71 – 15 – 13

NR: non rapporté

Comme le montre la Figure 3, à partir des données recueillies entre les saisons 1988 - 2004 par la National Collegiate Athletic Association (NCAA) dans 15 sports (plus d'un million d'expositions et un total de 182 000 blessures), l'analyse des blessures par partie du corps a montré que sur le total des blessures tête-cou, environ 44 % étaient des commotions cérébrales (Hootmann et al., 2007). Les commotions causées par un seul impact étaient un sujet d'intérêt depuis plusieurs décennies. Cependant, depuis la dernière décennie, un certain nombre d'études se concentrent sur les commotions cérébrales répétitives, également connues sous le nom de commotions multiples ou de traumatismes cérébraux légers répétitifs (TCLMR). La littérature a émis l'hypothèse que l'exposition à des impacts répétitifs à la tête subis par un sportif d'un sport de contact pourrait être la cause de la commotion cérébrale (Stemper et al., 2019). Une étude, basée sur les saisons 2015-2017, sur 608 athlètes de football américain de la NCAA Division III, collège et lycée, dans huit établissements, a mesuré les accélérations des impacts de la tête pour analyser les commotions et l'exposition répétitive aux impacts de la tête (Stemper et al., 2018). On a constaté qu'à la date de la commotion cérébrale, 44 % des athlètes ayant subi une commotion cérébrale ont subi des impacts crâniens à risque élevé, ce qui est directement lié à l'apparition de la commotion. Pour les autres, soit 56 % des athlètes ayant subi une commotion cérébrale, il semble que d'autres facteurs auraient contribué à l'apparition de la commotion. De plus, 33 % des athlètes ayant subi une commotion cérébrale ont subi des expositions

répétitives à des impacts crâniens élevés au cours de la saison, ce qui a mené à une commotion cérébrale.

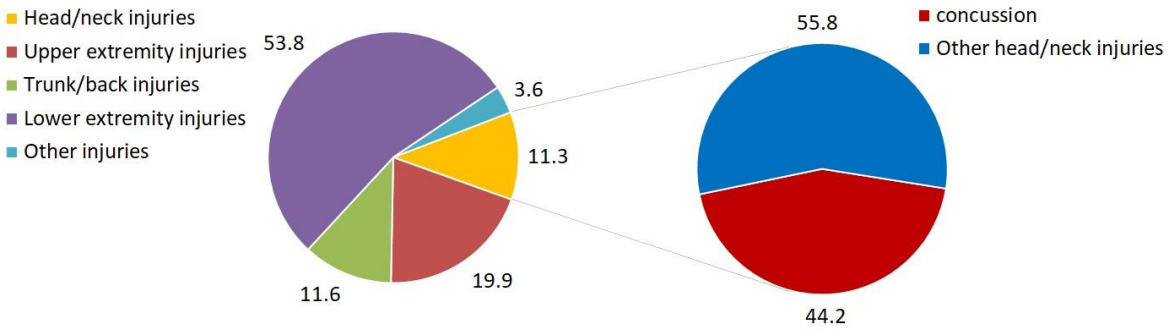

Figure 3: Diagramme illustrant la répartition en pourcentage des blessures dans les sports par parties du corps (Hootman et al., 2007).

Bien que la commotion cérébrale soit une blessure légère, ses conséquences à long terme ont un effet négatif sur la vie d'une personne. Le plus grand défi réside dans le fait que les conséquences immédiates d'une commotion cérébrale ne sont généralement que des troubles fonctionnels, qui ne peuvent être diagnostiqués par les techniques de neuroimagerie structurelle standard actuellement disponibles. Il est bien connu que la commotion cérébrale est causée par un mouvement soudain de la tête. Il devient donc essentiel d'améliorer les outils de prédiction des lésions cérébrales et d'optimiser les systèmes de protection, tels que les casques de sport, de manière à ce que la gravité et donc les conséquences de la commotion cérébrale puissent au moins être réduites, voire complètement évitées. A cet effet, la quantification de la commotion cérébrale en termes de paramètre mécanique sera d'une grande aide. Les modèles de calcul se sont avérés efficaces dans l'étude des lésions cérébrales. C'est pourquoi cette étude tente de quantifier la commotion cérébrale au moyen d'un modèle éléments finis de cerveau de rat. Cette étude est un premier pas vers une meilleure compréhension du mécanisme des lésions cérébrales en obtenant des informations sur le cerveau de rat, en termes d'élongation axonale, en cas de commotion cérébrale. Cette étude ouvre également la porte à de nombreuses autres possibilités concernant les investigations liées aux commotions cérébrales, telles que les investigations sur les commotions répétitives ou les rmTBI. Voyons les grandes lignes de ce travail dans les paragraphes suivants.

Le premier chapitre présente une revue de la littérature concernant cette étude afin de mieux comprendre les motivations de cette étude. L'objectif principal de cette étude est d'étudier le seuil mécanique de la commotion cérébrale en termes d'étirement axonal en cas de commotion. Cet objectif est atteint en développant un modèle anisotrope de cerveau de rat en éléments finis et en simulant des scénarios de commotion. Tout d'abord l'anatomie de la tête et du cerveau, au niveau

macroscopique et au niveau microscopique, est présentée. La connaissance de l'anatomie facilite la compréhension des mécanismes de la lésion. Les principales structures anatomiques et leurs fonctions sont décrites ainsi que les similitudes et les différences entre le cerveau humain et celui d'un rat. Une brève description d'une technique avancée de neuroimagerie, communément appelée imagerie du tenseur de diffusion (ITT ou DTI en anglais), est également fournie. Cette technique de neuroimagerie utilise la diffusion de molécules d'eau à l'intérieur du tissu cérébral et permet d'identifier l'anatomie et les propriétés microscopiques des fibres nerveuses. Comme on sait que la commotion cérébrale est un type de lésion bénigne et qu'elle entraîne des troubles fonctionnels, on suppose que la lésion structurelle se produit au niveau microstructural. Avec cette notion, les mécanismes potentiels de blessure pour la commotion cérébrale sont présentés ci-après. Les perturbations fonctionnelles sont le résultat d'une neurotransmission interrompue causée par un traumatisme mécanique. Les axones sont le principal moyen de neurotransmission et, par conséquent, les mécanismes de lésion potentiels sont considérés comme des altérations des éléments du cytosquelette axonal dues à un étirement soudain. Par conséquent, il est supposé que l'estimation de l'élongation axonale peut fournir une métrique pour la commotion cérébrale. Dans la section suivante, les échelles de classement des lésions cérébrales, les critères et les limites de tolérance, disponibles dans la littérature, sont présentés. Une prise de conscience à ce sujet non seulement élargit notre horizon en ce qui concerne les différentes possibilités d'évaluation des commotions cérébrales, mais nous fait également prendre conscience de la façon dont les commotions cérébrales ont été définies différemment dans diverses études. Vers la fin, la littérature concernant la modélisation par éléments finis du cerveau du rat est présentée. La modélisation par éléments finis est une procédure systématique comprenant la connaissance du matériau, le développement d'un modèle maillé, l'incorporation des propriétés du matériau et la validation du modèle. Par conséquent, les études expérimentales disponibles dans la littérature pour la détermination des propriétés des matériaux du cerveau de rat sont brièvement décrites dans la première partie de cette section. La partie suivante fait la lumière sur les modèles de cerveau de rat à éléments finis existants et fournit des détails sur leur maillage, leur matériau, leur validation et leurs résultats, tout en soulignant leurs limites. La dernière partie de cette section parle brièvement des méthodes de validation des modèles disponibles dans la littérature. La validation d'un modèle de calcul est une partie importante et essentielle du développement d'un modèle, car c'est seulement alors que nous pouvons être sûrs des résultats estimés et les mettre en œuvre. Ce chapitre conclut en résumant les principaux aspects de la littérature et fournit ainsi la motivation de cette étude.

Le deuxième chapitre présente le développement et la validation d'un modèle anisotrope de cerveau de rat aux éléments finis (FERBM). Le chapitre commence par souligner les avantages des modèles de

calcul dans l'étude de la biomécanique des blessures et l'importance de valider un modèle de calcul avant de pouvoir l'utiliser. La base de l'étude, c'est-à-dire le rat Sprague Dawley, est ensuite présentée. Cette espèce particulière de rat est choisie car les simulations de commotion expérimentale présentées dans le dernier chapitre sont basées sur des rats de cette espèce. Un atlas du DTI, disponible dans la littérature, pour cette espèce de rat est ensuite choisi. Cet atlas DTI fournit la géométrie du cerveau du rat ainsi que les paramètres de diffusion. Pour le développement du modèle, les limites géométriques sont d'abord rendues à partir de l'atlas DTI. Les détails sur la modélisation géométrique et le maillage du cerveau du rat sont ensuite présentés. Le cerveau du rat est maillé comme une seule structure, car il n'était ni possible ni nécessaire de mailler le cerveau du rat de manière segmentée. Cependant, pour identifier les caractéristiques régionales et fonctionnelles du cerveau de rat, le modèle maillé est classé uniquement pour l'analyse des résultats de simulation. C'est pourquoi les détails de cette catégorisation anatomique et fonctionnelle sont présentés ci-après. La section suivante présente la méthodologie pour l'identification des paramètres de diffusion. Après le maillage et la connaissance des paramètres de diffusion pour chaque élément du modèle maillé, l'étape suivante consiste à décider du modèle de matériau et des propriétés du matériau. Ainsi, la section suivante fournit des détails sur la loi constitutive choisie et les propriétés du matériau. De plus, l'incorporation des propriétés du matériau et des paramètres de diffusion dans la FERBM est expliquée. Des détails sur le matériau du liquide céphalorachidien et du crâne sont également fournis. Ainsi, la première moitié de ce chapitre expose la méthodologie complète du développement d'un modèle anisotrope de cerveau de rat aux éléments finis. La deuxième moitié de ce chapitre présente la validation de la FERBM anisotrope visqueuse hyperélastique développée. Le modèle développé est validé par rapport à deux expérimentations disponibles dans la littérature. Dans un premier temps, la validation par rapport au déplacement cortical dynamique expérimental sur l'application de l'impulsion de pression sous vide est présentée. Ensuite, la validation par rapport au déplacement relatif du crâne du cerveau sur l'application d'une charge d'accélération rotationnelle dans le plan sagittal est conduite. Pour les deux types d’expériences les spécifications sont d'abord détaillées, puis la simulation est conduite et une comparaison des résultats expérimentaux et numériques est proposée. Une étude paramétrique, présentée à la fin du chapitre, montre l'importance du choix de la loi de la matière cérébrale, de la compressibilité du liquide céphalorachidien et du contrôle du sablier sur la réponse cérébrale. L'objectif de cette étude de disposer d'un modèle validé de cerveau de rat par éléments finis. Ce modèle anisotrope fournira des informations approfondies sur le cerveau en termes d'élongation axonale en cas de commotion cérébrale et ouvrira de nouvelles portes à diverses investigations liées aux commotions cérébrales.

Le dernier chapitre présente les simulations de commotion cérébrale expérimentale. Les données pour vingt-six cas de commotion cérébrale expérimentale ont été mises à notre disposition par le Medical College of Wisconsin (MCW), aux États-Unis, dans le cadre d'une collaboration. Dans un premier temps, l'approche expérimentale est présentée pour détailler la méthodologie utilisée pour induire une commotion cérébrale chez le rat. Ensuite, la méthodologie expérimentale utilisée pour l'évaluation des réponses comportementales après la commotion est présentée. La gravité des blessures aiguës a été évaluée en utilisant le temps de récupération (temps d'inconscience). On a utilisé l'évaluation EPM (Elevated plus maze) pour analyser les changements dans les aspects comportementaux, l'activité et l'émotivité, à la suite de la commotion cérébrale. L'évaluation du labyrinthe d'eau de Morris (MWM) a été utilisée pour analyser l'amnésie antérograde post-traumatique et l'apprentissage spatial après la commotion cérébrale. Des détails sur la simulation de ces cas expérimentaux sont présentés ci-après. Les résultats de la simulation sont extraits pour le cerveau dans son ensemble ainsi que pour les régions anatomiques et fonctionnelles du cerveau. Pour une meilleure compréhension des résultats, la relation entre les résultats de simulation et les résultats expérimentaux est établie à travers différentes perspectives. Enfin, une analyse statistique des résultats de simulation en termes de différentes mesures statistiques est fournie. L'analyse statistique est faite pour identifier le meilleur prédicteur de commotion cérébrale et pour estimer les niveaux de tolérance à la commotion. Ce chapitre conclut en soulignant les avantages du modèle éléments finis anisotrope de cerveau de rat.

En fin de compte, une conclusion générale sous forme de synthèse de cette recherche est exposée et les principaux résultats sont rapportés. Par ailleurs, des perspectives de développement futur de ces travaux sont fournies, car un certain nombre d'étapes sont encore nécessaires à l'avenir pour une compréhension avancée des rmTBI.

Chapter 1: Synthèse bibliographique

Une synthèse bibliographique détaillée est donnée dans la version originale anglaise de la thèse. Les principaux éléments de la synthèse bibliographique sont présentés ci-dessous.

- La modélisation informatique s'est avérée être un outil efficace pour l'étude des lésions cérébrales.

- La non-faisabilité de l'expérimentation sur des sujets humains limite la possibilité d'une investigation détaillée liée à une commotion cérébrale. Ainsi, les modèles animaux ont été un choix privilégié pour ces recherches.

- Le rat a été choisi pour cette étude, car il existe des preuves publiées qu'au niveau des tissus, les cerveaux inter-espèces réagissent de façon similaire et qu'un cerveau de rat adulte peut être considéré comme neurologiquement équivalent à un cerveau humain adulte.

- Les modèles existants de cerveau de rat par éléments finis sont très simplifiés à bien des égards pour l'étude des commotions cérébrales, car ils sont isotropes et partiellement validés.

- Par conséquent, un modèle de cerveau de rat anisotrope à éléments finis entièrement validé était très nécessaire pour les investigations détaillées liées aux commotions cérébrales.

Chapter 2: Développement et validation d'un modèle anisotrope de cerveau de rat en éléments finis

1 Introduction

Les modèles informatiques, également connus sous le nom de modèles éléments finis, se sont avérés être des outils efficaces pour l'étude des lésions cérébrales. Par rapport à l'expérimentation, les modèles informatiques sont plus précis, plus économiques et plus faciles à utiliser. En outre, ils ne soulèvent pas les préoccupations éthiques qui sont toujours présentes en cas d'expérimentation sur des sujets biologiques. Le chapitre précédent a souligné la nécessité d'un modèle anisotrope de cerveau de rat à éléments finis (FERBM), pour l'étude approfondie des commotions cérébrales. Ce chapitre présente la méthodologie pour le développement et la validation d'un FERBM anisotrope.

La première moitié de ce chapitre porte sur l'élaboration des modèles. Ce modèle a été développé progressivement en différentes étapes, qui sont décrites en détail dans les sections suivantes. Dans un premier temps, on a choisi comme base de cette étude un jeune rat adulte Sprague Dawley, pesant environ 290 g. Après avoir choisi le rat, un atlas DTI (imagerie du tenseur de diffusion) disponible, pour le même type de rat, a été choisi pour créer la géométrie du cerveau du rat. Dans une étape ultérieure, le volume du cerveau du rat a été maillé pour créer le modèle géométrique des éléments finis. Ensuite, le même atlas DTI, comme mentionné précédemment, a été utilisé pour identifier les paramètres de diffusion - anisotropie fractionnelle (FA) et direction principale des fibres (PFD), pour chaque élément de la FERBM. Dans une étape ultérieure, une loi constitutive des matériaux et les propriétés des matériaux pour la FERBM, le liquide céphalorachidien (LCR) et le crâne ont été décidées. Enfin, l'implémentation du DTI, pour rendre le FERBM anisotrope, a été complétée par la mise à jour de la définition du matériau du cerveau afin d'intégrer les informations du DTI en termes de paramètres de diffusion.

La deuxième moitié de ce chapitre porte sur la validation des modèles. La validation des modèles est une étape très importante dans les études biomécaniques qui utilisent la modélisation informatique. C'est la validation du modèle qui confirme que les résultats des simulations effectuées sur ce modèle ont une fidélité suffisante et sont acceptables par rapport aux réponses de la vie réelle. Ainsi, cela aide à atteindre l'objectif de l'étude. Pour la validation d'un modèle computationnel, des scénarios expérimentaux sont recréés en termes de simulations numériques et la réponse du modèle est comparée à la réponse expérimentale. La réponse de simulation d'un modèle biofidélique est proche de la réponse expérimentale. Ainsi, le modèle développé dans le cadre de cette étude, FERBM, a été validé avec deux types d'expériences disponibles dans la littérature. La première validation est contre le déplacement cortical dynamique expérimental sur l'application d'une impulsion de pression sous vide sur la surface du cerveau. La deuxième validation est contre le déplacement relatif cerveau-crâne

expérimental sur l'application d'une charge d'accélération rotationnelle dans le plan sagittal. Ces deux expériences ont été réalisées in-vivo. Les détails de ces expériences sont expliqués dans les sections suivantes. En définitive, cette FERBM visqueuse anisotrope hyperélastique permet de mieux comprendre le cerveau du rat, en cas de commotion cérébrale, en termes d'élongation axonale, ce qui est expliqué dans le dernier chapitre.

2 Modélisation géométrique et maillage du cerveau du rat

Un atlas anatomique tridimensionnel du cerveau d'un rat adulte au 72e jour postnatal, élaboré par Rumple et al. (2013), a été utilisé pour la construction géométrique du modèle de cerveau de rat. Une description détaillée de l'atlas du DTI est fournie plus loin dans la section correspondante. Dans un premier temps, la géométrie du cerveau du rat a été rendue à partir de l'atlas du DTI sous la forme d'une représentation STL. Ensuite, le logiciel HyperMesh a été utilisé pour générer la surface du cerveau à partir de la représentation STL et pour mailler le modèle de cerveau de rat (Figure 2.1).

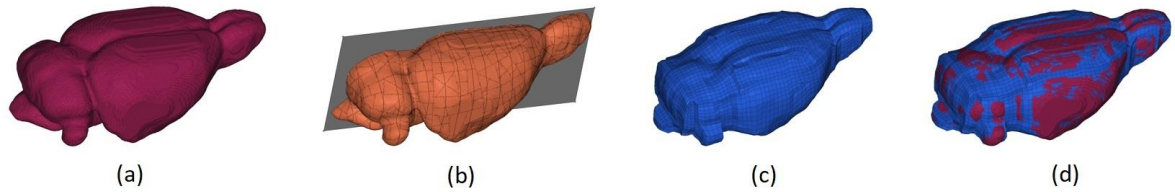

Figure 2.1: Processus de modélisation géométrique et de maillage, (a) représentation STL ; (b) surfaçage ; (c) modèle maillé et (d) représentation STL et modèle maillé coïncidents.

Le maillage du modèle était basé sur l'hypothèse que la géométrie du cerveau est identique à peu près au plan mi-sagittal. Par conséquent, seule la moitié droite du cerveau a été maillée et reproduite à gauche, pour générer le modèle géométrique maillé complet du cerveau de rat. La Figure 2.2 montre les dimensions du modèle de cerveau de rat maillé. Le modèle final de cerveau de rat pesait 1,94 g.

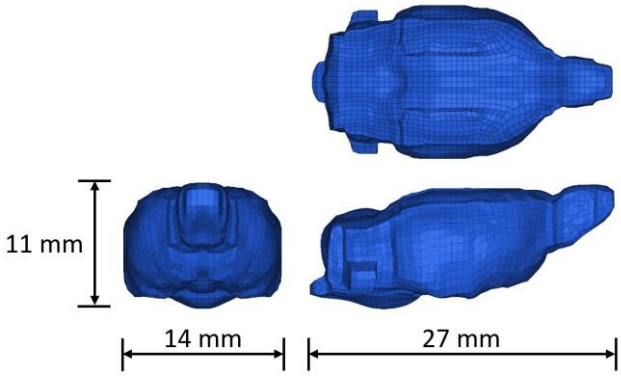

Figure 2.2: Diagramme représentant les vues sagittales, axiales et coronales et les dimensions du cerveau maillé du rat.

Ce modèle de cerveau de rat en éléments finis est constitué de 13 236 éléments hexaédriques solides. La taille des éléments varie de 0,4 mm à 0,8 mm, avec une valeur moyenne d'environ 0,5 mm. Le maillage a été réalisé en maintenant une bonne qualité d'éléments. Ainsi, pour tous les éléments du cerveau, le gauchissement maximum est inférieur à 30 degrés, le rapport d'aspect maximum est inférieur à deux, l'inclinaison maximum est de 45 degrés et le jacobien minimum est égal à 0,5. Le cerveau de rat maillé est enveloppé dans une couche de liquide céphalorachidien (LCR). Le LCR a été modelé comme une couche d'éléments hexaédriques solides, consistant en 3 252 éléments et ayant une épaisseur moyenne de 0,7 mm. Le cerveau et le modèle de LCR sont enfermés à l'intérieur du crâne, qui a été modélisé avec 3 252 éléments de coquille quadrilatérale.

Au départ, on pensait que la division du cerveau du rat en parties principales (selon la segmentation fournie dans l'atlas du DTI par Rumple et al., 2013) et le maillage de ces parties séparément, en maintenant la continuité entre le maillage des différentes parties, seraient à privilégier. Cependant, il a été constaté par la suite qu'il n'était pas possible de développer un tel maillage compte tenu des restrictions en termes de taille et de qualité des éléments, et qu'il n'était pas non plus indispensable. Globalement, le cerveau du rat étant très simple dans sa structure, contrairement au cerveau humain qui présente de multiples plis ; et plus petites dans leur taille, les parties ne peuvent être différenciées que sur la base de leurs fonctions, mais pas sur la base de leur structure géométrique. Il s'agit plutôt d'une structure unique et continue, mais avec une ségrégation ventriculaire. Cependant, cette ségrégation ventriculaire était censée être négligée en raison des restrictions de résolution. De plus, même si le cerveau avait été maillé avec la division partielle, il n'aurait pas été possible d'attribuer les propriétés matérielles partielles à ces régions à un stade ultérieur. En effet il existe très peu de données expérimentales dans la littérature pour les propriétés matérielles du cerveau du rat, ce qui n'était pas suffisant pour une telle division du cerveau. C'est pourquoi, sur la base de l'hypothèse formulée, le modèle a été maillé de la meilleure façon possible, nécessaire pour cette étude.

3 Catégorisation du cerveau pour l'analyse des résultats de simulation

Sur la base de la segmentation fournie dans l'atlas du DTI par Rumple et al. (2013), la FERBM a été classée en vingt-quatre régions différentes pour l'analyse des résultats de simulation. Ces régions sont l'hippocampe, la capsule externe, le caudé - putamen - globus pallidus en un seul, la commissure antérieure, la substantia nigra, la capsule interne, le thalamus, le cervelet, le collicule supérieur, l'hypothalamus, Collicule inférieur, gris central, néocortex, amygdale, bulbe olfactif, tronc cérébral, fimbria, fornix, région tegmentale ventrale (VTA), corps calleux, genu, aqueduc, splénium et reste du

cerveau comme un tout. Plus tard, cette catégorisation anatomique a permis de mieux comprendre les résultats des simulations sur des bases régionales. Le Table 2.1 fournit des détails sur cette catégorisation anatomique et la Figure 2.3 montre l'emplacement de certaines de ces parties dans le cerveau du rat selon la segmentation de l'atlas DTI fournie par Rumple et al. (2013).

Table 2.1: Détails de la catégorisation anatomique des régions cérébrales du rat.

#	Region description	Number of elements	% Brain volume
1	Hippocampus	614	4.6%
2	External capsule	1083	8.2%
3	Caudate – Putamen – Globus pallidus	572	4.3%
4	Anterior commissure	122	0.9%
5	Substantia nigra	64	0.5%
6	Internal capsule	104	0.8%
7	Thalamus	434	3.3%
8	Cerebellum	2869	21.7%
9	Superior colliculus	92	0.7%
10	Hypothalamus	421	3.2%
11	Inferior colliculus	272	2.1%
12	Central gray	192	1.5%
13	Neocortex	3474	26.2%
14	Amygdala	124	0.9%
15	Olfactory bulb	676	5.1%
16	Brainstem	1459	11.0%
17	Fimbria	136	1.0%
18	Fornix	53	0.4%
19	Ventral tegmental area (VTA)	20	0.2%
20	Corpus callosum	118	0.9%
21	Genu	48	0.4%
22	Aqueduct	14	0.1%
23	Splenium	16	0.1%
24	Rest of the brain	259	2.0%

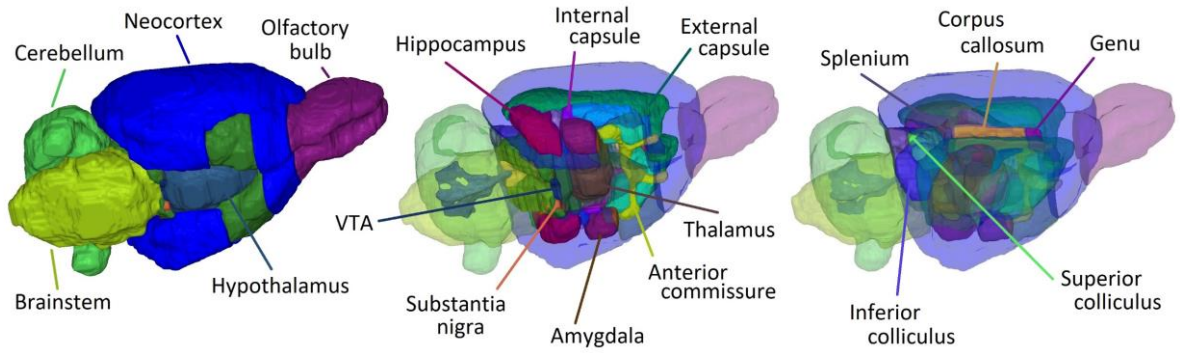

Figure 2.3: Diagramme représentant les différentes parties du cerveau du rat selon la segmentation du cerveau fournie par Rumple et al., 2013.

Une autre catégorisation du cerveau qui a été considérée était fonctionnelle et basée sur les aspects comportementaux. Les régions du cerveau associées à quatre aspects comportementaux - la conscience, l'activité, l'émotivité et la cognition - ont été identifiées. En raison de la complexité du cerveau et du peu de connaissances disponibles, il n'a' pas été possible d'identifier clairement les régions cérébrales associées à ces aspects comportementaux. Cependant, il a été supposé que la conscience est associée au thalamus, au néocortex et au tronc cérébral ; que l'activité est associée à l'hippocampe, à la substance noire, au cervelet, au gris central et au néocortex ; que l'émotivité est associée à l'hippocampe, au gris central, au néocortex, à l'amygdale, au tronc cérébral, aux fimbria et au fornix ; et que la cognition est associée à l'hippocampe, à la substance noire, au cervelet, au néocortex, aux fimbria et au fornix. Le Table 2.2 fournit les détails sur cette catégorisation fonctionnelle et la Figure 2.4 présente les régions du cerveau associées à ces aspects comportementaux. Plus tard, en se fondant sur cette catégorisation fonctionnelle, les résultats de simulation ont été analysés pour ces régions fonctionnelles ou pour différents aspects comportementaux.

Table 2.2: Détails de la catégorisation fonctionnelle des régions cérébrales du rat.

#	Function / behavioural aspect	Region description	Number of elements
1	Consciousness	Thalamus, Neocortex and Brainstem	5367
2	Activity	Hippocampus, Substantia nigra, Cerebellum, Central gray and Neocortex	7213
3	Emotionality	Hippocampus, Central gray, Neocortex, Amygdala, Brainstem, Fimbria and Fornix	6052
4	Cognition capability	Hippocampus, Substantia nigra, Cerebellum, Neocortex, Fimbria and Fornix	7210

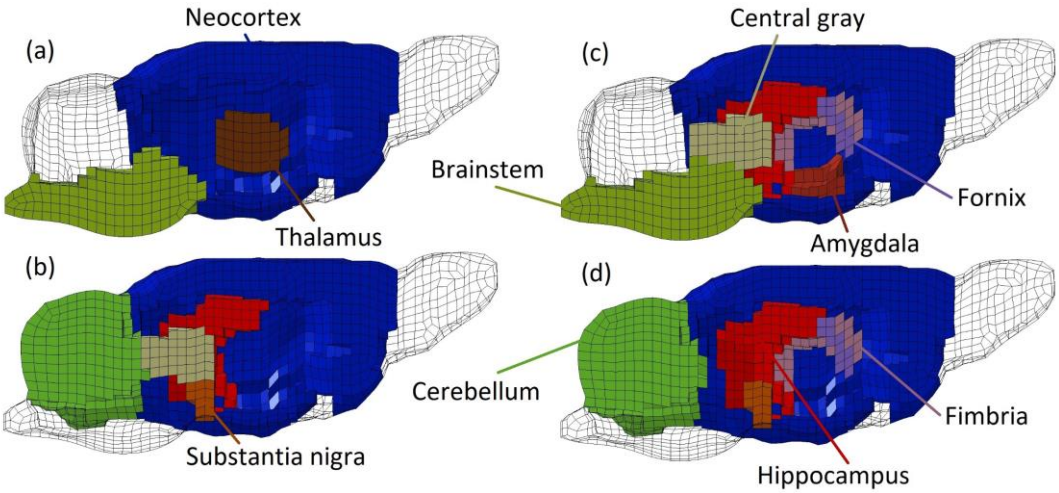

Figure 2.4: Diagramme représentant uniquement les régions fonctionnelles associées à différents aspects comportementaux : (a) conscience, (b) activité, (c) émotivité et (d) cognition au moyen d'une coupe dans le plan mi-sagittal.

Cette catégorisation anatomique et fonctionnelle du cerveau des rats en diverses régions a permis, au chapitre 3 corréler les résultats des simulations avec les résultats expérimentaux sur des bases régionales.

4 Identification des paramètres de diffusion

4.1 Introduction

Comme il a été mentionné précédemment, un atlas anatomique tridimensionnel du cerveau d'un rat adulte au jour postnatal 72, élaboré par Rumple et al. (2013) a été utilisé pour l'identification des paramètres de diffusion du cerveau du rat. Cet atlas est basé sur l'acquisition par IRM de six rats femelles Sprague Dawley, pesant 289,3 ± 20,5 g. Une séquence tridimensionnelle DTI RARE avec deux échos de navigateur a été utilisée sur le scanner horizontal 9,4 T de Bruker, avec les paramètres d'imagerie suivants : TR = 700 ms, TE = 23,662 ms, espacement des échos RARE = 11,9 ms et facteur RARE = 3. L'acquisition a été faite à une résolution de 0,16 x 0,125 x 0,16 mm3 dans douze directions de gradient avec deux images de ligne de base (b = 1600 s/mm2). La durée totale de l'acquisition a été d'environ 10 heures. La résolution isotrope finale de l'atlas DTI était de 0,125 x 0,125 x 0,125 mm3. Ainsi, cet atlas DTI a une dimension de 192 x 256 x 103 voxels, avec un espacement de voxels de 0,125 x 0,125 x 0,125, origine à (0, 0, 0) et une orientation spatiale L-P-S. Cet atlas DTI contient six volumes au total, chacun appartenant à l'une des six composantes de diffusion uniques d'un tenseur de diffusion typique et donc, les données de diffusion pour chaque voxel du cerveau du rat.

L'identification des paramètres de diffusion, de l'anisotropie fractionnelle et de la direction des fibres principales a suivi une procédure systématique, qui est expliquée en détail dans les paragraphes suivants. Cette méthodologie a été adaptée de celle de Chatelin et al. (2011) et de Sahoo et al. (2014). Tout d'abord, les paramètres de diffusion pour chaque voxel du cerveau ont été calculés mathématiquement à partir des données de diffusion disponibles pour chaque voxel du cerveau dans l'atlas DTI. Dans un deuxième temps, la FERBM développée a été alignée sur le volume du DTI, de sorte que les deux volumes se rapportent au même endroit dans l'espace. Par la suite, comme la résolution des voxels est inférieure à la résolution des éléments du modèle, les voxels qui se trouvent à l'intérieur de chaque élément du FERBM ont été identifiés. Enfin, comme les paramètres de diffusion ont déjà été calculés pour chaque voxel, une moyenne pondérée, à partir des voxels identifiés par élément, a été calculée pour estimer les paramètres de diffusion par élément. Ces paramètres de diffusion estimés ont été incorporés dans la définition du matériau par élément, qui sera expliquée plus loin dans ce chapitre. Tout ce calcul, alignement, identification, estimation et incorporation ultérieure a été fait par programmation Python.

4.2 Calcul de l'anisotropie fractionnelle et de la direction de la fibre principale par voxel

L'anisotropie fractionnelle (FA) et la direction principale des fibres (PFD) sont deux paramètres d'anisotropie de base. L'anisotropie fractionnelle est un indice quantitatif et sans dimension (scalaire) permettant de mesurer la fraction de la grandeur de la diffusivité ou, en d'autres termes, de définir le degré d'anisotropie de la diffusion à un endroit donné. L'AF n'est rien d'autre que l'orientation du vecteur d'anisotropie à un endroit donné. La valeur de l'AF est évaluée à partir des valeurs propres (λ1, λ2, λ3) du tenseur de diffusion (D) telles qu'exprimées dans l'Equation 2.1 (Basser and Pierpaoli, 1996).

$$Fractional\ anisotropy, FA = \sqrt{\frac{3}{2}} \frac{\sqrt{(\lambda_1 - \tilde{\lambda})^2 + (\lambda_2 - \tilde{\lambda})^2 + (\lambda_3 - \tilde{\lambda})^2}}{\sqrt{\lambda_1{}^2 + \lambda_2{}^2 + \lambda_3{}^2}} \quad 2.1$$

Où, $\tilde{\lambda} = (\lambda_1 + \lambda_2 + \lambda_3) / 3$ et tenseur de diffusion, $D = \begin{bmatrix} D_{xx} & D_{xy} & D_{xz} \\ D_{xy} & D_{yy} & D_{yz} \\ D_{xz} & D_{yz} & D_{zz} \end{bmatrix}$

Pour un milieu isotrope, la valeur de FA est égale à zéro et pour un milieu anisotrope, qui est cylindriquement symétrique et où λ1 >> λ2 = λ3, la valeur de FA est égale à un. Ainsi, pour un voxel, FA égal à zéro indique une isotropie parfaite et FA égal à un indique une anisotropie parfaite c'est-à-dire que tous les axones sont orientés le long du vecteur d'anisotropie ou dans la direction de la fibre

principale. Le vecteur propre associé à la valeur propre maximale du tenseur de diffusion représente la direction principale de la fibre, c'est-à-dire le PFD. L'atlas DTI contient les données du tenseur de diffusion pour chaque voxel du cerveau. Dans un premier temps, les valeurs propres et les vecteurs propres ont été calculés à partir de ces données, puis les valeurs FA et PFD par voxel ont été déterminées par programmation python. La Figure 2.5 montre les cartes DTI de l'AF et du PFD dans le plan mi-sagittal du cerveau du rat obtenues par l'atlas DTI.

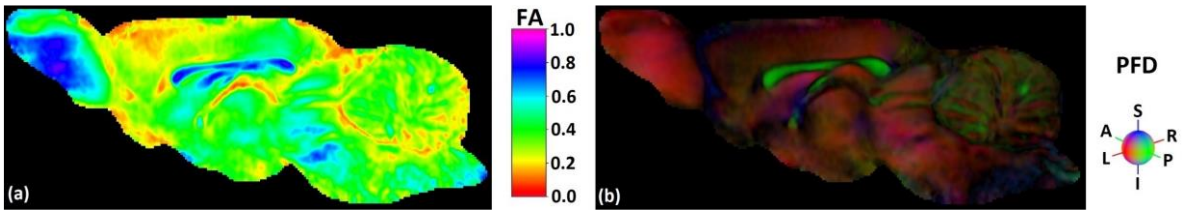

Figure 2.5: Diagramme représentant les données DTI en termes de (a) carte d'anisotropie fractionnelle (FA), et (b) carte de la direction principale des fibres (PFD), dans le plan mi-sagittal du cerveau du rat. FA=0 représente un voxel parfaitement isotrope, tandis que FA=1 représente un voxel parfaitement anisotrope. Pour le PFD, le rouge représente la direction droite-gauche (R-L), le vert représente la direction antéro-postérieure (A-P) et le bleu représente la direction inférieure-supérieure (I-S).

4.3 Alignement du modèle et identification des voxels par élément

Avant d'identifier les voxels par élément et d'estimer les paramètres de diffusion pour la FERBM, il est important d'aligner le modèle d'éléments finis sur le volume du DTI. C'est l'alignement du modèle qui garantit que le modèle FE et le volume DTI sont dans le même cadre de coordonnées et correspondent à la même position et orientation dans l'espace. L'alignement du modèle a été effectué en trois étapes principales. Tout d'abord, sept repères (au centre et sur la surface externe du cerveau à l'extrémité droite, gauche, antérieure, postérieure, inférieure et supérieure) ont été identifiés à la fois sur le volume du DTI et sur le modèle FE (Figure 2.6).

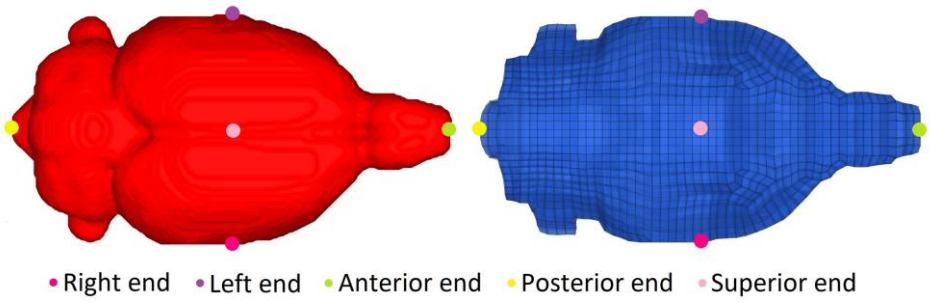

Figure 2.6: Diagramme représentant l'emplacement des cinq points de repère visibles sur le volume DTI (à gauche) et le modèle FE (à droite) pour l'alignement.

Les points de repère du modèle d'EF ont été pris comme points de repère sources et ceux du volume DTI ont été pris comme points de repère cibles. Tout d'abord, la transformation des points de repère du modèle EF en points de repère du volume DTI a permis de calculer la cartographie la mieux adaptée de la manière la moins carrée et de rapprocher les deux modèles. Ensuite, l'algorithme itératif du point le plus proche (ICP) a été utilisé pour optimiser cet alignement et une matrice de transformation a été identifiée pour aligner de façon optimale le modèle d'éléments finis sur le volume de l'ITD. Enfin, tous les nœuds du modèle FERBM ont été transformés à l'aide de cette matrice de transformation afin d'aligner de façon optimale le modèle FERBM sur le volume du DTI. Toutes les étapes de l'alignement du modèle ont été réalisées par programmation Python. La Figure 2.7 illustre brièvement cet alignement du modèle.

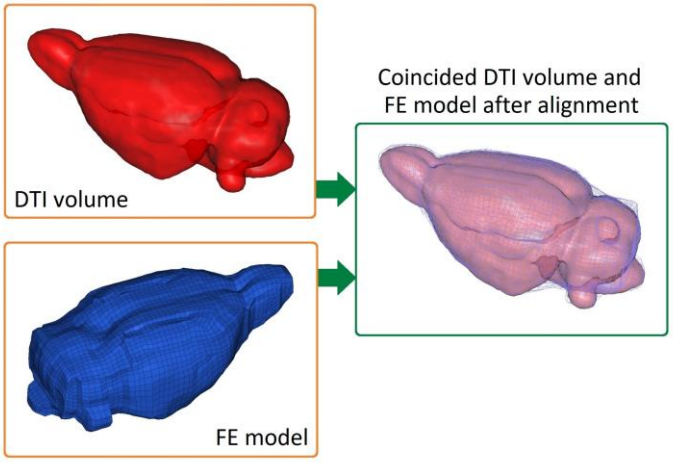

Figure 2.7: Diagramme représentant le volume DTI et le modèle FE avant et après l'alignement.

Pour l'identification des voxels par élément, un volume hexaédrique de sélection de voxels a été construit autour de l'élément de telle sorte que l'élément tombe complètement à l'intérieur de ce volume. Pour tous les voxels compris à l'intérieur de ce volume, il a été vérifié si le voxel est à l'intérieur du volume de l'élément ou sur l'une des faces de l'élément. Tous les voxels qui tombent à l'intérieur ou sur la limite de l'élément ont été sélectionnés. La Figure 2.8 illustre un élément, le volume de sélection des voxels autour de l'élément et les voxels sélectionnés pour l'élément.

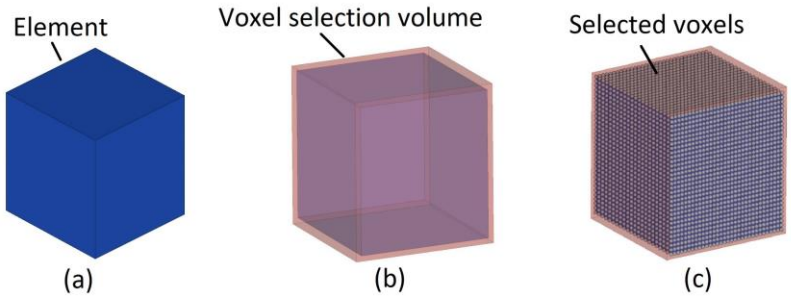

Figure 2.8: Diagramme représentant (a) un élément, (b) le volume de sélection de voxels autour de l'élément et (c) les voxels sélectionnés pour l'élément.

Ainsi, des voxels ont été sélectionnés pour chacun des 13 236 éléments de la FERBM. Ceci a également été réalisé par la programmation Python. L'identification des voxels par élément a permis d'estimer les paramètres de diffusion par élément, ce qui est expliqué dans la section suivante. La Figure 2.9 illustre le nombre de voxels identifiés par élément ainsi que le nombre minimum, maximum et moyen de voxels identifiés. Les nombres minimum, maximum et moyen de voxels identifiés pour un élément étaient respectivement de 21, 177 et 68. Par conséquent, chaque élément avait un nombre de voxels suffisamment bon pour l'estimation des paramètres de diffusion.

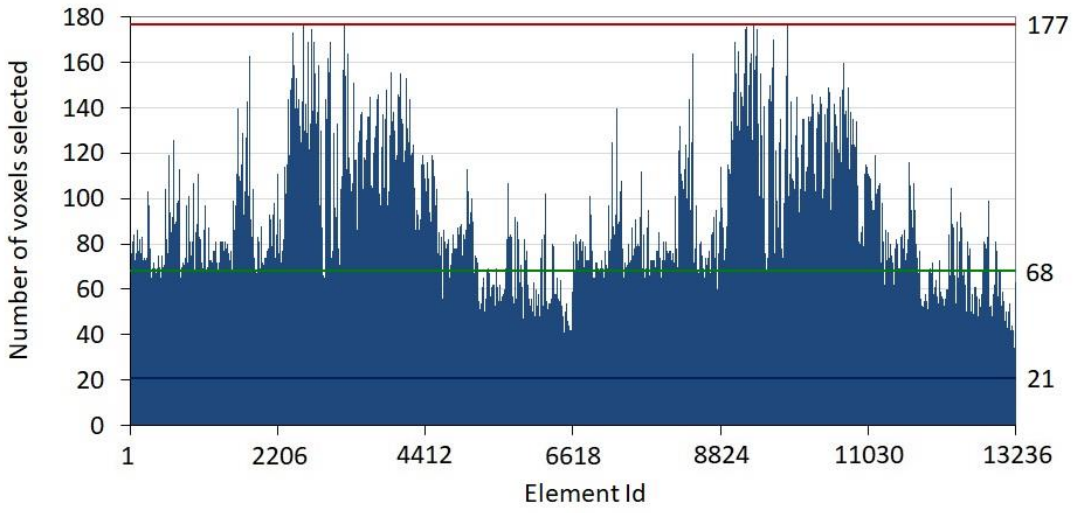

Figure 2.9: Diagramme représentant le nombre de voxels sélectionnés par élément, avec le minimum sélectionné égal à 21, le maximum sélectionné égal à 177 et une moyenne sélectionnée égale à 68 ± 24.

4.4 Estimation de l'anisotropie fractionnelle et de la direction des fibres principales par élément

Pour estimer les paramètres de diffusion - anisotropie fractionnelle (FA) et direction principale des fibres (PFD) par élément, une moyenne pondérée des valeurs de FA et PFD de tous les voxels à l'intérieur d'un élément a été calculée pour chaque élément du FERBM. La moyenne a été pondérée

de façon à ce que les voxels situés près du centre de l'élément aient une influence plus importante que ceux situés à la limite de l'élément. Par conséquent, la fonction de pondération exponentielle a été basée sur la distance du voxel par rapport au centre de l'élément (D) et est donnée dans l'Equation 2.2.

$$f(D_i) = e^{-D_i/L_e} \tag{2.2}$$

Où, L_e est la demi-longueur de la diagonale maximale de l'élément et D_i est la distance du ième voxel au centre de l'élément. La Figure 2.10 illustre cette pondération de manière plus comprehensible.

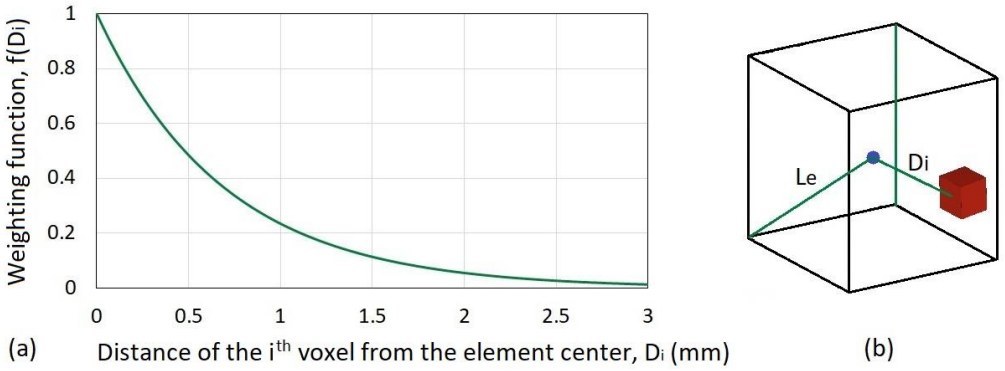

Figure 2.10: Diagramme illustrant (a) la fonction de pondération exponentielle basée sur la distance du voxel par rapport au centre de l'élément et (b) un voxel (rouge) à l'intérieur d'un élément, la distance entre le centre de l'élément et le voxel (D_i) et la demi-longueur de la diagonale maximale de l'élément (L_e). Les voxels proches du centre de l'élément ont une influence plus importante que ceux à la limite de l'élément (Sahoo et al., 2014).

Par conséquent, les paramètres de diffusion pondérés, l'AF et le VFI par élément ont été calculés selon les formules données dans l'Equation 2.3 et l'Equation 2.4.

$$FA_{element} = \frac{\sum_{i=1}^{n} FA_i \, e^{-\frac{D_i}{L_e}}}{\sum_{i=1}^{n} e^{-\frac{D_i}{L_e}}} \tag{2.3}$$

$$\overrightarrow{PFD}_{element} = \frac{\sum_{i=1}^{n} \overrightarrow{PFD}_i \, e^{-\frac{D_i}{L_e}}}{\sum_{i=1}^{n} e^{-\frac{D_i}{L_e}}} \tag{2.4}$$

Où, FA_i et $\overrightarrow{PFD}_i$ sont respectivement l'anisotropie fractionnaire et la direction principale des fibres (vecteur d'anisotropie) pour le ième voxel et n est le nombre total de voxels sélectionnés à l'intérieur d'un élément.

La Figure 2.11 illustre la valeur moyenne pondérée estimée de l'AF pour chaque élément, ainsi que l'écart-type et les moyennes générales. Les valeurs minimales et maximales réelles de l'AF se sont

avérées être de zéro et de 0,9579 respectivement. Les valeurs minimales et maximales pondérées de l'AF étaient de zéro et de 0,9595. Les valeurs réelles et pondérées de l'AF se situaient dans la même fourchette, avec une moyenne de 0,31.

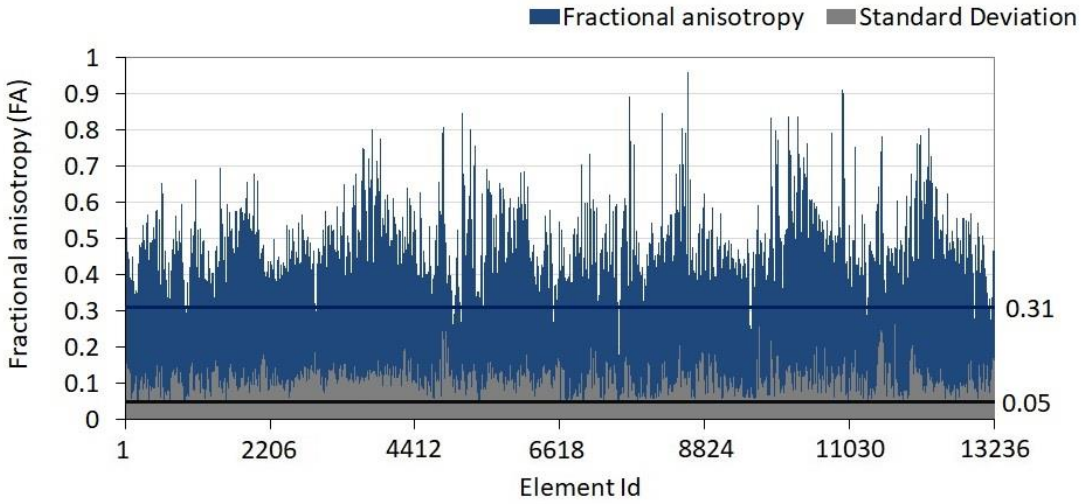

Figure 2.11: Diagramme représentant la valeur moyenne pondérée estimée de l'AF par élément ainsi que l'écart-type. La moyenne globale des AF est égale à 0,31 et avec un écart-type de 0,05.

Comme nous l'avons déjà mentionné, les régions du cerveau dont la valeur de l'AF est égale à zéro indiquent des régions parfaitement isotropes et une valeur de l'AF proche de un indique des régions fortement anisotropes. En général, comme la matière grise est principalement composée de corps de cellules neuronales, la valeur de l'AF dans les régions de la matière grise est habituellement faible. Comme la substance blanche est généralement composée de faisceaux d'axones ou de trajets de fibres, qui sont très anisotropes, la valeur de l'AF dans les régions de la substance blanche est généralement élevée.

La Figure 2.12 représente une illustration comparative des cartes FA et des cartes VFI, dans le plan mi-sagittal du cerveau du rat, obtenues par l'atlas DTI et telles qu'estimées pour le FERBM.

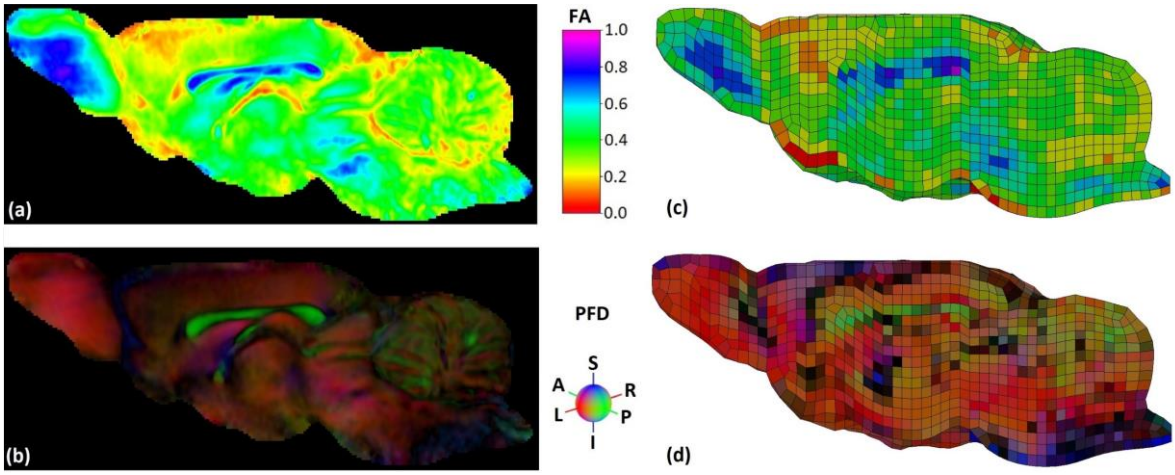

Figure 2.12: Diagramme représentant les données DTI à gauche et l'implémentation FERBM à droite en termes de (a) et (c) carte d'anisotropie fractionnelle (FA), et (b) et (d) carte de direction de la fibre principale (PFD), dans le plan mi-sagittal du cerveau du rat. FA=0 représente un voxel/élément parfaitement isotrope, tandis que FA=1 représente un voxel/élément parfaitement anisotrope. Pour le PFD, le rouge représente la direction droite-gauche (R-L), le vert représente la direction antéro-postérieure (A-P) et le bleu représente la direction inférieure-supérieure (I-S).

On peut observer sur le diagramme que les paramètres de diffusion identifiés pour les éléments sont conformes aux données d'imagerie réelles. Dans la Figure 2.12, les cartes FA et PFD des données d'imagerie sont représentées à gauche et les cartes FA et PFD du modèle FE après la mise en œuvre du DTI sont affichées à droite. Les cartes d'AF indiquent la valeur d'AF d'un voxel ou d'un élément sur une échelle de zéro à un. Les cartes PFD ne sont rien d'autre que des cartes en couleurs codées par direction, où chaque direction (c'est-à-dire la direction principale de la fibre dans ce voxel ou dans l'élément) est indiquée par une couleur différente, de sorte que la couleur rouge représente la direction droite-gauche (R-L), la couleur verte représente la direction antéro-postérieure (A-P) et la couleur bleue représente la direction inférieure-supérieure (I-S).

4.5 Conclusion

Dans cette section, la méthodologie d'identification des paramètres de diffusion pour chaque élément de la FERBM a été expliquée et implémentés dans le maillage dub cerveau du rat. Il a été démontré que les paramètres de diffusion identifiés sont conformes aux données d'imagerie du DTI.

5 Loi constitutif et propriétés matérielles

5.1 Introduction

Après avoir identifié les paramètres de diffusion par élément, l'étape suivante consistait à définir de la loi constitutive et des propriétés des matériaux pour la FERBM développée. Comme évoque dans le

premier chapitre, après une analyse bibliographique approfondie, il existe une énorme variation dans la compréhension du matériau cérébral. D'après les diverses expériences menées, les propriétés du matériel cérébral diffèrent selon qu'elles sont mesurées in vitro ou in vivo ; selon l'emplacement, selon qu'il s'agit de matière grise ou de matière blanche, même dans les subdivisions des régions cérébrales ; selon l'âge ; selon l'espèce ; selon les protocoles expérimentaux, etc. (Chatelin et al., 2010; Budday et al., 2019). Cependant, lorsque nous examinons la microstructure, il s'agit du même tissu mou, où les corps des cellules neuronales et les axones sont répartis dans la glie. Il existe également des preuves dans la littérature, qui soutiennent le fait qu'un cerveau de rat adulte peut être considéré comme neurologiquement équivalent à un cerveau humain adulte (Shreiber et al., 1997) et au niveau des tissus, le matériel cérébral inter-espèces répond de manière similaire (Gefen et al., 2003). Une comparaison des propriétés des matériaux identifiées par différentes études a montré que les propriétés des matériaux du cerveau du rat suivent le même schéma que celles des autres espèces et se situent également dans la même fourchette. Par conséquent, la loi constitutive et les propriétés de la matière cérébrale, telles qu'identifiées par Chatelin et al. (2013) pour le cerveau humain adulte, ont été adaptées pour la FERBM développée. Ces propriétés matérielles ont été adaptées pour le rat en incorporant les propriétés de diffusion anisotropique du cerveau du rat par la mise en œuvre du DTI. Une description détaillée de cette procédure est fournie dans les sections suivantes.

5.2 Matière cérébrale

Le modèle matériel choisi pour cette étude a été élaboré par Chatelin et al. (2013) et est basé sur Weiss et al. (1996) et Puso et Weiss (1998). Le modèle de matériau choisi considère que les fibres axonales influencent le comportement mécanique du tissu cérébral de la même manière que les fibres de collagène influencent les ligaments. La structure complexe du tissu cérébral, où le neurone et les voies de la substance blanche sous la forme d'axones densément comprimés, restent répartis dans les neurones, a été simplifiée sous la forme d'un matériau composite renforcé par des fibres. Cette simplification a été basée sur l'hypothèse que les fibres axonales sont les principaux composants, qui influencent le comportement mécanique anisotrope global du tissu cérébral et donc, l'influence des névroglies environnantes peut être négligée. Le tissu cérébral était censé être constitué d'un matériau matriciel isotrope avec un renforcement des fibres dans la direction principale des fibres, a0 comme le montre la Figure 2.13.

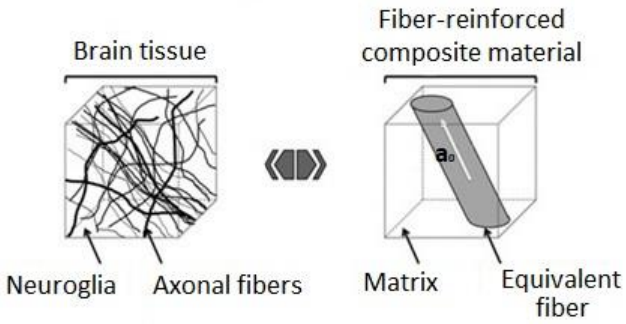

Figure 2.13: Diagramme représentant la simplification de la structure complexe du tissu cérébral en tant que matériau composite renforcé par des fibres (Chatelin et al., 2013; Sahoo et al., 2014).

L'énergie de déformation d'un matériau hyperélastique anisotrope renforcé par des fibres peut être entièrement décrite par les cinq invariants de la déformation droite 'C' de Cauchy-Green tels qu'exprimés dans les Equations 2.5 to 2.10 (Spencer, 1984).

$$W = W(I_1,\ I_2,\ I_3, I_4, I_5), \text{ où} \qquad 2.5$$

$$I_1 = tr(C) \qquad 2.6$$

$$I_2 = \frac{1}{2}\ (tr(C)^2 - \ tr(C^2)) \qquad 2.7$$

$$I_3 = det(C) = \ (J)^2 \qquad 2.8$$

$$I_4 = \ a_0 \,.\, C \,.\, a_0 = \ \lambda^2 \qquad 2.9$$

$$I_5 = \ a_0 \,.\, (C)^2 \,.\, a_0 \qquad 2.10$$

Où, J est le Jacobien de déformation et est égal au déterminant du gradient de déformation, a_0 est le vecteur unité dans la direction principale de la fibre et λ est l'étirement de la fibre.

Cependant, pour l'identification des coefficients paramétriques du matériel du tissu cérébral à partir des données expérimentales de l'étirement biaxial, on a supposé que l'énergie de déformation peut être décrite comme une fonction des quatre premiers invariants seulement (Criscione et al., 2001). Par conséquent, la fonction de l'énergie de déformation pour le matériau du tissu cérébral pourrait être exprimée sous la forme de l'Equation 2.11.

$$W = W^d_{Matrix}(\tilde{I}_1,\ \tilde{I}_2) + \ W^d_{Fiber}(\tilde{I}_4) + \ W^v(\tilde{I}_3) \qquad 2.11$$

Où, les énergies de déformation de la matrice et de la fibre sont représentées par les fonctions W^d_{Matrix} et W^d_{Fiber} respectivement. Les premier et deuxième invariants de distorsion de C peuvent

être exprimés comme dans l'Equation 2.12 et l'Equation 2.13 and $\tilde{I}_4$ est le quatrième invariant de distorsion de C.

$$\tilde{I}_1 = I_3^{-\frac{1}{3}} I_1 \qquad 2.12$$

$$\tilde{I}_2 = I_3^{-\frac{2}{3}} I_2 \qquad 2.13$$

L'énergie volumétrique, $W^v(\tilde{I}_3)$, est représentée dans l'Equation 2.14.

$$W^v(\tilde{I}_3) = \frac{1}{2} K \ln(J)^2 \qquad 2.14$$

Où, K est le module effectif en vrac et donc l'énergie volumétrique dépend de la compressibilité du matériau. Une hypothèse d'incompressibilité parfaite rend l'énergie volumétrique négligeable.

D'après Franceschini et al. (2006), il a été pris en considération que le matériau cérébral présente un comportement mécanique non linéaire et que, à des contraintes importantes, la rigidité augmente de manière significative. Ainsi, le matériau du tissu cérébral a été modélisé comme un solide non linéaire avec une incompressibilité volumétrique négligeable. Par conséquent, le modèle de matériau Mooney-Rivlin, tel que donné dans l'Equation 2.15, a été choisi pour le matériau de la matrice du tissu cérébral.

$$W^d_{Matrix}(\tilde{I}_1, \tilde{I}_2) = C_{10}(\tilde{I}_1 - 3) + C_{01}(\tilde{I}_2 - 3) \qquad 2.15$$

Où, C_{10} et C_{01} sont deux coefficients de modèle (Rivlin and Saunders 1951). On a supposé que l'énergie de déformation de la matrice est responsable du raidissement du tissu cérébral aux grandes déformations. La quasi-incompressibilité a été assurée en définissant une valeur très élevée du module K global, au moins trois fois supérieure à $(C_{10} + C_{01})/2$, qui correspond au module de cisaillement isotrope initial.

Sur la base d'études expérimentales (Miller and Chinzei 2002), qui ont démontré que la substance blanche du cerveau présente une rigidité différente en tension et en compression, plusieurs hypothèses ont été faites pour le modèle d'énergie de déformation de la fibre. La première hypothèse était que l'influence des fibres en compression peut être considérée comme négligeable. Deuxièmement, l'influence des fibres en tension a été supposée augmenter la rigidité de façon exponentielle avec l'étirement des fibres. La troisième hypothèse était que l'étirement local déviant de la fibre, λ dépend de la direction de la fibre principale, a_0 et peut être exprimé comme indiqué ci-dessous dans l'Equation 2.16.

$$\lambda = \sqrt{a_0 . C . a_0} = \sqrt{I_4} \quad 2.16$$

Où, C est le tenseur de déformation déviatoire droit Cauchy-Vert.

Par conséquent, la fonction d'énergie de déformation pour le matériau fibreux du tissu cérébral a été adaptée et est donnée par l'Equation 2.17 (Puso and Weiss, 1998).

$$\lambda \frac{\partial W^d_{Fibers}}{\partial \lambda}(\lambda) = \begin{cases} 0 & 0 \leq \lambda < 1 \\ C_3\left(e^{FA*C_4(\lambda-1)} - 1\right) & \lambda \geq 1 \end{cases} \quad 2.17$$

Où, C_3 et C_4 sont les coefficients hyperélastiques et dépendent des propriétés mécaniques et de la densité des fibres axonales. FA est l'anisotropie fractionnaire, qui a été incluse pour pondérer l'influence de la fibre par la fraction anisotrope. Par conséquent, les fibres axonales n'ont aucune influence mécanique sur le tissu cérébral, que ce soit en compression ou lorsque la tension est perpendiculaire à la direction principale des fibres.

En raison de la sensibilité élevée à la vitesse de déformation, la viscosité joue un rôle important dans la réponse du matériel cérébral à la charge quasi statique ainsi qu'à la charge d'impact (Prevost et al., 2011). Comme le proposent Fung et al. (1993), en considérant la seconde contrainte de Piola-Kirchhoff S(C, t) dépendante du temps, le comportement viscoélastique peut être décrit comme indiqué ci-dessous dans l'Equation 2.18.

$$S(C,t) = S^e(C) + S^v(C,t) \quad 2.18$$

Où, $S^e(C)$ est la contrainte d'équilibre et représente le comportement élastique à long terme du matériau.

Les effets de taux ont été pris en compte par viscoélasticité linéaire, en utilisant une représentation intégrale convolutive telle qu'exprimée dans l'Equation 2.19.

$$S^v(C,t) = \int_0^t 2G(t-s)\frac{\partial W}{\partial C(s)}\, ds \quad 2.19$$

Où, $G(t-s)$ est la fonction de relaxation réduite, qui peut être exprimée sous la forme d'une série de Prony d'ordre n, comme le montre l'Equation 2.20.

$$G(t) = \sum_{i=1}^{n} S_i\, e^{-\frac{t}{T_i}} \quad 2.20$$

Où, S_i est le module de relaxation du cisaillement et T_i est le temps de relaxation caractéristique et ceux-ci caractérisent la sensibilité du modèle à la vitesse de déformation.

Les paramètres de ce modèle de matériel cérébral anisotrope visqueux et hyperélastique ont été identifiés à partir de diverses études in vivo et in vitro disponibles dans la littérature (Chatelin et al., 2013). Pour identifier les valeurs des paramètres, le modèle théorique a été exprimé en termes de contrainte-étirement pour la compression et la tension uniaxiale, le long de la direction principale des fibres (a_0). Pour cette configuration, la première contrainte principale hyperélastique de Cauchy, sous l'hypothèse d'incompressibilité, est donnée par l'Equation 2.21.

$$\sigma^e(\lambda) = \lambda \frac{\partial W^d_{Matrix}}{\partial \lambda} + \lambda \frac{\partial W^d_{Fibers}}{\partial \lambda} - p \qquad 2.21$$

Où, λ est le rapport d'étirement et p est la pression hydrostatique. En compression ($0 \leq \lambda < 1$), lorsque les fibres n'ont aucune influence, l'Equation 2.21 devient l'Equation 2.22, comme indiqué ci-dessous.

$$\sigma^e(\lambda) = 2\left(\lambda^2 - \frac{1}{\lambda}\right)\left(C_{10} + \frac{C_{01}}{\lambda}\right) \qquad 2.22$$

Les coefficients hyperélastiques Mooney-Rivlin (C_{10} and C_{01}) pour la matrice du cerveau ont été identifiés à partir des données d'expériences d'élastographie par résonance magnétique (ERM) in vivo réalisées par Kruse et al. (2008) sur des sujets humains adultes en bonne santé. Les valeurs identifiées ont été adaptées pour prendre en compte le raidissement du tissu cérébral entre 50% et 60% de compression ($0.5 \leq \lambda < 0.6$) à des taux de déformation faibles comme élevés (Pervin et al., 2009 and Prevost et al., 2011). Sous un étirement faible ($0 \leq \lambda < 0.1$) le comportement du tissu cérébral était supposé être linéaire (Nicolle et al., 2004). Les valeurs des paramètres ont été optimisées par la méthode du simplex descendant. En tension ($\lambda \geq 1$), l'Equation 2.21 devient l'Equation 2.23, où la matrice cérébrale et les fibres ont une influence combinée.

$$\sigma^e(\lambda) = 2\left(\lambda^2 - \frac{1}{\lambda}\right)\left(C_{10} + \frac{C_{01}}{\lambda}\right) + C_3\left(e^{FA*C_4\,(\lambda\,-\,1)} - 1\right) \qquad 2.23$$

Le coefficient d'anisotropie fractionnaire (FA) pondère la projection de l'étirement principal dans le sens de la fibre. En cas d'isotropie pure, FA = 0 et donc, le terme de la fibre devient zéro. De même, en cas de tension, orthogonale à la direction de la fibre principale ou de compression, λ=1 et donc, le terme de la fibre devient zéro. Le taux d'étirement critique des fibres a été maintenu à un niveau exceptionnellement élevé, afin d'évaluer les contraintes du matériau sous l'influence de la matrice et de la fibre. Les coefficients hyperélastiques Mooney-Rivlin identifiés ont permis l'interpolation du comportement de la matrice cérébrale en tension. Pour l'identification des paramètres viscoélastiques, S_i et T_i, on a utilisé les données expérimentales de relaxation de l'analyse mécanique dynamique en cisaillement, telles que rapportées par Shuck and Advani (1972). La courbe du module de relaxation en fonction du temps qui en résulte a été mise à l'échelle à 13,6 kPa (Kruse et al., 2008),

de telle sorte que la continuité entre les modèles hyperélastiques (non linéaires) et viscoélastiques (linéaires) puisse être assurée. Les fibres cérébrales ont été modélisées uniquement en tant que matériau hyperélastique en raison du manque de données viscoélastiques expérimentales sur les fibres cérébrales.

Ce modèle de matériau hyperélastique visqueux anisotrope a été validé par rapport aux données expérimentales et a été publié dans Chatelin et al. (2013). Le même modèle de matériau est incorporé dans le FERBM développé avec quelques modifications nécessaires pour l'adaptation au cerveau du rat. La Figure 2.14 illustre le comportement d'étirement sous contrainte de ce modèle de matériau (Chatelin et al., 2013).

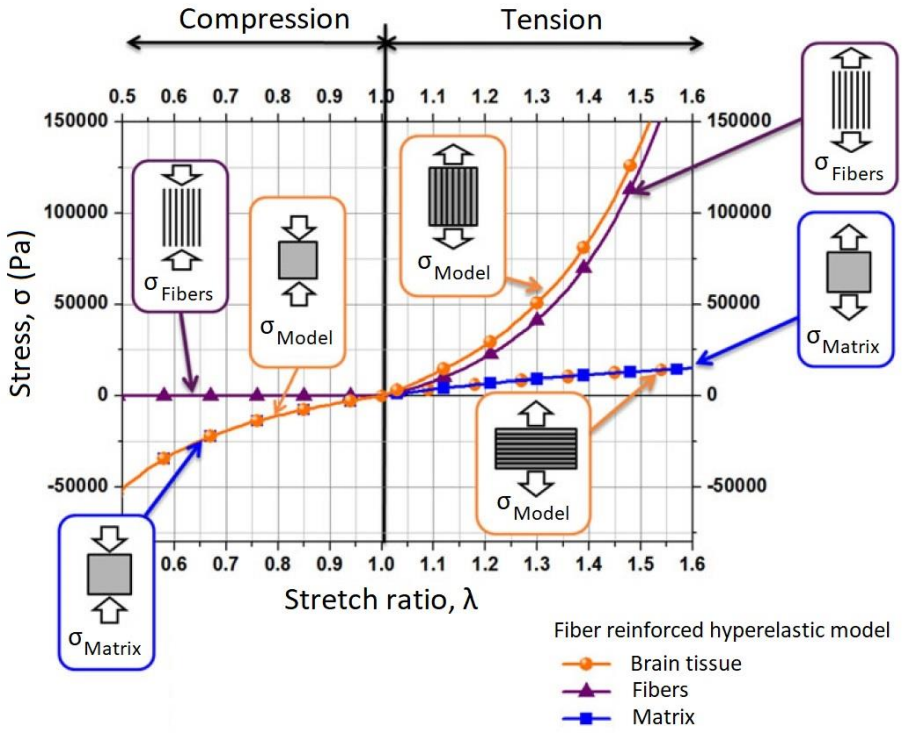

Figure 2.14: Diagramme illustrant le comportement en contrainte-étirement du modèle de matériau cérébral hyperélastique renforcé de fibres développé par Chatelin et al. (2013).

Les paramètres identifiés par Chatelin et al. (2013) ont été incorporés dans le modèle de matériau *MAT_092 i.e. *MAT_SOFT_TISSUE_VISCO de LS-DYNA, ainsi que les paramètres de diffusion, qui ont été identifiés à partir de l'atlas DTI de Rumple et al. (2013). Le Table 2.3 présente les détails de ces paramètres, ainsi que le paramètre LS-ADN équivalent. Le paramètre de diffusion FA a été incorporé avec le coefficient hyperélastique C_4. Par contre, le PFD, qui est le vecteur d'anisotropie, a été incorporé en attribuant ses trois composantes aux paramètres LA_1, LA_2 et LA_3 du modèle de matériau LS-DYNA (*MAT_SOFT_TISSUE_VISCO) respectivement.

Table 2.3: Détails paramétriques pour l'incorporation de la loi de matériau hyperélastique visqueux anisotrope dans le modèle de matériau LS-DYNA *MAT_092 i.e. *MAT_SOFT_TISSUE_VISCO.

LS-DYNA parameter	Model parameter	Unit	Description	Value
RO	ρ	Kg/m^3	Density	1040
C_1	C_{10}	kPa	Mooney-Rivlin hyperelastic coefficient for matrix	-1.034
C_2	C_{01}	kPa		7.809
C_3	C_3	kPa	Fiber reinforcement hyperelastic coefficient	13.646
C_4	C_4	-		4.64 x FA[#]
C_5	C_5	kPa	Hyperelastic coefficient	68.72
XK	K	MPa	Bulk modulus	1125
XLAM	λ	-	Critical fiber stretch ratio	11
AX, AY, AZ, BX, BY, BZ	-	-	To define local element axes	1, 0, 0, 1, 1, 0 (for AOPT = 2)
LA1, LA2, LA3	a_{0x}, a_{0y}, a_{0z}	-	Principal fiber direction vector (a_0) defined in local element frame	[#]
S1	S_i	kPa	Long-term shearing relaxation moduli	4.5
S2				9.11
T1	T_i	ms	Characteristic relaxation times	$1x10^{-6}$
T2				145

[#]les paramètres DTI, qui ont été incorporés via la programmation python

La programmation en python a été faite pour assigner les propriétés matérielles à chaque élément du cerveau. Ainsi, tous les 13 236 éléments de la FERBM se sont vus attribuer des propriétés matérielles différentes distinctes. Tous les éléments ont des propriétés de matériaux visqueux hyperélastiques similaires pour le matériau de la matrice ; mais des propriétés de matériaux de fibres différentes en termes d'anisotropie fractionnelle (FA) et de direction principale des fibres (PFD) comme déterminé à partir de l'atlas DTI.

5.3 Matériau pour fluide cérébrospinal

Le fluide cérébrospinal (CSF) se trouve entre le cerveau et le crâne comme matériau d'amortissement pour protéger le cerveau contre les chocs mécaniques et pour servir à diverses autres fins neurologiques. De nombreuses études rapportées dans la littérature, caractérise différemment le matériau du CSF pour son utilisation dans les simulations biomécaniques. Certains considèrent le CSF comme un matériau élastique, d'autres comme un matériau viscoélastique et d'autres encore comme un fluide élastique. La plupart des études ont fourni des arguments à l'appui de leurs choix de caractérisation du matériau. Cependant, les propriétés utilisées dépendent fortement du type de chargement et des conditions limites. Jin et al. (2015) ont réalisé des simulations biomécaniques sur la tête humaine, avec différentes propriétés matérielles du CSF, pour recréer certains cas expérimentaux. En comparant les résultats, on a constaté que le CSF modélisé comme un fluide élastique et avec un module de masse très élevé reproduisait les résultats plus fidèlement que toute autre méthode de modélisation. Par conséquent, pour le FERBM développé, le matériau du CSF a été supposé être un fluide élastique, ayant une densité de 1000 kg/m^3 et un module de masse élevé de 6750 MPa. Le modèle de matériau LS-DYNA choisi pour le CSF est *MAT_001 i.e. *MAT_ELASTIC_FLUID.

5.4 Matériau du crâne

Dans cette étude, le crâne a été modélisé comme un matériau rigide, ayant une densité de 1900 kg/m^3, un module de Young de 10 GPa et un coefficient de Poisson de 0,22. Le modèle de matériau LS-DYNA choisi pour le crâne était *MAT_20 i.e. *MAT_RIGID. Le crâne a été modélisé comme un matériau rigide, de sorte que la charge sur le cerveau puisse être appliquée de manière appropriée en assignant des conditions aux limites appropriées sur le crâne.

5.5 Conclusion

Cette section a fourni des détails sur les propriétés des matériaux et sur la façon dont ils ont été incorporés dans le FERBM anisotrope. Le modèle de matériau développé par Chatelin et al. (2013) avait été utilisé avec le cerveau humain (dans le modèle de tête aux éléments finis de l'Université de Strasbourg, SUFEHM) et s'est avéré très utile. Nous avons alors émis l'hypothèse que ce modèle de matériau, avec l'incorporation des propriétés de diffusion du cerveau de rat, sera également utile pour les recherches sur le cerveau de rat. Il est important de rappeler ici que cette hypothèse est basée sur les preuves littéraires de similitudes au niveau des tissus entre les cerveaux de rat et humain, qui ont

été mentionnées plus haut également. Ainsi, le FERBM développé consiste en un modèle de matériau anisotrope visqueux hyperélastique.

6 Validation vis-à-vis du déplacement cortical dynamique expérimental

6.1 Introduction

Shreiber et al. (1997) ont réalisé des expériences sur des rats Sprague Dawley mâles adultes pesant de 350 à 400 g. La charge a été appliquée sous forme d'une impulsion de pression sous vide sur la surface du cerveau et le déplacement cortical du cortex exposé a été mesuré au moyen d'un transducteur de déplacement à laser. Ces données expérimentales sur le déplacement cortical dynamique ont été utilisées pour comparer la réponse du modèle de calcul à des fins de validation. Le paragraphe suivant présente les spécifications expérimentales qui ont été utilisées pour la reconstruction en termes de simulations numériques.

6.2 Spécification expérimentales

Pour appliquer une impulsion de pression à vide sur la surface du cerveau du rat, une craniectomie de 5 mm de diamètre a été effectuée sur le cortex pariétal du côté gauche du cerveau. La dureté a été enlevée de cette région, afin d'éviter toute résistance mécanique à l'impulsion de pression à vide. Les expériences ont été réalisées pour trois amplitudes d'impulsion de pression de vide, qui sont 2 psi (13,8 kPa), 3 psi (20,7 kPa) et 4 psi (27,6 kPa) et pour trois durées différentes (25 ms, 50 ms et 100 ms). Ainsi, les expériences ont été effectuées sur le cerveau de rats pour neuf charges différentes et un total de sept animaux a été testé pour chaque condition de charge. Toutefois, comme la littérature ne contient que six courbes de charge, seules six conditions de charge expérimentales ont été simulées. La Figure 2.15 présente ces courbes expérimentales de pression en fonction du temps, qui ont également été utilisées pour les simulations de validation du modèle.

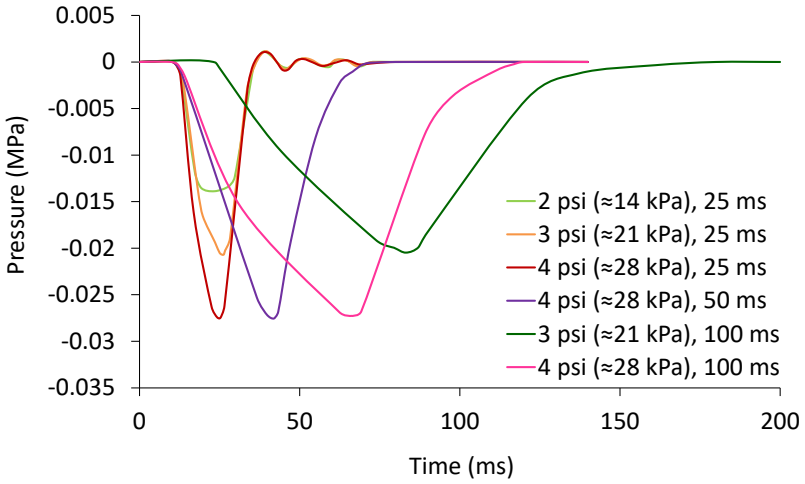

Figure 2.15: Diagramme représentant les courbes de charge de pression en fonction du temps appliquées dans les expériences de déplacement cortical dynamique ainsi que les simulations de validation (Shreiber et al., 1997).

Pour chaque condition de chargement, le déplacement cortical moyen de crête a été mesuré à l'aide d'un capteur de déplacement laser. Les mesures expérimentales du déplacement cortical dynamique sont indiquées au Table 2.4.

Table 2.4: Mesures expérimentales du déplacement cortical dynamique (DCD) (où le nombre d'animaux par scénario de chargement, n = 7) (Shreiber et al., 1997).

Experimental DCD (mm)	2 psi, 25 ms	3 psi, 25 ms	4 psi, 25 ms	4 psi, 50 ms	3 psi, 100 ms	4 psi, 100 ms
Mean	1.0	1.1	1.2	1.5	1.3	1.7
Standard deviation	0.4	0.3	0.5	0.6	0.4	0.6

6.3 Simulations numériques

Pour reconstruire numériquement les expériences de déplacement cortical dynamique, quelques modifications ont été apportées au modèle. Dans un premier temps, pour représenter la craniectomie, des éléments de la coque du crâne et des éléments solides du LCR, provenant du cortex pariétal gauche, ont été retirés pour une zone d'environ 5 mm de diamètre. Ensuite, un critère d'érosion du matériau a été attribué aux éléments de la couche de LCR. Cela a été fait pour reproduire la fuite du LCR entre le cerveau et le crâne, à la suite de la craniectomie et de l'ablation de la dure-mère. En se basant sur la pression intracrânienne (PIC) à l'intérieur de la tête du rat, qui est habituellement égale à 4 mmHg - 10 mmHg (0,5 kPa - 1,3 kPa), les éléments du LCR étaient érodés, si la valeur maximale de la pression était supérieure à 1,1 kPa ou si la valeur minimale de la pression était inférieure à -1,1 kPa. En cas d'érosion complète des éléments du LCR, un contact LS-DYNA, *CONTACT_AUTOMATIC_SURFACE_TO_SURFACE, a été défini entre le crâne et les éléments du

cerveau avec un faible coefficient de frottement de 0,2. Le crâne a été fixé dans l'espace et la charge a été appliquée au moyen d'une impulsion de pression sous vide sur les éléments cérébraux exposés (Figure 2.16).

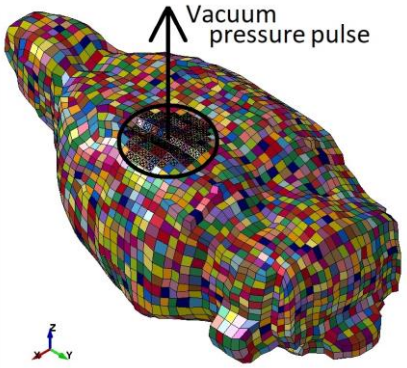

Figure 2.16: Diagramme représentant le modèle, mettant en évidence la région où l'impulsion de pression de vide a été appliquée.

Au total, six simulations ont été réalisées pour les impulsions de pression disponibles, comme le montre la Figure 2.15. Pour mesurer le déplacement cortical dynamique, nous avons mesuré le déplacement maximal des nœuds au centre de la craniectomie, dans une région d'un mm de diamètre, et on en a fait la moyenne pour la comparer aux résultats expérimentaux. Un diamètre de 1 mm a été choisi en fonction du diamètre du faisceau laser du transducteur de déplacement, qui a été utilisé pour mesurer le DCD expérimental comme indiqué dans Shreiber et al. (1997). La Figure 2.17 montre le modèle avant le chargement et après le chargement à la position de déplacement de pointe pour un scénario de chargement de 4 psi (≈28 kPa), 25 ms.

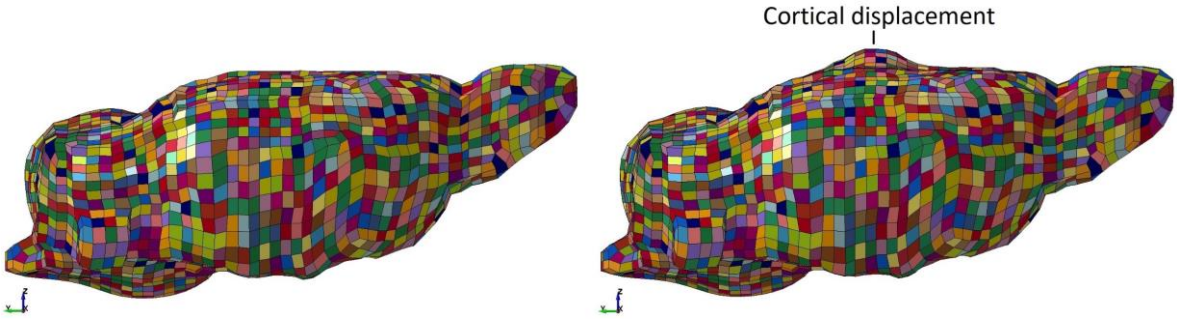

Figure 2.17: Diagramme représentant le modèle avant chargement (à gauche) et après chargement à la position de déplacement maximale (à droite) pour un scénario de chargement de 4 psi (≈28 kPa), 25 ms.

Les résultats de la simulation sont donnés dans le Table 2.5 et une comparaison des résultats de la simulation avec les résultats expérimentaux est fournie dans la section suivante.

Table 2.5: Mesures de simulation du déplacement cortical dynamique (DCD).

Simulation DCD (mm)	2 psi, 25 ms	3 psi, 25 ms	4 psi, 25 ms	4 psi, 50 ms	3 psi, 100 ms	4 psi, 100 ms
Mean	0.7	0.9	1.1	1.1	0.9	1.1
Standard deviation	0.01	0.02	0.04	0.04	0.03	0.04

Toutes les simulations ont été réalisées sur la plateforme LS-DYNA et le temps moyen de simulation était d'environ cinq heures.

6.4 Résultats de la validation du déplacement cortical dynamique

Pour différents scénarios de chargement, les résultats de la simulation en termes de des déplacements corticaux dynamiques expérimentaux sont rapportés en Figure 2.18. Les résultats expérimentaux sont donnés sous forme de valeur moyenne du déplacement cortical de pointe et de l'écart-type, tandis que les résultats de simulation sont donnés sous forme de valeur moyenne du déplacement cortical maximal.

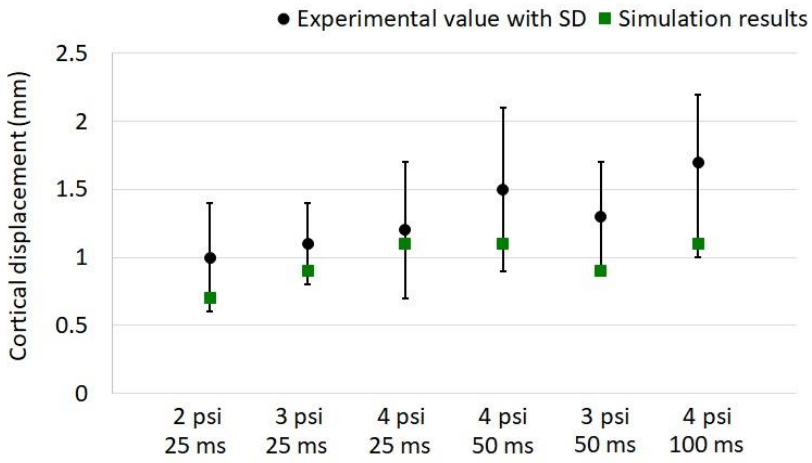

Figure 2.18: Diagramme représentant les mesures expérimentales et de simulation du déplacement cortical dynamique pour différents scénarios de chargement.

Il apparaît, d'après le diagramme, que les résultats de la simulation se situent dans la fourchette expérimentale pour presque tous les scénarios. Nous pouvons donc conclure que le modèle est validé par rapport au déplacement cortical dynamique expérimental. Si nous observons de près, nous pouvons clairement voir l'influence de l'ampleur de l'impulsion de pression. Comme pour une durée similaire de 25 ms, avec une augmentation de l'amplitude de la pression de 2 psi à 3 psi et à 4 psi, le déplacement cortical dynamique (DCD) a augmenté de 0,7 mm à 0,9 mm et à 1,1 mm respectivement. Par contre, l'influence de l'augmentation de la durée de l'impulsion, qui est clairement apparente dans

le résultat expérimental, n'a pas été observée dans le résultat de la simulation. Cette différence dans les résultats pourrait s'expliquer par de multiples raisons. L'une des raisons possibles pourrait être les propriétés des matériaux. Les paramètres de diffusion des propriétés des matériaux ont été identifiés grâce à un atlas de DTI in vitro. Cependant, le cerveau in vivo se comporte différemment d'un cerveau in vitro. Une autre raison pourrait être la différence de poids de l'animal. Tous les détails requis (par exemple l'atlas DTI et le protocole expérimental) ne sont pas toujours disponibles pour le même sujet. L'atlas du DTI a été construit à partir de rats Sprague Dawley d'environ 290 g, alors que le poids des rats Sprague Dawley expérimentaux du DCD variait de 350 g à 400 g. On ne peut pas négliger la possibilité que cela puisse influencer d'une manière ou d'une autre la réponse du cerveau. D'autres paramètres de simulation influencent également la réponse du cerveau, qui sont expliqués plus loin dans la section sur les études paramétriques.

6.5 Conclusion

La validation du FERBM anisotrope développée vis-à-vis du déplacement cortical dynamique expérimental, sous impulsion de pression sous vide a été conduite dans cette section. Avec différentes valeurs des paramètres de simulation, il a été possible d'obtenir des résultats de simulation encore meilleurs, c'est-à-dire une réponse plus proche de la moyenne expérimentale. Cependant, pour que le modèle passe également l'autre validation (déplacement relatif cerveau-crâne), celle présentée dans la Figure 2.18 était la meilleure solution possible. De plus, le but principal de cette étude n'était pas seulement de développer un modèle validé, mais d'aller plus loin et de pouvoir obtenir des informations supplémentaires sur le cerveau du rat en termes d'élongation axonale en cas de commotion cérébrale. À la connaissance de l'auteur, il s'agit de la première étude de ce type sur le cerveau de rat. Par conséquent, le modèle a été considéré comme validé par rapport au déplacement cortical dynamique expérimental.

7 Validation vis-à-vis du déplacement relatif expérimental cerveau-crâne

7.1 Introduction

Antona-Makoshi et al. (2014) ont réalisé des expériences sur trois rats Sprague Dawley mâles adultes, pesant environ 500 g. La charge a été appliquée en termes d'impulsion d'accélération de rotation dans le plan sagittal pour mesurer le déplacement du cerveau par rapport au crâne. Pour ce faire, on a inséré une aiguille dans le cerveau, de telle sorte que l'aiguille soit maintenue fermement fixée au crâne. Ainsi, la rotation de la tête a produit une cicatrice sur le cerveau en raison du mouvement relatif

entre le cerveau et le crâne. Cette longueur de cicatrice a été mesurée, à quatre profondeurs de la surface du cerveau, pour identifier le déplacement relatif cerveau-crâne à quatre profondeurs différentes. Afin de valider le modèle, ces longueurs de cicatrices expérimentales à quatre profondeurs ont été comparées aux résultats de la simulation qui ont été mesurés en termes de déplacements nodaux à ces endroits précis. Le paragraphe suivant présente les spécifications expérimentales qui ont été utilisées pour les simulations numériques.

7.2 Spécification expérimentales

Pour appliquer une charge d'accélération en rotation sur la tête du rat dans le plan sagittal, les auteurs ont placé le rat sur une base et fixé la tête du rat à une barre rotative de l'équipement de production de traumatismes (Figure 2.19). Pour rendre cet ajustement possible, il a d'abord été pratiqué une incision médiane sur le scalpe du rat, puis on a retiré les tissus au-dessus de la région frontale de l'os pariétal du crâne. Une calotte crânienne métallique a ensuite été collée sur le crâne et a été fixée avec une plaque de fixation. Cette plaque de fixation a permis l'ajustement entre la tête du rat et l'équipement.

La calotte crânienne a été conçue de manière à ce qu'un trou de 0,6 mm de diamètre soit percé dans le crâne pour l'insertion d'une aiguille de 0,5 mm de diamètre. Cette aiguille a été insérée jusqu'à une profondeur de 3 mm à l'intérieur du cortex cérébral à un endroit, 3,5 mm à l'arrière et 2,2 mm à droite de la bregma et a été solidement fixée avec le crâne. Une brève rotation vers l'arrière de la tête du rat dans le plan sagittal a été induite par une impulsion d'accélération de rotation, en frappant un percuteur sur le bloc de caoutchouc ciblé de l'équipement produisant le traumatisme. Cette rotation vers l'arrière se poursuit jusqu'à ce que la cible du percuteur entre en contact avec la traverse rigide recouverte de mousse, comme le montre la Figure 2.19.

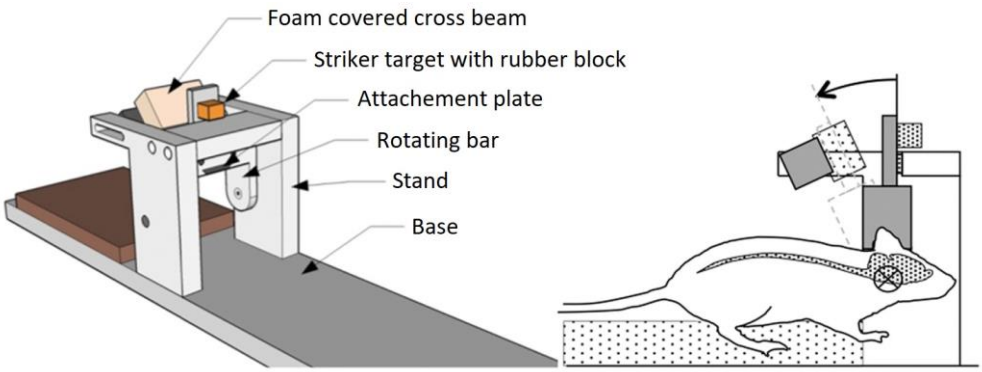

Figure 2.19: Diagramme représentant l'équipement produisant un traumatisme à gauche et une représentation schématique de la vue latérale de la tête de rat, montée dans l'équipement (Davidsson and Risling, 2011).

La courbe expérimentale moyenne de l'accélération rotationnelle en fonction du temps, qui a également été utilisée pour recréer l'expérience par simulation numérique, est présentée à la Figure 2.20. L'aiguille insérée a provoqué une cicatrice sur le cortex cérébral en raison du mouvement relatif entre le cerveau et le crâne. Immédiatement après le traumatisme, l'aiguille a été retirée et le cerveau a été fixé. Ensuite, le cerveau a été tranché, dans un plan perpendiculaire à l'aiguille insérée, à quatre profondeurs de la surface du cerveau, de façon à mesurer la longueur de la cicatrice à ces quatre différentes profondeurs, qui sont 0,5 mm, 1,0 mm, 1,5 mm et 2,0 mm. La longueur de cicatrice mesurée à ces profondeurs est la donnée expérimentale de déplacement relatif cerveau-crâne, par rapport à laquelle le modèle a été validé. Le Table 2.6 présente les mesures expérimentales du déplacement relatif cerveau-crâne selon Antona-Makoshi et al. (2014).

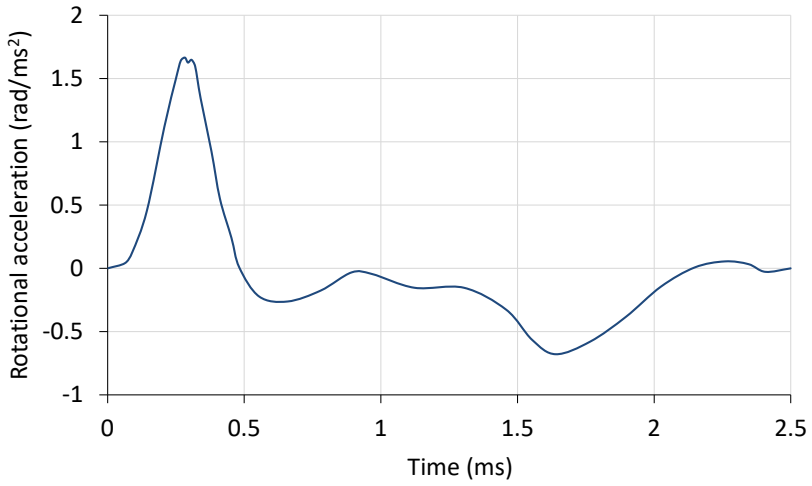

Figure 2.20: Diagramme représentant la courbe de charge expérimentale moyenne de l'accélération rotationnelle en fonction du temps (Antona-Makoshi et al., 2014), également appliquée dans les simulations de validation du déplacement relatif cerveau-crâne.

Table 2.6: Mesures expérimentales du déplacement relatif cerveau-crâne (BSRD).

Experimental BSRD (mm)	0.5 mm below surface	1.0 mm below surface	1.5 mm below surface	2.0 mm below surface
Rat 1	1.1	1.1	0.9	0.6
Rat 2	1.3	1.4	1.1	0.7
Rat 3	1.1	1.2	1.1	0.6
Average	1.2	1.2	1.0	0.6

7.3 Simulations numériques

Dans la mesure où une seule charge a été appliquée à la tête du rat, une seule simulation a été effectuée pour calculer le déplacement relatif cerveau-crâne. La courbe de chargement appliquée en termes d'accélération rotationnelle en fonction du temps est celle donnée à la Figure 2.20. Le centre de rotation a été choisi de manière à ce que le centre de gravité du cerveau se trouve à environ 6,5 mm au-dessus du centre de rotation (Davidsson and Risling, 2011). La Figure 2.21 présente le modèle avant et après le chargement.

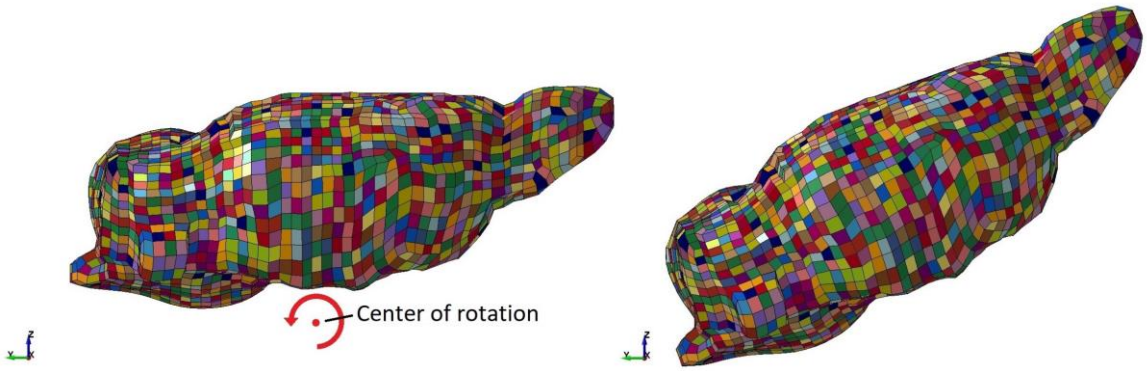

Figure 2.21: Diagramme représentant le modèle avant (à gauche) et après (à droite) la charge d'accélération rotationnelle dans le plan sagittal.

Les nœuds représentatifs choisis pour la mesure du déplacement relatif cerveau-crâne à quatre profondeurs différentes sont illustrés à la Figure 2.22. Le nœud le plus haut se trouve sur le crâne, par rapport auquel on a mesuré le déplacement des quatre nœuds situés en dessous. Les nœuds représentatifs ont été choisis à un endroit, 3,5 mm à l'arrière et 2,2 mm à droite du bregma, conformément à l'emplacement de l'aiguille donné par Antona-Makoshi et al. (2014).

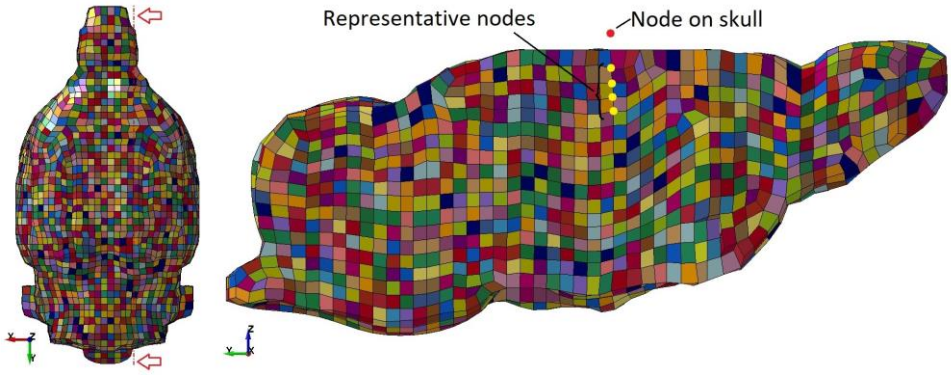

Figure 2.22: Diagramme illustrant les nœuds représentatifs en jaune (à droite) à travers une coupe sagittale (à gauche) à 2,2 mm à droite de la bregma. Le déplacement de ces nœuds a été mesuré par rapport au nœud sur le crâne (rouge) pour connaître le déplacement relatif cerveau-crâne à quatre profondeurs sous la surface du cerveau.

La simulation a été réalisée sur la plateforme LS-DYNA et le temps de simulation était d'environ 20 minutes. La stabilité de la simulation a également été vérifiée et l'énergie maximale du sablier du modèle se situait à 15 % près de l'énergie interne maximale. Les résultats de la simulation du déplacement relatif cerveau-crâne à quatre profondeurs sont donnés dans le Table 2.7.

Table 2.7: Mesures de simulation du déplacement relatif cerveau-crâne (BSRD).

Simulation BSRD (mm)	0.5 mm below surface	1.0 mm below surface	1.5 mm below surface	2.0 mm below surface
FERBM	1.1	1.1	1.1	1.2

7.4 Résultats de la validation du déplacement relatif cerveau-crâne

En comparant les résultats de la simulation avec ceux de l'expérience (Figure 2.23), il apparaît qu'il y a un accord raisonnable entre les deux, aux trois premières profondeurs. Cela nous permet de conclure que le modèle a été validé par rapport au déplacement relatif cerveau-crâne expérimental. Cependant, une différence significative est observée pour la quatrième profondeur. Il pourrait y avoir de nombreuses raisons possibles à cette différence. Comme nous l'avons déjà mentionné, une des raisons possibles pourrait être les propriétés des matériaux. Une autre pourrait être le poids de l'animal, qui était très différent dans ce cas (290 g contre 500 g). L'influence d'une variation paramétrique est expliquée dans la section suivante et peut nous aider à mieux comprendre la réponse du cerveau.

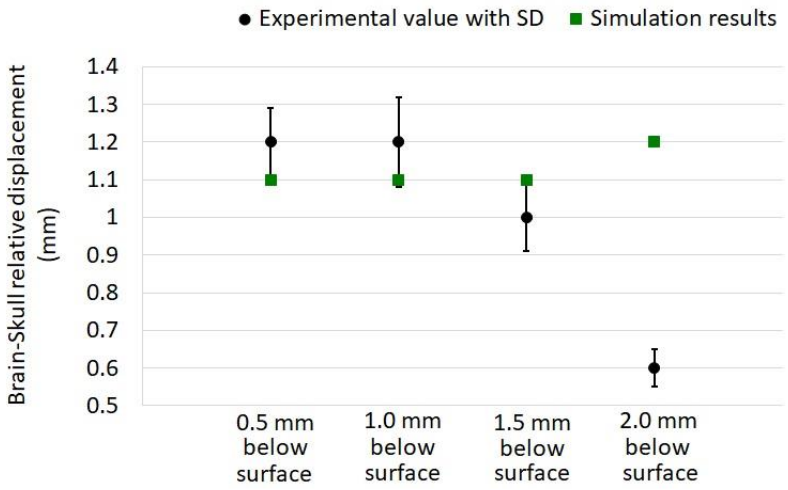

Figure 2.23: Diagramme représentant les mesures expérimentales et de simulation du déplacement relatif cerveau-crâne.

7.5 Conclusion

Cette section expose la validation du FERBM anisotrope développée vis-à-vis du déplacement-relatif entre le crâne et le cerveau sous chargement d'accélération rotationnelle dans le plan sagittal. Pour les trois premières profondeurs, les résultats de la simulation sont en bon accord avec les résultats expérimentaux. Cependant, la différence dans la mesure de la FERBM à la quatrième profondeur est significative. Malgré tous les autres facteurs, nous ne pouvons pas négliger le fait que dans l'expérimentation, une aiguille a été insérée dans le cerveau, ce qui aurait influencé la réponse du cerveau d'une manière ou d'une autre. Cependant, dans les simulations, ce n'était pas le cas et il a été supposé que le comportement nodal des nœuds sélectionnés représentait le comportement réel comme dans les expériences. Par conséquent, le modèle a été considéré comme validé par rapport au déplacement relatif cerveau-crâne expérimental.

8 Étude paramétrique

L'étude paramétrique joue un rôle important dans l'évaluation de la robustesse d'un modèle à éléments finis développé. La variation de la valeur des paramètres et la vérification de l'influence de ce changement sur la réponse du cerveau aident non seulement à identifier les paramètres critiques, mais aussi à soutenir le choix des valeurs des paramètres. Dans le cadre de cette étude, nous avons d'abord observé l'influence de la variation des propriétés matériel du cerveau. Le modèle anisotrope de cerveau de rat aux éléments finis (FERBM) développé utilise une loi de matériau hyperélastique visqueux anisotrope. Pour l'étude paramétrique, les simulations effectuées pour la validation du

déplacement cortical dynamique (DCD) et pour la validation du déplacement relatif cerveau-crâne (BSRD) ont été refaites avec la loi générale de la matière viscoélastique du cerveau de rat. Le modèle de matériau LS-DYNA *MAT_076, c'est-à-dire *MAT_GENERAL_VISCOELASTIC, a été utilisé à cette fin. Cette variation a été choisie car de nombreuses études biomécaniques sur le cerveau du rat ont utilisé ce matériau pour la modélisation du tissu cérébral.

Une autre variation paramétrique a été choisie concernant l'anisotropie uniquement. Les valeurs des paramètres de diffusion, c'est-à-dire l'anisotropie fractionnaire (FA) et la direction principale des fibres (PFD), ont été ramenées à zéro et les simulations de validation ont été effectuées à nouveau. Ceci a été fait pour voir l'influence des paramètres de diffusion sur la réponse du cerveau. Une autre étude paramétrique a été réalisée pour observer l'influence du module global (K) du liquide céphalorachidien (LCR) sur les mesures du DCD et du BSRD. La valeur du module global du LCR pour le FERBM anisotrope validé est égale à 6570 MPa. Pour cette étude paramétrique, la réponse du cerveau a été identifiée à un dixième, un tiers, la moitié, deux fois et dix fois la valeur réelle du module global, qui sont respectivement de 657 MPa, 2190 MPa, 3285 MPa, 13140 MPa et 65700 MPa, alors que tous les autres paramètres sont restés les mêmes.

L’énergie de hourglass joue un rôle important dans la vérification de la qualité de toute simulation. Dans LS-DYNA, une des méthodes pour contrôler l'énergie du sablier est de contrôler la formulation du sablier. Par conséquent, une autre étude paramétrique a été réalisée pour voir l'influence des paramètres du sablier sur les mesures de DCD et de BSRD. La variation de deux paramètres du sablier, IHQ, c'est-à-dire le type de contrôle du sablier, et QH, c'est-à-dire le coefficient du sablier, a été observée. Les valeurs réelles de ces paramètres de contrôle dans le FERBM validé sont IHQ = 7 et QH = 1,0. La réponse du cerveau a été observée pour des valeurs IHQ égales à 1, 2, 3 et 6 avec une valeur QH de 1,0 et ensuite pour une valeur QH de 0,1, 0,3, 0,5 et 0,7 avec une valeur IHQ de 7. Comme mentionné précédemment, QH n'est rien d'autre que le coefficient de sablier. Cependant, IHQ fait référence à différents types de contrôle de sablier, selon le manuel LS_DYNA, IHQ = 1 appartient à la forme visqueuse standard, IHQ = 2 appartient à la forme visqueuse (intégration de Flanagan-Belytschko pour l'élément solide), IHQ = 3 appartient à la forme visqueuse (Flanagan-Belytschko avec intégration volumique exacte pour l'élément solide) et IHQ = 6 appartient à la forme de rigidité co-rotative en déformation supposée de Belytschko-Bindeman pour les éléments solides 2D et 3D.

Les résultats détaillés des études paramétriques sont fournis dans la version originale anglaise de la thèse. L'étude paramétrique a révélé que le choix du matériel cérébral influence fortement la réponse du cerveau pour une condition de charge donnée. Une loi isotrope générale viscoélastique de la matière cérébrale semblait moins rigide que la loi anisotrope visqueuse hyperélastique de la matière

cérébrale. Il a également été observé que la compressibilité du liquide céphalorachidien influençait de façon significative la réponse cérébrale. D'autre part, le coefficient de sablier (QH) de la formulation du sablier n'influence pas considérablement l'énergie du sablier ni la réponse du cerveau ; alors que pour le type de contrôle du sablier (IHQ) de la formulation du sablier, on a pu observer une influence significative à la fois sur l'énergie du sablier et sur la réponse du cerveau.

9 Conclusion

Ce chapitre présente le développement d'un modèle éléments finis de cerveau de rat (FERBM) anisotrope visqueux hyperélastique. À notre connaissance, c'est la première fois qu'un modèle d'éléments finis anisotrope d'un cerveau de rat a été développé. Comme point de départ, un atlas DTI a été choisi pour la construction géométrique du cerveau de rat. La surface cérébrale numérisée a été rendue à partir de l'atlas DTI sous forme de représentation STL, puis la surface et le maillage du volume cérébral enfermé ont été réalisés sur la plateforme HyperMesh. Le modèle de cerveau maillé est constitué de 13 236 éléments solides hexaédriques. Ce modèle maillé a été enfermé dans une autre couche de 3 252 éléments solides hexaédriques représentant le liquide céphalorachidien. Ces deux éléments ont été enfermés dans un crâne rigide, qui a été modélisé par 3 252 éléments quadrilatéraux. Tous les éléments ont été maillés de manière à maintenir les continuités entre les éléments du cerveau et du LCR et entre le LCR et les éléments du crâne.

Dans la deuxième phase du développement, les paramètres de diffusion pour chaque élément de la FERBM ont été estimés. Le même atlas du DTI, comme mentionné précédemment, a été utilisé pour calculer les paramètres de diffusion par voxel. Une fois les voxels par élément identifiés, les paramètres de diffusion par élément ont été estimés par une fonction de moyenne pondérée, de sorte que les voxels situés près du centre de l'élément avaient un poids plus élevé que ceux situés à la limite de l'élément. Les paramètres de diffusion estimés par élément sont l'anisotropie fractionnelle (AF) et la direction principale des fibres (PFD). Tout ce qui précède a été fait par programmation Python.

La dernière phase de développement du modèle a consisté à définir la loi constitutive et des propriétés matérielles. Un modèle de matériau anisotrope visqueux hyperélastique développé par Chatelin et al. (2013) a été choisi et adapté pour le cerveau du rat. Bien que ce modèle matériel ait été développé pour un humain adulte, sur la base des preuves disponibles dans la littérature, on a émis l'hypothèse qu'avec l'inclusion des paramètres de diffusion du cerveau du rat, il pourrait être utilisé pour le cerveau du rat. Au niveau des tissus, ce sont les mêmes neurones et axones qui se propagent à l'intérieur des cellules gliales. Par conséquent, ce modèle matériel a été incorporé dans FERBM par le biais du modèle matériel *MAT_SOFT_TISSUE_VISCO de LS-DYNA. L'implémentation des propriétés

du matériau et des paramètres de diffusion pour chaque élément de la FERBM a été faite par programmation Python. Ainsi, le FERBM développé est un modèle anisotrope visqueux hyperélastique de cerveau de rat à éléments finis, où chaque élément du cerveau a une propriété matérielle différente.

La deuxième moitié de ce chapitre a présenté la validation d'un nouveau modèle éléments finis anisotrope de cerveau de rat. Le modèle est validé par rapport à deux types d'expérimentations disponibles dans la littérature. La première validation a été faite par rapport aux mesures de déplacement cortical dynamique, comme le rapportent Shreiber et al. (1997) et la seconde par rapport aux mesures de déplacement relatif cerveau-crâne, comme le rapportent Antona-Makoshi et al. (2014). Bien que le modèle ait été validé, on ne peut pas conclure qu'il s'agit d'une validation optimale. Cela est dû à deux raisons. Premièrement, le modèle a été validé pour deux mesures expérimentales différentes simultanément et, par conséquent, l'optimalité a été compromise. Deuxièmement, l'objectif principal de cette étude était de pouvoir obtenir des informations supplémentaires sur le cerveau du rat en termes d'élongation axonale en cas de commotion cérébrale et pas seulement la validation du modèle. Néanmoins, le modèle peut être considéré comme validé de manière raisonnable. L'étude paramétrique a montré l'importance de la loi de la matière cérébrale, de la compressibilité du liquide céphalo-rachidien et du contrôle du sablier sur la réponse du cerveau. Par ailleurs il existe toujours des incertitudes concernant les données expérimentales disponibles. Malgré tout, le comportement global du modèle anisotrope de cerveau de rat à éléments finis développé a été validé. Maintenant que nous disposons d'un FERBM anisotrope validé, le chapitre suivant présente des simulations de commotion cérébrale expérimentale ainsi que les résultats et leur analyse.

La motivation principale du développement d'un FERBM anisotrope était de pouvoir obtenir des informations sur la réponse du cerveau du rat en termes d'élongation axonale sous chargement dynamique conduisant à la commotion. Une fois les paramètres de diffusion incorporés dans le cerveau du rat et la direction principale des fibres par élément connus, l'identification de l'allongement axonal par élément devient possible. Finalement, après avoir simulé un traumatisme léger, les éléments à élongation axonale élevé ont permis d'identifier les régions du cerveau les plus susceptibles d'être blessées. Enfin, cela a permis d'identifier le seuil mécanique de la commotion cérébrale en termes d'allongement axonal.

Chapter 3: Simulations de commotion cérébrale expérimentale

1 Introduction

Comme nous l'avons déjà mentionné, la modélisation numérique s'est avérée un outil prometteur pour l'étude des lésions cérébrales. Un modèle numérique validé est utilisé au mieux lorsque des scénarios réels ou expérimentaux sont simulés, afin d'étudier les détails biomécaniques qui ne peuvent être mesurés expérimentalement. En ce qui concerne un scénario accidentel, l'étude du mécanisme de la lésion, l'analyse des causes et des événements, et la conclusion en termes de tolérance de la lésion peuvent être réalisées au mieux par la méthode scientifique de reconstruction d'accident, sous forme de simulation numérique. L'analyse des résultats des simulations numériques permet d'améliorer les outils de prédiction des lésions cérébrales et, par conséquent, d'optimiser les systèmes de protection. Dans les chapitres précédents, la nécessité d'un modèle anisotrope de cerveau de rat par éléments finis (FERBM) a été démontrée et la méthodologie de développement d'un tel modèle a été présentée, ainsi que la validation de ce modèle. Le présent chapitre s'intéresse aux expériences relatives aux commotions cérébrales choisies pour les simulations numériques, ainsi que les résultats de ces simulations. Enfin, une analyse statistique des résultats des simulations a été effectuée afin de déterminer la limite de tolérance du traumatisme crânien pour les commotions cérébrales. Commençons par décrire l'approche expérimentale telle qu'elle a été établie par nos partenaires du MCW.

2 Approche expérimentale

Notre partenaire du Medical College of Wisconsin (MCW), aux États-Unis, effectue des expériences des commotions cérébrales chez les rats depuis plus de dix ans. Les données expérimentales de vingt-six de ces expériences ont été transférées à l'Université de Strasbourg dans le cadre d'une collaboration basée sur l'étude de Stemper et al. (2016). Dans ces expériences, des lésions cérébrales traumatiques légères ou commotions cérébrales ont été induites au cerveau du rat par une mise en accélération en rotation dans le plan coronal selon le modèle de lésions en rotation de MCW, comme le montre la Figure 3.1.

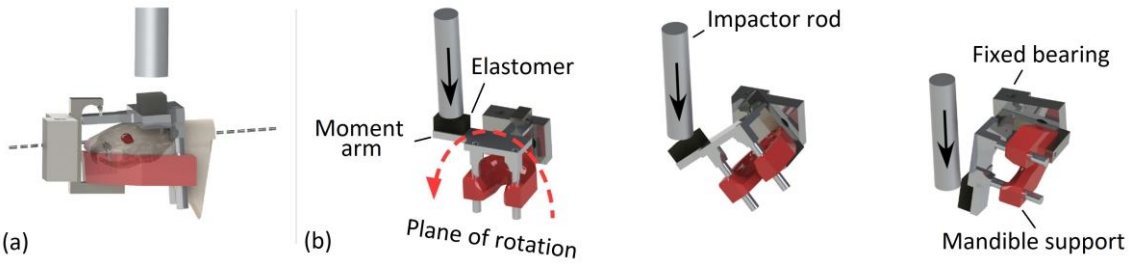

Figure 3.1: Diagramme représentant le modèle de blessure par rotation MCW, qui a été utilisé pour induire une commotion cérébrale chez des rats par une charge d'accélération de rotation de la tête du rat dans le plan coronal ; (a) placement de la tête du rat dans le dispositif, (b) rotation séquentielle du casque (Stemper et al., 2016).

La tête du rat était solidement fixée dans le << casque >> sans aucune attache extérieure et le casque était fixé au dispositif par une articulation à broche, de manière à permettre une rotation pure de la tête de rat dans le plan coronal autour de la colonne cervicale. On a signalé que l'utilisation de ce modèle n'a entraîné aucune mortalité et aucune fracture ou dislocation de la colonne cervicale (Stemper et al., 2016). Le chargement accélérometrique en rotation appliqué à la tête du rat a été matérialisée par l'impact d'un impacteur à accélération pneumatique sur le bras de moment latéral du casque. Cette accélération de rotation contrôlée en fonction du temps a entraîné une accélération de rotation de la tête du rat, qui a été limitée à environ 90˚ de rotation.

Les expériences ont été effectuées sur des rats Sprague Dawley femelles adultes, pesant 289 ± 22 g. Les rats ont été anesthésiés et placés dans le casque, puis le casque a été fixé au dispositif d'essai. Dès que l'anesthésie a été retirée, la tige de l'impacteur a été lancée pour frapper le bras de levier afin d'induire l'accélération de la rotation du casque. Immédiatement après l'exposition à la rotation, les rats ont été retirés du dispositif et placés sur une couverture pour se rétablir. Les rats ont été remis dans les cages après avoir acquis le réflexe de redressement et ont été surveillés de façon continue pendant les trente premières minutes, puis périodiquement jusqu'à six heures après l'exposition à la blessure.

La gravité de la lésion aiguë a été évaluée à l'aide du temps de récupération (temps d'inconscience), c'est-à-dire le temps écoulé entre le retrait de l'anesthésie juste avant l'exposition à la rotation et l'acquisition du réflexe de redressement après la lésion. L'évaluation du labyrinthe surélevé (EPM) a été utilisée pour analyser les changements dans les aspects comportementaux, l'activité et l'émotivité, suite à la commotion cérébrale. L'activité a été surveillée en observant la distance totale parcourue et le nombre total de changements au niveau du bras dans l'évaluation EPM. Alors que l'émotivité a été surveillée en observant le temps total passé dans les régions ouvertes pendant l'évaluation EPM. La

Figure 3.2 illustre le type de labyrinthe surélevé et de labyrinthe plus utilisé dans les expériences pour l'évaluation du comportement.

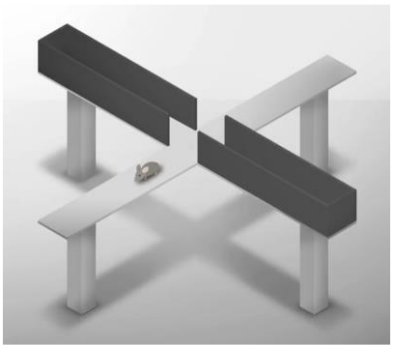

Figure 3.2: Diagramme représentant un labyrinthe surélevé plus (EPM) pour l'évaluation de l'activité et de l'émotivité post-commotion.

L'évaluation du labyrinthe aquatique de Morris (MWM) a été utilisée pour analyser l'amnésie antérograde post-traumatique et l'apprentissage spatial après la commotion cérébrale. Les changements dans les capacités cognitives après la commotion ont été suivis en observant la latence, c'est-à-dire le temps nécessaire pour les rats pour trouver la plateforme cachée au cours de trois sessions différentes (sur trois jours consécutifs après la blessure) de l'évaluation du MWM. La Figure 3.3 illustre le type de labyrinthe aquatique de Morris utilisé dans les expériences pour l'évaluation comportementale.

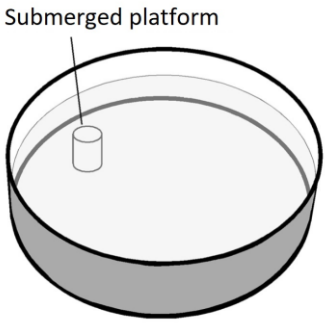

Figure 3.3: Diagramme représentant le labyrinthe d'eau de Morris (MWM) pour l'évaluation des capacités cognitives post-commotionnelles.

Les détails concernant le chargement expérimental de la tête, c'est-à-dire l'amplitude de crête et la durée positive de l'impulsion d'accélération rotationnelle appliquée pour les vingt-six cas expérimentaux, sont donnés dans le Table 3.1.

Table 3.1: Apports expérimentaux en termes d'amplitude de pic et de durée de l'accélération de rotation appliquée des vingt-six cas expérimentaux, tels que fournis par MCW.

Animal ID	Peak rotational acceleration (rad/ms^2)	Duration (ms)	Animal ID	Peak rotational acceleration (rad/ms^2)	Duration (ms)
1RAT17	0.3903	3.2	**14RAT107**	0.3049	2.4
2RAT18	0.3932	2.9	**15RAT119**	0.3107	1.3
3RAT19	0.3903	3.7	**16RAT123**	0.1659	2.4
4RAT77	0.3457	1.4	**17RAT141**	0.1922	3.2
5RAT78	0.3700	1.6	**18RAT142**	0.2580	3.0
6RAT79	0.3061	3.4	**19RAT148**	0.2721	1.4
7RAT80	0.4596	1.5	**20RAT152**	0.3817	1.8
8RAT84	0.3923	1.5	**21RAT296**	0.2468	0.8
9RAT85	0.3640	1.7	**22RAT299**	0.2348	0.7
10RAT86	0.4629	1.3	**23RAT301**	0.2262	0.8
11RAT93	0.4146	1.5	**24RAT303**	0.2392	0.8
12RAT95	0.3836	1.6	**25RAT306**	0.1953	2.3
13RAT105	0.3953	1.5	**26RAT311**	0.2116	2.0

D'après l'amplitude maximale et la durée de l'accélération de rotation, ces vingt-six expériences peuvent être répartir en quatre groupes de chargement, comme indiqué dans la publication de Stemper et al. (2016). Il s'agit du groupe à faible amplitude et courte durée (M1D1), du groupe à faible amplitude et longue durée (M1D2), du groupe à amplitude élevée et courte durée (M2D1) et du groupe à amplitude élevée et longue durée (M2D2). Le Table 3.2 regroupe brièvement les détails de cette catégorisation. Huit rats se retrouvent dans le groupe M1D1, deux dans le groupe M1D2, douze dans le groupe M2D1 et quatre dans le groupe M2D2. La magnitude faible, M1, était égale à 0,2242 ± 0,03 rad/ms2 et la magnitude élevée, M2, était égale à 0,3791 ± 0,05 rad/ms2. La courte durée, D1, était égale à 1,5 ± 0,5 ms et la longue durée était égale à 3,2 ± 0,3 ms.

Table 3.2: Détails de la catégorisation de vingt-six cas expérimentaux en différents groupes de charge en fonction de l'ampleur et de la durée de l'accélération rotationnelle appliquée. Le codage couleur représente la classification basée sur une impulsion de charge identique.

	Short duration, D1 1.5 ± 0.5 ms	**Long duration, D2 3.2 ± 0.3 ms**
Low magnitude, M1 0.2242 ± 0.03 rad/ms²	**n = 8 16RAT123, 19RAT148, 21RAT296, 22RAT299, 23RAT301, 24RAT303, 25RAT306, 26RAT311**	**n = 2 17RAT141, 18RAT142**
High magnitude (M2) 0.3791 ± 0.05 rad/ms²	**n = 12 4RAT77, 5RAT78, 7RAT80, 8RAT84, 9RAT85, 10RAT86, 11RAT93, 12RAT95, 13RAT105, 14RAT107, 15RAT119, 20RAT152**	**n = 4 1RAT17, 2RAT18, 3RAT19, 6RAT79**

Les résultats comportementaux aigus après blessure de ces vingt-six cas expérimentaux et ceux de la simulation numérique (groupe témoin sans blessure par rotation) tels qu'ils sont donnés dans Stemper et al. (2016) sont fournis ci-dessous dans le Table 3.3.

Table 3.3: Résultats comportementaux aigus post-lésionnels de la simulation (tels que donnés dans Stemper et al., 2016) et des vingt-six cas expérimentaux tels que fournis par MCW.

Animal ID	**Unconscious time (s)**	**EPM distance travelled (cm)**	**EPM arm changes (#)**	**EPM open duration (s)**	**MWM session I latency (s)**	**MWM session II latency (s)**	**MWM session III latency (s)**
Sham	178 ± 52 (n = 16)	724 ± 410 (n = 8)	15.6 ± 10.2 (n = 8)	42.2 ± 29.6 (n = 8)	48.8 ± 8.0 (n = 8)	17.8 ± 10.6 (n = 8)	21.2 ± 12.4 (n = 8)
1RAT17	256	1053	18	56.7	34.0	34.4	21.7
2RAT18	134	1325	28	24.8	45.9	19.6	11.6
3RAT19	212	1067	26	86.7	60.0	33.7	10.4
4RAT77	99	1356	35	51.6	46.7	8.1	7.0
5RAT78	198	1293	24	30.8	45.4	2.9	6.9
6RAT79	298	2095	62	107.9	30.2	41.7	3.9
7RAT80	97	1604	42	73.0	38.8	25.2	15.7
8RAT84	179	1354	37	81.5	22.1	7.5	6.5
9RAT85	294	1092	22	31.6	32.3	8.7	7.8
10RAT86	394	572	19	36.2	43.6	19.1	47.4
11RAT93	318	715	20	49.2	32.2	19.8	8.8
12RAT95	180	1623	44	79.5	46.7	22.7	3.1

Animal ID	Unconscious time (s)	EPM distance travelled (cm)	EPM arm changes (#)	EPM open duration (s)	MWM session I latency (s)	MWM session II latency (s)	MWM session III latency (s)
13RAT105	238	958	18	14.7	60.0	10.1	60.0
14RAT107	373	1429	36	49.1	49.7	5.0	5.9
15RAT119	264	1362	32	75.3	18.0	44.5	24.2
16RAT123	311	1235	29	33.3	26.7	22.9	33.5
17RAT141	190	1509	38	83.3	44.8	23.0	37.7
18RAT142	158	952	25	31.8	40.3	11.8	10.6
19RAT148	75	957	35	140.1	40.2	27.8	9.5
20RAT152	183	1778	44	109.4	25.6	30.7	23.0
21RAT296	165	1054	18	48.3	48.7	30.4	18.0
22RAT299	147	1169	25	82.0	27.0	15.2	17.1
23RAT301	135	1639	36	114.3	45.7	32.6	15.1
24RAT303	126	898	17	60.3	41.7	23.0	10.6
25RAT306	113	1869	39	144.6	26.3	10.1	18.2
26RAT311	144	932	21	55.2	15.0	15.2	23.9

Une variation des valeurs de la mesure de la réponse comportementale de vingt-six cas expérimentaux par rapport à celle de la simulation est un indicateur clair du changement de comportement après une blessure. Le Table 3.4 présente l'association des données d'entrées expérimentales (l'amplitude de crête et la durée de l'accélération de rotation appliquée) avec les données de sorties expérimentales (temps inconscient, distance parcourue par le MPE, changements de bras du MPE, durée d'ouverture du MPE et latence des sessions I, II et III du MPE) pour analyser l'effet de l'impulsion du chargement appliquée sur la réponse comportementale. Comme mentionné précédemment, les résultats expérimentaux s'associent à quatre aspects comportementaux, tels que le temps d'inconscience avec la conscience, la distance parcourue par l'EPM et les changements de bras de l'EPM avec l'activité, la durée d'ouverture de l'EPM avec l'émotivité et les latences de la session MWM avec les capacités cognitives. Même les courbes de charge appartenant à un même groupe de charge n'étaient pas identiques et par conséquent, les groupes ont été subdivisés. Le groupe M1D1 comptait huit cas au total. En fonction de la nature de l'impulsion de charge, les cas ont été divisés en deux sous-groupes M1D1a et M1D1b, avec quatre cas chacun. Les courbes de charge dans les sous-groupes étaient plus ou moins semblables. De même, les groupes M2D1a (7 cas), M2D1b (5 cas), M2D2a (3 cas) et M2D2b (1 cas) ont été créés. Le codage couleur fourni dans le Table 3.2 représente ces sous-groupes.

Table 3.4: Association entre les entrées expérimentales (amplitude et durée maximales de l'accélération de rotation appliquée) et les sorties expérimentales (temps inconscient, distance parcourue par le MPE, changements de bras du MPE, durée d'ouverture du MPE et latence dans les sessions I, II et III du MWM) sur la base des groupes de charge.

Unconscious time

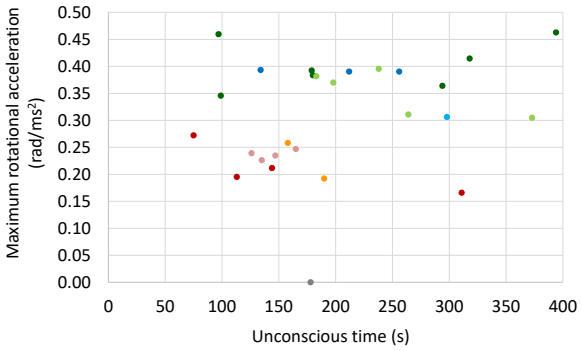

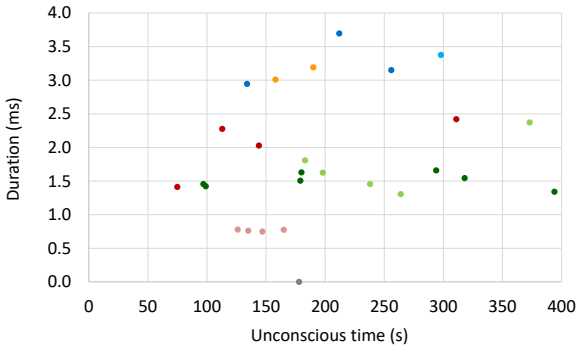

EPM distance travelled

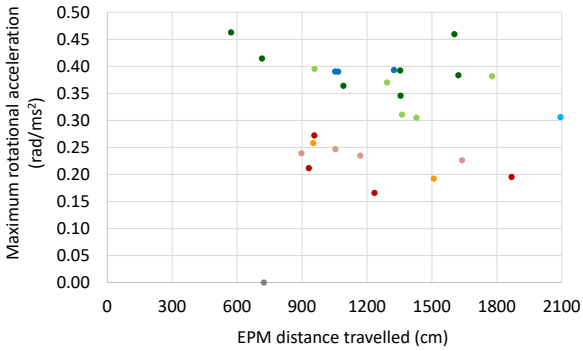

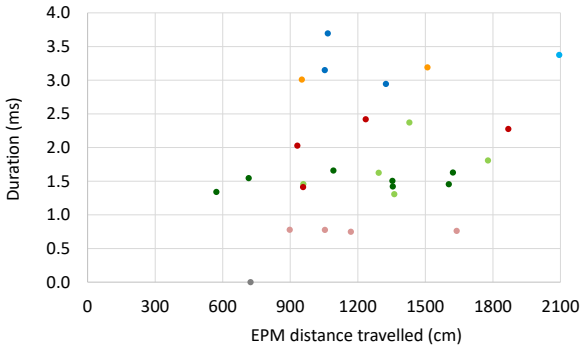

EPM arm changes

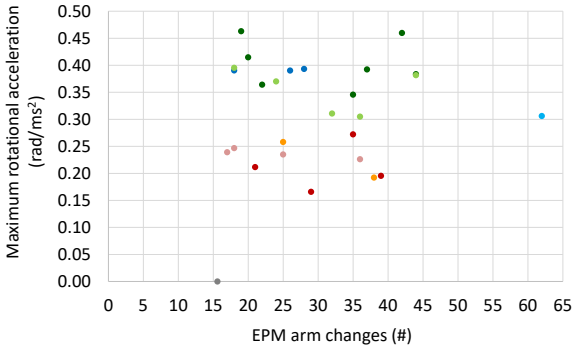

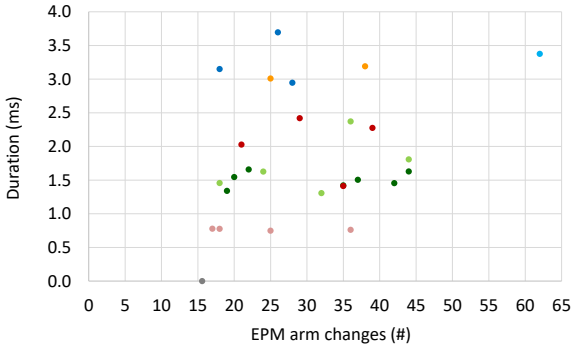

EPM open duration

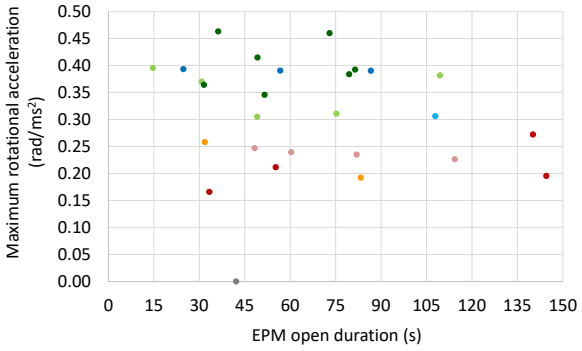

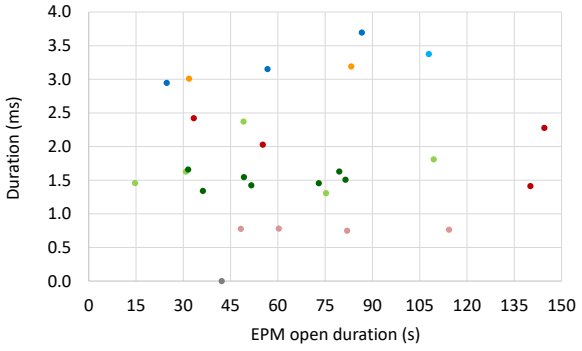

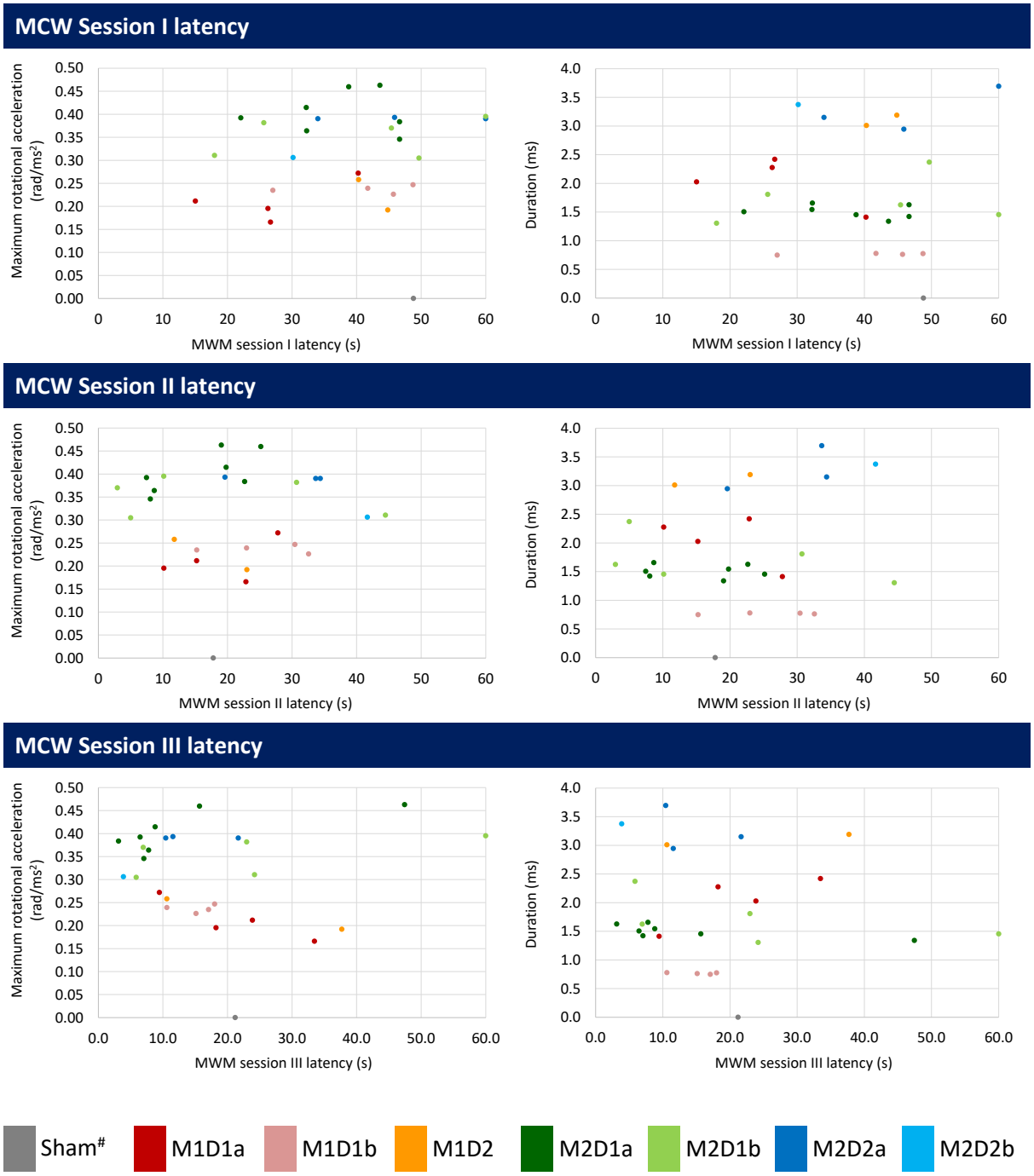

[#] Comme les simulacres n'ont pas subi de charge de rotation, seule leur réponse expérimentale est marquée.

Les graphiques de la Table 3.4 montrent que même les cas d'un même il n'apparaît pas de corrélation directe entre les caractéristiques de l'accélération de rotation et les mesures expérimentales de la réponse comportementale. Cela signifie qu'il est difficile d'expliquer les changements comportementaux en se basant uniquement sur l'accélération de rotation maximale et la durée. Les courbes de charge expérimentales de vingt-six cas expérimentaux illustrant les impulsions d'accélération rotationnelle appliquées sont fournies à l'Annexe B (version originale en anglais) à titre de référence. Une autre façon d'examiner la relation entre les caractéristiques de l'accélération et les

réactions comportementales consiste à classer les cas simulés en groupes de personnes non blessées et de personnes blessées. D'après la réponse comportementale de la simulation, 26 cas peuvent être classés en deux groupes. Le groupe non blessé, dont la valeur de la réponse comportementale est inférieure à celle du groupe simulé et le groupe blessé, dont la valeur de la réponse comportementale est supérieure à celle du groupe simulé. Le Table 3.5 présente l'association des données d'entrée expérimentales (amplitude de crête et durée de l'accélération de rotation appliquée) et des données de sortie expérimentales (temps d'inconscience, distance parcourue par l'EPM, changements de bras de l'EPM, durée d'ouverture de l'EPM et latence des sessions I, II et III du MWM) afin d'analyser l'effet de l'impulsion de charge appliquée sur la réponse comportementale sur la base des catégories non blessés et blessés.

Table 3.5: Association entre les entrées expérimentales (amplitude et durée maximales de l'accélération de rotation appliquée) et les sorties expérimentales (temps inconscient, distance parcourue par le MPE, changements de bras du MPE, durée d'ouverture du MPE et latence dans la session I, II et III du MWM) sur la base des catégories non blessées et blessées.

Unconscious time

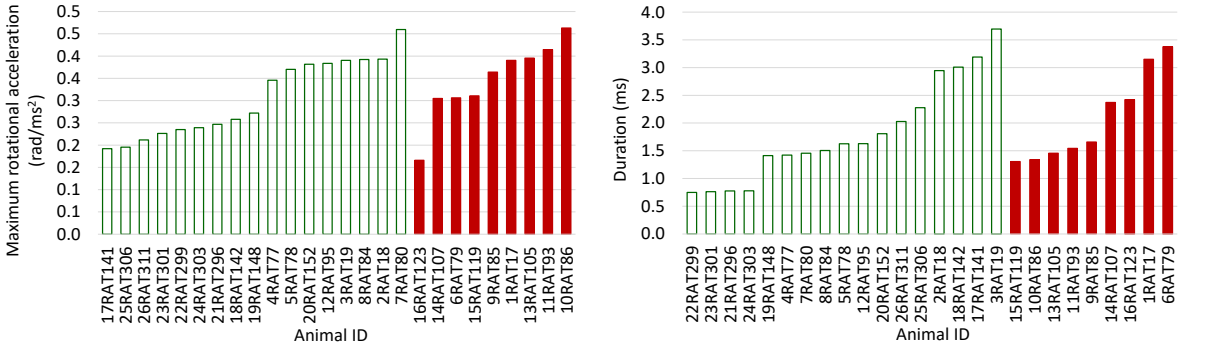

EPM distance travelled

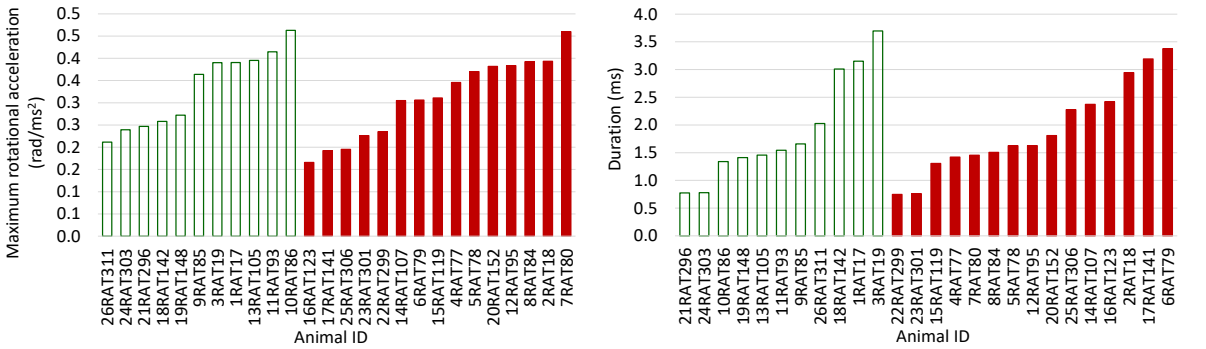

cont.

EPM arm changes

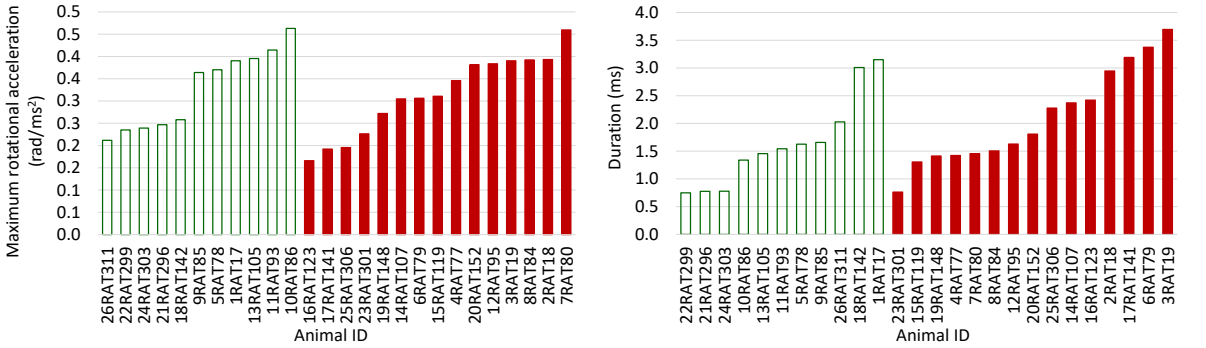

EPM open duration

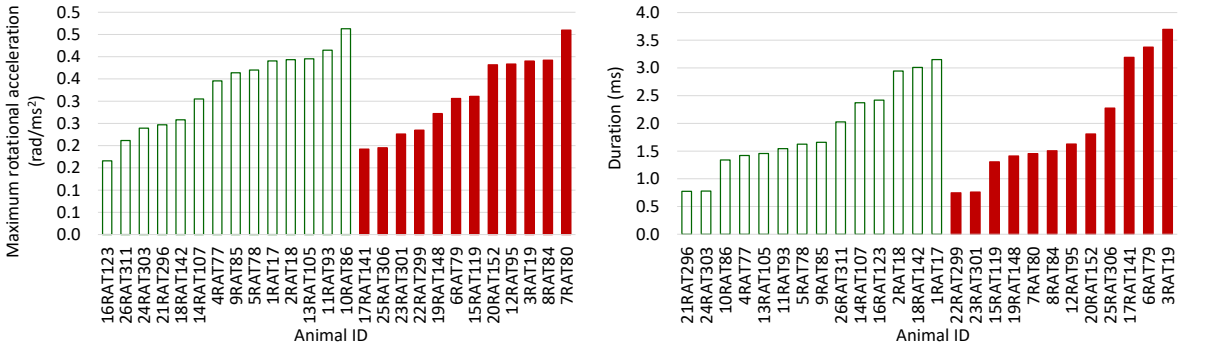

MCW Session I latency

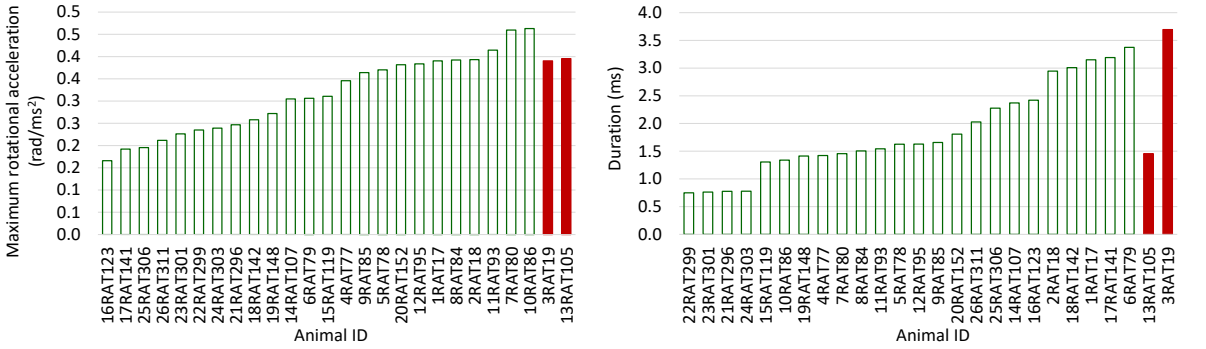

MCW Session II latency

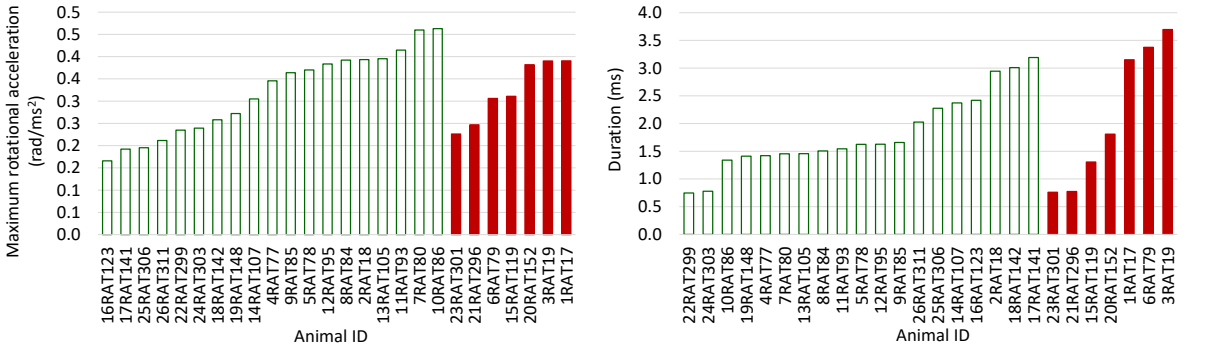

cont.

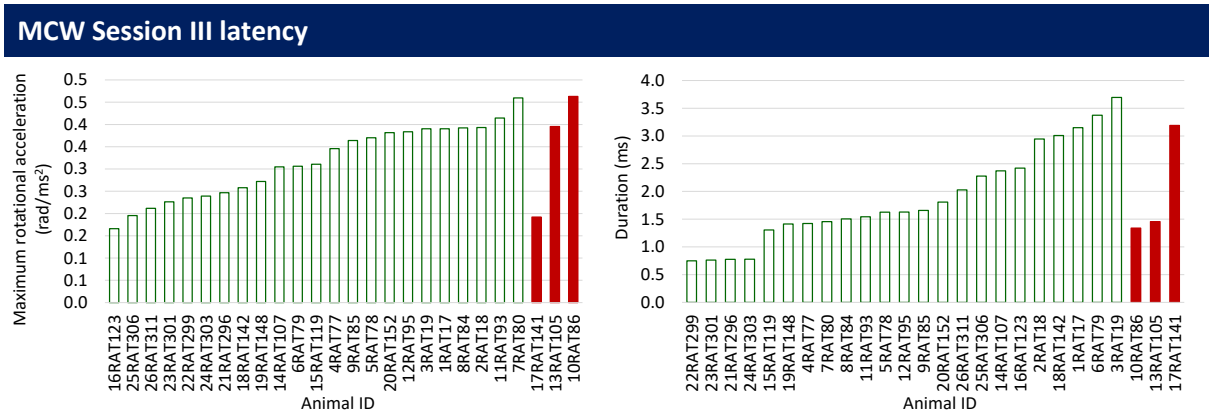

On peut voir sur les graphiques du Table 3.5 que les amplitudes des groupes non blessés et blessés varient de faibles à élevées et qu'il n'y a pas de différence significative entre les amplitudes globales des deux groupes. Par conséquent, nous ne voyons pas de corrélation directe entre les caractéristiques de l'accélération de rotation et les mesures expérimentales de la réponse comportementale. Cela signifie qu'en se basant également sur la catégorisation des non blessés et des blessés, il est difficile d'expliquer les changements de comportement en se basant uniquement sur l'accélération de rotation maximale et la durée.

3 Simulations numérique des chocs expérimentaux

Les vingt-six cas expérimentaux mentionnés ci-dessus ont été simulés avec le modèle de cerveau de rat développé au chapitre 2, sur la base des impulsions d'accélération de rotation du chargement en rotation fournies par le MCW, comme indiqué à l'Annexe B (version originale en anglais). Il apparaît que les courbes diffèrent même au sein d'un groupe de chargement. Par conséquent, comme mentionné précédemment, pour une meilleure compréhension des résultats de la simulation, ces groupes ont été subdivisés afin de comparer la réponse comportementale des rats en fonction du type de charge. Comme il est décrit au chapitre 2, le modèle de cerveau de rat a été enfermé dans un crâne rigide. Pour reproduire les expériences, une impulsion d'accélération de rotation a été appliquée au crâne autour d'un axe situé dans la moitié inférieure du cerveau, qui passe par le plan mi-sagittal, de manière à obtenir une rotation pure du cerveau du rat dans le plan coronal. La rotation maximale du cerveau de rat dans les vingt-six simulations est restée dans les 90 degrés.

Un solveur d'éléments finis non linéaire, dynamique et explicite, LS-DYNA SMP version R10.1.0 (Livermore Software Technology Corporation (LSTC), CA) a été utilisé pour les simulations. La durée de la simulation a varié entre trente minutes et trois heures trente minutes. La stabilité des simulations a été vérifiée et l'énergie maximale du sablier du modèle se trouvait dans des limites acceptables. La

Figure 3.4 montre le FERBM avant et après une telle simulation. Comme le montre la figure, la vue de droite du modèle avant la simulation est présentée à gauche. Après une rotation pure dans le plan coronal, la vue pivotée du modèle est présentée à droite.

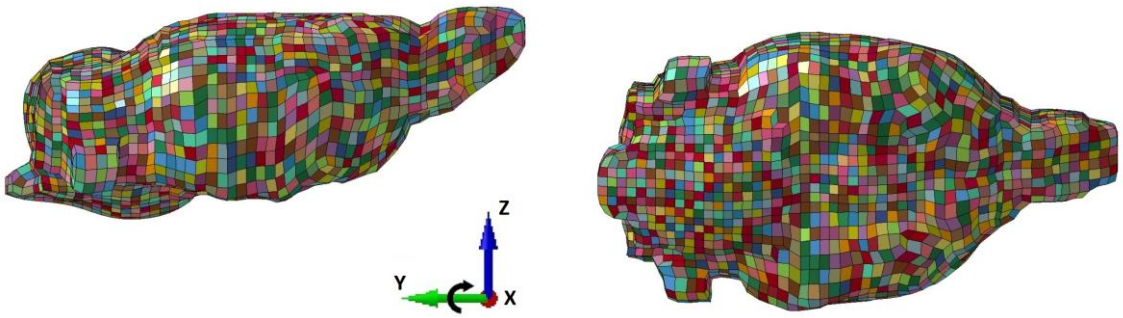

Figure 3.4: Diagramme représentant FERBM avant et après la simulation basée sur l'expérience de MCW liée à la commotion cérébrale pour l'un des cas.

4 Résultats des simulations

4.1 Introduction

Après avoir effectué les vingt-six simulations, dix paramètres mécaniques ont été extraits, à savoir la contrainte et la déformation maximale de von Mises, la contrainte et la déformation principale maximale, la contrainte et la déformation maximale de cisaillement, les pressions minimales et maximales, l'énergie de déformation et le tenseur de déformation, pour calculer la déformation axonale. Le post-traitement des résultats de simulation a été effectué sur le logiciel LS-PrePost version 4.5 (LSTC). Comme le modèle de calcul est anisotrope, chaque élément du FERBM avait une direction de fibre principale (PFD) qui est l'orientation du faisceau d'axones principal (expliqué en détail au chapitre 2). Ainsi, à l'aide de ce vecteur d'orientation, la déformation axonale par élément a été calculée à partir des données du tenseur de tache par programmation python. Ces données de déformation axonale ont aidé à estimer la déformation axonale maximale (DMA) pour tous les cas et à identifier les régions du cerveau qui subissent des déformations élevées. Tous ces paramètres mécaniques ont été calculés non seulement pour l'ensemble du cerveau (Table 3.6), mais aussi pour chacune des vingt-quatre régions anatomiques du cerveau ainsi que pour les régions fonctionnelles du cerveau associées à la conscience, à l'activité, à l'émotivité et aux capacités cognitives (la catégorisation des régions du cerveau pour l'analyse des résultats de simulation est décrite au chapitre 2). Ces résultats peuvent être considérés de différentes manières. Les sections suivantes représentent ces résultats de simulation avec différentes perspectives.

Table 3.6: Résultats de la simulation des vingt-six cas, en termes de dix paramètres mécaniques, pour l'ensemble du cerveau.

Animal ID	Max. axonal strain	Max. strain energy (mJ)	Max. von Mises stress (kPa)	Max. von Mises strain	Max. shear stress (kPa)	Max. shear strain	Max. principal stress (kPa)	Max. principal strain	Min. pressure (kPa)	Max. pressure (kPa)
1RAT17	0.1169	6.6E-05	7.4	0.1431	4.2	0.1234	348.3	0.1402	-346.7	374.2
2RAT18	0.1102	6.1E-05	6.9	0.1358	4.0	0.1172	332.6	0.1324	-331.2	365.5
3RAT19	0.1020	5.3E-05	6.4	0.1269	3.7	0.1095	312.8	0.1230	-311.4	352.3
4RAT77	0.1088	5.7E-05	6.9	0.1341	3.9	0.1157	333.6	0.1308	-332.1	371.8
5RAT78	0.0846	3.7E-05	5.3	0.1084	3.0	0.0936	272.7	0.1040	-272.2	315.1
6RAT79	0.1080	5.7E-05	6.9	0.1344	3.9	0.1159	330.3	0.1310	-328.9	366.6
7RAT80	0.1232	6.9E-05	7.9	0.1502	4.5	0.1295	363.4	0.1483	-361.6	385.6
8RAT84	0.1187	6.7E-05	7.2	0.1422	4.1	0.1226	344.7	0.1395	-343.1	377.8
9RAT85	0.1144	6.2E-05	7.4	0.1421	4.2	0.1225	346.5	0.1394	-345.0	376.4
10RAT86	0.1195	6.9E-05	7.5	0.1461	4.3	0.1259	351.4	0.1434	-349.8	377.6
11RAT93	0.1239	7.1E-05	8.0	0.1510	4.5	0.1304	363.5	0.1504	-361.7	386.6
12RAT95	0.1197	6.7E-05	7.9	0.1493	4.5	0.1287	359.1	0.1483	-357.4	381.2
13RAT105	0.1286	7.9E-05	8.2	0.1576	4.7	0.1358	367.1	0.1558	-365.3	379.2
14RAT107	0.1225	7.3E-05	7.8	0.1522	4.4	0.1312	355.9	0.1499	-354.2	373.7
15RAT119	0.0934	4.3E-05	6.0	0.1177	3.4	0.1016	292.6	0.1137	-291.4	350.7
16RAT123	0.0731	2.8E-05	4.6	0.0951	2.6	0.0822	247.9	0.0911	-247.6	285.5
17RAT141	0.0767	3.1E-05	4.7	0.0984	2.7	0.0848	256.9	0.0946	-256.6	297.4
18RAT142	0.0789	3.2E-05	4.9	0.1001	2.8	0.0864	267.8	0.0961	-267.4	309.6
19RAT148	0.0869	3.8E-05	5.5	0.1100	3.1	0.0950	277.3	0.1057	-276.8	326.3
20RAT152	0.1462	9.7E-05	8.9	0.1745	5.1	0.1503	407.3	0.1743	-405.0	394.4
21RAT296	0.0569	1.4E-05	3.3	0.0734	1.9	0.0634	205.2	0.0688	-204.4	206.6
22RAT299	0.0577	1.4E-05	3.3	0.0746	1.9	0.0644	208.9	0.0700	-208.0	209.5
23RAT301	0.0560	1.3E-05	3.2	0.0722	1.8	0.0623	200.4	0.0675	-199.6	201.8
24RAT303	0.0571	1.4E-05	3.3	0.0737	1.9	0.0637	203.8	0.0690	-202.9	205.8
25RAT306	0.0725	2.8E-05	4.5	0.0934	2.6	0.0806	250.4	0.0897	-250.1	285.2
26RAT311	0.0708	2.8E-05	4.3	0.0921	2.5	0.0793	243.1	0.0885	-242.7	275.2

Globalement, le cas de l'animal ID 20RAT152, qui appartient au groupe de chargement de courte durée de grande amplitude, a subi le chargement le plus sévère, car la réponse mécanique de ce cas est la plus élevée parmi tous les autres cas. Bien que, pour les cas 7RAT80 et 10RAT86, les amplitudes de l'accélération rotationnelle appliquée aient été plus élevées et les durées plus courtes que pour le cas

20RAT152, la qualité de l'impulsion d'accélération du cas 20RAT152 a permis d'expliquer la gravité relative de ce cas. Examinons les résultats de la simulation pour le cerveau entier en fonction de la catégorisation des groupes de charge dans la section suivante.

4.2 Pour le cerveau entier : basé sur la catégorisation des groupes de chargement

Cette section fournit des résultats de simulation pour l'ensemble du cerveau. Les résultats sont rapportés pour la déformation axonale maximale et la contrainte maximale de von Mises (Table 3.7). Annexe C (Table C1 à Table C7, version originale en anglais) présente les résultats pour l'ensemble des dix paramètres mécaniques en association avec sept mesures expérimentales de la réponse comportementale. Ces résultats sont basés sur les groupes de charge, en ce qui concerne l'amplitude et la durée de l'accélération rotationnelle expérimentale.

Table 3.7: Résultats de la simulation pour le cerveau entier basés sur la catégorisation des groupes de charge.

With respect to unconsciousness time

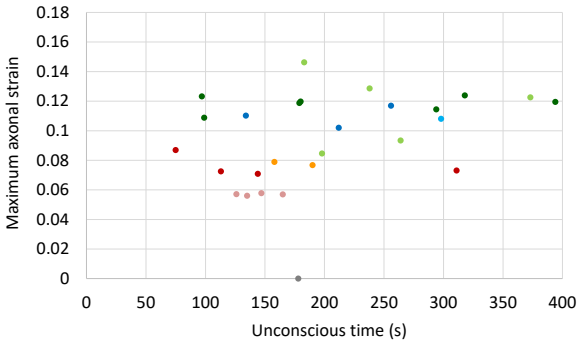

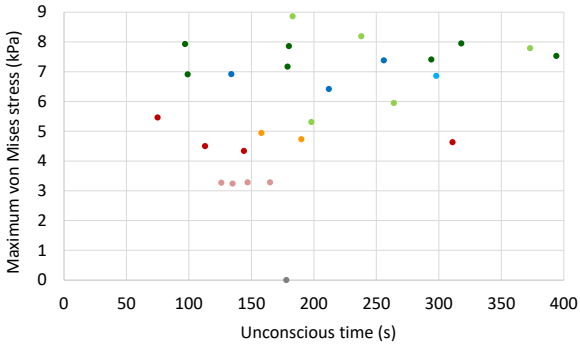

With respect to EPM distance travelled

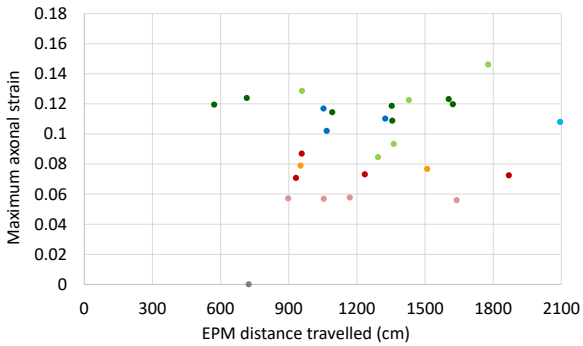

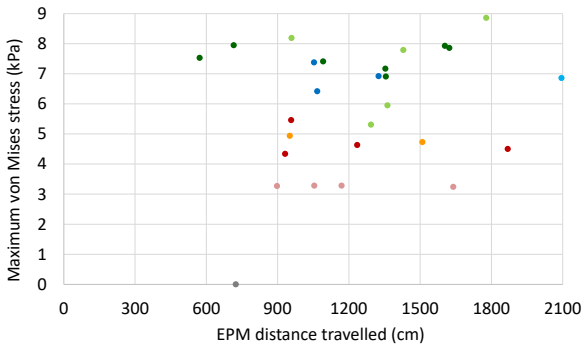

cont.

With respect to EPM arm changes

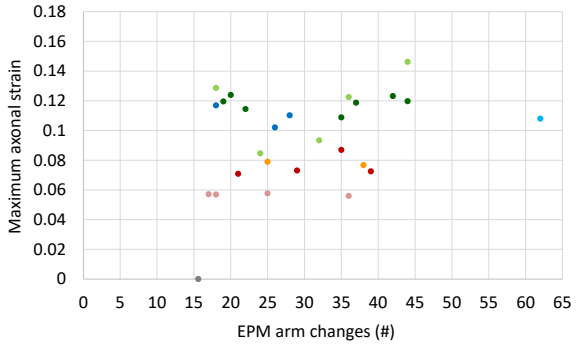

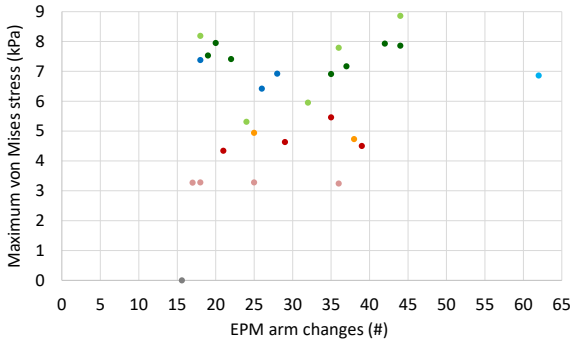

With respect to EPM open duration

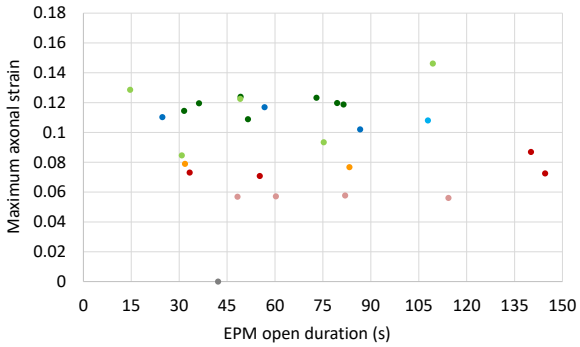

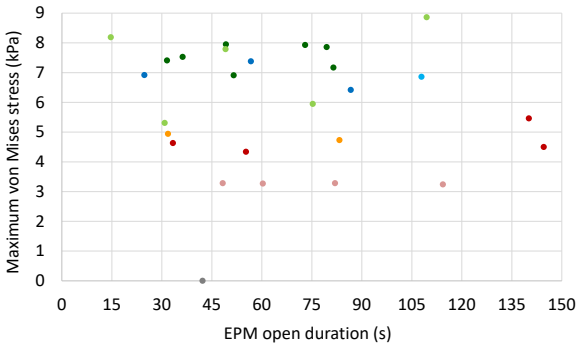

With respect to MWM session I latency

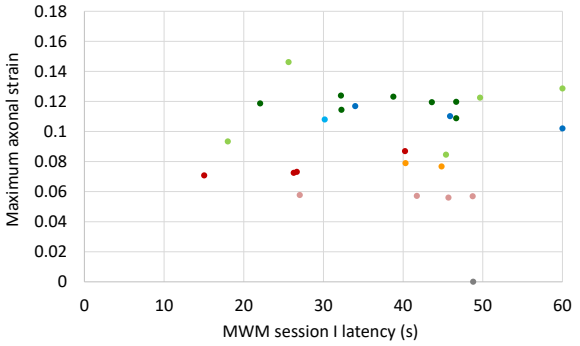

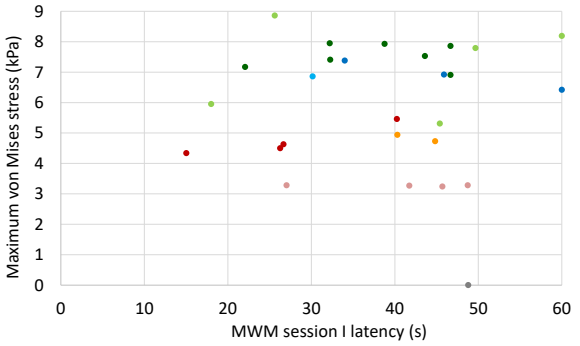

With respect to MWM session II latency

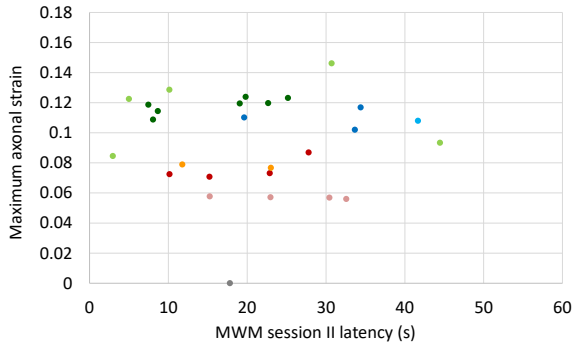

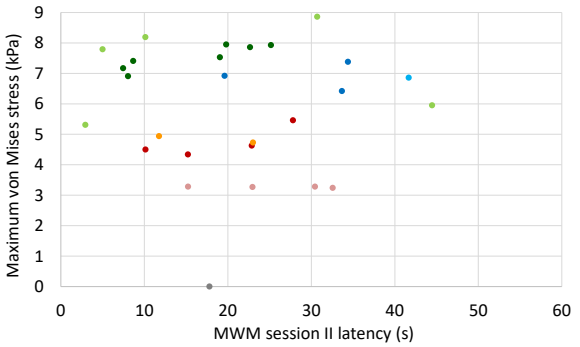

cont.

With respect to MWM session III latency

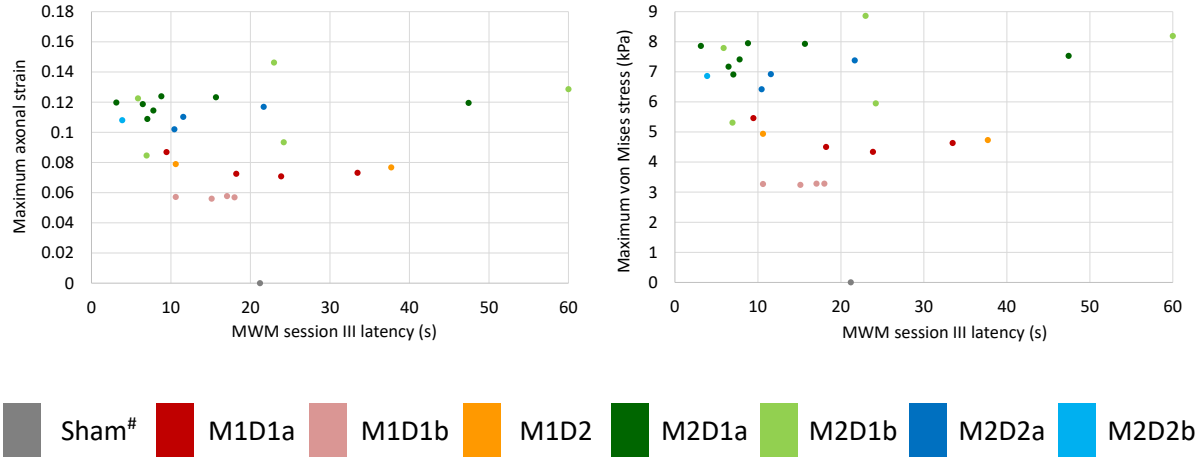

Sham[#] M1D1a M1D1b M1D2 M2D1a M2D1b M2D2a M2D2b

[#] Comme les simulacres n'ont pas subi de charge de rotation, seule leur réponse expérimentale est marquée.

Il ne semble pas y avoir de corrélation directe entre les mesures de la réponse comportementale expérimentale et les paramètres mécaniques calculés, car les cas appartenant au même groupe de charge présentent une grande variation de la réponse comportementale expérimentale. Par contre, les résultats mécaniques du groupe de charge se situent plus ou moins dans une plage raisonnablement étroite. Un écart dans la réponse par rapport à la valeur fictive indique clairement des changements post-blessure dans la mécanique du cerveau.

En ce qui concerne le temps d'inconscience, il existe quelques cas où le temps d'inconscience des rats blessés est inférieur à celui de la simulation. L'une des raisons possibles pourrait être que dans ces cas, l'impulsion d'accélération de rotation a agi comme un stimulant dans la prise de conscience précoce. La reprise de conscience d'un cerveau inconscient peut être catalysée par des stimuli externes dans des régions spécifiques du cerveau et la charge de rotation pourrait avoir déclenché ces stimulants.

En ce qui concerne la distance parcourue par l'EPM, il est clairement évident qu'à part un cas ou deux, la distance parcourue par les rats a augmenté de façon significative après l'application de la charge rotatoire. Cela indique une augmentation significative de l'activité après la blessure.

En ce qui concerne les changements de bras de l'EPM, il est clairement évident que le nombre de changements de bras pour tous les cas a augmenté considérablement après l'application de l'accélération rotationnelle. Cela indique une augmentation significative de l'activité après la blessure.

Concernant la durée d'ouverture des MPE, pour certains des cas, la durée d'ouverture des MPE a diminué. Par contre, dans la plupart des cas, une augmentation de la durée d'ouverture des MPE est clairement visible. Cela indique que la charge de rotation a clairement influencé l'émotivité des rats.

En ce qui concerne la latence de la session I du MWM, pour certains des cas, la latence de la session I du MWM a augmenté. Par contre, pour la plupart des cas, une diminution de la latence de la session MWM I est clairement visible. Cela indique que la charge d'accélération rotationnelle a influencé la capacité cognitive des rats de telle manière qu'ils ont pu trouver la plateforme cachée en moins de temps. La plupart des rats ont été capables de trouver la plateforme cachée en 30 à 50 secondes.

En ce qui concerne la latence de la session II du MWM, dans certains cas, la latence de la session II du MWM a diminué. Par contre, pour la plupart des cas, une augmentation de la latence de la session II du MWM est clairement visible. Cependant, la plupart des rats ont pu trouver la plateforme cachée en 10 à 30 secondes. Cela indique que la session I a permis un apprentissage spatial et la capacité de cognition de la plupart des rats a été améliorée de telle sorte qu'ils ont pu trouver la plateforme cachée en moins de temps que lors de la session I. Une amélioration significative de la capacité de cognition du simulacre est également clairement évidente. Cependant, pour certains des rats blessés, l'amélioration n'a pas été aussi significative, ce qui pourrait être dû à l'influence de la charge d'accélération de rotation.

En ce qui concerne la latence de la session III du MWM, dans certains cas, la latence de la session III du MWM a augmenté. Par contre, dans la plupart des cas, une diminution de la latence de la session III du MWM est clairement visible. La plupart des rats ont pu trouver la plateforme cachée dans les 20 premières secondes. Cela indique que les sessions I et II ont permis un apprentissage spatial et que la capacité cognitive de la plupart des rats a été améliorée de telle sorte qu'ils ont pu trouver la plateforme cachée en moins de temps que lors de la session I ou II. Au contraire, pour la simulation, la latence de la session III était légèrement supérieure à celle de la session II. Cependant, la plupart des rats blessés ont montré une amélioration significative de leurs capacités cognitives. Ceux qui n'ont pas pu le faire ont peut-être été influencés négativement par la charge d'accélération de la rotation.

Nous observons que sur la base de la catégorisation des groupes de charge, les résultats de la simulation, en termes de déformation axonale maximale et de contrainte maximale de von Mises, ne semblent pas avoir de corrélation directe avec les mesures expérimentales de réponse comportementale. Ceci est cohérent même avec les huit autres paramètres mécaniques (Annexe C, version originale en anglais). Cependant, il est important de considérer que globalement, pour les cas appartenant au groupe de courte durée de grande amplitude, la réponse mécanique est la plus élevée.

Elle est suivie par les cas appartenant au groupe de longue durée à forte amplitude, puis par les cas appartenant au groupe de longue durée à faible amplitude. La réponse mécanique des cas appartenant au groupe de courte durée de faible amplitude est la plus faible. Examinons maintenant ces résultats sous un autre angle.

4.3 Pour le cerveau entier : basé sur la catégorisation des groupes blessés et non blessés

Comme nous l'avons déjà mentionné, pour chaque aspect comportemental, la valeur de contrôle ou la valeur fictive était connue de Stemper et al. (2016). En se fondant sur cette valeur fictive de la mesure expérimentale de la réponse comportementale, les vingt-six cas expérimentaux ont été divisés en deux groupes. Ceux dont les résultats expérimentaux étaient inférieurs à la valeur fictive se retrouvent dans le premier groupe et sont appelés des cas non blessés et ceux dont les résultats expérimentaux étaient supérieurs à la valeur fictive se retrouvent dans le deuxième groupe et sont appelés des cas blessés. Le Table 3.8 ci-dessous présente les résultats de simulation, en termes de deux paramètres mécaniques (déformation axonale maximale et contrainte maximale de von Mises), de l'ensemble des vingt-six cas pour chaque aspect comportemental, c'est-à-dire la conscience, l'activité, l'émotivité et les capacités cognitives. On peut se référer à l'Annexe D (version originale en anglais) pour obtenir les résultats en termes de dix paramètres mécaniques calculés pour sept mesures expérimentales de réponse comportementale. Les colonnes vertes vierges représentent les cas non blessés, tandis que les colonnes rouges pleines représentent les cas blessés. Les deux sont présentées en ordre croissant.

Table 3.8: Résultats de la simulation des vingt-six cas expérimentaux pour deux paramètres mécaniques, soit la déformation axonale maximale et la contrainte maximale de von Mises pour l'ensemble du cerveau, selon la catégorisation des blessés (colonnes rouges pleines) et des non-blessés (colonnes vertes vierges) en ce qui concerne sept mesures expérimentales de réponse comportementale.

Injured and non-injured groups based on unconsciousness time

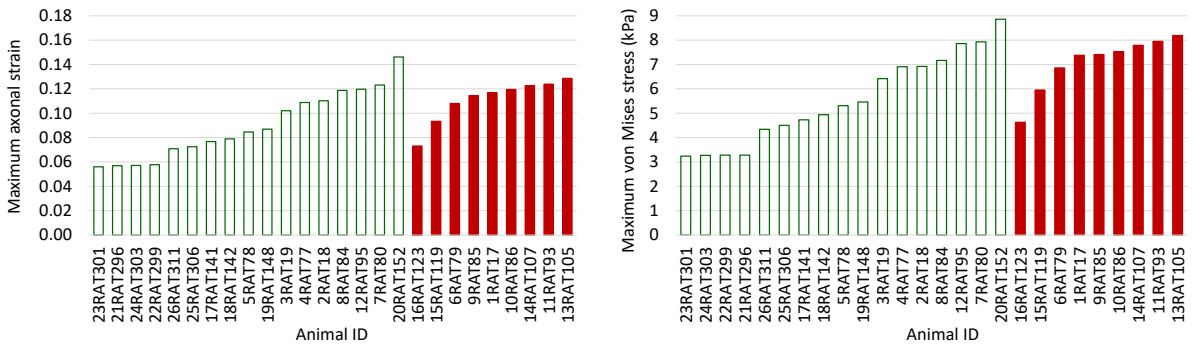

cont.

Injured and non-injured groups based on EPM distance travelled

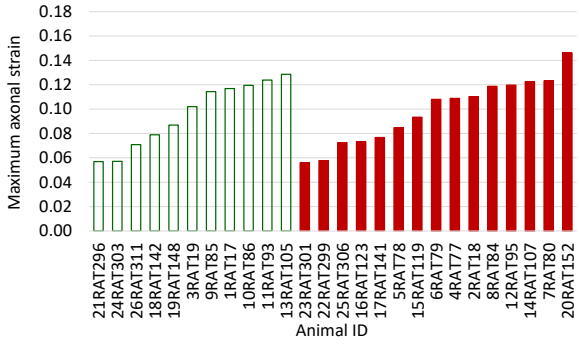

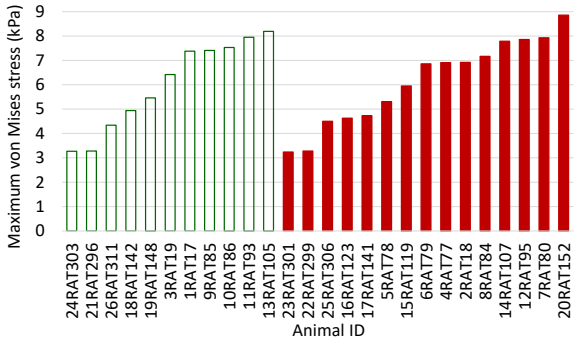

Injured and non-injured groups based on EMP arm changes

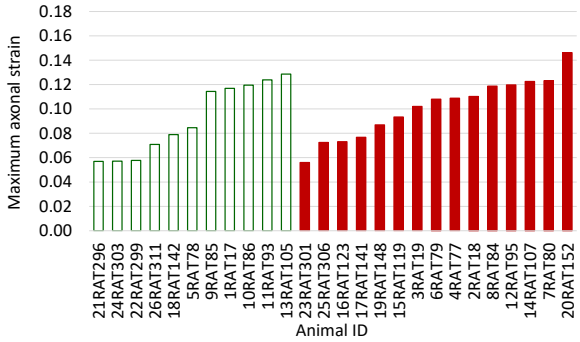

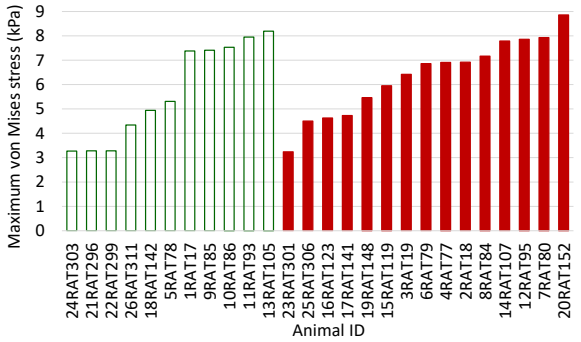

Injured and non-injured groups based on EPM open duration

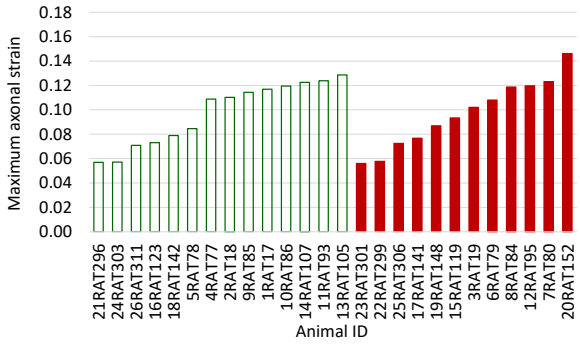

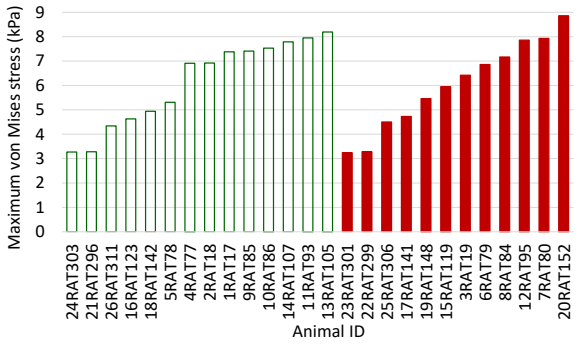

Injured and non-injured groups based on MWM session I latency

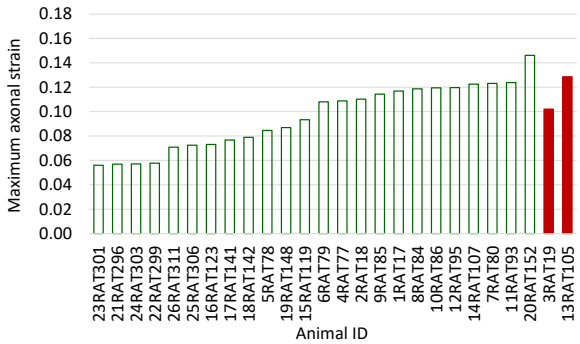

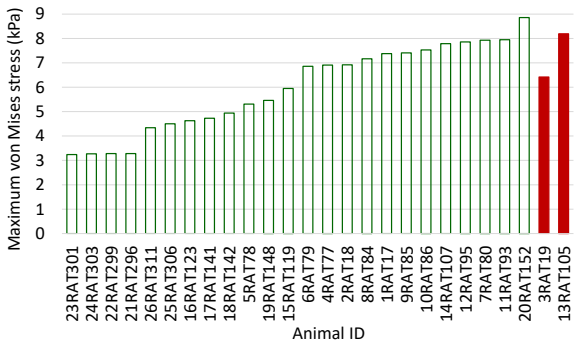

cont.

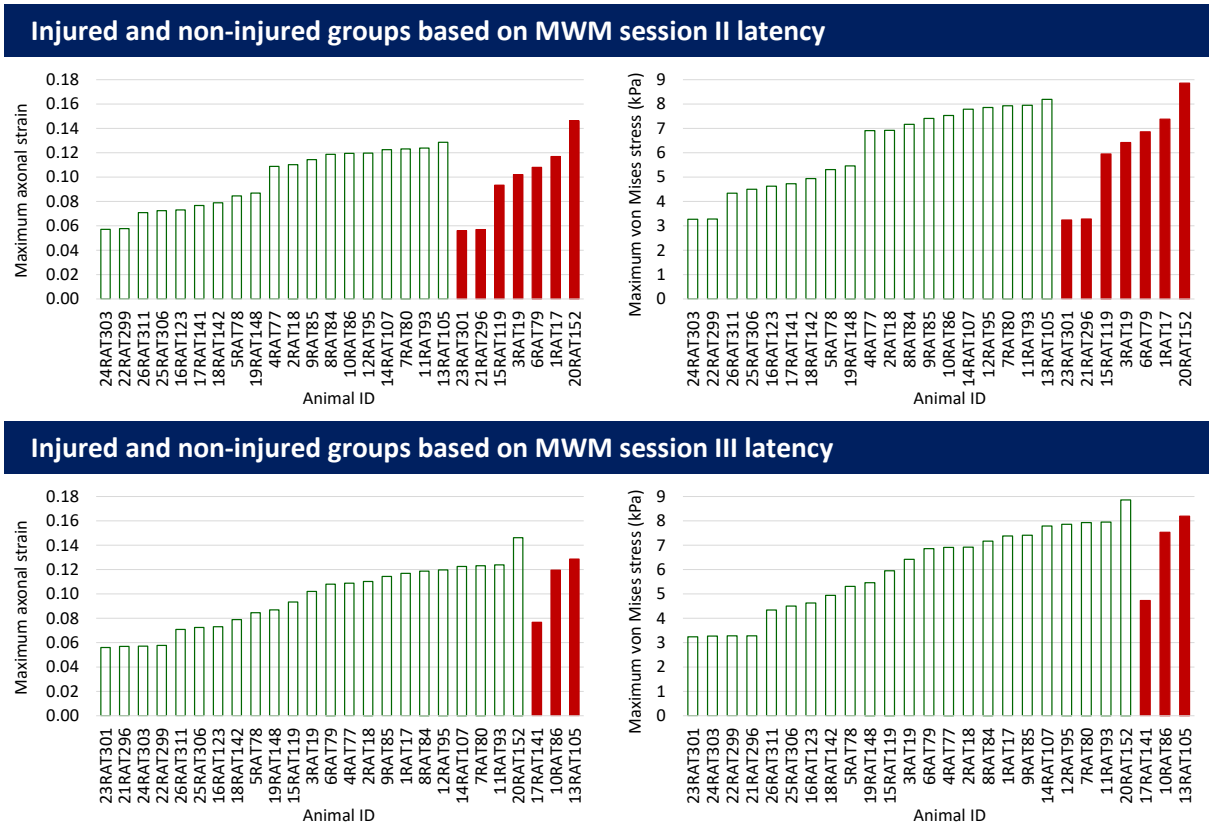

En ce qui concerne la mesure du temps d'inconscience, nous voyons qu'en prenant en considération le temps d'inconscience maximum, neuf cas sur vingt-six tombent dans le groupe des blessés et les dix-sept autres dans le groupe des non blessés. Cela indique que pour seulement 35 % de tous les animaux, qui ont été exposés à une charge en rotation, le temps d'inconscience a augmenté après la blessure. Nous constatons également que pour un des cas non blessés, soit l'animal id 20RAT152, l'amplitude mécanique subie est la plus élevée, voire plus élevée que dans le groupe blessé. Pour cet animal, le fait d'être dans le groupe non blessé ne signifie pas réellement que le rat n'a pas été blessé. Comme on l'a dit plus tôt, une charge légère peut agir comme un stimulant dans la récupération de la conscience plus tôt que la cause de toute blessure aiguë. Cela pourrait être vrai pour l'animal id 20RAT152 et pour beaucoup d'autres aussi. Comme on peut le voir sur les graphiques, il n'y a pas beaucoup de différence dans l'amplitude mécanique subie par le groupe blessé par rapport à celle subie par le groupe non blessé. Il en a été de même pour tous les autres paramètres mécaniques sélectionnés (Annexe D, Table D1, version originale en anglais). Ainsi, en nous basant sur le temps d'inconscience, nous ne pouvons pas commenter la blessure en fonction d'un paramètre mécanique choisi.

En ce qui concerne les mesures d'activité, c'est-à-dire la distance parcourue par l'EPM et les changements de bras de l'EPM, nous constatons qu'en prenant en considération soit la distance

maximale parcourue par l'EPM, soit le nombre maximal de changements de bras de l'EPM par le simulateur, quinze cas sur vingt-six tombent dans le groupe des blessés et les onze autres dans le groupe des non blessés. Cela indique que pour plus de 50 % des animaux, qui ont été exposés à la charge de rotation, l'activité après la blessure a augmenté de façon significative. De plus, les groupes non blessés et blessés ont subi des amplitudes mécaniques allant du plus faible au plus élevé, et la gamme des amplitudes mécaniques subies par les deux groupes est plus ou moins la même. Cela était vrai même pour tous les autres paramètres mécaniques sélectionnés (Annexe D, Table D2 et Table D3, version originale en anglais). Par conséquent, compte tenu de la distance parcourue et des changements de bras de l'EPM, il n'est pas possible de commenter la blessure en fonction d'un paramètre mécanique choisi. Néanmoins, nous devons garder à l'esprit qu'une augmentation de l'activité ainsi qu'une diminution de l'activité sont toutes deux des changements de comportement. Bien que, ici, nous supposons que les cas d'augmentation de l'activité sont ceux des blessés, d'autres ont également été commotionnés.

En ce qui concerne la mesure de l'émotivité, c'est-à-dire la durée ouverte de l'EPM, nous constatons qu'en tenant compte de la durée ouverte maximale de l'EPM de la feinte, douze cas sur vingt-six tombent dans le groupe des blessés et les quatorze autres dans le groupe des non blessés. Cela indique que 46 % des animaux, qui ont été exposés à la charge de rotation, ont été fortement influencés sur le plan émotionnel après la blessure. De plus, les groupes non blessés et blessés ont subi des amplitudes mécaniques allant du plus faible au plus élevé, et la gamme des amplitudes mécaniques subies par les deux groupes est plus ou moins la même. Cela était vrai même pour tous les autres paramètres mécaniques sélectionnés (Annexe D, Table D4, version originale en anglais). Ainsi, sur la base de la durée de l'EPM, il n'est pas possible de commenter la blessure en fonction d'un paramètre mécanique choisi. Néanmoins, nous devons garder à l'esprit qu'une augmentation de la durée d'ouverture de l'EPM ainsi qu'une diminution de la durée d'ouverture de l'EPM sont toutes deux des changements au niveau de l'émotivité. Même si nous supposons ici que l'augmentation de la durée d'ouverture de l'EPM est due à la blessure, d'autres cas de commotion cérébrale ont également été observés.

En ce qui concerne les mesures de cognition, c'est-à-dire les latences des sessions MWM, nous constatons qu'en prenant en considération la latence maximale de la session MWM I de la feinte, seuls deux cas sur vingt-six tombent dans le groupe des blessés et les vingt-quatre autres dans le groupe des non blessés. Cela indique que seulement 8 % des animaux, qui ont été exposés à la charge de rotation, ont été influencés de manière significative de telle sorte qu'ils ont pris plus de temps que la feinte pour trouver la plate-forme cachée. Comme on peut le voir sur les graphiques, l'amplitude

mécanique subie par le groupe blessé se situe dans la fourchette du groupe non blessé. Cela est vrai même pour tous les autres paramètres mécaniques sélectionnés (Annexe D, Table D5, version originale en anglais). Ainsi, sur la base de la latence de la session I du MWM, il n'est pas possible de commenter la blessure en fonction d'un quelconque paramètre mécanique choisi. Néanmoins, nous devons garder à l'esprit que le nombre de cas de blessés étant trop faible, rien de concluant ne peut être affirmé de toute façon. Comme la plupart des cas ont réussi à trouver la plate-forme cachée avec la feinte ou avant que la feinte ne le fasse, cela signifie que les capacités cognitives ont été modifiées positivement par la charge de rotation.

Nous constatons qu'en prenant en considération la latence maximale de la session II du MWM de la mascarade, sept cas sur vingt-six tombent dans le groupe des blessés et les dix-neuf autres dans le groupe des non blessés. Cela indique que seulement 27 % des animaux, qui ont été exposés à la charge de rotation, ont été influencés de manière significative de telle sorte qu'ils ont pris plus de temps que la feinte pour trouver la plate-forme cachée. De plus, les groupes non blessés et blessés ont subi des amplitudes mécaniques allant du plus faible au plus élevé, et la gamme d'amplitudes mécaniques subies par les deux groupes est plus ou moins la même. Cela était vrai même pour tous les autres paramètres mécaniques sélectionnés (Annexe D, Table D6, version originale en anglais). Ainsi, compte tenu du temps de latence de la deuxième session du MWM, il n'est pas possible de faire des commentaires sur la blessure en fonction d'un quelconque paramètre mécanique choisi. Néanmoins, nous devons garder à l'esprit que l'apprentissage spatial en termes d'amélioration des capacités cognitives s'est produit à la fois pour les cas blessés et non blessés. Comme pour tous les animaux, le temps nécessaire pour trouver la plateforme cachée a été inférieur à celui de la première session.

Nous constatons qu'en tenant compte de la latence maximale de la session III du MWM, seuls trois cas sur vingt-six tombent dans le groupe des blessés et les vingt-trois autres dans le groupe des non blessés. Cela indique qu'environ 12 % des animaux, qui ont été exposés à la charge de rotation, ont été influencés de manière significative de telle sorte qu'ils ont mis plus de temps que le simulacre à trouver la plate-forme cachée. Comme on peut le voir sur les graphiques, l'amplitude mécanique subie par le groupe blessé se situe dans la fourchette du groupe non blessé. Ceci est vrai même pour tous les autres paramètres mécaniques sélectionnés (Annexe D, Table D7, version originale en anglais). Ainsi, sur la base de la latence de la session III du MWM, il est difficile de commenter la blessure en termes de tout paramètre mécanique choisi. Néanmoins, nous devons garder à l'esprit que le nombre de cas de blessés étant trop faible, rien de concluant ne peut être affirmé de toute façon. Comme la plupart des cas ont réussi à trouver la plate-forme cachée avec la feinte ou avant que la feinte ne le fasse, cela signifie que les capacités cognitives ont été modifiées positivement par la charge de

rotation. Nous constatons également que l'apprentissage spatial en termes d'amélioration des capacités cognitives s'est produit pour les cas blessés et non blessés. Comme pour la plupart des animaux, le temps nécessaire pour trouver la plate-forme cachée lors de la troisième session était inférieur à celui de la première ou de la deuxième session.

Nous constatons que, sur la base de la catégorisation des blessés et des non blessés pour l'ensemble du cerveau, les résultats de la simulation ne semblent pas avoir de corrélation directe avec la lésion d'après les mesures expérimentales de réponse comportementale. Même pas pour la souche axonale, qui était clairement un prédicteur évident dans l'étude de Sahoo (2013). Les résultats présentés à l'Annexe D (version originale en anglais) permettent de tirer une conclusion similaire à partir des huit autres paramètres calculés. Voyons si ces résultats au niveau des régions fonctionnelles du cerveau pourraient fournir des indications précieuses.

4.4 Pour les différentes régions fonctionnelles du cerveau

Examinons maintenant les résultats des simulations pour les régions fonctionnelles du cerveau (détaillées au Chapter 2, Table 2.2 et Figure 2.4) consacrées à un aspect comportemental spécifique, c'est-à-dire la conscience, l'activité, l'émotivité et la cognition. Pour rappel, la conscience est associée au thalamus, au néocortex et au tronc cérébral ; l'activité est associée à l'hippocampe, à la substantia nigra, au cervelet, au gris central et au néocortex ; l'émotivité est associée à l'hippocampe, au gris central, au néocortex, à l'amygdale, au tronc cérébral, aux fimbria et au fornix ; et la cognition est associée à l'hippocampe, à la substantia nigra, au cervelet, au néocortex, aux fimbria et au fornix. Au lieu de présenter les résultats pour les dix paramètres mécaniques, nous présentons ici les résultats uniquement en termes de déformation axonale et de contrainte de von Mises. On peut se référer à l'Annexe E (version originale en anglais) pour voir les résultats en termes de l'ensemble des dix paramètres mécaniques calculés, basés sur sept réponses comportementales expérimentales. Les résultats sont présentés en fonction de la catégorisation en groupes blessés et non blessés selon différentes mesures expérimentales de réponse comportementale. Les colonnes vertes vierges représentent les cas non blessés, tandis que les colonnes rouges pleines représentent les cas blessés. Les deux sont présentées en ordre ascendant.

Le Table 3.9 représente les résultats de la simulation, en termes de déformation axonale maximale et de contrainte maximale de von Mises, de l'ensemble des vingt-six cas pour les régions du cerveau associées à la conscience.

Table 3.9: Résultats de la simulation des vingt-six cas expérimentaux pour deux paramètres mécaniques, soit la déformation axonale maximale et le contrainte maximal de von Mises pour les régions spécifiques du cerveau associées à la conscience ; basés sur la catégorisation des blessés (colonnes rouges pleines) et des non blessés (colonnes vertes vides) en ce qui concerne sept réponses comportementales expérimentales.

Injured and non-injured groups based on unconsciousness time

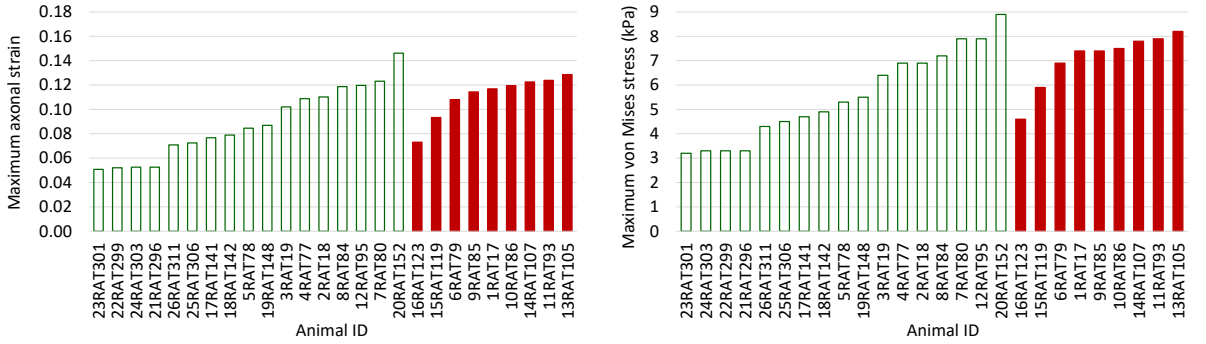

Injured and non-injured groups based on EPM distance travelled

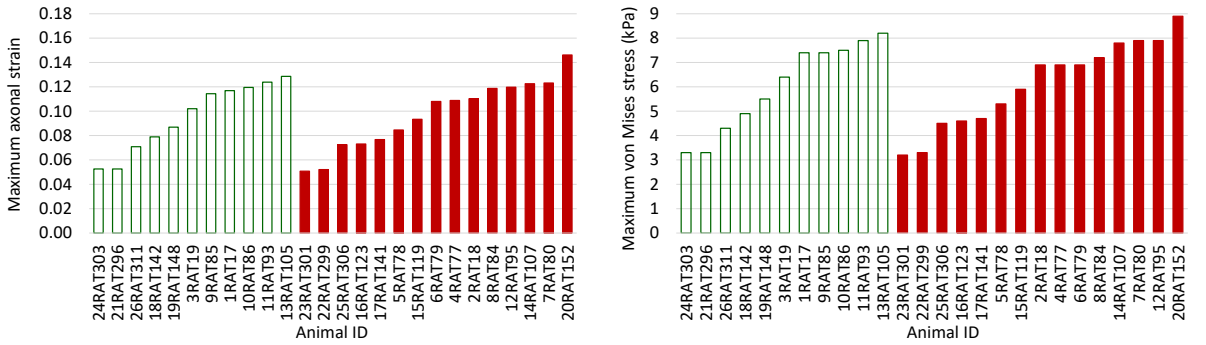

Injured and non-injured groups based on EPM arm changes

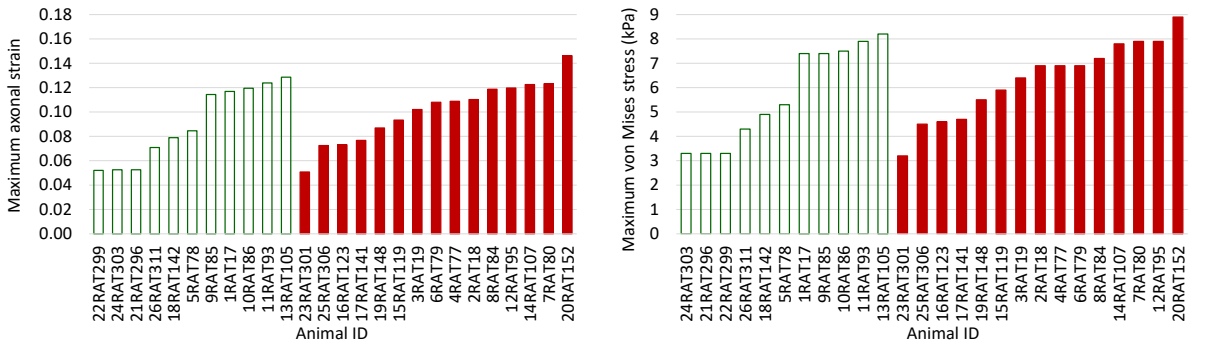

cont.

Injured and non-injured groups based on EPM open duration

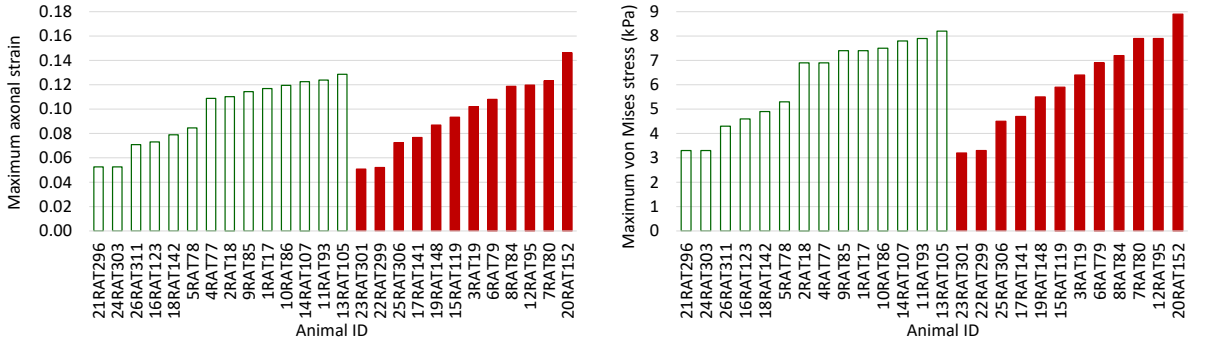

Injured and non-injured groups based on MWM session I latency

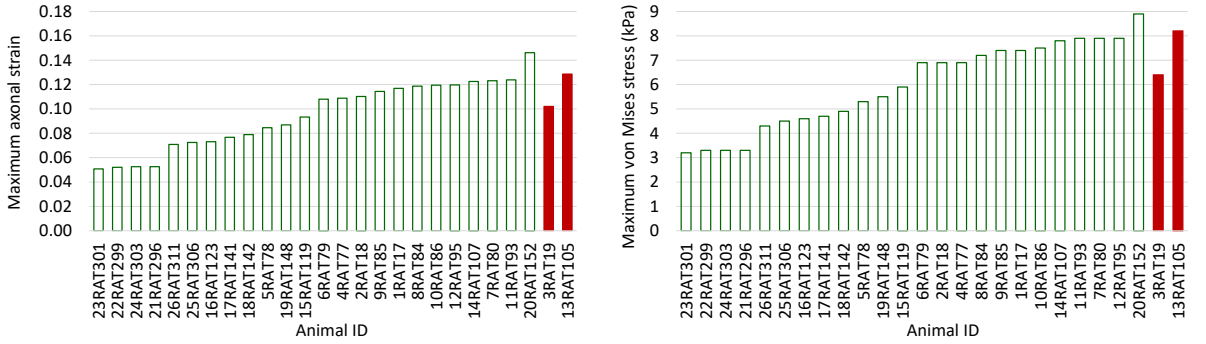

Injured and non-injured groups based on MWM session II latency

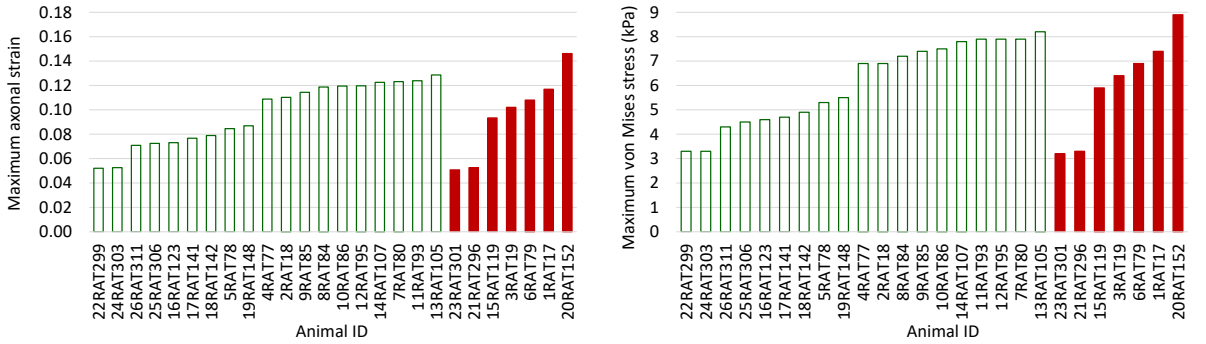

Injured and non-injured groups based on MWM session III latency

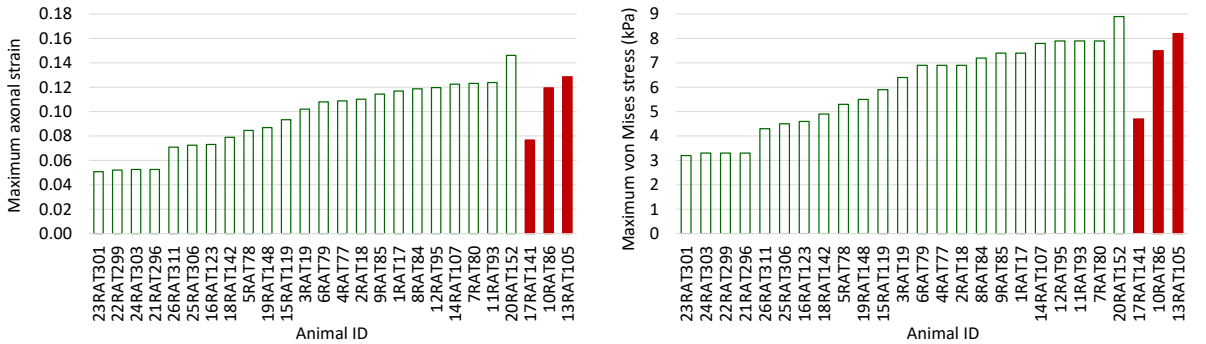

Comme on peut le voir sur ces graphiques, ni la déformation axonale maximale, ni le contrainte maximal de von Mises ne peuvent prédire l'occurrence d'une commotion cérébrale en association avec l'une des sept mesures expérimentales de la réponse comportementale pour les régions du

cerveau associées à la conscience. C'était également vrai pour d'autres paramètres mécaniques (Annexe E, Table E1 à Table E7, version originale en anglais).

Le Table 3.10 présente les résultats de la simulation, en termes de déformation axonale maximale et de contrainte maximale de von Mises, des 26 cas pour les régions cérébrales associées à l'activité.

Table 3.10: Résultats de la simulation des vingt-six cas expérimentaux pour deux paramètres mécaniques, soit la déformation axonale maximale et le contrainte maximal de von Mises pour les régions spécifiques du cerveau associées à l'activité ; basés sur la catégorisation des blessés (colonnes rouges pleines) et des non blessés (colonnes vertes vides) en ce qui concerne sept réponses comportementales expérimentales.

Injured and non-injured groups based on unconsciousness time

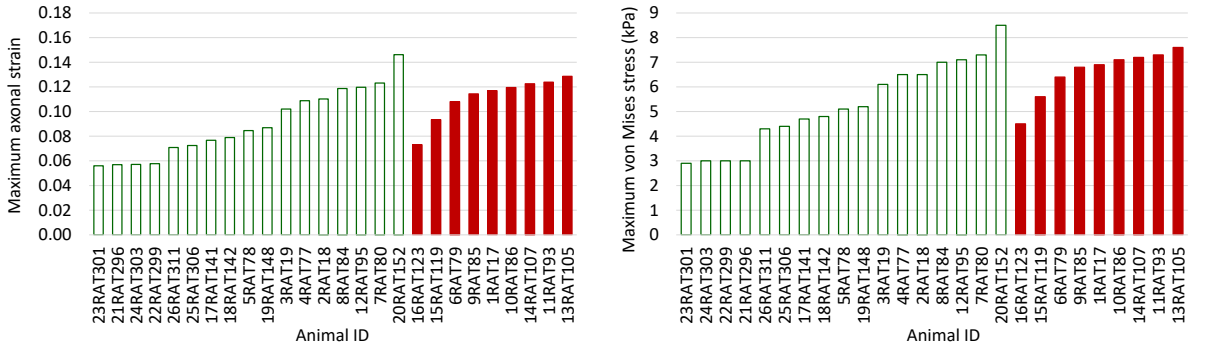

Injured and non-injured groups based on EPM distance travelled

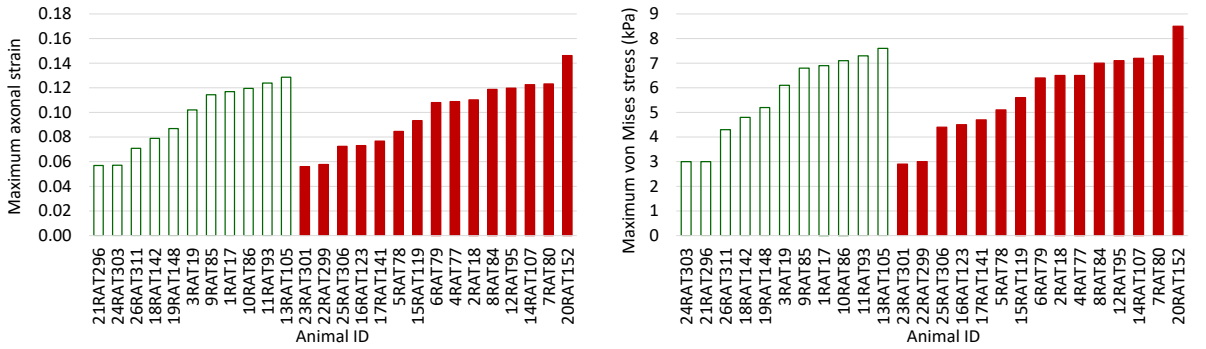

Injured and non-injured groups based on EPM arm changes

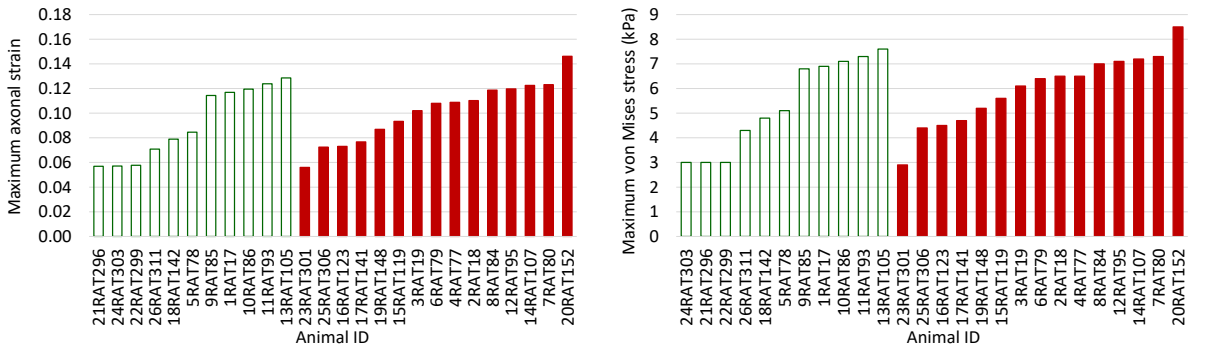

cont.

Injured and non-injured groups based on EPM open duration

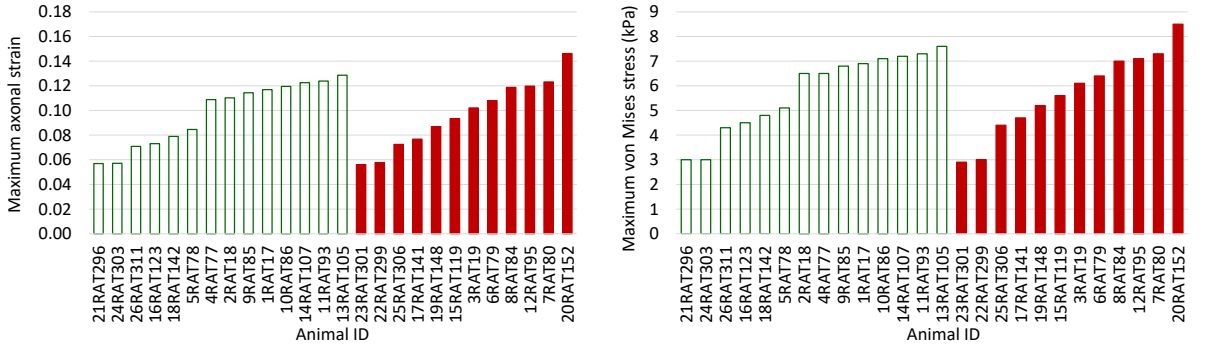

Injured and non-injured groups based on MWM session I latency

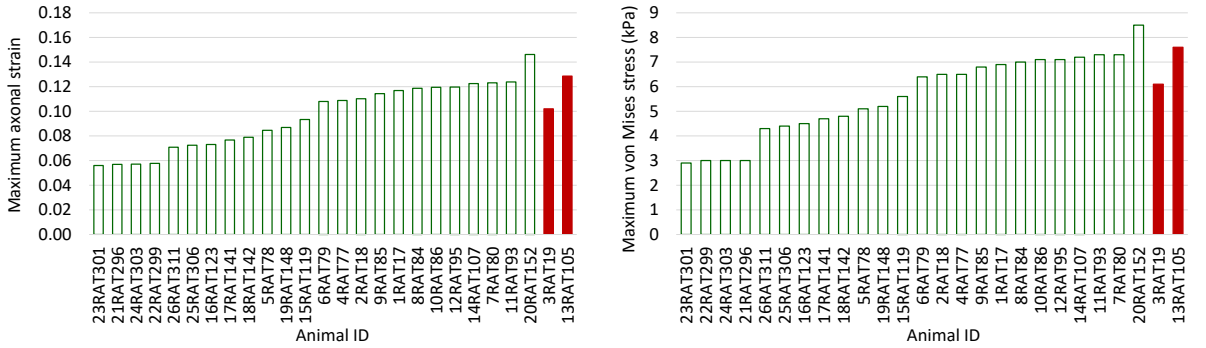

Injured and non-injured groups based on MWM session II latency

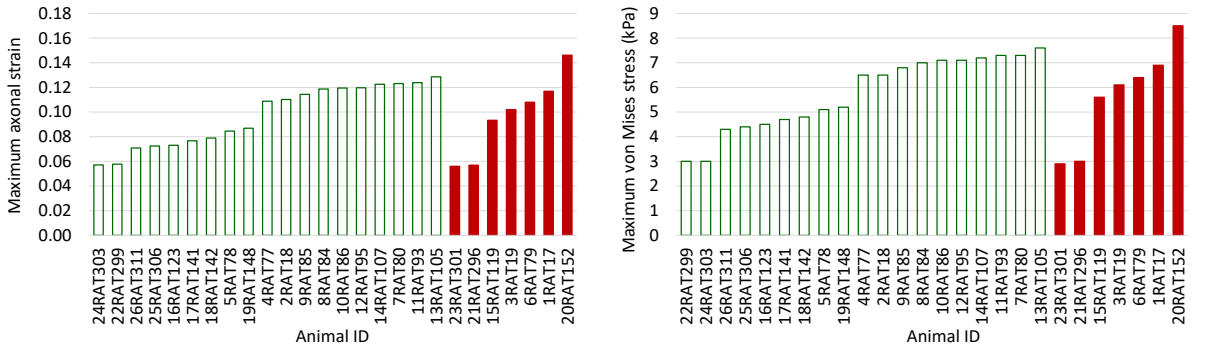

Injured and non-injured groups based on MWM session III latency

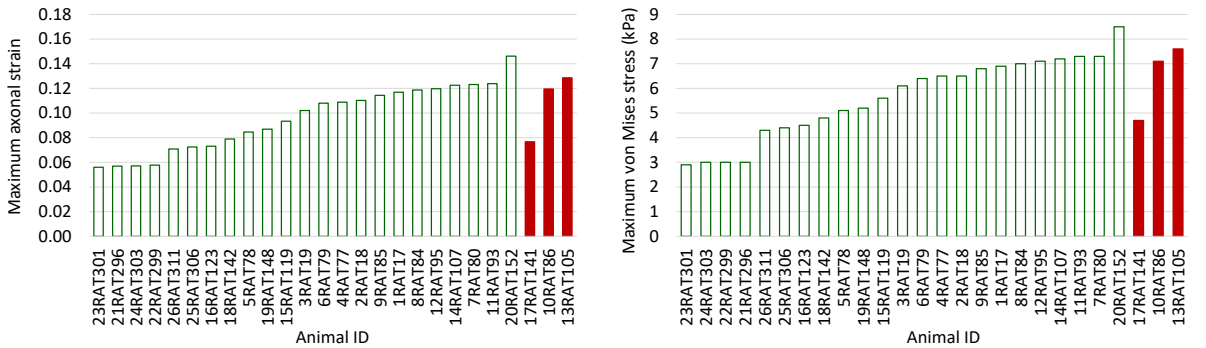

Comme on peut le voir sur ces graphiques, ni la déformation axonale maximale, ni la contrainte maximale de von Mises ne peuvent prédire l'occurrence d'une commotion cérébrale en association

avec l'une des sept mesures expérimentales de la réponse comportementale pour les régions du cerveau associées à l'activité. C'était vrai aussi pour d'autres paramètres mécaniques (Annexe E, Table E8 à Table E14, version originale en anglais).

Le Table 3.11 représente les résultats de la simulation, en termes de déformation axonale maximale et de contrainte maximale de von Mises, des vingt-six cas pour les régions cérébrales associées à l'émotivité.

Table 3.11: Résultats de la simulation des vingt-six cas expérimentaux pour deux paramètres mécaniques, soit la déformation axonale maximale et la contrainte maximale de von Mises pour les régions spécifiques du cerveau associées à l'émotivité ; basés sur la catégorisation des blessés (colonnes rouges pleines) et des non blessés (colonnes vertes vides) en ce qui concerne sept réponses comportementales expérimentales.

Injured and non-injured groups based on unconsciousness time

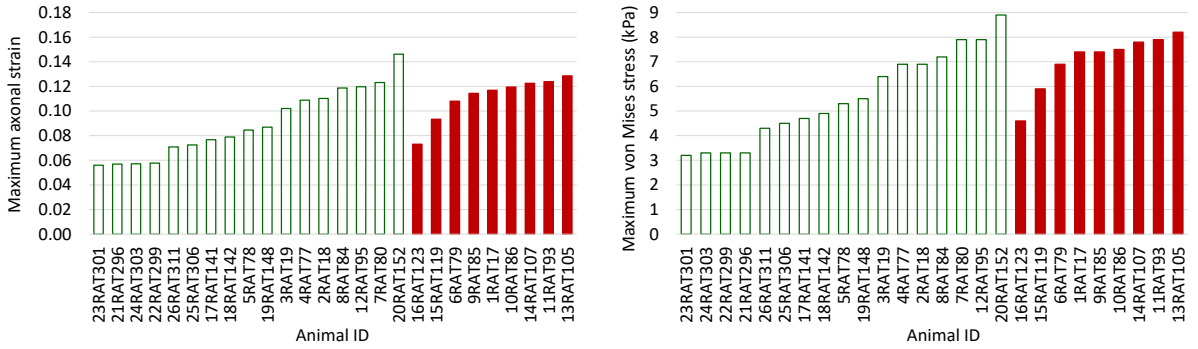

Injured and non-injured groups based on EPM distance travelled

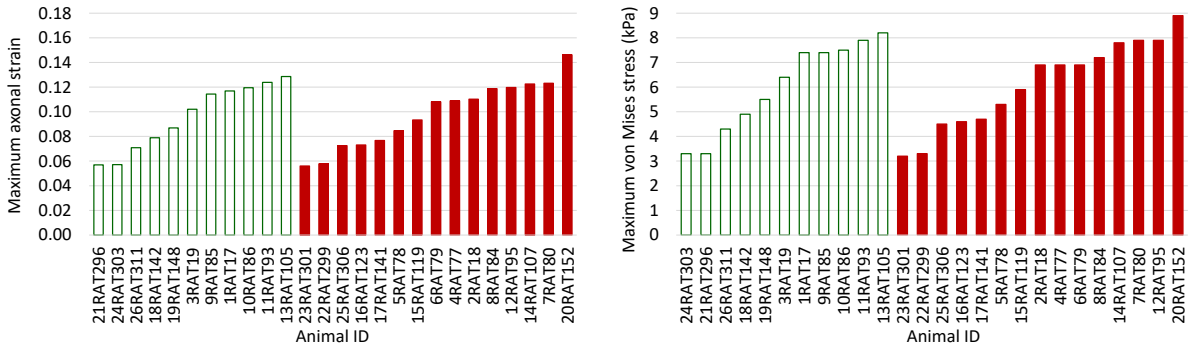

Injured and non-injured groups based on EPM arm changes

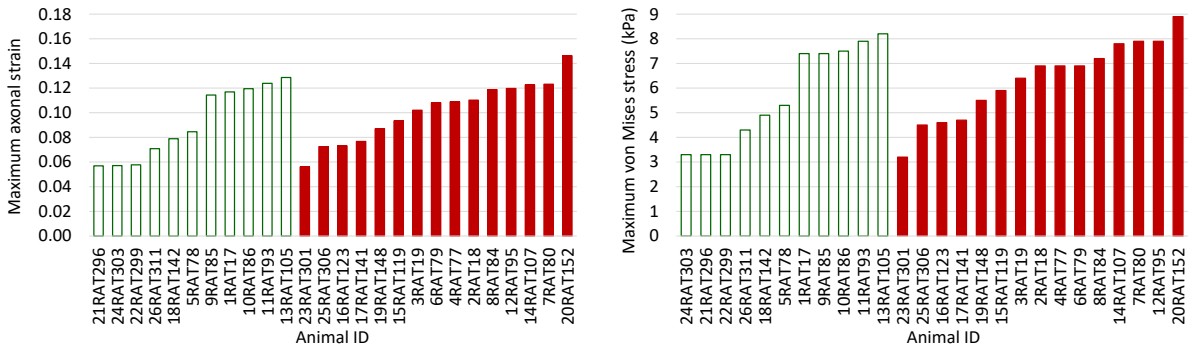

Injured and non-injured groups based on EPM open duration

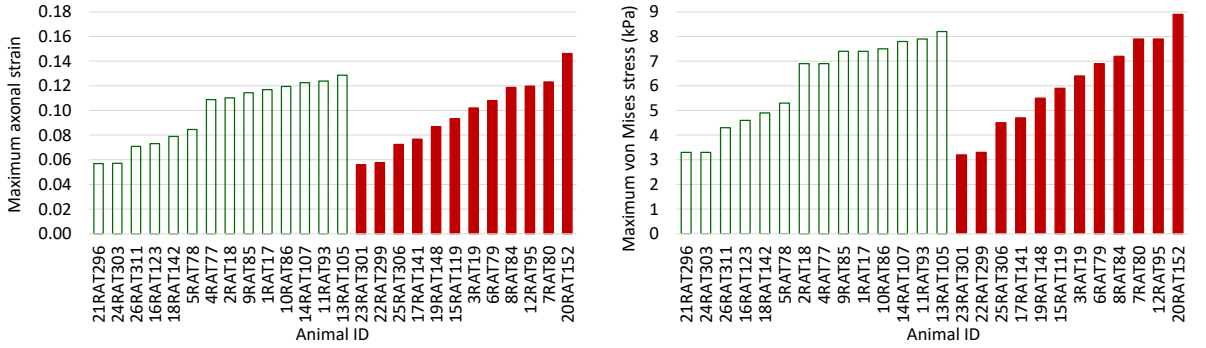

Injured and non-injured groups based on MWM session I latency

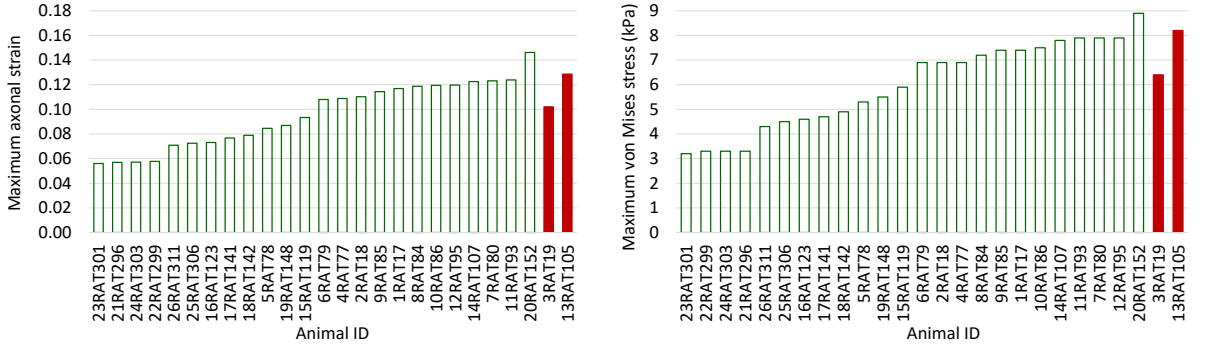

Injured and non-injured groups based on MWM session II latency

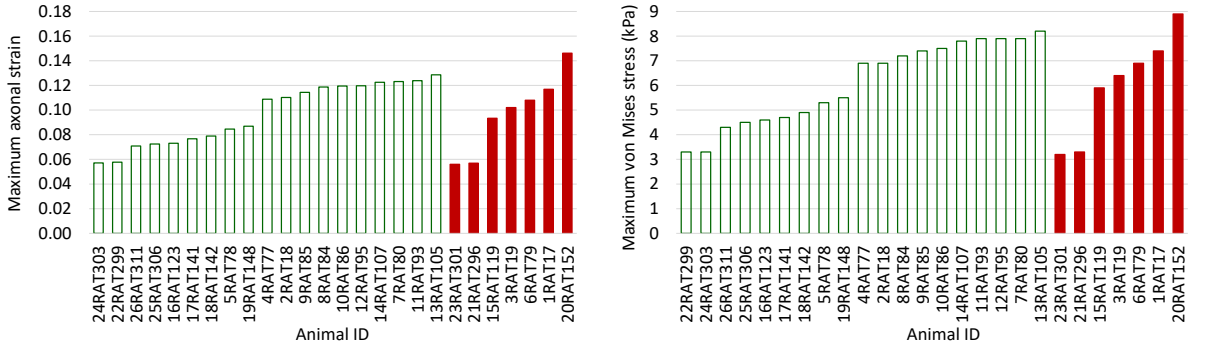

Injured and non-injured groups based on MWM session III latency

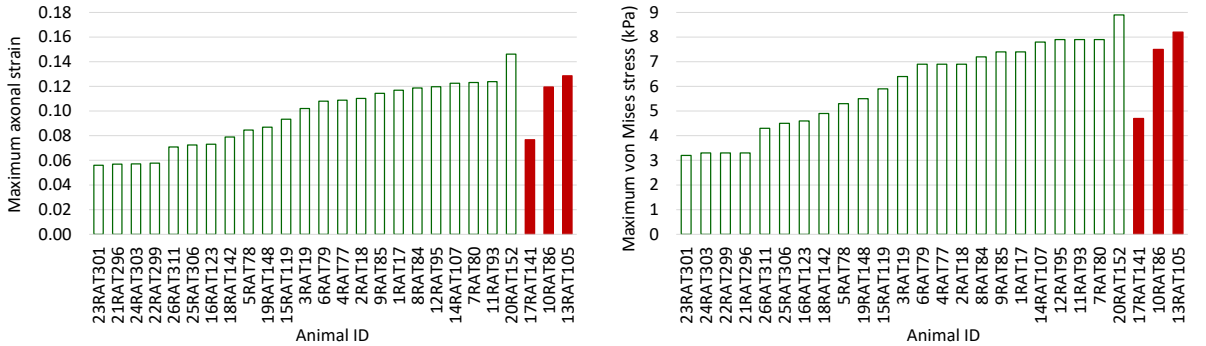

Comme on peut le voir sur ces graphiques, ni la déformation axonale maximale, ni la contrainte maximale de von Mises ne peuvent prédire l'occurrence d'une commotion cérébrale en association

avec l'une des sept mesures expérimentales de la réponse comportementale pour les régions du cerveau associées à l'émotivité. C'était également vrai pour d'autres paramètres mécaniques (Annexe E, Table E15 à Table E21, version originale en anglais).

Le Table 3.12 montre les résultats de la simulation, en termes de déformation axonale maximale et de contrainte maximale de von Mises, pour les 26 cas dans les régions du cerveau associées à la cognition.

Table 3.12: Résultats de la simulation des vingt-six cas expérimentaux pour deux paramètres mécaniques, soit la déformation axonale maximale et le contrainte maximal de von Mises pour les régions spécifiques du cerveau associées à la cognition ; basés sur la catégorisation des blessés (colonnes rouges pleines) et des non blessés (colonnes vertes vides) en ce qui concerne sept réponses comportementales expérimentales.

Injured and non-injured groups based on unconsciousness time

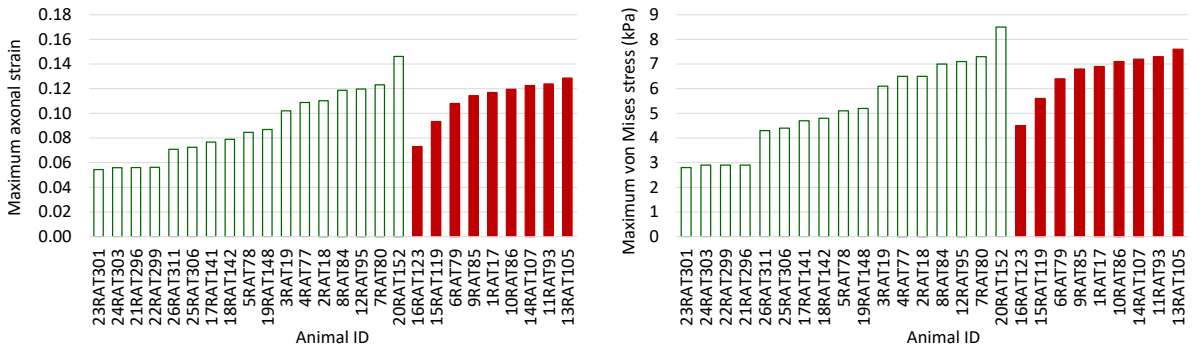

Injured and non-injured groups based on EPM distance travelled

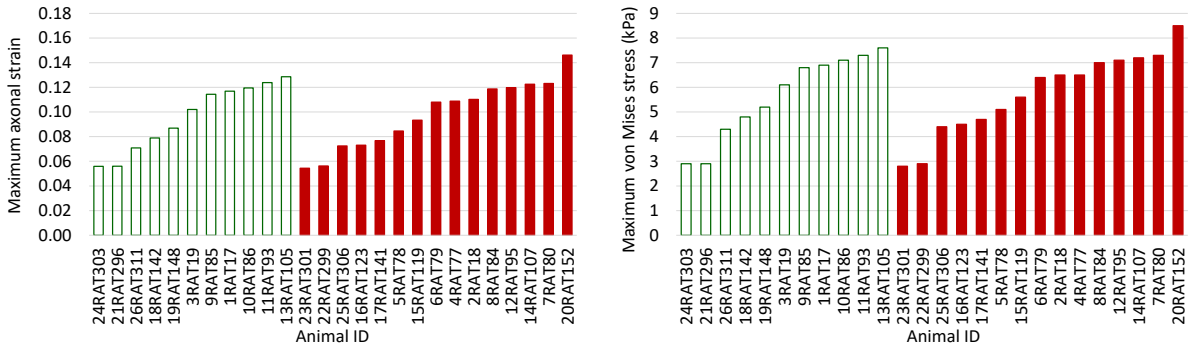

Injured and non-injured groups based on EPM arm changes

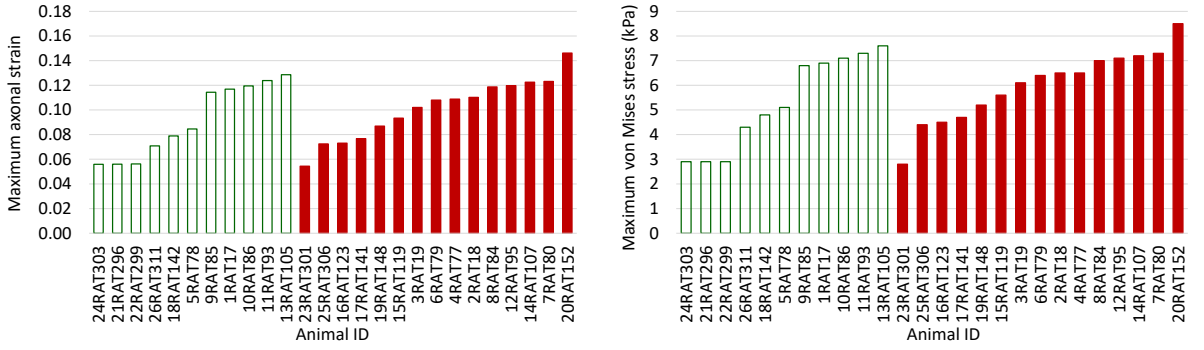

cont.

Injured and non-injured groups based on EPM open duration

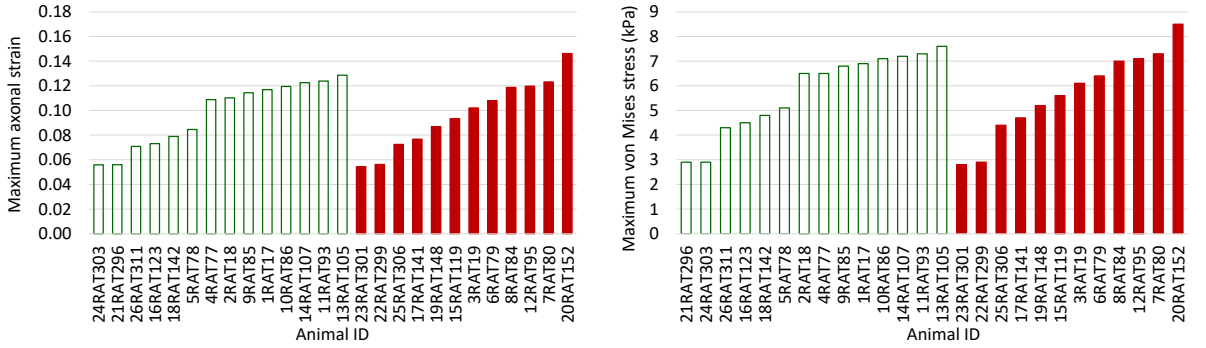

Injured and non-injured groups based on MWM session I latency

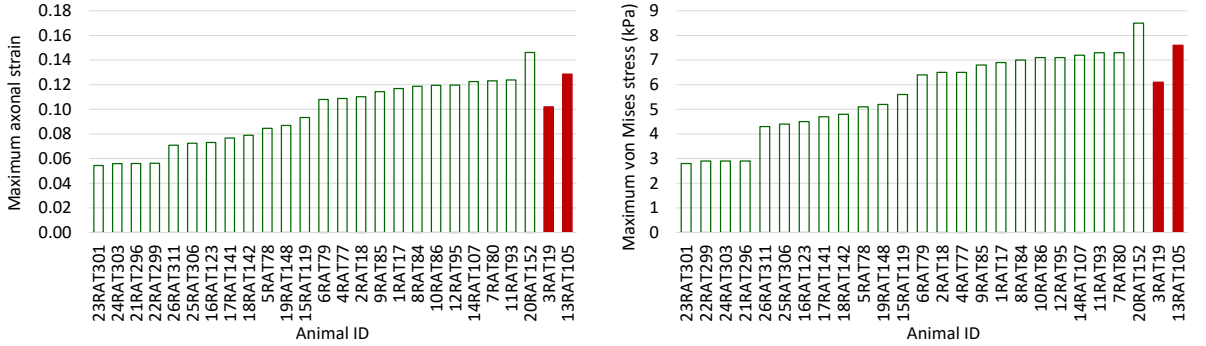

Injured and non-injured groups based on MWM session II latency

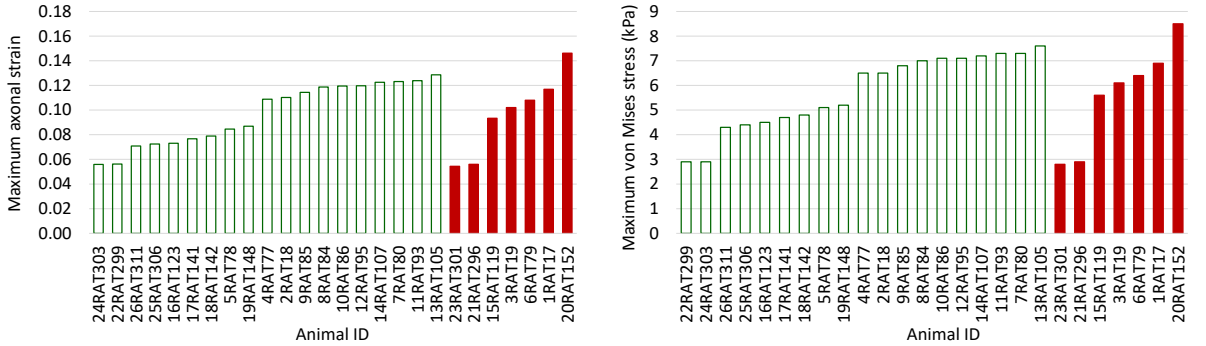

Injured and non-injured groups based on MWM session III latency

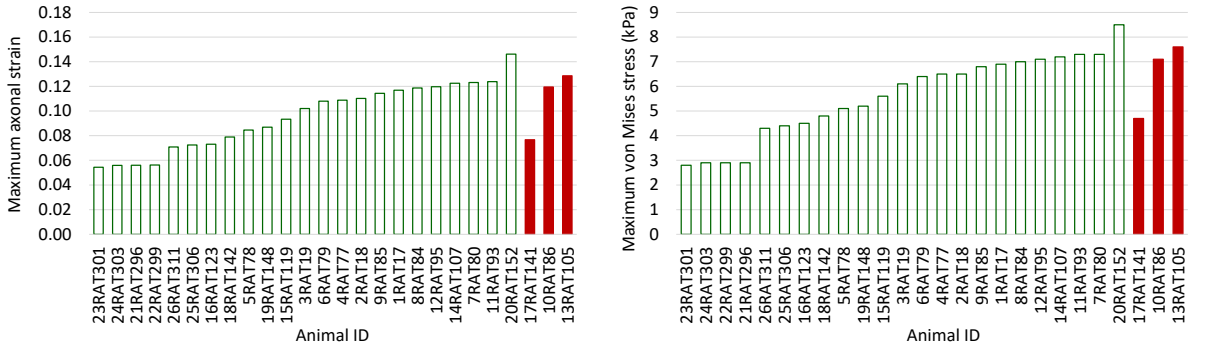

Comme on peut le voir sur ces graphiques, ni la déformation axonale maximale, ni la contrainte maximale de von Mises ne peuvent prédire l'occurrence d'une commotion cérébrale en association

avec l'une des sept mesures expérimentales de la réponse comportementale pour les régions du cerveau associées à la cognition. C'était également vrai pour d'autres paramètres mécaniques (Annexe E, Table E22 à Table E28, version originale en anglais).

Nous constatons que, d'après la catégorisation des blessés et des non-blessés pour différentes régions fonctionnelles du cerveau, les résultats de la simulation ne semblent pas avoir de corrélation directe avec la blessure d'après les sept mesures expérimentales de réponse comportementale. Cependant, il est important de noter que la relation avec le temps d'inconscience semble meilleure que tout autre paramètre mécanique calculé. Par conséquent, examinons maintenant ces résultats dans des régions individuelles du cerveau avec une perspective différente.

4.5 Pour différentes régions anatomiques du cerveau

Comme mentionné au Chapter 2 (Figure 2.3), la catégorisation anatomique du cerveau a divisé le cerveau en vingt-quatre régions, rappelées ici pour référence dans le Table 3.13. Les résultats de la simulation pour ces régions anatomiques du cerveau sont présentés ci-dessous. Comme nous l'avons vu plus haut, la catégorisation des blessés et des non blessés, fondée sur les sept mesures comportementales expérimentales, n'a pas permis d'obtenir des renseignements utiles. Par conséquent, au lieu de présenter les résultats basés sur la catégorisation des blessés et des non-blessés, on présente les résultats réels, en termes de déformation axonale maximale, par région du cerveau, par cas, en fonction de différents groupes de charge.

Table 3.13: Catégorisation anatomique du cerveau du rat en diverses régions.

#	Region description	#	Region description
1	Hippocampus	**13**	Neocortex
2	External capsule	**14**	Amygdala
3	Caudate – Putamen – Globus pallidus	**15**	Olfactory bulb
4	Anterior commissure	**16**	Brainstem
5	Substantia nigra	**17**	Fimbria
6	Internal capsule	**18**	Fornix
7	Thalamus	**19**	Ventral tegmental area (VTA)
8	Cerebellum	**20**	Corpus callosum
9	Superior colliculus	**21**	Genu
10	Hypothalamus	**22**	Aqueduct
11	Inferior colliculus	**23**	Splenium
12	Central gray	**24**	Rest of the brain

La Figure 3.5 illustre les valeurs maximales de la déformation axonale des vingt-quatre régions du cerveau pour quatre cas appartenant au groupe de charge M1D1a. Pour ce groupe de courte durée de faible amplitude, la déformation axonale maximale moyenne était égale à 4,96 %. Comme on peut l'observer sur le diagramme, la déformation axonale maximale a été ressentie par la région cérébrale numéro treize, c'est-à-dire le néocortex, et la SMA moyenne ressentie par le néocortex pour le groupe de charge M1D1a était égale à 7,58 % ± 0,6 %.

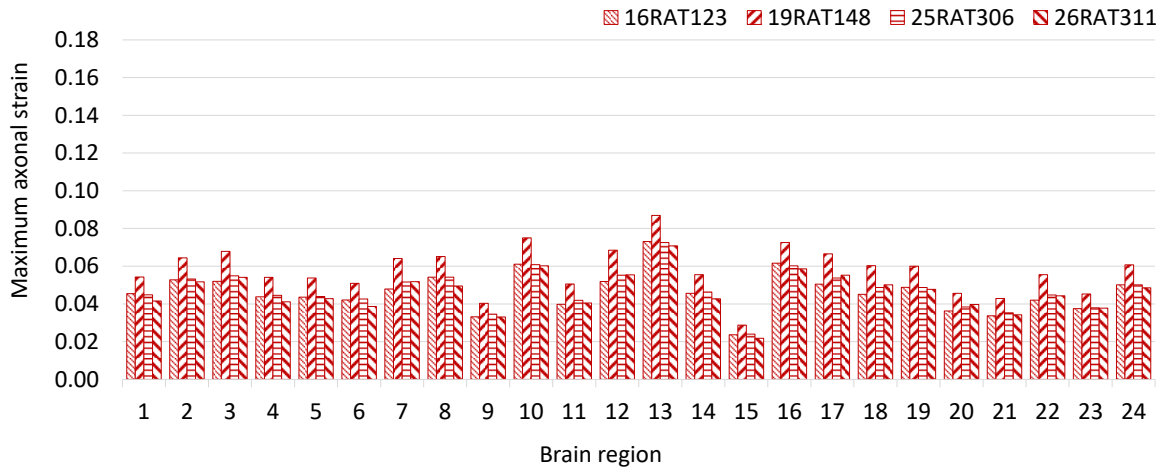

Figure 3.5: Diagramme illustrant les valeurs maximales de la déformation axonale des vingt-quatre régions du cerveau pour quatre cas appartenant au groupe de charge M1D1a.

La Figure 3.6 illustre les valeurs maximales de la déformation axonale des vingt-quatre régions du cerveau pour quatre cas appartenant au groupe de charge M1D1b.

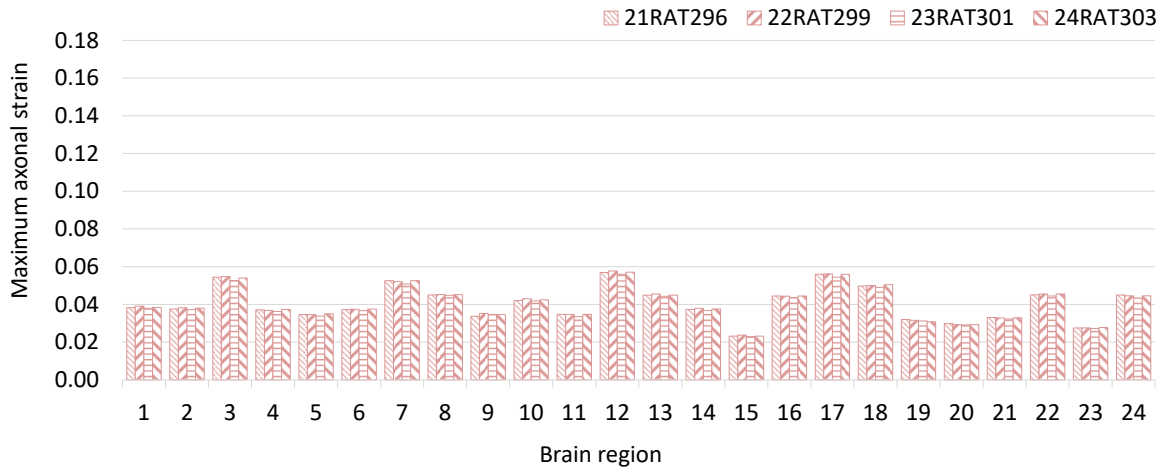

Figure 3.6: Diagramme illustrant les valeurs maximales de la déformation axonale des vingt-quatre régions du cerveau pour quatre cas appartenant au groupe de charge M1D1b.

Pour ce groupe de courte durée de faible amplitude, la déformation axonale maximale moyenne était égale à 4,04 %. Comme on peut le voir sur le diagramme, la déformation axonale maximale a été ressentie par la région cérébrale numéro douze, c'est-à-dire la région grise centrale, et par la région

dix-sept, c'est-à-dire les fimbria. La déformation axonale maximale moyenne subie par la région grise centrale pour le groupe de charge M1D1b était égale à 5,69 % ± 0,1 % et celle subie par les fimbria était de 5,56 % ± 0,1 %.

La Figure 3.7 illustre les valeurs maximales de la déformation axonale des vingt-quatre régions du cerveau pour deux cas appartenant au groupe de charge M1D2. Pour ce groupe de longue durée de faible amplitude, la déformation axonale maximale moyenne était égale à 5,2 %. Comme on peut le voir sur le diagramme, la déformation axonale maximale a été subie par la région cérébrale numéro treize, c'est-à-dire le néocortex. La déformation axonale maximale moyenne subie par le néocortex pour le groupe de charge M1D2 était égale à 7,78 % ± 0,1 %.

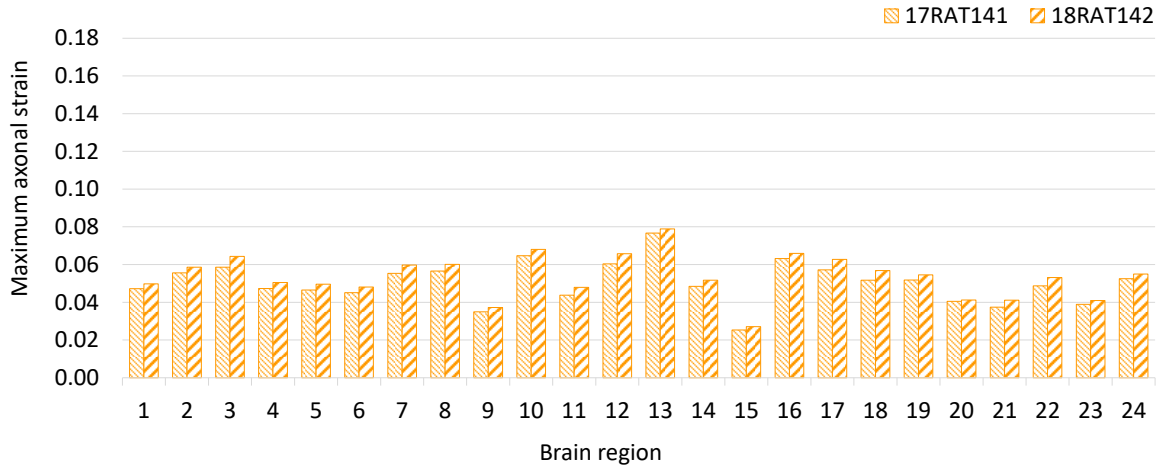

Figure 3.7: Diagramme illustrant les valeurs maximales de la déformation axonale des vingt-quatre régions du cerveau pour quatre cas appartenant au groupe de charge M1D2.

La Figure 3.8 illustre les valeurs maximales de la déformation axonale des vingt-quatre régions du cerveau pour sept cas appartenant au groupe de charge M2D1a. Pour ce groupe de courte durée de grande amplitude, la déformation axonale maximale moyenne était égale à 8,24 %. Comme on peut l'observer sur le diagramme, la déformation axonale maximale a été ressentie par la région cérébrale numéro treize, c'est-à-dire le néocortex. La déformation axonale maximale moyenne subie par le néocortex pour ce groupe de charge était égale à 11,83 % ± 0,5 %.

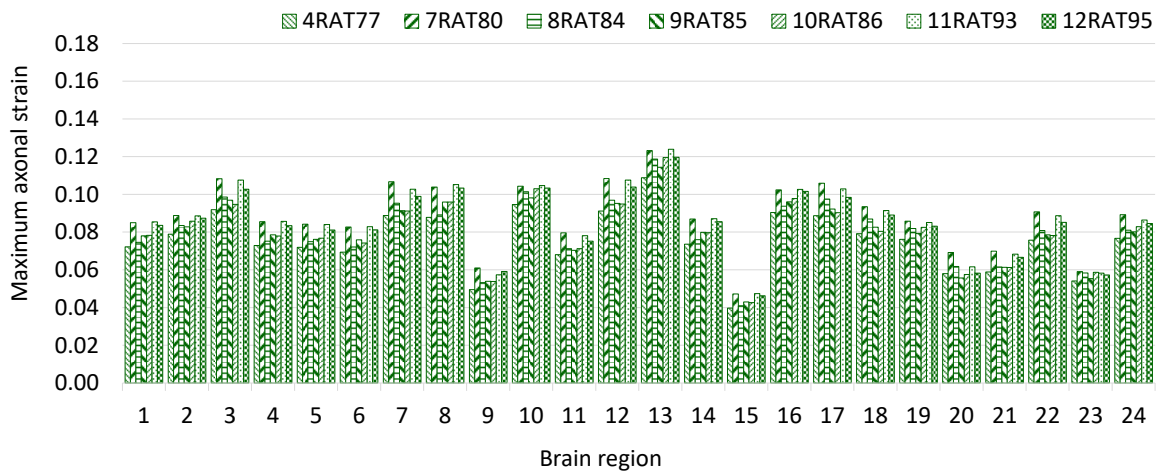

Figure 3.8: Diagramme illustrant les valeurs maximales de la déformation axonale des vingt-quatre régions du cerveau pour quatre cas appartenant au groupe de charge M2D1a.

La Figure 3.9 illustre les valeurs maximales de la déformation axonale des vingt-quatre régions du cerveau pour cinq cas appartenant au groupe de charge M2D1b. Pour ce groupe de courte durée de grande amplitude, la déformation axonale maximale moyenne était égale à 7,45 %. Comme on peut l'observer sur le diagramme, la déformation axonale maximale a été ressentie par la région cérébrale numéro treize, c'est-à-dire le néocortex. La déformation axonale maximale moyenne subie par le néocortex pour ce groupe de charge était égale à 11,51 % ± 2,3 %.

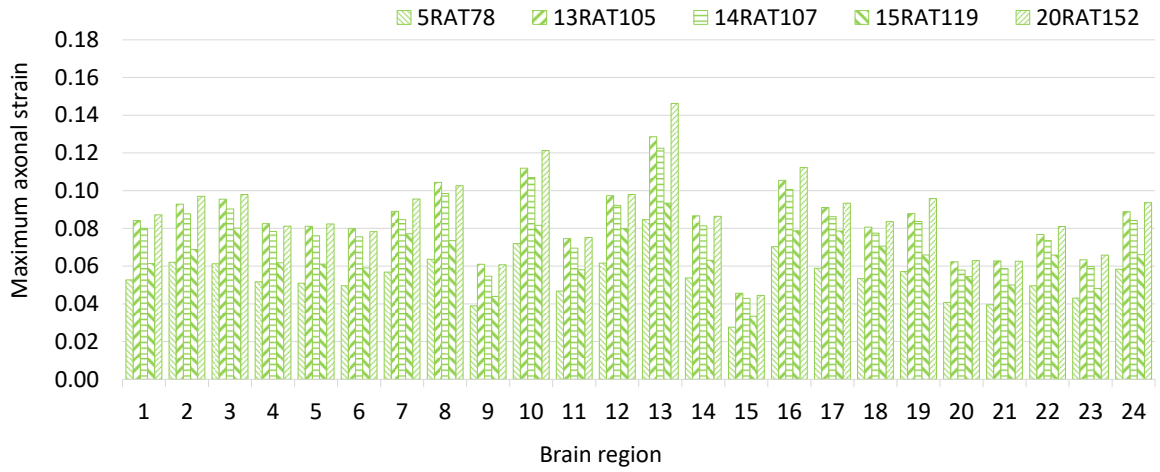

Figure 3.9: Diagramme illustrant les valeurs maximales de la déformation axonale des vingt-quatre régions du cerveau pour quatre cas appartenant au groupe de charge M2D1b.

La Figure 3.10 illustre les valeurs maximales de la déformation axonale des vingt-quatre régions du cerveau pour quatre cas appartenant aux deux groupes de charge M2D2. Pour ce groupe de longue durée de magnitude élevée, la déformation axonale maximale moyenne était égale à 7,31 %. Comme on peut l'observer sur le diagramme, la déformation axonale maximale a été ressentie par la région

cérébrale numéro treize, c'est-à-dire le néocortex. La déformation axonale maximale moyenne subie par le néocortex pour ce groupe de charge était égale à 10,93 % ± 0,5 %.

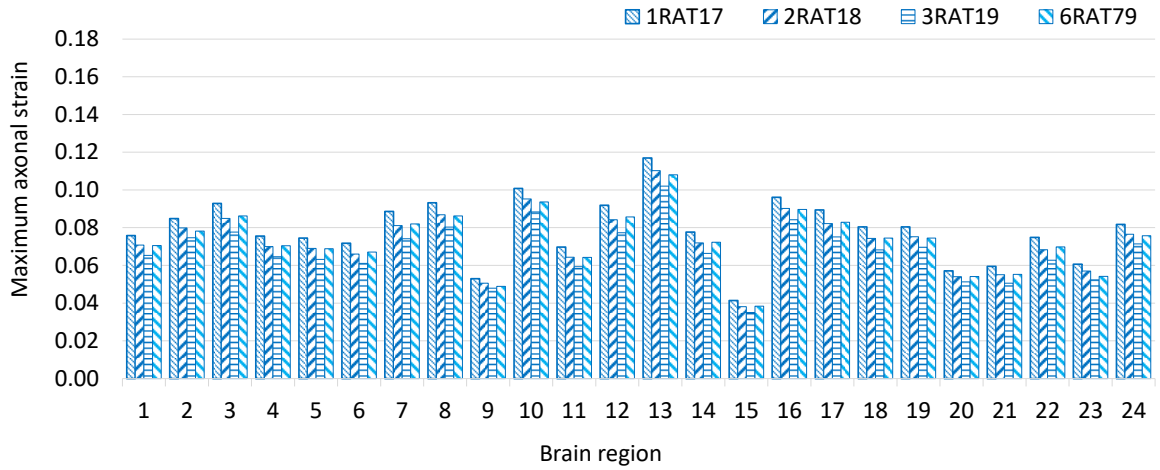

Figure 3.10: Diagramme illustrant les valeurs maximales de déformation axonale des vingt-quatre régions du cerveau pour quatre cas appartenant au groupe de charge M2D2.

Nous pouvons donc constater que la déformation axonale maximale a été subie par les cas appartenant au groupe de charge de courte durée de grande amplitude, ce qui est conforme à la littérature. Ces résultats ont également permis d'identifier les régions du cerveau qui ont subi des déformations élevées et qui, par conséquent, étaient plus vulnérables aux blessures. Les diagrammes montrent que les régions qui ont subi des déformation axonales élevées sont le néocortex (#13), l'hypothalamus (#10), le tronc cérébral (#16), le gris central (#12), le caudate-putamen-globus pallidus (#3), le thalamus (#7), le fimbria (#17) et le cervelet (#8). Toutes ces régions sont connues pour influencer d'une manière ou d'une autre la réponse comportementale (conscience, activité, émotivité et capacités cognitives).

4.6 Conclusion

Dans cette section, nous avons vu les résultats de la simulation pour l'ensemble du cerveau ainsi que pour les régions fonctionnelles et anatomiques du cerveau avec différentes perspectives. D'une part, il faut constater que nous n'avons pas pu établir de relation directe entre les résultats de simulation, en termes de divers paramètres mécaniques, et la lésion, en termes de mesures expérimentales de réponse comportementale. D'autre part, nous avons pu déterminer les déformations axonales pour chaque région du cerveau et identifier les régions du cerveau les plus vulnérables à la commotion cérébrale. Cette importante découverte n'a été possible que grâce au modèle anisotrope de cerveau de rat à éléments finis.

D'après les résultats de simulation de vingt-six cas expérimentaux, il ne semble pas y avoir de relation directe entre les caractéristiques d'accélération et les mesures expérimentales de réponse comportementale. On a constaté que les cas ayant des caractéristiques d'accélération similaires présentaient une grande variation dans les valeurs des mesures expérimentales de réponse comportementale. De plus, les cas blessés et non blessés variaient de faibles amplitudes, de courte durée, à des amplitudes élevées, de longue durée. Habituellement, les caractéristiques d'accélération dans la charge d'accélération en rotation, pour induire une blessure, peuvent être corrélées dans une certaine mesure avec la gravité de la blessure. Toutefois, ce n'est pas le cas ici. Une des raisons possibles pourrait être que le nombre de cas simulés était trop faible pour pouvoir révéler une telle relation.

Les autres paramètres mécaniques (déformation axonale maximale, énergie de déformation maximale, contrainte et déformation maximales de von Mises, contrainte et déformation maximales de cisaillement, contrainte et déformation principales maximales et pressions minimales et maximales) choisis pour l'analyse, ne montrent pas non plus de relation directe avec la blessure, en termes de mesures expérimentales de réponse comportementale. On a constaté que les cas ayant des caractéristiques d'accélération similaires présentaient une grande variation dans les valeurs des mesures expérimentales de réponse comportementale. Globalement, on a pu observer que pour les cas appartenant à un groupe de courte durée de grande amplitude, la réponse mécanique était la plus élevée. Elle était suivie par les cas appartenant au groupe de longue durée à forte amplitude, puis par les cas appartenant au groupe de longue durée à faible amplitude. La réponse mécanique des cas appartenant au groupe de courte durée de faible amplitude était la plus faible. De plus, la réponse mécanique des cas blessés et non blessés variait de faible à élevée et, bien que les amplitudes globales de ces réponses pour les cas blessés aient parfois été légèrement supérieures à celles des cas non blessés, les différences n'étaient pas significatives.

Les cas ont été classés en deux groupes, blessés et non blessés, selon l'hypothèse qu'une valeur de réponse comportementale inférieure à la valeur de réponse simulée peut être considérée comme non blessée et vice versa. Cette hypothèse peut ne pas convenir à ces cas expérimentaux parce que la commotion cérébrale est un type de traumatisme cérébral léger. L'impact de la commotion cérébrale est un trouble fonctionnel. Par conséquent, un écart entre la réponse et la réponse fictive indique un changement de comportement. Ce changement peut être positif ou négatif. Cependant, dans les deux situations, le changement est dû à la commotion cérébrale induite. Par conséquent, les cas où la réponse est tombée en dessous de la valeur de la simulation constituent également un changement et pourraient ne pas avoir été considérés comme non blessés.

Une comparaison partielle des déformations axonales maximales a montré que les principales régions où les déformations axonales maximales étaient les plus élevées étaient le néocortex, l'hypothalamus, le tronc cérébral, le gris central, le caudate-putamen-globus pallidus, les fimbria, le cervelet et le thalamus. Toutes ces régions sont connues pour influencer d'une manière ou d'une autre la réponse comportementale (conscience, activité, émotivité et capacités cognitives).

Sur la base des amplitudes faibles et élevées (M1 et M2) et des durées courtes et longues (D1 et D2) de l'accélération rotationnelle, une comparaison de la déformation axonale maximale par groupe de charge a montré que les régions du cerveau qui subissent la déformation axonale maximale la plus élevée dans les quatre groupes (M1D1, M1D2, M2D1 et M2D2) sont plus ou moins les mêmes. Cependant, les valeurs les plus élevées de la déformation axonale maximale diffèrent comme prévu. Par exemple, pour le groupe de courte durée de faible amplitude, les valeurs de déformation axonale maximale étaient plus faibles et se situaient autour de 7 %, tandis que pour le groupe de courte durée de forte amplitude, les valeurs étaient plus élevées et se situaient autour de 11 % et même 14,6 % pour l'un des cas.

Il serait intéressant d'avoir accès à quelques cas expérimentaux complémentaires, pour conclure. Cependant, pour voir la signification de ces résultats de simulation, procédons à une analyse statistique des données de simulation.

5 Analyse statistique

5.1 Introduction

Dans le but d'identifier le paramètre le plus approprié pour la prédiction de la commotion cérébrale, une analyse statistique a été effectuée pour différents paramètres mécaniques calculés numériquement en association avec différentes mesures expérimentales de réponse comportementale. La méthode de régression logistique binaire a été utilisée pour analyser statistiquement la corrélation entre les paramètres intracérébraux évalués et la survenue de la commotion cérébrale. L'analyse a été réalisée à l'aide du logiciel IBM SPSS Statics, version 21. Selon Sahoo et al. (2016) basés sur le rapport de Hynd and colleagues (2004), la régression logistique binaire s'est avérée être la meilleure méthode statistique par rapport aux autres mesures de cette évaluation. Le comportement mécanique du modèle, en termes de douze paramètres mécaniques (deux globaux et dix locaux), qui sont l'accélération rotationnelle maximale, la durée de l'accélération rotationnelle, la déformation axonale maximale, l'énergie de déformation maximale, la contrainte et la déformation de von Mises maximale, la contrainte et la déformation de cisaillement maximale, la contrainte et la

déformation principales maximales et les pressions minimales et maximales, a été analysée statistiquement sur la base de sept mesures expérimentales de la réponse comportementale, qui sont le temps d'inconscience, la distance parcourue par l'EPM, les changements de bras de l'EPM, la durée d'ouverture de l'EPM et les latences des sessions I, II et III de la MWM, afin de déterminer les meilleurs paramètres candidats pour la prédiction des commotions cérébrales. La régression logistique binaire tente d'ajuster un modèle de régression entre diverses mesures possibles de lésions cérébrales (commotions cérébrales). Avec cette méthode, la probabilité de lésion cérébrale (commotion) est définie comme indiqué dans l'Equation 3.1.

$$P(x) = 1/\left(1 + e^{-(b_0 + b_1 x)}\right) \quad 3.1$$

Où, b_0 et b_1 sont deux variables calculées par régression.

Comme nous l'avons décrit plus haut, la valeur maximale de la mesure expérimentale de la réponse comportementale de la simulation a été utilisée comme facteur décisif pour classer les cas dans les groupes non blessés et blessés pour la binarisation. Les valeurs de Nagelkerke R-carré ont été calculées pour identifier le meilleur prédicteur de blessure. La qualité de l'ajustement de la régression logistique a été testée au moyen des valeurs p de Hosmer-Lemeshow. De plus, l'analyse de la courbe caractéristique de fonctionnement du récepteur a été utilisée pour vérifier la robustesse de la mesure estimée. Les sections suivantes présentent une comparaison de ces prédicteurs de blessures à l'aide de trois méthodes statistiques, fondées sur la valeur R au carré de Nagelkerke, la valeur p de Hosmer-Lemeshow (valeur p de HL) et l'aire sous la courbe caractéristique de fonctionnement du récepteur (AUROC). Examinons maintenant les résultats de ces analyses statistiques.

5.2 Basé sur la régression logistique binaire pour la valeur R au carré de Nagelkerke

La valeur R au carré de Nagelkerke a été utilisée pour identifier la signification de divers prédicteurs de blessures. La comparaison des paramètres candidats utilisant la valeur de Nagelkerke R au carré a permis d'identifier la métrique de lésion cérébrale la mieux corrélée avec l'occurrence de la commotion cérébrale. La valeur de Nagelkerke R au carré varie entre zéro et un, où zéro représente un mauvais ajustement et un, un bon ajustement. Le Table 3.14 présente les valeurs de Nagelkerke R au carré calculées pour les douze prédicteurs de traumatismes en fonction de sept mesures expérimentales de la réponse comportementale pour l'ensemble du cerveau.

Table 3.14: Les valeurs de Nagelkerke R au carré pour tout le cerveau.

Injury predictor	Unconscious time	EPM distance travelled	EPM arm changes	EPM open duration	MWM session I latency	MWM session II latency	MWM session III latency
Max. rotational acceleration	0.071	0.019	0.006	0.009	0.163	0.000	0.034
Duration	0.025	0.000	0.096	0.001	0.112	0.033	0.002
Max. axonal strain	0.211	0.002	0.043	0.000	0.105	0.000	0.048
Max. strain energy	0.201	0.002	0.040	0.001	0.122	0.000	0.058
Max. von Mises stress	0.247	0.001	0.043	0.001	0.110	0.001	0.046
Max. von Mises strain	0.229	0.002	0.045	0.001	0.112	0.000	0.051
Max. shear stress	0.233	0.001	0.043	0.001	0.125	0.001	0.052
Max. shear strain	0.230	0.002	0.045	0.001	0.112	0.000	0.050
Max. principal stress	0.213	0.002	0.045	0.001	0.091	0.001	0.041
Max. principal strain	0.225	0.002	0.043	0.001	0.106	0.001	0.050
Min. pressure	0.214	0.002	0.045	0.001	0.090	0.001	0.042
Max. pressure	**0.261**	0.003	0.076	0.000	0.096	0.007	0.040

On peut observer que les valeurs de Nagelkerke R-carré pour toutes les combinaisons possibles sont assez faibles. Relativement, la meilleure corrélation des prédicteurs de blessure se trouve avec le temps d'inconscience. La valeur R au carré de la pression maximale pour prédire la commotion cérébrale est de 0,261 et est la plus élevée. La deuxième valeur R au carré la plus élevée est celle du contrainte de von Mises et est égale à 0,247. La valeur R au carré de la déformation axonale est de 0,211 seulement.

D'après cette analyse statistique, les courbes de risque de lésion pour l'ensemble du cerveau afin de prédire la commotion cérébrale en ce qui concerne le temps d'inconscience sont fournies dans le Table 3.15.

Table 3.15: Courbes de risque de blessure pour l'ensemble du cerveau afin de prédire la probabilité de commotion en fonction du temps d'inconscience en termes de différents prédicteurs de blessure

(les cercles verts creux représentent les cas non blessés et les cercles rouges pleins représentent les cas blessés).

Maximum axonal strain (MAS)

For a 50% risk of concussion: MAS = 0.1182

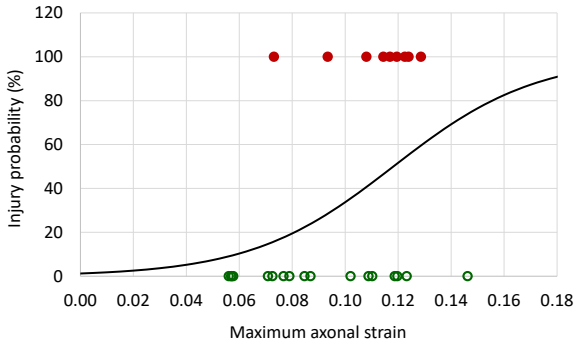

Maximum strain energy (MSE)

For a 50% risk of concussion: MSE = 6.77E-5 mJ

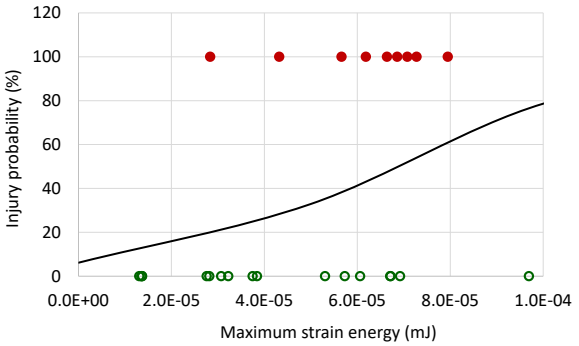

Maximum von Mises stress (MvMSs)

For a 50% risk of concussion: MvMSs = 7.4 kPa

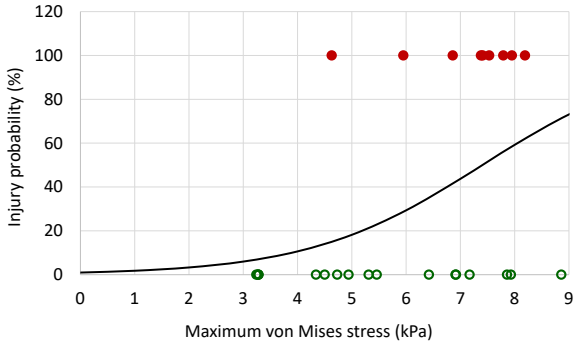

Maximum von Mises strain (MvMSn)

For a 50% risk of concussion: MvMSn = 0.1443

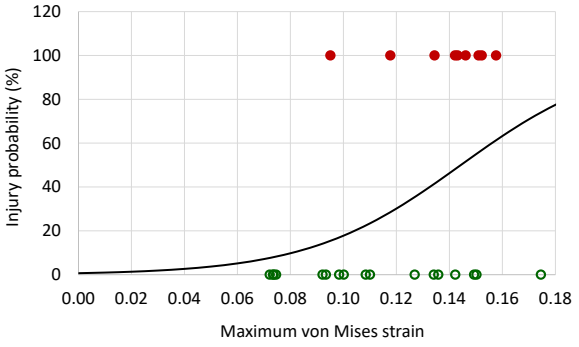

Maximum shear stress (MSSs)

For a 50% risk of concussion: MSSs = 4.2 kPa

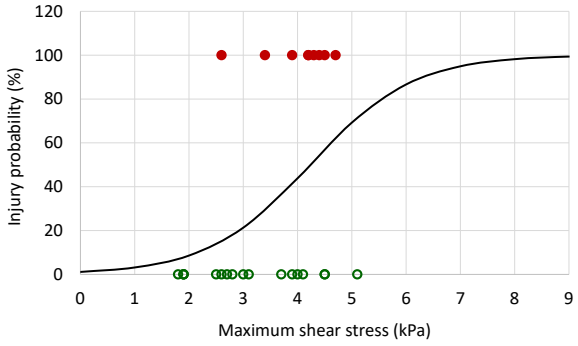

Maximum shear strain (MSSn)

For a 50% risk of concussion: MSSn = 0.1244

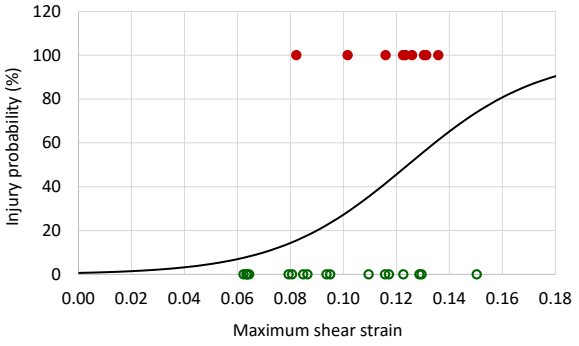

cont.

Maximum principal stress (MPSs)

Maximum principal strain (MPSn)

For a 50% risk of concussion: MPSs = 349.6 kPa

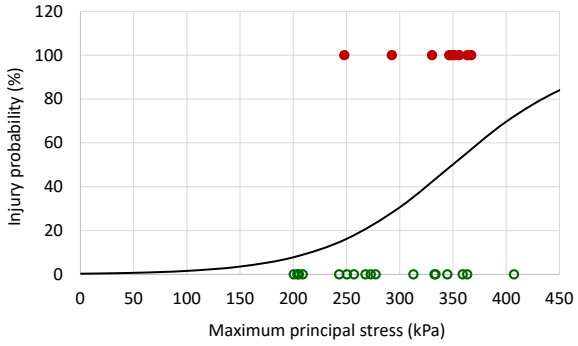

For a 50% risk of concussion: MPSn = 0.1421

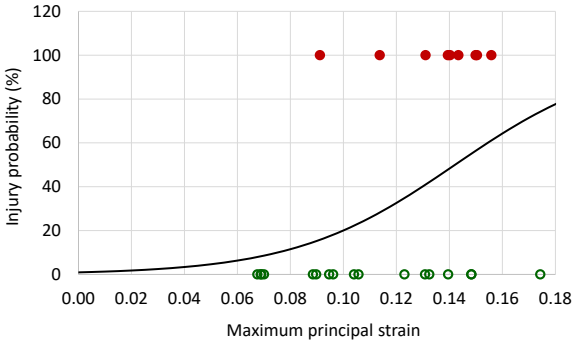

Minimum pressure (MinP)

For a 50% risk of concussion: MinP = -348 kPa

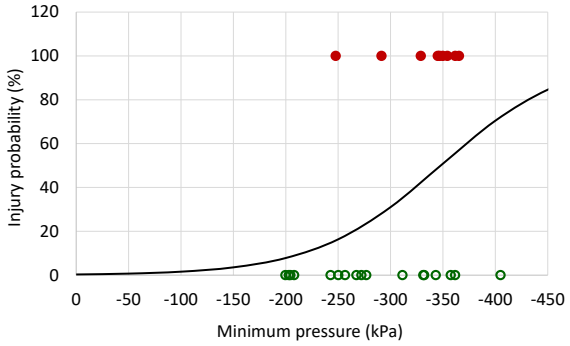

Maximum pressure (MaxP)

For a 50% risk of concussion: MaxP = 372.7 kPa

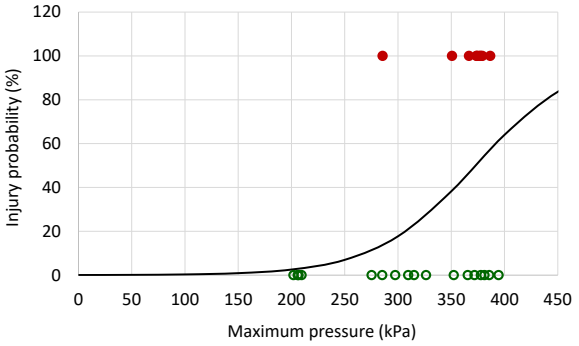

Ces courbes de risque de blessure indiquent que, sur la base du temps d'inconscience, pour une probabilité de 50 % de commotion, les niveaux de tolérance sont les suivants : 11,82 % de la déformation axonale, 6,77E-5 mJ d'énergie de contrainte, 7,4 kPa de contrainte de von Mises, 14,43 % de contrainte de von Mises, 4,2 kPa de contrainte de cisaillement, 12,44 % de contrainte de cisaillement, 349,6 kPa de contrainte principale, 14,21 % de contrainte principale, -348 kPa de pression minimale et 372,7 kPa de pression maximale. Une déformation axonale maximale de 14,65 % a été identifiée par Sahoo et al. (2016) pour un risque de 50 % de DAI par rapport à la valeur identifiée dans cette étude, soit 11,82 % de la déformation axonale maximale pour un risque de 50 % de commotion en ce qui concerne le temps d'inconscience.

Le Table 3.16 présente les valeurs R au carré de Nagelkerke de dix prédicteurs de blessures fondés sur sept mesures expérimentales de la réponse comportementale pour les régions du cerveau associées à la conscience.

Table 3.16: Valeurs de Nagelkerke R-carré pour les régions du cerveau associées à la conscience.

Injury predictor	Unconscious time	EPM distance travelled	EPM arm changes	EPM open duration	MWM session I latency	MWM session II latency	MWM session III latency
Max. axonal strain	0.217	0.002	0.048	0.001	0.107	0.000	0.051
Max. strain energy	0.201	0.002	0.040	0.001	0.122	0.000	0.058
Max. von Mises stress	0.241	0.002	0.044	0.001	0.112	0.001	0.047
Max. von Mises strain	0.235	0.003	0.051	0.001	0.114	0.001	0.054
Max. shear stress	0.233	0.001	0.043	0.001	0.125	0.001	0.052
Max. shear strain	0.236	0.003	0.051	0.001	0.114	0.001	0.053
Max. principal stress	0.213	0.002	0.045	0.001	0.091	0.001	0.041
Max. principal strain	0.232	0.002	0.050	0.001	0.108	0.002	0.054
Min. pressure	0.214	0.002	0.045	0.001	0.090	0.001	0.042
Max. pressure	**0.261**	0.003	0.076	0.000	0.096	0.007	0.040

On peut observer que les valeurs de Nagelkerke R-carré pour toutes les combinaisons possibles sont assez faibles. Relativement, la meilleure corrélation est trouvée avec le temps d'inconscience. La valeur R au carré de la pression maximale pour prédire la commotion cérébrale est de 0,261 et est la plus élevée. La deuxième valeur R au carré la plus élevée est celle du contrainte de von Mises et est égale à 0,241. La valeur R au carré de la déformation axonale est de 0,217 seulement. La courbe de risque de lésion (Table 3.20) pour les régions du cerveau associées à la conscience indique que, selon le temps passé inconscient, pour une probabilité de 50 % de commotion cérébrale, le niveau de tolérance est de 11,80 % de la déformation axonale.

Le Table 3.17 présente les valeurs R au carré de Nagelkerke de dix prédicteurs de blessures fondés sur sept mesures expérimentales de la réponse comportementale pour les régions du cerveau associées à l'activité.

Table 3.17: Valeurs de Nagelkerke R-carré pour les régions du cerveau associées à l'activité.

Injury predictor	Unconscious time	EPM distance travelled	EPM arm changes	EPM open duration	MWM session I latency	MWM session II latency	MWM session III latency
Max. axonal strain	0.211	0.002	0.043	0.000	0.105	0.000	0.048
Max. strain energy	0.201	0.002	0.040	0.001	0.122	0.000	0.058
Max. von Mises stress	0.226	0.002	0.052	0.001	0.114	0.002	0.059
Max. von Mises strain	0.225	0.002	0.043	0.001	0.106	0.000	0.049

Injury predictor	Unconscious time	EPM distance travelled	EPM arm changes	EPM open duration	MWM session I latency	MWM session II latency	MWM session III latency
Max. shear stress	0.233	0.003	0.055	0.000	0.105	0.001	0.049
Max. shear strain	0.226	0.002	0.043	0.001	0.106	0.000	0.048
Max. principal stress	0.213	0.002	0.045	0.001	0.091	0.001	0.041
Max. principal strain	0.215	0.002	0.045	0.000	0.107	0.000	0.050
Min. pressure	0.214	0.002	0.045	0.001	0.090	0.001	0.042
Max. pressure	**0.261**	0.003	0.076	0.000	0.096	0.007	0.040

On peut observer que les valeurs de Nagelkerke R-carré pour toutes les combinaisons possibles sont assez faibles. Relativement, la meilleure corrélation est trouvée avec le temps d'inconscience. La valeur R au carré de la pression maximale pour prédire la commotion cérébrale est de 0,261 et est la plus élevée. La deuxième valeur R au carré la plus élevée est celle de la contrainte de cisaillement et est égale à 0,233. La valeur R au carré de la déformation axonale et de la contrainte de von Mises est seulement de 0,211 et 0,225 respectivement. La courbe de risque de lésion (Table 3.20) pour les régions du cerveau associées à l'activité indique que, selon le temps passé inconscient, pour une probabilité de 50 % de commotion cérébrale, le niveau de tolérance est de 11,82 % de la déformation axonale.

Le Table 3.18 présente les valeurs R au carré de Nagelkerke de dix prédicteurs de blessures fondés sur sept mesures expérimentales de la réponse comportementale pour les régions du cerveau associées à l'émotivité.

Table 3.18: Valeurs de Nagelkerke R-carré pour les régions du cerveau associées à l'émotivité.

Injury predictor	Unconscious time	EPM distance travelled	EPM arm changes	EPM open duration	MWM session I latency	MWM session II latency	MWM session III latency
Max. axonal strain	0.211	0.002	0.043	0.000	0.105	0.000	0.048
Max. strain energy	0.201	0.002	0.040	0.001	0.122	0.000	0.058
Max. von Mises stress	0.241	0.002	0.044	0.001	0.112	0.001	0.047
Max. von Mises strain	0.229	0.002	0.045	0.001	0.112	0.000	0.051
Max. shear stress	0.233	0.001	0.043	0.001	0.125	0.001	0.052
Max. shear strain	0.230	0.002	0.045	0.001	0.112	0.000	0.050
Max. principal stress	0.213	0.002	0.045	0.001	0.091	0.001	0.041
Max. principal strain	0.225	0.002	0.044	0.001	0.106	0.001	0.050

Injury predictor	Unconscious time	EPM distance travelled	EPM arm changes	EPM open duration	MWM session I latency	MWM session II latency	MWM session III latency
Min. pressure	0.214	0.002	0.045	0.001	0.090	0.001	0.042
Max. pressure	**0.261**	0.003	0.076	0.000	0.096	0.007	0.040

On peut observer que les valeurs de Nagelkerke R-carré pour toutes les combinaisons possibles sont assez faibles. Relativement, la meilleure corrélation est trouvée avec le temps d'inconscience. La valeur R au carré de la pression maximale pour prédire la commotion cérébrale est de 0,261 et est la plus élevée. La deuxième valeur R au carré la plus élevée est celle du contrainte de von Mises et est égale à 0,241. La valeur R au carré de la déformation axonale est de 0,211 seulement. La courbe de risque de lésion (Table 3.20) pour les régions du cerveau associées à l'émotivité indique que, selon le temps passé inconscient, pour une probabilité de 50 % de commotion cérébrale, le niveau de tolérance est de 11,82 % de la déformation axonale.

Le Table 3.19 présente les valeurs de Nagelkerke R au carré de dix prédicteurs de blessures fondés sur sept mesures expérimentales de la réponse comportementale pour les régions du cerveau associées à la cognition.

Table 3.19: Valeurs de Nagelkerke R-carré pour les régions du cerveau associées à la cognition.

Injury predictor	Unconscious time	EPM distance travelled	EPM arm changes	EPM open duration	MWM session I latency	MWM session II latency	MWM session III latency
Max. axonal strain	0.213	0.002	0.044	0.000	0.106	0.000	0.049
Max. strain energy	0.201	0.002	0.040	0.001	0.122	0.000	0.058
Max. von Mises stress	0.227	0.002	0.053	0.001	0.115	0.002	0.060
Max. von Mises strain	0.233	0.002	0.046	0.001	0.109	0.001	0.052
Max. shear stress	0.235	0.002	0.055	0.001	0.105	0.001	0.050
Max. shear strain	0.234	0.002	0.045	0.001	0.109	0.001	0.052
Max. principal stress	0.213	0.002	0.045	0.001	0.091	0.001	0.041
Max. principal strain	0.224	0.002	0.048	0.001	0.110	0.001	0.053
Min. pressure	0.214	0.002	0.045	0.001	0.090	0.001	0.042
Max. pressure	**0.261**	0.003	0.076	0.000	0.096	0.007	0.040

On peut observer que les valeurs de Nagelkerke R-carré pour toutes les combinaisons possibles sont assez faibles. Relativement, la meilleure corrélation est trouvée avec le temps d'inconscience. La

valeur R au carré de la pression maximale pour prédire la commotion cérébrale est de 0,261 et est la plus élevée. La deuxième valeur R au carré la plus élevée est celle de la contrainte de cisaillement et est égale à 0,235. La valeur R au carré de la déformation axonale et de la contrainte de von Mises est seulement de 0,213 et 0,233 respectivement. La courbe de risque de lésion (Table 3.20) pour les régions du cerveau associées à la cognition indique que, selon le temps passé inconscient, pour une probabilité de 50 % de commotion cérébrale, le niveau de tolérance est de 11,82 % de la déformation axonale.

Les valeurs de Nagelkerke R-carré pour les régions fonctionnelles du cerveau se situent dans la même fourchette que celles de l'ensemble du cerveau, qui sont très faibles et donc non significatives. Par conséquent, les courbes de risque de lésion pour les régions fonctionnelles du cerveau pour les dix paramètres mécaniques calculés ne sont pas fournies. Toutefois, les courbes de risque de lésion pour les régions fonctionnelles du cerveau permettant de prédire la commotion cérébrale en termes de déformation axonale maximale par rapport à la durée d'inconscience sont données ci-dessous dans le Table 3.20.

Table 3.20: Courbes de risque de lésion pour les régions fonctionnelles du cerveau afin de prédire la probabilité de commotion par rapport au temps d'inconscience en termes de déformation axonale maximale (SMA) (les cercles verts creux représentent les cas non blessés et les cercles rouges pleins représentent les cas blessés).

For regions associated with consciousness	For regions associated with activity
For a 50% risk of concussion: MAS = 0.1180	For a 50% risk of concussion: MAS = 0.1182
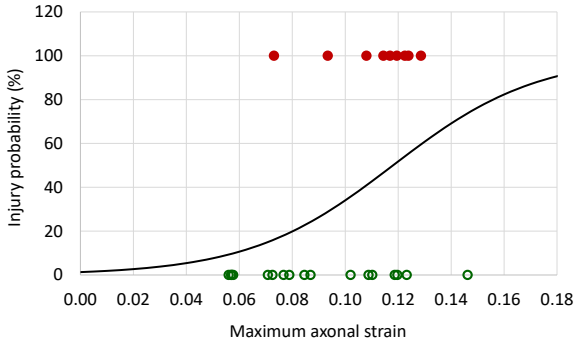	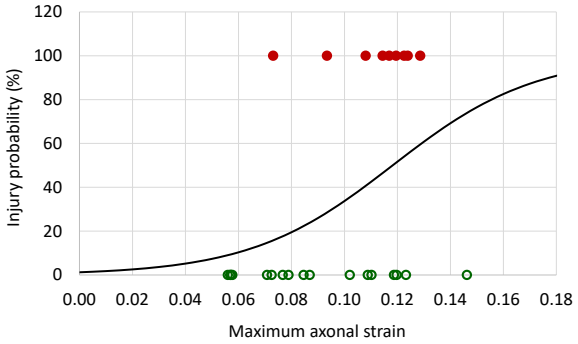

For regions associated with emotionality

For a 50% risk of concussion: MAS = 0.1182

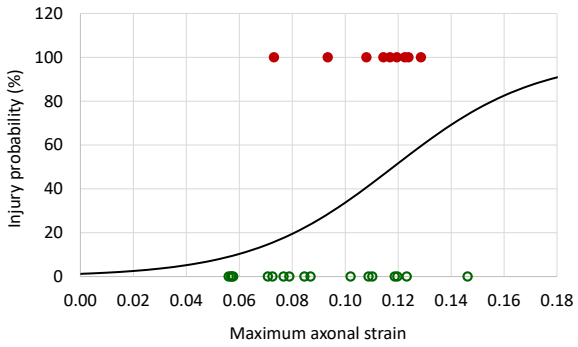

For regions associated with cognition

For a 50% risk of concussion: MAS = 0.1182

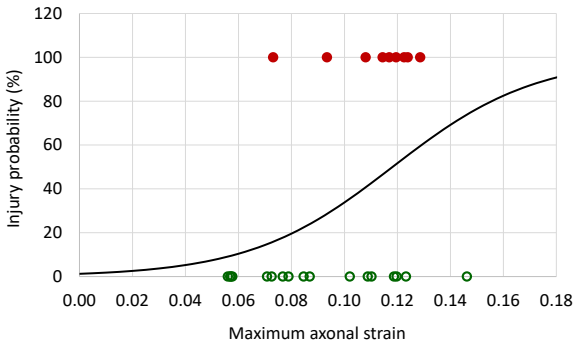

5.3 Basé sur une régression logistique binaire pour la valeur p de Hosmer-Lemeshow

Le test de Hosmer-Lemeshow a été effectué et les valeurs p ont été identifiées pour voir la qualité de l'ajustement de la régression logistique. Ce test permet de vérifier si les taux d'événements observés dans les sous-groupes de la population du modèle correspondent aux taux d'événements attendus. Ce test identifie spécifiquement les sous-groupes comme étant des déciles de valeurs de risque ajustées. Les valeurs de probabilité ou les valeurs p sont calculées sur la base de la distribution chi carré, afin de tester l'ajustement du modèle logistique (Hosmer and Lemeshow, 1980). Une valeur p comprise entre 0,7 et 0,8 indique une discrimination acceptable, une valeur p comprise entre 0,8 et 0,9 indique une excellente discrimination et une valeur p supérieure à 0,9 indique une discrimination exceptionnelle. Le Table 3.21 présente les valeurs p de HL des douze prédicteurs de lésion en fonction de sept mesures expérimentales de la réponse comportementale pour l'ensemble du cerveau.

Table 3.21: HL p valeurs pour l'ensemble du cerveau.

Injury predictor	Unconscious time	EPM distance travelled	EPM arm changes	EPM open duration	MWM session I latency	MWM session II latency	MWM session III latency
Max. rotational acceleration	0.318	0.488	0.218	0.936	0.800	0.586	0.314
Duration	0.257	0.679	0.250	0.406	0.254	0.099	0.485
Max. axonal strain	0.906	0.956	0.736	0.345	0.619	0.008	0.432
Max. strain energy	0.893	0.955	0.725	0.348	0.629	0.192	0.440
Max. von Mises stress	0.869	0.513	0.200	0.304	0.348	0.338	0.536
Max. von Mises strain	0.939	0.954	0.719	0.926	0.621	0.092	0.429
Max. shear stress	0.649	0.760	0.407	0.247	0.357	0.296	0.338

Injury predictor	Unconscious time	EPM distance travelled	EPM arm changes	EPM open duration	MWM session I latency	MWM session II latency	MWM session III latency
Max. shear strain	0.939	0.954	0.720	0.925	0.621	0.092	0.429
Max. principal stress	0.532	0.955	0.728	0.347	0.609	0.065	0.442
Max. principal strain	0.927	0.964	0.695	0.925	0.651	0.093	0.547
Min. pressure	0.532	0.955	0.729	0.347	0.608	0.065	0.443
Max. pressure	0.941	0.960	0.774	0.632	0.705	0.469	0.543

On peut observer que les valeurs p HL en association avec le temps d'inconscience, la distance parcourue par l'EPM et la durée d'ouverture de l'EPM montrent une bonne discrimination. Le Table 3.22 présente les valeurs p de HL de dix prédicteurs de lésions basés sur sept mesures expérimentales de la réponse comportementale pour les régions du cerveau associées à la conscience.

Table 3.22: HL p valeurs pour les régions du cerveau associées à la conscience.

Injury predictor	Unconscious time	EPM distance travelled	EPM arm changes	EPM open duration	MWM session I latency	MWM session II latency	MWM session III latency
Max. axonal strain	0.839	0.650	0.291	0.085	0.405	0.065	0.515
Max. strain energy	0.893	0.955	0.725	0.348	0.629	0.192	0.440
Max. von Mises stress	0.647	0.759	0.404	0.248	0.360	0.297	0.340
Max. von Mises strain	0.946	0.949	0.725	0.925	0.624	0.097	0.436
Max. shear stress	0.649	0.760	0.407	0.247	0.357	0.296	0.338
Max. shear strain	0.946	0.949	0.726	0.925	0.624	0.097	0.436
Max. principal stress	0.532	0.955	0.728	0.347	0.609	0.065	0.442
Max. principal strain	0.802	0.650	0.297	0.412	0.400	0.482	0.524
Min. pressure	0.532	0.955	0.729	0.347	0.608	0.065	0.443
Max. pressure	0.941	0.960	0.774	0.632	0.705	0.469	0.543

On peut observer que les valeurs p de HL en association avec le temps d'inconscience, la distance parcourue par l'EPM et la durée d'ouverture de l'EPM montrent une bonne discrimination pour les régions du cerveau associées à la conscience. Le Table 3.23 présente les valeurs p de HL de dix prédicteurs de blessures basés sur sept mesures expérimentales de la réponse comportementale pour les régions du cerveau associées à l'activité.

Table 3.23: HL p valeurs pour les régions du cerveau associées à l'activité.

Injury predictor	Unconscious time	EPM distance travelled	EPM arm changes	EPM open duration	MWM session I latency	MWM session II latency	MWM session III latency
Max. axonal strain	0.906	0.956	0.736	0.345	0.619	0.008	0.432
Max. strain energy	0.893	0.955	0.725	0.348	0.629	0.192	0.440
Max. von Mises stress	0.848	0.650	0.298	0.608	0.398	0.348	0.516
Max. von Mises strain	0.942	0.955	0.721	0.346	0.613	0.008	0.434
Max. shear stress	0.814	0.703	0.355	0.248	0.663	0.385	0.396
Max. shear strain	0.943	0.955	0.722	0.346	0.611	0.008	0.434
Max. principal stress	0.532	0.955	0.728	0.347	0.609	0.065	0.442
Max. principal strain	0.940	0.954	0.718	0.345	0.616	0.008	0.438
Min. pressure	0.532	0.955	0.729	0.347	0.608	0.065	0.443
Max. pressure	0.941	0.960	0.774	0.632	0.705	0.469	0.543

On peut observer que les valeurs p de HL en association avec le temps d'inconscience et la distance EPM parcourue montrent une bonne discrimination pour les régions du cerveau associées à la conscience. Le Table 3.24 présente les valeurs p de HL de dix prédicteurs de blessures basés sur sept mesures expérimentales de la réponse comportementale pour les régions du cerveau associées à l'émotivité.

Table 3.24: HL p valeurs pour les régions du cerveau associées à l'émotivité.

Injury predictor	Unconscious time	EPM distance travelled	EPM arm changes	EPM open duration	MWM session I latency	MWM session II latency	MWM session III latency
Max. axonal strain	0.906	0.956	0.736	0.345	0.619	0.008	0.432
Max. strain energy	0.893	0.955	0.725	0.348	0.629	0.192	0.440
Max. von Mises stress	0.647	0.759	0.404	0.248	0.360	0.297	0.340
Max. von Mises strain	0.939	0.954	0.719	0.926	0.621	0.092	0.429
Max. shear stress	0.649	0.760	0.407	0.247	0.357	0.296	0.338
Max. shear strain	0.939	0.954	0.720	0.925	0.621	0.092	0.429
Max. principal stress	0.532	0.955	0.728	0.347	0.609	0.065	0.442
Max. principal strain	0.927	0.964	0.695	0.925	0.651	0.093	0.546
Min. pressure	0.532	0.955	0.729	0.347	0.608	0.065	0.443
Max. pressure	0.941	0.960	0.774	0.632	0.705	0.469	0.543

On peut observer que les valeurs p de HL en association avec le temps d'inconscience, la distance parcourue par l'EPM et la durée d'ouverture de l'EPM montrent une bonne discrimination pour les régions du cerveau associées à l'émotivité. Le Table 3.25 présente les valeurs p de HL de dix prédicteurs de lésions basés sur sept mesures expérimentales de la réponse comportementale pour les régions du cerveau associées à la cognition.

Table 3.25: HL p valeurs pour les régions du cerveau associées à la cognition.

Injury predictor	Unconscious time	EPM distance travelled	EPM arm changes	EPM open duration	MWM session I latency	MWM session II latency	MWM session III latency
Max. axonal strain	0.908	0.956	0.738	0.345	0.620	0.065	0.433
Max. strain energy	0.893	0.955	0.725	0.348	0.629	0.192	0.440
Max. von Mises stress	0.851	0.650	0.300	0.608	0.400	0.350	0.518
Max. von Mises strain	0.945	0.950	0.726	0.346	0.620	0.065	0.440
Max. shear stress	0.792	0.474	0.196	0.248	0.299	0.387	0.425
Max. shear strain	0.945	0.951	0.726	0.346	0.618	0.065	0.440
Max. principal stress	0.532	0.955	0.728	0.347	0.609	0.065	0.442
Max. principal strain	0.809	0.650	0.294	0.345	0.406	0.065	0.520
Min. pressure	0.532	0.955	0.729	0.347	0.608	0.065	0.443
Max. pressure	0.941	0.960	0.774	0.632	0.705	0.469	0.543

On peut observer que les valeurs p de HL en association avec le temps d'inconscience et la distance EPM parcourue montrent une bonne discrimination pour les régions du cerveau associées à la cognition.

En comparaison avec l'évaluation de la valeur R au carré de Nagelkerke, on peut observer qu'en plus du temps d'inconscience, la distance EPM parcourue semble également être une mesure significative. Pour quelques paramètres mécaniques calculés, la durée d'ouverture de l'EPM démontre également une discrimination significative. Examinons les statistiques AUROC dans la section suivante.

5.4 Basé sur les courbes caractéristiques de fonctionnement du récepteur

Les courbes des caractéristiques de fonctionnement du récepteur (ROC) ont été tracées pour différents paramètres candidats en association avec des mesures expérimentales de réponse comportementale afin de prédire l'occurrence d'une commotion cérébrale. La capacité de diagnostic d'un classificateur binaire (dans cette étude, blessé comme 1 et non blessé comme 0) avec la variation

de sa valeur seuil est illustrée par la courbe ROC. Une courbe ROC est créée en traçant la sensibilité, c'est-à-dire le taux de vrais positifs, par rapport à la spécificité 1, c'est-à-dire le taux de faux positifs, afin de prédire un résultat dichotomique. Une autre mesure pour tester la performance est l'aire sous la courbe ROC (AUROC). Lorsque la sensibilité est égale à un et la spécificité à zéro, la valeur de l'AUROC est de 1 et le test est précis à 100 %. Par contre, un test qui n'est pas capable de distinguer entre normal et anormal, donne une diagonale de (0, 0) à (1, 1) et pour cela l'AUROC est égale à 0,5. Par conséquent, la métrique correspondant à AUROC égale à un est censée être le meilleur prédicteur de commotion cérébrale. Le Table 3.26 présente les valeurs AUROC de différents prédicteurs de lésion en fonction de sept mesures expérimentales de la réponse comportementale pour l'ensemble du cerveau.

Table 3.26: Valeurs AUROC pour l'ensemble du cerveau.

Injury predictor	Unconscious time	EPM distance travelled	EPM arm changes	EPM open duration	MWM session I latency	MWM session II latency	MWM session III latency
Max. rotational acceleration	0.650	0.400	0.445	0.438	0.823	0.496	0.652
Duration	0.588	0.521	0.636	0.476	0.688	0.541	0.493
Max. axonal strain	0.745	0.509	0.570	0.476	0.729	0.436	0.681
Max. strain energy	0.758	0.509	0.570	0.464	0.729	0.444	0.696
Max. von Mises stress	0.758	0.491	0.558	0.470	0.729	0.455	0.681
Max. von Mises strain	0.765	0.509	0.570	0.470	0.729	0.451	0.681
Max. shear stress	0.745	0.497	0.564	0.476	0.729	0.451	0.681
Max. shear strain	0.765	0.509	0.570	0.470	0.729	0.451	0.681
Max. principal stress	0.745	0.497	0.558	0.476	0.729	0.451	0.681
Max. principal strain	0.765	0.503	0.564	0.470	0.729	0.451	0.681
Min. pressure	0.255	0.503	0.442	0.524	0.271	0.549	0.319
Max. pressure	0.719	0.509	0.570	0.512	0.667	0.451	0.638

On peut observer que pour l'ensemble du cerveau, AUROC n'est significatif qu'en association avec le temps d'inconscience et la latence de la session I de MWM. Sur la base de cette analyse statistique, les courbes ROC permettant de prédire la commotion cérébrale par rapport au temps d'inconscience sont données ci-dessous dans le Table 3.27.

Table 3.27: Courbes ROC pour l'ensemble du cerveau afin de prédire la probabilité de commotion cérébrale par rapport au temps d'inconscience en termes de différents prédicteurs de lésions.

Maximum axonal strain

AUROC = 0.745

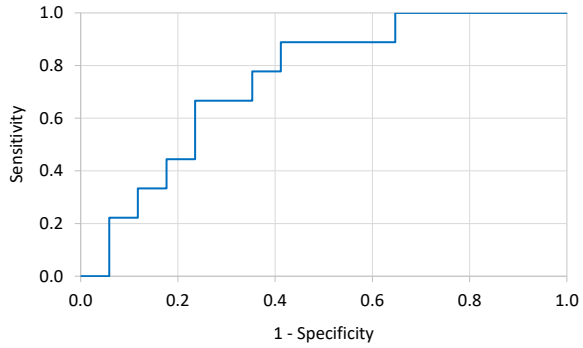

Maximum strain energy

AURCO = 0.758

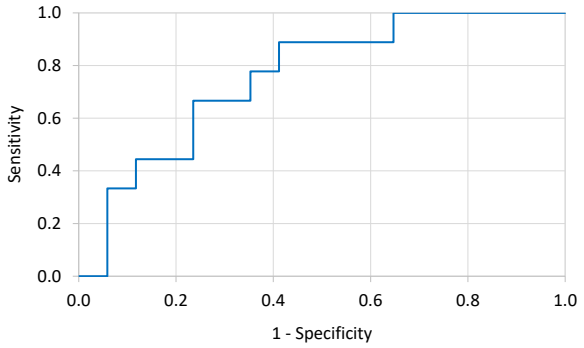

Maximum von Mises stress

AUROC = 0.758

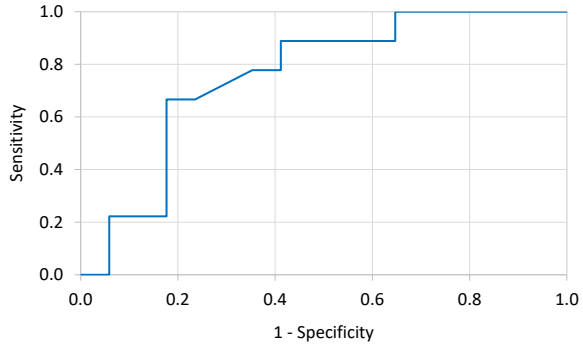

Maximum von Mises strain

AUROC = 0.765

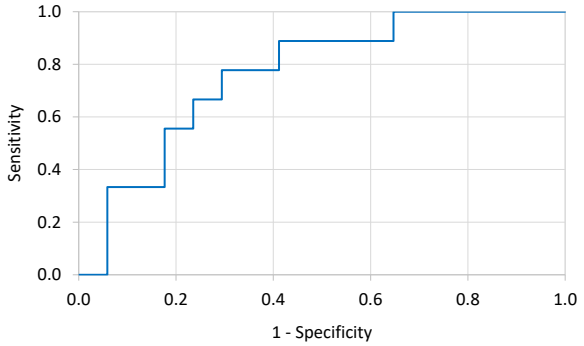

Maximum shear stress

AUROC = 0.745

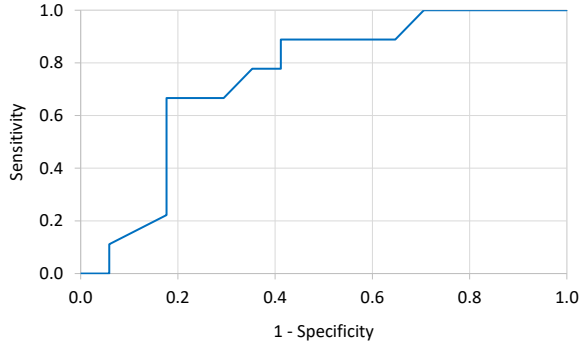

Maximum shear strain

AUROC = 0.765

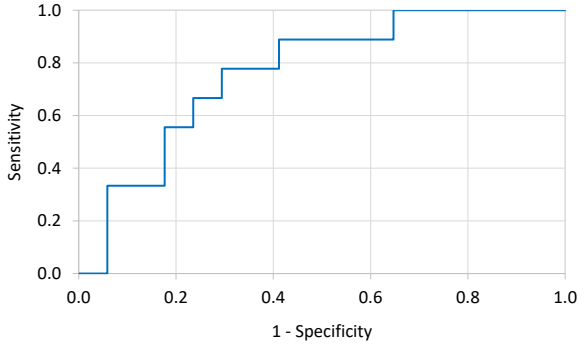

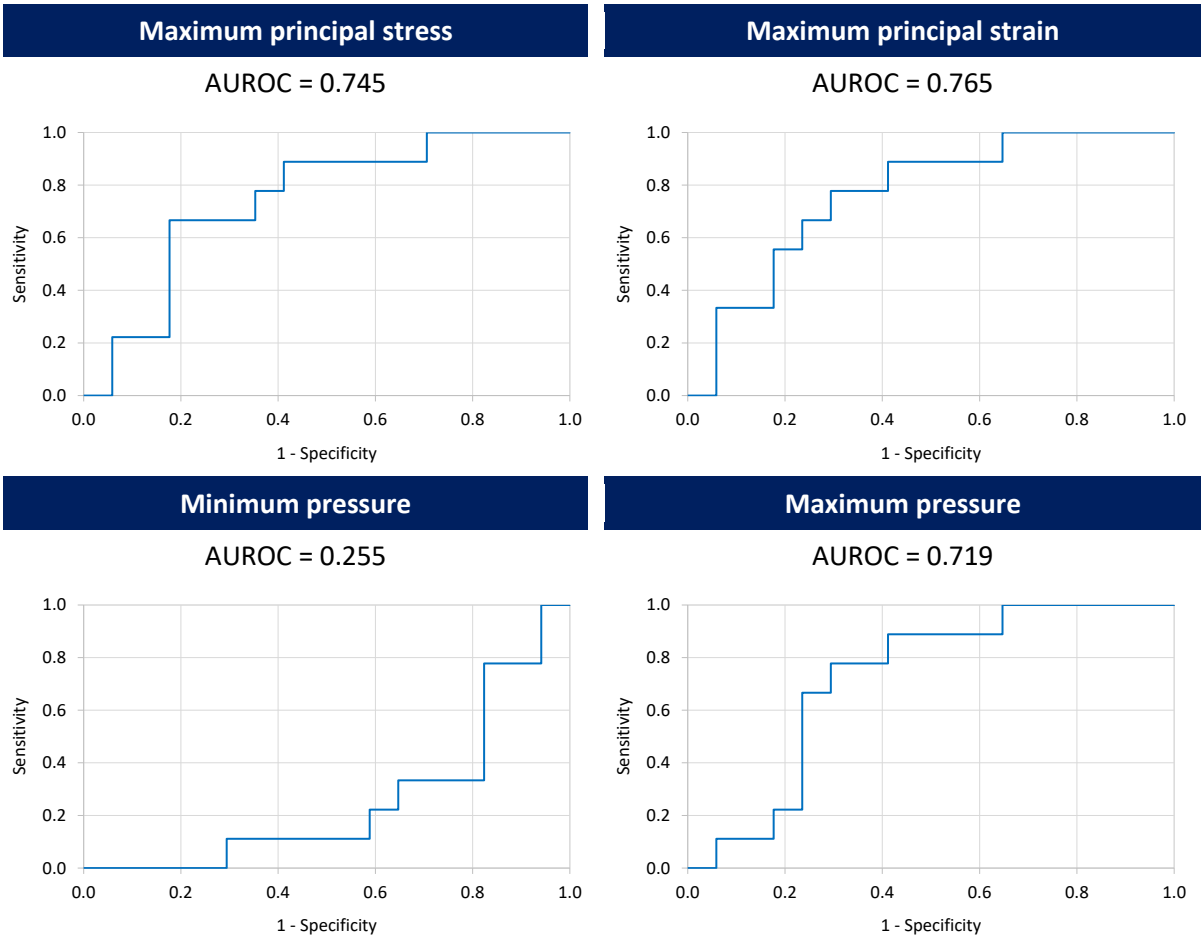

Ces courbes ROC indiquent que, sur la base du temps inconscient, les valeurs AUROC sont de 0,745 pour la déformation axonale, 0,758 pour l'énergie de déformation, 0,758 pour la contrainte de von Mises, 0,765 pour la contrainte de von Mises, 0,745 pour la contrainte de cisaillement, 0,765 pour la contrainte principale, 0,765 pour la contrainte principale, 0,255 pour la pression minimale et 0,719 pour la pression maximale. Le Table 3.28 présente les valeurs AUROC de dix prédicteurs de blessures basés sur sept mesures expérimentales de la réponse comportementale pour les régions du cerveau associées à la conscience.

Table 3.28: Valeurs AUROC pour les régions du cerveau associées à la conscience.

Injury predictor	Unconscious time	EPM distance travelled	EPM arm changes	EPM open duration	MWM session I latency	MWM session II latency	MWM session III latency
Max. axonal strain	0.745	0.497	0.570	0.464	0.729	0.447	0.681
Max. strain energy	0.758	0.509	0.570	0.464	0.729	0.444	0.696
Max. von Mises stress	0.752	0.497	0.564	0.476	0.729	0.455	0.681
Max. von Mises strain	0.765	0.503	0.570	0.464	0.729	0.451	0.681
Max. shear stress	0.745	0.497	0.564	0.476	0.729	0.451	0.681

Injury predictor	Unconscious time	EPM distance travelled	EPM arm changes	EPM open duration	MWM session I latency	MWM session II latency	MWM session III latency
Max. shear strain	0.765	0.503	0.570	0.464	0.729	0.451	0.681
Max. principal stress	0.745	0.497	0.558	0.476	0.729	0.451	0.681
Max. principal strain	0.765	0.491	0.564	0.458	0.729	0.462	0.681
Min. pressure	0.255	0.503	0.442	0.524	0.271	0.549	0.319
Max. pressure	0.719	0.509	0.570	0.512	0.667	0.451	0.638

On peut observer que pour les régions cérébrales associées à la conscience, AUROC n'est significatif qu'en association avec le temps d'inconscience et la latence de la session I du MWM. Le Table 3.29 présente les valeurs AUROC de dix prédicteurs de blessures basés sur sept mesures expérimentales de la réponse comportementale pour les régions du cerveau associées à l'activité.

Table 3.29: Valeurs AUROC pour les régions du cerveau associées à l'activité.

Injury predictor	Unconscious time	EPM distance travelled	EPM arm changes	EPM open duration	MWM session I latency	MWM session II latency	MWM session III latency
Max. axonal strain	0.745	0.509	0.570	0.476	0.729	0.436	0.681
Max. strain energy	0.758	0.509	0.570	0.464	0.729	0.444	0.696
Max. von Mises stress	0.745	0.503	0.570	0.470	0.729	0.444	0.688
Max. von Mises strain	0.752	0.503	0.564	0.470	0.729	0.444	0.681
Max. shear stress	0.758	0.518	0.579	0.482	0.729	0.459	0.674
Max. shear strain	0.752	0.503	0.564	0.470	0.729	0.444	0.681
Max. principal stress	0.745	0.497	0.558	0.476	0.729	0.451	0.681
Max. principal strain	0.752	0.503	0.564	0.470	0.729	0.444	0.681
Min. pressure	0.255	0.503	0.442	0.524	0.271	0.549	0.319
Max. pressure	0.719	0.509	0.570	0.512	0.667	0.451	0.638

On peut observer que pour les régions du cerveau associées à l'activité, l'AUROC n'est significative qu'en association avec le temps d'inconscience et la latence de la session I du MWM. Le Table 3.30 présente les valeurs AUROC de dix prédicteurs de blessures en fonction de sept mesures expérimentales de la réponse comportementale pour les régions du cerveau associées à l'émotivité.

Table 3.30: Valeurs AUROC pour les régions du cerveau associées à l'émotivité.

Injury predictor	Unconscious time	EPM distance travelled	EPM arm changes	EPM open duration	MWM session I latency	MWM session II latency	MWM session III latency
Max. axonal strain	0.745	0.509	0.570	0.476	0.729	0.436	0.681
Max. strain energy	0.758	0.509	0.570	0.464	0.729	0.444	0.696
Max. von Mises stress	0.752	0.497	0.564	0.476	0.729	0.455	0.681
Max. von Mises strain	0.765	0.509	0.570	0.470	0.729	0.451	0.681
Max. shear stress	0.745	0.497	0.564	0.476	0.729	0.451	0.681
Max. shear strain	0.765	0.509	0.570	0.470	0.729	0.451	0.681
Max. principal stress	0.745	0.497	0.558	0.476	0.729	0.451	0.681
Max. principal strain	0.765	0.503	0.564	0.470	0.729	0.451	0.681
Min. pressure	0.255	0.503	0.442	0.524	0.271	0.549	0.319
Max. pressure	0.719	0.509	0.570	0.512	0.667	0.451	0.638

On peut observer que pour les régions cérébrales associées à l'émotivité, AUROC n'est significatif qu'en association avec le temps d'inconscience et la latence de la session I de MWM. Le Table 3.31 présente les valeurs AUROC de dix prédicteurs de blessures basés sur sept mesures expérimentales de la réponse comportementale pour les régions du cerveau associées à la cognition.

Table 3.31: Valeurs AUROC pour les régions du cerveau associées à la cognition.

Injury predictor	Unconscious time	EPM distance travelled	EPM arm changes	EPM open duration	MWM session I latency	MWM session II latency	MWM session III latency
Max. axonal strain	0.745	0.509	0.570	0.476	0.729	0.444	0.681
Max. strain energy	0.758	0.509	0.570	0.464	0.729	0.444	0.696
Max. von Mises stress	0.745	0.503	0.570	0.470	0.729	0.444	0.688
Max. von Mises strain	0.758	0.497	0.564	0.458	0.729	0.459	0.681
Max. shear stress	0.758	0.506	0.573	0.470	0.729	0.459	0.674
Max. shear strain	0.758	0.497	0.564	0.458	0.729	0.459	0.681
Max. principal stress	0.745	0.497	0.558	0.476	0.729	0.451	0.681
Max. principal strain	0.758	0.500	0.564	0.461	0.729	0.455	0.681
Min. pressure	0.255	0.503	0.442	0.524	0.271	0.549	0.319
Max. pressure	0.719	0.509	0.570	0.512	0.667	0.451	0.638

On peut observer que pour les régions cérébrales associées à la cognition, AUROC n'est significatif qu'en association avec le temps d'inconscience et la latence de la session I du MWM.

En comparaison avec l'évaluation de la valeur R au carré de Nagelkerke, on peut observer qu'en plus du temps d'inconscience, la latence de la session I de MWM semble être une mesure significative également.

5.5 Conclusion

Cette section présentait l'analyse statistique des résultats de simulation basés sur les mesures expérimentales de la réponse comportementale afin d'identifier le paramètre le plus approprié pour prédire la commotion cérébrale. Le Table 3.32 présente une synthèse de cette analyse pour l'ensemble du cerveau en association avec l'une des mesures expérimentales de la réponse comportementale, c'est-à-dire le temps d'inconscience.

Table 3.32: Comparaison des résultats de la régression logistique pour différents paramètres mécaniques calculés à partir de vingt-six simulations de chargement rotationnel pour prédire la commotion cérébrale (pour le cerveau entier et sur la base du temps d'inconscience).

Injury predictor	Estimated tolerance level for 50% risk of concussion	Nagelkerke R-squared value	HL p-value	AUROC
Max. axonal strain	0.1182	0.211	0.906	0.745
Max. strain energy	6.77E-5 mJ	0.201	0.893	0.758
Max. von Mises stress	7.4 kPa	0.247	0.869	0.758
Max. von Mises strain	0.1443	0.229	0.939	0.765
Max. shear stress	4.2 kPa	0.233	0.649	0.745
Max. shear strain	0.1244	0.230	0.939	0.765
Max. principal stress	349.6 kPa	0.213	0.532	0.745
Max. principal strain	0.1421	0.225	0.927	0.765
Min. pressure	-348 kPa	0.214	0.532	0.255
Max. pressure	372.7 kPa	0.261	0.941	0.719

Sahoo et al. (2016) a également établi des limites de tolérance aux lésions cérébrales en se fondant sur le calcul de la déformation axonale. Cependant, leur étude était basée sur le cerveau humain et le SUFEHM (Strasbourg University Finite Element Head Model) a été utilisé pour reconstruire 109 cas de traumatismes crâniens à cette fin. Les résultats de leur analyse statistique ont montré clairement que

la déformation axonale est le meilleur prédicteur de lésion pour l'IAD (lésion axonale diffuse) parmi divers paramètres sélectionnés. La présente étude ne voit pas de distinction aussi nette dans les résultats. Sur les sept mesures expérimentales de la réponse comportementale, seul le temps d'inconscience semble être relativement significatif. Cependant, les valeurs de Nagelkerke R-carré pour le temps d'inconscience sont également assez faibles en général. Bien que la valeur p de HL et l'AUROC fournissent des informations supplémentaires, on ne peut pas dire qu'il existe une corrélation certaine entre ces deux indicateurs. Cela pourrait s'expliquer par le fait que le nombre de cas simulés était très faible et n'était pas identique. Comme nous l'avons déjà mentionné, ces cas peuvent être divisés en quatre grands groupes de chargement et, selon l'ampleur et la durée de l'accélération de rotation appliquée, la gravité des blessures aurait été différente pour chaque cas, ce qui réduit davantage le nombre de cas évalués par groupe de chargement. Un autre facteur important est le choix du classificateur binaire. Nous avons divisé les cas en groupes blessés et non blessés en nous basant sur la valeur fictive de la mesure expérimentale de la réponse comportementale. Selon cette hypothèse, les cas ayant une valeur de réponse inférieure à celle du simulacre ont été considérés comme non blessés et vice versa. Néanmoins, cette classification peut ne pas être appropriée pour les commotions cérébrales. La commotion cérébrale est un type de traumatisme cérébral léger qui entraîne des troubles fonctionnels. Une augmentation de la valeur de réponse par rapport à la simulation est un changement de comportement après la blessure, tout comme la diminution de la valeur de réponse. Par conséquent, un autre classificateur binaire peut être nécessaire pour différencier convenablement les groupes blessés et non blessés afin de pouvoir identifier avec certitude le meilleur prédicteur de blessure pour la commotion cérébrale.

6 Avantage d'un modèle anisotrope de cerveau de rat à éléments finis

Le modèle anisotrope de cerveau de rat à éléments finis développé dans cette étude présente plusieurs aspects originaux. C'est avec ce modèle que nous avons pu identifier les déformations axonales par région du cerveau. Le tableau 3.33 donne des détails sur la déformation axonale maximale (SMA) subie par chaque région du cerveau chez les 26 cas. La déformation axonale maximale de 14,62 % subie par le néocortex était la plus élevée. Le SAM moyen subi par le néocortex était de 9,54 % ± 2,89 %.

Table 3.33: Détails sur la déformation axonale maximale régionale parmi les vingt-six cas.

#	Brain region	Maximum axonal strain	Average maximum axonal strain
1	Hippocampus	0.0872	0.0631 ± 0.0173
2	External capsule	0.0970	0.0696 ± 0.0188
3	Caudate - Putamen - Globus pallidus	0.1083	0.0783 ± 0.0195
4	Anterior commissure	0.0857	0.0625 ± 0.0174
5	Substantia nigra	0.0842	0.0613 ± 0.0174
6	Internal capsule	0.0829	0.0601 ± 0.0165
7	Thalamus	0.1067	0.0747 ± 0.0191
8	Cerebellum	0.1052	0.0765 ± 0.0219
9	Superior colliculus	0.0610	0.0461 ± 0.0100
10	Hypothalamus	0.1213	0.0823 ± 0.0238
11	Inferior colliculus	0.0796	0.0576 ± 0.0155
12	Central gray	0.1084	0.0789 ± 0.0188
13	Neocortex	**0.1462**	0.0954 ± 0.0289
14	Amygdala	0.0871	0.0642 ± 0.0180
15	Olfactory bulb	0.0474	0.0345 ± 0.0091
16	Brainstem	0.1123	0.0797 ± 0.0214
17	Fimbria	0.1059	0.0762 ± 0.0178
18	Fornix	0.0935	0.0684 ± 0.0157
19	Ventral tegmental area (VTA)	0.0958	0.0654 ± 0.0197
20	Corpus callosum	0.0692	0.0491 ± 0.0120
21	Genu	0.0699	0.0499 ± 0.0129
22	Aqueduct	0.0907	0.0642 ± 0.0160
23	Splenium	0.0658	0.0482 ± 0.0120
24	Rest of the brain	0.0936	0.0681 ± 0.0166

Comme on peut l'observer au Table 3.33, les régions du cerveau qui ont subi une déformation axonale élevée sont le néocortex, l'hypothalamus, le tronc cérébral, le gris central, le caudate-putamen-globus pallidus, les fimbria, le cervelet et le thalamus. La Figure 3.11 illustre les cent premiers éléments cumulatifs des vingt-six cas qui ont subi la plus forte déformation axonale maximale (232 éléments au total).

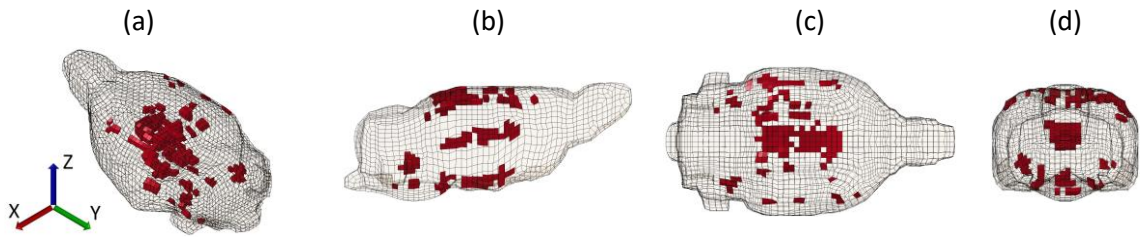

Figure 3.11: Diagramme illustrant les cent premiers éléments cumulatifs des vingt-six cas qui ont subi la plus forte déformation axonale maximale ; (a) vue isométrique, (b) vue sagittale, (c) vue axiale et (d) vue coronale du cerveau du rat.

Les éléments de déformation les plus élevés se trouvent dans les régions du cerveau, qui influencent d'une manière ou d'une autre la réponse comportementale, et ce, conformément aux résultats expérimentaux, car les changements de la réponse comportementale étaient évidents dans les résultats expérimentaux. La connaissance de la déformation axonale et des régions subissant une forte déformation axonale peut aider à l'étude des commotions cérébrales, car les lésions axonales diffuses sont l'une des caractéristiques les plus importantes des lésions cérébrales traumatiques. Néanmoins, il faut disposer d'un grand nombre de données accidentelles réelles ou de données expérimentales pour pouvoir tirer des conclusions définitives.

7 Conclusion

Ce chapitre a présenté des simulations d'expériences de commotions cérébrales sur le modèle animal. Au total, vingt-six cas expérimentaux ont été simulés avec le modèle de cerveau de rat anisotrope visqueux hyperélastique à éléments finis développé. Au début du chapitre, des détails sur l'approche expérimentale et les résultats expérimentaux ont été donnés. Dans le cadre de l'expérimentation, le chargement en accélération de rotation de la tête du rat était censé induire une commotion cérébrale. La réponse comportementale des animaux après la blessure a été mesurée à l'aide de sept paramètres, à savoir le temps d'inconscience, la distance parcourue par l'EPM, les changements de bras de l'EPM, la durée d'ouverture de l'EPM (par l'évaluation de l'élévation plus le labyrinthe) et la latence dans les sessions I, II et III de l'EPM (par l'évaluation du labyrinthe d'eau de Morris). Une comparaison des caractéristiques de l'accélération de la charge en rotation avec ces sept mesures expérimentales de la réponse comportementale n'a fait ressortir aucune relation entre elles. Par la suite, des informations relatives aux simulations ont été fournies, puis les résultats des simulations ont été communiqués. En ce qui concerne les résultats des simulations, dix paramètres mécaniques au total ont été extraits, à savoir la déformation axonale maximale, l'énergie de déformation maximale, la contrainte et la déformation maximales de von Mises, la contrainte et la déformation maximales de cisaillement, la contrainte et la déformation principales maximales et les pressions minimales et maximales. Les résultats de la simulation ont été évalués pour le cerveau entier ainsi que

pour les régions fonctionnelles et anatomiques du cerveau. L'évaluation de base des résultats était basée sur deux hypothèses. La première hypothèse était que les vingt-six cas peuvent être divisés en quatre groupes de charge (et sept autres sous-groupes) en fonction des caractéristiques de l'accélération rotationnelle appliquée. La deuxième hypothèse était basée sur la réponse comportementale expérimentale de la simulation. Vingt-six cas ont été divisés en groupes blessés et non blessés sur la base des résultats expérimentaux de l'animal fictif. On espérait que cette catégorisation aiderait à mieux cerner les limites de la tolérance du cerveau. Cependant, l'analyse des résultats fondés sur ces deux hypothèses n'a pas été très conforme à notre attente. En effet, aucun des paramètres mécaniques ne s'est avéré être en lien étroit avec l'une ou l'autre des mesures expérimentales de la réponse comportementale. Par conséquent, une analyse statistique a été effectuée pour voir la signification de ces résultats de simulation en association avec les résultats expérimentaux et pour trouver le paramètre mécanique le plus approprié pour prédire la commotion cérébrale. Une régression logistique binaire a été utilisée pour analyser les données en termes de statistiques de Nagelkerke R-carré, de statistiques de Hosmer-Lemeshow sur la valeur p et de statistiques sur la courbe caractéristique de fonctionnement du récepteur. On a constaté que les valeurs globales du R-carré de Nagelkerke étaient très faibles. Relativement, la seule mesure expérimentale de la réponse comportementale qui pouvait être corrélée avec les données de simulation était le temps d'inconscience avec une valeur MAS de 11,8 % pour un risque de commotion cérébrale de 50 %. Dans l'ensemble, aucun paramètre candidat n'a pu prédire rapidement la commotion cérébrale. D'après les études disponibles dans la littérature, au moins la déformation axonale aurait dû être évidente pour prédire la commotion cérébrale. Mais, cela n'a pas été fortement démontré dans cette étude. Une des possibilités est que le nombre de cas simulés était trop faible pour pouvoir révéler quoi que ce soit à cet égard. Deuxièmement, un paramètre autre que les dix paramètres sélectionnés peut être un candidat approprié pour prédire la commotion cérébrale.

Bien que les résultats de l'analyse statistique n'aient pas montré de corrélation intéressante, l'importance du modèle anisotrope visqueux hyperélastique de cerveau de rat à éléments finis prévaut. C'est avec ce modèle que nous avons pu identifier les régions cérébrales les plus vulnérables et leurs niveaux de tolérance aux commotions cérébrales.

Conclusion générale et perspectives

La commotion cérébrale, bien qu'elle soit une lésion cérébrale traumatique légère, entraîne des conséquences graves à long terme et peut avoir des effets néfastes sur la vie d'une personne, de sa famille et de la société. La commotion cérébrale est une perturbation neurologique causée par une force mécanique impulsive directe ou indirecte exercée sur la tête. Ces perturbations neurologiques entraînent des déficiences fonctionnelles du cerveau. Les lésions axonales diffuses (DAI) étant l'une des caractéristiques pathologiques les plus fréquentes des traumatismes crâniens, la connaissance du seuil mécanique de la commotion en termes d'élongation axonale peut aider à développer de meilleurs outils de numériques se sont avérés des moyens efficaces pour de telles études. Par rapport à l'expérimentation, les modèles informatiques sont plus précis, plus économiques et plus faciles à utiliser. En outre, ils ne soulèvent pas les préoccupations éthiques qui sont toujours présentes en cas d'expérimentation sur des sujets biologiques. Néanmoins, les données expérimentales sont essentielles pour la validation d'un modèle computationnel. L'impossibilité de conduire des expériences sur le cerveau humain limite l'étude détaillée des commotions cérébrales. Cependant, les petits animaux, comme le rat, semblent être une opportunité intéressante pour de telles investigations. Les observations littéraires selon lesquelles un cerveau de rat adulte peut être considéré comme neurologiquement équivalent à un cerveau humain adulte et qu'au niveau des tissus, les cerveaux interespèces réagissent de la même façon, confirment l'importance des études par modèle de cerveau de rat. Par conséquent, dans le cadre de cette thèse de doctorat, un modèle de cerveau de rat anisotrope, visqueux, hyperélastique en éléments finis a été élaboré, validé et utilisé pour l'étude du seuil mécanique de la commotion cérébrale. Ce travail de doctorat contribue à la recherche sur le développement de meilleurs outils de prédiction des lésions cérébrales et l'optimisation des systèmes de protection de la tête.

Cette étude a commencé par une analyse documentaire approfondie sur l'anatomie du cerveau, les mécanismes potentiels de lésions pour les commotions cérébrales, les lésions cérébrales - échelles de notation, critères et niveaux de tolérance, et la modélisation du cerveau des rats par éléments finis. Un résumé de cette analyse documentaire est présenté ci-dessous.

- L'anatomie du cerveau, présentée aux niveaux macroscopique et microscopique, a permis de préciser les similitudes et les différences entre le cerveau d'un humain et celui d'un rat et de nous familiariser avec l'intérieur du cerveau.
- Les mécanismes potentiels de commotion cérébrale ont mis en évidence l'importance de la quantification de l'élongation axonale, puisque la déficience des éléments du cytosquelette axonal semblait être la principale raison du début de la commotion cérébrale.

- Une prise de conscience des lésions cérébrales - échelles de classement, critères et niveaux de tolérance - a non seulement élargi notre horizon en ce qui concerne les différentes possibilités d'évaluation des commotions cérébrales, mais nous a également fait réaliser à quel point les commotions cérébrales avaient été définies différemment dans diverses études. De plus, nous avons appris que pour le cerveau du rat, il n'existe pas de limites de tolérance aux commotions cérébrales, en termes de paramètres mécaniques.
- Les données expérimentales disponibles dans la littérature concernant les propriétés des matériaux du cerveau de rat sont très limitées. Néanmoins, les propriétés des matériaux du cerveau de rat semblent être conformes à celles du cerveau humain.
- Les modèles existants de cerveau de rat aux éléments finis sont isotropes et ont été mis au point pour analyser les lésions cérébrales traumatiques modérées et graves. Ils ne peuvent pas être utilisés pour des investigations liées à des commotions cérébrales sans modifications supplémentaires.
- Les données expérimentales sur la déformation du cerveau de Shreiber et al. (1997) et Antona-Makoshi et al. (2014) peuvent être utilisées pour la validation d'un modèle de cerveau de rat à éléments finis.

Par conséquent, la restriction des études approfondies sur le cerveau humain et l'incapacité des modèles de cerveau de rat en éléments finis existants à étudier les commotions cérébrales nous ont fait réaliser la nécessité d'un modèle de cerveau de rat en éléments finis anisotrope pour l'étude du seuil mécanique de commotion en termes d'élongation axonale.

À cette fin, un modèle de cerveau de rat aux éléments finis anisotrope, visqueux et hyperélastique (FERBM) a été développé. Un résumé de la méthodologie de développement du modèle est donné ci-dessous.

- Des rats Sprague Dawley adultes, pesant environ 290 g, ont été choisis comme base pour cette étude.
- Un atlas tridimensionnel d'imagerie du tenseur de diffusion du cerveau du rat Sprague Dawley adulte (pesant environ 290 g) au 72e jour postnatal, élaboré par Rumple et al. (2013), , a été utilisé pour déterminer la géométrie et les paramètres de diffusion du cerveau du rat.
- En se basant sur la géométrie du cerveau de rat rendue par l'atlas du DTI, le modèle a été maillé à l'aide du logiciel HyperMesh. Le maillage FERBM était constitué de 13 236 éléments hexaédriques solides, avec une taille moyenne des éléments de 0,5 mm. Le modèle cérébral a été

enveloppé dans une couche de liquide céphalorachidien (LCR), modélisé avec 3 252 éléments hexaédriques solides, ayant une épaisseur moyenne de 0,7 mm. Le cerveau et le modèle de LCR ont été enfermés à l'intérieur du crâne, modélisé avec 3 252 éléments quadrilatéraux.

- Deux paramètres de diffusion - l'anisotropie fractionnelle (FA) et la direction principale des fibres (PFD) - ont été identifiés à partir de l'atlas du DTI. L'anisotropie de la FERBM développée a été obtenue en implémentant cette information du DTI dans le modèle.
- L'atlas DTI contenait les données de diffusion stockées pour chaque voxel (la subdivision cubique (taille : 0,125 mm) du volume du cerveau du rat). Ainsi, dans un premier temps, les valeurs d'AF et de PFD pour chaque voxel du cerveau de rat ont été calculées à partir des données stockées dans l'atlas du DTI.
- Le FERBM a été aligné avec le volume du DTI, de sorte que les deux correspondent à la même localisation et orientation dans l'espace. Les voxels tombant à l'intérieur de chaque élément du FERBM ont ensuite été identifiés. Le nombre moyen de voxels à l'intérieur d'un élément était égal à 68 ± 24.
- Les valeurs de FA et de PFD pour chaque élément du FERBM ont ensuite été estimées. Cette estimation a été faite en prenant la moyenne pondérée des valeurs d'AF et de PFD de tous les voxels à l'intérieur d'un élément. La fonction de pondération exponentielle a été choisie de manière à ce que les voxels situés près du centre de l'élément aient une influence plus importante que ceux situés à la limite de l'élément. La valeur de l'AF variait de zéro à 0,96, avec une valeur moyenne pondérée de l'AF égale à 0,31 ± 0,12.
- L'ensemble du processus, c'est-à-dire le calcul des paramètres de diffusion pour chaque voxel, l'alignement du modèle EF et du volume DTI, l'identification des voxels par élément et l'estimation des paramètres de diffusion par élément, a été réalisé par codage dans un langage de programmation de haut niveau - Python. Une comparaison des paramètres de diffusion identifiés avec ceux de l'atlas DTI a démontré un bon accord.
- Une loi constitutive anisotrope visqueuse hyperélastique validée pour le matériel cérébral, élaborée par Chatelin et al. (2013) a été jugée appropriée pour cette étude. Cette loi suppose que le tissu cérébral est constitué d'un matériau matriciel isotrope avec un renforcement anisotrope des fibres dans la direction principale des fibres. De plus, il a été supposé que les fibres n'ont aucune influence sur la compression et sur la situation où la tension est appliquée orthogonalement à la direction principale des fibres. Le matériau de la matrice a pris en compte à la fois l'hyperélasticité et la viscosité. Cependant, le matériau fibreux a été modélisé uniquement

comme hyperélastique en raison du manque de données viscoélastiques expérimentales sur les fibres cérébrales.

- Les propriétés du matériau du cerveau ont été implémente dans le modèle FERBM développé au moyen de *MAT_092, c'est-à-dire *MAT_SOFT_TISSUE_VISCO, le modèle de matériau de LS-DYNA. Ce modèle inclut à la fois les propriétés de la matière cérébrale visqueuse hyperélastique et les paramètres de diffusion anisotropique du cerveau du rat. En se basant sur les preuves littéraires, on a émis l'hypothèse qu'au niveau des tissus, le cerveau de rat adulte et le cerveau humain adulte sont neurologiquement équivalents. Ainsi, les propriétés des matériaux cérébraux utilisées par Chatelin et al. (2013) pour l'humain adulte ont été adaptées pour le cerveau de rat en incluant les paramètres de diffusion du cerveau de rat.
- Comme la propriété anisotrope du matériau diffère pour chaque élément du FERBM, l'incorporation des propriétés du matériau dans le FERBM, ainsi que les paramètres de diffusion, a été réalisée par codage dans un langage de programmation de haut niveau - Python.
- Le CSF a été modélisé avec *MAT_001 c'est-à-dire *MAT_ELASTIC_FLUID modèle de matériau de LS-DYNA et le crâne avec *MAT_20 c'est-à-dire *MAT_RIGID. Le crâne a été modélisé comme étant rigide afin d'appliquer la charge sur le cerveau de manière appropriée, en assignant des conditions aux limites appropriées sur le crâne.
- La FERBM visqueuse hyperélastique anisotrope développée a été validée par rapport à deux expérimentations disponibles dans la littérature. La première validation a été faite par rapport à un déplacement cortical dynamique expérimental sur l'application d'une impulsion de pression sous vide selon Shreiber et al. (1997). Au total, six simulations ont été réalisées pour différentes combinaisons d'amplitudes de pression et de durées d'impulsion. La deuxième validation a été faite par rapport au déplacement relatif cerveau-crâne (BSRD) expérimental sur l'application d'une charge d'accélération rotationnelle dans le plan sagittal selon Antona-Makoshi et al. (2014). Une simulation a été réalisée pour l'impulsion d'accélération rotationnelle disponible.
- Une étude paramétrique a révélé que le choix du matériau du cerveau influence fortement la réponse du cerveau pour une condition de charge donnée. Une loi isotrope générale viscoélastique de la matière cérébrale semblait plus flexible que la loi anisotrope visqueuse hyperélastique de la matière cérébrale. De plus, on a constaté que la compressibilité du liquide céphalorachidien influençait de façon significative la réponse cérébrale. De plus, le type de contrôle du sablier (IHQ) a démontré une influence significative sur l'énergie du sablier et la réponse du cerveau, mais pas sur le coefficient du sablier (QH).

Ainsi, un modèle validé de cerveau de rat anisotrope visqueux hyperélastique en éléments finis a été élaboré pour l'étude du seuil mécanique de la commotion cérébrale.

Des simulations numériques de commotion cérébrale expérimentale ont été réalisées pour obtenir des informations sur le cerveau du rat. Le résumé des expériences choisies pour les simulations et les détails des simulations, leurs résultats et l'analyse statistique sont donnés ci-dessous.

- Les données de vingt-six cas de commotion cérébrale expérimentale ont été reçues du Medical College of Wisconsin (MCW), aux États-Unis, dans le cadre d'une collaboration. Ces données faisaient partie de leur étude publiée - Stemper et al. (2016).
- Les sujets des expériences étaient des rats Sprague Dawley adultes (pesant environ 290 g) et la commotion a été induite par la charge d'accélération de rotation de la tête du rat dans le plan coronal. Pour les vingt-six cas expérimentaux, l'amplitude moyenne de l'accélération de rotation maximale était de 319,5 ± 85,5 krad/s2 et la durée moyenne était de 1,9 ± 0,8 ms.
- La gravité des lésions aiguës expérimentales a été évaluée en fonction du temps d'inconscience. On a utilisé l'évaluation EPM (Elevated plus maze) pour analyser les changements d'activité et d'émotivité après la commotion. L'évaluation du labyrinthe d'eau de Morris (MWM) a été utilisée pour analyser les changements post-commotionnels dans les capacités cognitives. Un total de sept mesures expérimentales des réponses comportementales ont été utilisées pour analyser les réponses post-commotion. Il s'agissait du temps d'inconscience, de la distance parcourue par l'EPM, des changements de bras de l'EPM, de la durée d'ouverture de l'EPM et des latences dans les sessions I, II et III du MWM.
- Les valeurs de ces sept mesures comportementales expérimentales étaient disponibles comme résultats expérimentaux pour les vingt-six cas. Les valeurs correspondantes pour le simulacre (sujet témoin qui n'a pas subi de charge de rotation) ont été tirées de Stemper et al. (2016).
- Pour l'analyse de la réponse post-commotion, basée sur la valeur maximale et la durée de l'accélération de rotation, ces vingt-six cas expérimentaux ont été divisés en quatre groupes de charge comme dans la publication de Stemper et al. (2016). Il s'agissait du groupe à faible amplitude et courte durée (M1D1), du groupe à faible amplitude et longue durée (M1D2), du groupe à amplitude élevée et courte durée (M2D1) et du groupe à amplitude élevée et longue durée (M2D2). L'amplitude moyenne basse M1 était égale à 224,2 ± 31,2 krad/s2 et l'amplitude moyenne haute M2 était égale à 379,1 ± 45,2 krad/s2. La durée moyenne courte D1 était égale à 1,5 ± 0,5 ms et la durée moyenne longue D2 était égale à 3,2 ± 0,3 ms.

- De plus, pour l'analyse de la réponse post-commotion dans une autre perspective, basée sur la valeur des résultats de la simulation, ces vingt-six cas expérimentaux ont été divisés en deux groupes. Ceux pour lesquels les résultats expérimentaux étaient inférieurs à la valeur fictive se retrouvent dans le premier groupe et sont appelés cas non blessés et ceux pour lesquels les résultats expérimentaux étaient supérieurs à la valeur fictive se retrouvent dans le deuxième groupe et sont appelés cas blessés.
- L'association des caractéristiques d'accélération avec les mesures expérimentales de réponse comportementale a été analysée. Aucune relation n'a été trouvée entre les caractéristiques de l'accélération et les mesures expérimentales de réponse comportementale. En se basant sur l'association des groupes de charge, on a constaté que les cas ayant des caractéristiques d'accélération similaires présentaient une grande variation dans les valeurs des mesures expérimentales de réponse comportementale. Cette variation a été observée même avec des cas ayant des caractéristiques d'accélération dissemblables. Cela signifie que le résultat expérimental des cas de faible amplitude ou de courte durée variait de faible à élevé, tout comme le résultat expérimental des cas de forte amplitude ou de longue durée. De plus, selon l'autre classification, les cas blessés et non blessés variaient de faibles amplitudes, de courtes durées à des amplitudes élevées, de longues durées sans différence significative entre les amplitudes globales.
- Au total, vingt-six simulations ont été effectuées, correspondant aux vingt-six expériences. Les résultats des simulations ou les réponses mécaniques ont été extraits en fonction de dix paramètres mécaniques. Ces paramètres étaient la contrainte et la déformation maximale de von Mises, la contrainte et la déformation principale maximale, la contrainte et la déformation maximale de cisaillement, les pressions minimales et maximales, l'énergie de déformation et le tenseur de déformation, pour calculer la déformation axonale.
- En se basant sur la direction de la fibre principale (PFD) par élément estimée précédemment, la déformation axonale pour chaque élément de FERBM a été calculée par programmation Python. Ainsi, la valeur maximale de la déformation axonale (MAS) a été identifiée pour chaque élément de la FERBM.
- Globalement, il a été observé que pour les cas appartenant au groupe de courte durée de grande amplitude (M2D1), l'amplitude des réponses mécaniques était la plus élevée. Viennent ensuite les cas appartenant au groupe de longue durée de forte amplitude (M2D2), puis les cas appartenant au groupe de longue durée de faible amplitude (M1D2). L'amplitude des réponses mécaniques des cas appartenant au groupe de courte durée de faible amplitude (M1D1) était la plus faible.

- Les paramètres mécaniques calculés (déformation axonale maximale, énergie de déformation maximale, contrainte et déformation maximales de von Mises, contrainte et déformation maximales de cisaillement, contrainte et déformation principales maximales et pressions minimales et maximales) n'ont pas montré de relation directe avec la blessure, en termes de mesures expérimentales de réponse comportementale. On a constaté que les cas ayant des caractéristiques d'accélération similaires présentaient une grande variation dans les valeurs des mesures expérimentales de réponse comportementale. En outre, la réponse mécanique des cas blessés et non blessés variait de faible à élevée et, bien que les amplitudes globales de ces réponses pour les cas blessés soient parfois légèrement supérieures à celles des cas non blessés, les différences n'étaient pas significatives. En ce qui concerne la durée de l'inconscience, la déformation axonale maximale moyenne pour le groupe de personnes non blessées était de 8,98 % ± 2,69 %. Par contre, la déformation axonale maximale moyenne pour le groupe de blessés était de 11,11 % ± 1,66 %.
- Une comparaison de la déformation axonale maximale entre les groupes de charge a montré que les régions du cerveau qui subissent la déformation axonale maximale la plus élevée dans les quatre groupes de charge (M1D1, M1D2, M2D1 et M2D2) sont plus ou moins les mêmes. Cependant, les valeurs les plus élevées de la déformation axonale maximale diffèrent, ce qui est logique. Par exemple, pour le groupe de courte durée de faible amplitude, les valeurs maximales de déformation axonale étaient d'environ 7 % seulement, alors que celles du groupe de courte durée de forte amplitude étaient d'environ 11 % et même de 14,6 % pour l'un des cas.
- Pour une analyse plus approfondie des résultats de la simulation sur une base régionale, la FERBM a été subdivisée en régions anatomiques et fonctionnelles. La catégorisation anatomique a divisé le cerveau en vingt-quatre régions - hippocampe, capsule externe, caudé - putamen - globus pallidus en un seul, commissure antérieure, substantia nigra, capsule interne, thalamus, cervelet, collicule supérieur, hypothalamus, collicule inférieur, gris central, néocortex, amygdale, bulbe olfactif, tronc cérébral, fimbria, fornix, région tegmentale ventrale (VTA), corps calleux, genu, aqueduc, splénium et reste du cerveau comme un tout. La catégorisation fonctionnelle était basée sur quatre aspects comportementaux - la conscience, l'activité, l'émotivité et la cognition. On a supposé que la conscience est associée au thalamus, au néocortex et au tronc cérébral ; l'activité est associée à l'hippocampe, à la substance noire, au cervelet, au gris central et au néocortex ; l'émotivité est associée à l'hippocampe, au gris central, au néocortex, à l'amygdale, au tronc cérébral, aux fimbria et au fornix ; et la cognition est associée à l'hippocampe, à la substance noire, au cervelet, au néocortex, aux fimbria et au fornix. Cependant, les paramètres mécaniques

calculés ont démontré une tendance similaire pour les régions anatomiques et fonctionnelles du cerveau que pour le cerveau entier.

- Une comparaison anatomique des déformations axonales maximales par région a montré que les principales régions où les déformations axonales maximales étaient les plus élevées étaient le néocortex (MAS = 14,62 %, moyenne : 9,54 % ± 2,89 %), l'hypothalamus (MAS = 12,13 %, moyenne : 8,23 % ± 2,38 %), le tronc cérébral (MAS = 11,23 %, moyenne : 7.97% ± 2,14%), gris central (MAS = 10,84%, moyenne : 7,89% ± 1,88%), caudate-putamen-globus pallidus (MAS = 10,83%, moyenne : 7,83% ± 1.95 %), le thalamus (SAM = 10,67 %, moyenne : 7,47 % ± 1,91 %), le fimbria (SAM = 10,59 %, moyenne : 7,62 % ± 1,78 %) et le cervelet (SAM = 10,52 %, moyenne : 7,65 % ± 2,19 %). Toutes ces régions sont connues pour influencer d'une manière ou d'une autre la réponse comportementale (conscience, activité, émotivité et capacités cognitives).
- L'analyse statistique des résultats de la simulation a été effectuée au moyen d'une régression logistique binaire, en termes de statistiques de Nagelkerke R-carré, de statistiques de valeur p de Hosmer-Lemeshow (HL) et de statistiques de caractéristiques d'exploitation de la zone sous récepteur (AUROC).
- Aucun des paramètres mécaniques choisis n'a montré une forte corrélation avec les mesures expérimentales de réponse comportementale. Cela pourrait s'expliquer par le fait que le nombre de cas simulés est assez faible, puisque les données expérimentales n'étaient disponibles que pour vingt-six cas. Relativement, le temps d'inconscience était assez corrélé avec les réponses mécaniques.
- Sur la base du temps d'inconscience, pour un risque de commotion cérébrale de 50 %, le niveau de tolérance estimé était de 11,82 % de la déformation axonale maximale, avec une valeur de Nagelkerke R au carré de 0,211, une valeur de HL p de 0,906 et une valeur AUROC égale à 0,745.
- Sahoo et al. (2016) ont reconstitué 109 cas de traumatismes crâniens en utilisant le modèle SUFEHM (Strasbourg University Finite Element Head Model) pour identifier la limite de tolérance des traumatismes crâniens en termes de déformation axonale. Pour un risque de 50 % d'IAD, le niveau de tolérance estimé était de 14,65 % de la déformation axonale maximale. Le niveau de tolérance aux commotions cérébrales identifié dans la présente étude est très proche du niveau de tolérance à l'IAD identifié par Sahoo et al. (2016).

C'est la première fois qu'un modèle de cerveau de rat anisotrope à éléments finis est développé. C'est grâce à ce modèle que nous avons pu obtenir des informations sur l'élongation axonale du cerveau du rat, ce qui n'était possible avec aucun des modèles de cerveau de rat à éléments finis existants. L'identification des déformations axonales maximales a permis d'identifier les régions du cerveau les

plus vulnérables aux commotions cérébrales. Les résultats expérimentaux ont clairement indiqué des changements post-commotionnels dans les réponses comportementales et les résultats de simulation semblaient être en lien, puisque les régions du cerveau identifiées comme étant vulnérables à la commotion cérébrale sont connues pour influencer le comportement d'une façon ou d'une autre. Néanmoins, il serait intéressant d'avoir accès à davantage de données expérimentales, afin d'identifier une forte corrélation et d'identifier le meilleur prédicteur de blessure et le niveau de tolérance. Cette étude est donc un premier pas vers des investigations liées aux commotions cérébrales par modélisation du cerveau des rats par éléments finis.

Un modèle de cerveau de rat anisotrope visqueux hyperélastique par éléments finis a été développé, validé et utilisé afin d'obtenir des informations sur le cerveau du rat en cas de commotion cérébrale. L'étude du seuil mécanique de la commotion cérébrale a démontré que pour un risque de commotion cérébrale de 50 %, le niveau de tolérance estimé de la déformation axonale maximale est de 11,82 %. Ce résultat est très proche du niveau de tolérance estimé par Sahoo et al. (2016) pour le cerveau humain, qui est de 14,65 % de la déformation axonale pour un risque de 50 % de DAI. Cette étude ouvre la porte à beaucoup plus de possibilités concernant les investigations liées aux commotions cérébrales.

A l'avenir, lorsque les propriétés expérimentales du matériau du cerveau du rat pour les différentes régions anatomiques du cerveau seront disponibles, il serait intéressant de savoir comment l'incorporation de ce type d'hétérogénéité influence les niveaux de tolérance. Dans ce cas, même le maillage du modèle peut être affiné pour avoir des frontières lisses distinctes entre les différentes régions anatomiques, ce qui rendra le modèle encore plus réaliste.

Les résultats expérimentaux, disponibles pour la présente étude, ne portent que sur les réponses comportementales. L'accessibilité aux données histologiques post-commotionnelles ou aux données d'imagerie médicale nous permettra d'obtenir de meilleures connaissances sur le cerveau du rat et nous aidera à prédire les commotions cérébrales avec plus de précision. De plus, un plus grand nombre de cas expérimentaux permettra d'effectuer des analyses statistiques plus robustes et, de plus, d'identifier plus efficacement le meilleur prédicteur de lésion et le niveau de tolérance aux commotions cérébrales.

Une autre possibilité intéressante est d'étudier les traumatismes cérébraux légers répétitifs (TTCmR) ou les commotions cérébrales multiples. Récemment, de nombreuses études ont commencé à se concentrer sur les traumatismes cérébraux légers répétitifs, car on suppose que les commotions

multiples pourraient être la principale raison des conséquences à long terme des commotions. À cet égard, un modèle anisotrope de cerveau de rat à éléments finis peut être utile pour de telles études.

References

Ahmadzadeh, H., Smith, D. H. and Shenoy, V. B. Viscoelasticity of Tau proteins leads to strain rat-dependent breaking of microtubules during axonal stretch injury: predictions from a mathematical model. Biophysical Journal, 2014, 106(4):1123-1133.

Antona-Makoshi, J., Davidsson, J., Ejima, S. and Ono, K. Development of a comprehensive injury criterion for moderate and mild traumatic brain injuries. International Journal of Automotive Engineering, 2016, 7(1):69-75.

Antona-Makoshi, J., Davidsson, J., Risling, M., Ejima, S. and Ono, K. Validation of local brain kinematics of a novel rat brain finite element model under rotational acceleration. International Journal of Automotive Engineering, 2014, 5(1):31-37.

Antona-Makoshi, J., Eliasson, E., Davidsson, J., Ejima, S. and Ono, K. Effect of ageing on brain injury prediction in rotational head trauma – a parameter study with a rat finite element model. Traffic Injury Prevention, 2015, 16:sup1, S91-S99.

Armstrong, R. C., Mierzwa, A. J., Marion, C. M. and Sullivan, G. M. White matter involvement after TBI: clues to axon and myelin repair capacity, Experimental Neurology, 2016a, 275(3):328-333.

Armstrong, R. C., Mierzwa, A. J., Sullivan, G. M. and Sanchez, M. A. Myelin and oligodendrocyte lineage cells in white matter pathology and plasticity after traumatic brain injury. Neuropharmacology, 2016b, 110(B):654-659.

Azevedo, F. A. C., Carvalho, L. R. B., Grinberg, L. T., Farfel, J. M., Ferretti, R. E. L., Leite, R. E. P., Filho, W. J., Lent, R. and Herculano-Houzel, S. Equal numbers of neuronal and nonneuronal cells make the human brain an isometrically scaled-up primate brain. The Journal of Comparative Neurology, 2009, 513(5):532-541.

Basser, P. J. and Pierpaoli, C. Microstructural and physiological features of tissues elucidated by quantitative-diffusion-tensor MRI. Journal of Magnetic Resonance, Series B, 1996, 111(3):209-219.

Basser, P. J., Mattiello, J. and LeBihan, D. MR diffusion tensor spectroscopy and imaging. Biophysical Journal, 1994, 66(1):259-267.

Baumgartner, D., Lamy, M., Willinger, R., Choquet, P., Goetz, C., Constantinesco, A. and Davidsson, J. Finite element analysis of traumatic brain injuries mechanisms in the rat. Proceedings of IRCOBI Conference, 2009, York, United Kingdom, 97-108.

Bayer, S. A., Altman, J., Russo, R. J. and Zhang, X. Timetables of Neurogenesis in the human brain based on experimentally determined patterns in the rat. NeuroToxicology, 1993, 14(1):83-144.

Bollen, A. and Bai, X. Effects of long-term calcium intake on body weight, body fat and bone in growing rats. Osteoporosis International, 2005, 16(12):1864-1870.

Briggs, D. I., Angoa-Perez, M. and Kuhn, D. M. Prolonged repetitive head trauma induces a singular chronic traumatic encephalopathy-like pathology in white matter despite transient behavioural abnormalities. The American Journal of Pathology, 2016, 186(11):2869-2886.

Broglio, S. P., Schnebel, B., Sosnoff, J. J., Shin, S., Feng, X., He, X. and Zimmerman, J. The biomechanical properties of concussions in high school football. Medicine and Science in Sports and Exercise, 2010, 42(11):2064-2071.

Budday, S., Ovaert, T. C., Holzapfel, G. A., Steinmann, P. and Kuhl, E. Fifty shades of brain: a review on the mechanical testing and modelling of brain tissue. Archives of Computational Methods in Engineering, 2019, https://doi.org/10.1007/s11831-019-09352-w.

Buki, A. and Povlishock, J. T. All roads lead to disconnection? – Traumatic axonal injury revisited. Acta Neurochirurgica, 2006, 148(2):181-194.

Cantu, R. C. Guidelines for return to contact sports after a cerebral concussion. The Physicians and Sportsmedicine, 1986, 14(10):75-83.

Cantu, R. C. Posttraumatic retrograde and anterograde amnesia: pathophysiology and implications in grading and safe return to play. Journal of Athletic Training, 2001, 36(3):244-248.

CDC, Centers for Disease Control and Prevention, Report to Congress on traumatic brain injury in the United States: epidemiology and rehabilitation. National Center for Injury Prevention and Control; Division of Unintentional Injury Prevention, 2014, Atlanta, GA.

Chang, K., Redmond, S. A and Chan, J. R. Remodeling myelination: implications for mechanisms of neural plasticity. Nature Neuroscience, 2016, 19(2):190-197.

Chatelin, S., Constantinesco, A. and Willinger, R. Fifty years of brain tissue mechanical testing: from in vitro to in vivo investigations. Biorheology, 2010, 47(5-6):255-276.

Chatelin, S., Deck, C. and Willinger, R. An anisotropic viscous hyperelastic constitutive law for brain material finite-element modeling. Journal of Biorheology, 2013, 27(1-2):26-37.

Chatelin, S., Deck, C., Renard, F., Kremer, S., Heinrich, C., Armspach, J. and Willinger, R. Computation of axonal elongation in head trauma finite element simulation. Journal of the Mechanical Behavior of Biomedical Materials, 2011, 4(8):1905-1919.

Christ, A. F., Franze, K., Gautier, H., Moshayedi, P., Fawcett, J., Franklin, R. J. M., Karadottir, R. T. and Guck, J. Mechanical difference between white and gray matter in the rat cerebellum measured by scanning force microscopy. Journal of Biomechanics, 2010, 43(15):2986-2992.

Colorado medical society - guidelines for the management of concussion in sports. Report of the Sports Medicine Committee, Denver, CO, 1990.

Conde C. and Caceres, A. Microtubule assembly, organization and dynamics in axons and dendrites. Nature review, Neuroscience, 2009, 10:319-332.

Coronado, V. G., Haileyesus, T., Cheng, T. A., Bell, J. M., Haarbauer-Krupa, J., Lionbarger, M. R., Flores-Harrera, J., McGuire, L. C. and Gilchrist, J. Trends in sports- and recreation- related traumatic brain injuries treated in US emergency departments: the national electronic injury surveillance system-all injury program (NEISS-AIP) 2001-2012. Journal of head trauma rehabilitation, 2015, 30(3):185-197.

Criscione, J. C., Douglas, A. S. and Hunter, W. C. Physically based strain invariant set for materials exhibiting transversely isotropic behavior. Journal of Mechanics and Physics of Solids, 2001, 49(4):871-897.

Davidsson, J. and Risling, M. A new model to produce sagittal plane rotational induced diffuse axonal injuries. Frontiers in Neurology, 2011, 2(41):58-68.

Davis, G. A., Purcell, L., Schneider, K. J., Yeates, K. O., Gioia, G. A., Anderson, V., Ellenbogen, R. G., Echemendia, R. J., Makdissi, M., Sills, A., Iverson, G. L., Dvorak, J., McCrory, P., Meeuwisse, W., Patricios, J, Giza, C. C. and Kutcher, J. S. The child sport concussion assessment tool 5th edition (Child SCAT5): background and rationale. British Journal of Sports Medicine, 2017a, 51(11):859-861.

Davis, G. A., Purcell, L., Schneider, K. J., Yeates, K. O., Gioia, G. A., Anderson, V., Ellenbogen, R. G., Echemendia, R. J., Makdissi, M., Sills, A., Iverson, G. L., Dvorak, J., McCrory, P., Meeuwisse, W., Patricios, J, Giza, C. C. and Kutcher, J. S. The child sport concussion assessment tool 5th edition (Child SCAT5): background and rationale. British Journal of Sports Medicine, 2017b, 51(11):862-869.

Deck, C. and Willinger, R. Head injury prediction tool for protective systems optimisation. Proceedings of 7th European LS-DYNA Conference, 2009.

Dewan, M. C., Rattani, A., Gupta, S., Baticulon, R. E., Hung, Y., Punchak, M., Agrawal, A., Adeleye, A. O., Shrime, M. G., Rubiano, A. M., Rosenfeld, J. V., and Park, K. B. Estimating the global incidence of traumatic brain injury. Journal of Neurosurgery, 2018, 130(4):1080-1097.

Duma, S. M. and Rowson, S. Chapter 7 – The biomechanics of concussion: 60 years of experimental research. In: Slobounov S., Sebastianelli W. (eds) Concussions in Athletics. Springer, New York, NY, 2014, 115-137.

Duma, S. M., Manoogian, S. J., Bussone, W. R., Brolinson, P. G., Goforth, M. W., Donnenwerth, J. J., Greenwald, R. L., Chu, J. J. and Crisco, J. J. Analysis of real-time head accelerations in collegiate football players. Clinical Journal of Sport Medicine, 2005, 15(1):3-8.

Echemendia, R. J., Meeuwisse, W., McCrory, P., Davis, G. A., Putukian, M., Leddy, J., Makdissi, M., Sullivan, S. J., Broglio, S. P., Raftery, M., Schneider, K., Kissick, J., McCrea, M., Dvorak, J., Sills, A. K., Aubry, M., Engebretsen, L., Lossemore, M., Fuller, G., Kutcher, J., Ellenbogen, R., Guskiewicz, K., Patricios, J and Herring, S. The sport concussion assessment tool 5th edition (SCAT5): background and rationale. British Journal of Sports Medicine, 2017a, 51(11):848-850.

Echemendia, R. J., Meeuwisse, W., McCrory, P., Davis, G. A., Putukian, M., Leddy, J., Makdissi, M., Sullivan, S. J., Broglio, S. P., Raftery, M., Schneider, K., Kissick, J., McCrea, M., Dvorak, J., Sills, A. K., Aubry, M., Engebretsen, L., Lossemore, M., Fuller, G., Kutcher, J., Ellenbogen, R., Guskiewicz, K., Patricios, J and Herring, S. The sport concussion assessment tool 5th edition (SCAT5). British Journal of Sports Medicine, 2017b, 51(11):851-858.

Elkin, B. S. and Morrison, B. Viscoelastic properties of the P17 and adult rat brain from indentation in the coronal plane. ASME, Journal of Biomechanical Engineering, 2013, 135(11):114507.

Elkin, B. S., Ilankovan, A. and Morrison III, B. Age-dependent regional mechanical properties of the rat hippocampus and cortex. ASME, Journal of Biomechanical Engineering, 2010, 132(1):011010.

Elkin, B. S., Ilankovan, A. I. and Morrison III, B. A detailed viscoelastic characterization of the P17 and adult rat brain. Journal of Neurotrauma, 2011, 28(11):2235-2244.

Fehily, B. and Fitzgerald, M. Repeated mild traumatic brain injury: potential mechanisms of damage. Cell Transplantation, 2017, 26(7):1131-1155.

Fernandes, F. A. O. and de Sousa, R. J. A. Head injury predictors in sports trauma – a state-of-the-art review. Journal of Engineering in Medicine, 2015, 229(8):592-608.

Fijalkowski, R. J., Stemper, B. D., Pintar, F. A., Yoganandan, N., Crowe, M. J. and Gennarelli, T. A. New rat model for diffuse brain injury using coronal plane angular acceleration. Journal of Neurotrauma, 2007a, 24(8):1387-1398.

Fijalkowski, R. J., Stemper, B. D., Pintar, F. A., Yoganandan and Gennarelli, T. A. Influence of angular acceleration duration on functional outcomes following mild diffuse brain injury. Proceedings of IRCOBI Conference, Maastricht, The Netherlands, 2007b, 161-171.

Fijalkowski, R. J., Yoganandan, N., Zhang, J. and Pintar, F. A. A finite element model of region-specific response for mild diffuse brain injury. Stapp Car Crash Journal, 2009, 53:193-213.

Finan, J. D. Biomechanical simulation of traumatic brain injury in the rat. Clinical Biomechanics, 2019, 64:114-121.

Finan, J. D., Elkin, B. S., Pearson, E. M., Kalbian, I. L. and Morrison III, B. Viscoelastic properties of the rat brain in the sagittal plane: effects of anatomical structure and age. Annals of Biomedical Engineering, 2012a, 40(1):70-78.

Finan, J. D., Pearson, E. M. and Morrison III, B. Viscoelastic properties of the rat brain in the horizontal plane. Proceedings of IRCOBI Conference, Dublin, Ireland, 2012b, 474-485.

Finan, J. D., Sundaresh, S. N., Elkin, B. S., McKhann II, G. M. and Morrison III, B. Regional mechanical properties of human brain tissue for computational models of traumatic brain injury. Acta Biomaterialia, 2017, 55:333-339.

Fliegauf, M. Benzing, T and Omran, H. When cilia go bad: cilia defects and ciliopathies. Nature Reviews Molecular Cell Biology, 2007, 8:880-893.

Flynn, K. C., Stiess, M. and Bradke, F. Chapter 2 - Role of the cytoskeleton and membrane trafficking in axon-dendrite morphogenesis. Cellular Migration and Formation of Neuronal Connections: Comprehensive Developmental Neuroscience, 2013, 2:19-50.

Fournier, A. J., Rajbhandari, L., Shrestha, S. and Venkatesan, A. In vitro and in situ visualization of cytoskeletal deformation under load: traumatic axonal injury, The FASEB Journal, 2014, 28(12):5277-5287.

Franceschini, G., Bigoni, D., Regitnig, P. and Holzapfel, G. A. Brain tissue deforms similarly to filled elastomers and follows consolidation theory. Journal of Mechanics and Physics of Solids, 2006, 54(12):2592-2620.

Fung, Y. C. Biomechanics: mechanical properties of living tissues. Second edition, Springer-Verlag New York, 1993.

Gabler, L. F., Crandall, J. R. and Panzer, M. B. Development of a metric for predicting brain strain responses using head kinematics. Annals of Biomedical Engineering, 2018, 46(7):972-985.

Gabler, L. F., Stone, J. R., Mourad, P. D., Crandall, J. R. and Salzar, R. S. Region specific viscoelastic properties of the adult rat brain under indentation following traumatic brain injury. Proceedings of IRCOBI Conference, Gothenburg, Sweden, 2013, 470-482.

Gadd, C. W. Use of a weighted-impulse criterion for estimating injury hazard. Proceedings of 10th Stapp Car Crash Conference, SAE Technical Paper 660793, 1966, 164-174.

Galford, J. E. and McElhaney, J. H. A viscoelastic study of scalp, brain and dura. Journal of Biomechanics, 1970, 3(2):211-221.

Gefen, A., Gefen, N., Zhu, Q., Raghupathi, R. and Margulies, S. S. Age-dependent changes in material properties of the brain and braincase of the rat. Journal of Neurotrauma, 2003, 20(11):1163-1177.

Gennarelli, T. A., Pintar, F. A. and Yoganandan, N. Biomechanical tolerances for diffuse brain injury and a hypothesis for genotypic variability in response to trauma. 47th Annual Proceedings, Association for the Advancement of Automotive Medicine, 2003, 47:624-628.

Genon, S., Reid, A., Langner, R., Amunts, K. and Eickhoff, S. B. How to characterize the function of a brain region. Trends in Cognitive Sciences, 2018, 22(4):350-364.

Giordano, C. and Kleiven, S. Evaluation of axonal strain as a predictor for mild traumatic brain injuries using finite element modeling. Stapp Car Crash Journal, 2014, 58:1-33.

Giza, C. C. and Hovda, D. A. The neurometabolic cascade of concussion. Journal of Athletic Training, 2001, 36(3):228-235.

Goldsmith, W. Biomechanics of head injury. In: Fung, Y. C., Perrone N. and Anliker, M. (eds) Biomechanics. Its foundation and objectives. Prentice-Hall, Englewood Cliffs, NJ, 1972, 585–634.

Gray's anatomy 41st edition, 2015.

Green, M. A., Bilston, L. E. and Sinkus, R. In vivo brain viscoelastic properties measured by magnetic resonance elastography. NMR in Biomedicine, 2008, 21(7):755-764.

Griffin, J. W., Price, D. L., Drachman, D. B. and Engel, W. K. Axonal transport to and from the motor nerve ending. Annals New York Academy of Sciences, 1976, 274(1):31-45.

Gross, A. G. Impact thresholds of brain concussion. The Journal of Aviation Medicine, 1958, 29(10):725-732.

Gurdjian, E. S., Webster, J. E. and Lissner, H. R. Observations on the mechanism of brain concussion, contusion and laceration. Surgery, Gynecology and Obstetrics, 1955, 101(6):680-690.

Gurdjian, E. S., Lissner, H. R. and Evans, F. G. Intracranial pressure and acceleration accompanying head impacts in human cadavers. Surgery, Gynecology, and Obstetrics, 1961, 113:185-190.

Gurdjian, E. S., Lissner H. R. and Patrick, L. M. Concussion-mechanism and pathology. 7th Stapp Car Crash Conference, 1963, 470-482.

Gurdjian, E. S., Roberts, V. L. and Thomas, L. M. Tolerance curves of acceleration and intracranial pressure and protective index in experimental head injury. The Journal of Trauma, 1966, 6(5):600-604.

Guskiewicz, K. M., McCrea, M., Marshall, S. W., Cantu, R. C., Randolph, C., Barr, W., Onate, J. A. and Kelly, J. P. Cumulative effects associated with recurrent concussion in collegiate football players: the NCCA concussion study. The Journal of the American Medical Association, 2003, 290(19):2549-2555.

Guskiewicz, K. M., Mihalik, J. P., Shankar, V., Marshall, S. W., Crowell, D. H., Oliaro, S. M., Ciocca, M. F. and Hooker, D. N. Measurement of head impacts in collegiate football players: relationship between head impact biomechanics and acute clinical outcome after concussion. Neurosurgery, 2007, 61(6):1244-1253.

Gysland, S. M., Mihalik, J. P., Register-Mihalik, J. K., Trulock, S. C., Shields, E. W. and Guskiewicz, K. M. The relationship between subconcussive impacts and concussion history on clinical measures of neurological function in collegiate football players. Annals of Biomedical Engineering, 2011, 40(1):14-22.

Heape, A., Cells of the nervous system, Neurobiology, 2010.

HEDDD - Human engineering design data digest, Department of defense human factors engineering technical advisory group, USA, 2000.

Herrmann, N. The creative brain. The Journal of Creative Behavior, 1991, 25(4):275-295.

Hodgson, V. R., Thomas, L. M., Gurdjian, E. S., Fernando, O. U., Greenberg, S. W. and Chason, J. L. Advances in understanding of experimental concussion mechanisms. Proceedings of 13th Stapp Car Crash Conference, SAE Technical Paper 690796, 1969, 18-37.

Holbourn, A. H. S. Mechanics of head injuries. The Lancet, 1943, 438-441.

Hootman, J. M., Dick, R. and Agel, J. Epidemiology of collegiate Injuries for 15 Sports: summary and recommendations for Injury prevention initiatives. Journal of athletic training, 2007, 42(2):311-319.

Hosmer, D. W. and Lemeshow, S. Goodnss of fit tests for the multiple logistic regression model. Communications in Statistics – Theory and Methods, 1980, 9(10):1043-1069.

Irvine, K. A. and Blakemore, W. F. Remyelination protects axons from demyelination-associated axon degeneration. Brain, 2008, 131(6):1464-1477.

Jafari, S. S., Maxwell, W. L., Neilson, M. and Graham, D. I. Axonal cytoskeletal changes after non-disruptive axonal injury, Journal of Neurocytology, 1997, 26(4):207-221.

Jafari, S. S., Nielson, M., Graham, D. I. and Maxwell, W. L. Axonal cytoskeleton changes after nondisruptive axonal injury. II. Intermediate sized axons, Journal of Neurotrauma, 1998, 15(11):955-966.

Jakel, S. and Dimou, L. Glial cells and their function in the adult brain: a journey through the history of their ablation. Frontiers in Neurology, 2017, 11(24):1-17.

Jin, J., Zhang, J., Song, X., Hu, H., Sun, X. and Gao, Z. Effect of cerebrospinal fluid modeled with different material properties on a human finite element head model. Journal of Mechanics in Medicine and Biology, 2015, 15(1):1550027(1-19).

Johnson, V. E., Stewart, W. and Smith, D. H. Axonal pathology in traumatic brain injury. Experimental Neurology, 2013, 246:35-43.

Jordan, B. D., Tsairis, P., Warren, R. F. (eds) Head injury in sports, Sports Neurology, Aspen Publications, 1989, 227.

Kelly, J. P. and Rosenberg, J. H. Diagnosis and management if concussion in sports. Neurology, 1997, 48(3):575-580.

King, A. I., Yang, K. H., Zhang, L., Hardy, W. and Viano, D. C. Is head injury caused by linear or angular acceleration? Proceedings of IRCOBI Conference, Lisbon, Portugal, 2003, 1-12.

Kleiven, S. Predictors for traumatic brain injuries evaluated through accident reconstructions. Stapp Car Crash Journal, 2007, 51:81-114.

Kruse, S. A., Rose, G. H., Glaser, K. J., Manduca, A., Felmlee, J. P., Jack Jr., C. R. and Ehman, R. L. Magnetic resonance elastography of the brain. NeuroImage, 2008, 39(1):231-237.

Lamy, M., Baumgartner, D., Yoganandan, N, Stemper, B. D. and Willinger, R. Experimentally validated three-dimensional finite element model of the rat for mild traumatic brain injury. Medical & Biological Engineering & Computing, 2013, 51(3):353-365.

LaPlaca, M. C., Lessing, M. C., Prado, G. R., Zhou, R., Tate, C. C., Geddes-Klein, D., Meaney, D. F. and Zhang, L. Mechanoporation is a potential indicator of tissue strain and subsequent degeneration following experimental traumatic brain injury. Clinical Biomechanics, 2019, 64:2-13.

Lee, S. J., King, M. A., Sun, J., Xie, H. K., Subhash, G. and Sarntinoranont, M. Measurement of viscoelastic properties in multiple anatomical regions of acute rat brain tissue slices. Journal of the Mechanical Behavior of Biomedical Materials, 2014, 29:213-224.

Levchakov, A., Linder-Ganz, E., Raghupathi, R., Margulies, S. S. and Gefen, A. Computational studies of strain exposures in neonate and mature rat brains during closed head impact. Journal of Neurotrauma, 2006, 23(10):1570-1580.

Li, H., Raun, J., Xie, Z., Wang, H. and Liu, W. Investigation of the critical geometric characteristics of living human skulls utilizing medical image analysis techniques. International Journal of Vehicle Safety, 2007, 2(4):345-367.

Ling, H., Hardy, J. and Zetterberg, H. Neurological consequences of traumatic brain injuries in sports. Molecular and Cellular Neuroscience, 2015, 66(B):114-122.

Lissner, H. R., Lebow, M. and Evans, F. G. Experimental studies on the relation between acceleration and intracranial pressure changes in man. Surgery, Gynecology and Obstetrics, 1960, 111:329–338.

Maday, S., Twelvetrees, A. E., Moughamian, A. J. and Holzbaur, E. L. F. Axonal transport: cargo-specific mechanisms of motility and regulation. Neuron, 2014, 84(2):292-309.

Maddocks, D. L., Dicker, G. D. and Saling, M. M. The assessment of orientation following concussion in athletes. Clinical Journal of Sport Medicine, 1995, 5(1):32-35.

Mao, H., Zhang, L., Yang, K. H. and King, A. I. Application of a finite element model of the brain to study traumatic brain injury mechanisms in rat. Stapp Car Crash Journal, 2006, 50:583-600.

Mao, H., Wagner, C., Guan, F., Yeni, Y. N. and Yang, K. H. Material properties of adult rat skull. Journal of Mechanics in Medicine and Biology, 2011, 11(5):1199-1212.

Maxwell, W. L., Povlishock, J. T. and Graham, D. L. A mechanistic analysis of nondisruptive axonal injury: a review. Journal of Neurotrauma, 1997, 14(7):419-440.

McAllister, T. W., Ford, J. C., Ji, S., Beckwith, J. G., Flashman, L. A., Paulsen, K. and Greenwald, R. M. Maximum principal strain and strain rate associated with concussion diagnosis correlates with changes in corpus callosum white matter indices. Annals of Biomedical Engineering, 2012, 40(1):127-140.

McCrory, P., Matser, E., Cantu, R. and Ferrigno, M. Sports neurology. The LANCET Neurology, 2004, 3(7):435-440.

McCrory, P., Meeuwisse, W., Dvorak, J., Aubry, M., Bailes, J., Broglio, S., Cantu, R. C., Cassidy, D., Echemendia, R. J., Castellani, R. J., Davis, G. A., Ellenbogen, R., Emery, C., Engebresten, L., Feddermann-Demont, N., Giza, C. C., Guskiewicz, K. M., Herring, S., Iversonm G. L., Johnston, K. M., Kissick, J., Kutcher, J., Leddy, J., J., Maddocks, D., Makdissi, M., Manley, G. T., McCrea, M., Meehan, W. P., Nagahiro, S., Patricios, J., Putukian, M., Schneider, K. J., Sills, A., Tator, C. H., Turner, M. and Vos, P. E. Consensus statement on concussion in sport-the 5th international conference on concussion in sport held in Berlin, October 2016. British Journal of Sports Medicine, 2017, 51(11):838-847.

McIntosh, A. S., Patton, D. A., Frechede, B., Pierre, P., Ferry, E. and Barthels, T. The biomechanics of concussion in unhelmeted football players in Australia: a case-control study. BMJ Open, 2014, 4(5): e005078.

Mierzwa, A. J., Marion, C. M., Sullivan, G. M., McDaniel, D. P. and Armstrong, R. C. Components of myelin damage and repair in the progression of white matter pathology after mild traumatic brain injury. Journal of Neuropathology and Experimental Neurology, 2015, 74(3):218-232.

Miller, K. and Chinzei, K. Mechanical properties of brain tissue in tension. Journal of Biomechanics, 2002, 35(4):483-490.

Moeendarbary, E., Weber, I. P., Sheridan, G. K., Koser, D. E., Soleman, S., Haenzi, B., Bradbury, E. J., Fawcette, J. and Franze, K. The soft mechanical signature of glial scars in the central nervous system. Nature communications, 2017, 8:14787.

Mori, S. and Zhang, J. Principals of diffusion tensor imaging and its applications to basic neuroscience research. Neuron, 2006, 51(5):527-539.

Mortera, P. and Herculano-Houzel, S. Age-related neuronal loss in the rat brain starts at the end of adolescence. Frontiers in Neuroanatomy, 2012, 6(45):1-9.

Murray, I. R., Murray, A. D. and Robson, J. Sports concussion: time for a culture change. Clinical Journal of Sports Medicine, 2015, 25(2):75-77.

Nelson, W. E., Jane, J. A. and Gieck, J. H. Minor head injury in sports: a new system of classification and management. The Physicians and Sportsmedicine, 1984, 12(3):103-107.

Newman, J. A. A generalized acceleration model for brain injury threshold (GAMBIT). Proceedings of IRCOBI Conference, Zurich, Switzerland, 1986, 121-131.

Newman, J., Barr, C., Beusenberg, M., Fournier, E., Shewchenko, N., Welbourne, E. and Withnall, C. A new biomechanical assessment of mild traumatic brain injury Part II – results and conclusions. Proceedings of IRCOBI Conference, Montpellier, France, 2000a, 223-233.

Newman, J. A., Shewchenko, N and Welbouren, E. A proposed new biomechanical head injury assessment function – the maximum power index. Proceedings of 44th Stapp Car Crash Conference, SAE Technical Paper 2000-01-SC16, 2000b, 362-394.

NHTSA (National Highway Traffic Safety Administration), Development of improved injury criteria for the assessment of advanced automotive restraint systems – II. 1999.

Nicolas, E., Calle, S., Nicolle, S., Mitton, D. and Remenieras, J. Biomechanical characterization of ex vivo human brain using ultrasound shear wave spectroscopy. Ultrasonics, 2018, 84:119-125.

Nicolle, S., Lounis, M. and Willinger, R. Shear properties of brain tissue over a frequency range relevant for automotive impact simulations: new experimental results. Stapp Car Crash Journal, 2004, 48():239-258.

Nowak, K., Mix, E., Gimsa, J., Strauss, U., Sriperumbudur, K. K., Benecke, R. and Gimsa, U. Optimizing a rodent model of Parkinson's disease for exploring the effects and mechanisms of deep brain stimulations. Parkinson's disease, 2011, 414682:1-19.

Ommaya, A. K., Yarnell, P., Horsch, A. E. and Harris, E. H. Scaling of experimental data on cerebral concussion in sub-human primates to concussion threshold for man. Proceedings of 11th Stapp Car Crash Conference, SAE Technical Paper 670906, 1967, 73-80.

Ommaya, A. K. and Hirsch, A. E. Tolerances for cerebral concussion from head impact and whiplash in primates. Journal of Biomechanics, 1971, 4(1):13-21.

Ommaya, A. K. and Gennarelli, T. A. Cerebral concussion and traumatic unconsciousness: correlation of experimental and clinical observations on blunt head injuries. Brain, 1974, 97(1):633-654.

Ommaya, A. K. Biomechanics of head injury: experimental aspects. In: Nahum AM, Melvin JW (eds) The Biomechanics of Trauma. Appleton-Century-Crofts, Norwalk, Connecticut, 1985, 245–269.

Ommaya, A. K., Goldsmith, W. and Thibault, L. Biomechanics and neuropathology of adult and paediatric head injury. British Journal of Neurosurgery, 2002, 16(3):220-242.

Ouyang, H., Nauman, E. and Shi, R. Contribution of cytoskeletal elements to the axonal mechanical properties, Journal of Biological Engineering, 2013, 7(21):1-8.

Papp, E. A., Leergaard, T. B., Calabrese, E., Johnson, G. A. and Bjaalie, J. G. Waxholm space atlas of the Sprague Dawley rat brain. NeuroImage, 2014, 97:374-386.

Patton, D. A., McIntosh, A. S. and Kleiven, S. The biomechanical determinants of concussion: finite element simulations to investigate brain tissue deformations during sporting impacts to the unprotected head. Journal of Applied Biomechanics, 2013, 29(6):721-730.

Patton, D. A., McIntosh, A. S. and Kleiven, S. The biomechanical determinants of concussion: finite element simulations to investigate tissue-level predictors of injury during sporting impacts to the unprotected head. Journal of Applied Biomechanics, 2015, 31(4):264-268.

Paxinos, G. and Watson, C. The rat brain in stereotaxic coordinates 7th edition, 2013.

Pellman, E. J., Viano, D. C., Tucker, A. M., Casson, I. R. and Waeckerle, J. F. Concussion in professional football: reconstruction of game impacts and injuries. Neurosurgery, 2003, 53(4):799-814.

Pena, A., Pickard, J. D., Stiller, D., Harris, N. G. and Schuhmann, M. U. Brain tissue biomechanics in cortical contusion injury: a finite element analysis. Acta Neurochirurgica Supplementum, 2005, 95:333-336.

Perge, J. A., Niven, J. E., Mugnaini, E., Balasubramanian, V. and Sterling, P. Why do axons differ in caliber? The Journal of Neuroscience, 2012, 32(2):626-638.

Pervin, F. and Chen, W. W. Dynamic mechanical response of bovine gray matter and white matter brain tissues under compression. Journal of Biomechanics, 2009, 42(6):731-735.

Pesaresi, M., Soon-Shiong, R., French, L., Kaplan, D. R., Miller, F. D. and Paus, T. Axon diameter and axonal transport: in vivo and in vitro effects of androgens. Neuroimage, 2015, 115:191-201.

Peschanel, F. D. The creative mind, the creative brain. Kyoto Conference on Japanese Studies 1994 II, 1996, .non01-02:50-58.

Pincemaille, Y., Trosseille, X., Tarriere, C., Breton, F. and Renault, B. Some new data related to human tolerance obtained from volunteer boxers. Proceedings of 33rd Stapp Car Crash Conference, SAE Technical Paper 892435, 1989, 177-190.

Prange, M. T., Meaney, D. F. and Margulies, S. S. Defining brain mechanical properties: effects of region, direction, and species. Stapp Car Crash Journal, 2000, 44:205-214.

Prevost, T. P., Balakrishnan, A., Suresh, S. and Socrate, S. Biomechanics of brain tissue. Acta Biomaterialia, 2011, 7(1):83-95.

Pudenz, R. H. and Shelden, C. H. The Lucite calvarium - a method for direct observation of the brain - cranial trauma and brain movement. Journal of Neurosurgery, 1946, 3(6):487-505.

Puso, M. A. and Weiss, J. A. Finite element implementation of anisotropic quasi-linear viscoelasticity using a discrete spectrum approximation. Journal of Biomechanical Engineering, 1998, 120(1):62-70.

Ren, L., Baumgartner, D., Davidsson, J., Yang, J. and Willinger, R. Effect of the inhomogeneous brain material characteristic on dynamic responses of head under trauma. Proceedings of IRCOBI Conference, 2014, Berlin, Germany, 93-105.

Rivlin, R. S. and Saunders, D. W. Large elastic deformations of isotropic materials VII. Experiments on the deformation of rubber. Philosophical Transactions of the Royal Society of London, Series B, Mathematical and Physical Sciences, 1951, 243(865):251-288.

Roberts, W. O. and Johnson, R. Who plays? Who sits? The Physician and Sportsmedicine, 1992, 20(6):66-72.

Rooker, S., Jorens, P. G., Reempts, J. V., Borgers, M. and Verlooy, J. Continuous measurement of intracranial pressure in awake rats after experimental closed head injury. Journal of Neuroscience methods, 2003, 131(1-2):75-81.

Rowson, S. and Duma, S. M. Development of the STAR evaluation system for football helmets: integrating player head impact exposure and risk of concussion. Annals of Biomedical Engineering, 2011, 39(8):2130-2140.

Rowson, S., Duma, S. M., Beckwith, J. G., Chu, J. J., Greenwald, R. M., Crisco, J. J., Brolinson, P. G., Duhaime, A., McAllister, T. W. and Maerlender, A. C. Rotational head kinematics in football impacts: an injury risk function for concussion. Annals of Biomedical Engineering, 2012, 40(1):1-13.

Rowson, S. and Duma, S. M. Brain injury prediction: assessing the combined probability of concussion using linear and rotational head acceleration. Annals of Biomedical Engineering, 2013, 41(5):873-882.

Rowson, S. and Rowson, B. Chapter 4 – Biomechanics of Head Trauma, Chronic Traumatic Encephalopathy, 2018, 51-62.

Rowson, S., Campolettano, E. T., Duma, S. M., Stemper, B. D., Shah, A., Harezlak, J., Riggen, L., Mihalik, J. P., Guskiewicz, K. M., Giza, C., Brooks, A., Cameron, K., McAllister, T., Broglio, S. P. and McCrea, M. Accounting for variance in concussion tolerance between individuals: comparing head accelerations between concussed and physically matched control subjects. Annals of Biomedical Engineering, 2019, 1-9.

Rubiano, A. M., Carney, N., Chesnut, R. and Puyana, J. C. Global neurotrauma research challenges and opportunities. Nature, 2015, 527(7578):S193-S197.

Rumple, A., McMurray, M., Johns, J., Lauder, J., Makam, P., Radcliffe, M. and Oguz, I. 3-Dimensional diffusion tensor imaging (DTI) atlas of the rat brain, PLOS ONE, 2013, 8(7):e67334.

Sahoo, D. Brain injury criteria based on computation of axonal elongation. PhD Thesis, University of Strasbourg, France, 2013.

Sahoo, D., Deck, C. and Willinger, R. Development and validation of an advanced anisotropic visco-hyperelastic human brain FE model. Journal of the Mechanical Behavior of Biomedical Materials, 2014, 33:24-42.

Sahoo, D., Deck, C. and Willinger, R. Brain injury tolerance limit based on computation of axonal strain. Accident Analysis and Prevention, 2016, 92:53-70.

Shafieian, M., Darvish, K. K. and Stone, J. R. Changes to the viscoelastic properties of brain tissue after traumatic axonal injury. Journal of Biomechanics, 2009, 42(13):2136-2142.

Shreiber, D. I., Bain, A. C. and Meaney, D. F. In vivo thresholds for mechanical injury to the blood-brain barrier. Proceedings of 41st Stapp Car Crash Conference, SAE Technical Paper 973335, 1997.

Shuck, L. Z. and Advani, S. H. Rheological response of human brain tissue in shear. ASME, Journal of Basic Engineering, 1972, 94(4):905-911.

Smith, D. H. and Meaney, D. F. Axonal damage in traumatic brain injury. The Neuroscientist, 2000, 6(6):483-495.

Snyder, J. M., Hagan, C. E., Bolon, B. and Keene, C. D. Chapter 20 - Nervous system. Comparative Anatomy and Histology (Second edition), Academic press, 2018, 403-444.

Spencer, A. J. M. Continuum theory of the mechanics of fibre-reinforced composites. Springer-Verlag New York, 1984.

Staal, J. A. and Vickers, J. C. Selective vulnerability of non-myelinated axons to stretch injury in an in vitro co-culture system. Journal of Neurotrauma, 2011, 28(5):841-847.

Steiner, L. A. and Andrews, P. J. D. Monitoring the injured brain: ICP and CBF. British Journal of Anaesthesia, 2006, 97(1):26-38.

Stemper, B. D., Shah, A. S., Chiariello, R., Olsen, C. M., Budde, M. D., Glavaski-Joksimovic, A., McCrea, M., Kurpad, S. N. and Pintar, F. A. Prediction of post-concussive behavioral changes in a rodent model based on head rotational acceleration characteristics. Annals of Biomedical Engineering, 2016, 44(11):3252-3265.

Stemper, B. D., Shah, A. S., Wild, A., Humm, J. R., Pintar, F. A., Broglio, S. P., McAllister, T. W. and McCrea, M. Role of repetitive head impact exposure in the onset of concussion: evidence of a possible second mechanism of concussion for contact sports. Proceedings of IRCOBI Conference, Athens, Greece, 2018, 334-335.

Stemper, B. D., Shah, A., Harezlak, J., Rowson, S., Duma, S. M., Mihalik, J. P., Riggen, L. D., Brooks, A., Cameron, K. L., Giza, C. C., Houston, M. N., Jackson, J., Posner, M. A., McGinty, G., DiFiori, J., Broglio, S. P., McAllister, T. W., McCrea, M. and the CARE Consortium Investigators. Repetitive head impact exposure in college football following an NCAA rule change to eliminate two-a-day preseason practices: a study from the NCAA-D0D CARE Consortium. Annals of Biomedical Engineering, 2019, 1-13.

Tadepalli, S. A., Bali, Z. K., Bruszt, N., Nagy, L. V., Amrein, K., Fazekas, B., Buki, A, Czeiter, E. and Hernadi, I. Long-term cognitive impairment without diffuse axonal injury following repetitive mild traumatic brain injury in rats. bioRxiv preprint, 2019.

Tagliaferri, F., Compagnone, C., Korsic, M., Servadei, F. and Kraus, J. A systematic review of brain injury epidemiology in Europe. Acta Neurochirurgica, 2006, 148:255-268.

Takhounts, E. G., Eppinger, R. H., Campbell, J. Q., Tannous, R. E., Power, E. D. and Shook, L. S. On the development of the SIMon finite element head model. Stapp Car Crash Journal, 2003a, 47:107-133.

Takhounts, E. G., Crandall, J. R. and Darvish, K. On the importance of nonlinearity of brain tissue under large deformations. Stapp Car Crash Journal, 2003b, 47:79-92.

Takhounts, E. G., Ridella, S. A., Hasija, V., Tannous, R. E., Campbell, J. Q., Malone, D., Danelson, K., Stitzel, J., Rowson, S. and Duma, S. M. Investigation of traumatic brain injuries using the next generation of simulated injury monitor (SIMon) finite element head model. Stapp Car Crash Journal, 2008, 52:1-31.

Takhounts, E. G., Hasija, V., Ridella, S. A., Rowson, S. and Duma, S. M. Kinematic rotational brain injury criterion (BRIC). International Technical Conference on the Enhanced Safety of Vehicles, Washington DC, 2011, 11-0263.

Takhounts, E. G., Craig, M. J., Moorhouse, K. and McFadden, J. Development of brain injury criteria (BrIC). Stapp Car Crash Journal, 2013, 57:243-266.

Tang-Schomer, M. D., Patel, A. R., Baas, P. W. and Smith, D. H. Mechanical breaking of microtubules in axons during dynamic stretch injury underlies delayed elasticity, microtubule disassembly, and axon degeneration, The FASEB Journal, 2010, 14(5):1401-1410.

Tang-Schomer, M. D., Johnson, V. E., Baas, P. W., Stewart, W. and Smith, D. H. Partial interruption of axonal transport due to microtubule breakage accounts for the formation of periodic varicosities after traumatic axonal injury, Experimental Neurology, 2012, 233(1):364-372.

Taylor, C. A., Bell, J. M., Breiding, M. J. and Xu L. Traumatic Brain Injury–Related Emergency Department Visits, Hospitalizations, and Deaths — United States, 2007 and 2013. Centers for disease control and prevention (CDC), Morbidity and mortality weekly report (MMWR), Surveillance summaries, 2017, 66(9):1-16.

Teasdale, G. and Jennett, B. Assessment of coma and impaired consciousness: a practical scale. The Lancet, 1974, 304(7872):81-84.

Torg, J. S. Athletic Injuries to the Head, Neck and Face. St Louis, MO: Mosby-Year Book; 1991:226.

Uldall, M., Juhler, M., Skjolding, A. D., Kruuse, C., Jansen-Olesen, I. and Jensen, R. A novel method for long-term monitoring of intracranial pressure in rats. Journal of Neuroscience Methods, 2014, 227:1-9.

Unnikrishnan, G., Mao, H., Sundaramurthy, A., Bell, E. D., Yeoh, S., Monson, K. and Reifman, J. A 3-D rat brain model for blast-wave exposure: effects of brain vasculature and material properties. Annals of Biomedical Engineering, 2019, 47(9):2033-2044.

Vappou, J., Breton, E., Choquet, P., Willinger, R. and Constantinesco, A. Assessment of in vivo and post-mortem mechanical behavior of brain tissue using magnetic resonance elastography. Journal of Biomechanics, 2008a, 41(14):2954-2959.

Vappou, J., Breton, E., Choquet, P., Constantinesco, A. and Willinger, R. Brain viscoelasticity measured by magnetic resonance elastography. Proceedings of IRCOBI Conference, Bern, Switzerland, 2008b, 441-444.

Versace, J. A review of the severity index. Proceedings of 15th Stapp Car Crash Conference, SAE Technical Paper 710881, 1971, 771-796.

Weiss, J. A., Maker, B. N. and Govindjee, S. Finite element implementation of incompressible, transversely isotropic hyperelasticity. Computer methods in applied mechanics and engineering, 1996, 135(1-2):107-128.

WHO, World Health Organization, Neurological disorders: public health challenges, 2006.

Willinger, R., Taleb, L. and Kopp, C. Modal and temporal analysis of head mathematical models. Journal of Neurotrauma, 1995, 12(4):743-754.

Yuan, A., Rao, M. V., Veeranna and Nixon, R. A. Neurofilaments at a glance. Journal of Cell Science, 2012, 125(14):3257-3263.

Zhang, L., Yang, K. H. and King, A. I. A proposed injury threshold for mild traumatic brain injury. Journal of Biomechanical Engineering, 2004, 126(2):226-236.